Advances in Laboratory Geophysics Using Bender Elements

by

João Filipe Meneses Espinheira Rio

supervised by

Dr. Paul Greening

University College London

Department of Civil & Environmental Engineering

A thesis submitted to the University of London

for the degree of Doctor of Philosophy.

April, 2006

Fall down seven times, get up eight. *Japanese Proverb*

Abstract

Bender element transducers are used to determine the small-strain shear stiffness, G_0, of soil, by determining the velocity of propagation of mechanical waves through tested samples. They are normally used in the laboratory, on their own or incorporated in geotechnical equipment such as triaxial cells or oedometers.

Different excitation signals and interpretation methods are presently applied, each producing different results. The initial assumptions of unbounded wave propagation, generally used in bender element testing and inherited from seismic cross-hole testing, are quite crude and do not account for specific boundary conditions, which might explain the lack of reliability of the results.

The main objective of this study is to establish the influence of the sample and transducer geometry in the behaviour of a typical bender element test system. Laboratory and numerical tests, supported by a theoretical analytical study, are conducted and the results presented in order to achieve this goal.

An independent monitoring of the dynamic behaviour of the bender elements and samples is also carried out. Using a laser velocimeter, capable of recording the motion of the subjects without interference, their dynamic responses can be obtained and their mechanical properties verified.

A parametric study dealing with sample geometry is presented, where 24 samples with different geometries are tested. Synthetic rubber is used as a substitute for soft clay, due to the great number of samples involved and the necessity of guarantee the

constancy of their properties.

The numerical analysis makes use of three-dimensional finite difference models with different geometries. A regressive analysis is possible since the elastic properties of the system are pre-determined and used to evaluate the results. A numerical analysis also has the benefit of providing the response not only at a single receiving point but at any node in the model.

Acknowledgements

My supervisor Dr. Paul Greening.

My parents and sister Maria Conceição Abreu, José Americo Rio and Ana Margarida Rio.

My sweetheart Ana Monterroso.

and Marcos Arroyo, Amar Bahra, Carlos Carneiro, Matthew Coop, EPSRC, Christopher Dano, Cristiana Ferreira, Antonio Viana da Fonseca, Yasmine Gaspar, Laurent Giampellegrini, Ana Paula Maciel, Patricia Maciel, Luis Medina, David Nash, Tristan Robinson, Malcom Saytch, Richard Sharp, CAMBRIDGE INSITU, Kenny Sørensen.

Declaration

The work presented in this dissertation was done exclusively by the author, under the supervision of Dr. Paul Greening, at the Department of Civil and Environmental Engineering, University College of London, University of London.

The results, ideas and convictions presented are those of the author, except when stated otherwise, and only he is accountable for them.

This dissertation, or any part of it, has not been submitted to any other university or institution.

João Filipe Rio

Signature: João Filipe Rio Date: 2006/10/19

Contents

List of Figures

List of Tables

List of Symbols

A	area
D	diameter
D_f	dynamic magnification ratio, $= \frac{a}{a_0/k}$
D_i	amplitude of incident compression wave
D_r	amplitude of reflected compression wave
E	Young's modulus
EI	flexural stiffness
F	force
F_P	far-field compression wave component
F_S	far-field shear wave component
G	shear stiffness
G_0	small-strain shear stiffness
H	height
I	cross-section moment of inertia
I_{Pi}	mass polar moment of inertia
$J_n(x)$	Bessel function
K	bulk modulus
L	length
M	concentrated mass
N	number of monomers in polymer chain
N_P	near-field compression wave component
N_S	near-field shear wave component
P	seismology term for compression wave

R_d	near-field effect indicative ratio
S	seismology term for shear wave
SH	horizontally polarised shear wave
SV	vertically polarised shear wave
T	period, $= 1/f$
T	temperature
T	thickness
T_i	amplitude of incident shear wave
T_r	amplitude of reflected shear wave
V_d	characteristic compression wave velocity
V_d^{ff}	far-field compression wave velocity, $= V_d$
V_d^{nf}	near-field compression wave velocity
V_s	characteristic shear wave velocity
V_s^{ff}	far-field shear wave velocity, $= V_s$
V_s^{nf}	near-field shear wave velocity
W	width
$Z(t)$	amplitude function
Δ	dilatation
Γ	Kelvin-Christoffel or acoustic tensor
Λ	wavelength, $= c_i/f$
β	frequency ratio, $= \overline{\omega}/\omega_n$
$\ddot{u}(t)$	response acceleration function
$\dot{u}(t)$	response velocity function
$\eta(x)$	shape function
γ_{ij}	strain
λ	Lamé's longitudinal elastic constant
μ	Lamé's transversal elastic constant also known as shear stiffness, $= G$
∇^2	Laplace operator
ν	Poisson's ratio

ω	circular frequency, $= 2\pi f$
ω_D	damped free-vibration circular frequency
ω_n	natural circular frequency
$\overline{\omega}$	harmonic load circular frequency
ϕ	scaler potential function
ψ	vector potential function
ρ	density
τ_{ij}	stress
θ	angular coordinate
ε	strain
ε_d	compression strain
ε_s	shear strain
ξ	damping ratio
ζ	hysteretic dampig ratio
a	response amplitude
a_0	load amplitude
a_{di}	angle of incident compression wave
a_{dr}	angle of reflected compression wave
a_{ti}	angle of incident shear wave
a_{tr}	angle of reflected shear wave
b	bond length
c	damping coefficient
c^*	generalised damping coefficient
c_R	velocity of Rayleight surface waves
c_c	critical damping coefficient, $= 2m\omega_n$
c_d	velocity of compression waves in unbounded media, $= \sqrt{(\lambda + 2\mu)/\rho}$
c_g	group velocity
c_i	wave velocity
c_p	phase velocity

c_t	velocity of shear waves in unbounded media, $= \sqrt{\mu/\rho}$
c_{ij}	elastic constant
d_{31}	piezoelectric strain constant
f_D	damped natural frequency, $= \omega_D/(2\pi)$
f_{wd}	frequency limit for waveguide dispersion
f_n	natural frequency, $= \omega_n/(2\pi)$
f_{nf}	near-field frequency limit, proposed by Arroyo *et al.* (2003*a*)
g_{31}	piezoelectric voltage constant
k^*	generalised stiffness
k_0	propagation constant in a particular direction
k_B	Boltzmann constant, $= 1.38 \times 10^{-23}\mathrm{JK}^{-1}$
k_d	longitudinal propagation constant
k_t	transversal propagation constant
l_b	embedment length
m	integer
m	mass
m^*	generalised mass
n	integer
n_P	near-field compression wavelength
n_S	near-field shear wavelength
$p(t)$	load function
$p^*(t)$	generalised load function
$p_T(t)$	harmonic torque load
r	radius
t	time
td	travel distance
u	component of displacement
$u(t)$	displacement function
u_θ	component of displacement

$u_p(t)$	transient dynamic response
u_r	component of displacement
$u_t(t)$	steady-state dynamic response
u_z	component of displacement
v	component of displacement
w	component of displacement
x	rectangular coordinate
y	rectangular coordinate
z	rectangular coordinate
LDV	laser Doppler velocimeter
LVDT	linear variable differential transformer
MDOF	multiple degrees of freedom
RTV	room temperature vulcanization
SASW	spectral analysis of surface waves
SDOF	single degree of freedom
UCL	University College London

Chapter 1

Introduction

1.1 Prologue

In normal working conditions, most part of the soil mass around a structure is subjected to small strains, less then 0.1%, with higher strains being achieved only locally, (Burland, 1989). Besides, the relationship between strain and stiffness of soils is generally non-linear, (Atkinson, 2000). Only at very small strains does the correlation between strain and stiffness behaves in a linear fashion. It is at these smaller strains that the shear stiffness reaches its maximum value, usually refered to as G_0 or G_{max}. For this reason it is also known as small-strain shear stiffness. A characteristic soil strain-stiffness curve is presented in figure 1.1.

When preparing a static or dynamic physical model of a geotechical structure it is relevant to take into account the non-linear behaviour of the soil. It is therefore necessary to obtain, among other properties of the medium, its small-strain shear stiffness, (Arulnathan *et al.*, 2000; Brignoli *et al.*, 1996). Dyvik and Madshus (1985) mentioned the relevance of using G_0 in the prediction of soil and soil-structures behaviour during earthquakes, explosions, traffic vibration, machine vibration, wind loading and wave loading. In analysis where large strains are considered, the knowl-

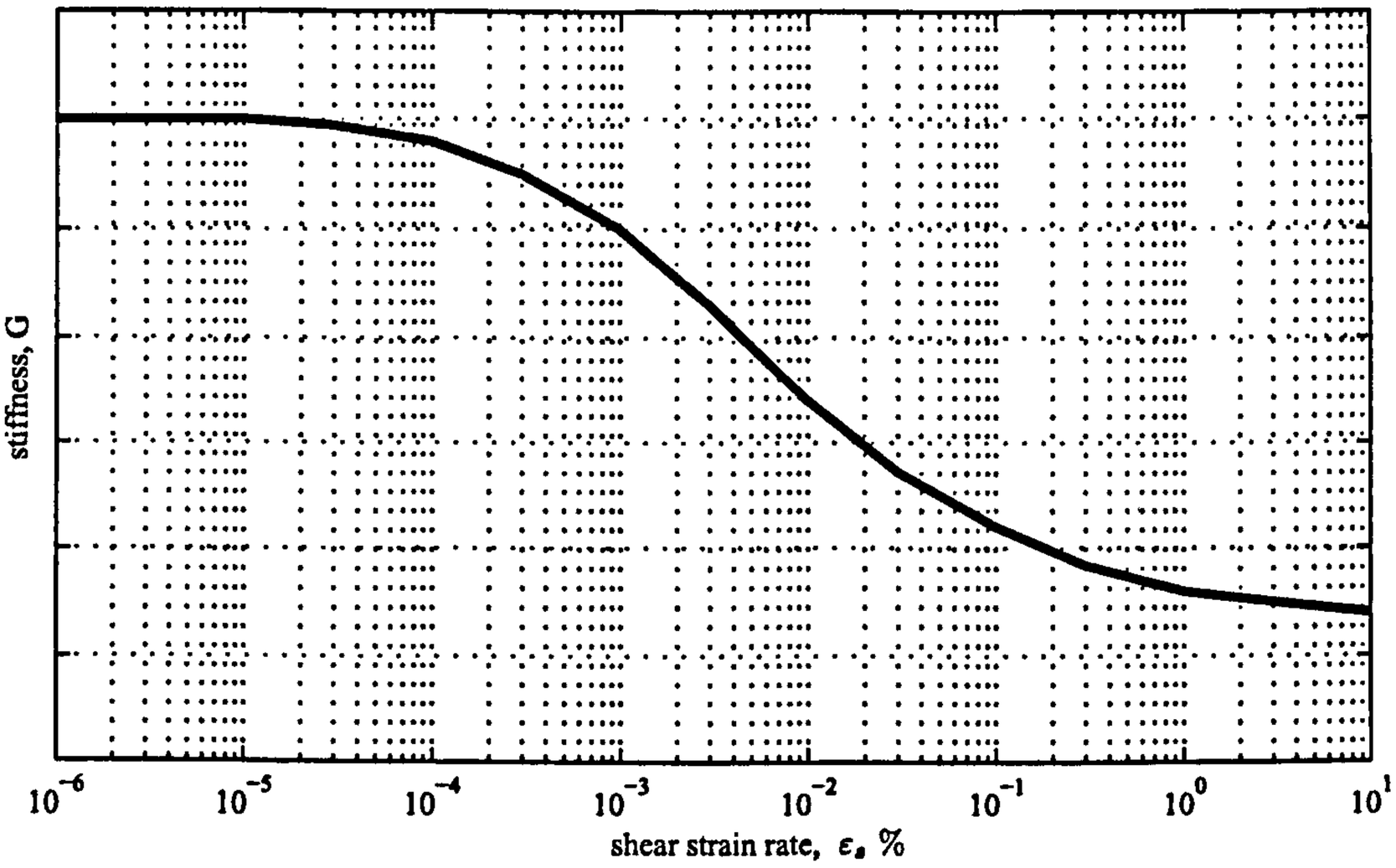

Figure 1.1: Characteristic strain-stiffness curve of soil's non-linear behaviour, collected from Atkinson (2000).

edge of G_0 is still relevant since it is one of the defining parameters when considering the soil's non-linear behaviour.

Stating the obvious, in order to obtain the small-strain stiffness, soils must be tested at small strains. Despite increasing precision from static test equipment such as local gauges, namely the use of LVDT[1], (Brocanelli and Rinaldi, 1998; Cuccovillo and Coop, 1997; Da-Re *et al.*, 2001), dynamic methods remain the natural option to test at small and very small strain ranges, (Atkinson, 2000).

Bender elements are piezoelectric ceramic instruments used in laboratory geotechnical dynamic testing. They work as cantilevers which flex or bend when excited by the voltage differential of an electric signal and vice-versa, i.e., they generate a voltage differential when forced to bend. These transducers are generally used in pairs where one bender element operates as a transmitter and the other as a receiver. The transmitting bender element tip is generally embedded at one end of a soil sample and the receiving bender element tip is, aligned with the transmitter, embedded at

[1]LVDT - Linear Variable Differential Transformer

the other end. The transmitting bender element transforms the input electric signal into a mechanical motion which disturbs the medium in which it is embedded. This disturbance propagates through the medium in the form of mechanical waves. Some components of these waves reach the other end of the sample where the receiving bender element is at. Wave components with motion transversal to the receiving transducer's tip are capable of forcing it to bend, and consequently of generating an output electric signal. An example of a pair of bender elements mounted on a triaxial-cell apparatus is presented in figure 1.2

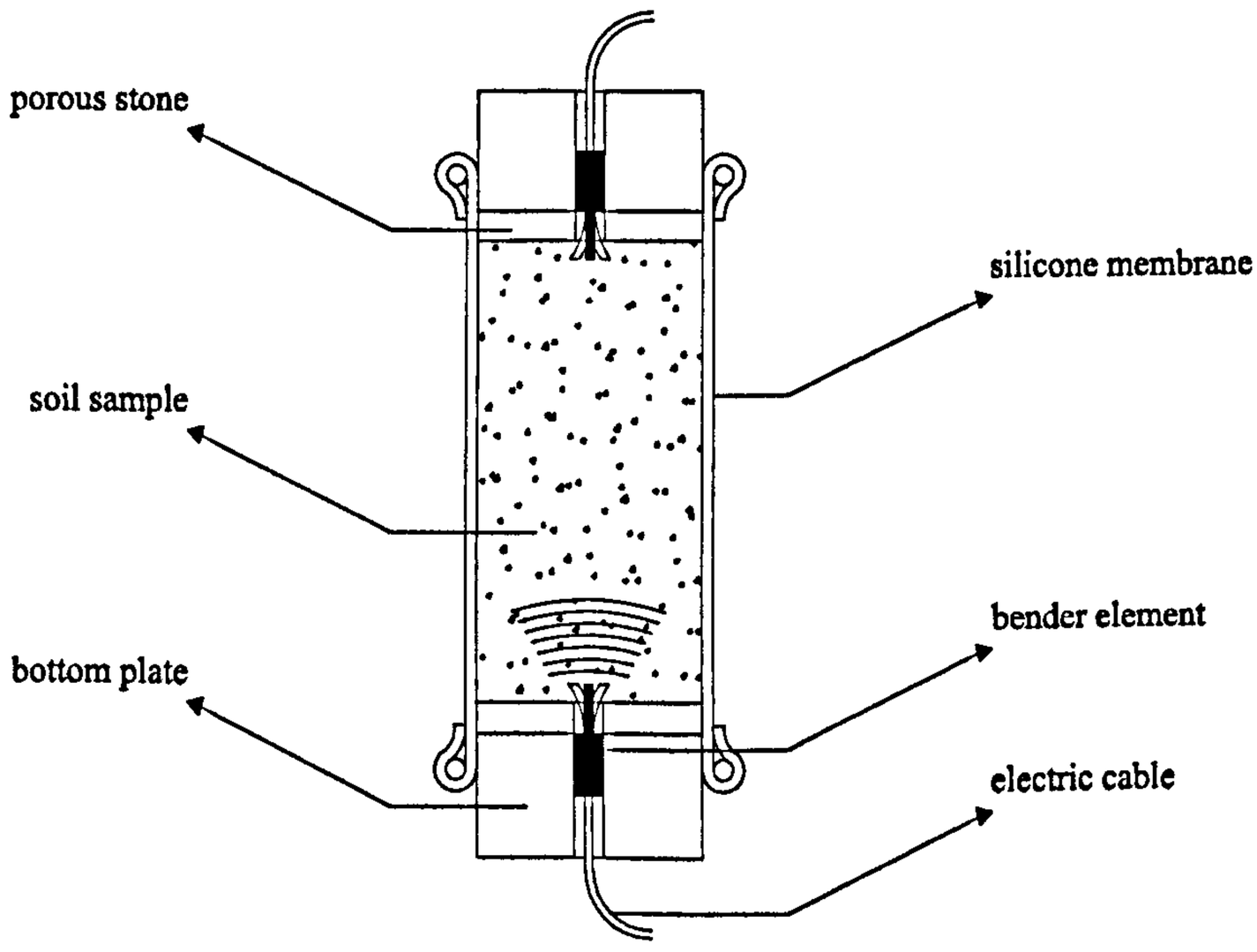

Figure 1.2: Pair of bender elements mounted in a triaxial-cell apparatus.

By comparing the input and output signals, it is presumably possible to obtain the shear wave velocity, which is a characteristic of the medium. The characteristic shear wave velocity can then be used to obtain the shear stiffness of the medium, (Redwood, 1960), as given by:

$$G_0 = \rho \cdot V_s^2 \tag{1.1}$$

where G_0 is the small-strain shear stiffness, ρ is the medium's density and V_s the characteristic shear wave velocity.

Other dynamic methods such as the cross-hole method used *in situ*, and different piezoceramic transducers such as shear-plate transducers and compression-plate transducers used in laboratory can also be used to determine wave travel times, (Bodare and Massarsch, 1984; Brignoli *et al.*, 1996). Resonant columns are another laboratory dynamic device used to determine the shear-stiffness and the damping coefficient of the soil, (ASTM, 1978). Unlike the previous example, resonant columns use the torsional or flexural resonance frequency, rather than a wave velocity, to estimate the medium's properties, (Stokoe *et al.*, 1994).

Arulnathan *et al.* (2000) used a mini-hammer in a centrifuge model together with a number of accelerometers to determine the propagation velocity of shear waves in sand. The obtained results were in good agreement with equivalent bender element results obtained for the same medium. AnhDan *et al.* (2002) have also used accelerometers together with LVDT apparatus to obtain the small-strain stiffness of coarse soils.

In Audisio *et al.* (1999) and Hope *et al.* (1999), another example can be found of *in situ* dynamic testing, known as spectral analysis of surface waves, SASW. Using surface waves, more particularly Rayleigh waves, to test soil as done with the cross-hole method but with no need for bore-holes, makes the SASW testing method less expensive than the cross-hole method, (Nazarian and Stokoe, 1984).

The advantages of using bender elements are that they are relatively cheap and simple to manufacture. They can be used on their own or can easily be integrated into existing and common geotechnical equipment such as triaxial cells, oedometers or direct shear apparatus, (Arroyo *et al.*, 2003*a*; Thomann and Hryciw, 1990). In this way it is possible to dynamically test soil samples under controlled load conditions, (Viggiani and Atkinson, 1997). They can be used together with other dynamic test apparatus such as the resonant column, as done by Connolly and Kuwano (1999).

Bender elements versatility allows them to be wired so as to operate both as a

bender and an extender, enabling the detection of compression waves as well as of shear waves, as done by Lings and Greening (2001) and later followed by Dano *et al.* (2003). When testing saturated soils, compression wave are able to propagate at a faster velocity through the relatively incompressible fluid, which might interfere with the detection of the media characteristic compression wave velocity, (Lings and Greening, 2001).

Due to their versatility, bender elements are also used to study the anisotropy of soils. If for the resonant column test one sample per direction needs to be obtained to study the anisotropy of a particular material, (M. and Ko, 1994), when using bender elements a pair of these transducers is needed for each chosen direction, while testing a single sample. Placing different pairs of bender elements with different orientations, mounted on the sides of the sample for example, enables the transmission of waves with different polarisations and/or different travel paths, to obtain the different values of the soil's shear stiffness. Nash *et al.* (1999) and Jovičić and Coop (1998) in the study of clay, and Belloti *et al.* (1996), Zeng and Ni (1998) and Kuwano *et al.* (2000) in the study of sand, for example, have used more than one pair of bender elements in triaxial cell devices in order to study the anisotropy at small-strains of those media. The influence of particle orientation, for example, can be studied in such way, (Lo Presti *et al.*, 1999). Figure 1.3 depicts two pairs of bender elements placed orthogonal to each other and the resulting wave polarisation.

Clayton *et al.* (2004) also used side-mounted bender elements in a triaxial cell but for different purposes. In this way he was capable of having more than one receiver for a single transmitter, enabling the determination of a more complete picture of the wave propagation properties.

The use of bender elements also carries some disadvantages. Their intrusive nature, when embedded in the soil, means that they disturb the sample near the

Figure 1.3: Study of soil anisotropy with vertical and horizontal bender element placement and consequent wave polarisation.

region where they are placed. Besides, having been originally design to transmit and receive shear wave components, if used in slender samples, and due to the anti-symmetric nature associated with the transmitting bender element flexion, they are expected to excite flexural modes of wave propagation rather than the simpler pure shear waves, (Arroyo and Muir-Wood, 2003). Flexural modes of wave propagation are dispersive in nature, (Redwood, 1960), which may difficult the detection of the actual shear wave velocity, and consequently the estimation of the medium's shear stiffness.

About the intrusive nature of bender elements, Fioravante (2000) and Fioravante and Capoferri (2001) attempted to use the inertia properties of the transducers by attaching them to the outside of the sample and permitting their free vibration, in air or in fluid but not embedded in the soil, both at transmitting or receiving transversal waves. This variation in the use of bender elements is well suited for the study of anisotropy, since in this type of test multiple pairs of bender elements are usually placed at the sides of the sample. This positioning is difficult to achieve

when the transducers' tips are embedded in the soil, since they must go through the protective latex membrane, which might jeopardise its impermeability.

Presently, some disagreement remains over the constitutive model of behaviour of a general bender element test system. Also, issues such as the optimum type of signal to excite the transmitting bender element or the best method of signal interpretation are also still not agreed upon. A more traditional behaviour model of bender element systems assumes the mechanical waves to propagate as if in a unbounded medium, similar to a cross-hole test. In this case, there is no dispersion caused by wave reflection and hence no added complexity from this factor. Another constitutive model, considering the geometry of the tested sample and its dynamic modal behaviour, the same as assumed in resonant column tests, is also possible.

The issue of sample geometry is central in this dissertation. Knowing that bars with different geometries have different modal responses, (Clough and Penzien, 1993), by establishing a relationship between sample geometry and general dynamic behaviour of the test system, with consequent interference in the obtained results, it is possible to establish this modal behaviour as the most suitable constitutive model of bender element testing in general. Besides, if this is accomplished, it is also possible to address the issues of optimum input signal and optimum result interpretation in the context of optimum dynamic response.

1.2 Historical Overview

References to the study of dynamic phenomena such as waves and body vibrations can be traced as far back as Pythagoras in 500 B.C., when he noticed the relationship between the length of vibrating strings and the harmony of the sound they produced. The history of dynamics cannot be separated from the history of physics itself, as well as that of its most influential protagonists. Galileo's study of the periodicity

of celestial body orbits, Newton's laws of motion, Euler's 'Theory of the Motions of Rigid Bodies' and Rayleigh's 'Theory of Sound' are but a few distinguished examples.

Seismic events are a relevant type of dynamic phenomena. They receive significant attention from the engineering community due to their potential of causing great impacts in human activity. Seismology is a well established field of study, being an important driving force for the development of general dynamic theory. Love's 'Some Problems in Geodynamics' is a noteworthy example. The field of theoretical seismology is in constant progress, (Aki and Richard, 2002), from which the dynamic testing of soils is but a part.

Burland (1989) and Atkinson (2000), have addressed the notion of non-linear soil stiffness, focussing on the importance of its small-strain behaviour. In this way, greater awareness was obtained for the testing of soils at small-strains, which could mainly be achieved with dynamic testing.

The dynamic testing of soils *in situ* is traditionally made using the cross-hole method, (Bodare and Massarsch, 1984). A number of sensors are placed in separate boreholes and the records of received shear waves compared. The objective is to determine the velocity of the shear wave, which in turn is used to obtain the medium's shear stiffness. In cross-hole testing the medium is generally assumed to be non-dispersive because of the considerable distance between wave source and receivers, and also because of the considerable distance between wave direct travel path and medium boundaries, (Hoar and Stokoe, 1979), making the estimation of the wave velocity a simpler task.

Laboratory dynamic testing, before the use bender elements, included the use of piezoceramic crystal transducers and resonant columns. In the case of piezocrystals, they too are used to directly measure the velocities of either compression or shear waves, (Brignoli *et al.*, 1996). Resonant columns tests are used according to a different principle. The soil samples are excited, usually in torsion, and the resonance

frequency of the first vibration mode is obtained and used to estimate the medium's shear stiffness, (Richart *et al.*, 1970). In resonant column testing, the wave dispersion on the soil sample is acknowledged. That is why the first mode of torsional frequency is frequently used, since it is a well known non-dispersive mode of vibration, (Stokoe *et al.*, 1994).

Shirley and Hampton (1978) combined the properties of piezorecamic transducers with the principles of cross-hole testing by using a pair of piezoelectric ceramic plates to transmit and receive mechanical waves. The use of shear wave transducers was not unheard of, (Lawrence, 1963), the merit of Shirley (1978) was the development of an innovative design for the transducers. Using relatively long thin plates permitted the production and detection of transversal motion through their bending deformation rather than through a shear deformation as done by shear wave transducers. Hence the name bender elements. This slender design significantly reduces the resonance frequency of the transducers approaching it to the frequencies at which waves propagate in soft soil media without being excessively attenuated. This bending design also permitted a better coupling between the medium and the transducers.

Schultheiss (1981) further developed the design of bender elements, optimising their dimensions so that they could be fitted into oedometers, triaxial cells and simple shear geotechnical apparatuses. Dyvik and Madshus (1985) presented with some detail, a study on bender element performance related with their wiring, concluding that parallel wiring suited the transmitting transducer and series wiring suited the receiver transducer. Dyvik and Madshus (1985) also presented a comparative study between bender element transducers and better established resonant columns, in order to validate their results. The work of Dyvik and Madshus (1985) has become a benchmark in the use of bender elements, and is amongst the most cited works related to this type of testing.

Dyvik and Madshus (1985) and Viggiani and Atkinson (1995) provided generally accepted guidelines in the study of bender element testing. They gave some insight about the issue of wave travel distance as well as having used a frequency domain analysis, in the form of a cross-spectrum between the input and output signal, which they then compared with time domain results.

Jovičić *et al.* (1996) and Brignoli *et al.* (1996) presented relevant work, focusing on the phenomena related to bender element testing. Both have explored how best to interpret time domain results and both give relevant consideration to near-field effect as a cause of wave velocity dispersion. Jovičić *et al.* (1996) also looked at the shape of the input signal and justified the use of an optimised sinusoidal pulse signal. Brignoli *et al.* (1996) verified the results of bender element tests with those of shear-wave transducers as well as also reflecting on the issue of travel distance.

Blewett *et al.* (2000) proposed the use of frequency domain technique, just as Viggiani and Atkinson (1995) had. This time using continuous signals with the objective of obtaining the response curves of the system. An interesting comparison between bounded and unbounded sample behaviour was also presented.

Presently, bender elements use has increased despite test standards and generally accepted guidelines not being established yet, (Viggiani and Atkinson, 1997), and the non-agreement about the actual behaviour of the dynamic system. Consequently there is no established method of interpreting the results. There is an ongoing debate about the benefits of using time or frequency domain analysis, pulse or continuous signals, about the relevance of different causes of dispersion, or even about the feasibility of actually obtaining the shear wave velocity using bender elements.

1.3 Strain Level

In normal working conditions most foundation structures cause strains lower than 0.1% to large volumes of the affected ground soil, only locally are higher strains achieved, (Burland, 1989). Besides, soil has a non-linear elastic behaviour where at small strains the stiffness is significantly higher than for larger strains, (Atkinson, 2000). Figure 1.1 ilustrates a characteristic strain level curve.

In situ soil testing, measuring strains above $10^{-1}\%$, does not offer the capability of determining soil stiffness at lower strain levels. In terms of laboratory testing, static methods such as local gauges have a limited precision that does not allow them to measure strains lower than $10^{-3}\%$ for which a maximum stiffness can generally be obtained. Dynamic laboratory testing is then left as the single option to obtain measurements for the lowest strains, $\epsilon < 10^{-2}\%$, of which bender elements are a suitable example, (Jovičić and Coop, 1997).

In terms of the shear strain levels involved in the use of bender elements, Dyvik and Madshus (1985) estimated the transmitting transducer to be in the range of $\epsilon \approx 10^{-3}\%$. Leong *et al.* (2005) estimated the strain level of the receiving bender element to be in the range of $\epsilon \approx 10^{-4}\%$, when touching the transmitting bender element. There is another estimate of strain level in the range of $\epsilon \approx 10^{-4}\%$, given by Pennington (1999).

1.4 Monitoring of Bender Element Behaviour

When testing with bender elements, the transmitted and received electric signals are used to characterise the system. When doing so, it is inherently assumed that the transducers have a mechanical motion with a time history equivalent to the corresponding input signal that forced their movement. This assumption is questionable since the bender elements have non-zero mass and non-zero stiffness, then they must

behave, mechanically, as a Newtonian system, where the effect of inertia is present.

If, for example, the body of the bender element is fixed to a cap and its tip free to move, these are common boundary conditions usually described as those of a cantilever. Clough and Penzien (1993) explain how the dynamic bending or flexural motion of a cantilever can be analytically modelled as a single degree of freedom system, SDOF, (section 3.10). The response of a generic SDOF to a harmonic excitation is presented in section 3.8.5, and illustrated in figures 3.25 and 3.24. For an excitation force of constant magnitude, the magnitude of the response varies with frequency, (equation 3.84). Also, there is a phase difference between the excitation and the response which also varies with the excitation frequency and can be as much as 180°, (equation 3.84). The observation that such a system can vibrate not in phase with the excitation force is well known in mechanical dynamics, but somehow not generally assumed when dealing with the behaviour of bender elements.

In order to better understand the behaviour of bender elements, some authors have monitored it. Shirley (1978) mentions the resonance frequency of the bender elements used, but does not mention the method to obtain such a value. The earliest reference about the monitoring of bender elements is given by Schultheiss (1982). The method consisted of wiring the piezoelectric ceramic to two independent electric circuits. One circuit is used to excite the transducer in the normal way and the other to transfer its response back to an electric signal. This method of monitoring initially appears to be quite ingenious, yet the results show a response which is perfectly faithful to the excitation, thus not plausible. Such a result can be explained by an electric leakage, where the exciting electric signal reaches the wiring circuit responsible for the response monitoring directly. Since the received signal corresponding to the actual mechanical bending of the transducer would have a significantly lower amplitude than that of the input signal; if an electric short-circuit does occur, it would dominate the received signal. One other possibility is

for the input signal to be harmonic with a frequency comparatively lower than the resonance frequency of the transducer, allowing a steady state response with barely no phase delay, (Clough and Penzien, 1993).

Schultheiss (1982) used the same self monitoring method proposed by Shirley (1978), and for two pulse signals with different frequencies obtained two distinct responses. For a lower frequency of 2.96kHz the transducer is observed to emulate the excitation signal perfectly. At a higher frequency of 29.6kHz, the transducer has shown again to emulate the excitation signal but now with some discontinuities in the response trace. This second behaviour, namely the observed discontinuities, was called overshooting.

Brocanelli and Rinaldi (1998) used an accelerometer to monitor the response of the bottom plate to which the transmitting bender element is mounted and fixed. Hitting the bottom plate and inducing a pulse load and then exciting the bender element with a sinusoidal signal enabled the determination of the magnitude response curve of the composed system. Such data allowed to distinguish and identify the individual resonance frequencies of both the bender element and the plate. Nevertheless, since the behaviour of the plate is dominant, the results concerning the bender element are less reliable.

Greening and Nash (2004) have monitored the behaviour of a transmitting bender element by placing a strain gauge in direct contact with the piezolectric ceramic plate and encapsulating them together in epoxy resin. Using a random signal, the response magnitude and phase delay curves were obtained for a comprehensive range of frequencies. The obtained curves are characteristic of a simple mechanical device, indicating a magnitude peak and phase shift of equal frequency, believed to be the resonance frequency of the bender element. See section 3.8.5 for details about similar response curves.

Since bender elements can work both as transmitters and receivers, a logical

step was to make a receiver bender element touch the transmitter and monitor it, (Lee and Santamarina, 2005; Leong *et al.*, 2005). The problem with this method is that the monitoring data is the signal from the receiver bender element. So, the receiving transducer is the one being directly monitored and not the transmitter. The application of this method requires the assumption of a perfect coupling between the tips of a pair of bender elements with the same electric wiring, series or parallel. In normal testing, it is not possible to verify such boundary condition. Besides, bender elements are used to excite and be excited by the soil through their much larger lateral surfaces, and not just by their tip end.

By making the receiver bender element touch the transmitter bender element, the dynamic behaviour of one transducer is influenced by the other. What is then actually being studied is this composed system and not the independent behaviour of one of the transducers. Neither Lee and Santamarina (2005) nor Leong *et al.* (2005) thoroughly describe the test system and it is taken into account, when associating the obtained results with the transducers' properties. Nevertheless, it is possible to compare the transmitted and received signals and estimate how faithfully the bender elements react to the transmitted signal. Leong *et al.* (2005) found no significant time delay between the transmitted and received signals. These were similar but not the same, making clear that the received signal has a different time history than that of the transmitted signal, with a different frequency and shape; particularly after the transmitted signal has ended. the received signal indicates some further movement from the transducers, as would be caused by inertia effects.

Lee and Santamarina (2005) mention another method of monitoring a bender element transducer which is quite simple. A single bender element tip is left free to vibrate, excited by an instantaneous impact and its response recorded, especially its resonance frequency. In this work, the result were compared with an analytical model allowing their association with the flexural stiffness of an equivalent beam,

and consequently, the calculation of the Young modulus stiffness constant.

Arulnathan *et al.* (1998) conducted numerical work where the propagation of waves in an elastic two dimensional medium is studied. The mechanical behaviour of the transmitting and receiving bender elements was also considered in the model and so their behaviour could be studied. A varying time delay between the applied force and the tip displacement was detected and estimated between 3.0% and 8.5% of the input signal period. No correlation was proposed between the observed time delay and the phase delay that occurs in simple mechanical systems, and which also varies with excitation frequency, (section 3.8.5). Therefore it is not possible to determine how faithfully the numerical result comply with such particular theoretical behaviour. It would also be interesting to compare the behaviour of the bender element, and the surrounding soil, but such results were not presented.

1.5 Travel Distance

Concerning the travel time and travel distance, necessary to calculate the wave velocity in bender element testing, the determination of travel distance is generally considered the less problematic of the two. Although related with the introduction of the use of bender elements, Shirley and Hampton (1978) did not elaborate on the subject of travel distance, simply referring to it as the distance between the transducers. Dyvik and Madshus (1985), followed by Brignoli *et al.* (1996) and Viggiani and Atkinson (1995) have proposed and justified the measurement of travel distance as the minimum distance between transducer tips, also known as tip-to-tip distance. The tip-to-tip travel distance is commonly assumed by a variety of authors, for instance Kuwano *et al.* (1999), Dano and Hicher (2002), Kawaguchi *et al.* (2001) or Pennington *et al.* (2001), with or without explicit justification.

Dyvik and Madshus (1985) compared the dynamic results from three different clay samples, using the resonant column and bender element tests. They observed that the results from the bender element test fitted best the resonant column results for travel distances measured tip-to-tip. An analysis of those same results can indicate that the effective travel distance for higher soil stiffness, if all other things remain equal, would in fact be even smaller than the tip-to-tip distance. The bender element tests were conducted using a square pulse signal associated with significant uncertainty in the interpretation of results, (Jovičić *et al.*, 1996), which must extend to the proposed conclusion of correct wave travel distance.

Viggiani and Atkinson (1995) used bender elements to test 3 samples with different heights, between 35mm and 85mm. For each sample, three travel time estimates were obtained for different stress states using square and sinusoidal pulse signals. The chosen linear relationship between the results from different samples, at similar stress states, indicate the correct travel distance to be the tip-to-tip distance. Brignoli *et al.* (1996) also came to the conclusion that the correct travel distance must be measured between tip-to-tip. Samples with different heights were tested with bender elements as well as with shear-plates which support his conclusion. Brignoli *et al.* (1996) used an alternative reference to sample and embedment heights by using the relative embedment heights of the transducers in relation to that of the samples. The two cases referred to were for relative embedment heights of 3% and 14%.

Alternatives to the tip-to-tip travel distance are not commonly proposed. Fam and Santamarina (1995) used the distance between mid-embedded height but did not justify it.

When dealing with direct wave travel times and imagining the wave first arrival, it seems intuitive to picture the receiver being first excited at its tip end. If the same principle is applied to the transmitter, even though it is forced to move as

a single body, again it is easy to picture the disturbance caused by the tip end to propagate ahead of other wave components. If, on the other hand, all the signal content is considered, and not just its first arrival, then both the transmitting and receiving transducers are fully engaged in a mechanical sense. One could suggest for the travel distance to be measured between the centres of applied and received pressure. Also, since the estimation of travel time is itself problematic, it cannot be used to undoubtedly verify the travel distance.

1.6 Scope of Thesis

Chapter 2 describes the different signals used to excite the transmitting bender element. Each type of transmitted signal and consequent received signal are commonly associated with a particular method of interpreting the results. These methods are also explained.

Chapter 3 presents the relevant theoretical background used to support the interpretations made of the bender element related phenomena. Wave propagation theory, body vibration theory, wave radiation and dispersion are some of the subjects referred to.

Chapter 4 explains the use of synthetic rubber as a replacement for soft soil samples. The properties of polyurethane rubber are explained and compared to those of soft soils.

In chapter 5 the dynamic properties of bender element transducers are studied in detail. The results from an independent monitoring of their behaviour is carried out and the results compared with simple numerical and analytical models.

Chapter 6 presents the results from the geometry parametric study. The sample geometry is related with the differences in results, according to established theory of body motion and wave propagation.

In chapter 7 the bender element and soil sample test system is modelled using specific numerical tools. Again the geometry of the sample is varied in order to establish a relationship with its dynamic behaviour.

Chapter 8 contains the relevant conclusions made from the observation of the presented results and consideration of relevant theoretic background.

Chapter 2

Signal Properties and Processing Methods

In this section, different types of input signals used when testing with bender elements are explained. These are electric signals which excite the piezoelectric ceramic plate by applying a voltage differential, forcing it to flex or bend. The electric signals are generated and transmitted by a function generator or similar device. Both a function generator and a personal computer, more specifically its sound card, are used henceforward.

There are a number of different methods of signal processing available, each permitting, in principle, the estimation of the desired wave velocity. A clear distinction between these methods can be placed at the domain in which the results are processed, time domain or frequency domain.

2.1 Pulse Signal

The impulse or pulse signal is a type of signal commonly used in dynamic testing. This type of signal has been employed since the beginning of testing with bender elements, (Shirley, 1978). It is possible to interpret pulse signal results in the fre-

quency domain, as done by Mancuso *et al.* (1989), for cross-hole test results for example. Still, pulse signals offer an intuitive interpretation of results in the time domain. The wave travel time can be measured directly in a graphic representation of the transmitted and received signals' time histories, (figure 2.2).

A well known dynamic geotechnical test, the cross-hole method, (Bodare and Massarsch, 1984; Hoar and Stokoe, 1979), uses the same method of wave travel time estimation, serving as a theoretical basis for its use in bender element testing. The cross-hole test method also uses impulse loads, and the response is measured at one or more points positioned away from the source. Even though the bender element and cross-hole test methods have similarities, especially when pulse signals are used to obtain results in the time domain, there are obvious differences between the two. Such differences relate to the boundary conditions and properties of the input signal. Bender elements are most used in somewhat small samples of relatively soft soil where the amplitude of the initial disturbance is small, with strains in the range of $\varepsilon \in [10^{-3}\ 10^{-5}]\%$, (Dyvik and Madshus, 1985). In the cross-hole method the transducers are placed much further apart and the impulse loads created by a significant impact of some kind. So, not only the dimensions and geometry of the media in which the waves propagate are significantly different, but in the cross-hole method the properties of the transmitted signals are limited due to their impact nature.

Because of the established use of the cross-hole test method, testing with bender elements 'inherited' some of the assumptions concerning the dynamic behaviour of the wave propagation. One such assumption is the consideration of unbounded wave propagations in bender element testing as for the cross-hole method, (Bodare and Massarsch, 1984). In this way the influence of the sample boundaries is disregarded. Such assumption of unbounded wave propagation is challenged with the results presented in chapter 6.

Pulse signals are characterised by their finite duration, implicit in their name. This finite nature of the pulse signals in the time domain means that the dynamic phenomena related with the consequent body vibration and wave propagation are transient, (Clough and Penzien, 1993). The relationship between transient and steady-state body responses, and specific benefits of each for testing with bender elements, is explored in theoretical terms in section 3.8 and in practical terms in chapter 5.

One property of the pulse signal is its shape or form. In figures 2.1(a) and 2.1(b) are represented two typical shapes of pulse signals, one sinusoidal and another square, commonly used in bender element testing, (Dyvik and Madshus, 1985; Pennington, 1999).

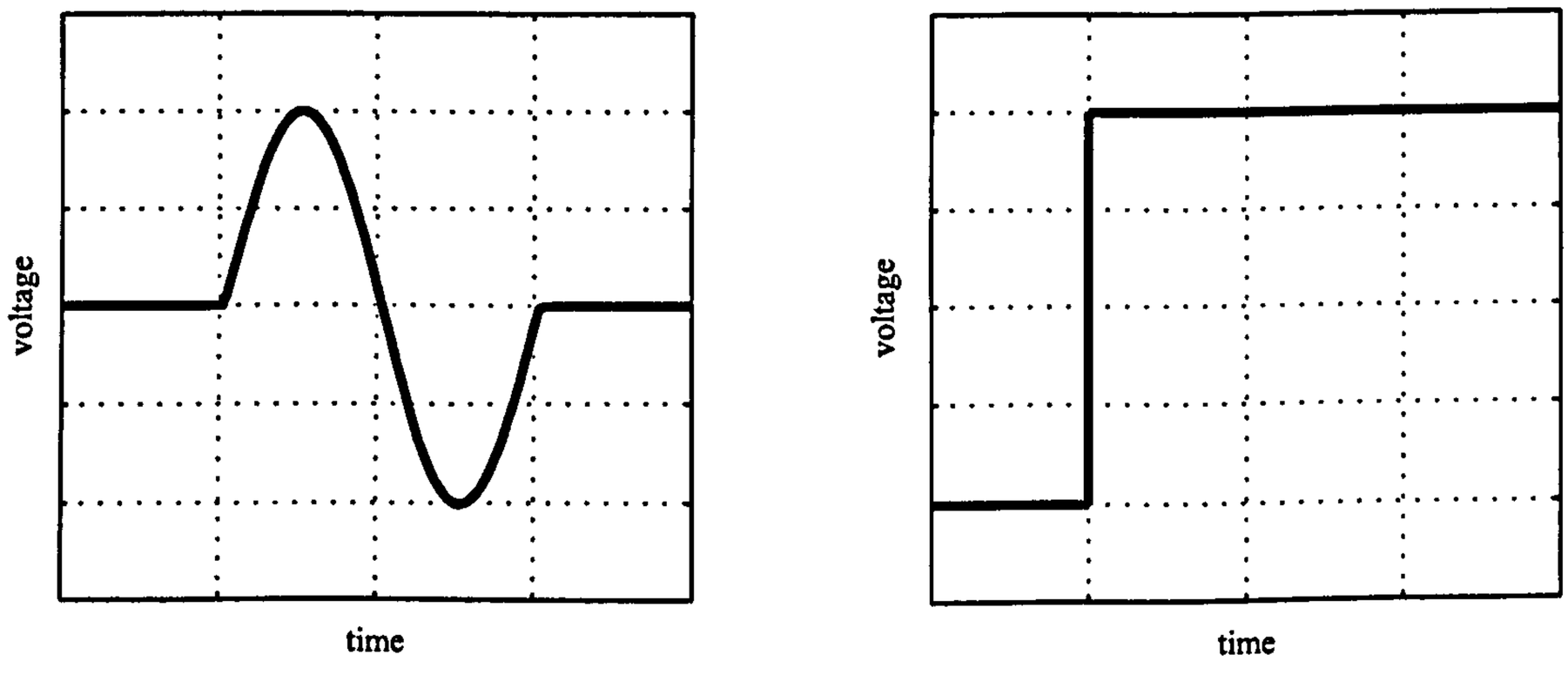

(a) sinusoidal (b) square

Figure 2.1: Sinusoidal and square pulse signals representation.

It became a matter of some discussion which of the two shapes of pulse signal, sinusoidal or square, is more appropriate for bender elements testing. The square pulse signal, (figure 2.1(b)), as used by Bates (1989), Viggiani and Atkinson (1995) or Shibuya *et al.* (1997) for example, has a very well defined start but no other noticeable features. The start of the square signal is point from which the travel time is measured, Jovičić *et al.* (1996). Square signals resemble the impact loads

used in the cross-hole test method, (Bodare and Massarsch, 1984), as does the direct time domain method used to estimate the wave travel time. A mathematical representation of a square pulse signal is given,

$$y(t) = \quad a \quad \text{for} \quad t_0 \leq t \leq (t_0 + T) \tag{2.1}$$

$$y(t) = \quad 0 \quad \text{for} \quad t < t_0 \text{ and } t > t_0 + T$$

where a is the amplitude, t is the time, T is the period of the signal and $y(t)$ its magnitude.

Problems concerning the use of square pulse signals are related to its sharp initial rise. An instantaneous variation can be expressed analytically as done in equation 2.1 and even reproduced as an electric signal by a digital function generator. But, mechanic devices with finite mass and stiffness, also known as Newtonian systems, cannot respond in such manner. Due to the presence of inertia forces it is not possible to obtain instantaneous variations in motions, equivalent to infinite accelerations. Therefore, when using square signals a discrepancy between the input signal and the actual movement of the transducer must be expected. Consequently, the correlation between the input signal and the transducer's motion is not straightforward and neither is the overall correlation between the input and output signals.

Due to their instantaneous variation in the time domain, square pulse signals have a very broad frequency content with no particular main or central frequency. This means that frequency dependent dispersion phenomena, such as the near-field effect, explained in section 3.6, and modal wave propagation, explained in section 3.2, cannot be avoided. This is another reason why the use of square pulse signals has gradually become less common in bender element testing, where the boundary conditions of the test system are more prone to the mentioned dispersive phenomena, (Arroyo, 2001; Jovičić *et al.*, 1996).

Sinusoidal pulse signals, as the one represented in figure 2.1(a), are also commonly used in bender element testing. Examples can be found in Brignoli *et al.* (1996) or Fioravante (2000). This type of pulse signal is defined,

$$\begin{aligned} y(t) = &\quad a\sin(\omega t+\theta) - a\sin(\theta) \quad \text{for} \quad t_0 \le t \le t_0 + T \\ y(t) = &\quad 0 \qquad\qquad\qquad\qquad\quad \text{for} \quad t < t_0 \text{ and } t > t_0 + T \end{aligned} \tag{2.2}$$

where a is the amplitude, ω is the pseudo-frequency, given by $\omega = 1/(2\pi T)$, and θ is the phase origin. Generally, the phase step is set at 0°, as in figure 2.1(a), but other values can also be used, (figure 2.3). The frequency of the signal is referred to as a pseudo-frequency because it is not he actual frequency of the signal, serving only as a reference. The sinusoidal pulse signal does not follow a Dirac function, with a single frequency, having instead a broad frequency content, accounting for he signal initial and final accelerations.

When using a pulse signal to excite the transmitting transducer, the time histories of the transmitted and received signals are used to obtain directly the wave travel time. An example of a transmitted and received pulse signal is given in figure 2.2. The input sinusoidal pulse signal has a phase of 0° hence the equilibrium. This example is similar to several other results from similar test set-ups and clay materials, (Hardy *et al.*, 2002). The travel time can be measured in the horizontal time axis between two characteristic points of the input and output curves.

In figure 2.2 some characteristic features of the transmitted and received signal curves are marked. From these a number of travel time estimates can be obtained. Features A, B and C mark the start, the first local maximum and the first local minimum of the transmitted signal. On the received signal the characteristic features marked are D - first deflection, E - first local minimum, F - first through zero, G - first maximum and H - second local minimum. Assuming that features in the transmitted

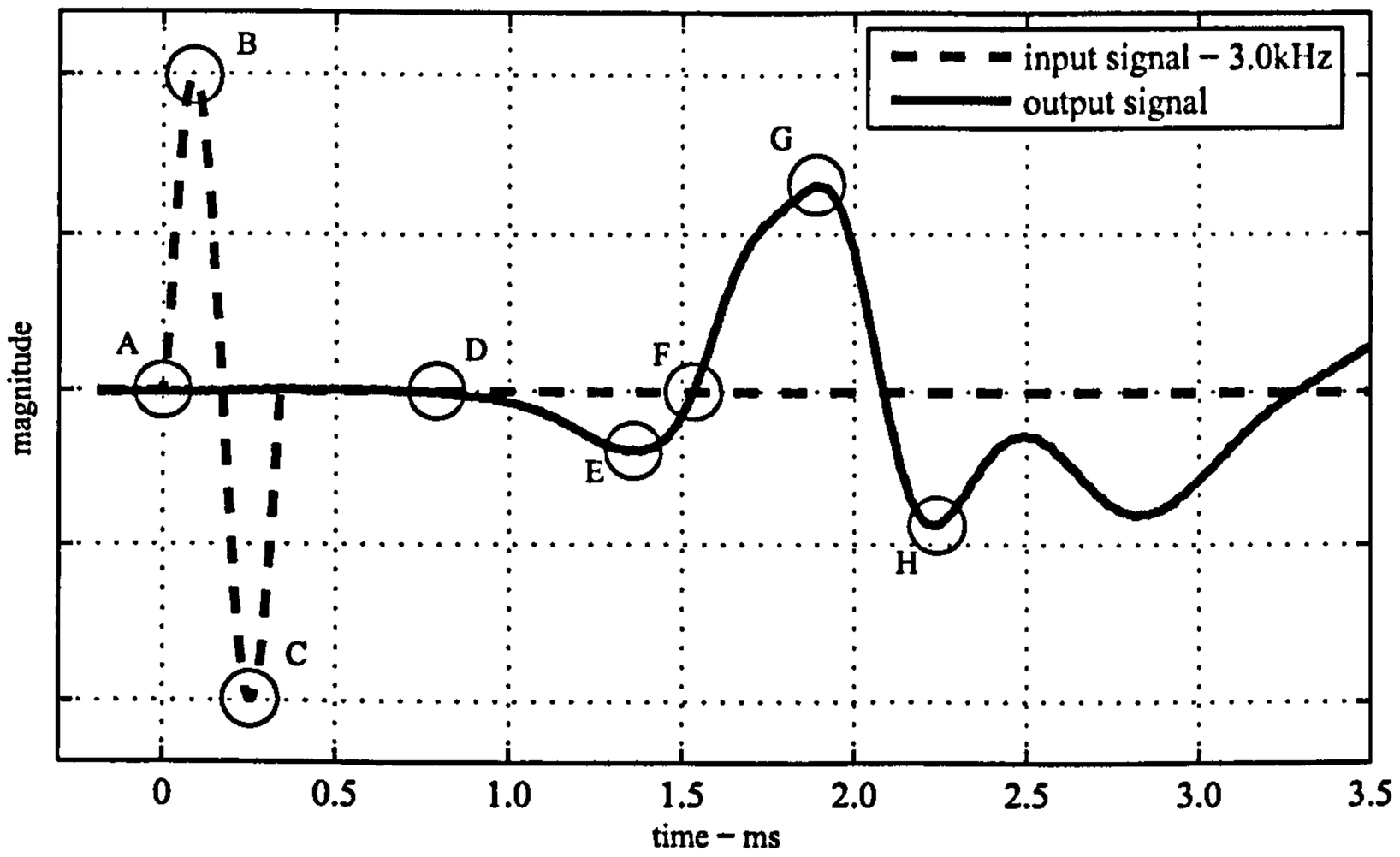

Figure 2.2: Transmitted sinusoidal pulse signal and correspondent received signal time histories, and relevant signal features for travel time estimation.

signal are related with features in the received signal, the time difference between such features gives the desired wave travel time. Table 2.1 presents the travel time estimates obtained using the time differences between the mentioned points which might possibly be related.

Peak Features	Travel Time
A-D	0.76ms
A-E	1.36ms
A-F	1.54ms
B-G	1.81ms
C-H	1.98ms

Table 2.1: Pulse signal travel time estimates from signal features given in figure 2.2.

It is clear, just by looking at the input and output curves, that the received signal is a distorted version of the transmitted signal. Plausible sources for the observed signal distortion are wave dispersion and particular mechanical response

from the system components. The tested system included a kaolin soil sample, a pair of bender elements, both connected in series and places at each top of the sample, aligned with each other, a function generator and a oscilloscope with a link to a PC. These test components are described with detail in chapters 5 and 6. Consequently the direct estimate of the wave travel time might not be as straightforward as for an ideal case, where the received signal would be a scaled copy of the transmitted signal. The discrepancy registered in table 2.1 between the travel time estimates reinforced this observation. For the present example, the difference between the longest and shortest travel time estimates is of 1.22ms, 62% of the maximum estimate.

The determination of the wave travel time, when measured directly from the signals' time histories, is clearly not as simple as it might have appeared initially. Redwood (1960) described the propagation of a pulse through a solid medium as complex, and Achenbach (1973) mentioned the complications caused by reflections of the transient wave motion at the bounding surfaces. The understanding of these phenomena and how to overcome the complications they introduce in the interpretation of the results is one of the main objectives of this dissertation.

Some effort has been made in the pursuit of a convenient method of interpreting time domain results from bender element testing in soil samples. One of the signal properties considered was the shape of the transmitted sinusoidal pulse signal. Figure 2.3 contains two sinusoidal pulse signals where the phase θ as given in equation 2.2 is established at -90° and +30°. The aim of using these variants of the sinusoidal pulse signal is to obtain results that provide a clearer, less ambiguous, determination of travel time, (Jovičić *et al.*, 1996).

Results obtained using variants of the sinusoidal input signal, as those seen in figure 2.3, were explored by Jovičić *et al.* (1996) and again by Greening *et al.* (2003) and Pennington *et al.* (2001). The objective was the optimisation of the input signal in order to obtain an output signal with none or minimum distortion, and

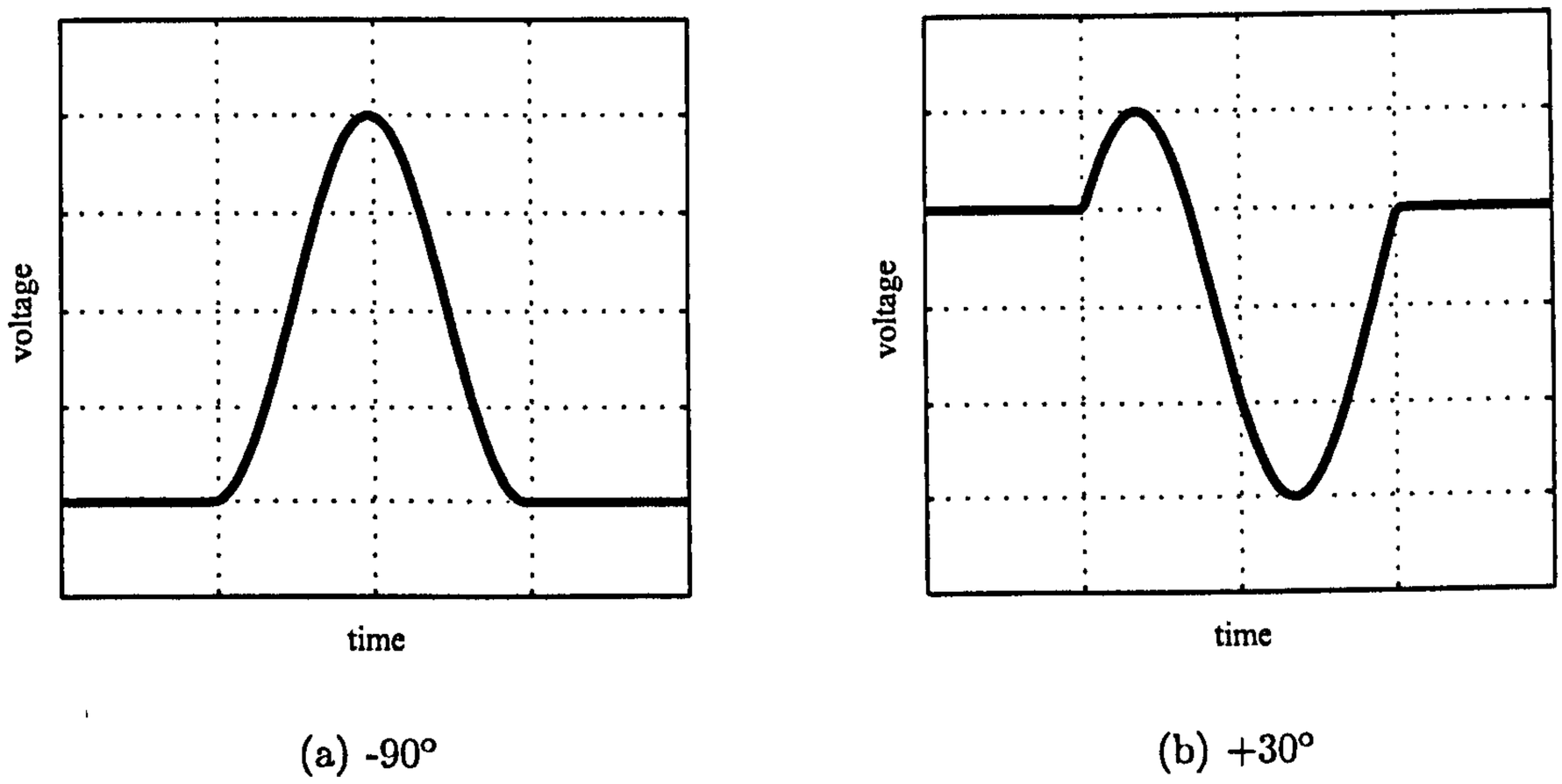

(a) -90°

(b) +30°

Figure 2.3: Variations of sinusoidal pulse signal with voltage phase shifts of -90° and +30°.

in particular with no early first arrival. In practical terms, and using figure 2.2 as a reference, the main objective of using variations of the sinusoidal pulse signal is to obtain a received signal where features D, E and F coincide. Even though the resulting received signal can be made to look clearer, the manipulation of the transmitted signal does not address the reasons for which such distortions occurs. The central frequency and the frequency range of the different pulse signals are the same and so frequency dependent dispersion phenomena cannot be assumed to vary significantly with relative phase of sinusoidal pulse signals.

A sinusoidal pulse signal, such as the one presented in figure 2.1(a), has a broad frequency content. In equation 2.2, only a single frequency is defined, but since the transducer starts its movement from a still position, it has to accelerate to reach the desired frequency and decelerate to return to its initial rest condition. The mentioned sinusoidal pulse signal has a central frequency of 3.0kHz, but its actual frequency content is much broader as seen in figure 2.4.

The frequency content presented in figure 2.4 was obtained using a Fast Fourier Transform function, FFT. This method consists of numerically decomposing the

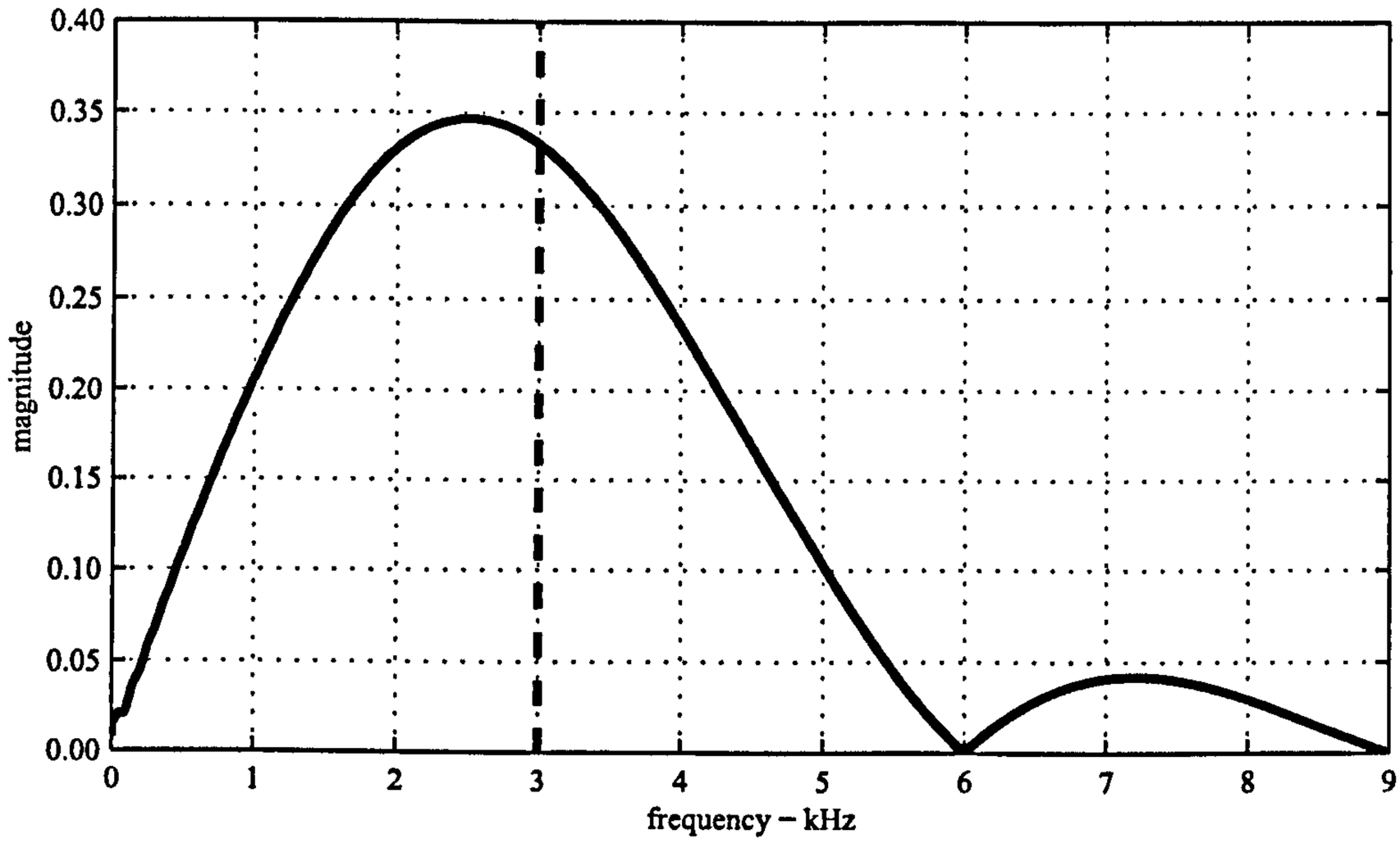

Figure 2.4: Frequency content of sinusoidal 3.0kHz pulse signal, obtained using a FFT method.

signal into a finite number of Fourier series, (Cooley and Tukey (1965)). It can be observed that the pulse signal has quite a broad frequency spectrum.

Because of the transient nature of a pulse signal, the discrete Fourier transform has some limitations concerning its decomposition as a series of continuous sinusoidal functions, (Doyle, 1977). A more recent method of signal decomposition and consequent processing is the wavelet analysis. In broad terms, the wavelet method uses finite length or fast decaying oscillating waveform to decompose a signal. This method is ideal to deal with finite signals such as the pulse signal, (Kumar and Foufoula-Georgiou, 1997). Its potential is acknowledged but is not pursued further, because of its extra degree of complexity and lack of accessible numerical tools.

Returning to the issue of interpreting wave travel time from the time histories of the signals, the discrepancy found between the results presented in table 2.1 is not an isolated case. A number of tests performed independently from a number of authors came up with similar results, (Kawaguchi *et al.*, 2001) for example. When dealing with wave propagation a relevant aspect of such phenomenon is the wave

front, the virtual varying position which marks the discontinuity between excited and 'at rest' particles. The travel time of the wave front could then, in principle, be measured between the transmitted and received signals first offsets. But, with the presence of wave dispersion, the wave front travels at the phase velocity of the fastest wave component, which is not necessarily the same as the group velocity of the wave centre, (Redwood, 1960).

The estimate travel time obtained from the received signal first offset is commonly judged to underestimate the travel time, thus overestimating the wave velocity and the medium's stiffness. For this reason, an explanation is sought as to why the received signal could arrive earlier than it should, or why the wave front travels at a velocity higher than the characteristic shear wave velocity of the medium. Sanchez-Salinero (1987) proposed the near-field effect as a plausible explanation.

The near-field effect is a wave radiation phenomenon which states that a propagating wave is formed by up to four different components, compression and shear far-field wave components and compression and shear near-field wave components. The near-field effect received such a name because its influence is significant near the source of the disturbance, dissipating quite rapidly as the wave propagates away from it. The subject of wave radiation is explored with more detail in section 3.6. The near-field wave components are dispersive, with different propagating velocities at different frequencies as well as at different distances from the source. If such near-field wave components are present, and since they propagate at velocities different than the characteristic wave velocities, the received wave has more than one propagation velocity. The higher propagation velocity of the near-field wave components could then provide a plausible explanation as to why the wave front can arrive early.

The distinction between the near-field and the far-field wave components in bender element analysis in the time domain has been attempted, (Brignoli *et al.*, 1996). The first out-of-phase or negative offset, described as feature E in figure 2.2, is usu-

ally assumed to be caused by the near-field effect. Eventually, it comes down to the experience and assumptions of the test operator. If both near and far-field wave components are present, they become overlaid throughout all of the response signal's length. Therefore, there is some degree of wishful thinking in the assumption that a clear distinction can be consistently made directly in the time history of the response.

Once the notion of a simple, undistorted received signal is questioned, it is relevant to indicate other wave components that might contribute to the distortion of a wave form. The case of a compression wave component, which takes a different propagation path to reach the receiving transducer is one such case, (Santamarina, 2001). Such propagation paths could involve the wave reflection at the sample's lateral or end boundaries, for example.

Wave reflection is related with a modal behaviour of sample, where the transmitted wave is propagated in a series of wave propagation modes, see Arroyo *et al.* (2002). This modal interpretation of wave propagation is also dispersive, with phase and group velocity varying with frequency. This subject is explored further in section 3.1.7.

2.2 Continuous Signals

A continuous signal can be used to excite the transmitting bender element transducer with no discernible beginning or end. If this signal is harmonic, i.e., is defined by a periodic sinusoidal function, it is possible to establish a steady state vibration of the system. Shirley (1978) and Redwood (1960) mention continuous harmonic signals in the fields of structure vibration and of wave propagation respectively. A

mathematical description of such a signal is given,

$$y(t) = a\sin(\omega t + \theta) \tag{2.3}$$

where a is the amplitude, ω the frequency of excitation and θ a phase step.

Harmonic continuous signals can be used to obtain travel time results directly, in the same way pulse signal are. But, it is their potential to provide results in the frequency domain which makes their use interesting. The transmitted and received signals can be manipulated in the frequency domain to indirectly obtain the wave travel time. These type of results can be used on their own or can complement the direct readings of travel time from pulse signals, in the time domain.

An example of a continuous signal with an amplitude of $a = 10$V, an angular frequency of $\omega = 3 \times 2\pi \text{rad.s}^{-1}$ and a phase step of $\theta = 0$rad is given in figure 2.5.

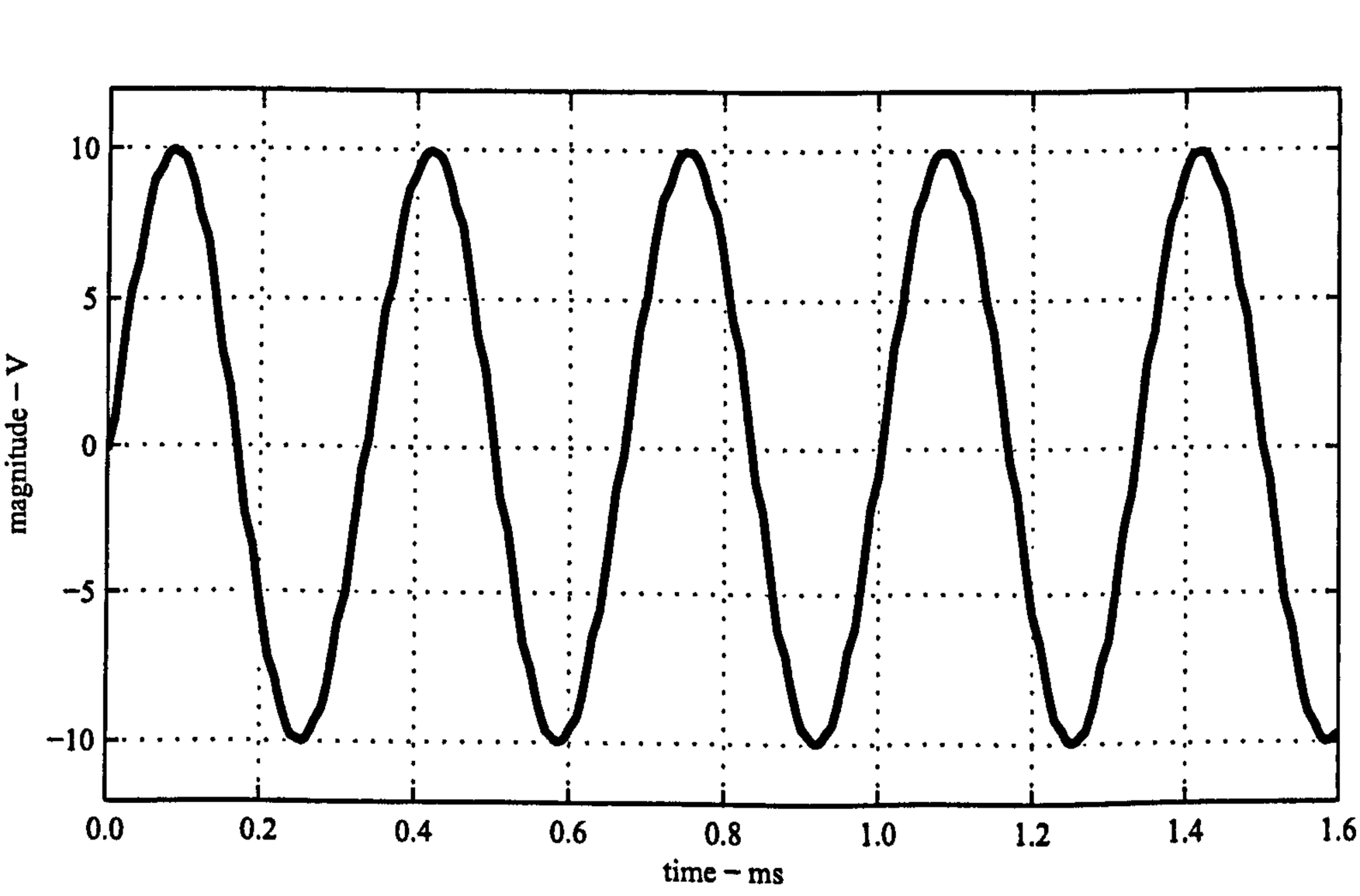

Figure 2.5: Example of a 3.0kHz sinusoidal continuous signal.

The frequency content of the 3.0kHz signal is given in figure 2.6. Again, the frequency content was obtained numerically using a FFT. The theoretical frequency content of a continuous signal, with no start and end, would be represented in figure

2.6 as a straight vertical line, but since a finite and discrete signal was used, the obtained frequency content is an approximation of the mentioned straight line.

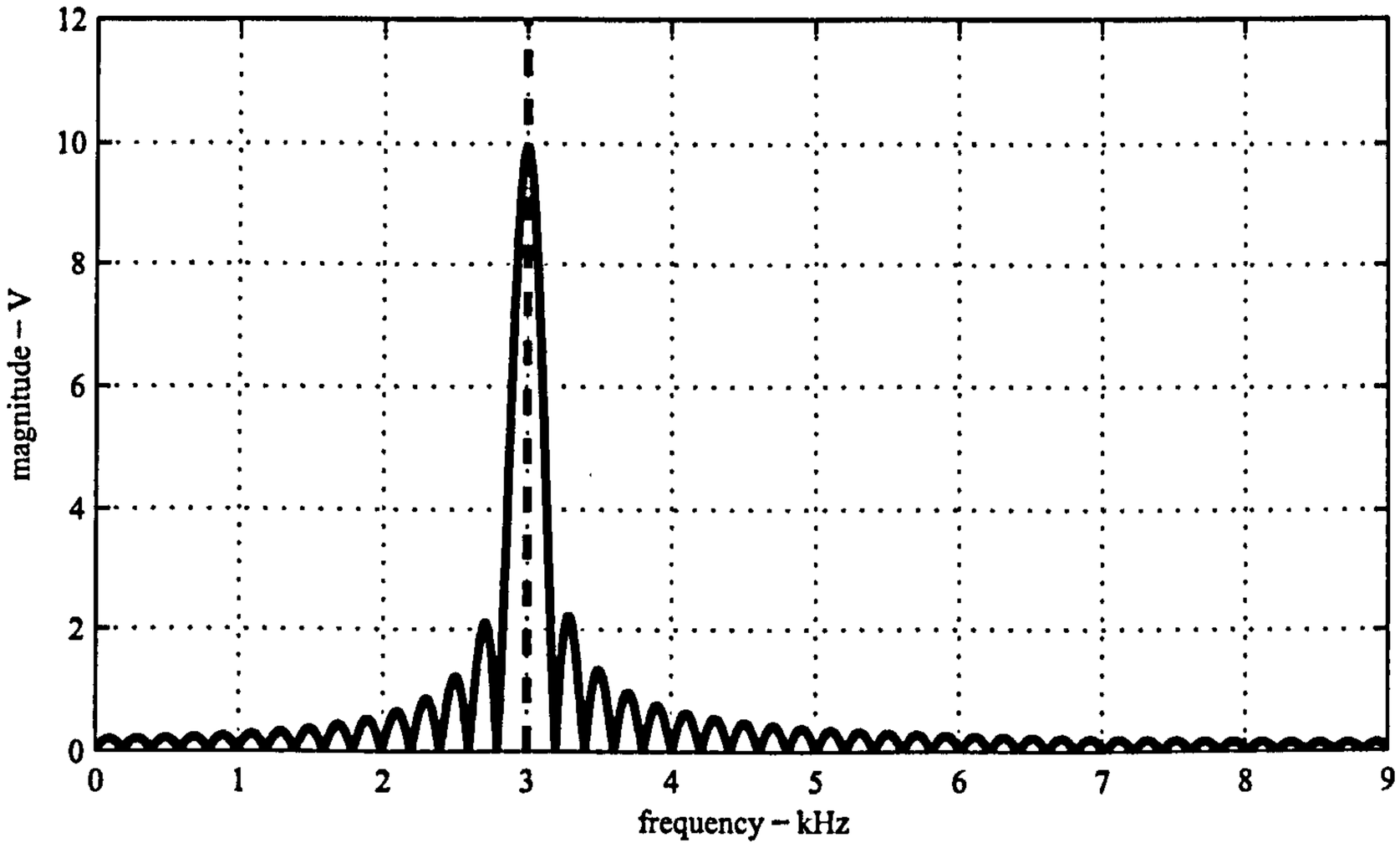

Figure 2.6: Frequency content of 3.0kHz sinusoidal continuous signal obtained using a FFT.

It is interesting to compare the frequency contents of the continuous signal with that of the equivalent 3.0kHz pulse given in figure 2.4. Note that the frequency content of the continuous signal is much narrower and its magnitude peak also coincides better with the desired frequency of 3.0kHz.

If a harmonic continuous signal is used to excite the transmitting bender elements, a steady state of body vibration can be obtained, which is terms of wave propagation is also known as a standing wave, (Achenbach, 1973). In this case the transmitted and received signals have the same frequency but different amplitudes and as phase delay between them. By determining the magnitude and phase delay of a number of received signal, for transmitted signals with different frequencies, the response curves of the system can be obtained, (section 3.8). Figure 2.7 presents an example of the same 3.0kHz sinusoidal signal being transmitted in a synthetic rubber sample.

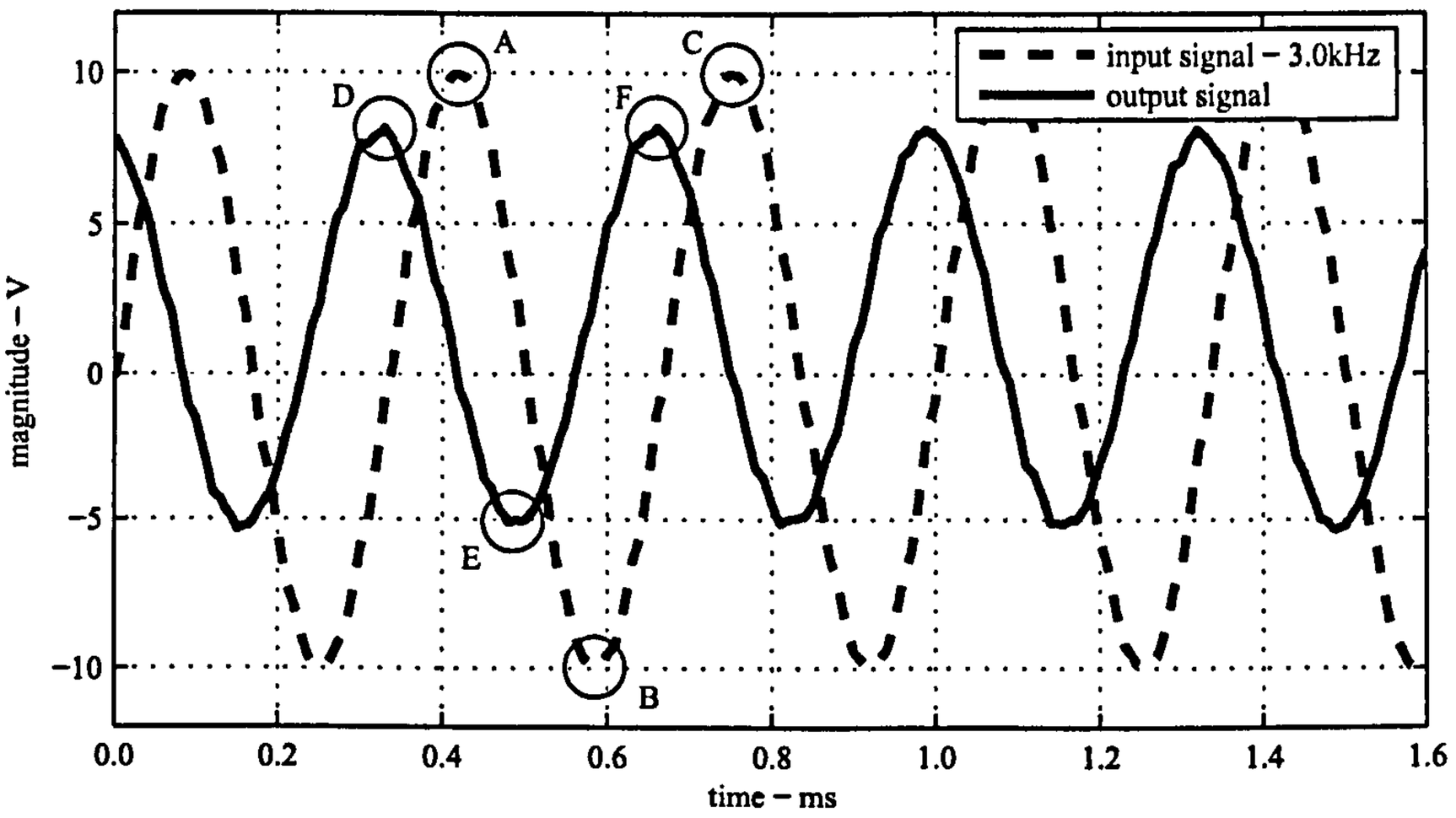

Figure 2.7: Example of transmitted and received sinusoidal continuous signal with 3.0kHz.

The curve features marked as A, B, C, D, E and F indicate local maximums and minimums of the transmitted and received signals. The x and y subscripts indicate the horizontal time axis, x, and the vertical magnitude axis, y, respectively. The indicated features can be related with each other in order to obtain a number of properties of the transmitted and received signals as well as to relate the two signals.

- $\mathrm{A}_y - \mathrm{B}_y = a_t$, magnitude of the transmitted signal.
- $\mathrm{D}_y - \mathrm{E}_y = a_r$, magnitude of the received signal.
- $\mathrm{C}_x - \mathrm{A}_x = T_t$, period of the transmitted signal, $f_t = 1/T_t$.
- $\mathrm{D}_x - \mathrm{F}_x = T_r$, period of the received signal, according to figure 2.7 and more generally with Clough and Penzien (1993), $f_r = f_t = f$.
- $(\mathrm{A}_x - \mathrm{D}_x) \times f \times 2\pi = \Delta\theta$, phase difference between transmitted and received signal.

If the magnitude of the transmitted signal is kept constant, and different predetermined frequencies are used to excite the system, a magnitude response curve can be obtained. This curve is formed by the amplitude values of all the received signals. Figure 2.8 provides an example of such a magnitude curve.

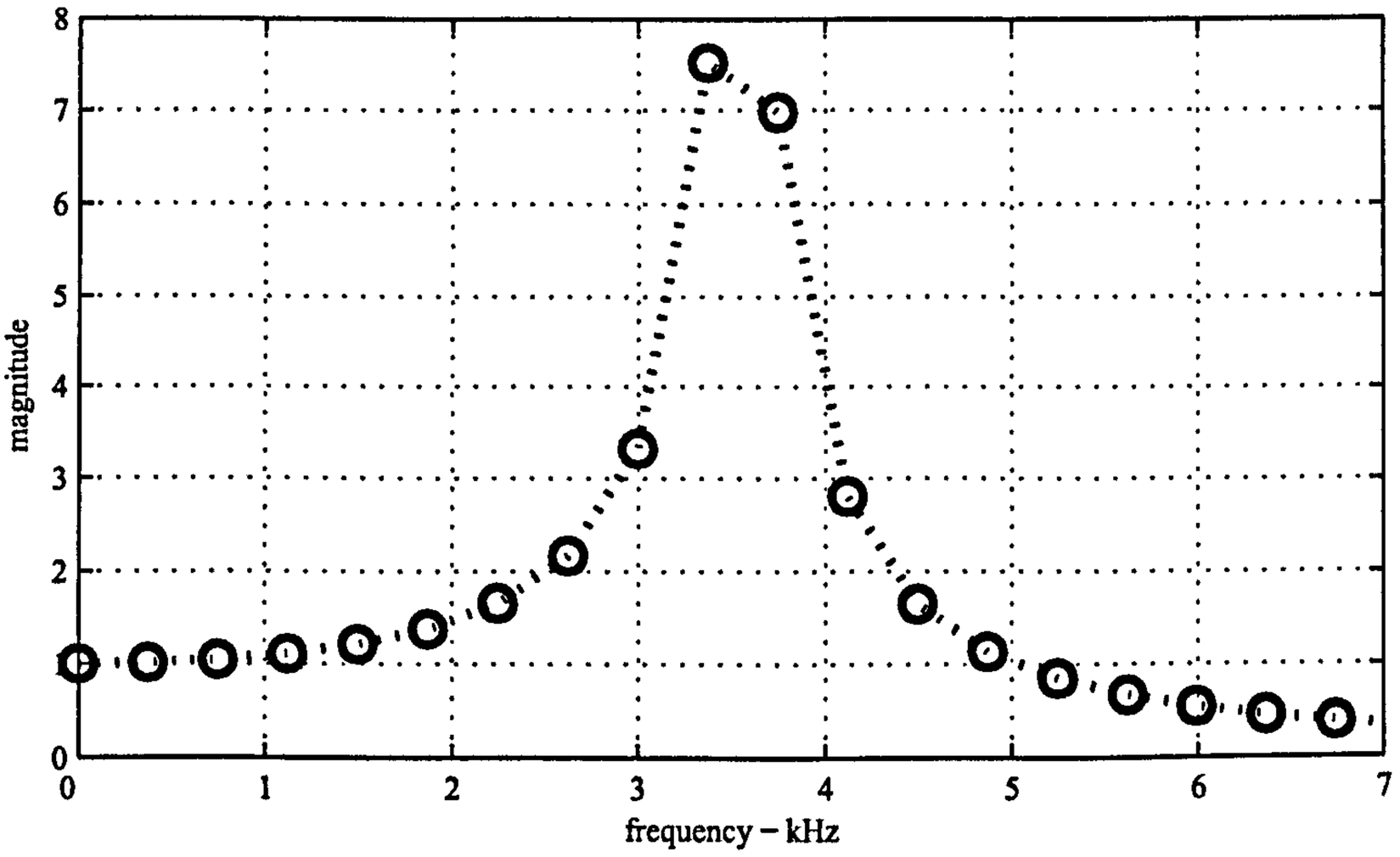

Figure 2.8: Magnitude curve constituted by a collection of received continuous signals with different frequencies.

Excitation signals with constant amplitude but different frequencies produce responses with different phase delays. The other component of the response curve is given by such results, comprising the phase difference between the transmitted and received signals. The transmitted signals used to obtain the magnitude response curve in figure 2.8 are used to obtain the correspondent phase delay curve, plotted in figure 2.9.

One relevant characteristic of the curve presented in figure 2.9 is its gradient, since a travel time can be obtained from it. Equation 2.4 describes the decomposition of the gradient units into time units. Dividing the gradient, in radians per Hertz,

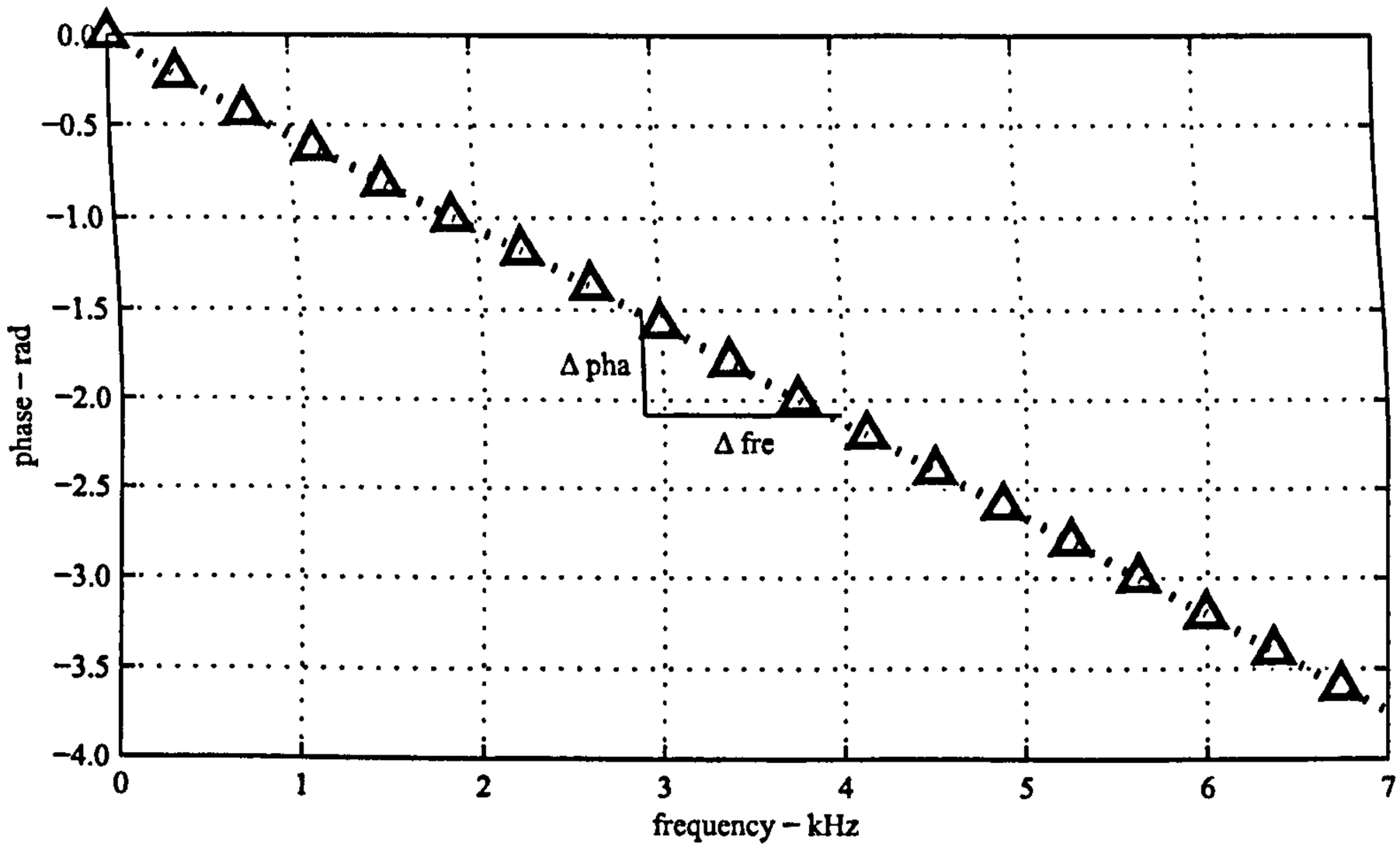

Figure 2.9: Phase delay curve constituted by a collection of received continuous signals with different frequencies.

by 2π leads to the determination of a time value in seconds.

$$\frac{\Delta\text{phase}}{(2\pi)\Delta\text{frequency}} \equiv \frac{\text{rad}}{(2\pi)\text{Hz}} \equiv \text{s} \tag{2.4}$$

The time obtained from the curve gradient is assumed to be that of the corresponding wave. In fact, at each frequency two gradients can be obtained, one of the curve tangent and another of the curve secant. Each of these two gradients possesses a different physical meaning. The gradient of the curve tangent is related with the group velocity and the gradient of the curve secant is related with the phase velocity.

Resonant torsional columns are an example of another dynamic geotechnical testing method which can be used to obtain the magnitude curve of a soil sample system. The magnitude response curve can also be used to estimate the damping coefficient of the medium, as seen in section 3.9.2. Further elaboration on testing with resonant columns can be found in Drnevich *et al.* (1978) or in section 3.11.

2.3 Pi-Points

The pi-points method is a variant of the continuous signal method described in section 2.2. With the continuous signal method, the frequency of the signals is pre-selected and the magnitude and phase difference of the corresponding responses are recorded. With the pi-points method, the opposite takes place; as the phase differences are pre-selected and the frequencies at which they occur are recorded. With this method a response phase delay curve can also be obtained and the correspondent travel time. Normally, the chosen phase differences are multiples of π, so the frequency of the signals are recorded when the transmitted and received signals are in and out-of-phase which is easily identifiable, hence the name pi-points method. The use of this method is common, for it can be performed with the same equipment as the time domain pulse testing, (Ferreira *et al.*, 2004; Greening *et al.*, 2003).

Unlike measuring the phase difference between the transmitted and received signals, which requires a small amount of calculus, the pi-point method can be obtained directly from an oscilloscope reading. Figure 2.10 provides an example of how to identify the pre-selected phase differences between two signals from a typical oscilloscope reading in the time domain.

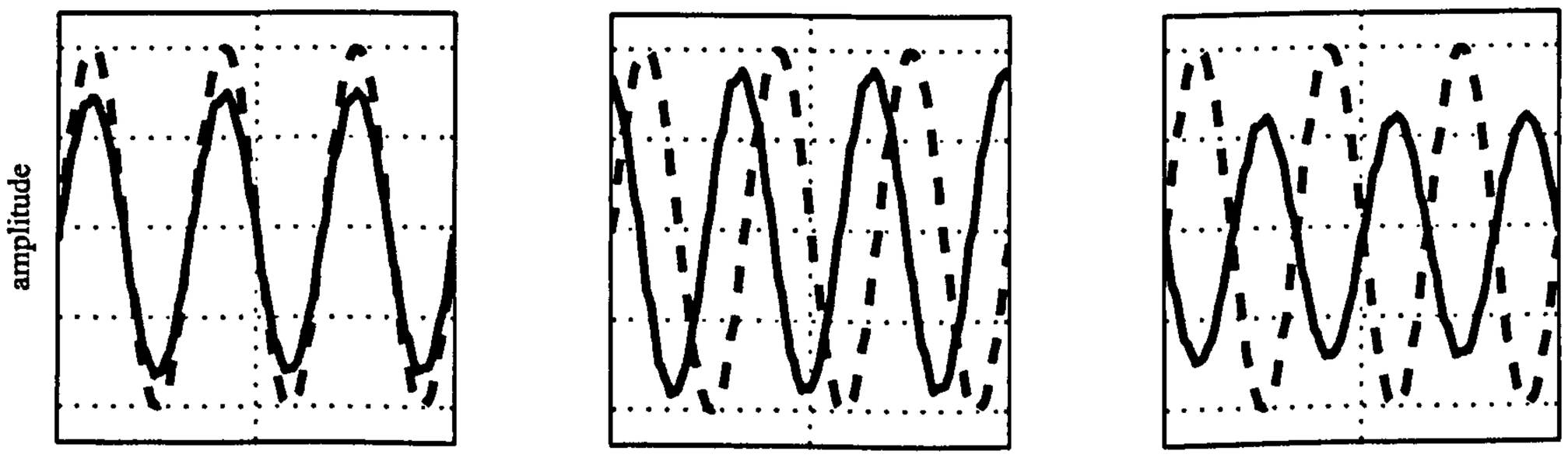

(a) in phase (b) other (c) out of phase

Figure 2.10: Relative position of two sinusoidal continuous signals in the time axis.

The oscilloscope can also be used to provide readings where the signals are presented in superposition, known as Lissajous curves. Using this feature, the added signals are represented as an ellipse, which varies in shape with relative phase difference. This ellipse eventually takes the shape of a straight line when the two signals are in or out-of-phase, enabling an easy identification of the particular relative phase differences, (figure 2.11). By varying the frequency of the transmitted signal and annotating the frequencies at which the signals are in and out-of-phase, a discrete response phase delay curve is constructed for the covered range of frequencies. The obtained response curve is similar to that shown in figure 2.9, and a wave travel time can be obtained from its gradient, just like in section 2.2.

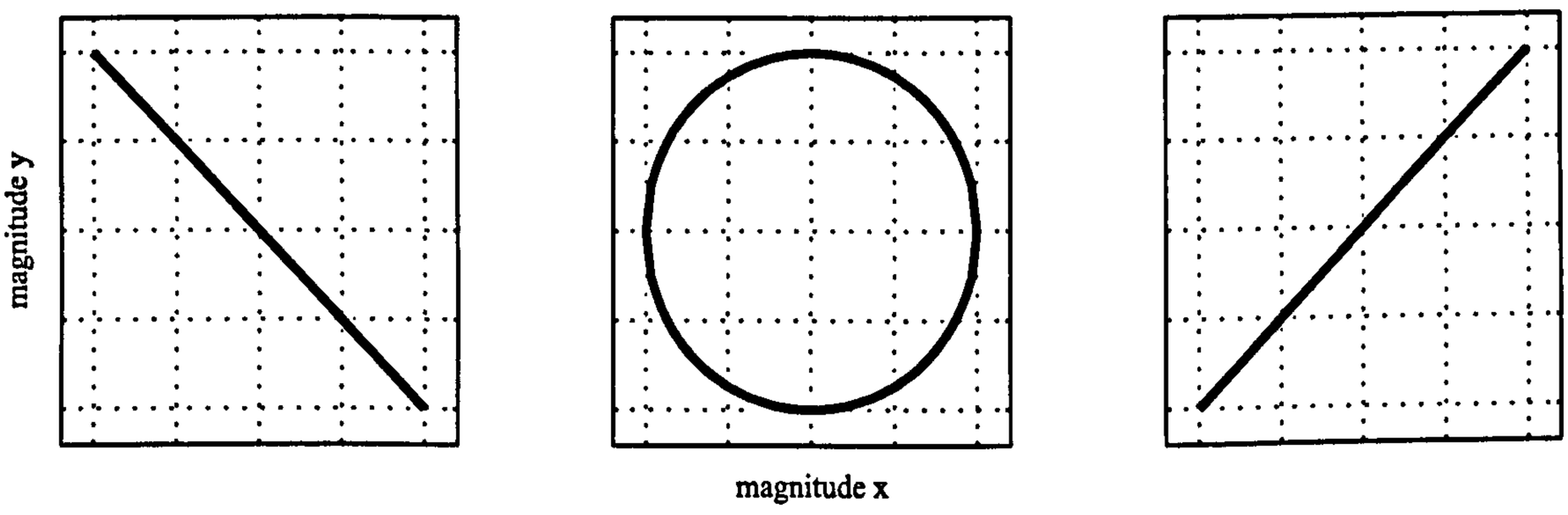

(a) in phase (b) other (c) out of phase

Figure 2.11: Typical oscilloscope displays of two superimposed sinusoidal continuous signals.

2.4 Sweep Signals

Sweep signals, in the context of bender element testing, are non-harmonic sinusoidal continuous signals, Greening and Nash (2004). These signals are similar to the continuous signals described in section 2.2, but have variable frequency with time.

Such a signal is described,

$$y(t) = a\sin(\omega(t) \times t) \quad \text{where} \quad \omega(t) = \omega(0) + \frac{\partial\omega}{\partial t}t \tag{2.5}$$

where a is the amplitude and $\omega(t)$ is the angular frequency. Figure 2.12 presents a typical time history of a sweep signal.

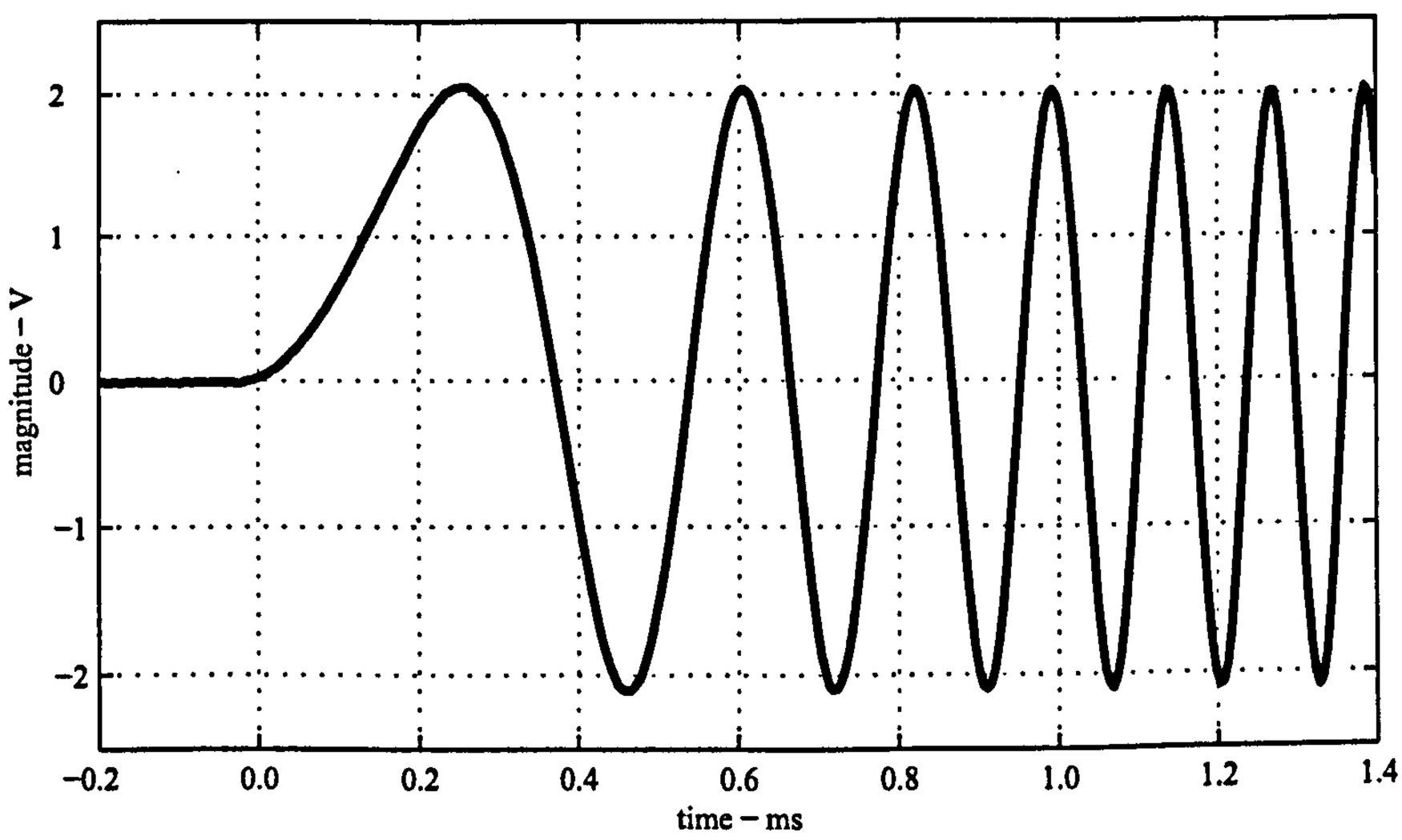

Figure 2.12: Example of a sweep signal time history.

The purpose of using sweep signals is the same as for the use of harmonic sinusoidal continuous signals, i.e., to obtain the response of the system in the form of its magnitude and phase delay curves. In the case of harmonic continuous signals, each used signal provide the response information concerning a single frequency, hence only one point of the response curves can be obtained. In order to obtain the response curves covering a broader range, more than one signal needs to be used in what becomes a time consuming process. The sweep signal contains a much broader frequency spectrum, and so has the potential of providing a near-continuous response curve from a single signal, (figure 2.13).

The use of a sweep signal is dependent on the numerical effort necessary to

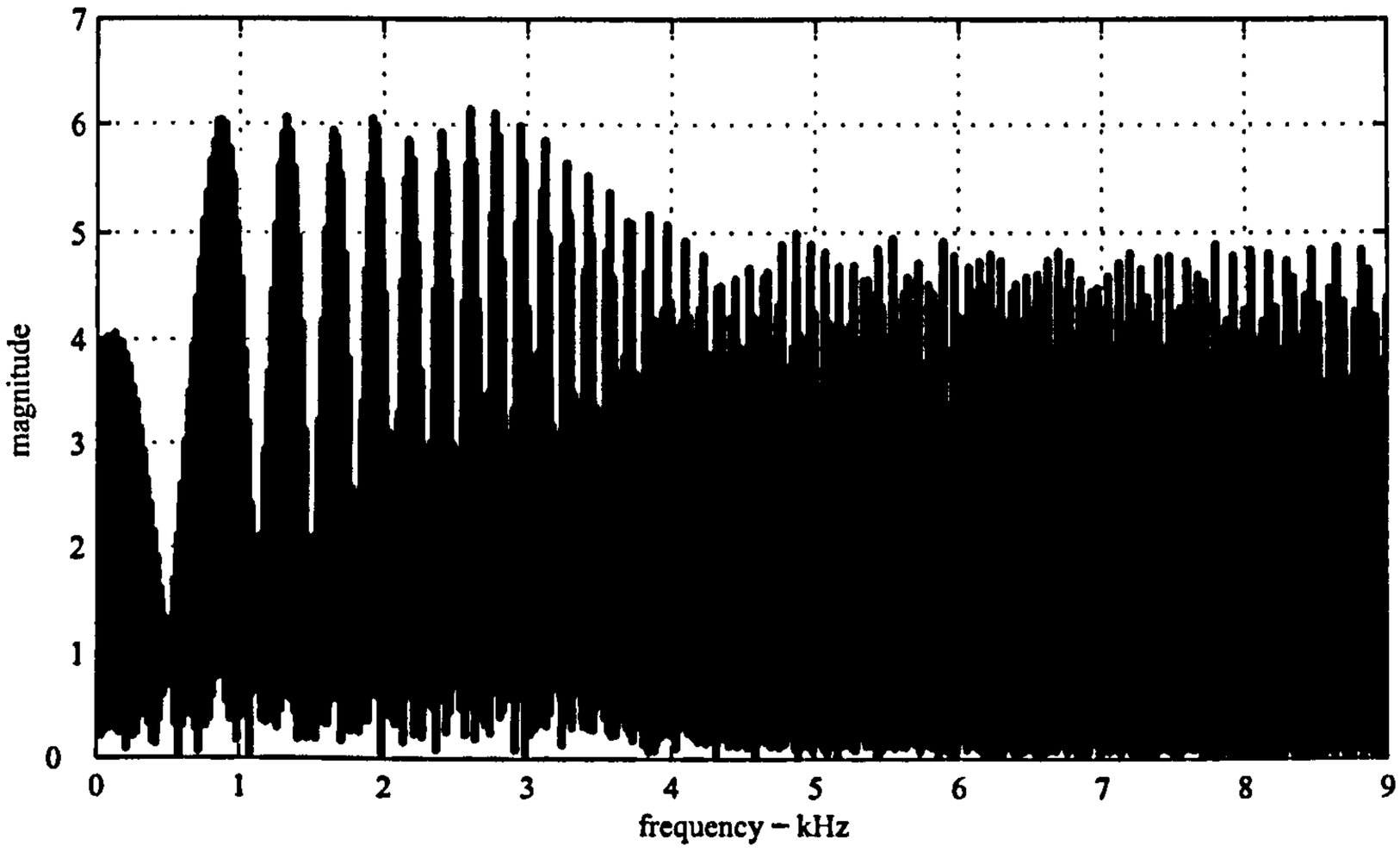

Figure 2.13: Frequency content of sweep signal.

process the signal and obtain the response curves from it. Greening and Nash (2004) have prepared a very useful automatic signal processing tool which, using a sweep signal to excite the transmitting bender element, handles the received signal and calculates the response curves of the system as well as the wave travel time. This numerical tool comprises a capacity for signal generation, using the computer sound card to transmit it. This enables to obtain the magnitude and phase delay curves in a few seconds and with a relatively high frequency sampling rate in the range of results at every 20Hz for example. A dynamic analysis using continuous signal method or the pi-points method would take at least a few minutes for a much lower sampling rate.

The harmonic continuous signals, the pi-points and the sweep signals are all used to obtain equivalent result, i.e, the response curves of the system, all three methods being used in the present study. The objective of using different methods is to obtain a certain degree of redundancy in order to consolidate the confidence in the results, especially the less intuitive sweep signal results. The sweep signal method is less intuitive, since the bulk of the processing is done numerically. But, it is also more

powerful, providing results concerning a much greater number of frequency points with just one signal. Besides it is also possible to obtain not only the magnitude and phase delay response curves but it is also possible to obtain a measure of the coherence between the transmitted and received signals. These results, which relate the transmitted and received signals, are also known as the transfer function of the system, (Arroyo *et al.*, 2006).

The transfer function used in the processing of the sweep signals can also be calculated for pulse signals and harmonic continuous signals. The obtained results have the same theoretical capacity of describing the system. But, these signals have a narrower frequency content than the sweep signal, compare the results in figures 2.4 and 2.6 with the results in figure 2.13. Therefore, the proposed numerical analysis is less reliable, than if sweep signals were used.

2.5 Cross-Correlation

The cross-correlation is a mathematical tool used to measure similarities between two numerical entities, capable of finding patterns between them. It can be used to compare the transmitted and received signals and to obtain a time delay between the most closely related features in the two signals. These time delays can be assumed to express a wave travel time, (Arulnathan *et al.*, 1998; Clayton *et al.*, 2004). This numerical method is able to compare pulse and continuous signals, harmonic or not, as is the use of the response phase delay gradient.

Assuming the transmitted and received signals to be represented by S_{in} and S_{out} respectively, the cross-correlation operation, represented by $\star$, also described by Arulnathan *et al.* (1998), is given,

$$\left(S_{\text{in}} \star S_{\text{out}}\right)(\Delta t) = \int_T S_{\text{in}}^{*}\left(t + \Delta t\right) S_{\text{out}}\left(t\right) dt \tag{2.6}$$

considering Δt to be the time delay between the two signals, T the time length of each signal and S_{in}^{*} the complex conjugate of the input signal. Note that Δt corresponds to the maximum of the cross-correlation function,

The cross-correlation is the most complex signal processing methods presented so far, it can only be obtained with the help of numerical processing tools, unlike the other time and frequency domain methods. The cross-correlation will not be used in the following analysis, where the phase delay curve gradient is chosen as the frequency domain wave velocity determination method.

2.6 Noise

Dynamic testing making use of bender elements involves the handling of electric signals, in the form of the transmitting and received signals. All of the electric circuit involved in the test set-up is potentially capable of picking up noise from the environment such as electro-magnetic signals. The bender elements can both serve as receivers of any residual vibration that might reach them, not only the vibration intended by the controlled excitation of the sample. As for example the vibrations from nearby roads traffic, people walking in or near the lab, any form of sound, etc. For these reasons, different forms of noise can be, and were indeed present in the laboratory work conducted. Three distinct sources of noise were distinguished during most of the experimental tests. These noises were classified as background electro-magnetic noise, residual vibrations and cross-talk.

2.6.1 Background Noise

Background noise from electro-magnetic signals is omnipresent in normal urban environments such as the one found at the civil engineering laboratory where the tests were carried out. Because the electric circuit is quite extensive, no reasonable

amount of secondary earthing circuit was capable of preventing some amount of electro-magnetic noise from being picked up. It was picked up at amplitudes of 50mV which makes its presence quite significant in the received signal and insignificant in the transmitted signal. This type of background noise, when compared with the transmitted and received signals, is random in nature and can therefore be eliminated by consistently averaging the results. This was the procedure of choice to eliminate background noise.

2.6.2 Residual Vibration

Residual vibration is also noticeable in the received signal. The laboratory where most of the tests were conducted is located in the vicinity of a busy road where a significant amount of traffic, including buses and other heavy vehicle, go through. Noticeable vibration from the building structure due to students and staff walking by is also present. As with electro-magnetic background noise, this type of disturbance is random in nature, thus the same process of averaging the received signal results is valid to eliminate it.

2.6.3 Cross-Talk

Cross-talk was observed between the transmitted and received signals where the transmitted signal 'leaks' into the received signal. Santamarina (2001) has frequently mentioned electromagnetic coupling phenomena related with bender element testing. These exit when the transmitting and receiving bender elements protrude into a conductive medium, such as a water saturated soil. The transmitted electric signal is potentially capable of reaching the received bender element by being electrically conducted through the sample water almost instantaneously. An example of electromagnetic coupling is explored by Lee and Santamarina (2005) and associated with

the different wiring of the transducers. The solution for this type of cross-talk involves the grounding of the bender element pair or the use of an ideal parallel/series bender element combination.

Cross-talk can occur at different points of the circuit but in the considered test cases it is believed to occur at the oscilloscope. This conclusion was achieved, through a process of trial and error, by handling the different elements of the circuit. The cross-talk takes place inside the oscilloscope equipment and could not be avoided by any amount of grounding the circuit. The wiring of the bender elements were also not observed to interfere with this form of noise. Figure 2.14 contains an example of such cross-talk.

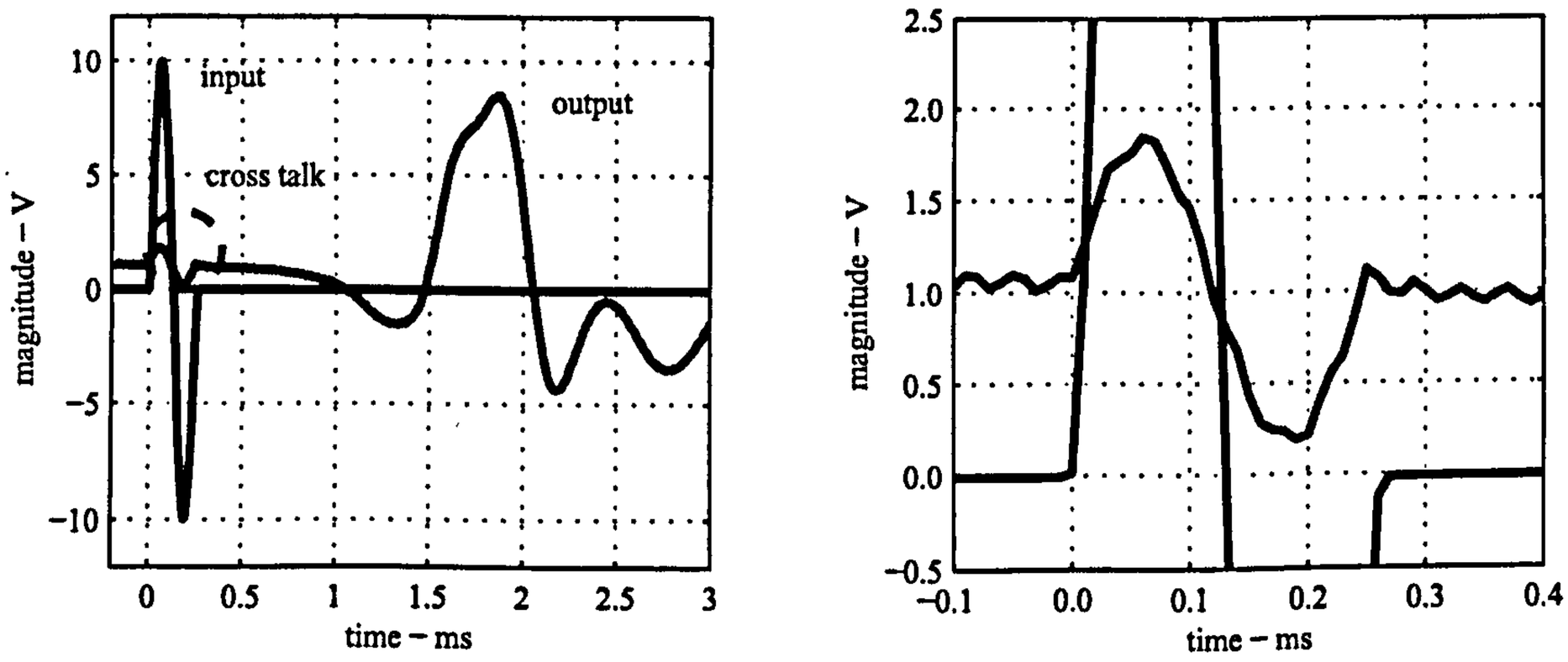

(a) example pulse signal

(b) cross-talk

Figure 2.14: Example of specific oscilloscope cross-talk noise for an input signal with an amplitude of 20V and a frequency of 4.0kHz.

Cross-talk, being a signal leakage between the transmitted and received signal channels, contaminates the received signal with the content of the transmitted signal. The noise caused by cross-talk is frequently in the same range of amplitude as the received signal and its influence is therefore a considerable source of error. This type of noise is not random in its nature. It mirrors the transmitted signal, except for a different amplitude and slight shift in phase. If the ratio between the transmitted

signal amplitude and that of the cross-talk is constant and known, b, as well as the phase shift, Δt, it is then possible to calculate the cross-talk signal component, $S_{ct}(t)$, and to subtract it from the received signal, $S_{out}(t)$,

$$S^*_{out}(t) = S_{out}(t) - S_{ct}(t) \quad \text{where} \quad S_{ct}(t) = bS_{in}(t - \Delta t) \tag{2.7}$$

where $S_{in}(t)$ is the transmitted signal and $S^*_{out}(t)$ is the received signal with the cross-talk noise removed.

After a careful analysis of some preliminary results, the cross-talk parameters were determined at $b = 1/(3.7 \times 10^4)$ and $\Delta t = 1/(\text{sampling rate})$. Using these parameters the cross-talk is numerically removed from the received signal. In figure 2.15(a) are given three examples of received pulse signals cross-talk. These signals were obtained using the same test set-up and sample and only the amplitude of the input signal was varied, at 20V, 10V and 5V. The equivalent filtered signals are presented in figure 2.15(b). In figure 2.15 is possible to confirm that the cross-talk noise is proportional to the input signal amplitude. It is also possible to confirm the efficiency of the proposed method of reducing the cross-talk in the received signals by a ratio of 10.

The proposed method of filtering cross-talk was generally applied to the results obtained in chapters 5 and 6, since all were obtained using the same oscilloscope equipment and hence all have been equally contaminated.

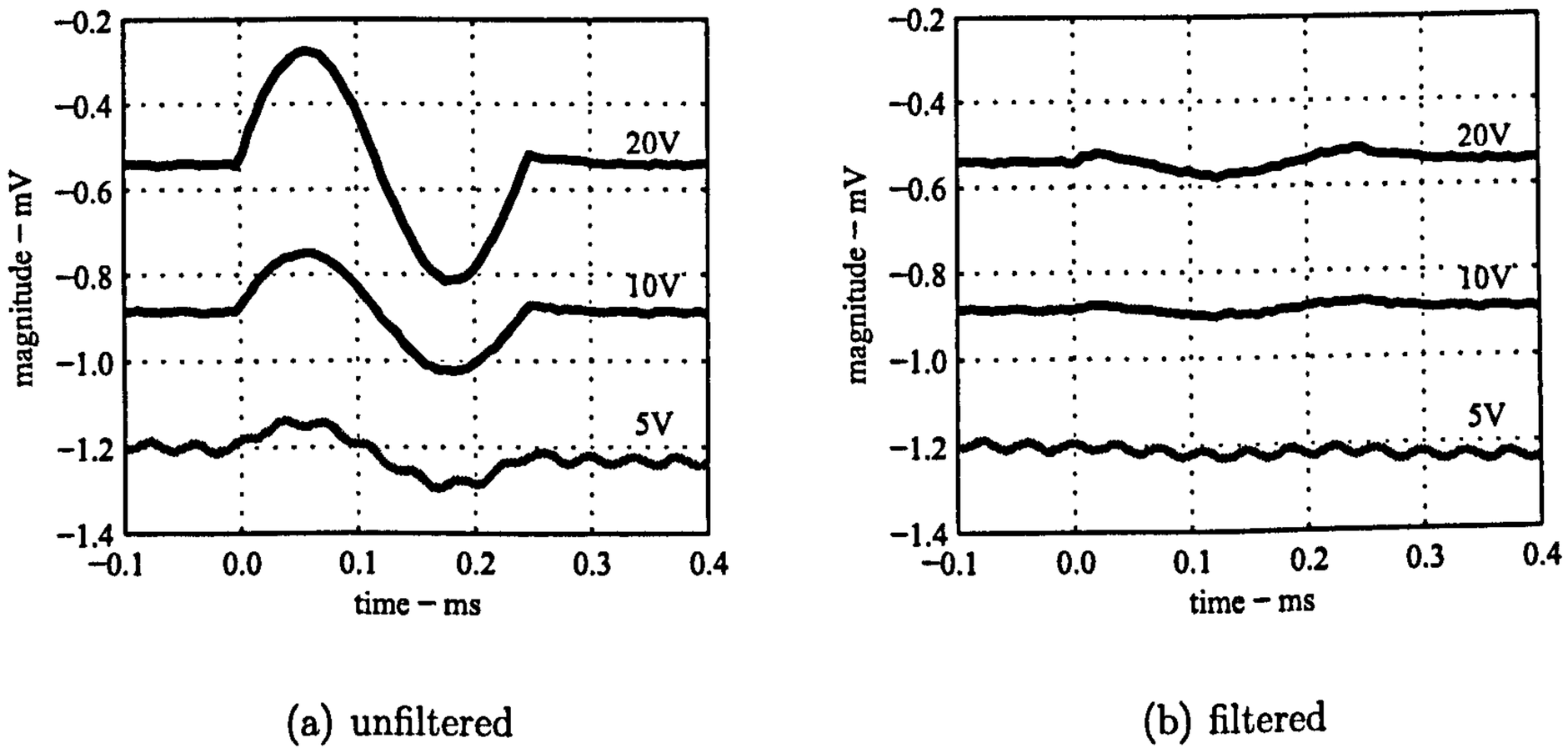

(a) unfiltered

(b) filtered

Figure 2.15: Example application of cross-talk filtering for pulse signals with central frequency of 4.0kHz and amplitudes of 20V, 10V and 5V.

Chapter 3

Theoretical Background

This chapter explores the theoretical concepts necessary to offer a better understanding of bender elements and soil sample dynamic systems. The mentioned theoretical concepts address basic dynamic mechanics. Wave propagation theory is at the basis of seismology studies and body vibration theory is most frequently used in structural analysis.

If the dynamic aspects of a mechanical system are analysed, it is necessary to distinguish between two important notions, each one describing a different aspect of body motion: wave and vibration.

> 'Vibration is an oscillation of the parts of a fluid or an elastic solid whose equilibrium has been disturbed.'
>
> 'Wave is a disturbance of the particles of a substance which may be propagated without net movement of the particles, as in the passage of undulating motion or sound.'
>
> *Concise Oxford English Dictionary*

In other words, vibration relates to the oscillation movement of a particle or body, and wave relates to the propagation of such disturbance along the body.

The use of bender elements to determine soil's shear stiffness makes use of wave propagation theory, explicit in equation 1.1. The application of equation 1.1 has its origins in the development of generic wave equations, (section 3.1). The application of the mentioned equation must assume a wave propagation context which might not be compatible with the bender element-soil system. Equation 1.1 is valid for bulk solids, (Podesta, 2002), which might not always be the case, depending on the tested sample geometry.

The wave and vibration theory presented in this chapter aim to describe some of the simpler relevant cases, for which the following mechanical assumptions need to be made:

- The studied properties are assumed to vary continuously with position in the medium, placing the present analysis in the discipline of continuum mechanics.
- The studied medium is assumed to have a constant and linear stress-strain behaviour, where the relationship between stress, τ_{ij}, and strain, γ_{ij}, is ruled by an elastic constant c_{ij}, enabling the general application of Hooke's law, $\tau_{ij} = \gamma_{ij} \cdot c_{ij}$.
- The studied medium is assumed to be a solid with constant elastic properties in all directions, i.e., it is an isotropic solid.

3.1 Planar Waves

The theory presented in this section considers planar wave propagation, which is a particular case of general wave radiation, where the wave properties are considered independent from the nature of the source. More general concepts of wave radiation are presented in section 3.6.

The concepts of strain and stress are addressed in order to bring them into context with the definition of the governing wave equations of the dynamic system.

3.1.1 Strain

Consider two points defining a three-dimensional body, point A with coordinates (x, y, z), and point B with coordinates $(x+\delta x, y+\delta y, z+\delta z)$. Now consider point A is displaced by (u, v, w) and point B by $(u+\delta u, v+\delta v, w+\delta w)$. Since the displacements of the two points are not equal, a strain is applied to the body. A two-dimension analogy, in an orthogonal plane x and y, is illustrated in figure 3.1.

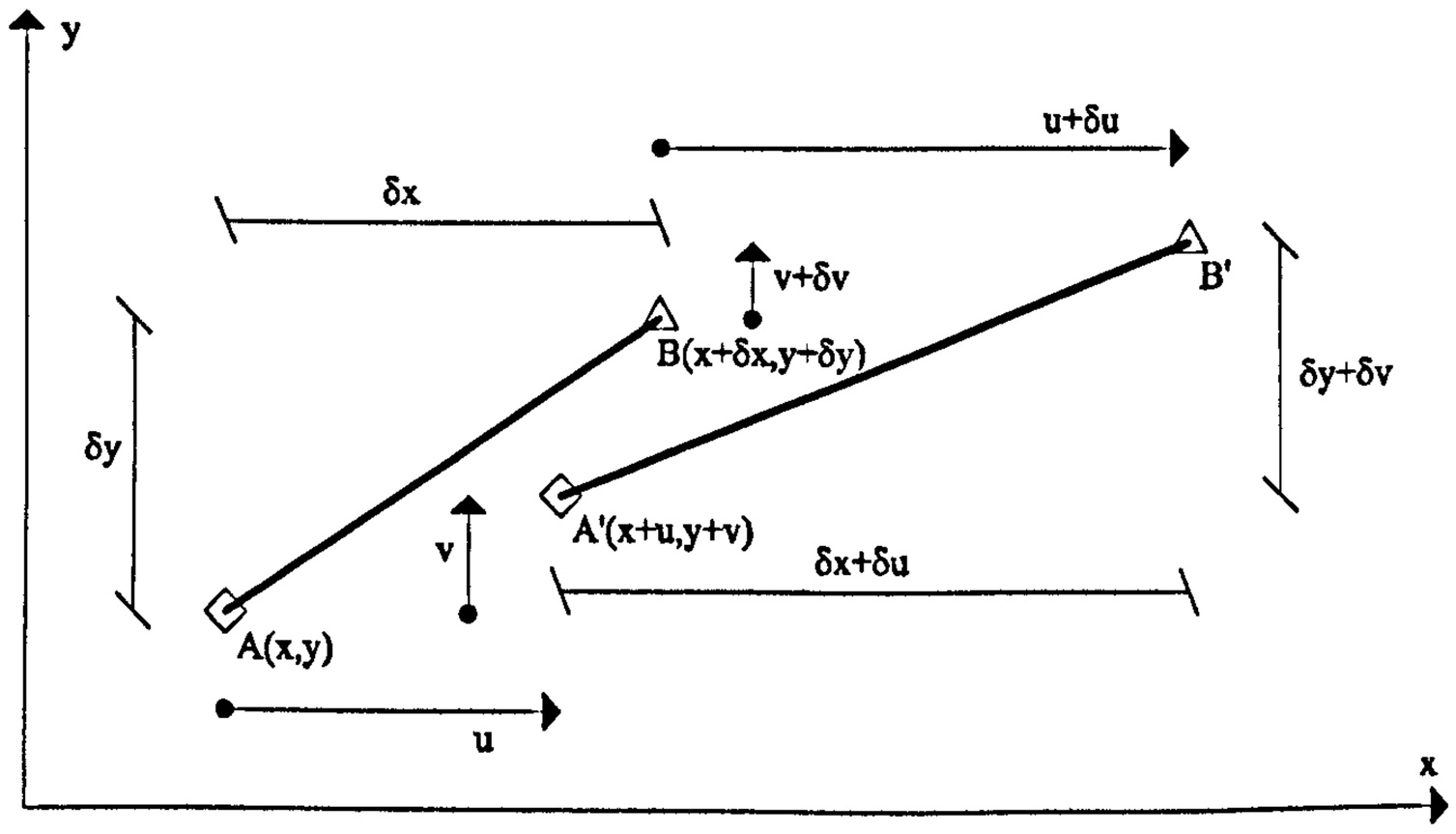

Figure 3.1: Two-dimension body strain.

If the terms of higher order are neglected, the displacement of point B is, according with Taylor's theorem, equivalent to:

$$\begin{aligned} u+\delta u &= u+\frac{\partial u}{\partial x}\cdot\delta x+\frac{\partial u}{\partial y}\cdot\delta y+\frac{\partial u}{\partial z}\cdot\delta z \\ v+\delta v &= v+\frac{\partial v}{\partial x}\cdot\delta x+\frac{\partial v}{\partial y}\cdot\delta y+\frac{\partial v}{\partial z}\cdot\delta z \\ w+\delta w &= w+\frac{\partial w}{\partial x}\cdot\delta x+\frac{\partial w}{\partial y}\cdot\delta y+\frac{\partial w}{\partial z}\cdot\delta z \end{aligned} \tag{3.1}$$

3.1.2 Stress

In its general form, nine components of stress are necessary to describe a force acting on a portion of area, (τ_{xx}, τ_{xy}, τ_{xz}, τ_{yx}, τ_{yy}, etc.). Each one is a linear function of six components of strain ($\frac{\partial u}{\partial x}$, $\frac{\partial v}{\partial y}$, $\frac{\partial w}{\partial z}$, etc), resulting in 54 elastic constants (e_{11}, e_{12}, etc) necessary to provide the complete elastic relationship between stress and strain of a solid volume. Because only six stress components are independent, ($\tau_{xy} = \tau_{yx}$, $\tau_{xz} = \tau_{zx}$, $\tau_{yz} = \tau_{zy}$), then only 36 elastic constants would be needed. Even so, according to Love (1944), from these 36 elastic constants, only 21 are co-independent and only them are need to be determined.

Since the assumption of isotropy is made, the number of necessary elastic constants can be reduced to two, λ and μ, known as Lamé's constants. μ is also known as shear modulus G. The relationship between Lamé's two elastic constants and three other well known elastic constants, Young's modulus E, bulk modulus K and Poisson's ratio ν is convenient.

$$\lambda = \frac{\nu E}{(1+\nu)(1-2\nu)}; \quad \mu = \frac{E}{2(1+\nu)}$$
$$E = \frac{\mu(3\lambda+2\mu)}{\lambda+\mu}; \quad \nu = \frac{\lambda}{2(\lambda+\mu)}; \quad K = \lambda + \frac{2}{3}\mu \tag{3.2}$$

The linear correlation between stress and strain, ruled by the elastic constants such as the ones presented by Lamé, are presented in equations 3.3 next.

$$\begin{aligned} \tau_{xx} &= \lambda\Delta + 2\mu \cdot \frac{\partial u}{\partial x}; & \tau_{yy} &= \lambda\Delta + 2\mu \cdot \frac{\partial v}{\partial y} \\ \tau_{zz} &= \lambda\Delta + 2\mu \cdot \frac{\partial w}{\partial z}; & \tau_{yz} &= \mu\left(\frac{\partial w}{\partial y} + \frac{\partial v}{\partial z}\right) \\ \tau_{zx} &= \mu\left(\frac{\partial u}{\partial z} + \frac{\partial w}{\partial x}\right); & \tau_{xy} &= \mu\left(\frac{\partial v}{\partial x} + \frac{\partial u}{\partial y}\right) \end{aligned} \tag{3.3}$$

The concept of cubical dilatation Δ, representing the volume variation with displacement, is useful to make the equations notation simpler.

$$\Delta = \frac{\partial u}{\partial x} + \frac{\partial v}{\partial y} + \frac{\partial w}{\partial z} \tag{3.4}$$

3.1.3 Equations of Motion

The equations of motion contain the basic relations between inertia forces, displacement, stiffness and time. They are necessary to understand and describe both wave and vibration theory.

Next is presented a version of the equation of motion best suited for handling the notation of planar wave propagation theory,

$$\begin{aligned} \rho \cdot \frac{\partial^2 u}{\partial t^2} &= (\lambda + \mu) \frac{\partial \Delta}{\partial x} + \mu \nabla^2 u \\ \rho \cdot \frac{\partial^2 v}{\partial t^2} &= (\lambda + \mu) \frac{\partial \Delta}{\partial y} + \mu \nabla^2 v \\ \rho \cdot \frac{\partial^2 w}{\partial t^2} &= (\lambda + \mu) \frac{\partial \Delta}{\partial z} + \mu \nabla^2 w \end{aligned} \tag{3.5}$$

∇ is the Laplace operator, expressed as:

$$\nabla = \sqrt{\left(\frac{\partial^2}{\partial x^2} + \frac{\partial^2}{\partial y^2} + \frac{\partial^2}{\partial z^2} \right)} \tag{3.6}$$

In equation 3.5 the only medium properties referred to are its density and elastic constants, ρ, λ and μ. Damping characteristics and external forces have been left out for now, making the equations independent from the source of the disturbance,

where the initial force or displacement is applied. Other versions of the equation of motion, best suited for the study of wave radiation near its source and particle and body vibration are presented in sections 3.6 and 3.8 respectively, including the mentioned damping and external forces.

3.1.4 Wave Equation

In order to express the wave equations in a practical and simple notation, one scalar potential function, ϕ, and a vector potential function, ψ, are used. Their relation with the displacement components, u, v and w, is given in equations 3.7 and 3.8.

$$\begin{aligned} u &= \frac{\partial \phi}{\partial x} + \frac{\partial \psi_z}{\partial y} - \frac{\partial \psi_y}{\partial z} \\ v &= \frac{\partial \phi}{\partial y} + \frac{\partial \psi_x}{\partial z} - \frac{\partial \psi_z}{\partial x} \end{aligned} \tag{3.7}$$

$$w = \frac{\partial \phi}{\partial z} + \frac{\partial \psi_y}{\partial x} - \frac{\partial \psi_x}{\partial y}$$

$$\nabla^2 \phi = \frac{\partial u}{\partial x} + \frac{\partial v}{\partial y} + \frac{\partial w}{\partial z} \tag{3.8}$$

In equations 3.9 and 3.10, is expressed, in rectangular coordinate, the wave propagation in an unbounded elastic solid,

$$\nabla^2 \phi = \frac{1}{{c_d}^2} . \frac{\partial^2 \phi}{\partial t^2} \tag{3.9}$$

$$\nabla^2 \psi_i = \frac{1}{{c_t}^2} \cdot \frac{\partial^2 \psi_i}{\partial t^2}, \quad i = x, y, z \tag{3.10}$$

where c_d and c_t are the characteristic compression and shear wave velocities given

by:

$$c_d{}^2 = \frac{\lambda + 2\mu}{\rho} \tag{3.11}$$

$$c_t{}^2 = \frac{\mu}{\rho} \tag{3.12}$$

ρ is the density of the medium and λ and μ are Lamé's elastic constants, presented before in equation 3.2.

Equation 3.12 is identical to equation 1.1, which has been at the base of the dynamic study of soil using bender elements. It is then possible to start describing equation 1.1 integrated in its theoretical context.

3.1.5 Planar Waves Types

Two simple types of planar waves, dilatational and distorsional, can be said to propagate in an infinite medium, (Graff, 1975). Equations 3.11 and 3.12 describe these two distinct waves. One type, represented by potential function ϕ, propagates with a characteristic velocity c_d, and can also be described as a longitudinal or compressional wave. This type of planar wave is also known, in seismic notation, as a P wave. The other type of planar wave, represented by potential function ψ, propagates with a characteristic velocity c_t and can be described as a transversal or shear wave. In seismic notation, this type of wave is also called S wave.

Longitudinal waves are characterised by particle oscillation in the same direction as the wave propagation. Transversal waves are characterised by particle oscillation perpendicular to the direction of wave propagation, (figures 3.2(a) and 3.2(b)).

There is a key difference between waves propagating in elastic fluids and solids. Perfect fluids have no shear stiffness, $\mu = 0$, and therefore only P waves are able to propagate in them, unlike in elastic solids, where both P and S waves are able to propagate.

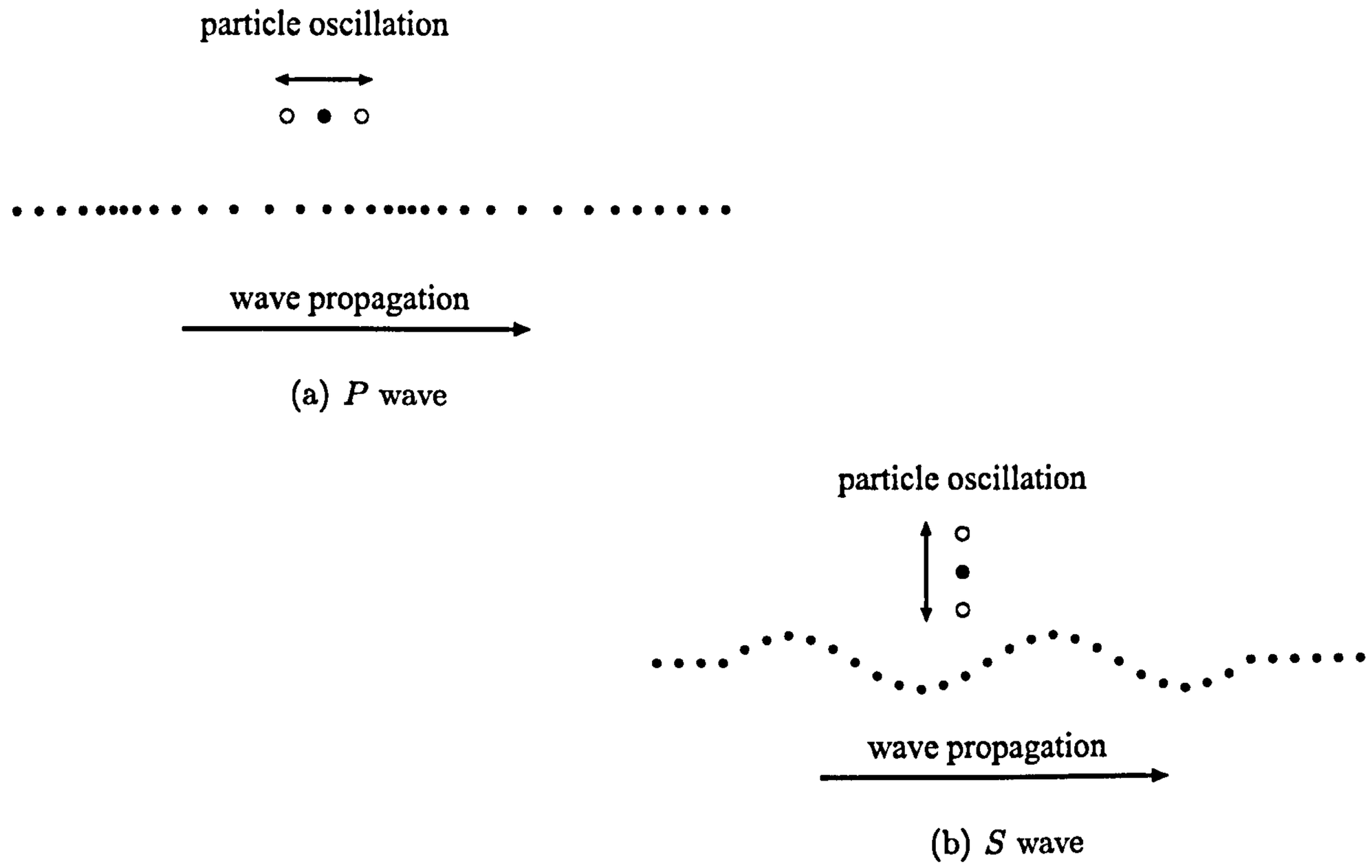

Figure 3.2: P and S wave propagation, and corresponding directions of particle oscillation.

3.1.6 Orthogonally Polarised Shear Waves

When dealing with anisotropic media, it is useful to divide plane transversal waves into two subtypes, each capable of propagating independently, according to their polarisation. These subtypes or modes are known, in seismology terms, as SV and SH waves. The particle oscillation for each mode is orthogonal to each other, as well as to the direction of wave propagation. Both modes travel with velocity c_t, which is constant along any direction in an isotropic solid. It can also be said that with a SV wave mode the particles oscillate within the vertical plane; and with a SH wave mode the particles oscillate within the horizontal plane.

Together with P waves, SV and SH form a orthogonal, three-dimension plane wave system, capable of describing other, more complex, types of wave.

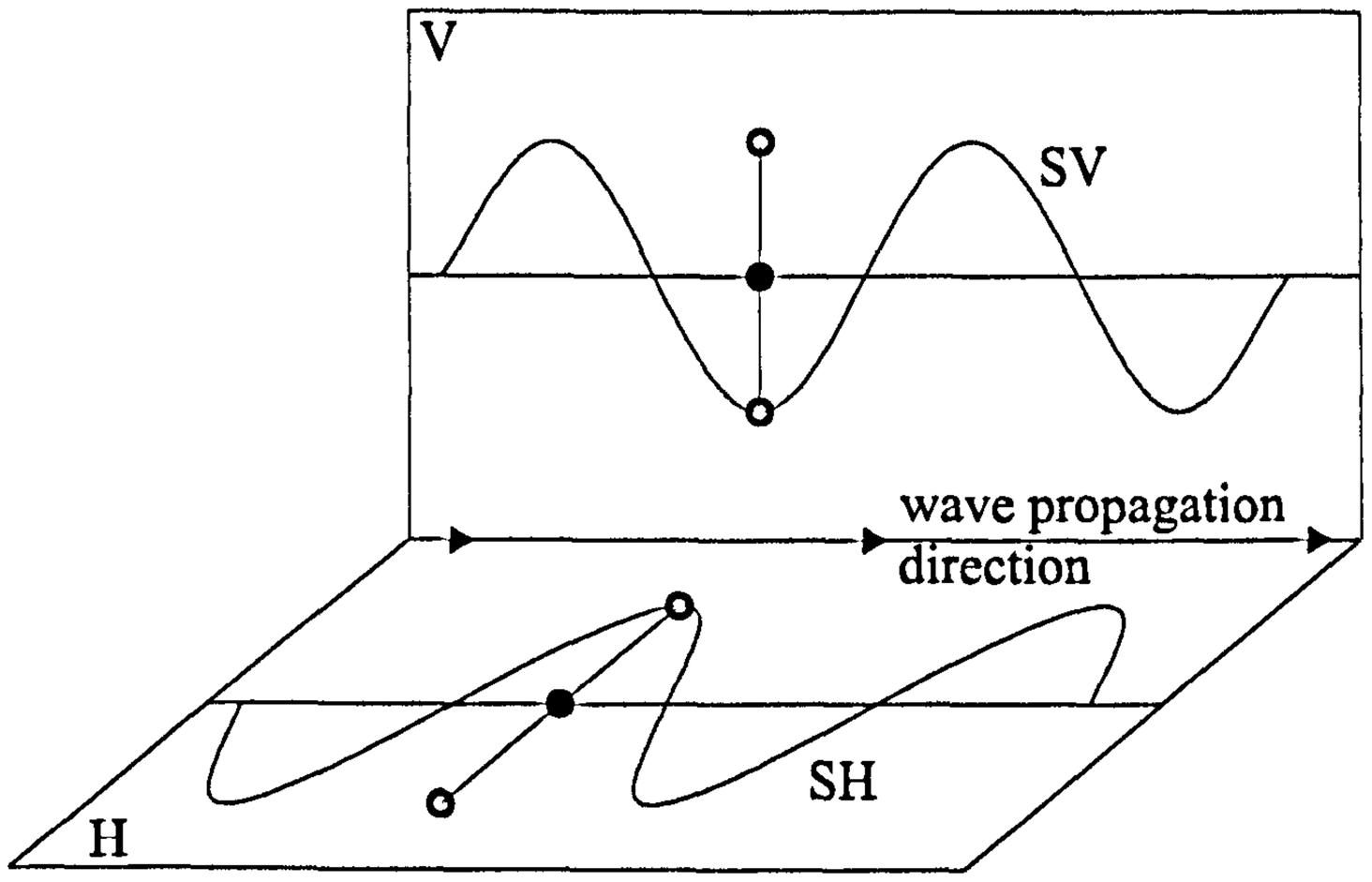

Figure 3.3: *SV* and *SH* transversal wave types.

3.1.7 Wave Propagation

After a body, or part of a body, has been disturbed either by the application of a displacement or stress, such disturbance is then propagated along the body, away from its source. The properties of how this propagation takes place are a function of both the initial disturbance properties and of the body properties, in which the propagation takes place. When it comes to describe the initial disturbance it is necessary to introduce the concept of wave source and wave front; and when it comes to describing the way in which the wave propagates it is necessary to introduce the concepts of wave reflection and waveguide.

The assumption of a linear elastic medium enables the application of linear superposition. This assumption has the potential of permitting the description of periodic disturbances as the sum of time-harmonic waves, through the use of a Fourier series. Pulse disturbances can also be decomposed into the sum of harmonic waves through the use of Fourier integrals even though not as efficiently, (Graff, 1975).

The nature of the wave source influences directly the shape of the propagating wave front. The wave front is an imaginary surface at which a discontinuity between the particles that have already been disturbed and the particles that are still at rest

is located. Considering geometric simple wave fronts with spheric, cylindrical and plane shapes, it is easy to associate these to point, line and surface wave sources, respectively.

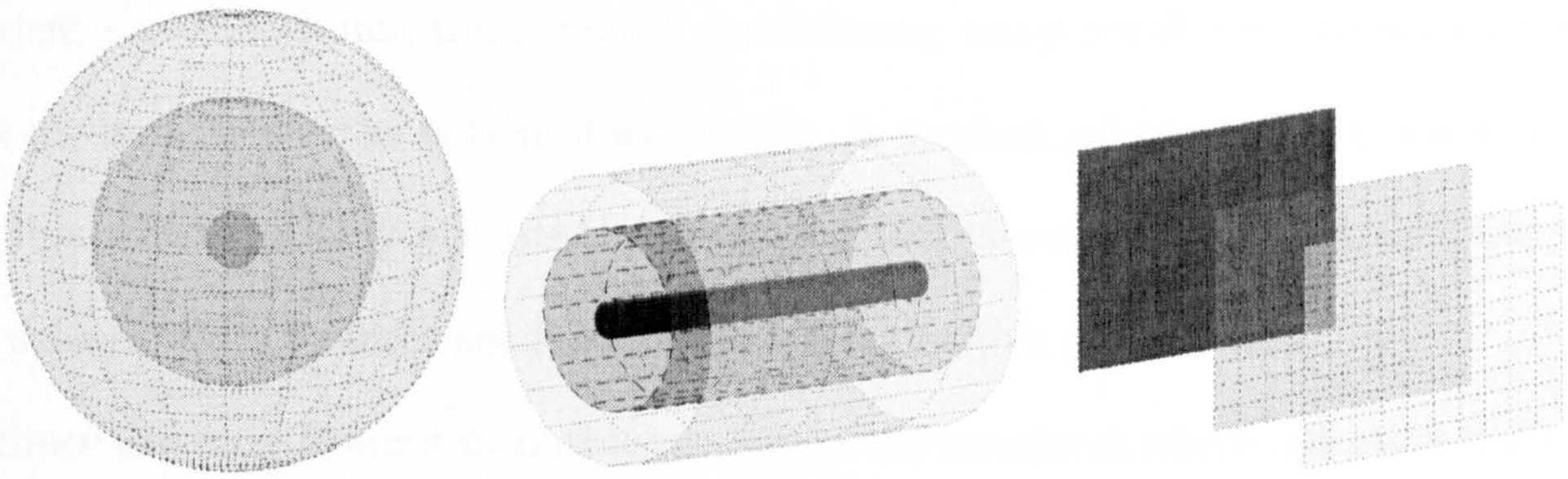

(a) spheric wave front (b) cylindrical wave front (c) planer wave front

Figure 3.4: Wave sources and corresponding wave fronts.

In practice it is difficult to find wave sources that are exact matches of theoretical points, lines or planes, like the ones described so far, but at a certain distance the wave sources can be perceived as such. The radiation of a wave away from its source is a complex problem from which the planar wave propagation mentioned here is a particular case, also known as the far-field. Wave propagation near its source is a dispersive phenomenon, where wave components travel at different velocities at different frequencies and at different distances from the source. This problem is addressed with more detail in section 3.6.

3.2 Waveguides

Wave propagation in a bounded medium is influenced by the reflection of wave components that encounter the boundaries. Considering the system to have a linear behaviour, reflected wave components do not interfere, in theory, with the non-reflected ones, nevertheless they might be perceived as if they did, when observing the composed wave front. For example, when analysing the pressure distribution

at any given cross-section of the waveguide, the observed stress is the sum of all the present wave component, and despite their independence of each other, it might not be possible to distinguish between them. The boundaries of a medium guide incident waves back into the medium, conditioning the general wave propagation in that medium, hence the notion of waveguide. A mechanical waveguide is a bounded medium which not only permits the propagation of vibration waves but also, due to the present of its boundaries, influences and guides this propagation.

Since the wave fronts are continuous, as are the interfaces where reflection occurs, it is not practical to calculate the resulting wave pressure in terms of each reflected and non-reflected component at each point of the surface and wave front.

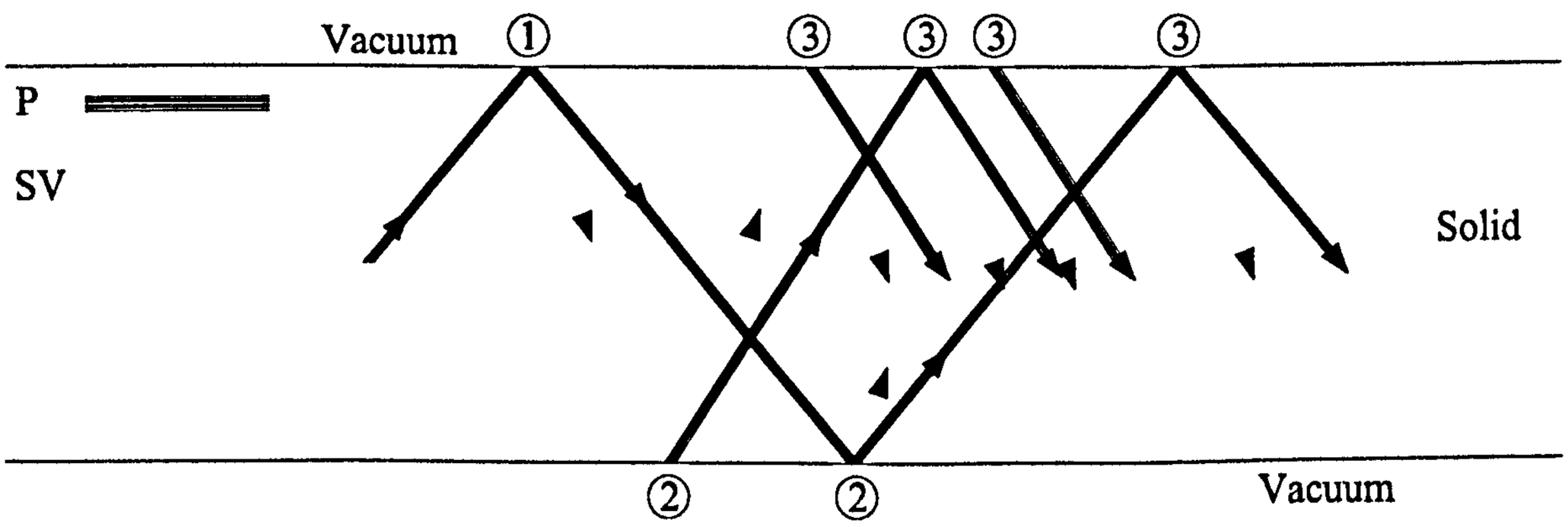

Figure 3.5: P wave multiple reflection inside a solid with finite cross-section.

This problem becomes even more complex if the body has a finite cross-section where a reflected wave is able to be reflected back and forwards between surfaces as it propagates. One P wave component propagating along a thin plate can produce up to 8 different wave components after 3 reflections. For each wave component, such as the one pictured in figure 3.5, it is convenient to consider not only its actual 'zig-zag' propagation directions, but also the general propagation direction along the axis of the waveguide.

3.3 Wave Reflection

When a wave propagating inside a body meets an obstacle, defined by a boundary between two different media, its interaction with this interface causes the original wave to change. The processes through which these changes take place are called wave reflection and refraction. Reflection addresses the case of an incident wave energy which is returned from the boundary back into the body. Refraction addresses the case of an incident wave energy transferred into the other medium. Diffraction is a particular case of wave disturbance, where the boundary or obstacle is smaller than the wave front. In this case some of the wave energy is reflected, some energy is refracted and some remains unaltered. The most relevant of the mentioned processes, for the analysis of a bender element test system, is the wave reflection, since it is concerned with the transformations of waves within one continuous body.

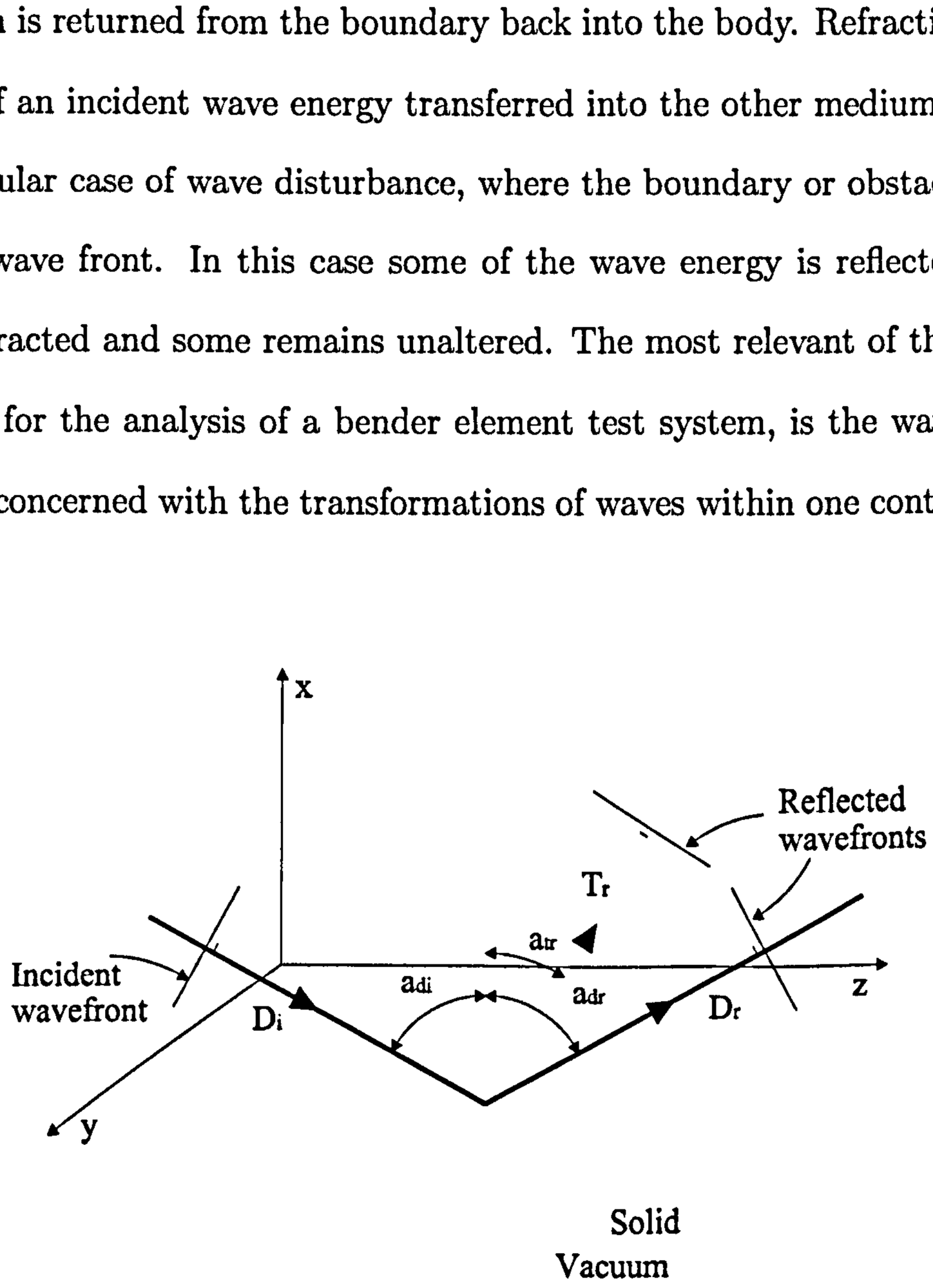

Figure 3.6: P wave reflection from a solid-vacuum boundary.

Wave reflection is a complex process that varies with the nature of the media at the interface as well as with the nature of the incident waves. The boundary, or interface, between two media causes different reflection and refraction phenomena

of incident waves, depending on the nature of each of the two media. Possible combinations of media defining a boundary between them are possible. Considering that a solid medium is capable of propagating P and S waves, a fluid medium is capable of propagating P waves and in vacuum no wave propagation is possible, then each case presents a different solution for the reflection problem.

The relevant cases for the present study involve a boundary with an interface between solid and either fluid or vacuum media. In most cases, laboratory soil samples, studied in apparatus such as triaxial cells and oedometers, are surrounded by a fluid such as water or oil, and raped by a latex membrane. In other cases, the samples can be tested directly on a bench for which the consideration of a solid and vacuum interface is appropriate. For either case the refracted waves are disregarded and only the reflected waves are considered. The solid-vacuum interface is enough for a first description of reflection of this type.

3.3.1 Solid-Vacuum Interface

Consider the case of wave reflection at the interface between a solid body and a vacuum medium, i.e., a surface of the solid medium, such as pictured in figure 3.6. This case is simpler than the more general solid-solid interface and can be applied to cases where the refracted part of the wave does not interfere with the reflected one, which is commonly assumed when testing soils samples in different apparatus.

Three simple independent planar wave types, P, SV and SH, are each reflected differently from a body surface. In order to interpret the reflection phenomenon using the same notation as the one used in wave equations 3.9 and 3.10, the boundary conditions at the interface must be satisfied. The normal and parallel stresses must be zero, $\tau_{xx} = \tau_{xy} = \tau_{xz} = 0$ at $x = 0$. The axes definition are presented in figure 3.6. These boundary conditions force a particular solution on wave equations, as

presented by the following equations.

$$\phi = \phi_0(x) \cdot \exp(-jk_0 z) \cdot \exp(j\omega t) \tag{3.13}$$

$$\psi_i = \psi_{i0}(x) \cdot \exp(-jk_0 z) \cdot \exp(j\omega t) \tag{3.14}$$

The wave equations solution take the form:

$$\phi_0(x) = D_i \exp(-jk_d x) + D_r \exp(+jk_d x) \tag{3.15}$$

$$\psi_{i0}(x) = T_i \exp(-jk_t x) + T_r \exp(+jk_t x) \tag{3.16}$$

$$i = x,\ y\ or\ z$$

where

$$k_d{}^2 = \left(\frac{\omega}{c_d}\right)^2 - k_0{}^2 \tag{3.17}$$

$$k_t{}^2 = \left(\frac{\omega}{c_t}\right)^2 - k_0{}^2 \tag{3.18}$$

D_i and D_r are the amplitudes of the incident and reflected P wave, and T_i and T_r are the amplitudes of the incident and reflected S wave; k_d, k_s and k_0 are constants of wave propagation and will be mentioned later in the development of particular solutions of the wave equations, and ω is the circular frequency.

3.3.2 P Wave Reflection

A P wave has a complex reflection from a solid-vacuum interface, as it is reflected as both P and S waves. According to figure 3.6, and considering the particle movement due to the incident P wave to be in the xz plane, then the reflected waves will also

only have particle movement in the same plane xz. In the present context, SV waves are assumed to have particle polarisation in the xz plane and that SH have particle polarisation in the y direction.

Three properties must be determined for each of the reflected wave components, the angle of reflection, the phase change and the amplitude. The angles of reflection, a_{dr} and a_{tr}, are the angles the reflected wave components propagation direction make with a plane orthogonal to the interface. Their relationship with the incidence angle, a_{di}, is:

$$a_{dr} = a_{di} \tag{3.19}$$

$$\sin a_{tr} = \frac{c_t}{c_d} \cdot \sin a_{di} \tag{3.20}$$

where a_{di}, a_{dr} and a_{tr} are the incident P wave, reflected P wave and reflected SV wave angles respectively.

Phase change describes the delay between oscillation movements of different wave components. The phase change that takes place between the incident P wave and the reflected SV wave, according to equations 3.19 and 3.20, can be either π for $D_r/D_i > 0$, or takes another value function of the medium's Poisson ratio ν, and the angle of incidence a_{di}. The phase change between the incident P wave and the reflected SV wave is zero for all cases.

The amplitude of the reflected waves is again a function of a_{di} and ν. An example of the reflected wave amplitude variation can be seen in figure 3.7, obtained as a particular solution of equations 3.15 and 3.16, where $T_i = 0$.

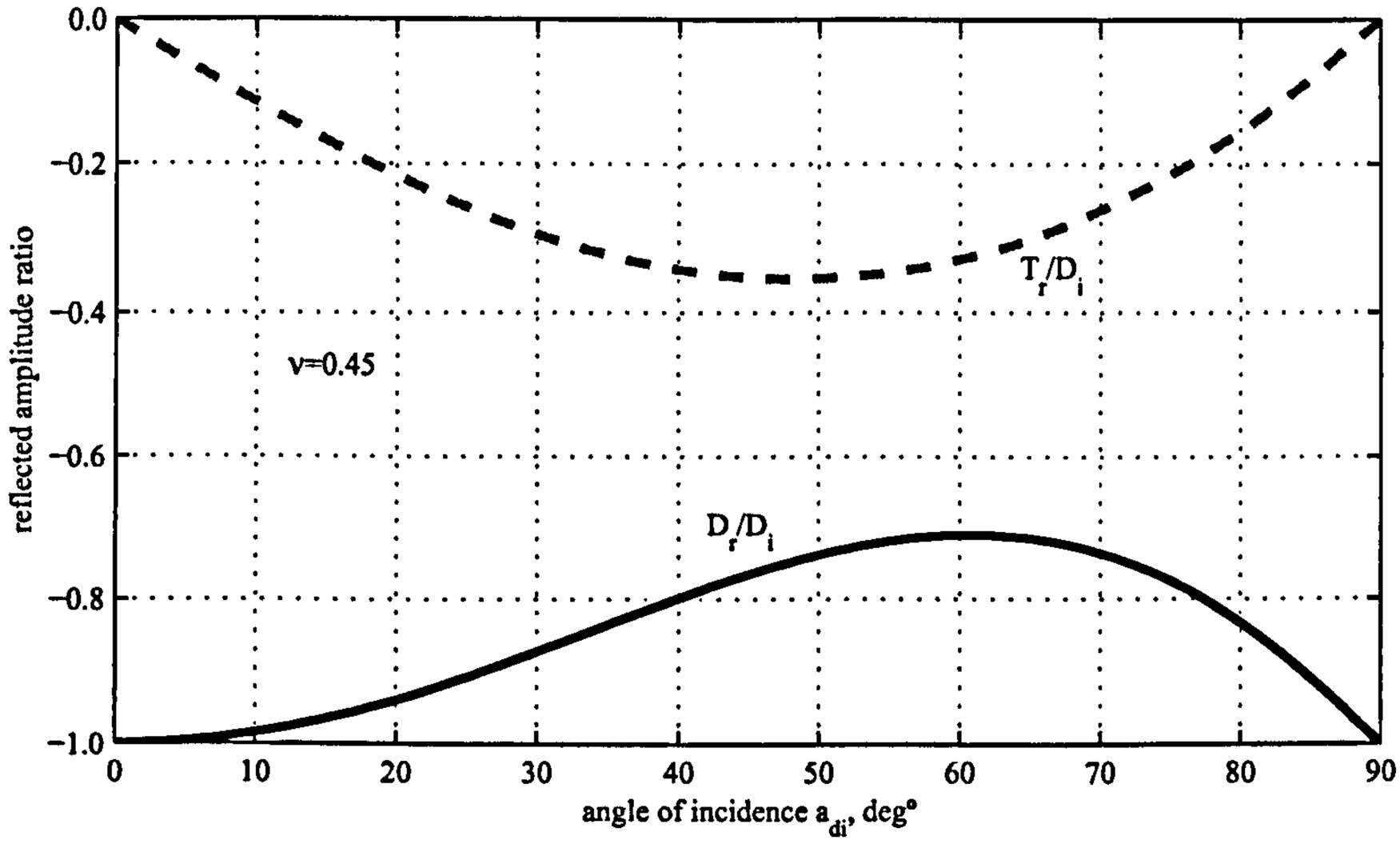

Figure 3.7: Reflected P and S waves amplitude from a incident P wave, at a solid-vacuum interface.

3.3.3 S Wave Reflection

The properties of the reflection of S waves from a solid-vacuum interface varies according to the S wave polarisation. The reflection of SH waves is the most simple of the three plane wave components, they are reflected as SH waves with the same horizontal polarisation and a symmetric incident angle of $a_{tr} = a_{ti}$. Besides, the reflected SH waves have the same phase and amplitude as the incident SH waves. The SV waves, with particle oscillation in the xz plane, are reflected into SV and P wave components. The reflected SV wave component has a symmetric angle of the incident wave, $a_{tr} = a_{ti}$. The reflected P wave component angle, a_{dr}, can be obtained using equations 3.19 and 3.20. The phase change between the incident SV wave and the reflected P and SV waves, as with the reflection of P waves, can either be π or 0, depending on the medium's Poisson ratio and the angle of incidence. The amplitudes of the reflected waves are determined by a particular solution of equations 3.15 and 3.16, making $D_i = 0$.

It is now possible to obtain values of reflected wave angles of $a_{dr} < 0$, according

to equations 3.19 and 3.20, using incident wave angles between 0^o and 90^o. In such cases, the reflected P waves do not behave as longitudinal waves, but as surface waves, which adds another degree of complexity to the wave reflection phenomenon.

3.3.4 Surface Waves

A surface wave is a wave that propagates along the surface of a medium. It is characterised by an exponential decrease in amplitude with distance from the surface. Even if the wave source is not at the body's surface, or close to it, it is also possible to obtain surface waves from the reflection of P and SV waves within specific ranges of incident angles. SH waves can also be reflected into surface waves, known as Love's waves.

Rayleigh waves, theoretically predicted by Lord Rayleigh in 1885, (Rayleigh and Lindsay, 1945), are surface waves which propagate along a free surface of an elastic medium, such as the interface between an elastic solid medium and vacuum. This type of surface wave is well known in the study of seismic phenomena, (Aki and Richard, 2002). It is characterised by a particular velocity of propagation, c_R, lower than the characteristic shear wave velocity, c_t, of the medium. The particle oscillations are elliptical and have relatively high amplitudes, which decays exponentially with distance from the surface.

A particular characteristic of the particle oscillation movement of this type of surface wave is its retrograde elliptical motion at the surface, pictured as a clockwise movement in figure 3.8. At depths of more than $x > \Lambda/5$ an opposing prograde movement of the particles can be observed, where *Lambda* is the wavelength. The value of Rayleigh wave propagation velocity, c_R, can be obtained with a good approximation as a function of ν and c_t, as given in equation 3.21, (Achenbach, 1973).

$$c_R = \frac{0.862 + 1.14\,\nu}{1 + \nu} \cdot c_t \tag{3.21}$$

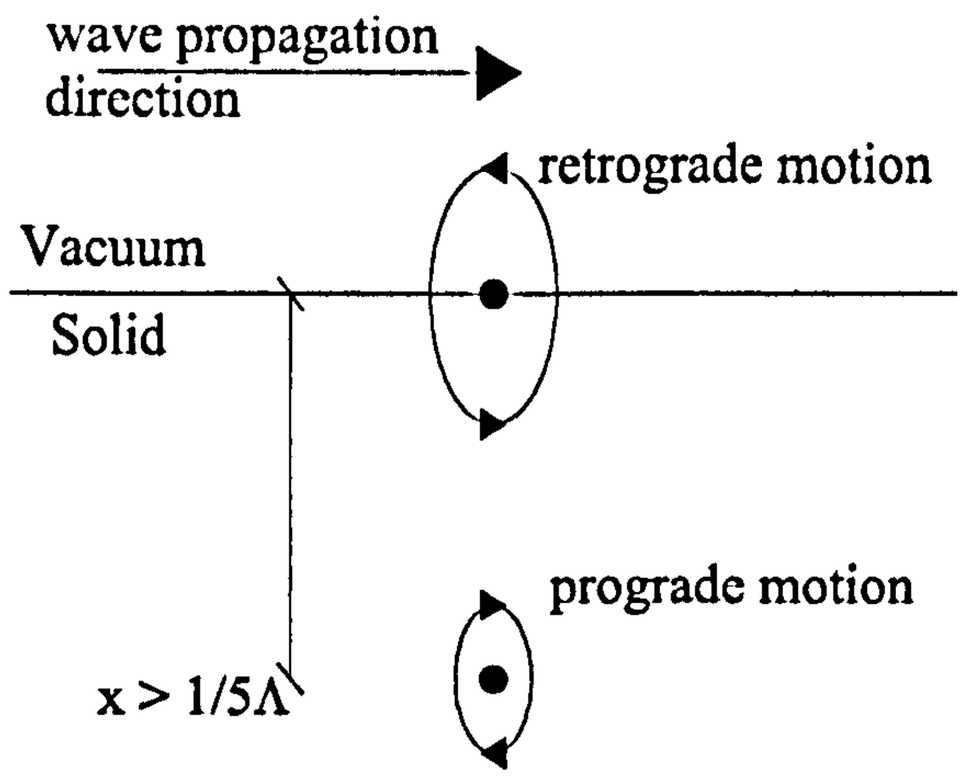

Figure 3.8: Particle motion of Rayleigh surface wave.

3.4 Modes of Wave Propagation

The pressure distribution in a cross-section of a simple waveguide, such as a layer of an homogeneous elastic solid medium, due to the propagation of a mechanical wave can be described as the sum of simple characteristic pressure distribution cases. Each one of this cases corresponds to a mode of propagation.

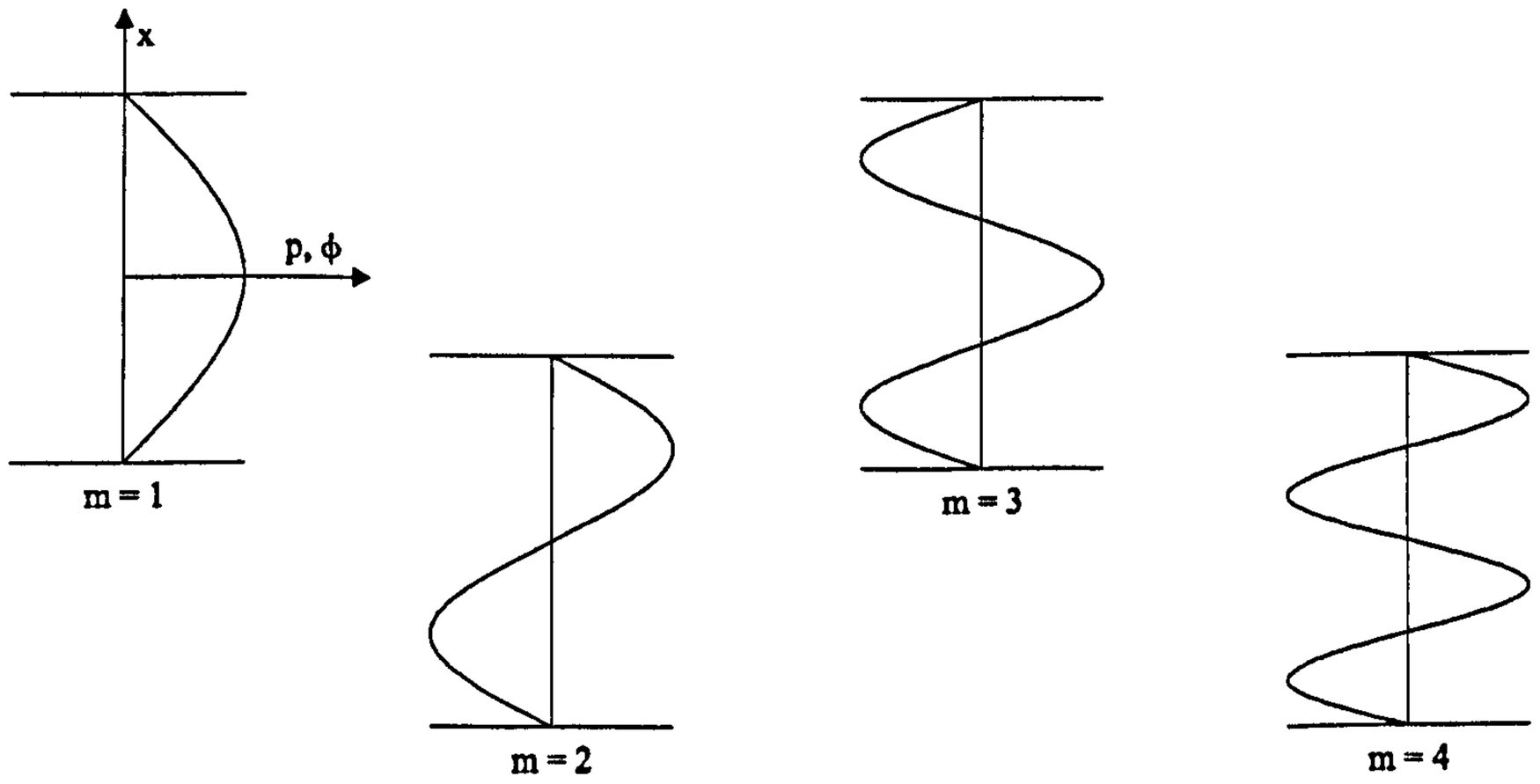

Figure 3.9: Simple cases of pressure distribution along the cross-section of a layer of fluid in vacuum.

In figure 3.9 are pictured four simple pressure distribution cases, in a cross-section of a fluid layer surrounded by vacuum. The odd modes, $m = 1$ and $m = 3$, have a symmetric pressure distribution, and the modes $m = 2$ and $m = 4$ have an asymmetric pressure distribution.

The modes of pressure distribution presented in figure 3.9 are also known as fundamental modes. They can be used to decompose less regular pressure distributions, in the same way as with a Fourier or Taylor series.

3.4.1 Continuous Waves in Solid Cylinders

The theoretical analysis presented is concerned with infinitely long solid cylinders. The study of wave propagation grows exponentially more difficult with body geometry increased complexity. Even for simple cases such as square cross-sections bar, the handling of the general wave equations is much more difficult than for circular cross-section, (Redwood, 1960). Numerical solutions often are the only suitable tool to handle complicated analysis. Fortunately, simple bounded media such as plates and cylinders can be analytically modelled with reasonable analytical effort. Even though the analysis of cylinders is not as simple as the analysis of plates, it still benefits from the symmetry about its axis.

It is an advantage that bender elements are often used with soil samples with cylindrical shapes. The expression of the wave equations in cylindrical coordinates z, r and θ, enables their simplification for particular waves with a symmetry about the z axis. This simplification also makes cylindrical waveguides a well documented case of wave propagation, (Fan *et al.*, 2003).

The equations describing the propagation of an harmonic wave along the axis of an infinitely long cylinder of a solid medium can now also be expressed in cylindrical

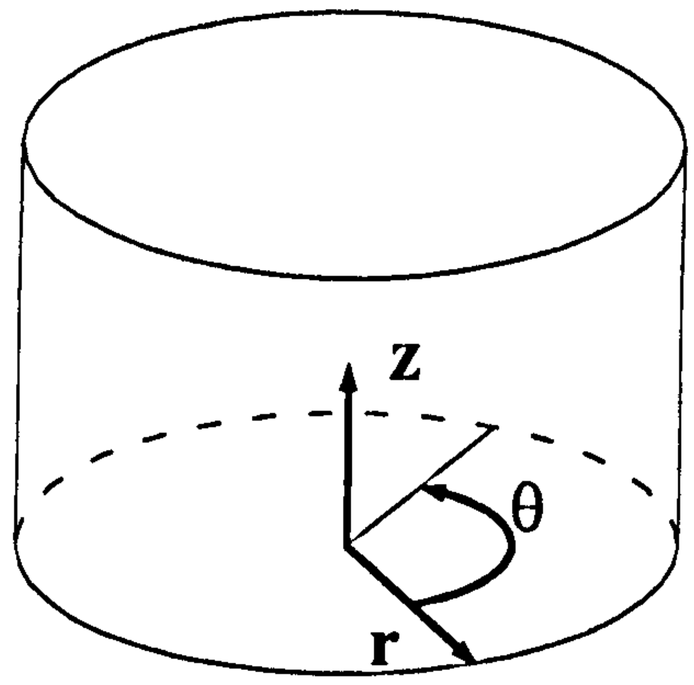

Figure 3.10: Cylindrical axis system.

coordinates. The correspondent displacement equations of motion are:

$$\nabla^2 u - \frac{u}{r^2} - \frac{2}{r^2}\frac{\partial v}{\partial \theta} + \frac{1}{1-2\nu}\frac{\partial \Delta}{\partial r} = \frac{1}{{c_t}^2}\frac{\partial^2 u}{\partial t^2} \tag{3.22}$$

$$\nabla^2 v - \frac{v}{r^2} - \frac{2}{r^2}\frac{\partial u}{\partial \theta} + \frac{1}{1-2\nu}\frac{1}{r}\frac{\partial \Delta}{\partial \theta} = \frac{1}{{c_t}^2}\frac{\partial^2 v}{\partial t^2} \tag{3.23}$$

$$\nabla^2 w + \frac{1}{1-2\nu}\frac{\partial \Delta}{\partial z} = \frac{1}{{c_t}^2}\frac{\partial^2 w}{\partial t^2} \tag{3.24}$$

∇^2 is the Laplace operator, and Δ the volumetric dilatation, now also expressed in cylindrical coordinates:

$$\nabla^2 = \frac{\partial^2}{\partial r^2} + \frac{1}{r}\frac{\partial}{\partial r} + \frac{1}{r^2}\frac{\partial^2}{\partial \theta^2} + \frac{\partial^2}{\partial z^2} \tag{3.25}$$

$$\Delta = \frac{\partial u}{\partial r} + \frac{1}{r}\left(\frac{\partial v}{\partial \theta} + u\right) + \frac{\partial w}{\partial z} \tag{3.26}$$

The relation between stress and strain is now expressed as:

$$\tau_r = \lambda\Delta + 2\mu\frac{\partial u}{\partial r} \tag{3.27}$$

$$\tau_{r\theta} = \mu\left[\frac{1}{r}\left(\frac{\partial u}{\partial \theta} - v\right) + \frac{\partial v}{\partial r}\right] \tag{3.28}$$

$$\tau_{rz} = \mu\left(\frac{\partial u}{\partial z} + \frac{\partial w}{\partial r}\right) \tag{3.29}$$

Potential functions ϕ and ψ are useful to describe displacements in z, r and θ, as was shown in equations 3.7 and 3.8. The scalar potential ϕ and vector potential component ψ_z enable the use of uncoupled equations 3.30 and 3.31.

$$\nabla^2\phi = \frac{1}{{c_l}^2}\frac{\partial^2\phi}{\partial t^2} \tag{3.30}$$

$$\nabla^2\psi_z = \frac{1}{{c_t}^2}\frac{\partial^2\psi_z}{\partial t^2} \tag{3.31}$$

Still, the remaining vector potential components ψ_r and ψ_θ, need to be determined as a pair of coupled equations.

$$\nabla^2\psi_r - \frac{\psi_r}{r^2} - \frac{2}{r^2}\frac{\partial\psi_\theta}{\partial\theta} = \frac{1}{{c_t}^2}\frac{\partial^2\psi_r}{\partial t^2} \tag{3.32}$$

$$\nabla^2\psi_\theta - \frac{\psi_\theta}{r^2} - \frac{2}{r^2}\frac{\partial\psi_r}{\partial\theta} = \frac{1}{{c_t}^2}\frac{\partial^2\psi_\theta}{\partial t^2} \tag{3.33}$$

In order to proceed with the handling of the wave equations, it is necessary to introduce boundary conditions according to the geometry and nature of the waveguide. Logically, the boundary conditions are concerned with the surface of the cylindrical waveguide, for which a constant value of radius $r = a$ is assumed. The cylindrical surface defines an interface between a solid medium and vacuum and is free of tension, therefore $\tau_r(a) = \tau_{r\theta}(a) = \tau_{rz}(a) = 0$.

3.5 Wave Propagation in a Solid Cylinder

An infinitely long solid cylinder waveguide has three different families of wave propagation modes, that can be used to describe harmonic wave propagation along the main axis z. The fundamental modes of wave propagation are either longitudinal, torsional or flexural, as pictured in figure 3.11.

Concerning the symmetry of the proposed fundamental modes of wave propaga-

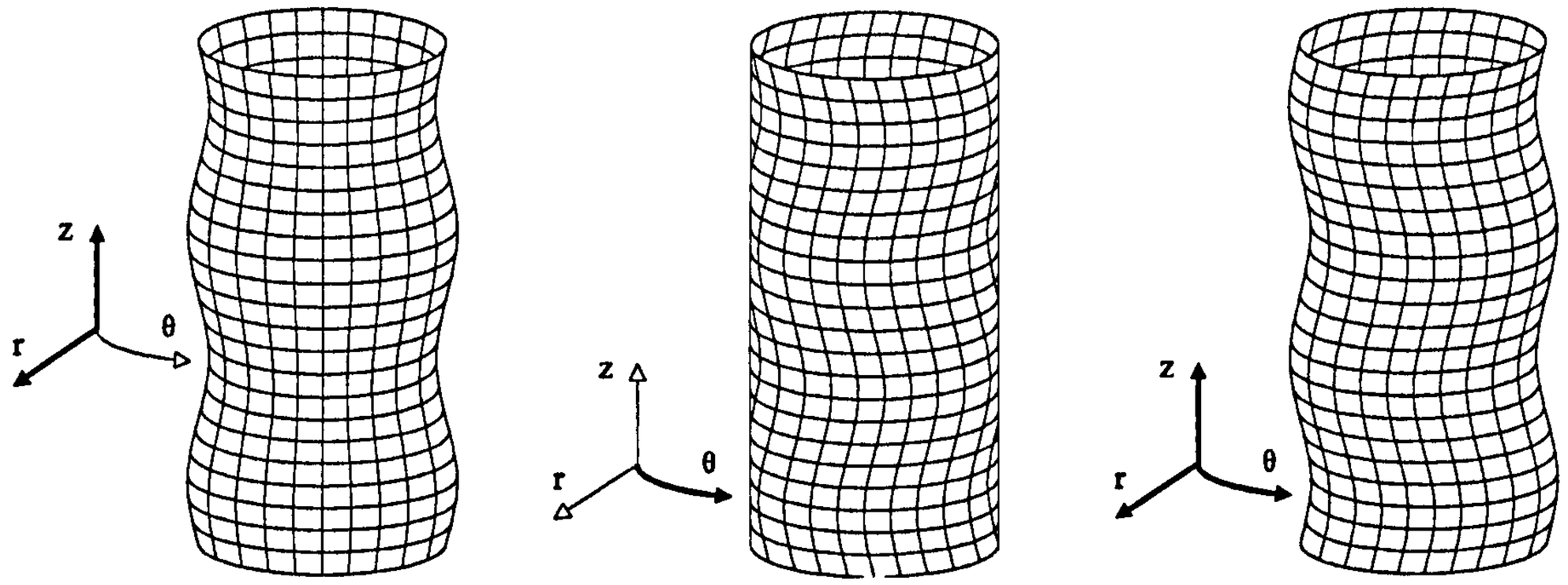

(a) longitudinal (b) torsional (c) flexural

Figure 3.11: Fundamental modes of wave propagation in a cylinder waveguide.

tion, the longitudinal and torsional modes are symmetric about the cylinder main axis and and the flexural modes are asymmetric.

Each type of mode of wave propagation has a specific set of wave equations, generally obtained by simplifying the general wave equations 3.30 to 3.33. Applying each mode properties to the manipulation of the wave equations leads to the specific solution in the form of a characteristic frequency equation.

3.5.1 Longitudinal Modes of Propagation

Longitudinal modes of wave propagation describe waves with symmetry about the z axis that are independent from θ, making $\frac{\partial}{\partial\theta} = 0$. A schematic graphic representation is given in figure 3.11(a).

The solution of the wave equations is a complex and time consuming process, thus only a summarised version of the condensed equations is presented, in order to introduce relevant variables. A more comprehensive solution can be found in Redwood (1960) or Achenbach (1973).

The radial and axial displacements are:

$$u_r = \frac{\partial \phi}{\partial r} + \frac{\partial^2 \psi}{\partial r \partial z} \tag{3.34}$$

$$u_z = \frac{\partial \phi}{\partial z} - \frac{\partial^2 \psi}{\partial r^2} - \frac{1}{r}\frac{\partial \psi}{\partial r} \tag{3.35}$$

These permit a differential solution to the wave equations, making use of Bessel function $J_n(x)$, the potentials ϕ and ψ can now be expressed as:

$$\phi = A J_{n-1}(k_d r) \exp[i(k_0 z - \omega t)] \tag{3.36}$$

$$\psi = C J_n(k_t r) \exp[i(k_0 z - \omega t)] \tag{3.37}$$

$$n = 1, 2, 3, ... \tag{3.38}$$

where n is the mode number.

Solving equations 3.36 and 3.37 permits the elimination of the constants A and C and the determination of a characteristic frequency equation.

$$k_0{}^2 \cdot \frac{k_t J_{n-1}(k_t a)}{J_n(k_t a)} - \frac{1}{2}\left(\frac{\omega}{c_t}\right)^2 + \left\{\frac{1}{2}\left(\frac{\omega}{c_t}\right)^2 - k_0{}^2\right\}^2 \frac{J_{n-1}(k_d a)}{k_d J_n(k_d a)} = 0 \tag{3.39}$$

The frequency equation 3.39 introduces a number of relevant parameters.

- k_0 is the wave-number of a particular wave mode for a given direction and a given frequency.

- k_d is a longitudinal wave propagation constant and can be obtained from equation 3.17.

- k_t is a transversal wave propagation constant and can be obtained from equation 3.18.

- ω is the circular frequency in $rad \cdot s^{-1}$, obtained from the frequency, f, in Hz:

$$\omega = 2\pi \cdot f$$

- $J_n(x)$ is the Bessel function obtained from a series expansion.

$$J_n(x) = \sum_{i=0}^{\infty} (-1)^i \cdot \frac{\left(\frac{1}{2}x\right)^{n+i^2}}{i!\,(n+i)!} \tag{3.40}$$

  - n is the mode number, taking integer values of $n = 1, 2, 3, ...$ Each mode number is associated with a specific pressure distribution along the cross-section of the waveguide, (figure 3.9). The mode number is associated with the number of nodes, through zero points, in each pressure distribution diagram.

- a is the cylinder radius, $a = r$.

3.5.2 Phase Velocity

The ratio between circular frequency, ω, and wavenumber, k_0, produces a velocity. This velocity is known as phase velocity, c_p.

$$c_p = \frac{\omega}{k_0} \tag{3.41}$$

The phase velocity is the velocity at which a wave component with unaltered shape, i.e., constant phase, propagates through a medium. In a linear system, a periodic wave can be described as the sum of a number of harmonic waves, each with its characteristic phase velocity. Each mode of wave propagation has a characteristic pressure distribution to which is associated a characteristic phase velocity.

The frequency equation 3.39, when solved in order of k_0 and making $n = 1$ or 2 in equation 3.41, enables the calculation of c_p. Since c_p varies with frequency, (equation 3.41), the obtained curves are known as dispersion curves. Figure 3.12 presents the

dispersion curves of the phase velocity in a solid cylinder relative to the wave length, Λ, and cylinder radius, r.

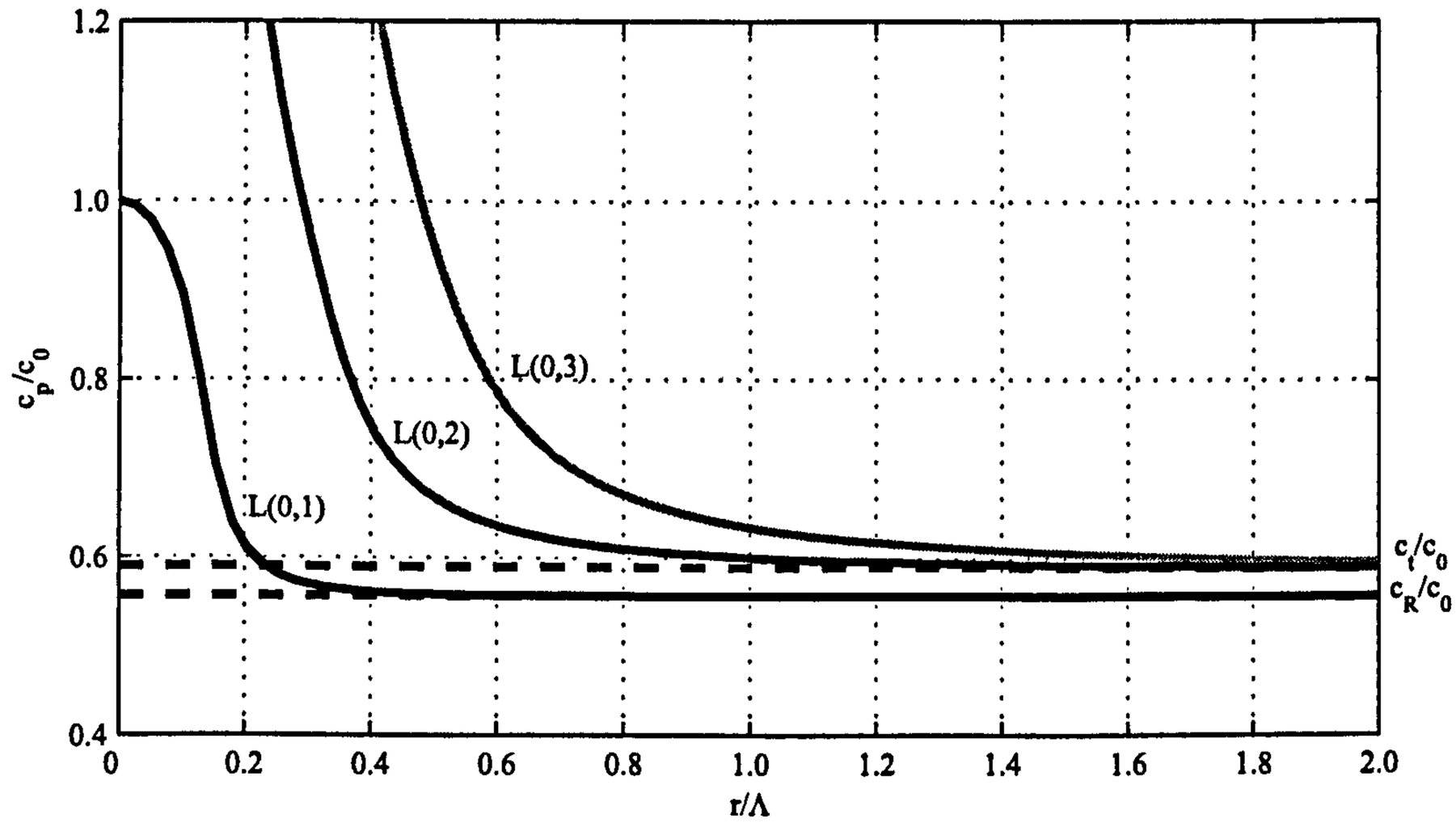

Figure 3.12: Phase velocity dispersion curves of the 3 first longitudinal modes of wave propagation.

Figure 3.12 was obtained using numerical routines developed by Seco *et al.* (2002). These routines were programmed to solve the frequency equations as the one given in equation 3.39. In figure 3.12 only the first three modes of wave propagation are presented for simplicity purposes, where in the reference $L(i,j)$, L describes a longitudinal mode, the first index, $i = 0$, describes a symmetric mode, and the second index, $j = 1$, 2 or 3, are the mode numbers.

The dispersion curves shown in figure 3.12, such as the remaining dispersion curves shown next, show how the wave velocity becomes more stable with cylinder radius and frequency.

The dispersion curves were obtained for dimensionless axis such as $\left(x \rightarrow \frac{a}{\Lambda}\right)$ and $\left(y \rightarrow \frac{c_p}{c_0}\right)$; but in the present case, to gain some sensitivity of soft medium's behaviour, the curves are presented for a particular material. The physical and geometric properties of the soft material used are given in table 3.1 and were chosen

to be similar to the properties of the synthetic material tested in chapter 6.

Property	Symbol	Units	Value
Bulk modulus	K	Pa	18.4E6
Poisson coefficient	ν	no units	0.45
Density	ρ	$kg.m^{-3}$	1000
Radius	a	mm	38

Table 3.1: Cylinder waveguide model material properties.

In figure 3.12 only the far-field wave components are considered and so the observed dispersion is due to the presence of the wave reflection at the lateral boundaries of the cylinder. In practice, boundary conditions are more complex than those considered for an infinitely long bar. The geometry of non-infinite samples and the presence of other components of the testing system are some of these boundary conditions. For this reason, the dispersion detected on real tests might not be possible to correlate directly with the geometry of the sample. Nevertheless, dispersion does have a theoretical explanation related to the present of geometric boundaries, as observed, and should also be evaluated in those terms.

The dispersion curves of the longitudinal modes of wave propagation have other relevant characteristics worth mentioning. The curve of each longitudinal mode, except the one corresponding to the first mode, tend to infinity, ∞, with decreasing frequency. These higher modes have a limit frequency below which no real values of c_p can be obtained. These limit frequencies are called cut-off frequencies and are a characteristic of the waveguide.

The velocity of the first mode of longitudinal wave propagation tends to the Rayleigh surface wave velocity, $c \Rightarrow c_R$, with increasing frequency. In the same conditions, all the other higher modes tend to the characteristic S wave velocity c_t.

3.5.3 Group Velocity

The gradient of the phase velocity, c_p, dispersion curves can be used to obtain the group velocity, c_g, see equations 3.42 or 3.43. Group velocity is the velocity at which the energy is propagated through the medium, and is not necessarily the same as c_p. It can be correlated with the modulation of a group of harmonic waves, and the average velocity at which the group as a whole propagates,

$$c_g = \frac{d\omega}{dk_0} \tag{3.42}$$

or

$$c_g = c_p + k_0 \frac{dc_p}{dk_0} \tag{3.43}$$

Figure 3.13 presents the first three modes of propagation group velocity dispersion curves.

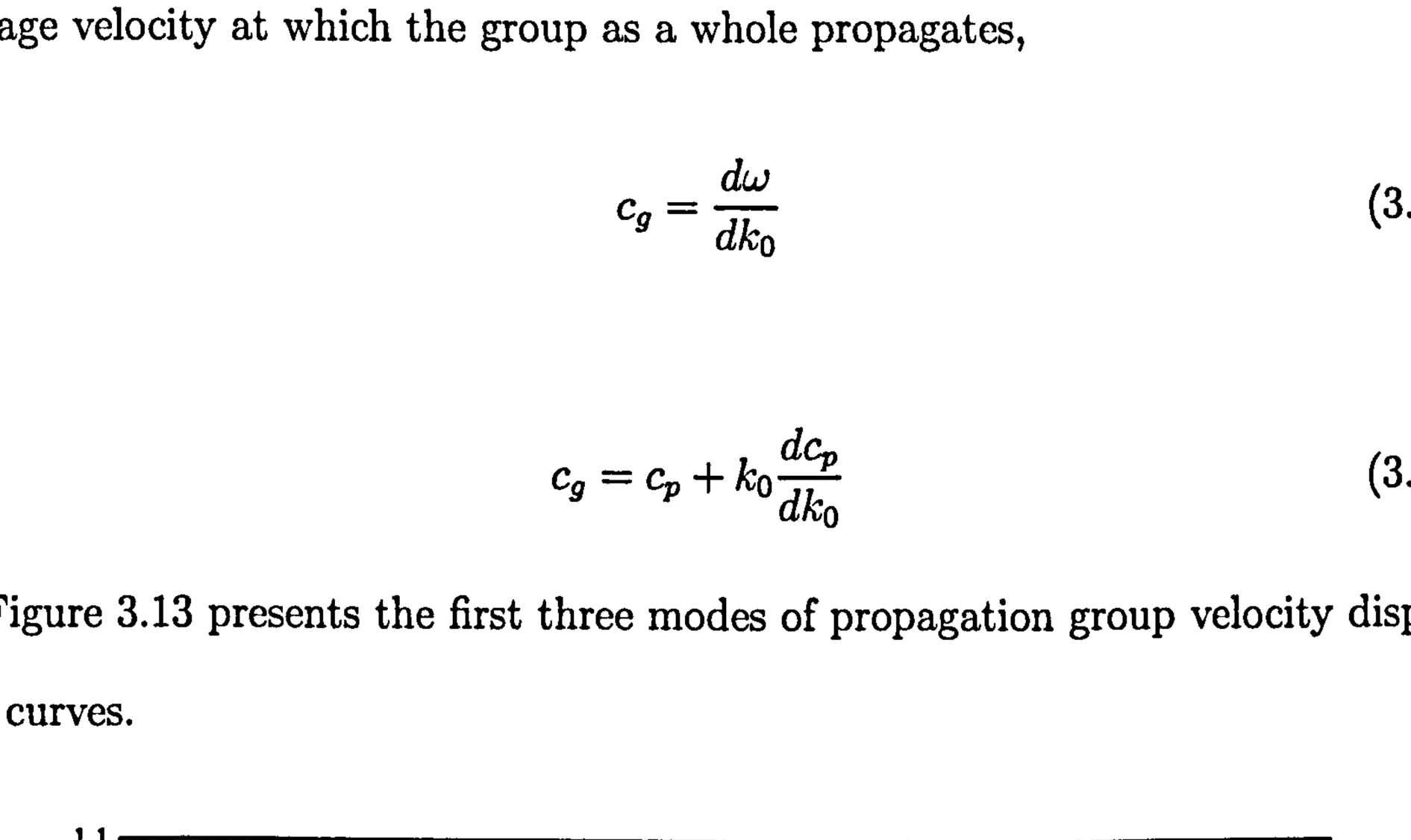

Figure 3.13: Group velocity dispersion curves of the 3 first longitudinal modes of wave propagation.

The dispersion curves representing group velocity have similar characteristics to those of phase velocity, especially with increasing frequency and radius, i.e., the first

mode of wave propagation tend to the Rayleigh wave velocity and the higher modes tend to the characteristic S wave velocity. At lower frequencies, the differences between group and phase velocities dispersion curves become more apparent. The most noticeable difference is how in the group velocity dispersion curves tend to zero at the cut-off frequencies.

3.5.4 Torsional Modes of Propagation

Torsional modes of wave propagation are symmetric, as seen in figure 3.11, and are characterised by circular particle displacement, again independent of θ, which can be expressed as $u_r = u_z = 0$. The wave equations concerned with the torsional modes of wave propagation can be reformulated into a much simpler form as a single equation,

$$\frac{\partial^2 u(r)}{\partial r^2} + \frac{1}{r}\frac{\partial u(r)}{\partial r} - \frac{1}{r^2}u(r) + \frac{\partial^2 u(z)}{\partial z^2} = \frac{1}{c_t^2}\frac{\partial^2 u(r)}{\partial t^2} \tag{3.44}$$

if

$$u_\theta = u(r)\exp(-ik_0 z)\exp(i\omega t) \tag{3.45}$$

The frequency equation then becomes:

$$\frac{J_{n-1}(k_t a)}{J_n(k_t a)} = \frac{2}{k_t a} \tag{3.46}$$

for which the Bessel functions J_n and J_{n-1} have been described in equation 3.40.

The dispersion curves for the torsional modes of vibration are presented in figures 3.14 and 3.15 for the same cylinder beam described in table 3.1.

The only non-dispersive mode of wave propagation in infinitely long cylinders is the first torsional mode. It is worth noting how the values of phase and group velocity given by curve T(0,1) in figures 3.14 and 3.15 remain constant with varying frequency and sample radius. This characteristic is appreciated in geotechnical

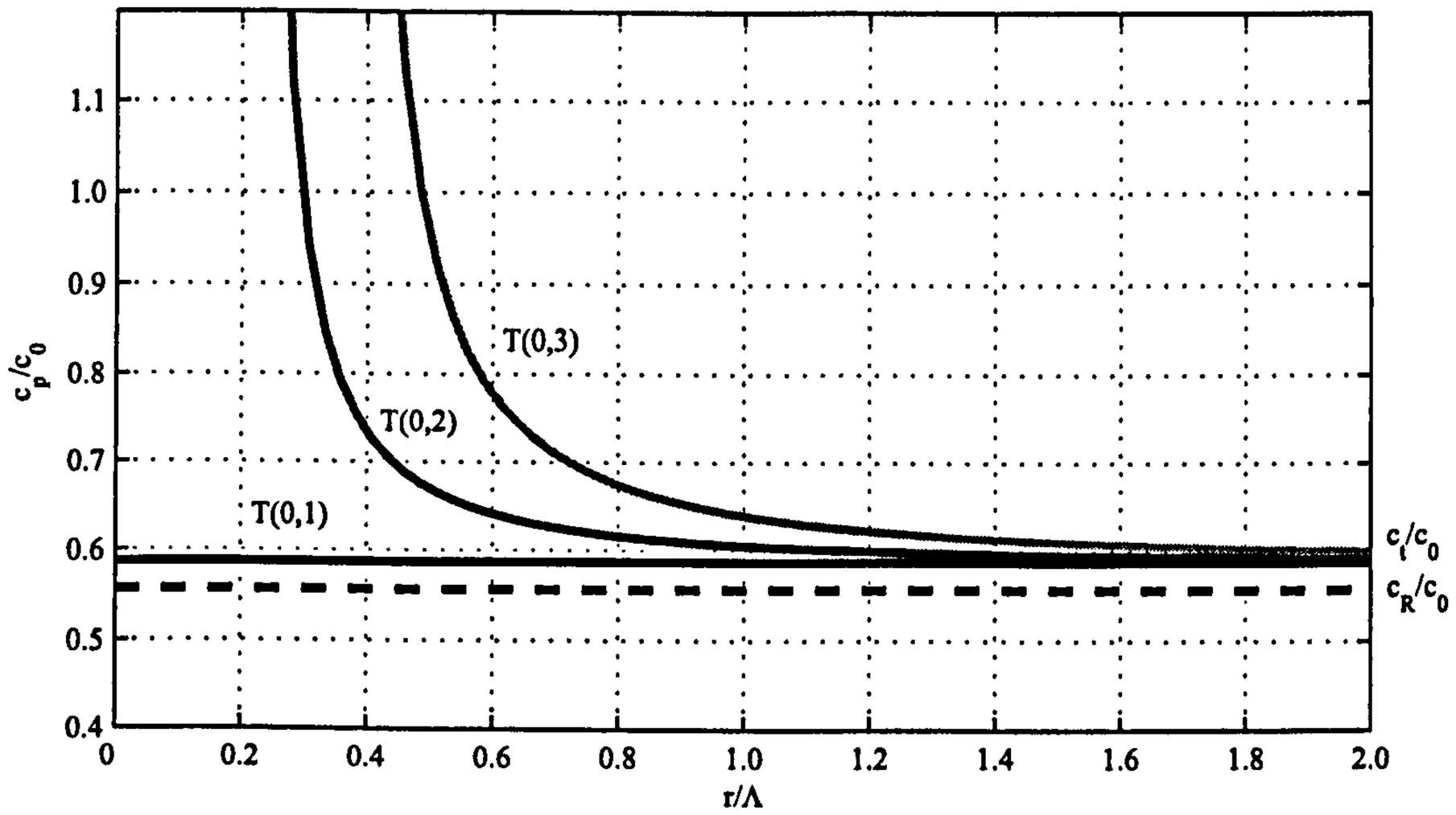

Figure 3.14: Phase velocity dispersion curves of the 3 first torsional modes of wave propagation.

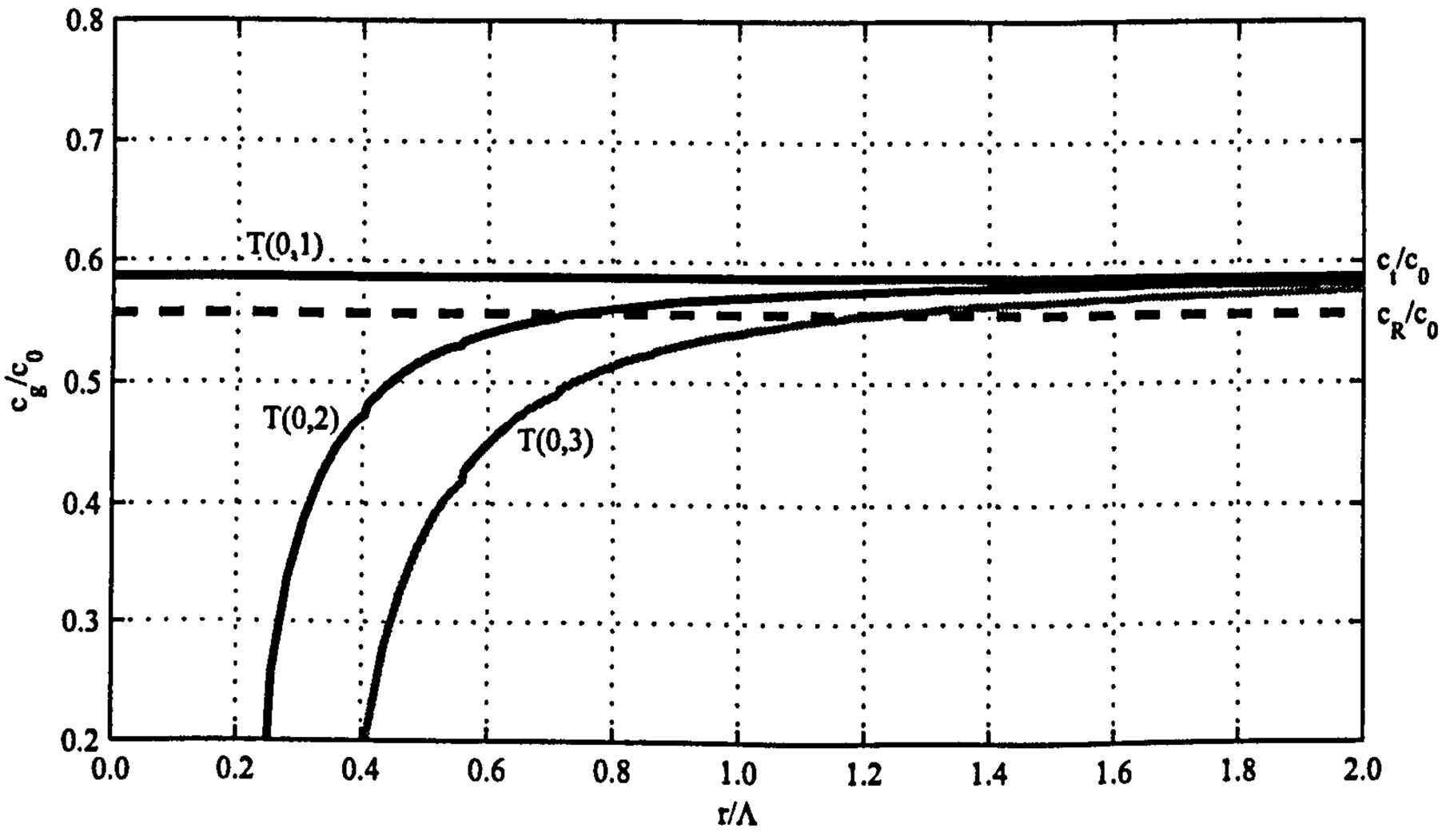

Figure 3.15: Group velocity dispersion curves of the 3 first torsional modes of wave propagation.

dynamic testing when testing with torsional resonant columns. Resonant columns are a laboratory device used to excite soil samples in torsion and read their responses. A classic citation of its normalised use is found in Drnevich *et al.* (1978). Further information about their use is also given in section 3.11.

3.5.5 Flexural Modes of Propagation

The flexural modes of wave propagation present the most elaborate solution of the three proposed fundamental types of wave propagation modes. Since these modes are asymmetric about the cylinder main axis, the particle motion is dependent of all three coordinates, r, z and θ. Therefore, the solution to the governing wave equations is more general than the previous longitudinal and torsional ones.

The application of the boundary conditions at the cylinder surface, $r = a$, is expressed by making the local tension equal to zero, $\tau_{rr}(a) = \tau_{rz}(a) = \tau_{r\theta}(a) = 0$. The development of the frequency equation for the present case has to make use of the general wave equations 3.30 to 3.33, and takes the form of the determinant:

$$\begin{vmatrix} n^2-1-a^2{k_0}^2(x-1) & n^2-1-a^2{k_0}^2(2x-1) & 2(n^2-1)[\gamma_n(k_ta)-n]-a^2{k_0}^2(2x-1) \\ \gamma_n(k_da)-n-1 & \gamma_n(k_ta)-n-1 & 2n^2-2[\gamma_n(k_ta)-n]-a^2{k_0}^2(2x-1) \\ \gamma_n(k_da)-n & -(x-1)[\gamma_n(k_ta)-n] & n^2 \end{vmatrix} = 0 \quad (3.47)$$

for which

$$\gamma_n(k_ia) = \frac{k_iaJ_{n-1}(k_ia)}{J_n(k_ia)} \quad (3.48)$$

$$x = \frac{1}{2}\frac{{c_p}^2}{{c_t}^2} \quad (3.49)$$

$$n = 1,\ 2,\ 3, \ldots$$

The dispersion curves of the phase and group velocity, for the medium described in table 3.1, are pictured in figures 3.16 and 3.17 respectively.

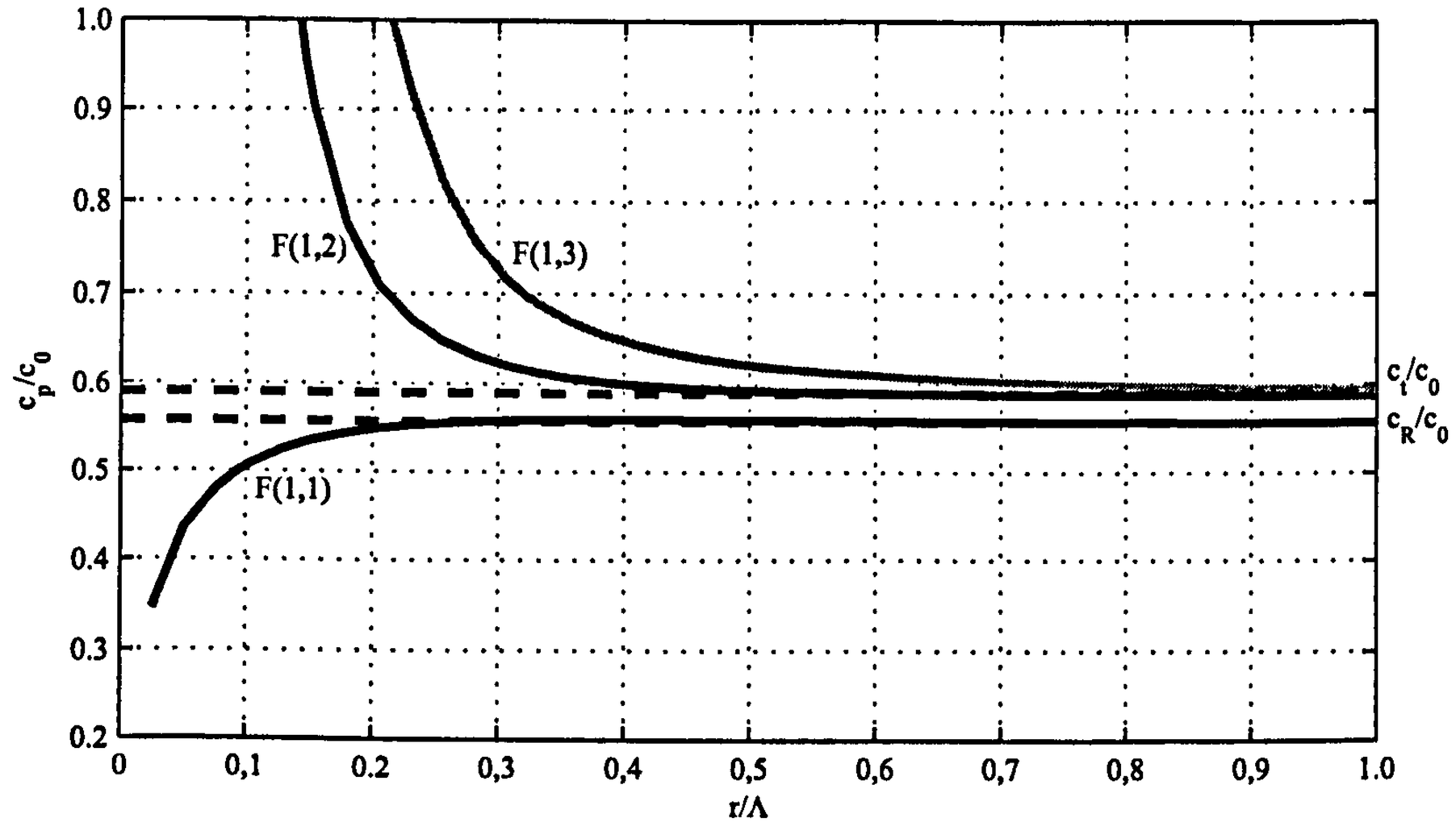

Figure 3.16: Phase velocity dispersion curves of the 3 first flexural modes of wave propagation.

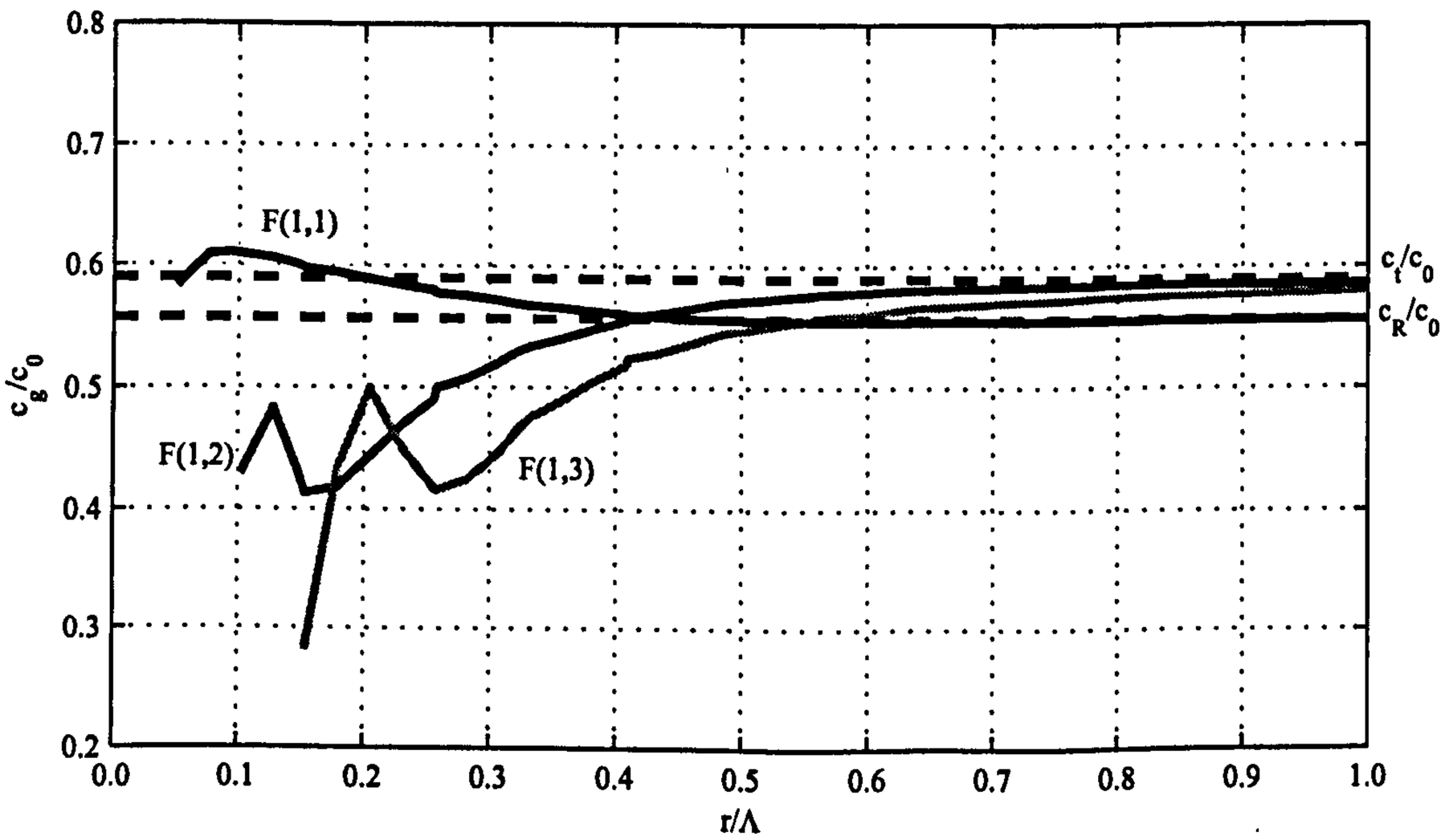

Figure 3.17: Group velocity dispersion curves of the 3 first flexural modes of wave propagation.

As with the dispersion curves of the longitudinal and torsional modes of wave propagation, the presence of cut-off frequencies is apparent. The velocity of the first mode curve, $n = 1$, tends to c_R with increasing frequency and the velocity of the higher modes tend to c_t.

3.6 Wave Radiation

The wave theory presented so far is applicable to the case of planar far-field wave propagation, which is a particular case of the general wave radiation theory. Testing with bender elements requires the understanding of the general wave radiation for relatively short wave travel lengths. Also, the understanding of wave radiation is important to determine how far away from a wave's source it becomes valid to replace general wave radiation theory with planar wave propagation theory.

The simpler case of a single isolated impulsive force acting at an isolated point in an infinite medium, which disturbed the medium and causes a wave to radiate from it, is presented. Such a wave source permits the presentation of the wave radiation phenomenon in simpler terms and is comparable to the bender element wave source. Assuming a linear behaviour from the test system permits the consideration of combinations of the mentioned load case to obtain more complex load cases.

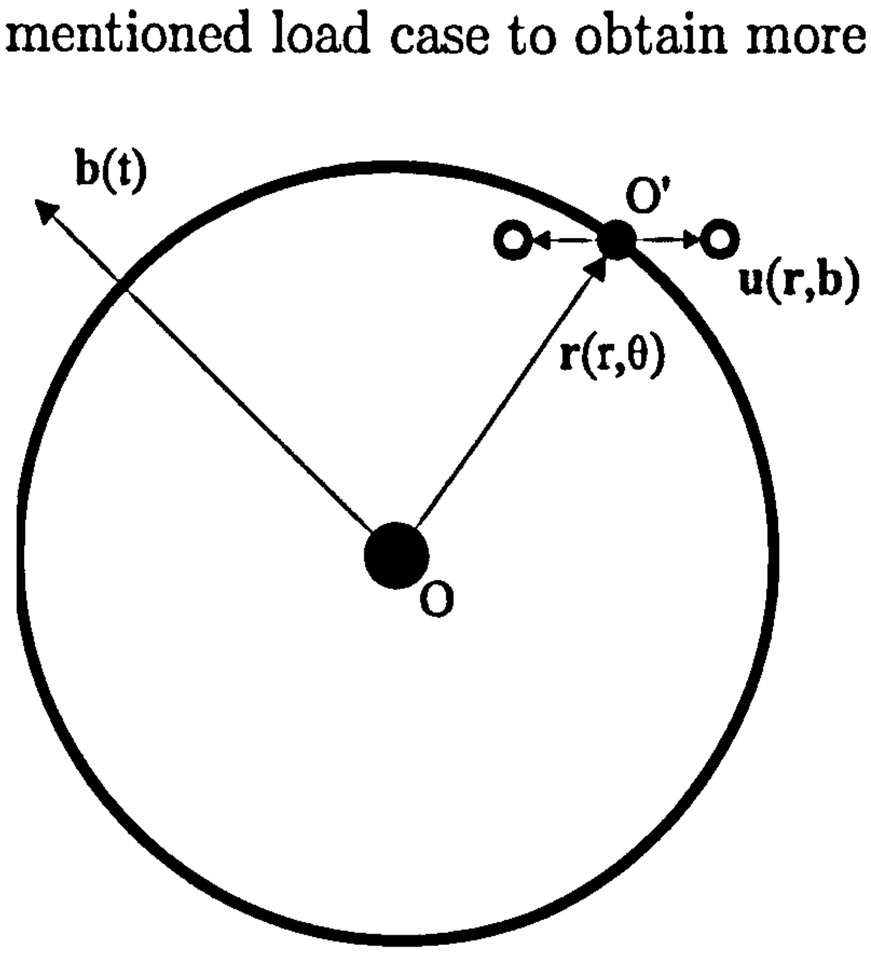

Figure 3.18: Wave source and wave radiation diagram.

A Lagrangian description of the problem is ideal, studying a specific particle movement. Assuming, as in figure 3.18, point O to be the source of the wave radiation, at which a single isolated impulsive load in the form of vector $\mathbf{b}(t)$ is applied; and point O' with relative position to the origin determined by vector $\mathbf{r}(r, \theta)$

and point O' movement history is given by $\mathbf{u}(\mathbf{r}, \mathbf{b})$. The used notation distinguishes between vector values in **bold** fonts and scalars in normal fonts. Because the wave radiates from a single origin point into an unbounded medium, it is convenient to use a system of spheric coordinates.

The description of this problem presents a transformation function that assumes the impulsive load at the origin and that is capable of determining the oscillation properties of a particular point at a particular time and at a particular position in the system. A mathematical fundamental solution provides the base for the determination of such transfer function, (Stokes, 1845). A known practical application of the fundamental solution can be found in Sanchez-Salinero (1987).

It is necessary to take as starting point the differential equation of motion for an homogeneous and isotropic medium, as in Aki and Richard (2002) or Arroyo (2001), given as:

$$\rho\ddot{\mathbf{u}} = \mathbf{b} + (\lambda + \mu)\,\nabla\,(\nabla \cdot \mathbf{u}) + \mu\nabla^2\mathbf{u} \tag{3.50}$$

where λ and μ are Lamé's elastic constants presented previously in equation 3.2, ρ is the medium's density and ∇^2 the Laplace operator also previously given in equation 3.6. In order to solve the differential equation 3.50, a mathematical tool known as the Green function $\mathbf{G_R}$ is used.

The assumed boundary conditions state that every point in the system starts its movement from its equilibrium position $\mathbf{u}(\mathbf{r}, 0) = 0$, and that every point, except the origin, is at rest when the impulsive load is first applied, $\dot{\mathbf{u}}(\mathbf{r}, 0) = 0$ for $\mathbf{r} \neq 0$. The displacement can now be expressed as a convolution $*$ between the Green function and the applied load.

$$\mathbf{u} = \mathbf{G_R} * \mathbf{b} \tag{3.51}$$

In the interest of this study, the particle oscillation is decomposed into two orthogonal polarisations, parallel and perpendicular to the direction of the wave

propagation. The particle movement can then be expressed in terms of two simple wave modes, $\mathbf{u}_P$ and $\mathbf{u}_S$, in reference to P and S waves.

$$\mathbf{u}_P = \quad (\mathbf{u}\cdot\mathbf{r})\mathbf{r} \quad = (\mathbf{r}\cdot\mathbf{b}) * [2N + F_P]\mathbf{r} \tag{3.52}$$

$$\mathbf{u}_S = \quad \mathbf{u}\wedge\mathbf{r} \quad = \mathbf{r}\wedge\mathbf{b} * [F_S - N] \tag{3.53}$$

When considering the characteristics of wave radiation and the relation between its simpler orthogonal wave modes, $\mathbf{u}_P$ and $\mathbf{u}_S$, and the impulsive load at the source properties, the following conclusions can be obtained:

- propagation in the direction of the source impulse load has particle oscillation with no shear component because $(\mathbf{r}\wedge\mathbf{b}) = 0$.

- propagation in the direction perpendicular to the source impulse load has particle oscillation with no compression component since $(\mathbf{r}\cdot\mathbf{b}) = 0$.

- generally, only when far-field coefficients F_p and F_s become much higher than near-field ones, N, i.e., $N/F \rightarrow 0$, can P wave components be associated with P wave velocity, c_l, and S wave components associated with S wave velocity, c_t.

The last point poses the principal condition for which plane wave propagation becomes an appropriate model of dynamic behaviour, (Aki and Richard, 2002).

3.6.1 Wave Field Components

In equations 3.52 and 3.53, N, F_P and F_S, represent the near-field, compression far-field and shear far-field wave components. They can be obtained in the frequency domain in the form of a complex exponential, enabling a more intuitive description

of the problem,

$$u = a + ib \quad \equiv \quad u = M\, e^{iF} \tag{3.54}$$

and the relation between these two expressions is expressed in

$$M = \sqrt{a^2 + b^2} \quad \text{and} \quad F = \arctan \frac{b}{a} \tag{3.55}$$

For the mentioned complex exponential, M is the modulus and F the phase of the function. Returning to the field problem at hand, the expression of the field components are expressed as:

$$N = N_S - N_P \tag{3.56}$$

and

$$F_P \;=\; \frac{k}{{c_l}^2}\, e^{-i n_P} \tag{3.57}$$

$$F_S \;=\; \frac{k}{{c_t}^2}\, e^{-i n_S} \tag{3.58}$$

where the near-field component N can be separated into its compression and shear parts, N_P and N_S. It is not always convenient to express the near-field components separately, (Aki and Richard, 2002), but for the sake of coherence with the expression of the far-field components, such decomposition of the near-field is presented,

$$N_P = \frac{k}{{c_l}^2} \frac{\sqrt{1 + {n_P}^2}}{{n_P}^2}\, e^{-i[n_P - \arctan(n_P)]} \tag{3.59}$$

$$N_S = \frac{k}{{c_t}^2} \frac{\sqrt{1 + {n_S}^2}}{{n_S}^2}\, e^{-i[n_S - \arctan(n_S)]} \tag{3.60}$$

k is a function constant at each point, given by:

$$k = \frac{1}{4\pi\rho r} \tag{3.61}$$

and n_P and n_S are dimensionless coefficients which contain the relation between frequency and wave velocity, also known as wavelength.

$$n_P = \frac{\omega}{c_l} r \quad \text{and} \quad n_S = \frac{\omega}{c_t} r \tag{3.62}$$

Of especial interest for this study are the properties of the shear wave mode, $\mathbf{u}_S$. The function that rules its behaviour, after equation 3.53, was given by Jovičić *et al.* (1996) and Arroyo *et al.* (2003*a*) as the sum of the field wave components.

$$\Gamma = \Gamma_1 + \Gamma_2 - \Gamma_3 \quad \text{or} \quad = F_S + N_P - N_S \tag{3.63}$$

The manipulation of these field components enables a better understanding of the radiation phenomenon and why it might be relevant in interpreting bender elements test results. The expressions of the far field components, F_P and F_S, attenuate with r^{-1} and a have a constant wave propagation velocity equal to the bulk velocities c_l and c_t respectively. The expressions of the near-field components, N_P and N_S, attenuate with a higher order value of r^{-2}. This means that the far field components of the radiation function become dominant as $r \rightarrow \infty$ and the near-field components are dominant as $r \rightarrow 0$, hence the name. For these near-field components the wave propagation velocity is not constant but varies with distance from the source, r.

3.6.2 Near-Field Amplitude

The study of the modulus of the field components and the calculation of the ratio between the amplitudes of the near and far-field components is performed to the soft material described in table 3.1 and presented next in figures 3.19(a) and 3.19(b).

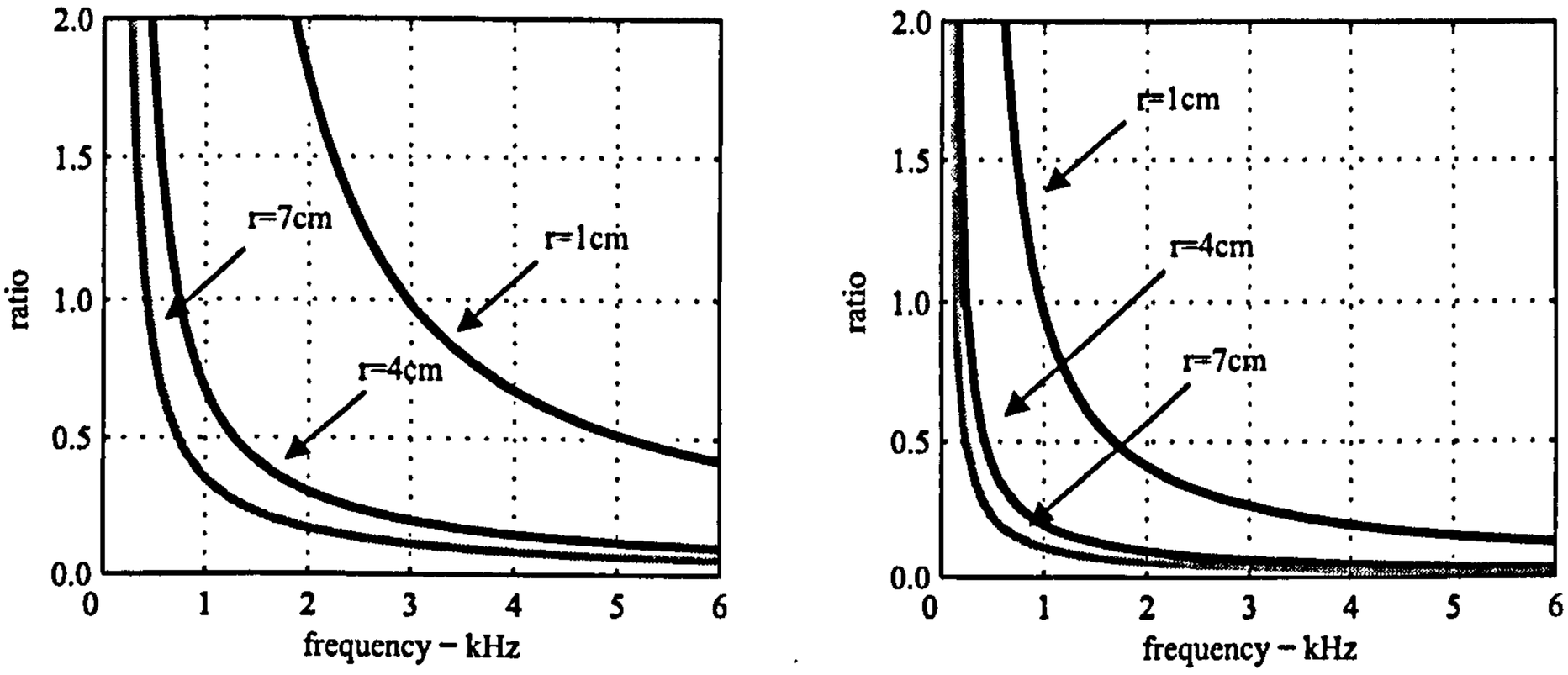

(a) N_P/F_P (b) N_S/F_S

Figure 3.19: Ratio between near and far-field wave components.

The pictured curves present the ratio between near and far-field components at different distances from the wave source, $r = 1$, 4 and 7cm. At 1cm from the source the near-field is significant up to 5kHz for its P component and up to 2kHz for its S component but it decays rapidly because at 4 and 7cm from the source the same ratio seems to stabilize and dive under 25% near 0.5kHz.

3.6.3 Near-Field Wave Velocity

When considering the influence of the near-field components, or the near-field effect, it is important not only to consider its ratio with the far-field components, but also the different phase velocities of each component. The far-field components are non-dispersive, i.e., they have a constant propagation velocity, regardless of the distance to the source and from the frequency of the source signal. The velocity of the P and S wave modes are the same as the characteristic equivalent wave velocities, c_d and c_t. The expression of the phase velocity can be obtained as the phase parcel derivative in r. The expression of the phase velocities is given below, after Arroyo

(2001).

$$\text{far-field:} \qquad V_d^{ff} = c_d \qquad V_s^{ff} = c_t \tag{3.64}$$

$$[1ex]\text{near-field:} \qquad V_d^{nf} = c_d\left(1 + \frac{1}{{n_p}^2}\right) \qquad V_s^{nf} = c_t\left(1 + \frac{1}{{n_s}^2}\right) \tag{3.65}$$

Next are presented the dispersive curves for the values of the near-field N_P and N_S components, V_d^{nf} and V_s^{nf} with varying frequency and at increasing distances from the wave source, obtained from equation 3.65 using the material properties given in table 3.1.

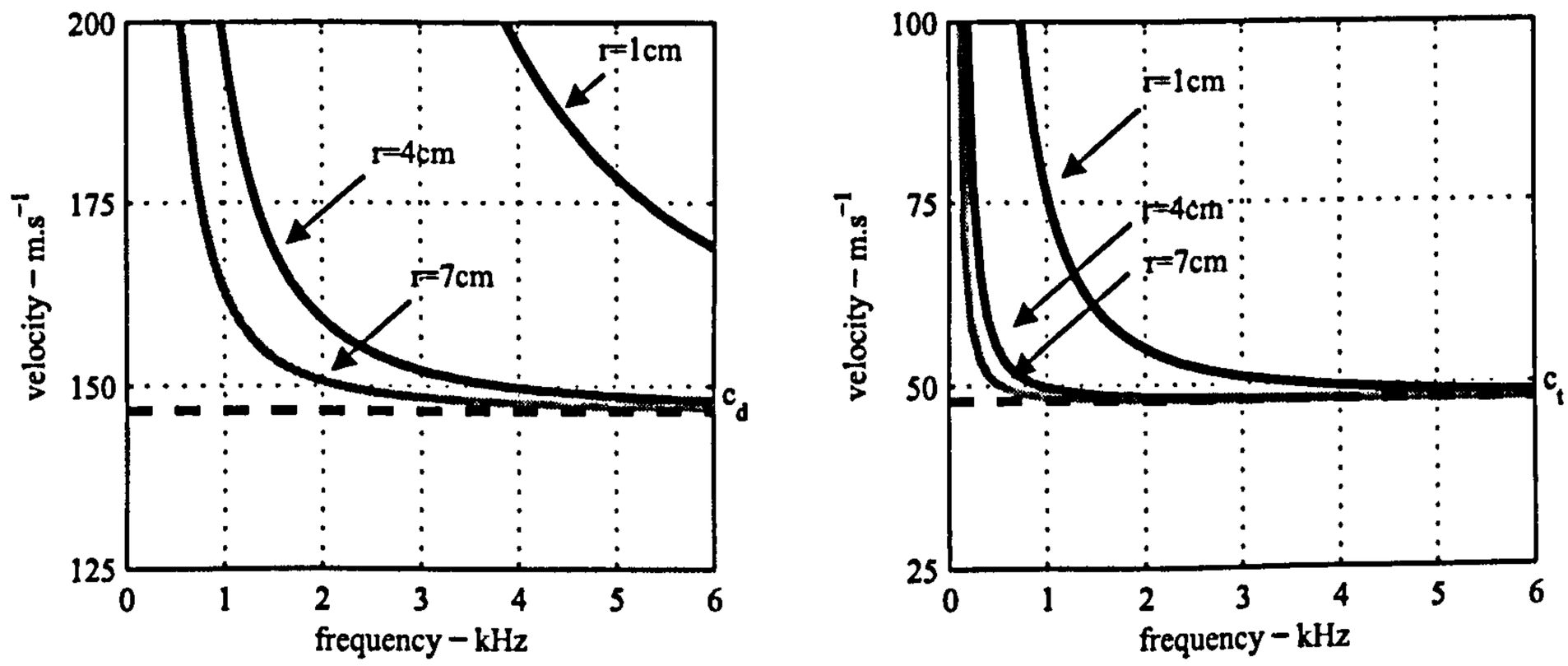

(a) near-field P component velocity

(b) near-field S component velocity

Figure 3.20: Near-field components velocity.

Figures 3.20(a) and 3.20(b) show how dispersive the near-field components are. The near-field compression component N_P is not only dispersive but tends to the characteristic P wave velocity c_d, with increasing distance from the source, $r \to \infty$, and with increasing frequency, $f \to \infty$. Therefore, at small distances from the source and at low frequencies its presence has the potential of disturbing the pursuit of the characteristic shear wave velocity. The near-field S wave component N_S is also dispersive, tending to the characteristic shear wave velocity c_t, with increasing distance to the source $r \to \infty$, and with increasing frequency $f \to \infty$.

According to the results presented so far, the importance of the near-field effect as a significant component of a travelling wave in particular domains of lower frequencies and short distances from the source becomes apparent. The near-field effect can have an amplitude of more than twice the amplitude of the far-field components and propagate with twice its velocity. Significant contributions from near-field wave components will therefore disturb the identification of the characteristic shear wave velocity.

Sanchez-Salinero (1987) studied the notion of near-field effect relating it to bender element testing by the use of the medium's wavelength and travel distance. He correctly observed that the dispersion due to the near-field effect diminished with increasing wave travel distance and with decreasing wavelength. These two factors can be combined to produce a ratio R_d which can serve as an indicator of the potential near-field effect,

$$R_d = \frac{td}{\Lambda} = td \cdot \frac{f_j}{V_s} \tag{3.66}$$

where R_d is the near-field effect indicative ratio, td is the wave travel distance, f_j is the signal frequency and V_s the characteristic shear wave velocity.

Jovičić *et al.* (1996) and Brignoli *et al.* (1996) in their studies of bender element testing have also referred to the near-field ratio and have used it to evaluate their results. A distinction is made in their analysis, Brignoli *et al.* (1996) noted a difference between the frequencies of the transmitted and received signals, and chose the received signal's frequency as the value f_j used to calculate R_d. Jovičić *et al.* (1996) did not distinguish between input and output signal frequencies, for pulse signals, and hence used the input frequency as the value f_j. More recently reference to the near-field ratio is also made in the work of Dano *et al.* (2003), for example.

In studying the near-field effect on bender element testing Arroyo *et al.* (2003*a*) went further and proposed a simple method of determining a frequency limit, after

which the near-field effect might be disregarded. The wave velocity of the near-field shear wave component is selected as the main parameter used in the method, and not its relative magnitude, (figures 3.19(b) and 3.20(b)). This is because the wave velocity of the near-field wave components decreases faster than its amplitude, both with signal frequency and distance to source. So, even though the near-field effect might still have a significant magnitude, its velocity becomes similar to that of the far-field shear wave components sooner, diminishing its influence in terms of dispersion. The proposed frequency limit is set so that difference between far and near-field wave components is lower than 5%,

$$\frac{V_s^{nf}}{V_s^{ff}} < 1.05$$

then the frequency limit becomes

$$f_{nf} > \frac{V_s}{1.6\,td} \tag{3.67}$$

where V_s^{nf} is the near-field shear wave velocity, V_s^{ff} is the far-field shear wave velocity, also known as the characteristic shear wave velocity V_s, td is the distance from the wave source also known as travel distance, which in the bender element test is usually measured between tip-to-tip, (Viggiani and Atkinson, 1995), and f_{nf} is the minimum frequency for which the proposed limit velocity ratio can be observed.

The frequency limit f_{nf} proposed by Arroyo *et al.* (2003*a*) can be related to the ratio R_d mentioned by Sanchez-Salinero (1987), for a single frequency signal, i.e., a harmonic continuous signal, as follows:

$$f > \frac{V_s}{1.6\,td} \quad \equiv 1.6 > \frac{V_s}{tf\,f} \quad \equiv R_d > \frac{1}{1.6} > 0.625 \tag{3.68}$$

3.7 Dispersion

Dispersion is the phenomenon in which a wave is decomposed into different frequency components, each has a different characteristic propagation velocity. When considered dynamic test methods involving wave propagation, to determine the elastic properties of a medium, such as its elastic constants or damping characteristics, dispersion must be considered. So far, two causes for dispersion have been discussed, the waveguide dispersion, caused by the reflection of wave components at the boundaries of the medium, and the near-field effect, where the near-field wave components have a different amplitude and propagating phase wave velocity than the far-field wave components.

The structure of the soil can be another source of dispersion, (Mah and Schmitt, 2001). Soils, being granular materials are locally heterogeneous, therefore causing a heterogeneous interaction between particles with wave propagation. One aspect of this heterogeneous wave propagation is the possibility of local dispersion caused by differentiated particle interaction. Still, for the present study the studied media are considered to be homogeneous. The other aspect of heterogeneity is related to how certain particle structures may cause more general specific anisotropic wave propagation. The subject of soil anisotropy has also been studied using bender elements, (Belloti *et al.*, 1996; Nash *et al.*, 1999), but is also not primary subject for the present study.

After acknowledging the existence of dispersion, the understanding of the concepts of group and phase velocities is also important. A mathematical interpretation has already been given in section 3.4.1 for different modes of wave propagation in a solid cylinder. Further, the analogy presented by Graff (1975), quoting from Rayleigh and Lindsay (1945), concerning a pool of still water and the propagation of waves due to an intense local disturbance is well worth repeating.

'It has often been remarked that, when a group of waves advances into still water, the velocity of the group is lower than that of the individual waves of which it is composed; the waves appear to originate at the rear of the group, propagate to the front, and disappear. Thus, the ripples have a higher velocity than the overall group.'

This example illustrates how a group of waves appears to propagate with a 'central' or group velocity different from the actual velocity of each of its components, where each component is characterised by its own frequency and phase velocity.

3.8 Body Vibration

Dynamic phenomena can be interpreted through the perspective of the travelling disturbance or through the perspective of the disturbed particles. A critical analysis of the use of bender elements indicates a closer relationship to wave propagation theory. Wave propagation is well suited to study transient states of response of the system. On the other hand, when establishing a dynamic steady state, by the use of continuous harmonic signals for example, the study of the vibration behaviour is better suited to providing theoretical support, in which is also known as the establishment of a standing wave, (Redwood, 1960). Also, if the focus is shifted from the primary quest of wave velocity to the particular behaviour of parts in the dynamic system, such as the behaviour of a bender element, then the study of the vibration behaviour can again provide suitable theoretical support.

The following vibration theory is not meant to be extensive; it is chosen to be simple and directly applicable to describe some dynamic phenomena associated with the use of bender elements, namely the behaviour of the bender elements themselves, as presented in chapter 5.

3.8.1 Reformulation of the Equation of Motion

A version of the equation of motion has already been presented in sections 3.1.3 and 3.6 in the form of equations 3.5 and 3.50. A third more popular version of the equation of motion is presented next with a notation suitable for the particular handling of vibration related phenomena.

$$m\ddot{u} + c\dot{u} + ku = p(t) \tag{3.69}$$

Equation 3.69, here presented in its scalar form, is suitable for single degree of freedom, SDOF, systems. This equation is used to describe a linear behaviour of the system with constant mass and stiffness in the time domain.

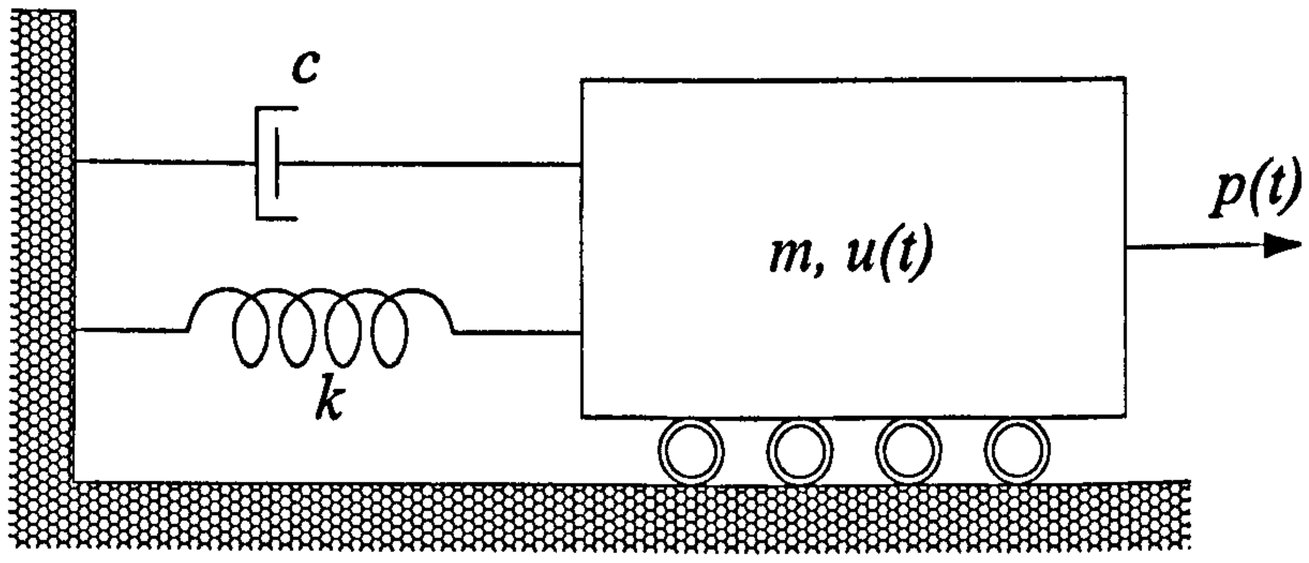

Figure 3.21: SDOF body vibration scheme.

In equation 3.69, u represents the position of the body, for which $\dot{u}$ and $\ddot{u}$ are the first and second order time derivatives, better known as velocity and acceleration respectively; m is the body mass, k is the spring stiffness, c is the damping of the system and $p(t)$ is an external force applied to the body.

3.8.2 Vibration of SDOF

A SDOF system provides a simple example of dynamic behaviour with several applications to testing with bender elements. It is most commonly used to describe

a lumped mass system concentrated in a single point. It is also possible to apply SDOF equations to simple multiple degree of freedom, MDOF, bars where the mass and elastic properties are uniformly distributed along the bar's length.

3.8.3 Undamped Free Vibration

The vibration of a system where no external force is applied and there is no damping is known as undamped free vibration. This vibration is usually started either by an initial displacement, $u(0) \neq 0$, or an initial velocity, $\dot{u}(0) \neq 0$; and the value of the damping coefficient is made equal to zero, $c = 0$. The frequency at which the system vibrates, in these circumstances, is a property of the system itself known as its natural frequency. The natural circular frequency of the system is a function of the square root of the ratio between the spring's stiffness and the system's mass, k and m.

$$\omega_n = \sqrt{\frac{k}{m}} \tag{3.70}$$

The natural circular frequency is expressed in radians per second and is related to the natural frequency in Hertz when divided by 2π, $f_n = \frac{\omega_n}{2\pi}$. The undamped free response of a SDOF system is expressed as an harmonic oscillation,

$$u(t) = a\cos(\omega_n t + \theta) \tag{3.71}$$

where a is the amplitude of the oscillation and θ is the phase angle. Both are a function of the natural circular frequency, ω_n, the mass initial position, $u(0)$, and

initial velocity, $\dot{u}(0)$.

$$a = \sqrt{u(0)^2 + \left[\frac{\dot{u}(0)}{\omega_n}\right]^2} \tag{3.72}$$

$$\theta = \tan^{-1}\left[\frac{-\dot{u}(0)}{\omega_n u(0)}\right] \tag{3.73}$$

3.8.4 Damped Free Vibration

When a mechanical system is damped, then it is worth considering the value of the damping coefficient $c > 0$. The damping coefficient can be so high as for the system to becomes incapable of oscillating. Such value of c is called the critical damping coefficient, c_c. The value of c_c is also a property of the system.

$$c_c = 2m\omega_n \tag{3.74}$$

The most relevant case of damped systems, for the present study, occurs when some oscillation remains possible, meaning $c < c_c$, in which is known as an under-critically damped system. Such a system is characterised by its damping ratio and by the damped free-vibration frequency, here represented by ξ and ω_D respectively. The damping ratio ξ is given by:

$$\xi = \frac{c}{c_c} \tag{3.75}$$

and the damped free-vibration frequency by

$$\omega_D = \omega\sqrt{1 - \xi^2} \tag{3.76}$$

The response of the undercritically damped SDOF system is given by:

$$u(t) = a\cos(\omega_D t + \theta)e^{-\xi\omega t} \tag{3.77}$$

for which the amplitude and phase angle, a and θ, are now also functions of ξ and ω_D.

$$a = \sqrt{u(0)^2 + \left(\frac{\dot{u}(0) + u(0)\xi\omega}{\omega_D}\right)^2} \tag{3.78}$$

$$\theta = -\tan^{-1}\left[\frac{\dot{u}(0) + u(0)\xi\omega}{\omega_D u(0)}\right] \tag{3.79}$$

An example of the response of a SDOF system undercritically damped free vibration is ilustrated in figure 3.22 for an initial body velocity at the origin, $\dot{u} \neq 0$ and $u = 0$.

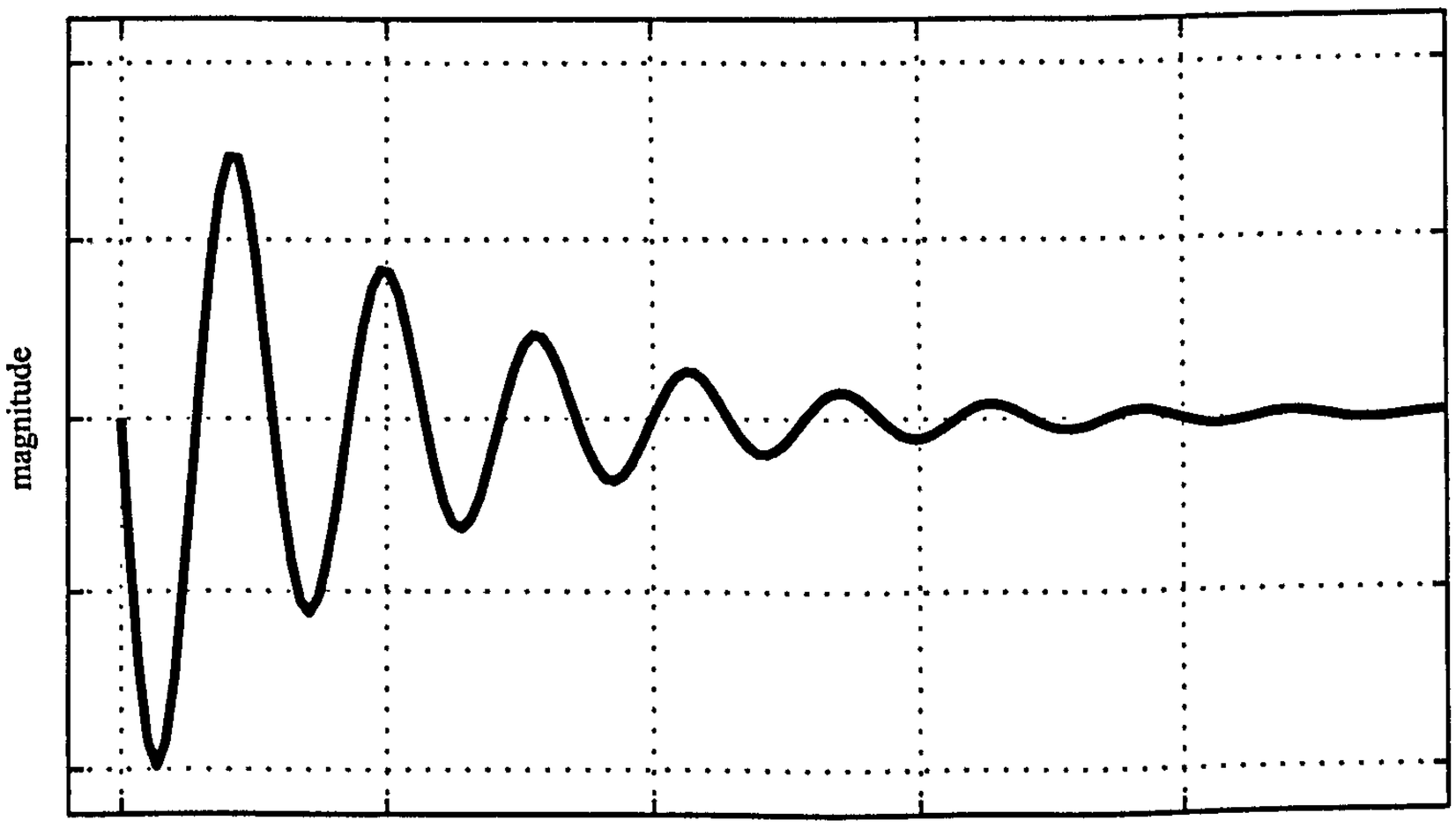

Figure 3.22: Time history of a SDOF damped free vibration.

3.8.5 Harmonic Loading

The application of an harmonic load to the system is a useful load case worth considering, especially when considering the possibility of applying a Fourier series to decompose more general signals into a sum of harmonic ones. The periodic nature of an harmonic loading enables its expression in similar terms as those used so far for the system's response,

$$p(t) = a_0 \sin(\overline{\omega} t) \tag{3.80}$$

where the amplitude of the loading is given by a_0 and the frequency by $\overline{\omega}$.

The response of the system to the harmonic loading has the contribution of a particular solution, $u_p(t)$, where it is forced to move in direct response to the load and its properties, and has a complementary solution $u_c(t)$, where it tries to move as if it were free.

$$u(t) = u_p(t) + u_c(t) \tag{3.81}$$

The complementary solution is also known as a transient response that sees its influence diminish in time, due to damping, until it disappears. The particular solution is known as the steady-state harmonic response. This second response is usually the more interesting as it can be isolated as soon as the transient response dies out. Again, the oscillation of the system can be expressed in the form of a sinusoidal function,

$$u_p(t) = a \sin(\overline{\omega} t - \theta) \tag{3.82}$$

where the response amplitude a and phase angle θ are given by:

$$a = \frac{a_0}{k} \sqrt{(1-\beta^2)^2 + (2\xi\beta)^2} \tag{3.83}$$

$$\theta = \tan^{-1}\left[\frac{2\xi\beta}{1-\beta^2}\right] \tag{3.84}$$

for which β is the ratio between the load frequency, $\overline{\omega}$, and the system natural free-vibration circular frequency, ω_n,

$$\beta = \frac{\overline{\omega}}{\omega_n} \tag{3.85}$$

An example of the transient and steady-state responses, as well as the total combined response, is given in figure 3.23.

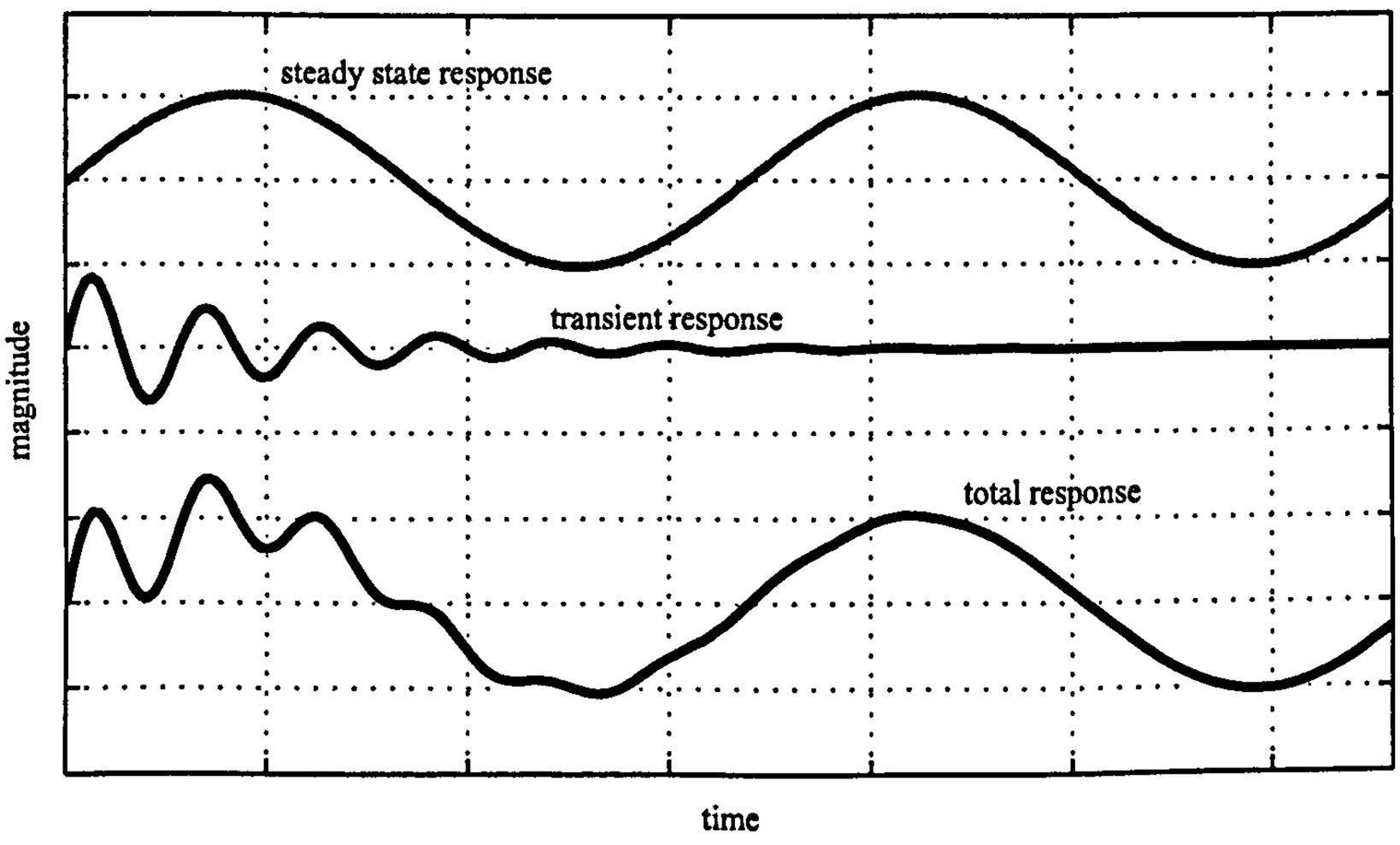

Figure 3.23: Steady-state, transient and total responses of a simple mechanical system.

In equation 3.84 it can be seen how the phase of the response, θ, varies with the load frequency. Given its somehow counter-intuitive nature of the response, it is important to keep in mind that a body does not always vibrate in-phase with an harmonic load being applied to it. The phase delay response curves for SDOF system with different damping coefficients are given in figure 3.24.

The damping of the system also influences the response magnitude. The magnitude response curves for a generic SDOF system are presented in figure 3.25 for

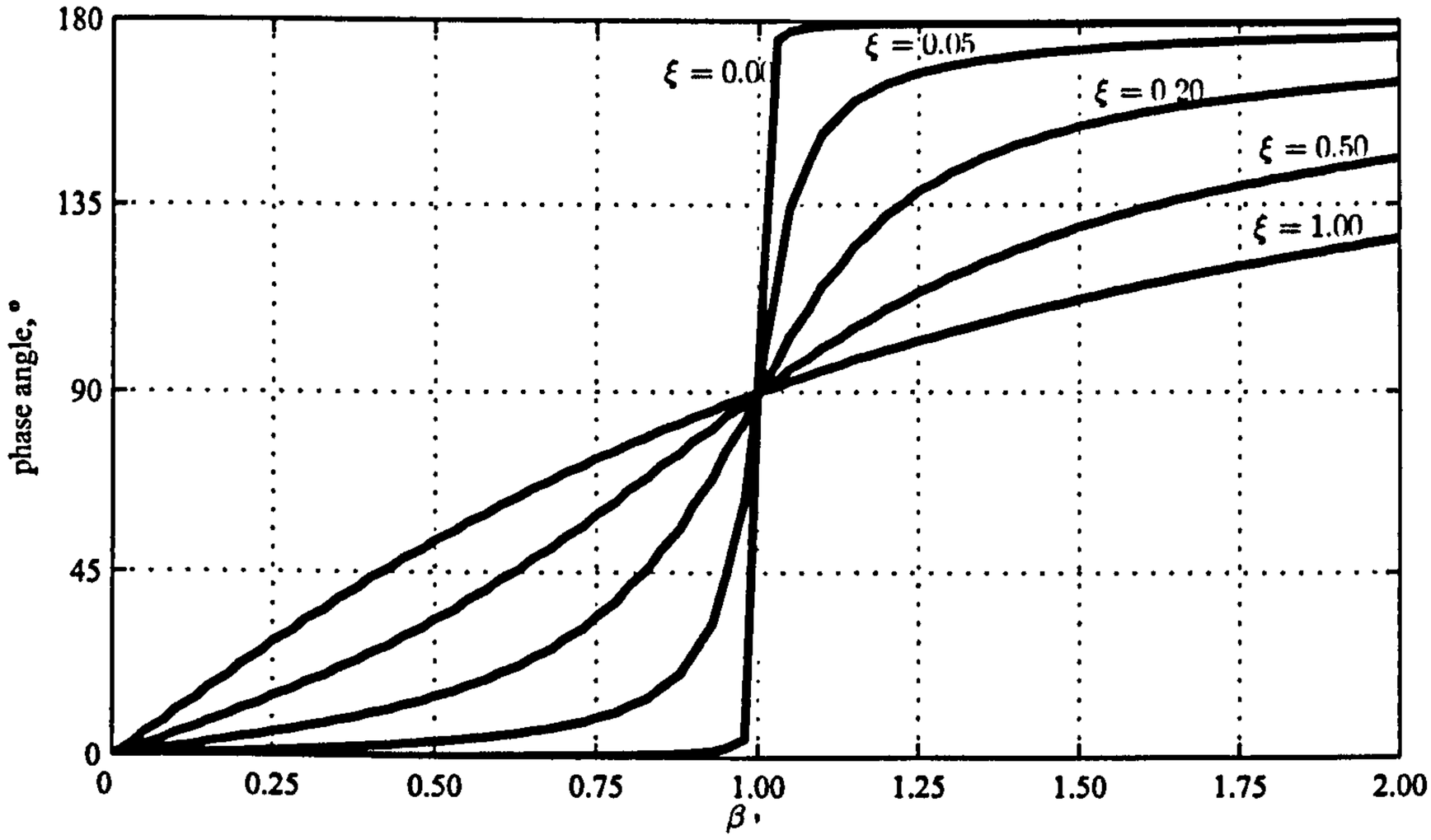

Figure 3.24: Phase difference between load and response of a SDOF system, for different damping coefficients.

different damping coefficients, ξ. The response magnitudes are presented as a ratio between the magnitude of the dynamic displacement and the equivalent static displacement, D_f. This ratio is known as the dynamic magnification factor, (Clough and Penzien, 1993).

$$D_f = \frac{a}{a_0/k} = \left[\left(1-\beta^2\right)^2 + \left(2\xi\beta\right)^2\right]^{-\frac{1}{2}} \tag{3.86}$$

3.9 Damping

Real physical systems always have some form of inherent damping. The concept of damping refers to the dissipation of vibration energy as waves travel through a medium. The damping phenomenon is applicable both to wave propagation and particle vibration dynamic phenomena. In the study of wave propagation, damping is also referred to as attenuation.

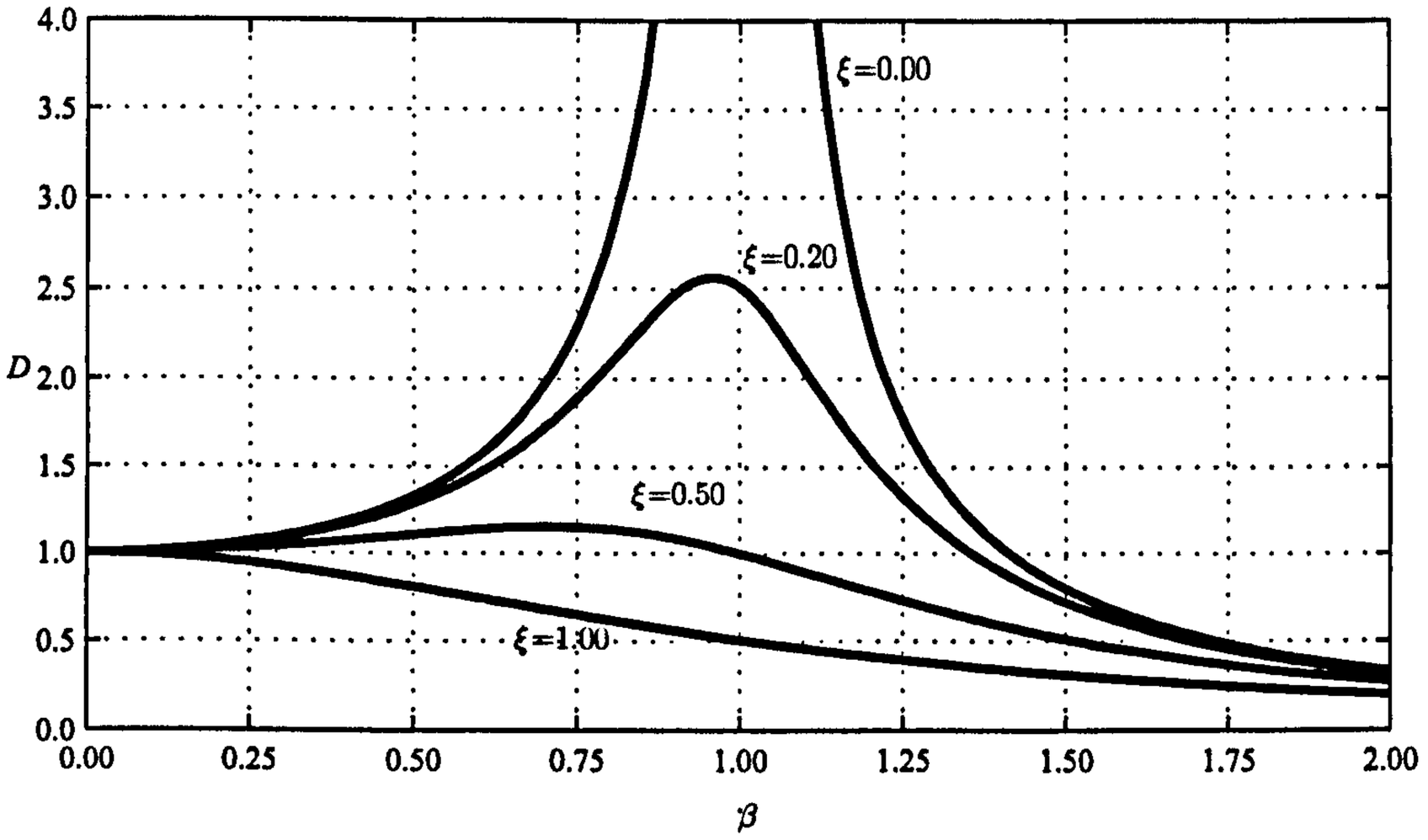

Figure 3.25: Magnitude response curves of a SDOF for different damping coefficients.

The concept of damping is not simple to define. Damping can be attributed to internal particle friction, plasticity and viscosity phenomena such as slippage at particles interfaces, (Graff, 1975). For simple systems, the actual damping that takes place can be associated, for simplicity purposes, to an equivalent mechanical viscous damping. This idealised viscous damping induces dissipation forces proportional to the velocity of the oscillating particles, and is therefore only frequency dependent, (Muscolino *et al.*, 2005).

A more realistic model of damping is provided by the notion of hysteretic damping. This form of damping is related to the actual properties of the system, such as its mass and stiffness, and is independent from the frequency of excitation. The particular cases of soils and rocks are good examples of occurrence of natural damping is largely of hysteretic nature, Gemant and Jackson (1937); Wegel and Walther (1935).

The force due to linear hysteretic damping, for an harmonically loaded system,

is provided in equation 3.87,

$$f_D(t) = i\zeta k u(t) \tag{3.87}$$

where ζ is the hysteretic damping ratio, k the system elastic stiffness and $u(t)$ the system's response. The imaginary constant i enables the damping force to be in phase with the velocity. Through its use, a complex stiffness of the system need also to be defined.

$$\hat{k} = k(1 + i\zeta) \tag{3.88}$$

This form of hysteretic damping leads to an equation of motion that is impractical to handle for simple analytical studies such as those carried out, and therefore will not be pursued further. Nevertheless, it can be said that even though viscous damping is frequency-dependent and hysteretic damping is amplitude-dependent, the response of the system's models are identical when excited at resonance frequency, (Clough and Penzien, 1993).

The equivalent viscous damping will be used henceforward rather than the hysteretic damping due to producing simpler analytical models and of being well accepted in the study of body vibration, (Clough and Penzien, 1993). Viscous damping is assumed to be a property of the medium but also a function of the particle oscillation velocity. Its determination is useful because it enables the use of the $c\dot{u}$ component of equation 3.69 which is the start point to characterise vibration behaviour of simple dynamic systems. Due to the added degree of complexity of using hysteretic damping, it will not be used in relation to the present study of testing with bender element.

The determination of the equivalent viscous damping coefficient, c, for a SDOF system can be made in a different number of ways. The methods for its determination make use of the system's response to different vibration and load conditions

and are presented next.

3.9.1 Free-Vibration Decay Method

In order to determine the damping of a simple mechanical system, one of the most intuitive methods is the free-vibration decay method. It consists of disturbing the system with a short duration impact and letting it oscillating freely afterwards. In this way, the main cause of decay is the system's own damping. An example of a decaying time history of such a free oscillation response is given in figure 3.26 which regards the free oscillation of an idealised damped SDOF system.

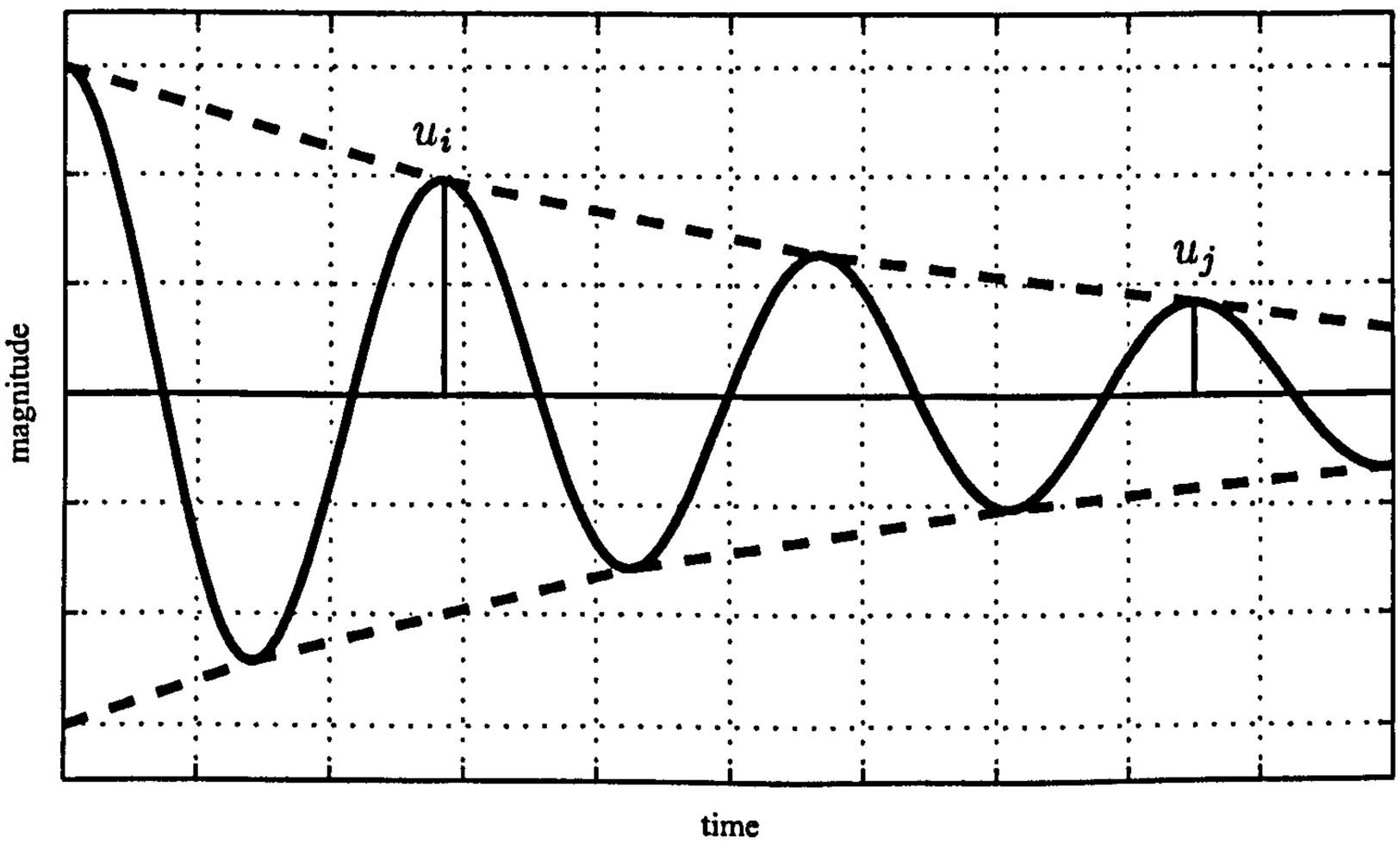

Figure 3.26: Time history response of damped SDOF system.

The decay takes a form of a logarithmic decrement, δ, given by:

$$\delta = \ln \frac{u_i}{u_j} = \frac{2(j-i)\pi\xi}{\sqrt{1-\xi^2}} \tag{3.89}$$

which, as described in Clough and Penzien (1993), allows an approximation to the

value of the damping ratio, ξ, by

$$\xi \cong \frac{u_i - u_j}{2n\pi u_j} \text{ where } \quad n = j - i \tag{3.90}$$

The estimated damping ratio obtained using the free-vibration decay method is higher than the actual exact value. The error of this approximation goes up to 25% for values of damping higher than 10%. The quantification of this error is given with more detail by Clough and Penzien (1993).

3.9.2 Half-Power Bandwidth

Another method of determining a system's equivalent viscous damping, c, is called half-power bandwidth method. It makes use of the frequency-response curve of the system, which is obtained by determining the amplitude of the response at different frequencies. An example of such a curve is given in figure 3.27.

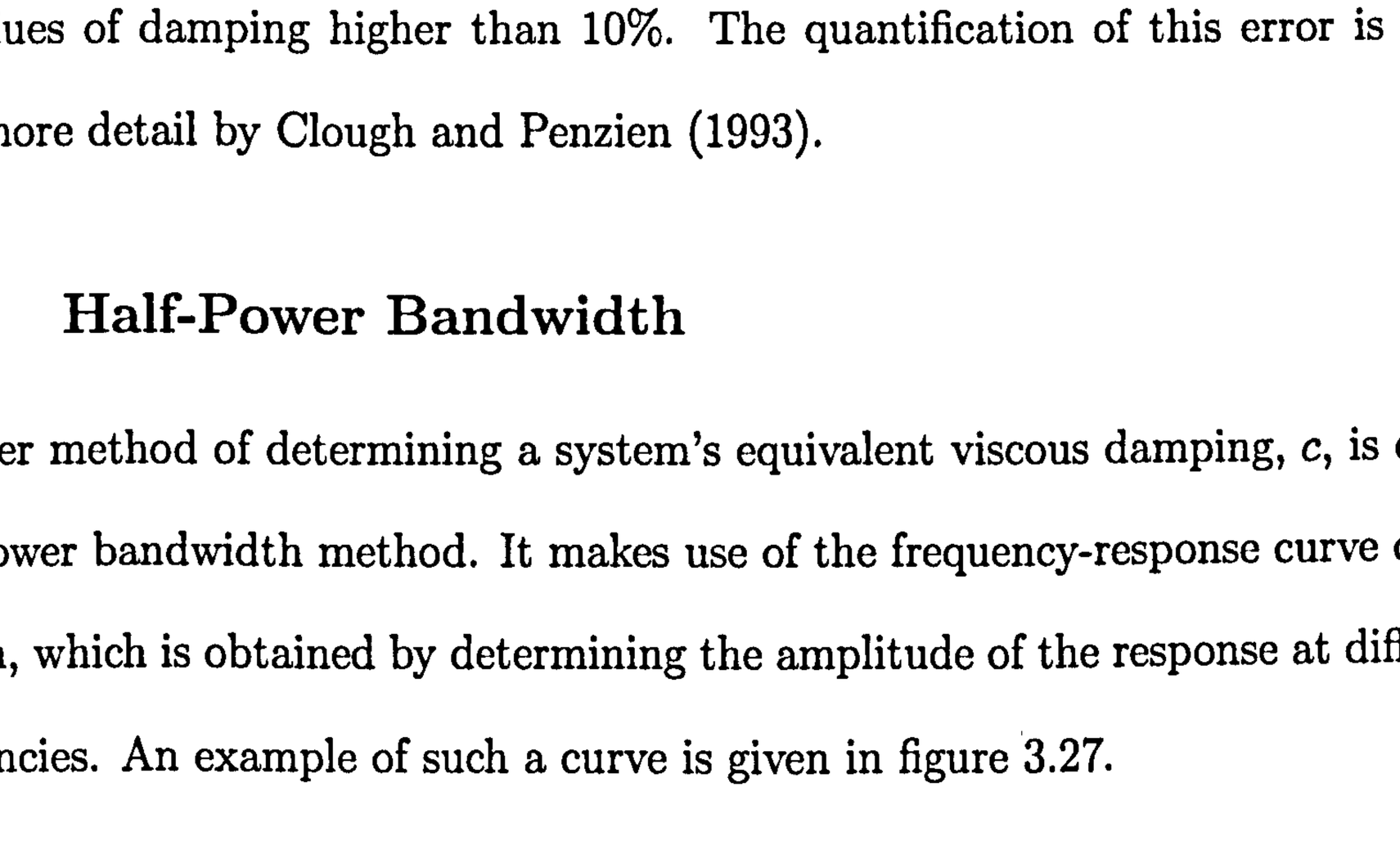

Figure 3.27: Magnitude frequency response of a damped harmonic-loaded SDOF system.

At the response curve in figure 3.27 it can be noted that for lower frequencies,

the amplitude of the response starts from the value of the static amplitude, which is given by the ratio of the initial load over the stiffness of the system, a_0/k. With increasing frequency the magnitude of the response is amplified until it reaches a maximum near the natural frequency, ω. Past the natural frequency the amplitude of the response diminishes, eventually becoming lower than the initial static response.

The half-power bandwidth method focuses on the response band around the maximum response, in the frequency range for which the response of the system is higher than at least $u(t)$ >peak/$\sqrt{2}$. The value of the damping ratio, ξ, can then be obtained by approximation, for low values of ξ, using the relation between the frequencies that limit the half-power bandwidth, as given by:

$$\xi \cong \frac{f_2 - f_1}{f_2 + f_1} \tag{3.91}$$

The obtained approximation to the value of the equivalent viscous damping contains an error. The approximated results are also higher than the exact value, although not as high as the approximation obtained using the free-vibration decay method. This means the half-power bandwidth can be used to estimate the value of damping with less error for systems with relatively higher values of damping.

3.10 Distributed Parameter Systems

3.10.1 Generalised SDOF Systems

The theoretical principles that apply to SDOF systems can, in some circumstances, be generalised to multiple degree of freedom, MDOF, systems, (Clough and Penzien, 1993). Two examples of MDOF systems which can be modelled using the dynamic principles of a SDOF system are:

- Systems with linked rigid bodies where the mass is concentrated in arbitrated

rigid bodies and the elastic behaviour is associated with weightless spring elements, and

- Systems with distributed mass and elastic properties. These systems can be described by generalised SDOF principles if the displacements are monotonic, i.e., the deformed body can only assume one deformed shape or form.

Systems with elastic properties and distributed mass are of special interest for the present study, since the dynamic principles of SDOF can be generalised to provide simple analytical tools, that can be used to model their dynamic behaviour. Bars with simple boundary conditions, such as bender element transducers and particular slender soil samples, can both be assumed to behave as distributed mass and elastic properties MDOF systems, (Lee and Santamarina, 2005; Richart *et al.*, 1970).

A system with distributed flexibility has an infinite number of degrees of freedom. The application of SDOF principles is possible for a number of simple deformed shape or modes of the vibrating body. The properties of the system that must be considered are its distributed stiffness, $EI(x)$, and its distributed mass, $m(x)$.

It is convenient to fragment each monotonic displacement into its amplitude that is function of time, $Z(t)$, and its shape, which is a function of position, $\eta(x)$.

$$u(x,t) = \eta(x) \cdot Z(t) \tag{3.92}$$

Because the amplitude of the displacement function varies with time, it can be used to produce an equation of motion more general than that presented by equation 3.69, and which takes the form:

$$m^* \ddot{Z}(t) + c^* \dot{Z}(t) + k^* Z(t) = p^*(t) \tag{3.93}$$

where m^* is the generalised mass, c^* is the generalised damping coefficient, k^* the generalised stiffness and $p^*(t)$ the generalised load function of the system.

Considering a bender element fixed to the end plate of a triaxial cell, it is possible to relate the generalised properties of the SDOF system to the actual properties of a cantilever beam system and actual load function, m, c, k and p, by integrating them along the bar's length. Figure 3.28 illustrates such a system,

$$m^* = \int_0^L m(x)\,\eta(x)^2 dx \tag{3.94}$$

$$c^* = \int_0^L c(x)\,\eta(x)^2 dx + C_1 \int_0^L EI(x)\,\eta''(x)^2 dx \tag{3.95}$$

$$k^* = \int_0^L k(x)\,\eta(x)^2 dx + \int_0^L EI(x)\,\eta''(x)^2 dx \tag{3.96}$$

$$p^*(t) = \int_0^L p(x,t)\,\eta(x) dx \tag{3.97}$$

where C_1 is a damping constant. Equations 3.94 to 3.97 describe the generalised mass, damping, stiffness and load for the cantilever beam with no axial force applied to it.

3.10.2 Partial Differential Equations of Motion

Partial differential equations can be used to formulate the equations of motion of a dynamic system with distributed parameters such as a cantilever. A cantilever beam provides a suitable example with potential application to bender element test analysis.

Consider the vertical cantilever beam, with section properties $EI(x)$ and $m(x)$, represented in figure 3.28, in a free-vibration state of motion. The relevant load cases for the present analysis are those involving flexural deformation. The properties of the beam section are considered to be constant along its length, i.e., its flexural

stiffness and its distributed mass become $EI(x) = EI$ and $m(x) = m$.

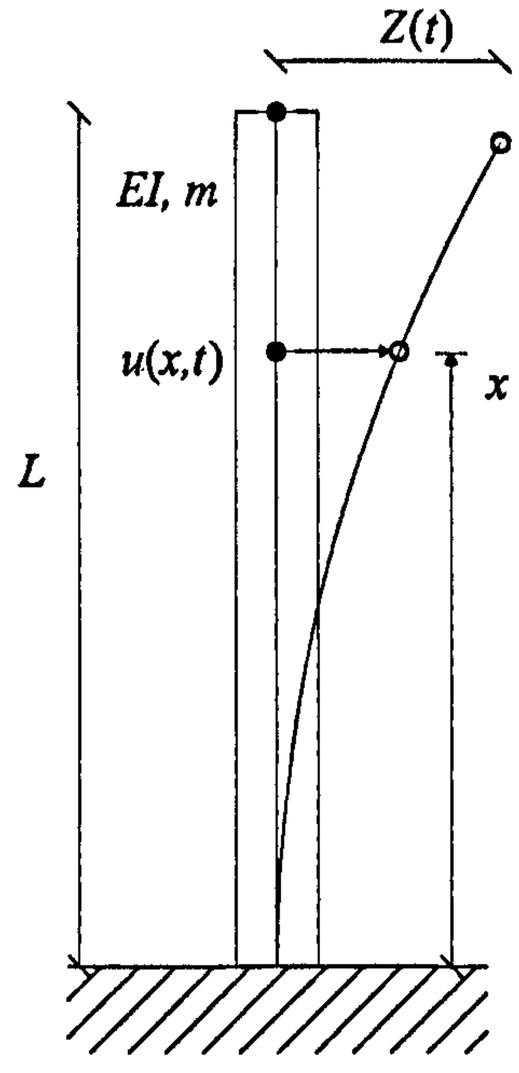

Figure 3.28: SDOF system of flexed cantilever.

According to the Bernoulli-Euler theory, which takes into account the transverse inertia forces and neglects the effects of shear deformation and rotational inertia forces, (Karnovsky and Lebed, 2001), the equation of motion can be expressed as:

$$EI\frac{\partial^4 u(x,t)}{\partial x^4} + m\frac{\partial^2 u(x,t)}{\partial t^2} = 0 \tag{3.98}$$

Other more complete and complicated theories could also be named. Timoshenko's theory, for example, takes into account the rotational inertia and the shear deformation of the beam, (Karnovsky and Lebed, 2001). Even though the Bernoulli-Euler theory is not the best to model an exact solution, it provides simpler analytical tools and is it produces first order results with sufficient precision, (Karnovsky and Lebed, 2001).

The beam displacement $u(x,t)$ is again divided into an amplitude and shape functions, $Z(t)$ and $\eta(x)$, as in equation 3.92. Equation 3.98 can now be expressed

in the form of two differential equations,

$$\ddot{Z}(t) + \omega^2 Z(t) = 0 \tag{3.99}$$

$$\eta^{iv}(x) - \delta^4 \eta(x) = 0 \tag{3.100}$$

where ω is the vibration circular frequency and δ is a function of the boundary conditions. The frequency equation 3.101 expresses the relation between ω and δ and is at the base of modal analysis, according with the Bernoulli-Euler theory.

$$\omega = (\delta L)_n^2 \sqrt{\frac{EI}{mL^4}} \quad \text{for} \quad n = 1, 2, 3, \ldots \tag{3.101}$$

Different solutions for the value of δ correspond to independent modes of vibration of the beam, which occur at different frequencies ω, and are associated with different shapes. The frequency of each mode of vibration, as well as its corresponding shape are dynamic characteristics of the system and are also known as eigenvalues, ω^2, and eigenvectors.

The expressions for the determination of δ for simply supported beams and cantilever beams with a mass at the free end are presented in equations 3.102 and 3.103 respectively.

- Simply supported beam:

$$\sin \delta L = 0 \tag{3.102}$$

- Cantilever with mass at the free end:

$$\delta L = \frac{1 + \cos \delta L \cosh \delta L}{\alpha \left(\sin \delta L \cosh \delta L - \sinh \delta L \cos \delta L \right)} \tag{3.103}$$

where α is the ratio between the mass at the free end, M, and the mass of the beam.

$$\alpha = M/(mL) \tag{3.104}$$

A simple cantilever with no concentrated mass is a particular case of the cantilever beam with a mass on top where $M = 0$ and therefore $\alpha = 0$. Its corresponding value of δ can be calculated using the simplified equation 3.105.

- Simple Cantilever:

$$\cos \delta L = -(1/\cosh \delta L) \tag{3.105}$$

3.11 Resonant Column

Resonant columns are well known laboratory devices for the dynamic testing of soil samples. Their use is related to the use of bender elements because they are also designed to determine the small-strain shear-stiffness of soils. It is therefore relevant to understand their application as well as its supportive theory, and to distinguish the differences and the similarities with bender element testing. A short summary of the application of bar vibration theory, as presented in section 3.10.2, is presented in the context of resonant column testing.

The resonant column apparatus is generally used to excite longitudinal or torsional modes of vibration of soil samples, (Richart *et al.*, 1970). Only the case of torsional excitation is discussed, for cylindrical columns of soil samples, since it is the most commonly used mode of excitation. The first mode of torsional vibration is favoured because it is the only mode of vibration where waveguide dispersion is not present, (section 3.5.4). When used this way, resonant columns are also known as torsional shear apparatus, (Kim and Stokoe, 1994). A generic schematic repre-

sentation of a resonant column is given in figure 3.29.

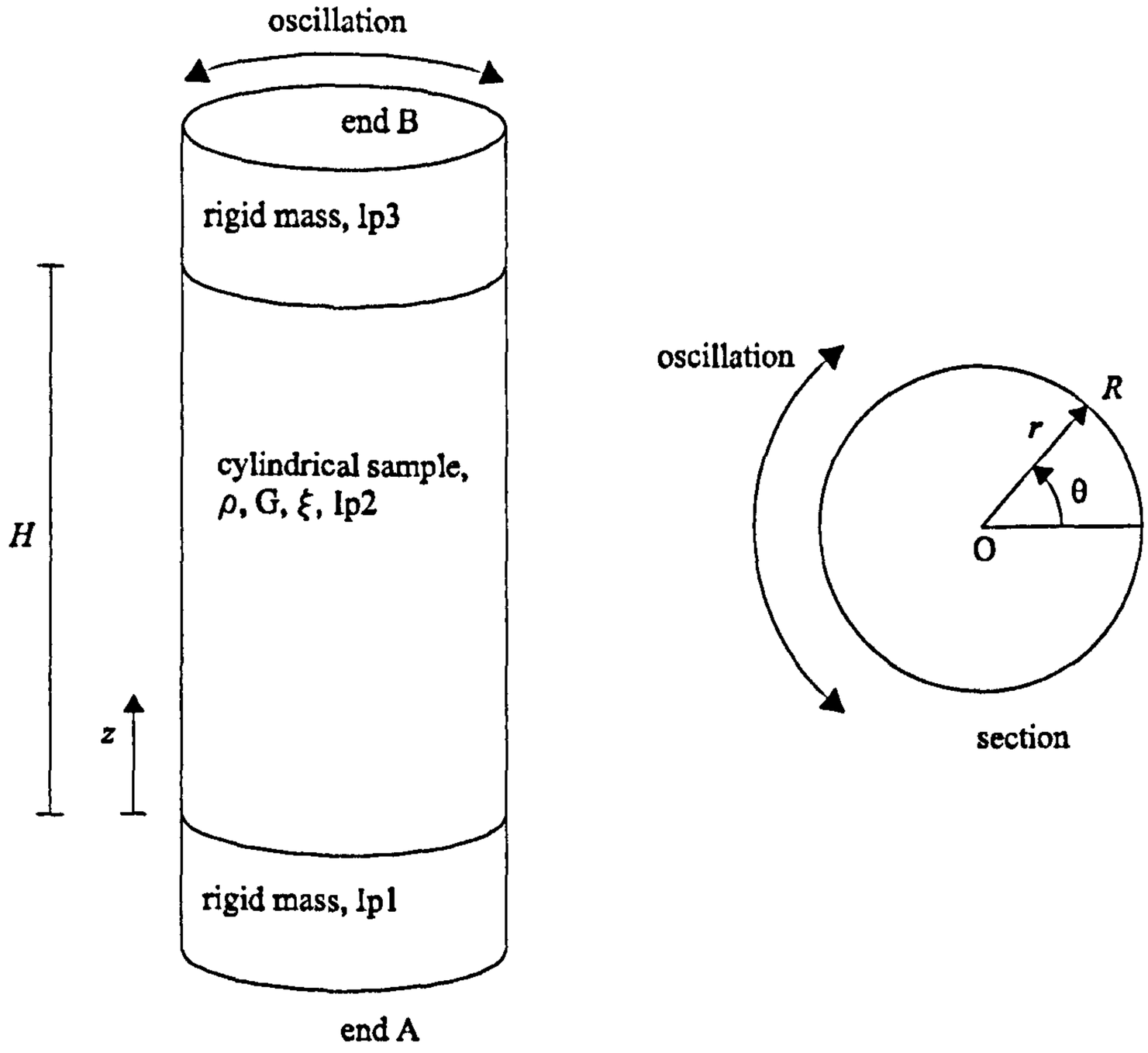

Figure 3.29: Generic resonant column model.

The sample can be excited in a torsional mode and its response monitored. The dynamic behaviour of the soil can be expressed as a response curve. This response curve contains the amplitude and phase delay of the response at each frequency of excitation. The properties of the response curve and its components enable the determination of the shear-stiffness of the sample's constitutive medium, as well as its attenuation in the form of a damping coefficient.

Soil stiffness is strain level dependent, (figure 1.1), except at low and very low strains, (Atkinson, 2000), where the elastic relation appears to be linear. The study of the first torsional mode of vibration of a cylindrical soil sample, applying small-strains, was devised to overcome some of the complexities of general soil dynamic behaviour.

The determination of the medium's shear stiffness is made by the application of the torsional equation of vibration, 3.44, (Rix and Meng, 2005). The boundary

conditions must be considered to enable the application of the main equation of vibration equation in a specific form. Primarily, these boundary conditions relate to the fixity of the ends of the cylindrical sample, the inertia of the caps attached to the free ends, which participate and influence the system dynamic response, and the torque driving the oscillation, (figure 3.29). Two types of end fixity are considered in the relevant literature, fixed-free and free-free ends, (Ashmawy and Drnevich, 1994).

3.11.1 Fixed-Free Boundary Conditions

The fixed-free boundary condition is the traditional set-up of the resonant column apparatus, as presented by Drnevich *et al.* (1978), and stated initially in ASTM (1978) geotechnical testing standards. In such a set-up, the mobility is restricted to one of the ends of the cylindrical sample, and torque load applied to the other end, also known as passive and active ends respectively. Referring back to figure 3.29, and according to ASTM-D-4015 (2000), the fixed end is assumed to be the bottom end A. This translates into the following boundary condition: $\theta(0,t) = 0$. The torque load, p_T, is then applied at the other end of the sample, in this case, the top rigid mass at end B. Again according to ASTM-D-4015 (2000), the geometry ratio height-diameter, of the cylinder sample must be of 2:1 with the sample placed vertically.

The torque load can either be impulsive or continuous, creating transient or steady-state responses from the system respectively. If the load is impulsive, the sample is left to rotate freely, in what is a damped free vibration response, as described in section 3.8.2. The sample is expected to assume a torsional mode of oscillation at its respective natural torsional frequency. Using an impulsive load and obtaining a damped free vibration allows to determine the natural frequency of the system, which is used together with the equation of vibration 3.44 to obtain the shear

stiffness of the sample. The determination of the viscous damping coefficient could also be obtained from the observation of the decrease of the oscillation amplitude, applying the method of free-vibration decay described in section 3.9.

If the torque load is harmonic continuous, then the sample response assumes a steady-state of vibration, oscillating at the same frequency as the load. By varying the load frequency, the magnitude and phase delay response curves of the sample can be obtained, making this the ideal load case to obtain the complete response curves of the system. When using a fixed-free configuration, the continuous harmonic oscillation is usually driven by a coil-magnet device, (Drnevich *et al.*, 1978). Some error can occur in the readings due to the nature of this test equipment. The coil-magnet, used to drive the oscillation of the sample, uses a magnetic field that adds extra damping to the system, which is known as the back electromagnetic force, back-EMF, (Wang *et al.*, 2003). If the damping of the medium is low to start with, the back-EMF can be a significant source of error, (Cascante *et al.*, 2005; Meng and Rix, 2003). Nevertheless, it does not significantly affect the determination of stiffness since the resonance frequency is little affected by damping, as expressed in equation 3.70.

The desired properties of the system are its stiffness and the damping. In order to determine them, other relevant properties of the cylindrical sample and rigid masses need to be determined prior to the use of the frequency equation 3.107. For a general resonant column test system, such as the one pictured in figure 3.29, the relevant properties to the determination of the shear-stiffness of the sample are presented in table 3.2.

The continuous harmonic torque imposing the torsional oscillation of the system can take the form of well known sinusoidal function,

$$p_T(t) = a_0 \exp(i\overline{\omega}t) \tag{3.106}$$

Part	Property	Symbol
rigid mass at end A	polar moment of inertia	I_{P1}
rigid mass at end B	polar moment of inertia	I_{P3}
sample	height	H
	radius	r
	volume	$V = \pi r^2 H$
	density	ρ
	mass	$M = V * \rho$
	mass polar moment of inertia	$I_{P2} = \frac{\pi R^4}{2} \cdot M$
(to be determined)	natural frequency	ω_n
(to be determined)	shear stiffness	G
(to be determined)	damping ratio	ξ

Table 3.2: Relevant properties of the sample and rigid masses of a resonant column apparatus according to figure 3.29.

where a_0 is the amplitude and $\overline{\omega}$ the forced circular frequency of the oscillation.

The dynamic response of the system is obtained by measuring the rotation at the free end B, $\theta(H,t)$. The theoretical frequency response equation translates the ratio between the harmonic torque and the angular response as given in Rix and Meng (2005),

$$\omega_n = \beta\sqrt{\frac{G}{\rho H}} = \beta\frac{c_t}{H} \tag{3.107}$$

where β is a parameter which reflects the boundary conditions. It is worth noting the similarities with the Euler-Bernoulli beam frequency equation 3.101, where essentially the flexural stiffness, EI, is replaced by a torsional stiffness.

Equation 3.108 describes a non-damped system, where $\xi = 0$. For such systems, the amplitude of the oscillation tends to infinity as the load frequency nears the characteristic frequencies of the system. The ratio between the load and the torsion

amplitude is given in equation 3.108:

$$\frac{p_T(t)}{\theta(H,t)} = I_{P2}\frac{\beta}{\tan\beta}\overline{\omega}^2 - I_{P3}\overline{\omega}^2 \tag{3.108}$$

which in the limit becomes

$$\lim_{\overline{\omega}\to\omega_n} \theta(H,t) = \infty \quad \Rightarrow \quad \lim_{\overline{\omega}\to\omega_n} \frac{p_T(t)}{\theta(H,t)} = 0 \tag{3.109}$$

giving

$$\beta\tan\beta = \frac{I_{P2}}{I_{P3}} \quad \text{for} \quad \overline{\omega} = \omega_n \quad \text{and} \quad n = 1,2,3,\ldots \tag{3.110}$$

where $\overline{\omega}$ is the load frequency and ω_n is the characteristic first mode torsional frequency of the system.

It is possible, knowing the torsional resonant frequency, to obtain the shear wave velocity and consequently, using equation 3.12, to obtain the shear stiffness of the medium. The torsional resonance frequency corresponds to the first mode of torsional vibration, (Richart *et al.*, 1970). Equation 3.107 is therefore the governing equation of resonant column testing in torsional with fixed-free ends boundary conditions, (Cascante and Santamarina, 1997).

3.11.2 Free-Free Boundary Conditions

More recently, resonant columns capable of free-free ends boundary conditions have also been used, (Stokoe *et al.*, 1994). This configuration was devised to provide an alternative to the fixed-free configuration and its inherent complexity due to the use of a coil-magnet device needed to drive the system, (Kalinski and Thummaluru, 2005). With the free-free set-up, a simpler torsional excitation device can be used to drive the system, which must now be placed horizontally.

The torsional frequency equation of a system with these boundary conditions is

the same as for the fixed-free boundary conditions provided by equation 3.107. The difference in analysis can be found in the determination of parameter β. With the free-free set-up, both mass inertias at each end of the sample participate in the oscillation of the system and must therefore be considered, (Kalinski and Thummaluru, 2005). Equation 3.111 is used to calculate β for the free-free torsional vibration case,

$$\tan\beta = \frac{(\mu_1 + \mu_2)\beta}{\mu_1\mu_2\beta^2 - 1} \tag{3.111}$$

where

$$\mu_1 = \frac{I_{P1}}{I_{P2}} \quad \text{and} \quad \mu_2 = \frac{I_{P3}}{I_{P2}} \tag{3.112}$$

Chapter 4

Synthetic Soil Samples

4.1 Introduction

Polyurethane synthetic rubber was chosen as replacement of soft clay soil for the geometry parametric study presented in section 6. The parametric study required different 32 samples with varied geometries and constant mechanical properties. The main practical advantage in the use of synthetic materials over real soil is the stability of its mechanical properties, particurlaly when compared with soft soils.

The process of natural soil sampling can disturb the original fabric of the soil. During the sampling process, the stress state and the moisture content of the soil are undoubtedly modified, (Craig, 1997). This might lead to reconfigurations of the particle skeleton but also to alterations in chemical-related phenomena such as leaching, ageing and cementation, (Nagaraj and Norihiko, 2001). During the handling and storage of the samples, similar aspects of physical and chemical alterations might also occur, (Head, 1998). The nature of these disturbances is random since they are not intended and besides, most can go undetected prior to testing the samples. Even if the disturbances to the soil were kept to an acceptable minimum, the heterogeneity found in the soil deposits can also lead to variations in the properties

of distinct samples samples.

For the parametric study natural or artificial clays, such as kaolin, where considered unsuitable due to the inherent difficulty of handling such a great number of samples, as well as to ensure their homogeneity, or even of being able to measure, quantify and control their heterogeneity. The differences in mechanical properties between samples would become an unwelcome source of error. It was therefore important to find a suitable alternative to soft clay which could behave in a similar way for the range of stresses and strains applied during bender element testing and which could overcome these inherent uncertainties. Synthetic rubber was a straightforward choice.

Appropriate synthetic materials can overcome the difficulties posed by actual soils concerning uniformity and consistency of the samples, which is one of the main requirements of a parametric study. The chosen synthetic material from which the tested samples were obtained was polyurethane rubber. This material is known for its elasticity, mechanical resilience and chemical stability, (Doi, 1996). Also, there was some history of using such materials in geotechnical laboratory studies by Stokoe *et al.* (1990) and Kim and Kweon (2000). Polyurethane rubber can be casted into moulds, facilitating the production of samples with the desired range of geometries, even including a slot to place the bender element transducers. Polyurethane rubber is commercially available at very reasonable prices.

4.2 Polymers

Polymers are one of the most common type of materials found in nature or in present human activity. The term polymer indicates a certain chemical configuration characterised by the inclusion of certain types of macromolecules in the molecular structure. These macromolecules are formed by chains of smaller molecules known

as monomers.

A monomer is a molecule, usually carbon based, with the potential of forming four chemical links. Two of these chemical links are usually with hydrogen atoms. One of the most common basic monomers is the hydrocarbon CH_2, also represented as:

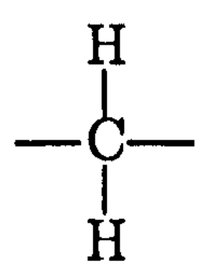

Figure 4.1: Typical monomer hydrocarbon molecule.

There are two types of chemical link between monomers forming a polymer. The main chemical link, and the one responsible for forming the polymer chain, is the covalent bond. The covalent bond is a strong chemical link involving the sharing of electrons between monomers, (Tabor, 1991). This bond forms a two-dimensional string macromolecule. A typical polymer formed by covalent bonds between CH_2 monomers is presented in figure 4.2.

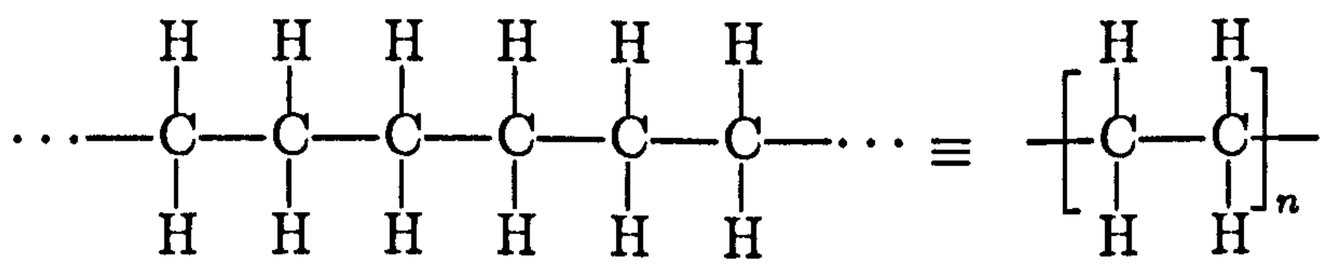

Figure 4.2: Typical polymer molecule.

The second possible chemical link between monomers, which is not universal for all polymers but is present in rubber-like materials such as the ones considered, is the cross-link bond, (Warner and Terentjev, 2003). This bond is weaker than the covalent bond and is responsible for some of the properties that make polymers have a rubber-like behaviour. Cross-links bonds between monomers of a polymer chain form a three-dimensional network skeleton. If it was not for these cross-link bonds,

the polymer would be in a liquid state, (Tabor, 1991).

Polymers are usually characterised by a particular monomers, nevertheless, their properties depend on a number of factors:

Skeleton Linearity describes the configuration of the macromolecule chains. The chain can be linear, or non-linear. A linear skeleton is a simple chain with two ends. Non-linear skeletons are either branched, forming a two-dimensional structure with more than two ends, or are organised as a network, forming a three-dimensional complex structure. The distinct skeleton organization is due to the functionality of the monomers present in the polymerization reaction. For monomer functionality of two or less, each monomer can only bond with two others. Monomer functionality higher than two permits the formation of non-linear skeletons of complex chains. Non-linear network skeletons have not only covalent bonds between monomers but also have, at certain junction points, cross-link bonds. The ratio of cross-link bonds is variable and actually plays an important role in the properties of the polymer.

Monomer Diversity is a simple differentiation between homopolymers and copolymers. Homopolymers have only one type of monomer, which can include one or more sub-types of monomers. Copolymers have more than one type of monomer.

Crystallinity describes the regularity of the polymer chain arrangement. In terms of regularity, a polymer chain varies between crystalline and amorphous arrangements. Polymer chain regularity, or lack of it, can be expressed in two senses, either referring to the intrinsic monomer disposition along the chain, and/or to the regularity of the chain arrangement in space.

Polymerization describes the reaction in which the polymer chains are formed. There is more than one way of distinguishing between polymerization reac-

tions. The activity potential of the monomers and polymer chains, where they can be classified either as step-polymerization or as chain-polymerization, (Feldman and Barbalata, 1996). In step-polymerization, any two monomers or molecules can react with each other which leads to the disappearance of monomers in the reaction. In chain-polymerization, monomers can only be added to active chain ends. The other characteristic of polymerization reactions is given by the concepts of poly-condensation and poly-addition. Poly-condensation is a reaction where small molecules are released during the polymerization and do not become part of the macromolecule. In poly-addition the reactions take place with no loss of molecules.

4.3 Polyurethane Rubber

Polyurethanes are a type of synthetic polymers relatively recently added to the polymer family, (Saunders and Frisch, 1962). Polyurethane rubbers have a low density network skeleton, are copolymers, have an amorphous molecule configuration and are formed by a step-polymerization of poly-addiction, (Feldman and Barbalata, 1996). Polyurethane rubber can contain a number of functional monomer groups but is characterised by the a monomer know as urethane, (Feldman and Barbalata, 1996).

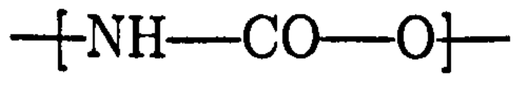

Figure 4.3: Representation of urethane monomer.

The development of polyurethane production is credited to Professor Otto Bayer. Through a chemical process of poly-addition, polyurethanes are generally obtained by the reaction of a diisocyanate group with a diol.

Such polymerization reaction is complex, involving a multi-step chemical process

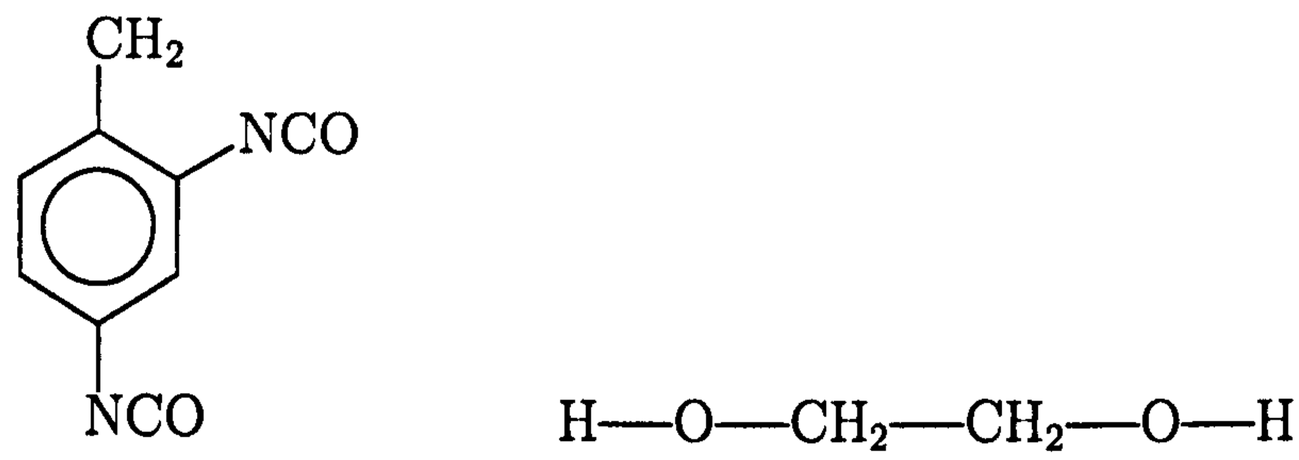

(a) diisocyanate (b) diol

Figure 4.4: Polyurethane main molecular groups.

which eventually leads to the formation of the polyurethane. Besides the polymerization reaction, where monomer molecules are added to the polymer chain, the chemical reactions that lead to the formation of cross-linking must also occur. The cross-linking reactions are also known as vulcanization, (The British Association of Synthetic Rubber Manufacturers, 1970). The chemical representation of a simple polyurethane monomer is given in figure 4.5.

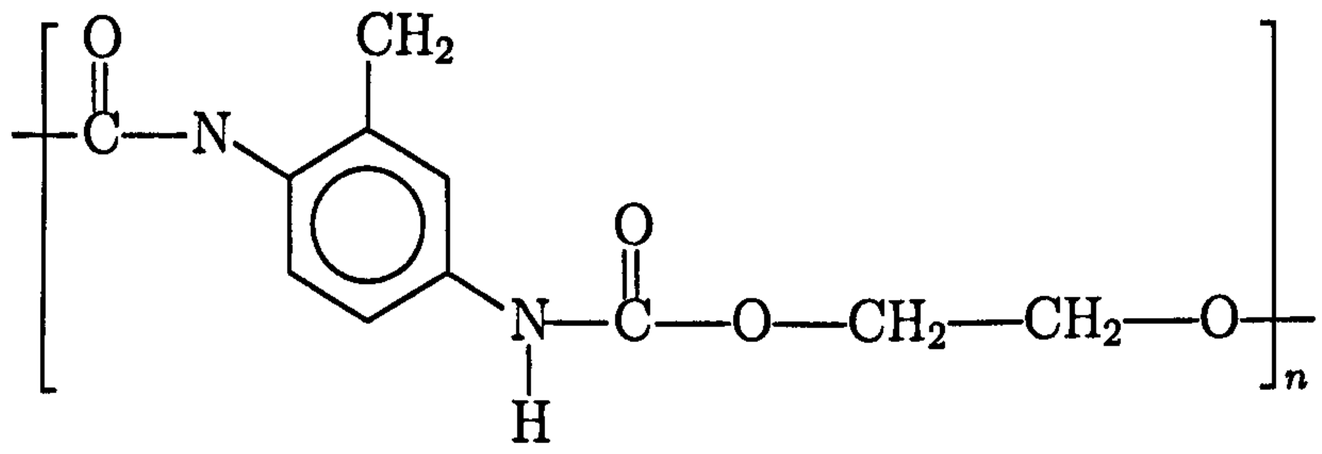

Figure 4.5: Chemical representation of a simple polyurethane monomer.

The properties of the polyurethane rubber depend on the density of cross-link bonds and on the rotation potential of the covalent bonds between monomers, (Warner and Terentjev, 2003). The reason why polyurethane can act like rubber or an elastomer is because of the ability of sliding between the monomer strings, enabled by flexible cross-link bonds and the capacity for molecular rotation at the covalent bonds. A representation of a polymer chain with cross-link bonds is given in figure 4.6.

The notion of elastomer derives from the capacity of a rubber-like material to withstand very large elastic strains which can go well over 100%, (Treloar, 1958).

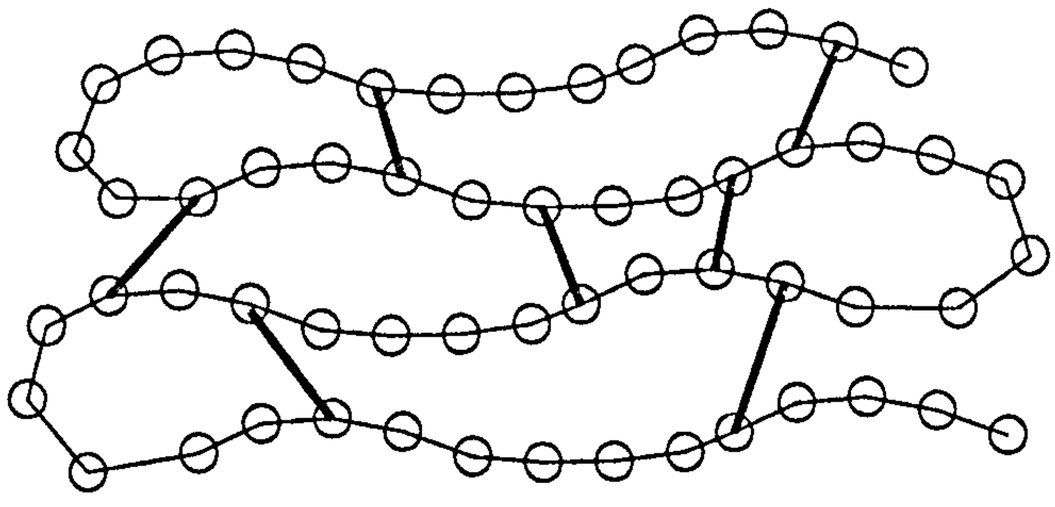

Figure 4.6: Polymer chain with covalent bonds in thin lines between monomers and cross-link bonds in thicker lines, forming an amorphous network skeleton.

Rubber-like materials are in fact viscous liquids with a solid behaviour due to the presence of the cross-links bonds, (Tabor, 1991). At small strains, rubber-like materials behave like liquids being near incrompressible, having a Poisson ratio near to 0.5, (Doi, 1996). For strains higher than 100% the Poisson's ratio varies with the elongation, (Claxton, 1958). Nevertheless, for the present study only small-strain behaviour is relevant and hence only contant Poisson ratios around 0.5 are considered.

4.4 Synthetic Rubber and Soft Soil

Besides the inherent practical advantages of using a synthetic material as a soil replacement to perform the parametric tests, it is important that a significant degree of comparability exists between the chosen material and actual soil. The mechanical behaviours of polyurethane rubber and soft soils are similar, for small-strains, since both can be assumed to be linear-elastic.

4.4.1 Soft Soil Consolidation

Time delayed strains are commonly referred to in the study of soft soils, for example when studying foundation settlements the application of a load to a soft soil enables the observation of instant and time delayed deformations, (Terzaghi and

Peck, 1967). In geotechnical terms the instant deformation is referred to as being an elastic deformation. The delayed deformation, or consolidation, is divided in two, known as primary and secondary consolidations, (Smith, 1990), where the secondary consolidation is also known as creep.

The primary consolidation is the deformation of soft soils due to the dissipation of the fluid phase pressure gained with the application of the load. The dissipation of the fluid pressure is accompanied by its flow according with the pressure gradient, being implicit that the soil is drained. The creep is the rearrangement of soil particles to accommodate the pressure transferred by the fluid. It is intuitive to assume that primary consolidation on its own is reversible and creep is not, and therefore is assumed to be a type of plastic deformation. Both primary and secondary consolidations can occur simultaneously if the soil structure has not experienced the applied stress before, or just primary consolidation, on what is referred to as an over-consolidated soil, (Smith, 1990).

The influence of time delayed deformation behaviour of soft soils is associated with what can also be understand as of viscous nature, (Marques *et al.*, 2004). Such viscous-like behaviour is influenced by temperature and strain level, (Campanella and Mitchell, 1968; Mitchell, 1964).

4.4.2 Viscosity

Viscosity is a concept usually applied in the Newtonian context of fluids resistance to flow, (Tabor, 1991). It can be observed when the shear for a given stress is not accomplished immediately but distributed in time. Some viscous-type behaviour is, to a lower degree, present in solid materials as well. Coincidently, both rubber-like materials and soft soils have considerable viscous behaviour. In fact, rubber-like materials are also known as non-Newtonian fluids, (Podesta, 2002).

The characteristics of rubbers viscous behaviour can be expressed by the decom-

position of strain into two components, making use of a differential equation relating stress σ, strain ε, and time t, (Maxwell and Niven, 1890),

$$\frac{d\varepsilon}{dt} = \frac{1}{K}\frac{d\sigma}{dt} + \frac{\sigma}{\beta} \tag{4.1}$$

where K is a constant modulus of elasticity and β a viscosity constant, characteristic of the material, (Treloar, 1958). The elastic and viscous components of the equation, in which the strain and the rate of strain increase, are proportional to the stress.

Synthetic rubbers and soft soils are both commonly described as having visco-elastic dynamic behaviour. Their complex behaviour has been studied making use of empiric mechanical models. A common reference in the modelling of both materials is made to the independent work of Kelvin (1887) and Voigt (1887) where such mechanical model is described.

A classic visco-elastic model for soft soil dynamic behaviour was given in Biot (1956). Since then further models have been developed, (Bardet, 1992). The key for the analysis of soft soil behaviour is the consideration of the two distinct solid and liquid phases of a nearly saturated soil, making the consideration of porosity fundamental. So much so that Biot (1956) described the visco-elastic behaviour of clays as poro-elastic, porosity being the percentage of soil volume occupied by the liquid phase, usually water. Polyurethane rubber is also known for its viscous behaviour, not due to the presence of two phases as in soft soils but due to its molecular configuration, (Warner and Terentjev, 2003).

To observe the significant time delay of a polyurethane rubber deformation, a simple compression test under constant load was carried out. Figures 4.7(a) and 4.7(b) show the deformation values of the compression of a cylindrical polyurethane rubber sample, during time interval past the initial load. The sample has a diameter of $D = 38\text{mm}$, a height of $H = 76\text{mm}$, a density of $\rho = 1000\text{kg.m}^{-3}$ and is under a

constant load of 1.0kg.

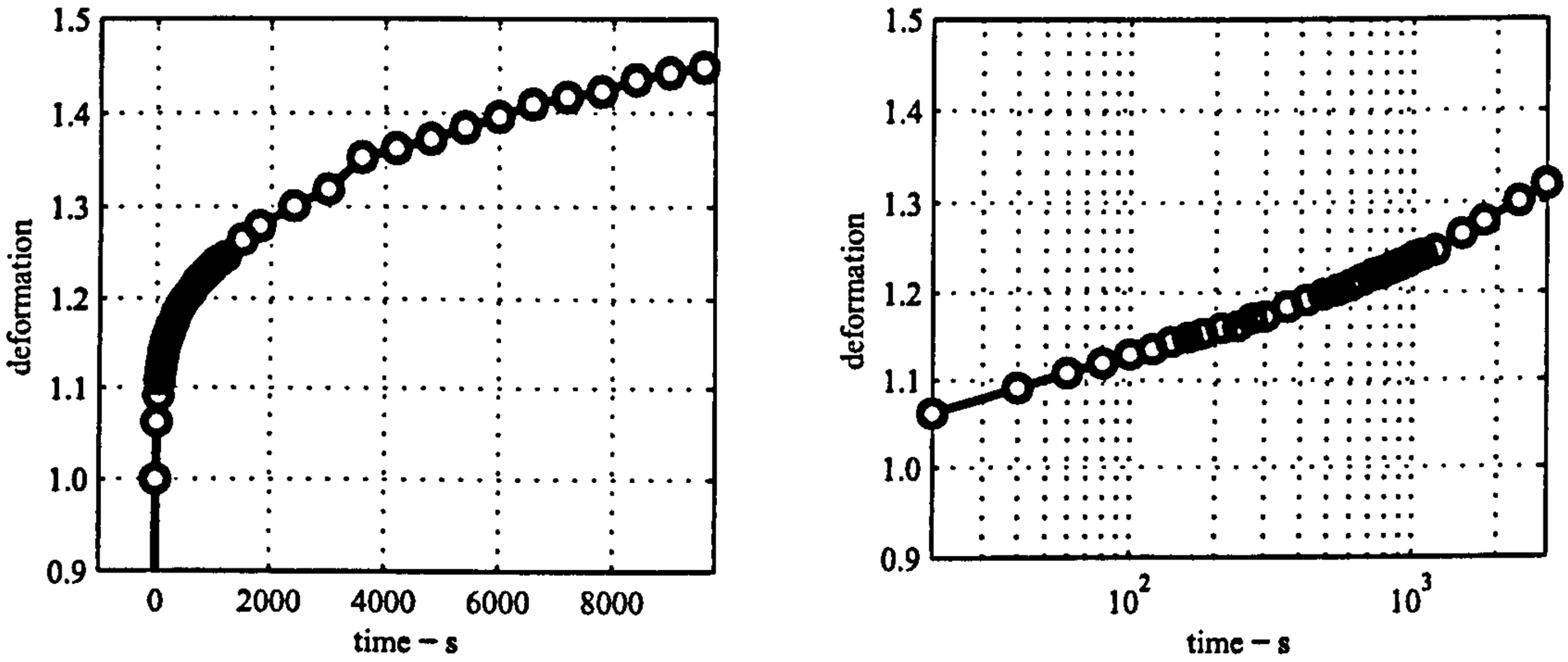

(a) linear time axis

(b) logarithmic time axis

Figure 4.7: Simple compression load test on polyurethane cylinder.

The sample deformation is presented normalised in relation to the initial elastic displacement of 8.20mm. After 10^3s, the differential deformation increased by around 40% of the initial deformation.

The dynamic loading of rubber-like materials within a frequency range of $f \in [0.5 \;\; 20.0]$kHz means that the duration of the load is quite small, in the range of $t \in [0.5 \;\; 20.0] \times 10^{-4}$s. Considering the solution of equation 4.1 in the form:

$$\varepsilon = \frac{\sigma}{K} + \int_0^t \frac{\sigma}{\beta} dt \tag{4.2}$$

such a short load duration makes the viscous term of the strain equation negligible, in comparison with the elastic term. So, for such short duration loads, the viscous component becomes negligible and can be omitted.

The duration of the load for soft soils and rubber-like materials is important to determine the extent of the consolidation and other viscous phenomena. The considered dynamic load frequencies result in stress being applied to the media for relatively short durations of time. Therefore, the viscous component of strain can

be assumed to be negligible, $\Delta t \cong 0 \Rightarrow \int_0^t \frac{\sigma}{\beta} dt \cong 0$, thus enabling the application of linear-elastic models of behaviour.

4.4.3 Molecular Structure

Soft soils, when saturated, have two phases, solid and liquid. That is the reason for its strong visco-elastic or poro-elastic behaviour, (Biot, 1956). The solid and liquid phases are not independent from each other but interact to form what can be considered, to some extent, a composite material. The cohesion between the solid particles can be obtained due to geometric nature of the solid particles and ionic nature of fluid particles. As the size of a particle decreases the ratio between the surface and the volume increases. Small enough particles, such as clay particles $D < 2\mu$m, have electrically charged surfaces, enabling a ionic bond between the solid particles and ionic fluid particles, such as water molecules. Some bonds between solid soil particles are also possible. For example, due to ageing chemical alterations can lead to the formation of new bonds in what is known as cementation, (Dano *et al.*, 2004; Sørensen *et al.*, 2006).

Even though rubber-like materials do not have two or three distinct phases as soils do, they would behave as viscous fluids if it was not for the cross-link monomer bonds. In fact, their molecular amorphous structure is more similar to that of a liquid than to that of a solid.

Both the cross-link bonds and the soft-soils ionic bonds are quite weak and flexible, despite the exact nature of the bonds being different, the similarities between the two materials molecular structure is worth mentioning.

4.4.4 Strain Level

Soil has a non-linear relation between stress and strain, (Burland, 1989). A constant maximum stiffness is found at a range of low strains, as seen in figure 1.1. When solicited at strain levels lower than $10^{-3}\%$ to $10^{-4}\%$, depending on the soil properties, the apparent constant value of stiffness observed allows to consider the soil as a linear elastic medium.

Rubber has an elastic behaviour up to much higher strain levels than soils do. Nevertheless, this does not mean that it has a linear-elastic behaviour. Rubber-like materials, despite being elastic up to much higher strains than soft soils or even hard solids, have in fact a non-linear elasticity, (Treloar, 1958). The non-linear elastic behaviour of rubber-like materials is apparent for very large strains, $\epsilon > 100\%$, (Doi, 1996). For smaller strains, such as the strains considered in bender element testing, rubber-like materials can be considered to have linear-elastic behaviour.

4.4.5 Temperature

Rubber-like materials are quite sensitive to temperature. In fact, they have a unique counter-intuitive characteristic; unlike crystalline solids, their stiffness modulus increases with temperature, (Tabor, 1991). The stiffness modulus of rubbers not only increases with temperature, but is believed to be approximately proportional to absolute temperature, (Doi, 1996). Remembering the amorphous molecular configuration of such materials, when tension is applied to them, the polymer chains are pulled and tend to align with each other, thus increasing its degree of crystallinity. Due to their amorphous molecular configuration and because of the nature of the molecular cross-link bonds between polymer chains, the more energy is added to the system, the higher its entropy. For higher entropies the polymer chains resist more at being aligned. So, by increasing the temperature of a rubber-like material, the

energy and entropy of the system also increase, adding to the resistance of polymer chain alignment, and consequently, increasing the resistance to deformation of the material, i.e., stiffening it.

Rubber-like materials can be expected to behave as springs with a spring constant of K:

$$K = \frac{3k_B T}{Nb^2} \tag{4.3}$$

where k_B is the Boltzmann constant, T is the absolute temperature in °K, N is the number of monomers in the polymer chain and b is the bond length.

4.5 Sample Preparation

The polyurethane samples used in the parametric study presented in chapter 6 were prepared in the geotechnics laboratory at UCL. A polyurethane rubber that goes by the commercial name of Poly RTV liquid rubber was chosen as the polymer to be used as soil replacement. This synthetic rubber is acquired in the form of two liquid components which, when mixed in the right proportions, vulcanize at room temperature; hence the abbreviation 'RTV'.

The density of the two liquid parts was known, and so the correct proportion of each part to use in the mixture was obtained by weighting it. After starting the mixture, a time window of ten minutes was available during which the rubber parts could be mixed and poured into the moulds, after that either of these operations became impractical or even impossible since the mixture quickly becomes too viscose to handle.

The moulds, seen in figure 4.8, are made of aluminium. They are composed by a fixed cap, to which two side parts can be screwed. Positioned inside the side parts is a movable cap. The position of the movable cap determines the sample height. One of the two side parts of each mould is perforated to allow the liquid rubber mixture

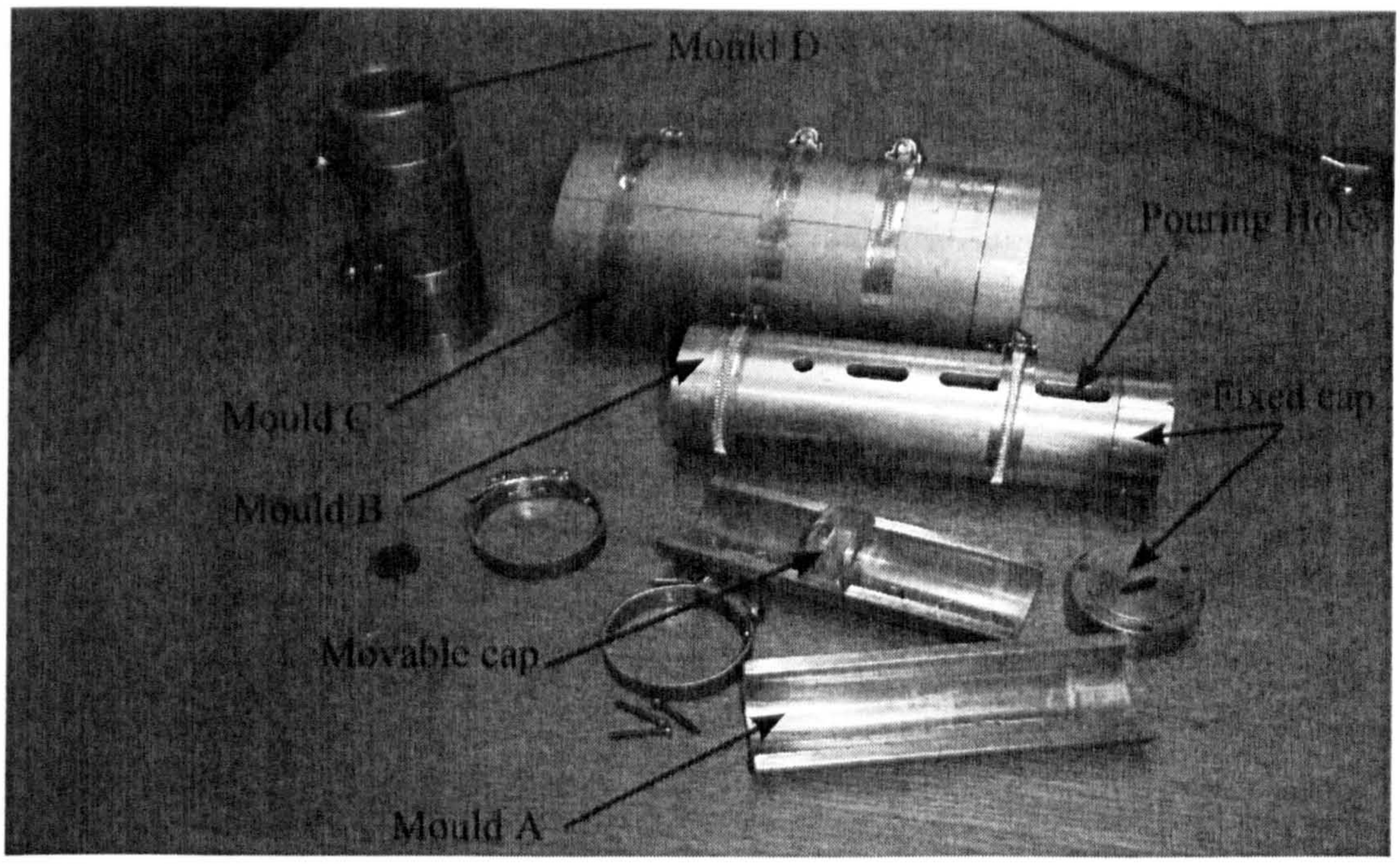

Figure 4.8: 4 moulds used to prepare the polyurethane rubber samples.

to enter the mould and to exhaust the air previously contained in it.

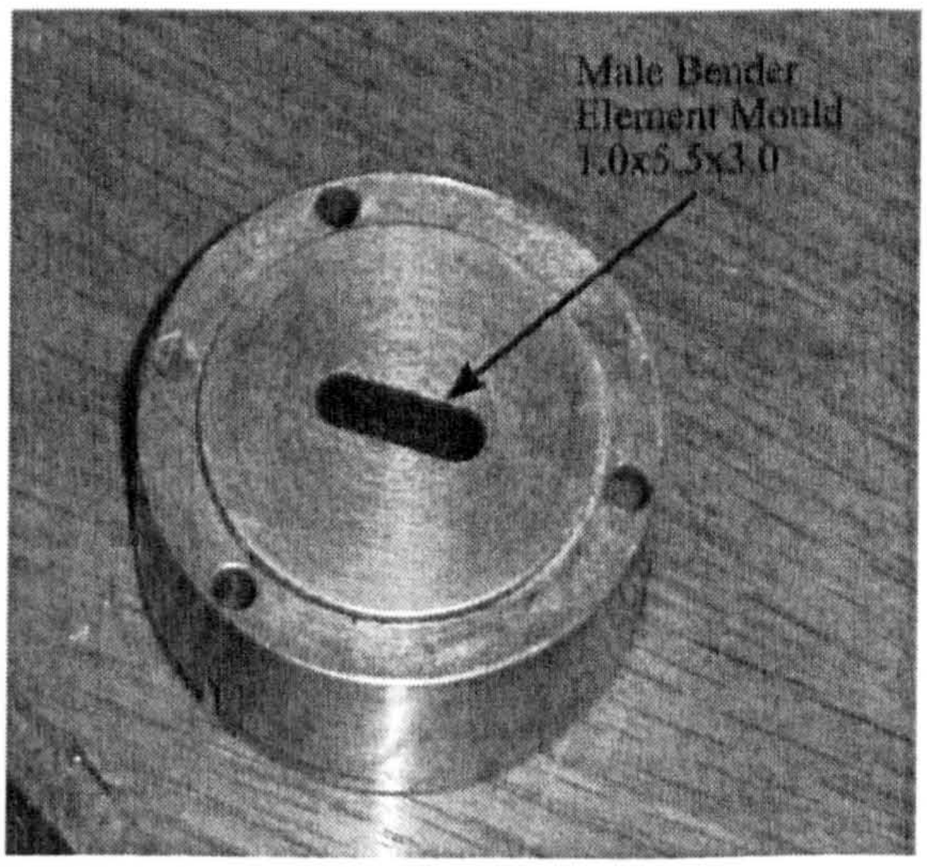

Figure 4.9: Male bender element mould in fixed cap.

Both the fixed and movable cap have a male bender element mould, as seen in figure 4.9, with thickness and width dimensions slightly smaller than the dimensions of the bender elements used in the parametric test, 1.0×5.5mm $< 1.5 \times 6.0$mm (UCL-BE in figure 5.7(a)). These smaller dimensions of the male bender element moulds were chosen to guaranty a tight fit between the transducers used in testing and the

corresponding gap left in rubber samples.

The liquid rubber mixture was prepared in quantities to guaranty the moulding of four cylindrical samples simultaneously. In each set of four samples, three of them had the same height and diameters of 38, 50 and 75mm, obtained from mould A, B and C respectively (figure 4.8). The fourth sample had, for all sets, constant diameter of 38mm and height of 76mm, being obtained from mould D. The justification for this choice of sample dimensions is given in section 6.1.1.

4.6 Repeatability

In order to verify the degree of repeatability offered by the use of polyurethane rubber as a soil replacement, a polyurethane sample was tested. For the repeatability test, a synthetic sample of polyurethane rubber with a commercial name of poly76 was tested six times with bender elements, during a period of 81 days counting from the time it was first casted. The sample used for this purpose was chosen from a group of samples used in the parametric study presented in section 6 and its geometry is described in table 6.2, being referred to as sample S08.

For each of the six tests the equipment was reset so that any error caused by variations in its installation and configuration could also be observed. Another parameter controlled, besides the sample age, was the room temperature of the laboratory during each test, due to the supposed sensitivity of polyurethane rubbers to it, as described in section 4.4.5.

The tests on the chosen sample where conducted in exactly the same way as each one of the parametric bender element tests. A detailed description of this test procedure is provided in section 6.1. For each test six velocity estimates were obtained using different input signals and signal processing methods. A summary of each velocity estimation method and the used parameters is given in table 4.1. A

detailed explanation of each of the used input signal properties and signal processing method is given in section 2.

Reference	Signal Type	Processing Method	Frequency
sweep1	sweep signal	phase delay gradient	$f \in [250\ \ 650]$Hz
sweep2	.....	.....	$f \in [1000\ \ 4000]$Hz
ps1	pulse signal	direct travel time	$f = 400$Hz
ps2	.....	.....	$f = 1200$Hz
pip	pi points	phase delay gradient	$f \in [1500\ \ 4000]$Hz
cs	continuous signal	.....	$f \in [1500\ \ 4000]$Hz

Table 4.1: Detailed notation of figure 4.10.

Figure 4.10 contains each of the 36 velocity estimates, according with the test type and the age of the sample when tested. The average velocity for each test type as well as the variation about that average is given are table 4.2.

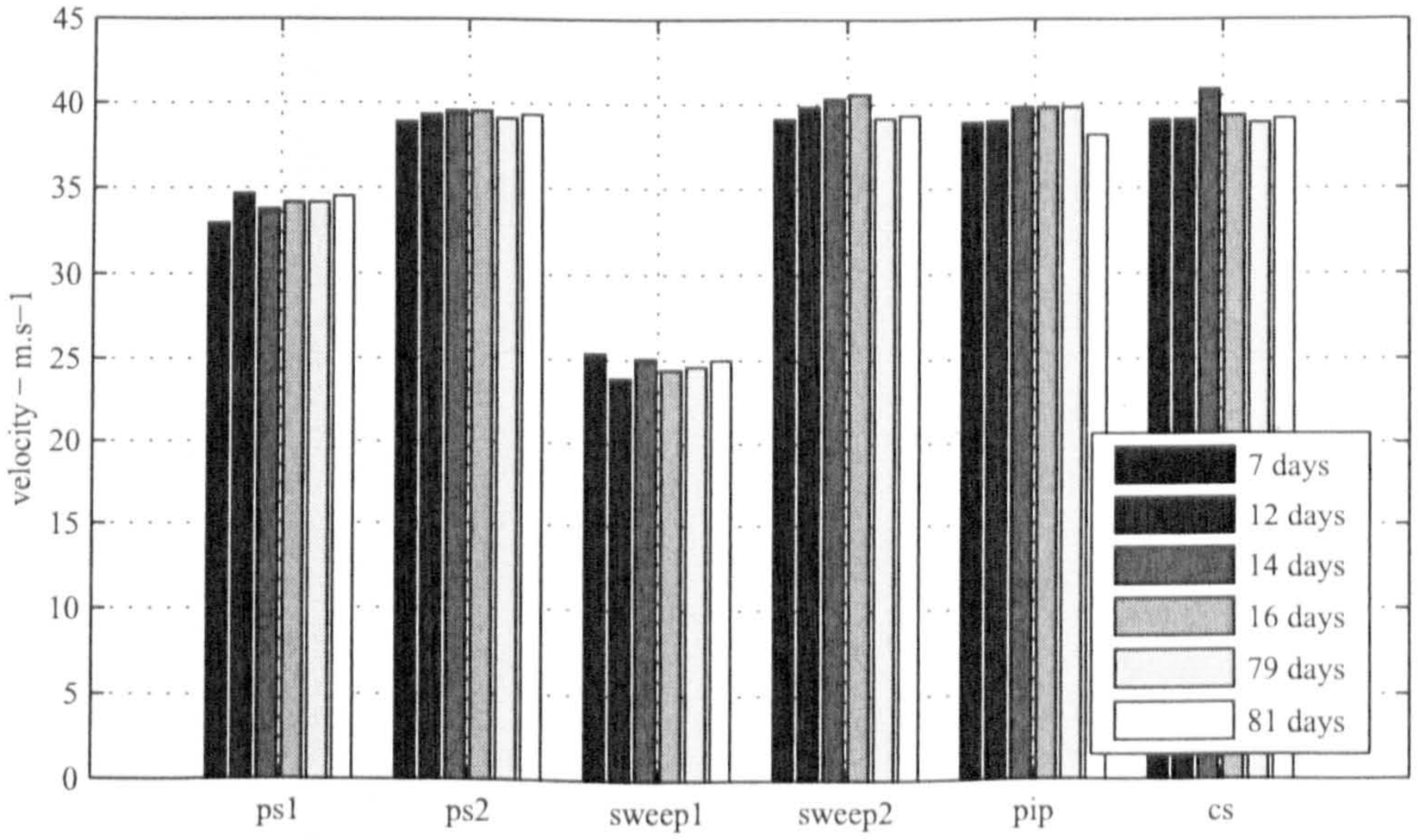

Figure 4.10: Estimated wave velocities from bender element testing on one sample over 81 days, determined with different input signals and different signal processing methods.

There are three parameters which might vary with each test, the sample age, the room temperature in the laboratory and the test set-up. The sample age is

Sample Age	Temperature	Wave Velocity Estimates ($m.s^{-1}$) / Deviation From The Average (%)					
(days)	°C	sweep1	sweep2	ps1	ps2	pip	cs
7	26.0°	25.4 / 2.7%	39.1 / -1.6%	32.9 / -3.2%	38.9 / -1.0%	38.9 / -0.8%	39.1 / -0.8%
12	26.0°	23.9 / -3.4%	39.8 / 0.2%	34.7 / 1.9%	39.3 / 0.1%	38.9 / -0.7%	39.1 / -0.8%
14	23.5°	25.1 / 1.5%	40.3 / 1.5%	33.7 / -0.8%	39.5 / 0.7%	39.8 / 1.4%	40.9 / 3.8%
16	23.5°	24.4 / -1.3%	40.6 / 2.2%	34.1 / 0.4%	39.5 / 0.7%	39.8 / 1.5%	39.3 / -0.2%
79	25.5°	24.6 / -0.5%	39.2 / -1.4%	34.1 / 0.4%	39.1 / -0.5%	39.8 / 1.5%	38.9 / -1.3%
81	24.5°	25.0 / 1.1%	39.3 / -1.0%	34.5 / 1.4%	39.3 / 0.1%	38.1 / -2.8%	39.1 / -0.7%
average		24.7	39.7	34.0	39.3	39.2	39.4

Table 4.2: Wave velocity estimates and deviation from average of each sample for each of the repeatability tests.

the factor with greater potential at indicating how stable the sample is to repeated testing at different times. The temperature, although being relatively stable, suffered variations from test to test. The maximum temperature difference for any two tests was 2.5°C; it will also be analysed together with the wave velocity results.

The test equipment was set-up always in the same way, but some human error cannot be avoided and so, if any variations occurred in the test set-up, they were undesired and consequently unaccounted for. The test equipment set-up must therefore also be considered a source of error, but that unlike the room temperature and sample age, cannot be directly monitored.

Of the two known variable parameters, the sample age was the first to be analysed. Figure 4.11 contains the representation of the variation about the average of each test for different test methods.

The observation of the results directly in figure 4.11 lead to no objective conclusion. Even though some variation does occur, it does not seam to be correlated with the sample age for any of the test methods. A linear regression curve was correlated with each set of results with no significant relation being observed either.

The variation of wave velocity with temperature is presented in figure 4.12. Again, the variation about the average is represented for each test method.

There seems to be no relation between room temperature and the wave velocity results. In figures 4.12(a) to 4.12(f), no noticeable trend in wave velocity can be seen with increasing temperature. If the stiffness of rubber materials is in fact approximately proportional to the absolute temperature, it was not possible to observe this phenomenon for the range of studied room temperatures. The maximum temperature difference observed was of 26.0°C−23.5°C= 2.5°C, which in terms of absolute temperature, is equivalent to a variation of $\Delta\text{temp} = 0.85\%$,

$$\Delta\text{temp} = \frac{2.5°\text{K}}{273°\text{K} + 25°\text{K}} \cong 0.85\% \tag{4.4}$$

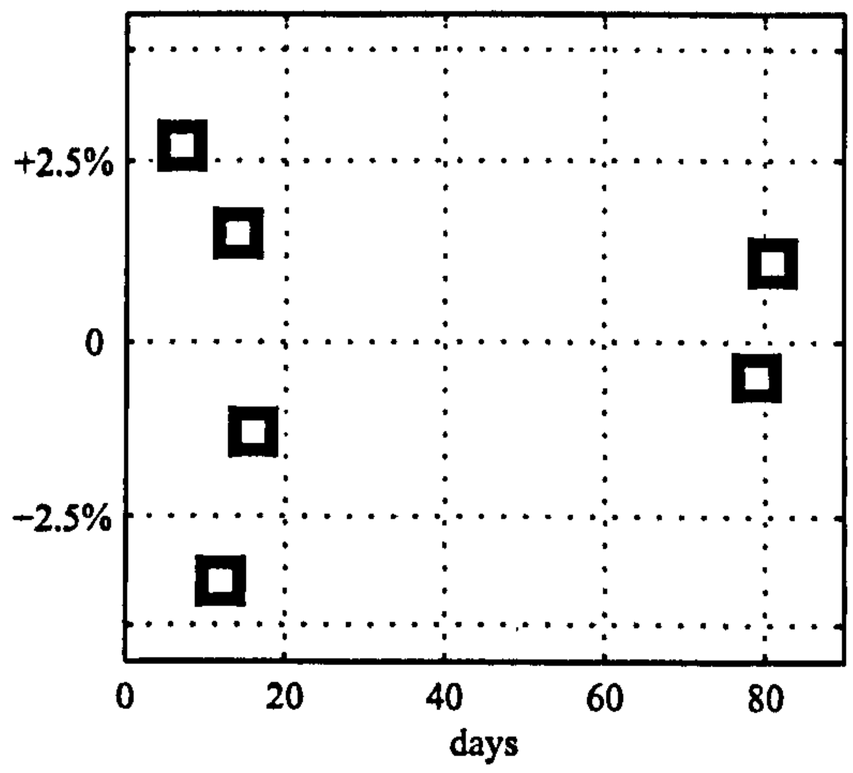

(a) sweep1

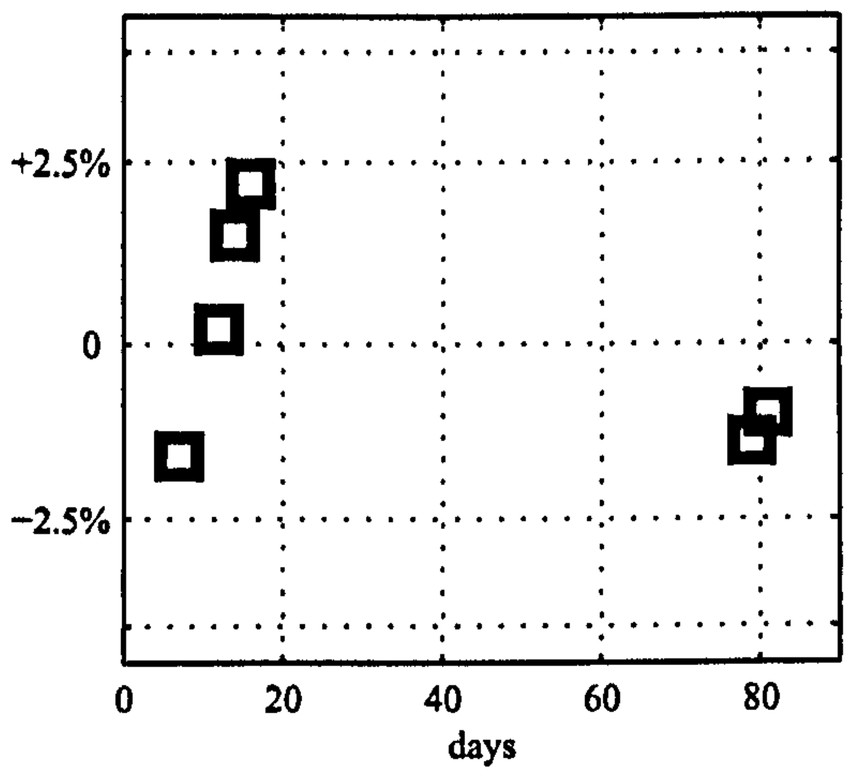

(b) sweep2

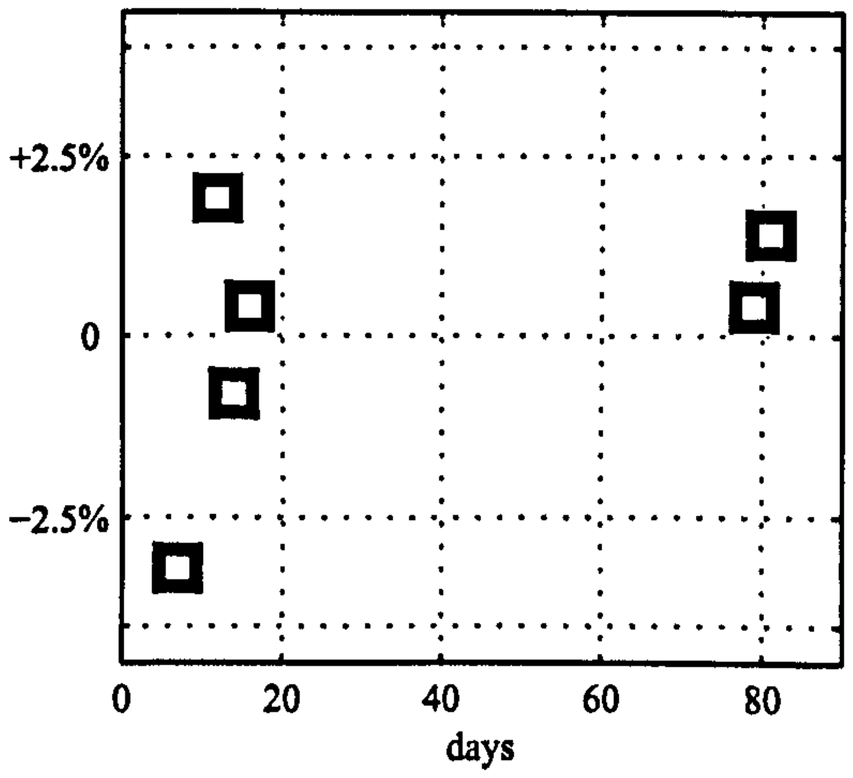

(c) ps1

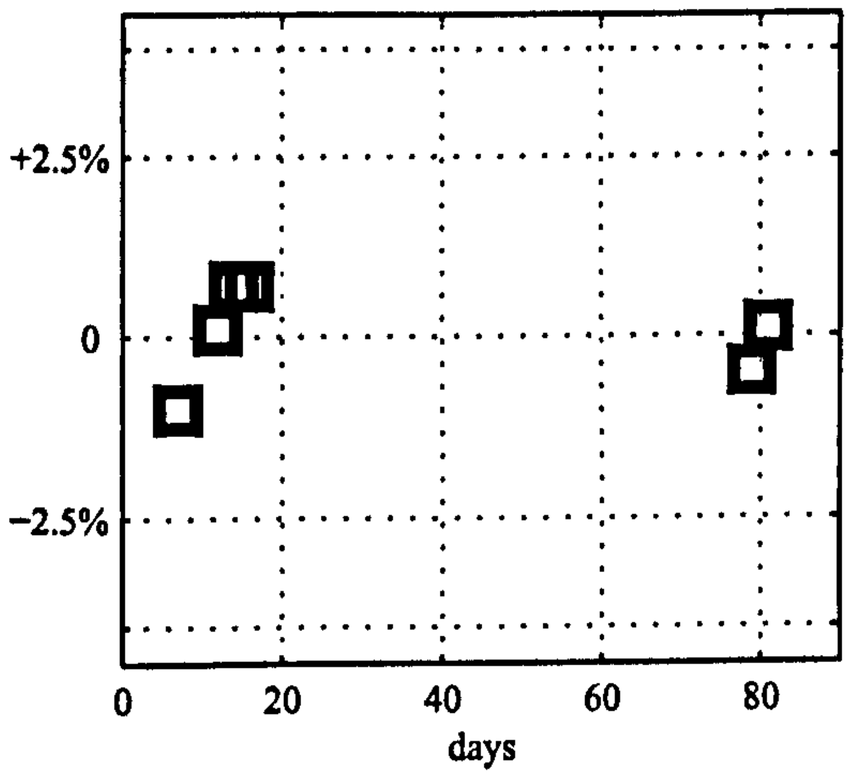

(d) ps2

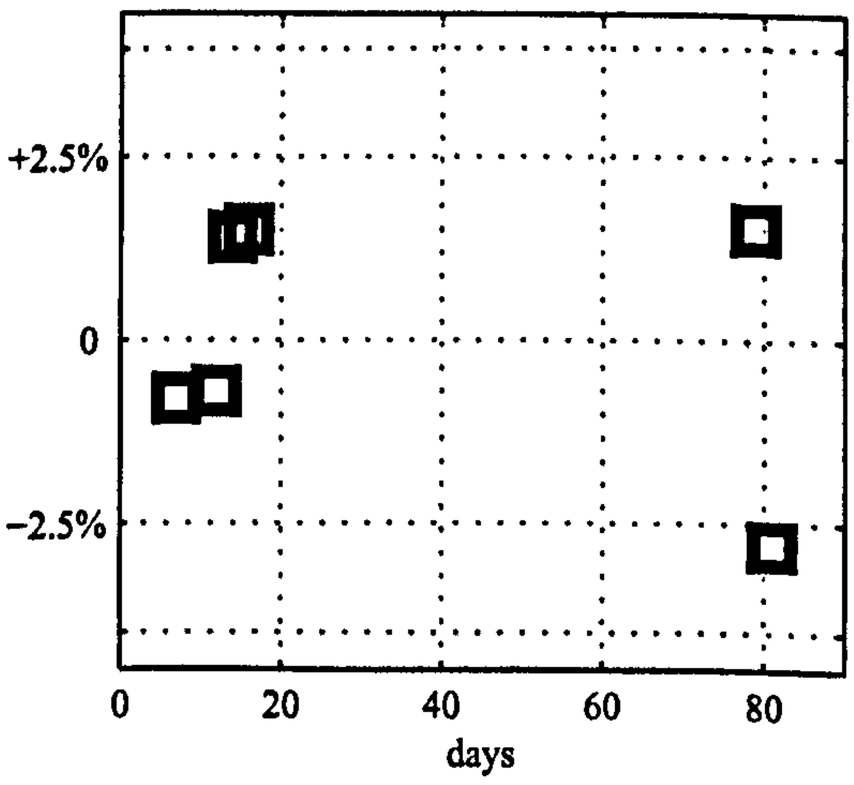

(e) pip

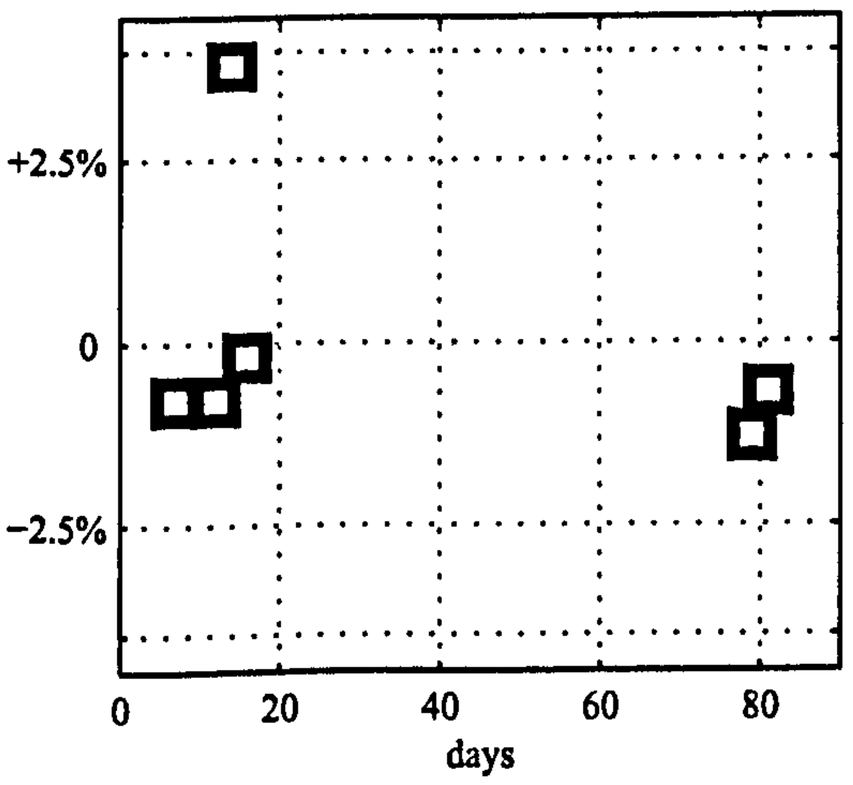

(f) cs

Figure 4.11: Repeatability of synthetic sample testing with sample age.

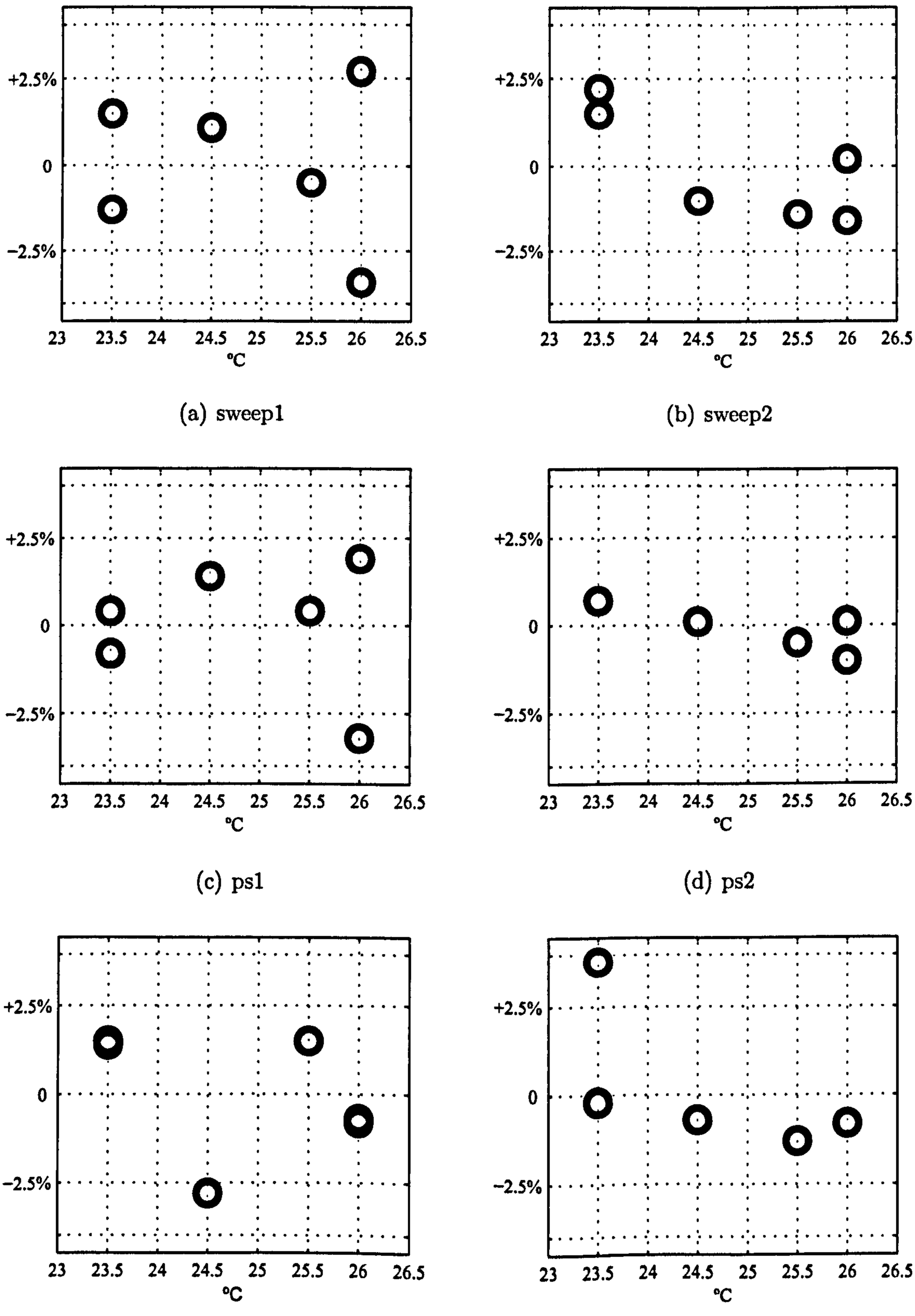

(a) sweep1

(b) sweep2

(c) ps1

(d) ps2

(e) pip

(f) cs

Figure 4.12: Repeatability of synthetic sample testing with room temperature.

where $273°K + 25°K$ is the average temperature. Such temperature variation could only, as expressed in equation 4.3, justify a stiffness variation of the same importance and consequently a velocity variation of around 0.9%. The observed velocity variation of 2.0% could only be explained by a temperature variation of $\Delta temp = 4\% \equiv \Delta temp = 11°C$.

In terms of repeatability, having tested the samples over a period of 81 days, and with a room temperature within a range of 2.5°C, obtaining 36 velocity estimate results, the highest deviation from average was of 3.8%. 31 of those results had a deviation which falls below the 2.5% mark. These results present a good case of how reliable synthetic rubber samples are. All things being equal, and considering the calculation effort necessary to obtain the results, an average deviation of 1.5% was obtained. This value of velocity deviation must be atributed in bulk to human error, room temperature and sample age since no particular relation could be atributed to any single parameter.

Chapter 5

Bender Element Behaviour

This chapter presents experimental work concerning the monitoring of the dynamic behaviour of bender elements and its correlation with analytical and numerical models.

Electric signals are used to excite (transmitting) bender elements, which transform them into mechanical vibration, and vice-versa. A specific correlation between the exciting electric signals and the actual mechanical oscillation performed by the bender elements is commonly neither mentioned nor assumed. Nevertheless, the transmitted and received electric signals time histories are usually compared as though they were the actual vibration of the bender elements, (Schultheiss, 1981). This assumption of similarity facilitates, and in fact enables, the direct correlation between the, otherwise unknown, transmitted and received vibration time histories, since only the electric signals are known. It is important to know the actual behaviour of the bender elements so that a possible error inherited from the use of the mentioned assumption can be determined.

An introduction to the study of bender elements by other authors has already been given in section 1.4. Shirley (1978) had referred to the dynamic properties of bender elements, namely how they influence the coupling with the medium. A

number of different methods have been used so far, such as the complementary wiring of the transducer, (Jovičić *et al.*, 1996; Schultheiss, 1982); the monitoring of the plate to which the bender element is clamped using an accelerometer, (Brocanelli and Rinaldi, 1998); by making the receiver bender element touch and monitor the transmitter, (Lee and Santamarina, 2005; Leong *et al.*, 2005); or by placing a strain gauge on the piezoelectric ceramic plate, (Greening and Nash, 2004). A numerical study was also conducted by Arulnathan *et al.* (1998), that considered the response of the bender element to a sinusoidal load.

Schultheiss (1982) found that the bender elements vibration and the exciting electric signal matched each other. These results can either be obtained for a particular case of a general mechanical simple system vibration, or they can be due to an error caused by the nature of the testing. The transmitted electric signal might have leaked to the complementary wiring, creating a received signal that is a copy of the transmitted one. Jovičić *et al.* (1996) found that for two different frequencies the transducer emulated the excitation signal, even though the response signal was not so clear for the highest frequency.

The remaining authors, Brocanelli and Rinaldi (1998), Lee and Santamarina (2005), Leong *et al.* (2005), Greening and Nash (2004) and Arulnathan *et al.* (1998), have observed a dynamic bender element behaviour that does not exactly match the excitation signals but indicates that the transducer may be behaving as a simple mechanical system, such as the detection of a resonance frequency. Lee and Santamarina (2005) go as far as proposing a theoretical mechanical model to explain the observed behaviour.

5.1 Dynamic Behaviour

It is important to separate two distinct phenomena concerning body vibration, the transient response and the steady-state response to a mechanical disturbance. When a body is initially disturbed, its movement goes through a transient stage and keeps doing so as long as the load is not tuned to the body movement. A body can eventually reach a steady-state if the load is continuous, harmonic and is applied long enough for the transient response to dissipate, (Clough and Penzien, 1993), (section 3.8.5). The total response of a linear system can be decomposed into the sum of the transient and steady-state responses, as described in equation 3.81 and illustrated in figure 3.23.

In simple terms, the steady-state response is thus a state in which a system's vibration is in tune with the applied load and vibrates at its frequency. During the transient response, a body's movement is strongly influenced by its own dynamic properties. The frequency of vibration that characterises the transient stage is the resonant frequency of the body and not the frequency of the load, as illustrated in figure 3.23.

A system vibrating freely, with no load acting on it, does so at its natural frequency for which the amplitude of the initial response decays due to damping. The properties of such a damped free vibration, its resonance frequency and rate of decay, are present in the transient component of the response of simple mechanical systems. An example of a transient response, both alone and combined with a steady-state response, is presented in figure 3.26.

The application of a short duration load, such as a pulse signal, to a transmitting bender element does not have enough time to force the system to reach a steady-state of vibration. Therefore, it will only behave in a transient state and vibrate at its own natural frequency, (Clough and Penzien, 1993).

During the steady-state response of a simple mechanical system, its response does not necessarily emulate the load function. The response of a system to a harmonic continuous load can be described as a complex curve with two components, magnitude and phase. The properties of the magnitude and phase of the steady-state response were described in equations 3.82 to 3.84. These equations are for a SDOF system but can be generalised to simple MDOF systems. Figures 3.25 and 3.24 illustrate the variation of the response magnitude and phase delay with the load frequency respectively. The relationship between the load and consequent response is also not straightforward even when a system vibrates in a steady-state. It is even less correlated during a transient response, such as the ones obtained when using pulse loads.

The experimental work presented addresses the relation between the actual response of the bender elements with the electric signals used to excite them. The monitoring of the bender elements was carried out using a laser velocimeter. The obtained results are presented and evaluated using well known theoretical mechanical vibration models. The dynamic vibration theory necessary to interpret the results was presented in section 3.8.

When using a laser velocimeter to monitor the transducers, the oscillation time histories can easily be recorded without influencing the bender elements behaviour. The non-contact nature of this type of monitoring is its main advantage, (Heymann *et al.*, 1997). The self-monitoring method presented by Schultheiss (1982), is technically simple to achieve and, in principle, does not modify the mechanical behaviour of the transducers significantly. This method appeared to lead to invalid results, where the response of the transducers is a scaled copy of the excitation signals, which is not possible for a mechanical Newtonian system. The other self-monitoring method, of using a strain gauge, presented by Greening and Nash (2004), requires a difficult manufacture procedure to attach the gauge to the piezoelectric ceramic plate. Fur-

thermore, since bender elements are generally very delicate pieces of equipment, the presence of the strain gauge can significantly alter the overall mechanic behaviour of the system. The accelerometer used by Brocanelli and Rinaldi (1998), connected to the plate rather than to the to bender element, provided results predominantly dominated by the plate's response. Even though it is possible to obtain some information from the bender element dynamic behaviour, it is strongly contaminated by the behaviour of the plate.

Touching bender elements is a simple monitoring method, as done by Lee and Santamarina (2005) and Leong *et al.* (2005). This method is possible to perform without the use of any extra equipment, which is a great advantage. However, it is not ideal since the boundary conditions of the monitored transducer are significantly altered in this way. The mechanical boundary conditions of fixity of touching bender elements are quite different from those of transmitting and receiving bender element transducers in a normal set-up. The obtained response is that of two touching bender elements and not that of a single operating bender element.

The main obstacle for the use of the laser velocimeter concerns its use when monitoring the behaviour of a bender element embedded in a sample. To work properly the laser beam needs to be reflected from the body it is monitoring and then be capable of reaching its source without obstacles. If the transducer's tip is embedded in the sample, the sample presents an unsurpassable obstacle to the laser beam. A compromise was achieved by cutting a small hole in the sample to allow a correct reflection of the laser beam from the monitored transducers

5.1.1 Boundary Conditions

Bender elements are commonly used in triaxial cells and oedometer devices, with their tip embedded in the soil sample and their body fixed to the top and bottom plates and porous stones. When placed in this manner, the bulkier part of the bender

element body is mounted on the plate, restricting its freedom of movement. This means that only the tip of the bender element is capable of mechanical vibration. A diagram of a typical bender element set-up in a triaxial cell with the mentioned boundary conditions is given in figure 5.1.

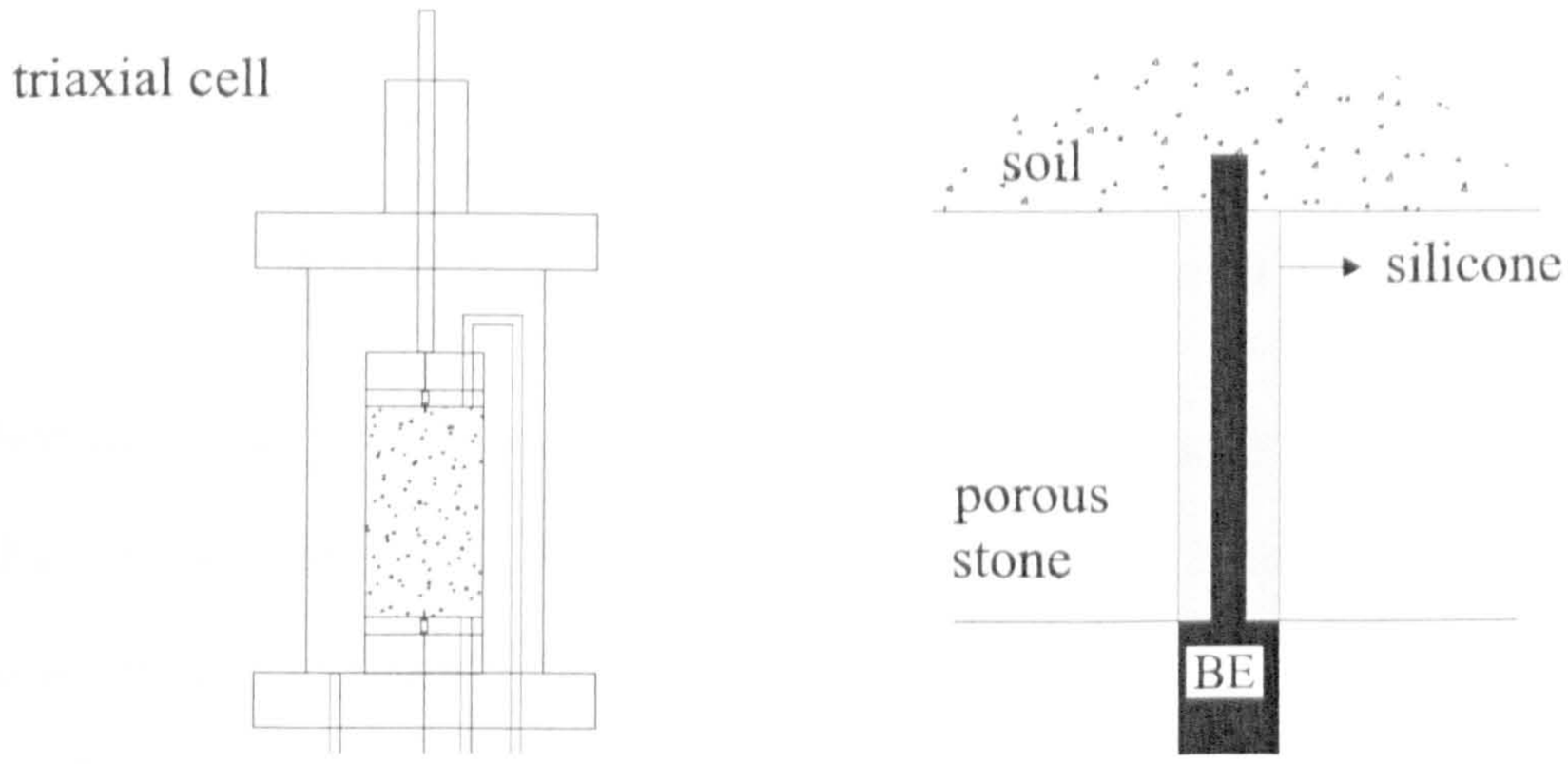

Figure 5.1: Bender element embedded in triaxial cell cap.

In normal testing conditions, the tip of the bender element protrudes into the soil sample by a variable length. The gap between the sample and the bulkier part of the bender element is usually filled with some impermeable flexible material such as silicone rubber.

The deformation of a bender element tip is usually assumed to be regular and with no axial strain, as illustrated in figure 5.2(a). Because of its significant width, a bender element can be expected to actually have a three-dimensional flexural deformation, as illustrated in figure 5.2(b). For a section with constant properties, the bending stiffness is lower near the lateral edges and so they are expected to flex more then near the centre.

A two-dimensional plane deformation can be decomposed into simple flexural and longitudinal modes, as for a simple cantilever rod. The consideration of a three-dimensional behaviour also needs to consider torsional and complex torsional-

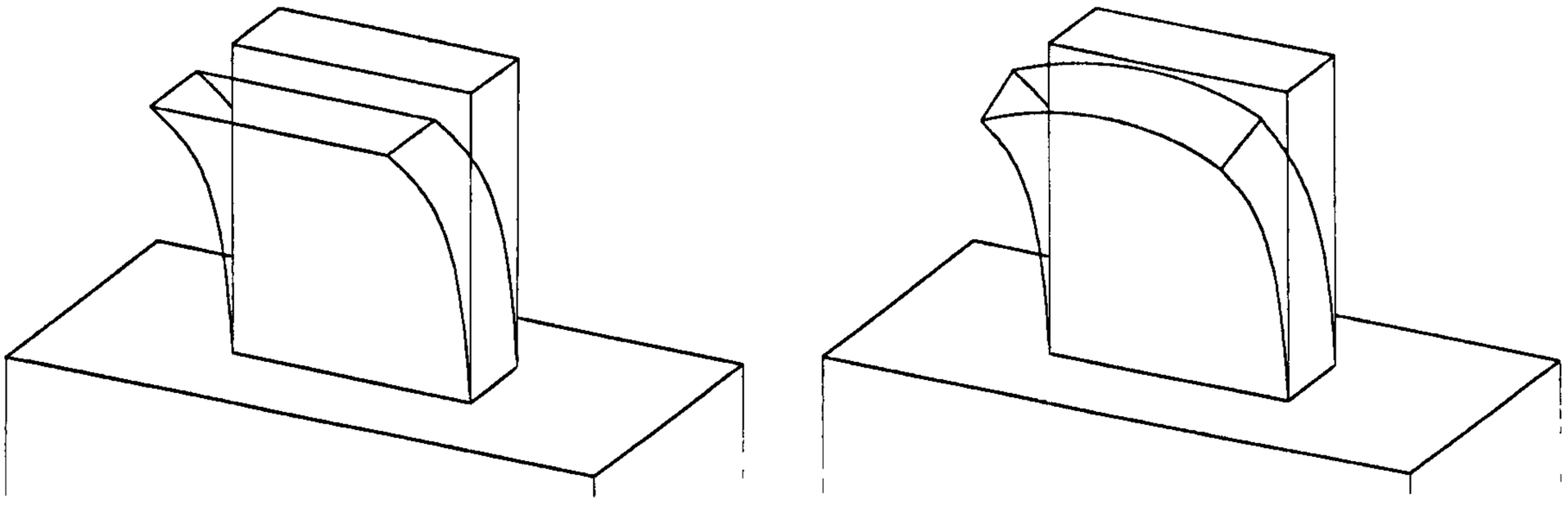

(a) ideal plane deformation (b) complex 3D deformation

Figure 5.2: Flexural deformation of a bender element tip.

flexural modes of deformation. It is reasonable to simplify the analysis by assuming that, in the range of excitation frequencies used, the bender elements does behave as a simple plane cantilever.

The laser velocimeter is used to monitor the bender elements in two distinct sets of boundary conditions. In both cases the bulk body of the bender element is fixed. The difference is in the tip boundary conditions. In one case the tip is left free to vibrate in air and in the other case the tip is embedded in a sample. The first case, with the free tip, is used to study the actual properties of the bender element. This study is better done with the simplest case of boundary conditions where only the properties of the bender element influence its behaviour. The second case serves to understand how the bender element tip interacts with the medium in which it is embedded.

The two different cases of boundary conditions are each modelled by a simple mechanical model. The free bender element tip is modelled as a simple plane cantilever, (figure 5.3(a)). The embedded bender element tip is modelled as a simple plane cantilever with a damped spring at the embedded end, (figure 5.3(b)). The damped spring replaces the reaction offered by the sample to the lateral surface of the embedded tip in normal testing conditions. The relevant dynamic properties of the free cantilever are its mass per unit length, m, and flexural stiffness, consti-

tuted by product of the medium's Young modulus, E, and the section's moment of inertia, I. The properties of the damped spring are its stiffness, k and its damping coefficient, c.

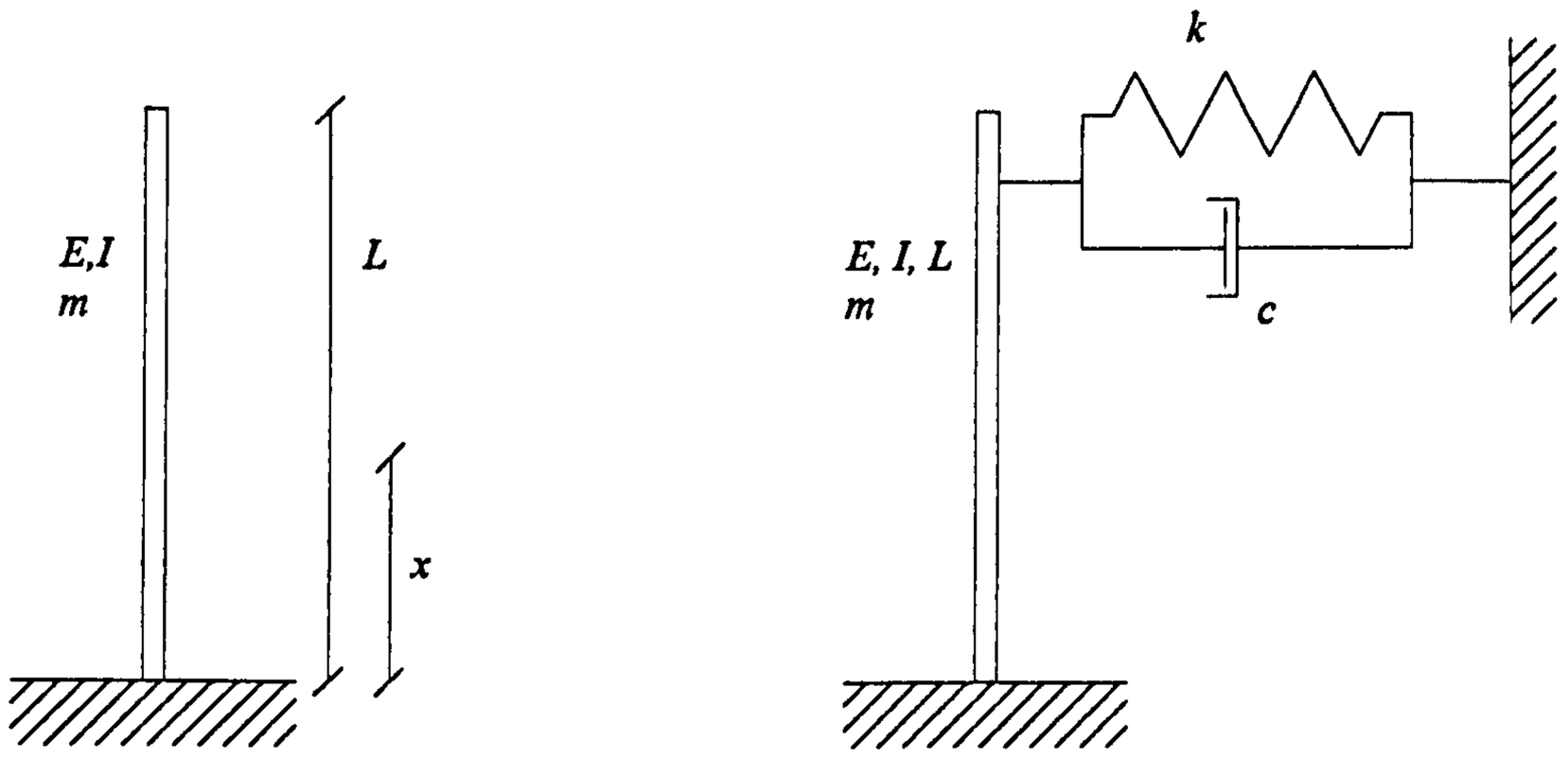

(a) free cantilever

(b) cantilever with spring

Figure 5.3: Boundary conditions for oscillating bender element.

These two cantilever models can be treated as simple MDOF systems. The theoretical background of the dynamic behaviour of simple MDOF mechanical systems is provided in section 3.10.1.

5.1.2 Load Conditions

When an electric signal is used to excite a bender element, it expands one of the two piezoelectric ceramic plates in its plane and shrinks the other. If one of the piezoceramic layers expands and the other shrinks uniformly, this type of load condition forces the system to bend in two directions, with a constant bending moment along the element. This behaviour is equivalent to the application of a temperature gradient. When considering the equivalent two-dimensional flexural deformation, such a load condition can be equally obtained by the application of a concentrated bending moment at the free end of the bender element tip, causing a constant bending moment along its section, (figure 5.4). For analysis purposes, it is convenient to

establish the load to the bender element in the form of such a concentrated moment.

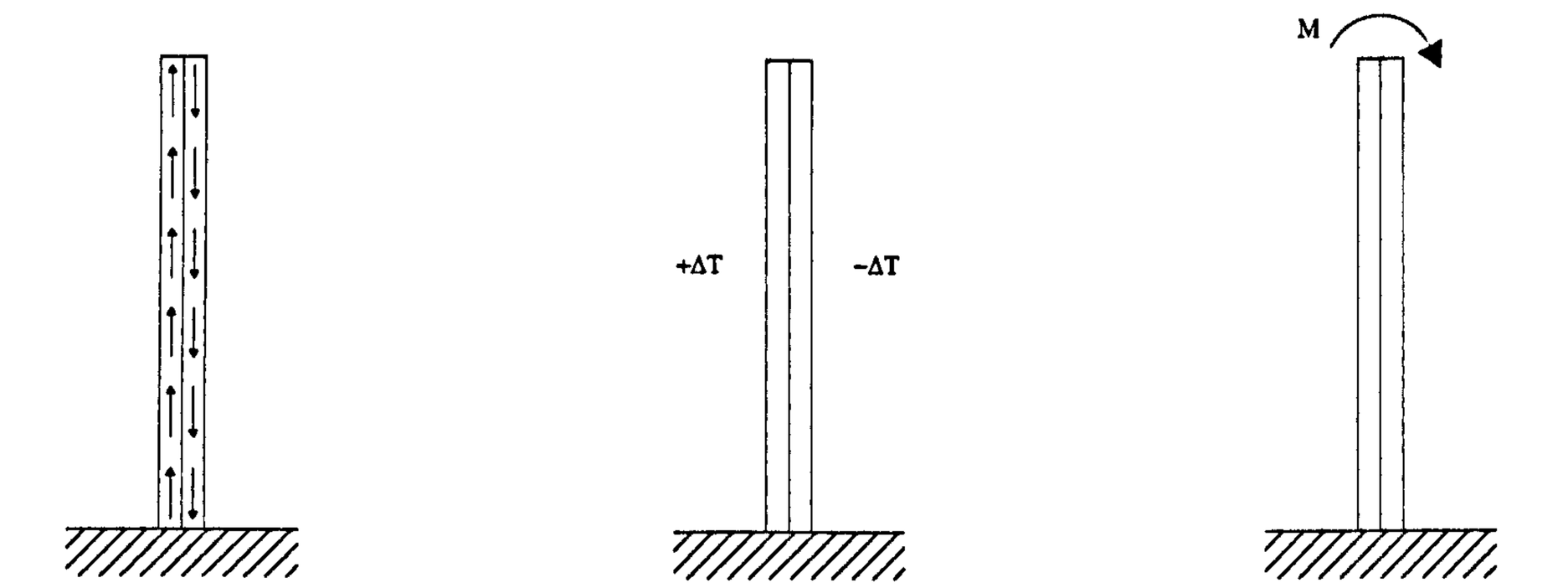

(a) piezoelectric load (b) thermic gradient (c) bending moment

Figure 5.4: Driving load of a transmitter bender element.

5.1.3 Dynamic Response

The dynamic behaviour of the two proposed cantilever models, that are subjected to the proposed load, can be theoretically described. The free cantilever model was the subject of theoretical analysis in section 3.10.1, (Clough and Penzien, 1993). It is convenient to determine a suitable equation of motion for this model. Referring back to equation 3.93 and assuming the following:

- constant flexural stiffness along the axis, $\frac{\partial EI(x)}{\partial x} = 0$.
- constant mass along the axis, $\frac{\partial m(x)}{\partial x} = 0$.
- constant damping along the axis, $\frac{\partial c(x)}{\partial x} = 0$.
- localised moment load at the tip, $p(x,t) = 0$ for $x \neq L$ and $p(x,t) = M(t)$ when $x = L$.
- considering a parabolic shape function of the cantilever of the form:

$$\eta(x) = \frac{x^2}{L^2} \tag{5.1}$$

The parabolic shape given in equation 5.1 describes a constant curvature, as consequence of having a constant bending moment along the length of the cantilever. A specific version of the generalised equation of motion 3.93 can be calculated by replacing equation 5.1 in equations 3.94 to 3.97,

$$m^* = m\int_0^L \left(\frac{x^2}{L^2}\right)^2 dx = \frac{mL}{5} \tag{5.2}$$

$$c^* = a_1 EI\frac{16}{L^4} = \frac{4C_1 EI}{L^3} \tag{5.3}$$

$$k^* = EI\int_0^L \left(\frac{2x}{L^2}\right)^2 dx = \frac{4EI}{L^3} \tag{5.4}$$

$$p^* = p(t)\int_0^L \left(\frac{x^2}{L^2}\right) dx = \frac{mL}{3}\cdot p(t) \tag{5.5}$$

producing a equation of motion now expressed as:

$$\left(\frac{mL}{5}\right)\ddot{Z}(t) + \left(\frac{4C_1 EI}{L^3}\right)\dot{Z}(t) + \left(\frac{4EI}{L^3}\right)Z(t) = \frac{mL}{3}\cdot p(t) \tag{5.6}$$

Equation 5.6 can now be used to calculate the dynamic behaviour of the free cantilever model under a concentrated moment load at the top.

In terms of modal behaviour, if the free cantilever is assumed to be undamped and linear-elastic, then its dynamic behaviour can be decomposed as the sum of characteristic modes of flexural vibration. Each mode of flexural vibration is associated with a characteristic frequency, being the first mode associated with the resonance frequency. The frequency equation and respective boundary condition parameters have been presented in section 3.10.2 as equations 3.101 and 3.103. From the mentioned equations simpler frequency equations can be expressed, (Chopra, 1995; Clough and Penzien, 1993). Equation 5.7 is one such equation for the first mode of flexural vibration.

$$\omega = (1.875)^2\sqrt{\frac{EI}{mL^4}} \tag{5.7}$$

Lee and Santamarina (2005) were able to develop a similar equation for a cantilever with a spring on top representing the soil stiffness, as illustrated in figure 5.3(b). Obtaining a composed mass and stiffness for an equivalent free cantilever it was possible to use a similar frequency equation:

$$\omega = (1.875)^2 \sqrt{\frac{E_c I / L^3 + \eta E_s L}{mL + (\rho_s b^2 L)\,\beta}} \tag{5.8}$$

where E_c and E_s are the Young modulus of the cantilever and sample respectively, L is the effective length of the cantilever, η is displacement influence factor at the interface, m is the mass per unit length, b is the width of the transducer, ρ is the density of the sample and β is an experimentally determined factor.

5.2 Laser Velocimeter

One of the main problems posed by the use of bender elements in the determination of a medium's dynamic properties is that they become an integrated part of the system they are supposed to be testing. For this reason, bender elements have a direct influence on the system's overall behaviour. This aspect of the use of bender elements raises difficulties in the determination of the actual properties of the medium targeted for study. It is therefore relevant to determine the transducers own properties to better understand how they might influence the overall behaviour of the system.

The use of a non-disturbing monitoring device to study the dynamic behaviour of piezoceramic transducers was chosen. An optical technique making use of a single point Laser Doppler velocimeter, LDV, was selected to perform the monitoring of the bender element dynamic behaviour, as done another type of piezoceramic transducers by Ahn *et al.* (2001) and for local displacement transducers by Heymann

et al. (1997). Using the LDV it was possible to monitor the behaviour of the bender elements without any physical contact between the monitoring equipment and the monitored subject, (Podesta, 2002).

An LDV is an equipment which is capable of sending a laser beam and collecting the light components, reflected from the target, that reach the source. The wave-length difference between the transmitted and received beams allows it to determine the velocity at which the target was moving, (Durst *et al.*, 1981). A single point LDV uses only a single point beam, meaning that it can only determine the movement velocity of one specific target point on a chosen body.

The LDV optical equipment used was an Ometron VH300+. This equipment is a single body LDV with both the transmitter and receiver integrated in the same piece of equipment. Relevant characteristics of the LDV equipment are presented next in table 5.1.

Ometron VH300+	
signal output	velocity
calibration	$1V = 100mm.s^{-1}$
velocity range	$2\mu m.s^{-1}$ to $425mm.s^{-1}$
frequency range	0.1Hz to 25kHz
recommended distance from target	385mm up to 10m, at intervals of 140mm

Table 5.1: Ometron VH300+ LDV properties, given in Image (2000).

The calibration given in table 5.1 enables the correlation between the amplitude of the electric signal in Volts and velocity in $mm.s^{-1}$.

5.3 Experimental Proceedings

5.3.1 Laboratory Set-Up

The basic experiment set-up consists of the monitored bender element, a function generator, the single point LDV, an oscilloscope and a personal computer. This equipment is configured so that the function generator sends an electric signal both to the bender element, forcing it to vibrate, and to one of the channels of the oscilloscope. The laser beam is pointed at the tip of the bender element monitoring its velocity time history, which in turn is sent to a second channel of the oscilloscope also in the form of an electric signal. The oscilloscope sends both channel inputs to the personal computer where the information is visualised, processed and stored. A representation of this set-up is given if figure 5.5.

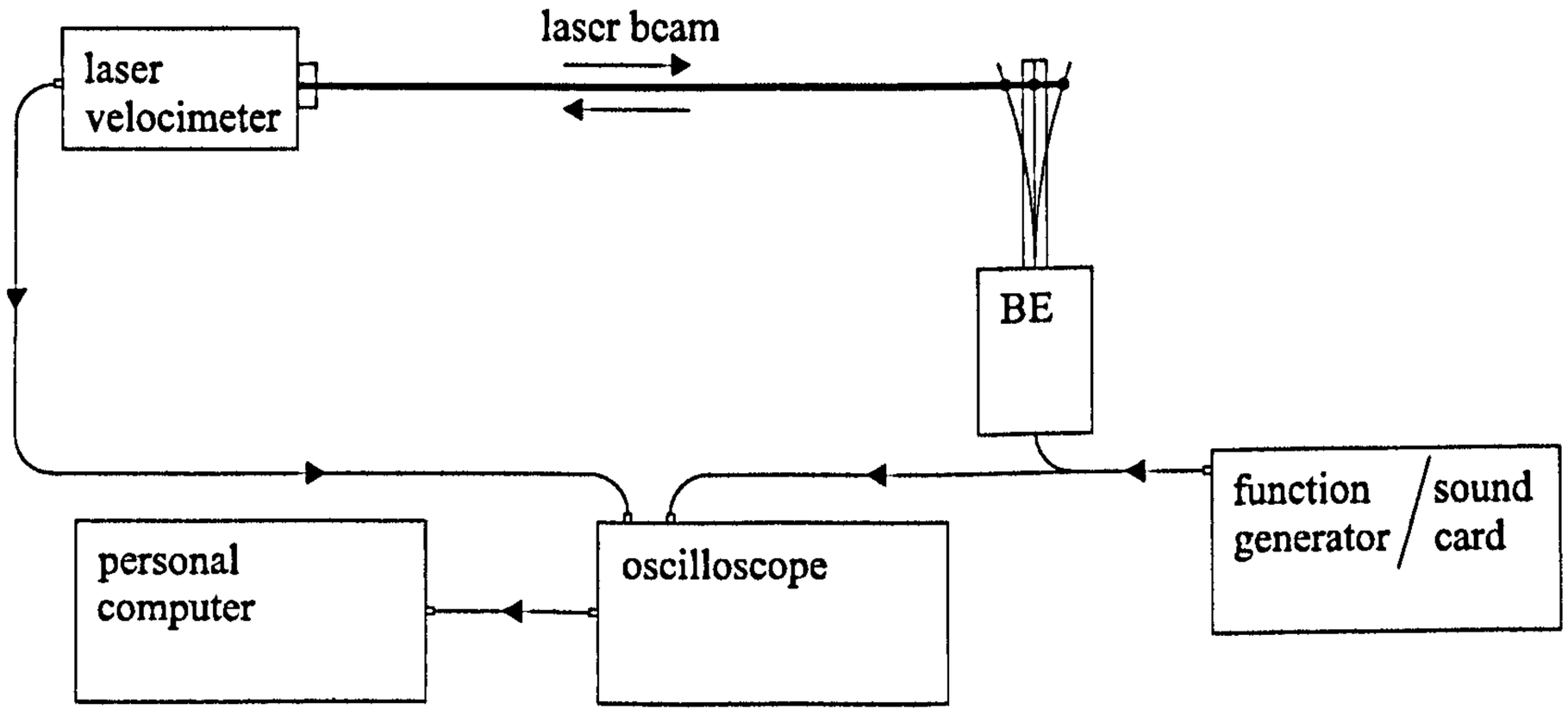

Figure 5.5: Bender element behaviour monitoring set-up, with a laser velocimeter.

Both the laser beam and received reflected light beam go through the same lens of the LDV. Special care was taken in levelling the LDV so that the incident laser beam was horizontal and perpendicular to the target surface, maximising the amount of light successfully reflected back to the LDV. Because of the laser beam's own modulation or wavelength, the working distance between the target and the lens can be arbitrated so as to optimise the quality of the reflected light beam.

The optimum working distance advised by the manufacturer is multiple of 140mm, (Image, 2000). A distance of 3.360 metres, 24 times the reference distance, was used. After pointing the laser at the bender element, it is necessary to focus the beam properly so that the reflected spot on the target's surface is as small as possible, enabling the minimisation of scattering from the reflected light and improving the quality of the reflected beam.

5.3.2 Test Programme

A set of dynamic tests was performed on two different pairs of bender elements. One of these bender element pairs was part of a set manufactured and supplied by Cambridge Insitu Ltd. The second tested pair of bender elements was designed and manufactured at University College London, where the tests were carried out. These two different pairs of bender elements have different geometries, which enables the proposed comparison to address the issue of bender element geometry influence on its performance. Conveniently, because the two distinct sets of bender elements were manufactured independently, the similarities between their dynamic behaviours might consolidate the knowledge of some of their general dynamic properties.

Image of transducers belonging to the UCL-BE and CIS-BE pairs are given in figure 5.6. The characteristics of each bender element set are illustrated in figure 5.7 and described in table 5.2.

Name	Manufacturer	Wiring	Dimensions (mm)
UCL-BE	UCL's Civil and Environmental Engineering Department	series	$1.5 \times 6.5 \times 8.0$
CIS-BE	Cambridge Insitu	series	$1.5 \times 12.0 \times 10.0$

Table 5.2: Description of the two tested bender element transducers.

The bender elements were tested with two different boundary conditions. Ini-

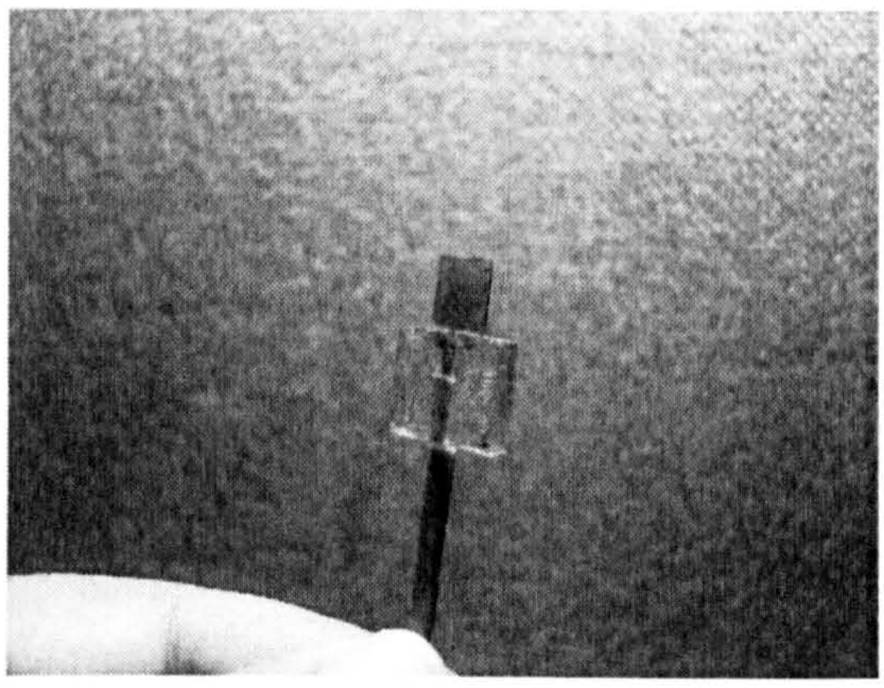

(a) UCL - UCL-BE

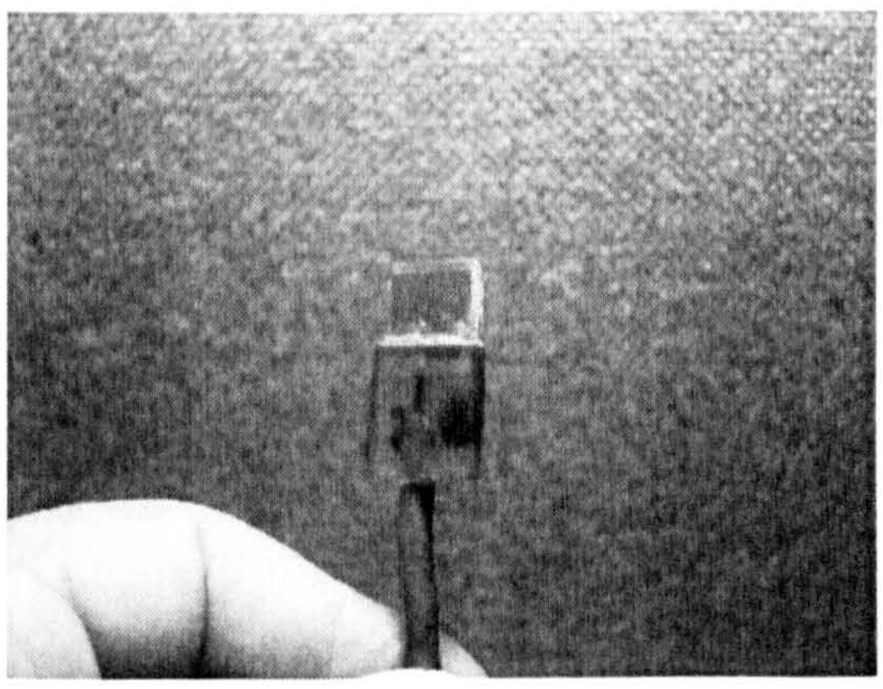

(b) Cambridge InSitu - CIS-BE

Figure 5.6: Tested UCL-BE and CIS-BE transducers.

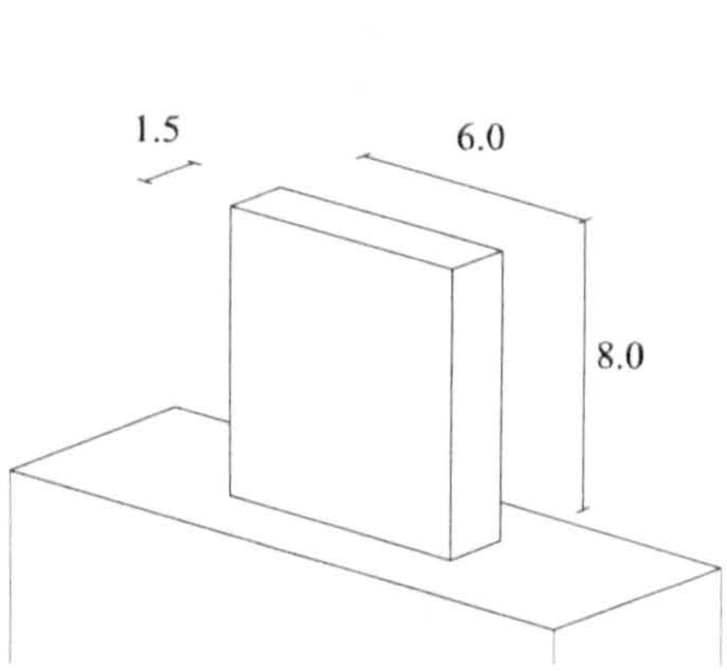

(a) UCL-BE

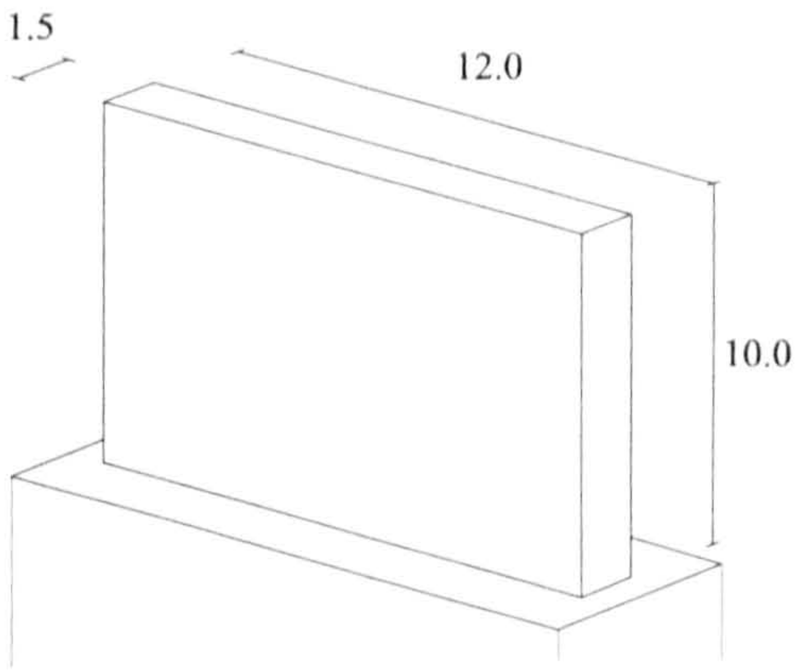

(b) CIS-BE

Figure 5.7: Illustration of the tested UCL-BE and CIS-BE transducers, dimensions in mm.

tially they were tested with their tips in air, with unrestricted movement and capable of free vibration. They were then tested with their tips embedded into a sample to better understand their behaviour under normal test conditions. A synthetic sample made of polyurethane rubber was used, its properties are detailed in section 4. The synthetic sample was similar to those used in the geometry parametric study presented in chapter 6. The motives for using a synthetic rubber sample were its availability, its similarities with soft viscous soils and to ensure the compatibility with the results obtained for the parametric study. This way, the dynamic behaviour of the complete system could be decomposed into the separate dynamic behaviours

of the transducers and synthetic samples.

A small hole had to be carved out of the rubber sample so that the laser beam could reach, unobstructed, its target at the bender element tip surface. This hole was made as small as possible so as to minimise the disturbance it might cause to the coupling between the bender and the sample.

In summary, there are two different test set-ups for each of the two bender elements studied, the UCL-BE and CIS-BE. This gives a total of four distinct test set-ups. A summarised description of each test set-up is given in table 5.3.

Number	Bender Element	Tip Embedment
1	UCL-BE	free
2	UCL-BE	embedded
3	CIS-BE	free
4	CIS-BE	embedded

Table 5.3: LDV monitoring test summary.

5.3.3 Hardware

Different pieces of hardware played different roles in the experiment: a function generator, an oscilloscope, a laser velocimeter and a personal computer. The personal computer was used both to store and process data and to serve as a function generator, not a conventional use. This method was first explored in a bender element testing context by Greening and Nash (2004) .

Each piece of equipment handles electric signals in a different way, namely the frequency range in which it is capable of operating and the sampling rate of the signal. These characteristics of the equipment might influence the range of results that can be obtained. They are presented in table 5.4.

The information about the sampling frequency and frequency range was obtained

Hardware	Name	Sampling Rate		Frequency Range
		transmitted	received	
function generator	TTi TG1010	not given	——	up to 10MHz
oscilloscope	Picoscope ADS-216	——	166kHz	up to 25kHz
LDV	Ometron VH300+	not given	——	up to 25kHz
PC sound card	Intel 82801 AC97	44.1kHz	——	11kHz

Table 5.4: Hardware frequency range of the equipment used in the laser monitoring of bender element behaviour.

in the user manuals or other product documentation, (Image, 2000; Intel, 2004; Pico, 2005; Thurlby, 1994).

5.3.4 Signal Properties

The function generator and the personal computer sound card generate the signals used to excite the bender element transducer. Three types of signals were chosen to perform the tests:

- sinusoidal impulsive signals, provided by the function generator. These signals had a constant amplitude of 20V, and frequencies arbitrated between 0.2kHz and 24kHz.

- sinusoidal continuous signals, provided by the function generator. These signals had an amplitude of 20V, and frequencies arbitrated between 0.2kHz and 24kHz.

- sinusoidal sweep signals, provided by the personal computer sound card. These signals had an amplitude of up to 4V, and a continuously varying frequency between 0.0Hz and 20.0kHz.

The mentioned signals will henceforward be referred to, in simpler terms, as continuous signal, pulse signal and sweep signal. The signals generated either by

the function generator or sound card are called transmitted signals, and the signals received by the LDV and bender element are called received signals.

Continuous Signal

The LDV readings give the velocity time history of the transmitting bender element. Its displacement time history can be obtained by integrating the velocity time history, as given by equation 5.9 for a continuous signal.

$$u(t) = \int \dot{u}(t)dt = \int a_{\dot{u}} \cos(\omega t) = \frac{a_{\dot{u}}}{\omega} sin(\omega t) + C_1 \tag{5.9}$$

The displacement response amplitude, a_u, is provided by:

$$a_u = \frac{a_{\dot{u}}}{\omega} \tag{5.10}$$

The constant of integration, C_1, adds a step shift in the magnitude curve. This shift does not interfere with the frequency, phase or intrinsic magnitude of the signal and therefore can be dismissed. There is a constant phase shift of $\frac{\pi}{2}$ between the velocity and displacement curves, as is the case between equivalent cosine and sine functions. Figure 5.8 provides an example of the relation between the velocity and displacement sinusoidal continuous curves.

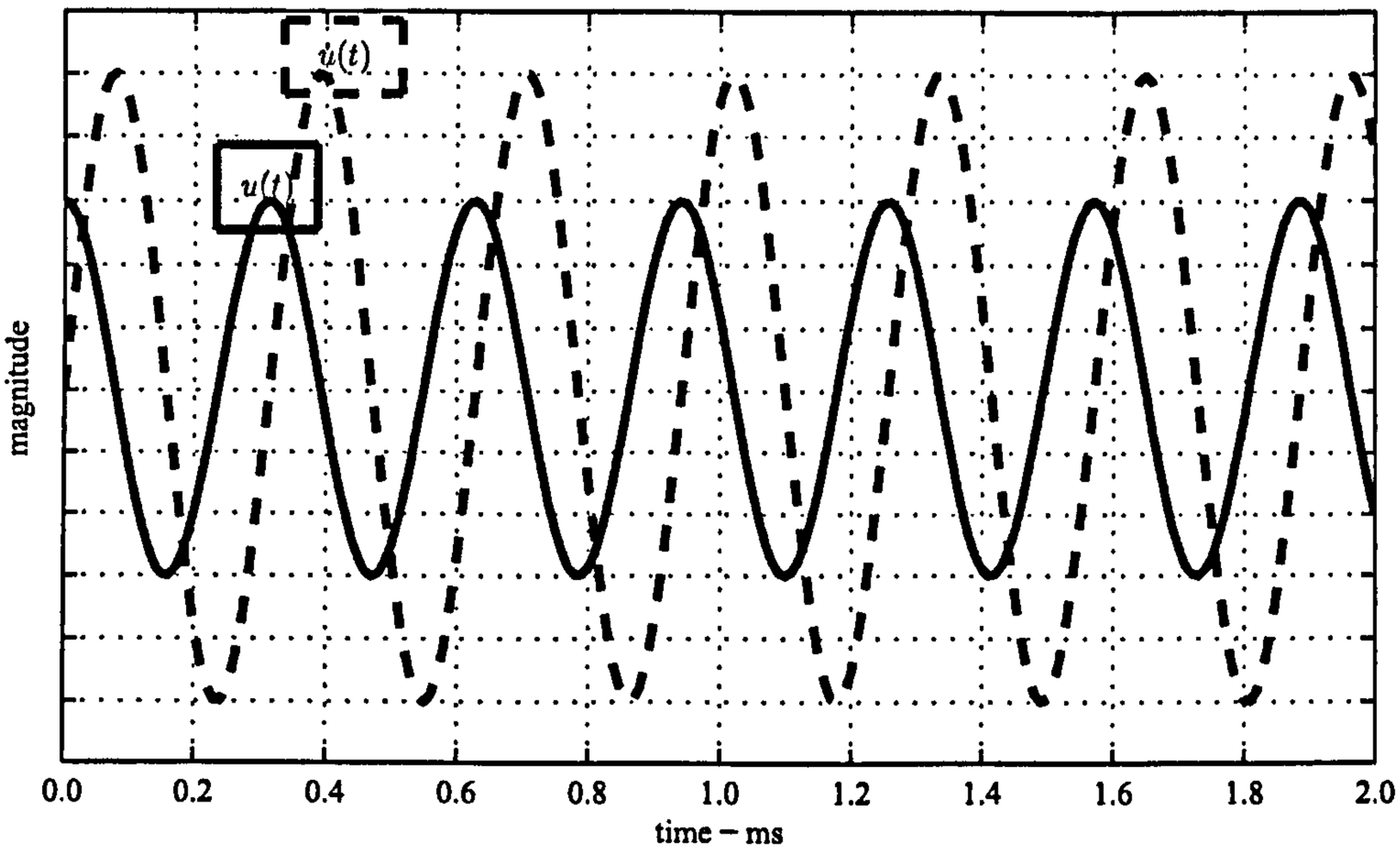

Figure 5.8: UCL-BE's monitored velocity and corresponding displacement, $\dot{u}(t)$ and $u(t)$, for a 4.0kHz harmonic continuous signal excitation.

Pulse Signal

The use of pulse signals in these tests enabled the observation of the system behaving in a free damped vibration. After the pulse signal was finished, the system carried on vibrating with no other external loading. This is a well-known case of theoretical dynamic behaviour, (section 3.8.4).

Another important reason to use pulse signals to excite and monitor the behaviour of the transducers in the present study is that pulse signals are popular when it comes to testing with bender elements. It is relevant to observe the bender elements actual behaviour under such load conditions, and determine the differences between its real and assumed behaviour.

Figure 5.9 presents an example of the monitored behaviour of a free bender element excited by a single pulse signal with a central frequency of 4.0kHz. The time history of the velocity was numerically integrated to obtain the time response of the displacement.

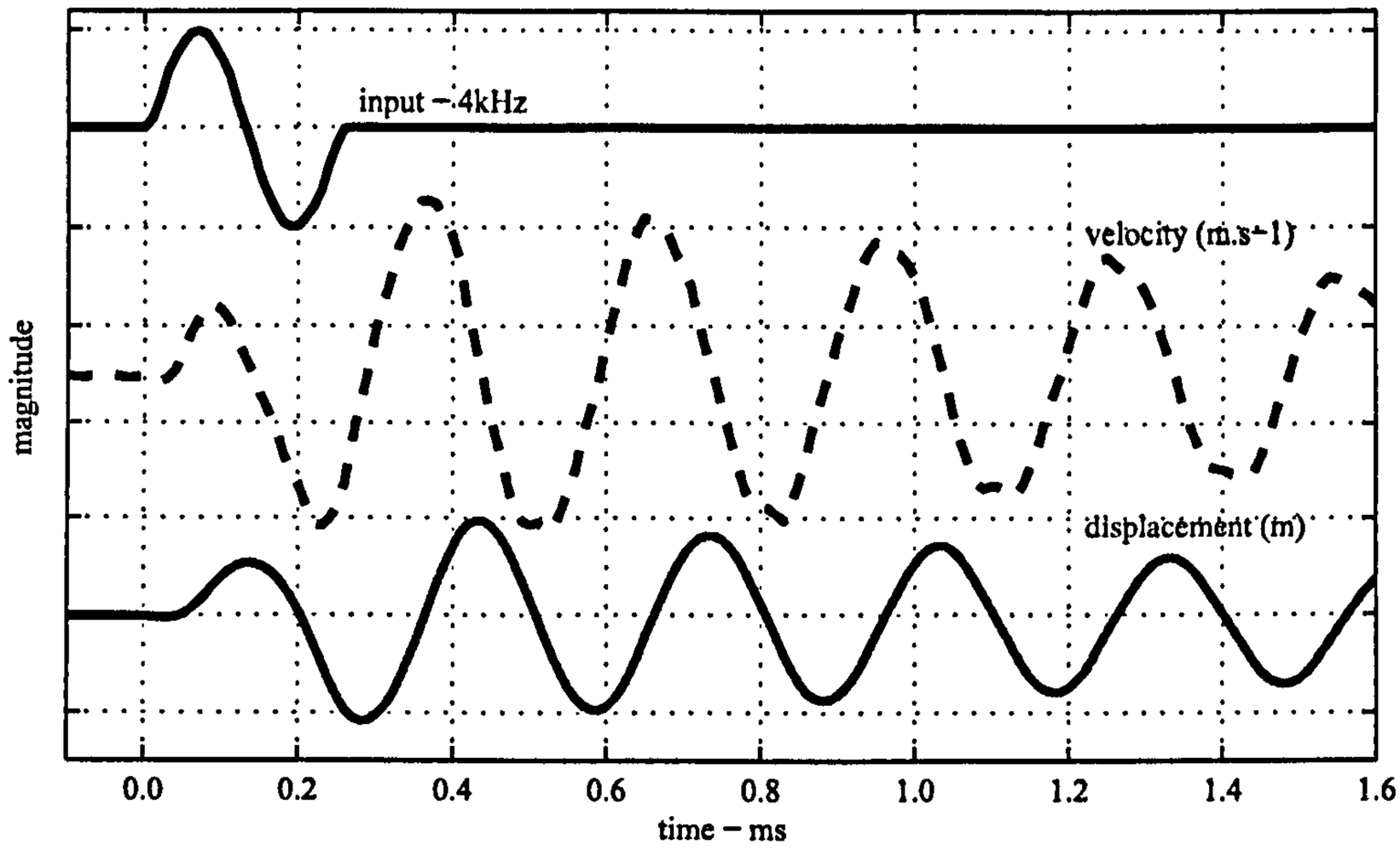

Figure 5.9: UCL-BE's monitored velocity response and corresponding numerically integrated displacement, for a 4.0kHz input pulse signal excitation.

Sweep Signal

Sweep signals will also be used to obtain the system's response curves. Greening and Nash (2004) have used a similar signal, also by transmitting it from a personal computer sound card. The properties of the used sweep signal are listed in table 5.5, and an introduction to the use of sweep signals is presented in section 2.4.

Property	Description
source	PC sound card
amplitude	2V
frequency range	from 0.0kHz to 20.0kHz
length	80ms
cycles	two cycles of 0.0Hz → 20.0kHz → 0.0Hz
cycle rate	10^{-6}Hz.s^{-1}

Table 5.5: Sweep signal properties

5.4 Results for Free Transducers

The results from the dynamic testing of the UCL-BE and CIS-BE are presented in this section. Having used sinusoidal pulse, continuous and sweep signals to excite the bender elements, time and frequency domain results are presented separately. Even though the time domain results are intuitive and easier to analyse, the frequency domain results will be presented first, because they provide information which introduces an interesting perspective to the time domain analysis.

5.4.1 Frequency Domain

The magnitude and phase response curves of the free UCL-BE are used to describe its behaviour. Figure 5.10 presents these two response curves obtained using continuous signals. The continuous signals used had different frequencies, at steps of 100Hz, and with even smaller steps near the frequency of the first resonance observed. Similar results were obtained using a sweep signal.

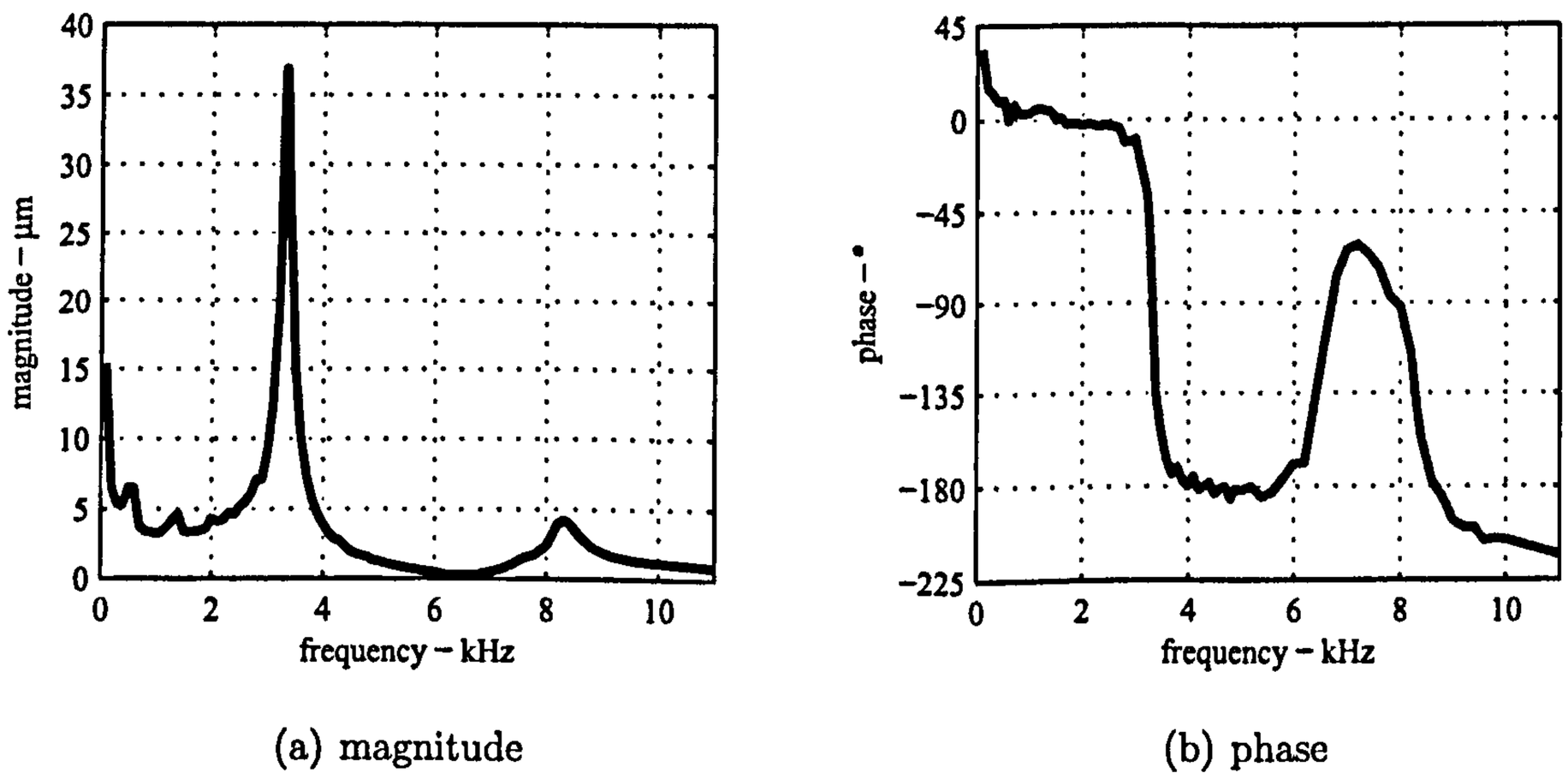

(a) magnitude (b) phase

Figure 5.10: Free UCL-BE's response function estimate from continuous signal dynamic excitation.

Figure 5.10 presents results which are quite similar to classic textbook responses of multiple degree of freedom systems with each of the presented peaks, at 3.4kHz

and 8.4kHz, corresponding to a different mode of vibration. Greening and Nash (2004) present a pair of magnitude and phase response curves quite similar to those presented in figure 5.10. The main difference is the value at which the main resonance frequency occurs, 1.1kHz. This difference can be explained by the different geometry of the transducer and by different boundary conditions. Details of this test and those of other authors are presented in table 5.6.

The magnitude is expressed in distance units, μm, obtained by using the calibration ratio of the laser velocimeter, given in table 5.1, and then by differentiating the velocity curve. In this manner it is possible to present an almost direct estimate of the actual amplitude of the bender element oscillation. So, when its tip is subjected to no lateral constraints and excited by a continuous signals with an amplitude of 20V, the maximum amplitude of the oscillation is of $u_a = 37.0\mu\text{m} \equiv \pm 18.5\mu\text{m}$.

The natural frequency of the system is easily identifiable in figure 5.10(a). It takes the value of $f_a = 3.4\text{kHz}$ and corresponds to the first peak of the magnitude curve. The resonance frequency is confirmed by a phase shift at that same frequency observed in the phase curve, (figure 5.10(b)), and as is expected in such simple dynamic systems. The second observed peak at 8.4kH is also accompanied by a phase shift.

An estimate of the damping ratio can be obtained from the magnitude response curve applying the half-power bandwidth method, (section 3.9), or (Clough and Penzien, 1993). For the case of the UCL-BE, the magnitude of the peak corresponding to the natural frequency was identified as $u_a = 37\mu\text{m}$. The frequencies at which the magnitude is $u_a/\sqrt{2} \approx 26.2\mu\text{m}$ are approximately $f_1 = 3244\text{Hz}$ and $f_2 = 3404\text{Hz}$. Equation 3.91 is then used to estimate the viscous damping ratio.

$$\xi_{\text{ucl}} = \frac{3404 - 3244}{3404 + 3244} \equiv 2.5\%$$

Similar results can be obtained for the CIS-BE. The necessary response curves are presented in figure 5.11.

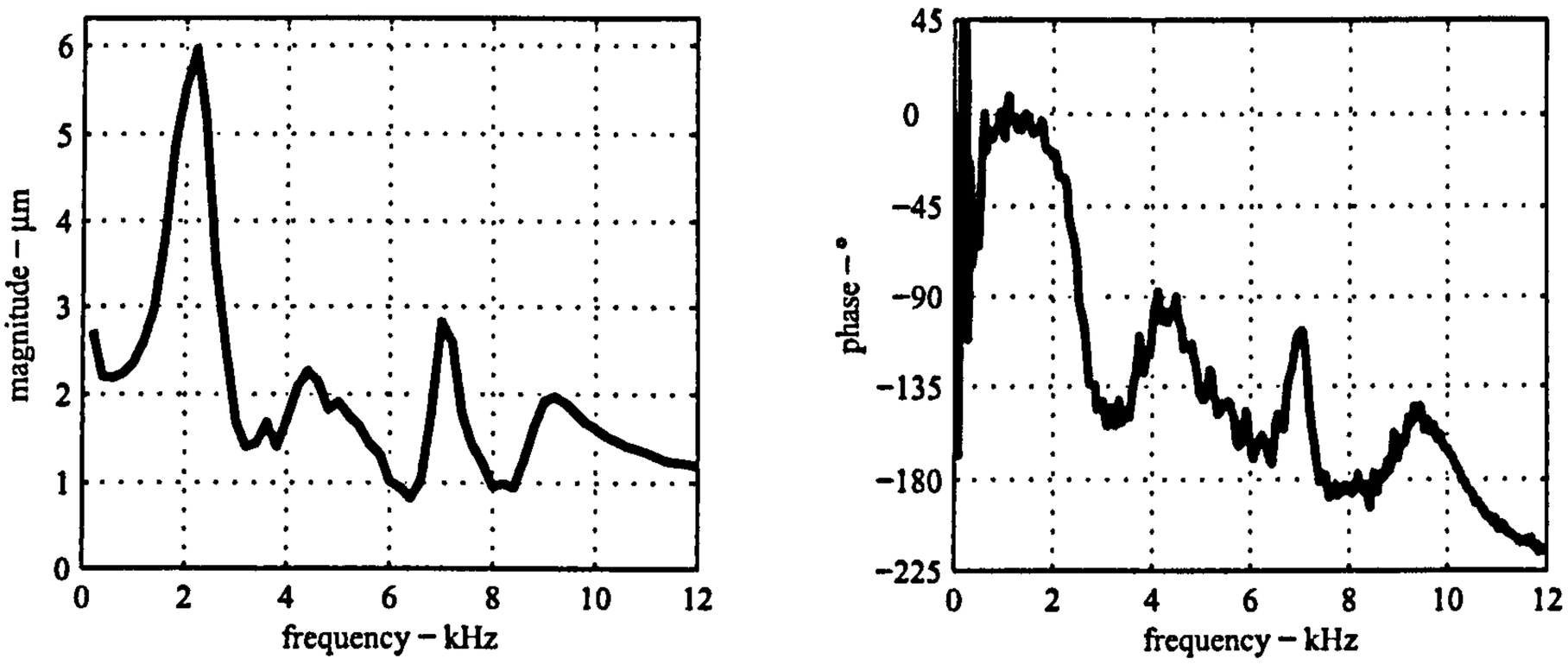

(a) magnitude (b) phase

Figure 5.11: Free CIS-BE response function estimate from sweep signal dynamic excitation.

The flexural natural frequency of the free CIS-BE appears to occur at 2.2kHz. This response is not as clear as was the response of the UCL-BE, in the sense that there are some other peaks occurring close together. The proximity between these peaks imply that they might interfere with each other, i.e., that more than one mode of vibration might be excited at a single frequency. The transducer might then behave not in a single, more simple, mode of vibration but in a more complex mode. The CIS-BE clearly has a more complex response than the UCL-BE. This increased complexity can be explained by the geometry of the transducer's tip. The CIS-BE tip has a relatively large width, even larger than its own height. Knowing also that the electric signal causes the bender element to bend, or flex, not in a planar manner but in a more complex three-dimension manner, (figure 5.2). This might explain why, for such a large width of the transducer's tip, other modes of vibration other than the flexural modes can be excited, such as torsional modes and flexural-torsional modes. A study of both the UCL-BE and CIS-BE modal

behaviour is presented in section 5.6.

The maximum magnitude of the response, occurring at the resonance frequency, is of $u_a = 5.9\mu$m. This value is around 6 times smaller than the free maximum magnitude of the UCL-BE response. This might indicate that its flexural response is not as efficient, either due to a more complex modal behaviour or maybe due to other parameters, such as the piezoelectric capacity of the ceramic plate, or due to a stiffer section.

A similar calculation of the CIS-BE damping ratio, for the corresponding main mode of vibration, using the magnitude curve, gives $\xi_{cis} = 8.0\%$. This value is higher than the one obtained for the free UCL-BE, it is even relatively high from what could be expected from a simple cantilever dynamic system with no added damping. Again this could signal a possible interference of the vibration mode .

5.4.2 Time Domain

The time domain results are obtained directly from the time histories of the transmitted sinusoidal pulse signals and corresponding received signals. This way, it is possible to observe the behaviour of the bender elements both during the period when the excitation signals are still acting on them, and also during the period when there is no more external excitation and the bender elements are left to vibrate freely. The natural frequency of both the UCL-BE and CIS-BE have already been estimated at 3.4kHz and 2.2kHz. Pulse signals with a central frequency lower, similar and higher than the mentioned resonance frequencies are used in order to observe possible differences in the responses.

The time histories of the UCL-BE transducer are presented in figure 5.12 for pulses with central frequency lower equal and higher than 3.4kHz.

The response caused by an exciting signal with a central frequency equal to the natural frequency of the system, 3.4kHz, reaches higher amplitudes than in cases

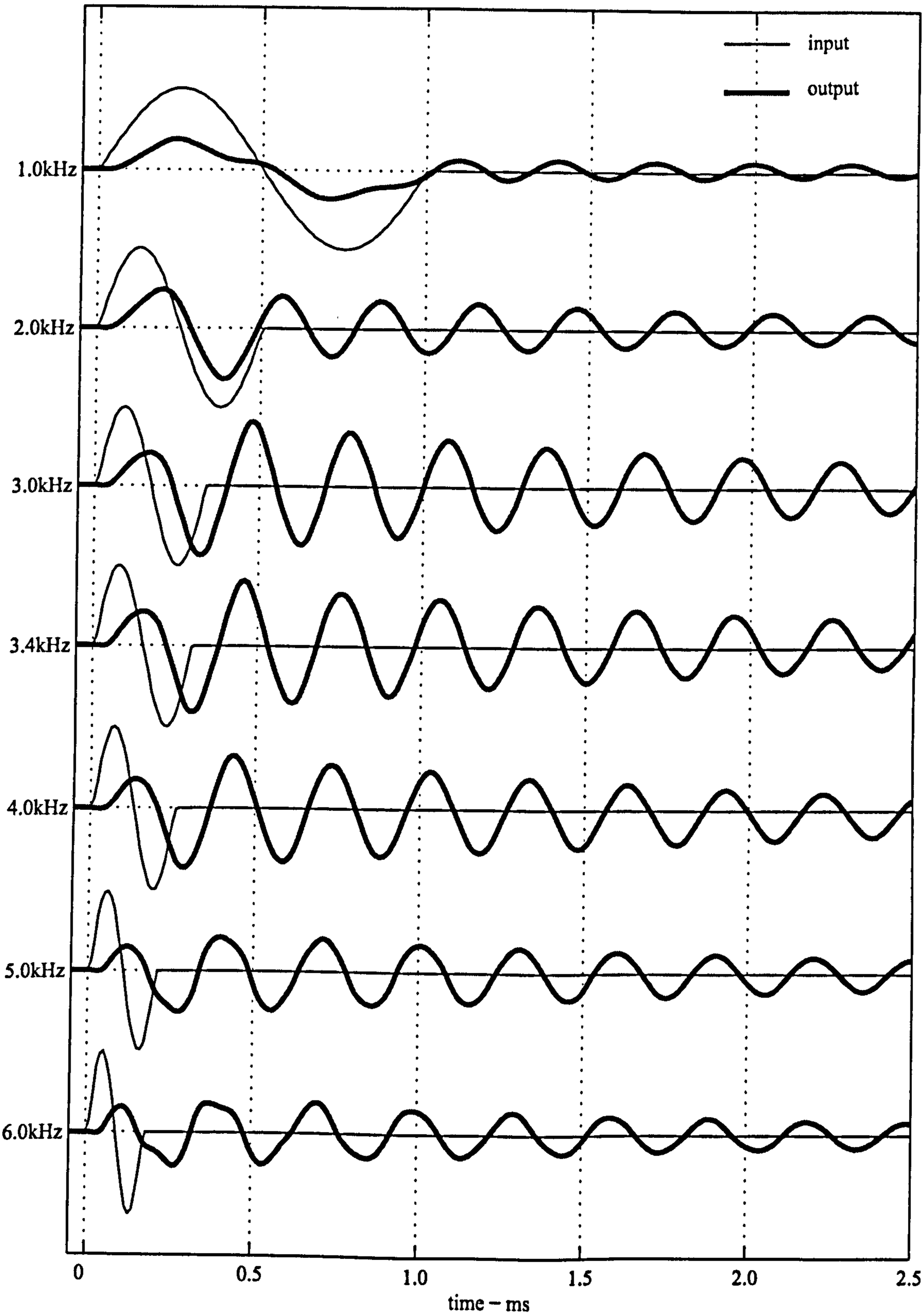

Figure 5.12: Free UCL-BE's time responses to pulse signals with various frequencies.

where the input signals had lower and higher frequencies, thereby strengthening the observation that 3.4kHz is in fact the resonance frequency of the system. It is relevant to note that the bender element oscillation reaches its maximum amplitude, not while the input signal is still acting, but after it has finished, at a value of $u_a = \pm 4\mu$m. This can easily be explained by the existence of inertia. According to Newton's second law of motion, $F = ma$, it would take an infinite force or a zero mass to be able to obtain an instantaneous or infinite acceleration. Therefore, the system cannot pass instantaneously from a stationary state to an oscillating state with the desired frequency, either using continuous or pulse signals. The same can be said of the amplitude of the oscillation, meaning it might only reach its maximum value after a number of oscillation cycles. This is evident by the relation of the maximum oscillation obtained using, at the resonance frequency, a pulse signal, $u_a = \pm 4.0\mu$m, and a continuous signal, $u_a = \pm 18.0\mu$m.

Considering the response time histories for input signals with frequency significantly lower than the resonance frequency, for example $f = 1.0$kHz and $f = 2.0$kHz, during the load stage it can be observed that the UCL-BE oscillation was not able to emulate the input signals precisely. In the case of $f = 1.0$kHz, it can be clearly observed that the oscillation is characterised by two distinct frequencies. One frequency that seems to be the frequency of the input signal, and another higher frequency that must be the resonance frequency of the system. This response, during the load stage, is quite similar to the composed steady-state and transient state responses given in figure 3.23.

For excitation with frequencies higher than the natural frequency, and again during the loading stage, there is a clear phase difference between input and response. Also, the frequency of the response seems to be lower than the frequency of the input. The difference in frequencies can again be explained by a transient state of vibration and the significant phase difference is characteristic of an excitation frequency higher

than the resonance frequency, (figure 3.24).

After the input signal is no longer acting on the transducer, all of the responses assume an oscillation that, although with different initial amplitudes, resemble each other in that they are similar to a free damped vibration, (section 3.8.4). Independent from the frequency of the now passed input signal, in all cases the UCL-BE assumes a vibration with constant frequency, equal to the resonance frequency, and decaying amplitude.

If the UCL-BE does behave as a damped SDOF, then the observed amplitude decay can be assumed to be logarithmic. It is thus possible to apply the free-decay method to evaluating the system's damping ratio. The free-decay method is described in section 3.9 and can be achieved by the application of equation 3.90. Taking the response of the system for an input signal with $f = 3.4$kHz, and using the magnitude of the 3rd and 7rd positive peaks, the estimation of the damping ratio goes as follows:

$$u_3 = 2.95\mu\text{m},\ u_7 = 1.84\mu\text{m}, \quad \text{and} \quad n = j - i = 7 - 3 = 4$$

giving

$$\xi \doteq \frac{u_i - u_j}{2n\pi u_j} = \frac{2.95 - 1.84}{2 \times 4 \times \pi \times 1.84} = 2.4\%$$

This estimate was obtained independently from the one made using the half-power bandwidth method presented in section 5.4.1, which gave a value of $\xi = 2.5\%$, and using different input signals. However they are reassuringly similar.

It has already been observed that, once the input signal is over, the system seems to vibrate at a constant frequency, believed to be its resonance frequency. In order to verify the actual frequency content of the pulse induced responses, an analysis of their time histories in the frequency domain is carried out. For this purpose a fast Fourier transform is performed on the time histories of both the input signals and

respective responses and presented in figure 5.13.

Some of the observations made possible by the analysis of time histories are confirmed by the frequency content of the pulse signals. The most apparent property of the FFT's is the common resonance frequency shared by all the responses, $f \approx$ 3.4kHz. It is also possible to observe how the frequency content of the responses is much narrower than the frequency content of the excitation.

A pulse signal is normally referred to by its known central frequency. But it is worth remembering it has a broad range of frequency content. This is a consequence of it having to accelerate from an immobility state up to the desired frequency, assuming every frequency in between. Once the signal is over, the opposite occurs, and the signal has to decelerate from its main frequency back to 0Hz, again assuming every frequency in between.

In figure 5.13, the signals with frequency lower than the natural frequency of the UCL-BE have responses with a significant range of frequencies, beyond the natural frequency. The case of exciting frequency $f = 1.0$kHz is the best example, since the free UCL-BE can be found to have the most significant response at frequencies lower than the natural frequency. As the exciting frequency increases, the response frequency content of the system at lower frequencies decreases. When excited above the natural frequency, the system apparently stops having any response at that initial range of lower frequencies. As the excitation frequency increases it is possible to start observing some response at a frequency range which corresponds to a second mode of vibration, at around 8.5kHz also detected in figure 5.10.

The pulse excited transducer behaviour described so far points to a response with a considerable degree of independence from a pulse signal exciting it. This observation is quite important for anyone operating a bender element testing system. It serves to reinforce the notion that the driving frequency of an exciting pulse signal might not be the frequency of the vibration actually being transmitted to the sample.

The consequence is that the test operator, not having control over the frequency of the vibration, cannot avoid dispersive phenomena, which are frequency dependent.

Unlike for the UCL-BE, the response curves of the CIS-BE transducer indicate a system behaving in a more complex manner than a simple cantilever would be expected to. The time histories of the response to excitation pulse signals are studied further to better understand such behaviour.

Figure 5.14 presents the mentioned time histories for a number of input signals with different frequencies, higher and lower than the resonance frequency. The observations made previously for the free UCL-BE in figure 5.12 can be made once again. For input signals with lower frequencies, the transducer apparently emulates the excitation signal while it lasts. For input signals with frequency higher than the resonance frequency, a significant phase difference exists between the input and the response. After the input signal is over, the response in all cases, even though with different magnitudes, tunes into the resonance frequency of the transducer.

The frequency content of the pulse input and response time histories are presented in figure 5.15. The resonance frequency of the system is observed to occur at 3.4kHz. This natural frequency is different from the value obtained using a continuous signal, 2.2kHz, (figure 5.11(b)). Besides, the same response curve appears to have a local minimum at this same frequency. When using continuous harmonic or sweep signals, the transducer is forced into a flexural vibration. However, the resonance frequency observed in figure 5.15, referring to the system's free oscillation, is not that of the flexural mode of vibration. It can be conclude that the flexural resonance occurs at 2.2kH and that if left to vibrate freely, the CIS-BE transducer does so at another mode of vibration. The local minimum in the magnitude response curve in figure 5.11(a), which appears to coincide with the flexural resonance frequency 3.4kHz, might be an anti-resonance feature of this curve, which occurs at the interference of the main mode of vibration with a neighbouring mode, (Ewins,

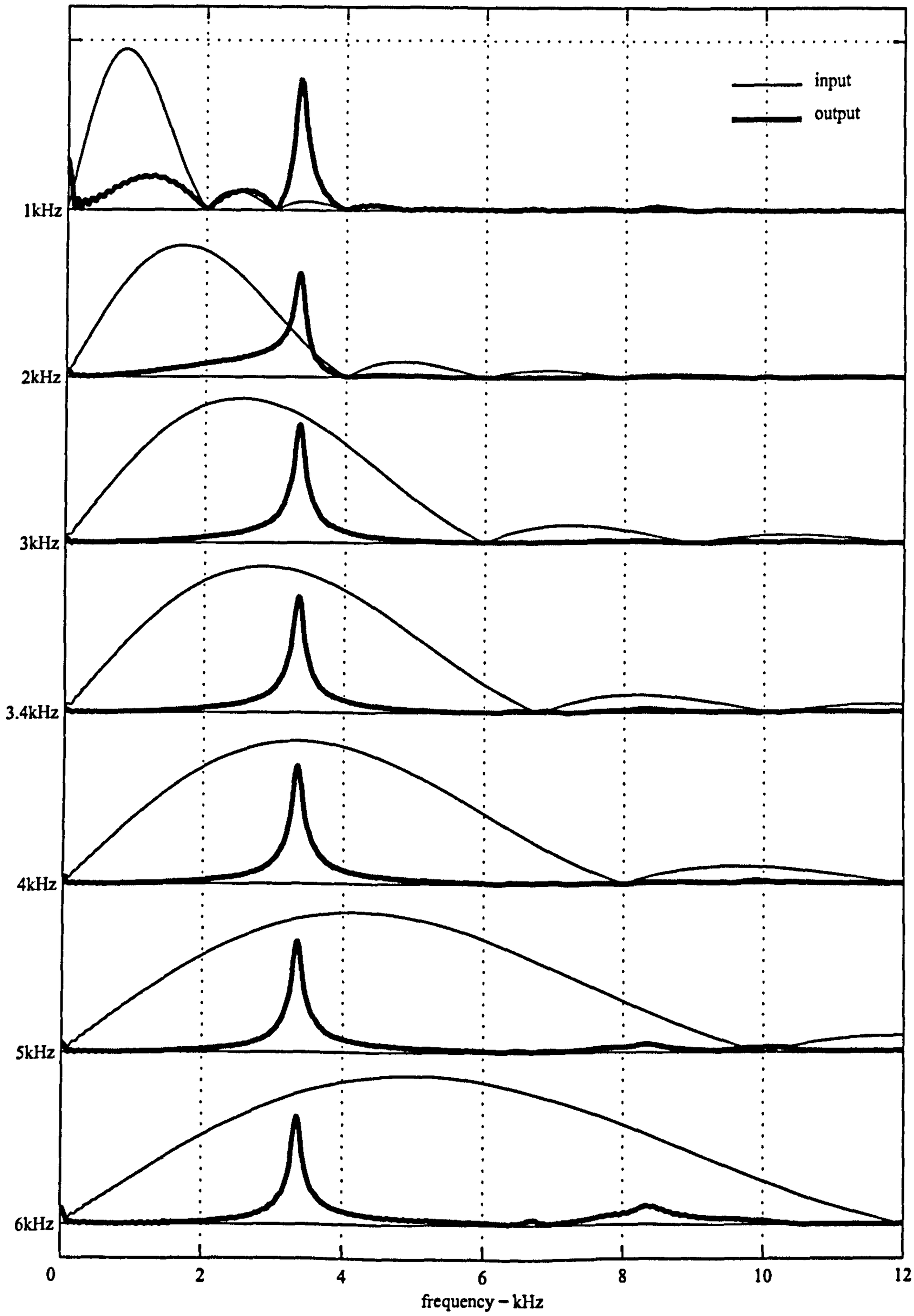

Figure 5.13: Free UCL-BE input and output signals' frequency content.

2000). This other mode of vibration, which occurs when the transducer vibrates freely, is probably a more complex flexural-torsional mode of vibration favoured by the relatively large width of the transducer.

The magnitude of the maximum oscillation, when in a free vibration is of $a = \pm 3.3\mu$m, higher than the maximum amplitude achieved when forced to oscillate in a flexural mode, $a = \pm 2.9\mu$m. Again, this is a sign of the importance of the free vibration mode.

The estimation of the damping ratio using the free decay component of the time history of one of the responses can be obtained using equation 3.90. The value of the damping ratio is calculated to be $\xi = 8.8\%$. This method of determining the damping ratio produces a value higher than the exact value, Shirley (1978) proposes a correction to the estimated damping ratio, which for the present case is of 75%, giving $\xi = 0.75 * 8.8 = 6.6\%$.

The damping ratio of the CIS-BE obtained from a time history curve provides a significant final clue for why, when left to oscillate with no interference from an excitation signal, the frequency of the oscillation differ from that of a forced vibration. Dominant modes of vibration have lower damping ratios, so since the damping ratio for the free vibration mode is lower than the damping ratio associated with the forced flexural vibration, $6.6\% < 8.0\%$, this is further proof of the importance of the free vibration mode. The presented complexity of the modal behaviour of the CIS-BE acts as a warning about the need to consider the geometry of bender element transducers when designing them. In this case, the geometry of the CIS-transducer leads to a free mode of vibration which is not a flexural mode. This raises doubts about the efficiency of the transducer at performing bending motions and hence producing shear waves, when excited by pulse signals.

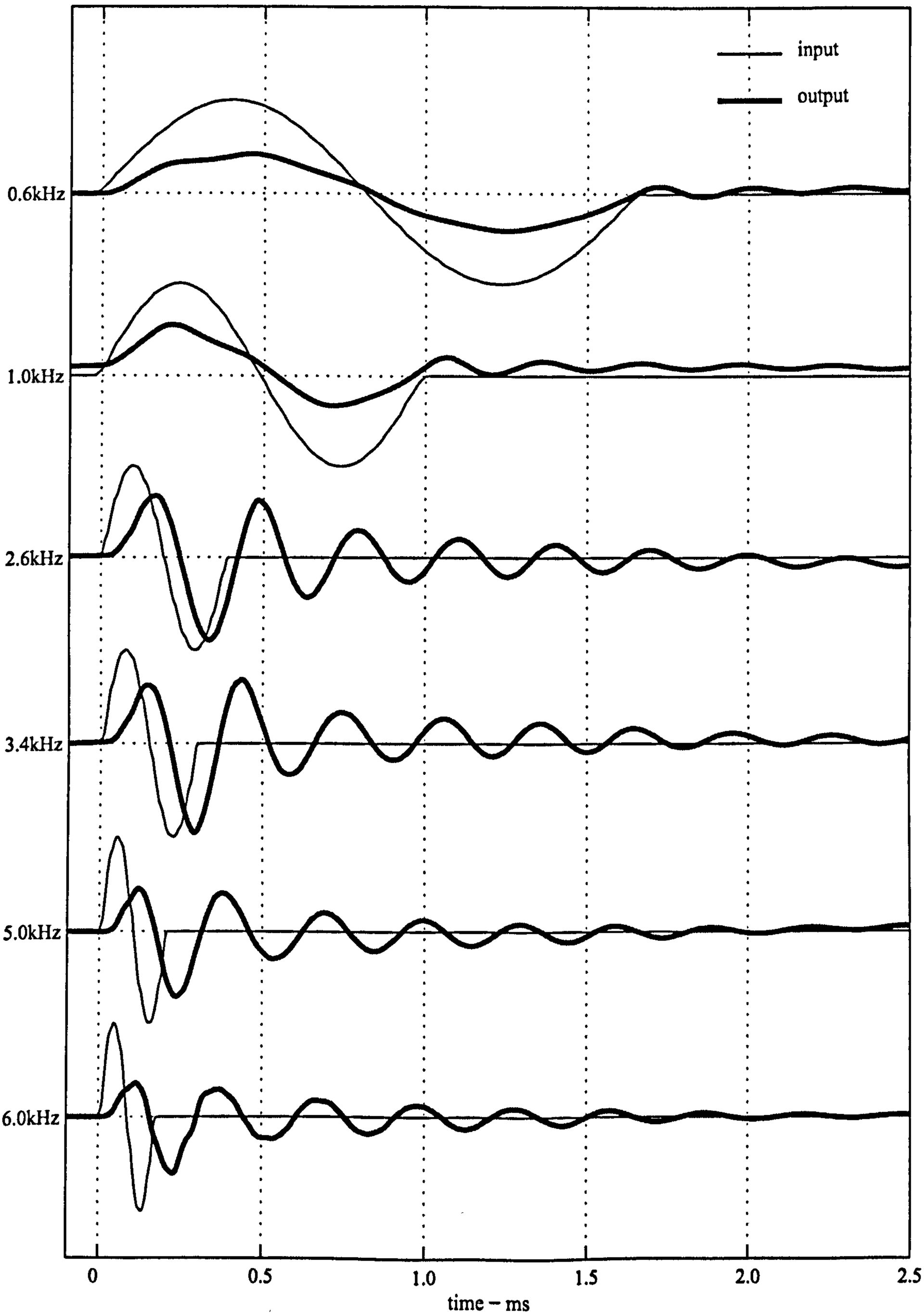

Figure 5.14: Free CIS-BE's time responses to pulse signals with various frequencies.

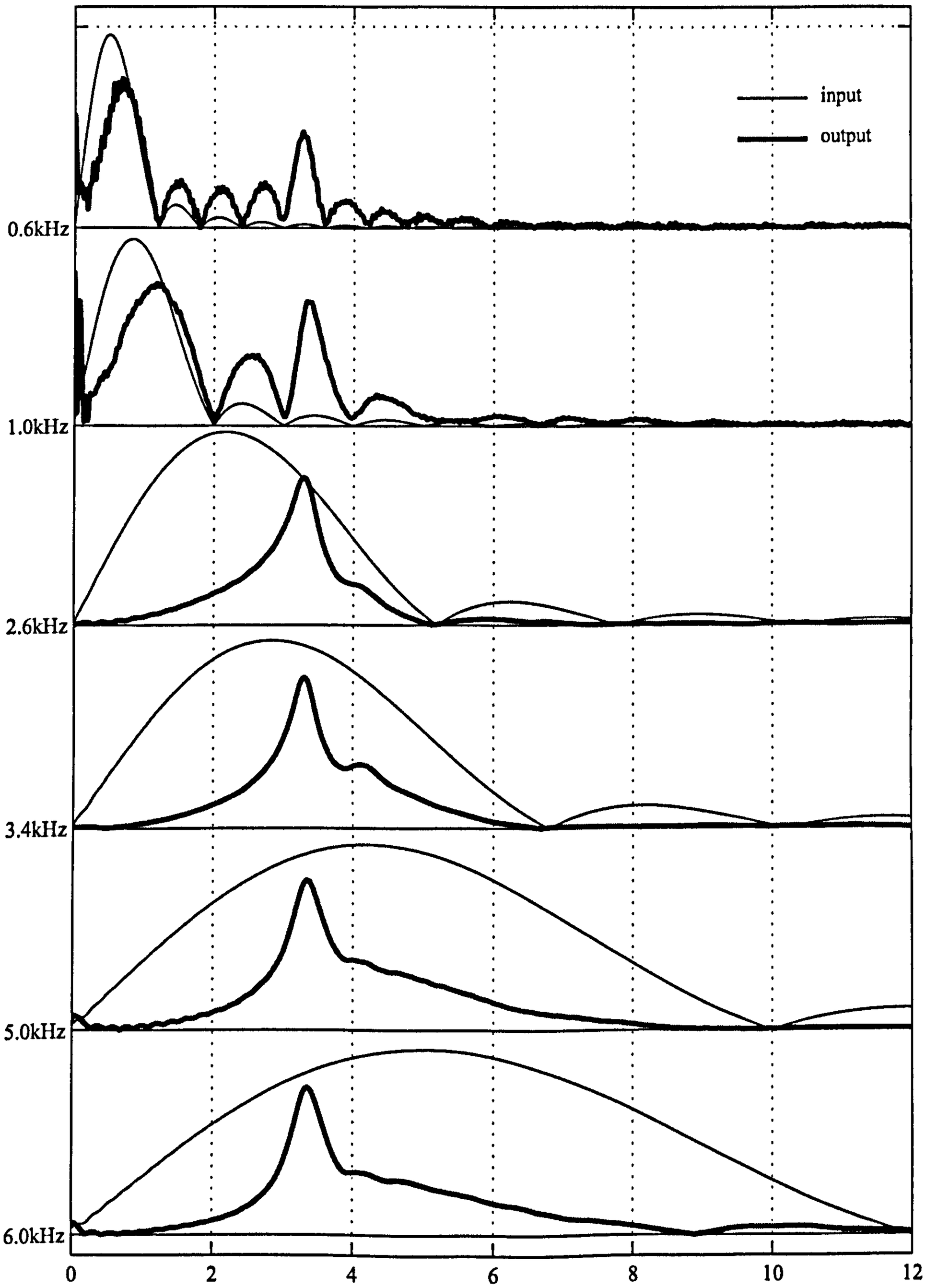

Figure 5.15: Free CIS-BE input and output signals' frequency contents.

5.5 Results for Embedded Transducers

The results concerning the behaviour of the UCL-BE and CIS-BE with their tips embedded 3mm in the synthetic rubber sample are now presented . This will enable the study of the transducers dynamic behaviour in conditions similar to normal testing conditions.

5.5.1 Frequency Domain

Figure 5.16 presents the magnitude and phase components of the response of the UCL-BE when excited with continuous signals.

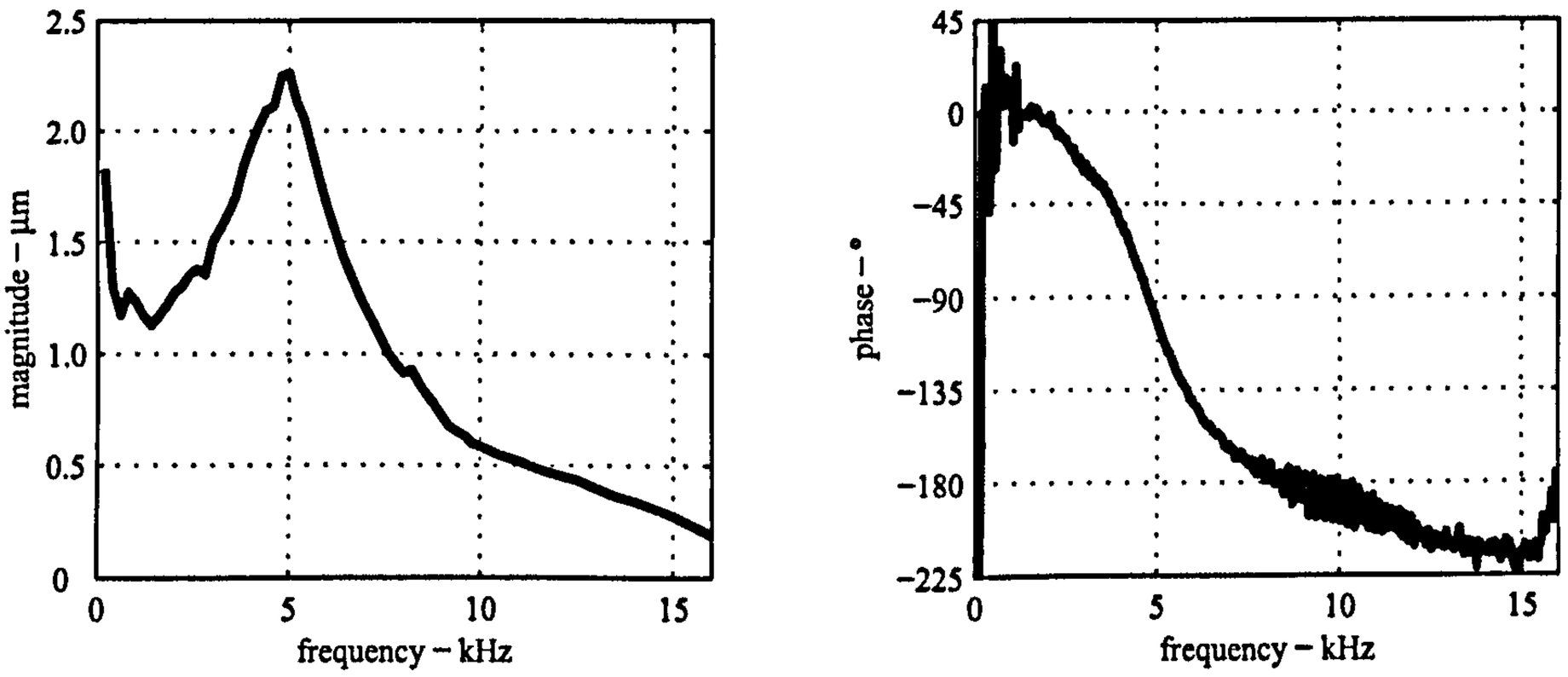

(a) magnitude

(b) phase

Figure 5.16: Embedded UCL-BE's response function estimate from sweep signal dynamic excitation.

The response curve in figure 5.16(a) enables the observation of a resonance frequency of 5.0kHz for the UCL-BE. The phase shift at 5.0kHz seen in figure 5.16(b) confirms this observation. Remembering that the resonance frequency of the free UCL-BE was at 3.4kHz, it can be noted how the presence of the sample in contact with its tip stiffens its overall behaviour.

The maximum magnitude of the oscillation of the embedded tip of the UCL-BE is now 2.3μm, much smaller than when it was free, 37μm. The decrease in

the maximum oscillation magnitude is a logical result since, having used the same magnitude of load, the sample acts as an obstacle to the transducer's movement. The sample adds stiffness to the system, which implies an increased resistance to deformation forces. There is also the question of increased damping, which decreases the maximum dynamic motion magnitude, (figure 3.25).

The estimation of the viscous damping ratio for the embedded UCL-BE, using the half-power bandwidth method and equation 3.91, produces a damping ratio value of $\xi = 25.0\%$. This value is significantly higher than the 2.5% found for the free UCL-BE. Nevertheless, it is still quite distant from the 100%, which would mean the transducer would behave as a critically damped system, (section 3.8.4). This observation is important because only for a critically, or overcriticaly damped system could one expect the response of the transducer not to last after the action of a transient pulse load, (Clough and Penzien, 1993).

The response curves of the CIS-BE system, obtained using sweep and continuous signals, are presented in figure 5.17.

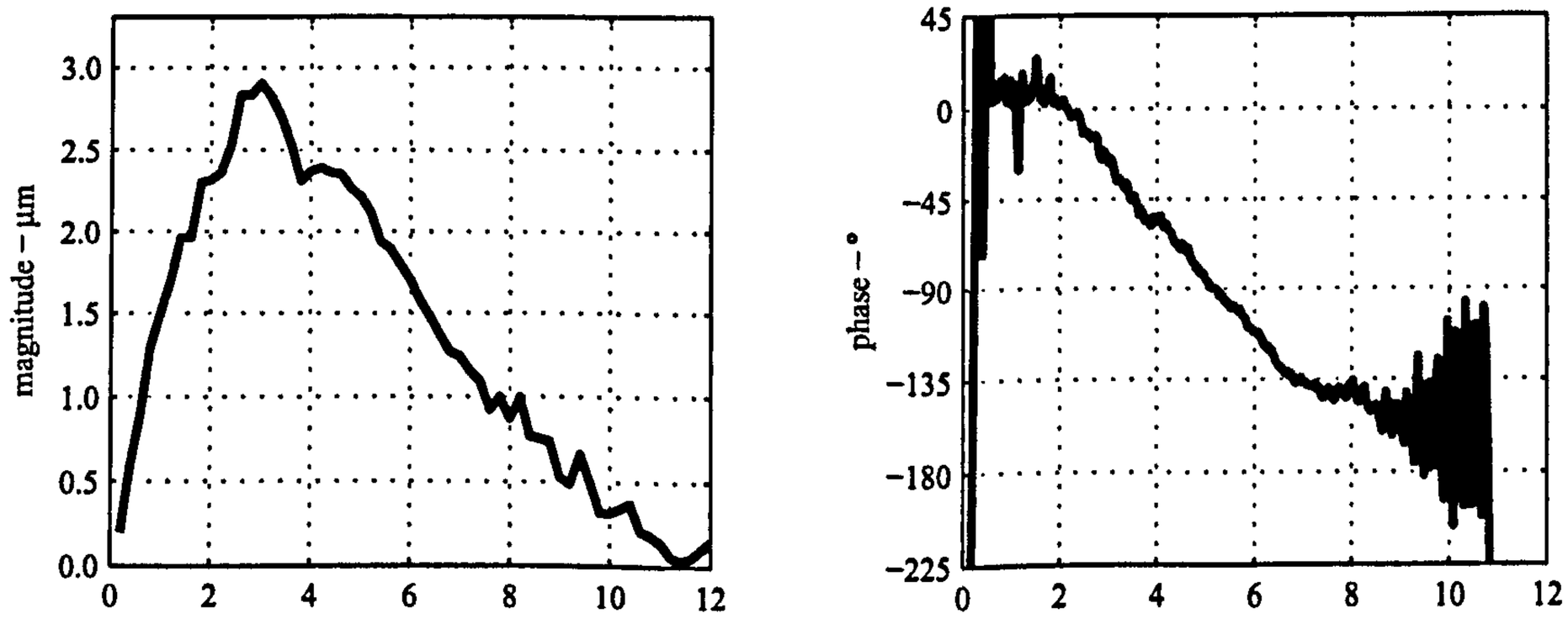

(a) magnitude (b) phase

Figure 5.17: Embedded CIS-BE's response function to sweep signal dynamic excitation.

As with the UCL-BE, the behaviour of the CIS-BE changes drastically when its

tip is inserted in the sample. In the CIS-BE case, in the considered frequency range, $f \in [0\ 12]$kHz, the magnitude curve now has a single broad single peak where before it had a number of narrower peaks. The system response to flexural excitation has a natural frequency of 3.2kHz.

It is clear that the damping ratio of the system has increased by embedding the tip of the transducer in the sample, as it had with UCL-BE, since the corresponding peak feature of the magnitude curve is now much broader. The estimation of the damping ratio, using equation 3.91, produces $\xi = 50\%$. The magnitude curve contains a second, less noticeable, peak near 4.2kHz with a lower magnitude of 2.4μm. This means that the observed peak covering a frequency range of $f \in [0.5\ 11.5]$ is composed by more than one mode of vibration, rendering the proposed damping ratio calculation meaningless.

The amplitude of the oscillation is $a = 2.9\mu$m. Even though the frequency domain results shown so far are ambiguous for the CIS-BE embedded test set-up, the shift in behaviour of the system when the tip of the transducer is inserted in the sample is similar to the UCL-BE on three aspects, namely: the natural frequency increase, the damping ratio increase and the magnitude of the oscillation decrease.

5.5.2 Time Domain

Figure 5.18 presents the input signals and the embedded UCL-BE time history oscillation responses. When compared with equivalent responses for a free tip boundary conditions, they can be observed to take around 1.2ms for the bender element to return to a stationary state. Before it took well over 5.0ms. This is a clear indication in the increase of the system's damping, as calculated in section 5.5.1.

The maximum amplitude of the response for pulse excitations with 5,0kHz is $u_a = 2.5\mu$m, which is almost the same value found for a continuous signal excitation with the same frequency, $u_a = 2.3\mu$m. It is in fact slightly higher for pulse

excitations. This observation appears to contradict the explanation given for the difference in steady and transient maximum oscillation magnitudes, when the UCL-BE tip was free. With a free transducer tip, the continuous signal produced higher oscillations magnitudes, since it took the system more than one cycle to achieve its limit state and the pulse signal did not have enough time to achieve the same magnitudes. The observed shift in oscillation magnitude for the embedded transducer tip is due to the much higher damping of the system. The maximum oscillation magnitude is now relatively lower, compared with the free boundary conditions, but most importantly compared with the equivalent static displacement, (Clough and Penzien, 1993). Therefore it now takes the transducer less time to reach the maximum oscillation magnitude.

The transducer's response is quite similar to the input signal with 1.0kHz. For 3.0kHz and 5.0kHz the response seems to have a similar frequency to the input signal but a significant phase delay. For the 7.0kHz and 9.0kHz cases, the response has a significant phase delay but is also clearly not at the same frequency as the input. Once the input signal is over, the frequency of the response is that of the resonance frequency in all cases.

The response can be observed to decay to a near stationary state in around 1ms past the end of the input signals in all cases. The determination of the damping ratio using the time history of the received signals, as done in section 5.4.2, estimates a value of $\xi = 31\%$, using the peaks features at 0.325ms and 0.535ms. This value is misleading since the free-vibration decay method becomes inaccurate for high values of damping ratios. In fact, Clough and Penzien (1993) do not even propose a correction factor for damping ratios higher than 20%. If a corrected value had to be estimated extrapolating the correction curve proposed by Clough and Penzien (1993), it would point to a value of around $\xi = 20\%$. This result is somewhat consistent with the result obtained in the frequency domain.

The observations of the time histories are well corroborated by their frequency content, (figure 5.19). The resonance frequency can be observed to occur at 4.8kHz, quite near the 5.0kHz value obtained when using continuous or sweep signals. The frequency content response peaks are now broader than for the free UCL-BE case, confirming the increased damping. A certain independence of the response frequency in relation to the input frequency content is again present, more so for input signals with frequencies higher than the resonance frequency of the system.

The results concerning the time domain responses of the embedded CIS-BE are presented in figure 5.20. The high values of damping obtained with the frequency domain results can also be observed in the form of some magnitude decrease for all the presented responses. If the free tip was observed to oscillate 3ms past the input signal end, it becomes stationary after approximately 1ms. The damping ratio using the free-vibration decay method is not possible to apply because there are no comparable decaying peaks. Further, it has already been shown that for high values of damping ratio, $\xi < 20\%$, the mentioned method is not reliable.

The magnitude of the maximum oscillation, in the case of the 3.0kHz input signal is $u_a = 2.6\mu$m. This value is similar to the value found for a steady-state load at 3.2 $u_a = 2.9\mu$m in section 5.5.1. As before, a high damping ratio can explain the similarities between maximum oscillation magnitude for a transient and steady-state responses.

Comparing the analysed test set-ups, the response of the embedded CIS-BE at low frequencies is the one apparently most capable of emulating the input signal, for input signal frequencies lower than the resonance frequency. Above the system's resonance frequency, a significant phase delay between input and response is again noticeable. For high input frequencies, the response of the transducer seems to be not a perfect sinusoidal signal, but the sum of two signal components with different frequencies.

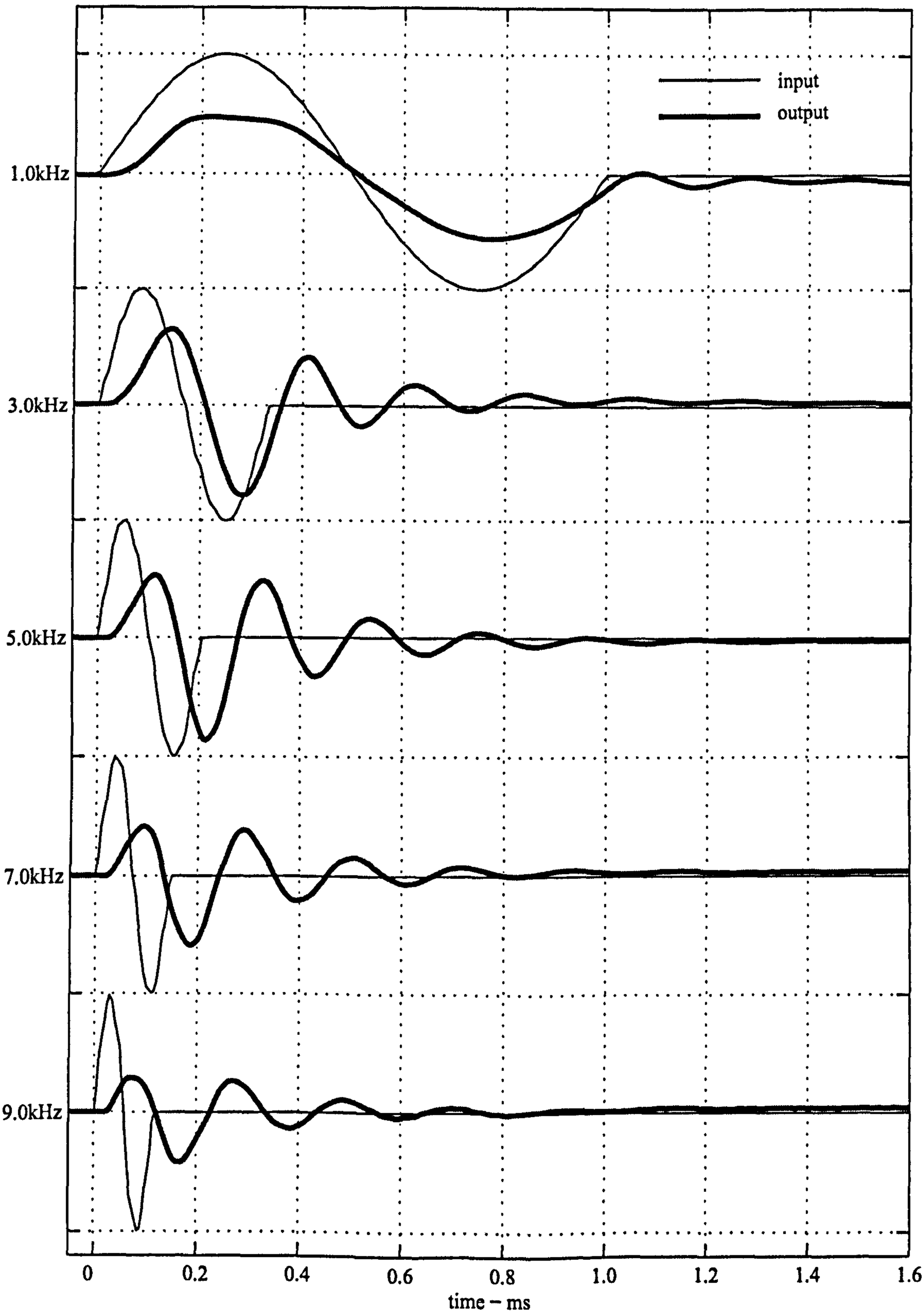

Figure 5.18: Embedded UCL-BE's time responses to pulse signals with various frequencies around the natural frequency.

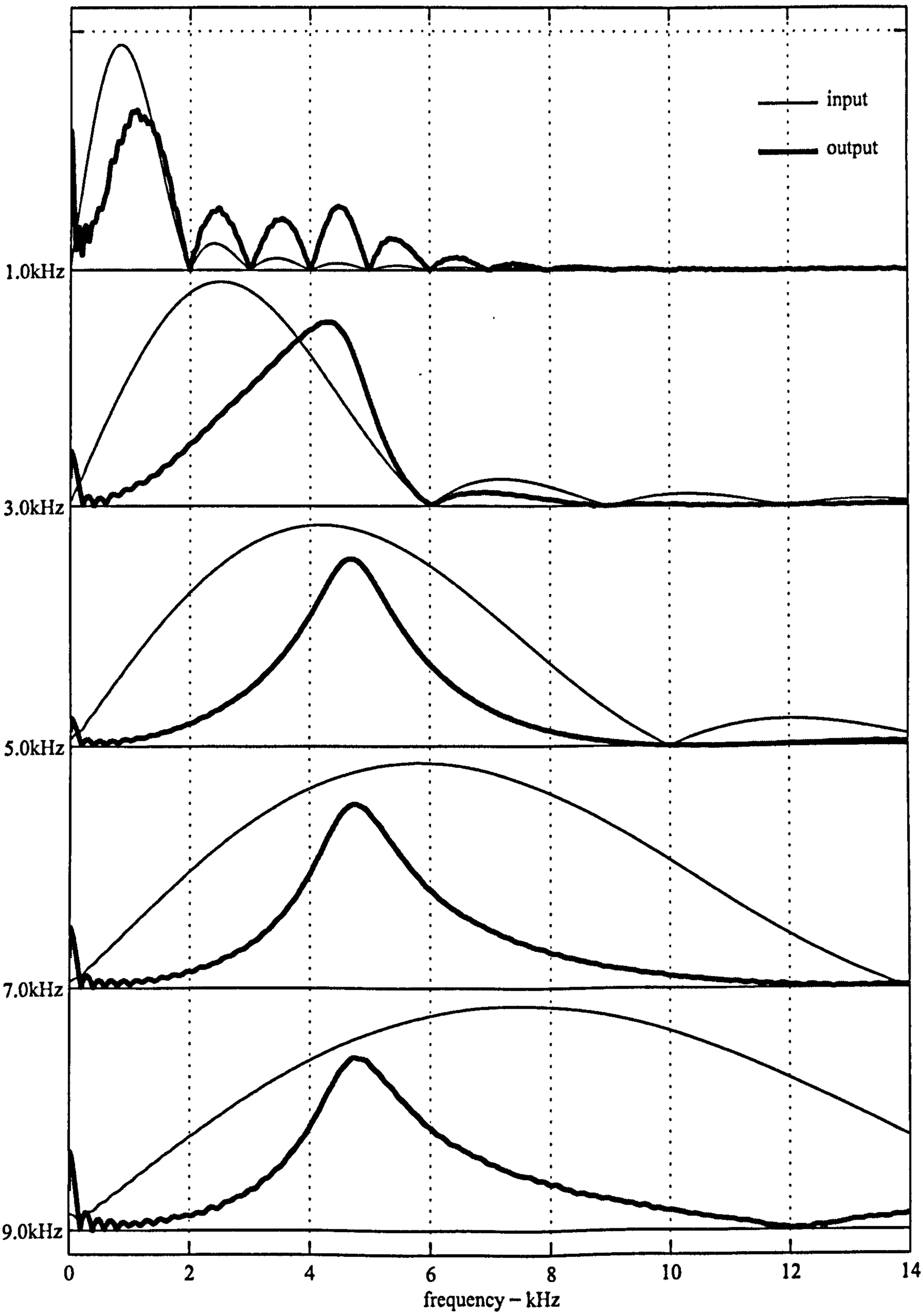

Figure 5.19: Embedded UCL-BE responses frequency content to pulse signals with various frequencies.

The frequency contents of the time responses of the pulse signals are presented in figure 5.21. The quality of the frequency contents is quite poor. This has to do with the nature of the Fast Fourier Transform. The FFT is in theory best suitable to handle long continuous signals, being less capable of processing short signals. In figure 5.20 it can be seen that the response time histories are quite short. Nevertheless, it is clear that more than a single response frequency is being picked up by the system. One peak at 3.2kHz and another peak at around 4.3kHz provide the highest responses for excitation pulses with central frequencies higher than 3.0kHz. This observation is in agreement with the results presented in figure 5.17.

Unlike the results from the free CIS-BE, there is no significant difference of behaviour detected for a steady-state vibration, obtained using sweep and continuous signal, and a transient state response, obtained using pulse signals. Both indicate a resonance frequency at 3.2kHz and at 4.3kHz. It is not possible to evaluate, without some form of modal analysis, if either or both resonances are related with which particular modes of vibration, either flexural or of a more complex mode.

It is finally possible to confront the assumption stating that the transmitting bender element transducer perfectly emulates the transmitted pulse signals. From the observations made of the actual behaviour of bender element transducers, it is plain that the transmitting bender element behaves as a dynamic multiple degree of freedom system with a certain degree of independence from the transient input pulse signals. Observed aspects of the oscillation behaviour of bender elements different from the input signal are its frequency, significant phase shifts and sufficient inertia to maintain oscillation movement after the exciting signal is over. Therefore, when operating a bender element testing system, the operator must acknowledge the different mechanical response of bender elements to transient and steady-state excitation signals, especially the differences between the transmitting signal and the transmitting transducer behaviour when using pulse signals.

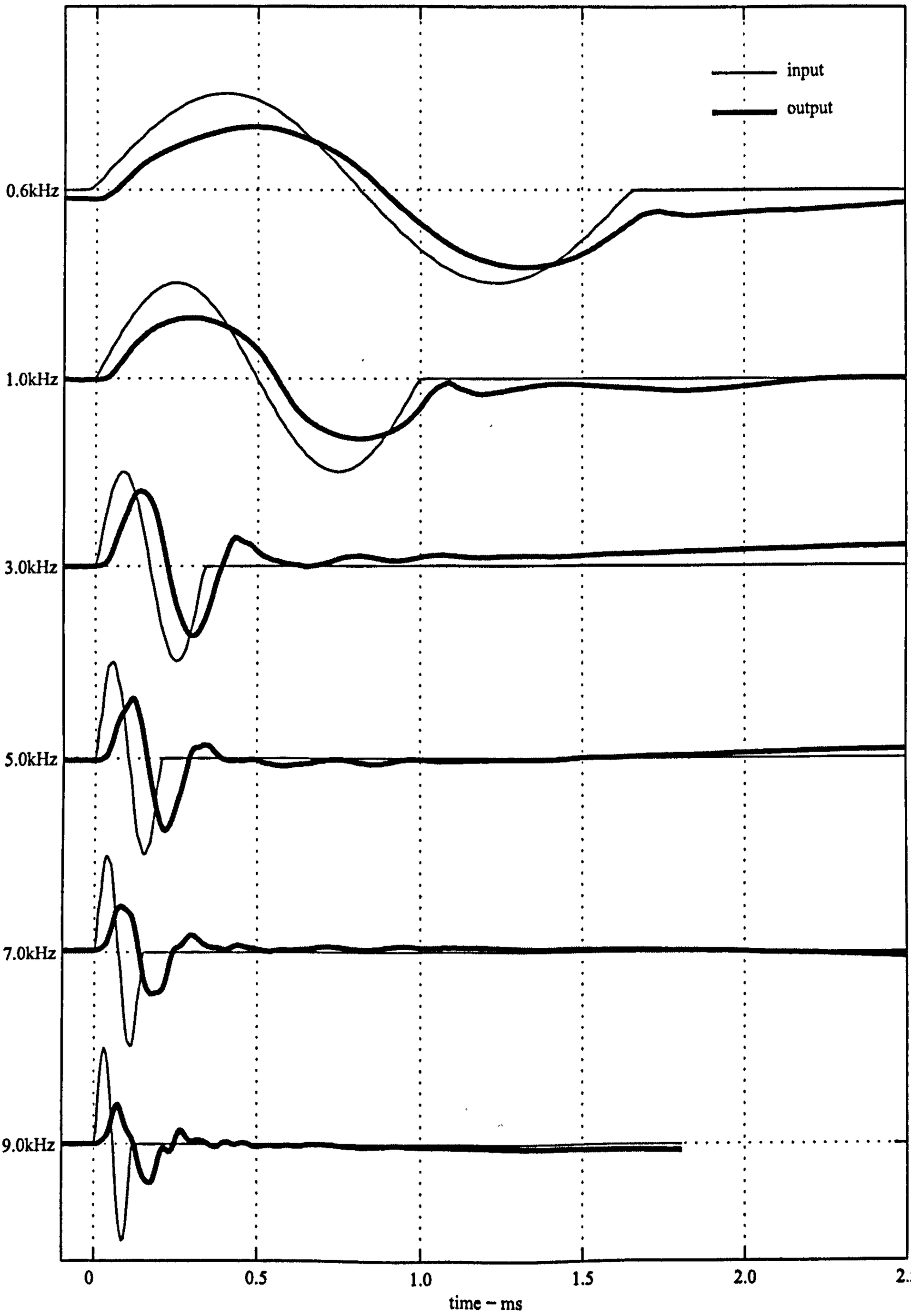

Figure 5.20: Embedded CIS-BE's time responses to pulse signals with various frequencies around the natural frequency.

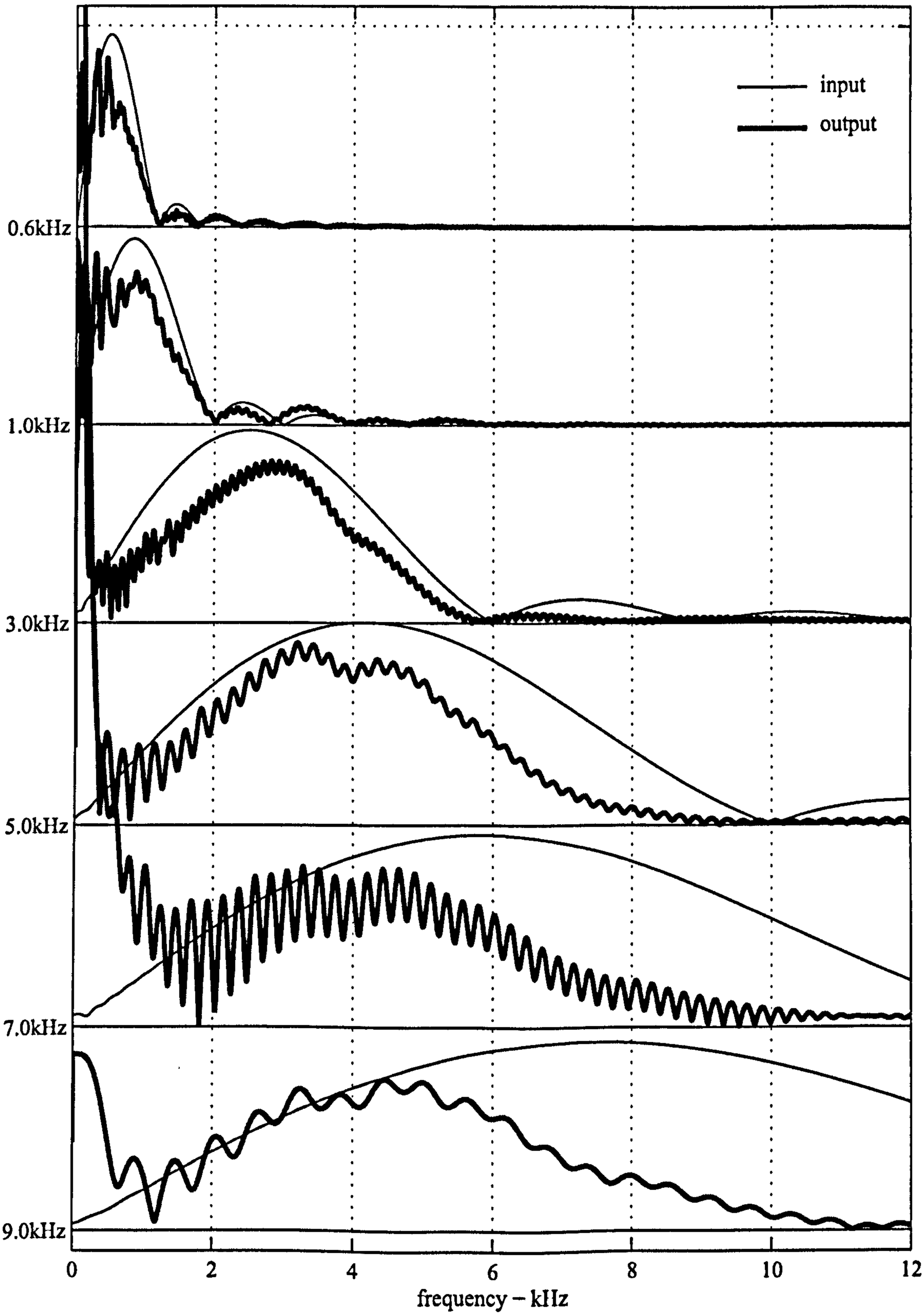

Figure 5.21: Embedded CIS-BE responses frequency content to pulse signals with various frequencies.

5.6 Bender Element Model

Having monitored the behaviour of the UCL-BE and CIS-BE, with their tips either free and embedded, it is possible to present the natural frequency, maximum oscillation magnitude and values of damping ratio, (table 5.6). Using these values together with simple analytical and numerical models the elastic properties of the transducers can be estimated. It is also possible to analyse some aspects of the excitation signals, such as their exerted force on the transducer or the properties of the medium in which the transducer tips were embedded.

Both transducers were manufactured using similar piezoelectric ceramic plates, supplied by the same company and with the same piezoelectric capacity. The plates used in the test were wired in series for both pairs of transducers.

In table 5.6 the oscillation amplitude, a, the natural damped frequency of the system, f_D, and the estimated damping ratio, ξ, are presented for the monitored bender elements, UCL-BE and CIS-BE, in the two tested scenarios, with free and embedded tips. Similar results available in relevant literature are also presented.

The observed natural frequency of the free transducer, $\omega = 2\pi f$, its dynamic maximum displacement, a, and the damping coefficient, ξ, are all used to characterise the system. The free bender element transducers are assumed to behave as simple cantilevers. The natural frequency is used with frequency equation 3.101 and boundary condition equation 3.105 to estimate the flexural stiffness of the free system, EI. The damping ratio is used to obtain the dynamic magnification factor, D_f, which is used to obtain an estimate of the equivalent static displacement, a_s, from the dynamic displacement, a, as described by equation 3.86 in section 3.8.5. With the flexural stiffness of the system, as well as with other properties such as its length, L, and mass per unit length, m, a numerical model is used to estimate the necessary static load, M. This is the load necessary to produce the same pre-

determined static displacement obtained from the dynamic displacement and the magnification factor.

Transducer	Tip Fixity		Properties		
	body	tip	a	f_D	ξ
UCL-BE	clamped	free	37.0μm	3400Hz	2.5%
(1.5×6.5×8.0mm)[1]	clamped	embedded	2.3μm	5000Hz	25.0%
CIS-BE	clamped	free	5.9μm	2200Hz	8.0%
(1.5×12.0×10.0mm)	clamped	embedded	2.9μm	3200Hz	—
Shirley (1978)	unspecified	free	—	8000Hz	—
(0.5×6.4×25.4mm)					
Dyvik and Madshus (1985)	clamped	free	—	2000Hz	—
(1.0×10.0×12.0mm)	clamped	embedded	—	4000Hz	—
Brocanelli and Rinaldi (1998)	clamped	free[2]	—	3170Hz	—
(no dimensions)					
Greening and Nash (2004)	free	embedded	—	1100Hz	—
(1.5×12.0×10.0mm)					
Lee and Santamarina (2005)	clamped	free	—	1500Hz	—
(0.6×8.0×12.7mm)[3]	clamped	embedded	—	5000Hz	—

Table 5.6: Summary of dynamic properties of tested bender elements.

Figure 5.22 shows the mechanical model of the bender element with tip embedded in soil used in the numerical model analysis. A similar numerical model is used for the free cantilever but with no spring stiffness, making $K = 0$N/m.

The embedded system is modelled as the free UCL bender element plus a number of springs at the corresponding embedded tip end. The flexural stiffness of the cantilever itself is the same as the one estimated for the free system. The load capable of producing the free static displacement, M, is considered to be the same for the case with embedded tip, since the boundary conditions of the transducer tip

[1] (Thickness×Width×Length)
[2] The transducer's tip is not embedded in soil but is partially embedded in silicone rubber.
[3] Tested with different free lengths. The value presented is for a free length of 11.5mm.

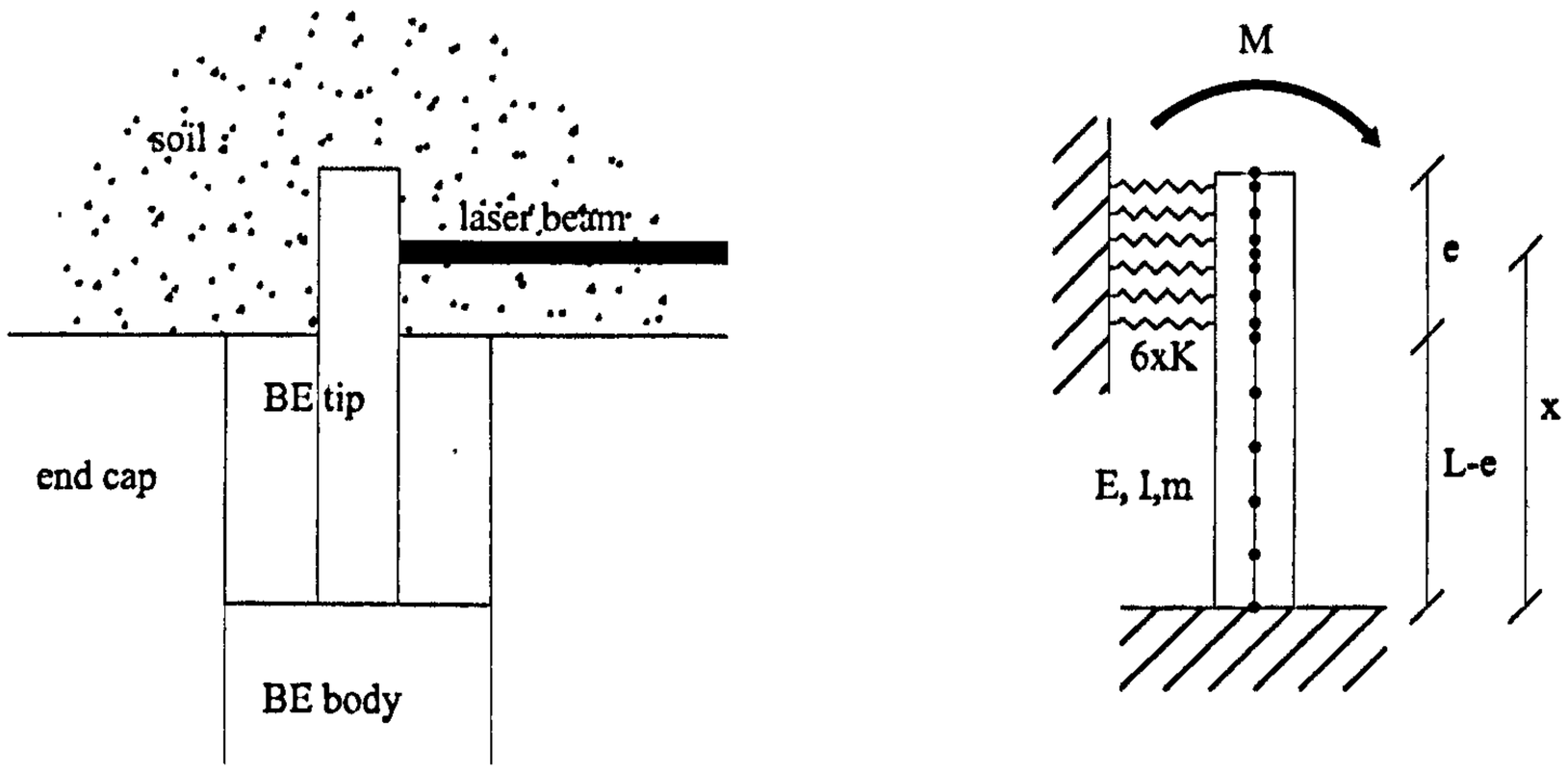

(a) bender element in soil (b) mechanical model

Figure 5.22: Mechanical model of bender element tip embedded in soil.

surface have no influence over the electric signal and the equivalent bending action it provides. Taking the equivalent static displacement obtained from the observed dynamic displacement and the acting moment load into account, the stiffness of the springs can be evaluated using a static numerical model.

Knowing the relevant properties of the embedded system, such as the flexural stiffness and the spring stiffness, two distinct verifications can be done. A dynamic model can be used to verify the embedded transducer resonance frequency and a static model can be used to verify the produced static displacement, applying the previously determined moment load, M.

The static and dynamic numerical models were calculated using a finite element program, (CALFEM, 1999). These numerical models, specifically the dynamic model, do not consider the damping ratio. In summary, the static models are used to correlate the flexural stiffness, the static displacement, the moment load and the spring stiffness. The dynamic models are used, together with all of the already estimated properties, in a regressive analysis to verify the natural frequency of the system. Figure 5.23 presents a diagram of the multi-step procedure to characterise the transducers and verify the results.

Thus, the natural frequency of the transducer, ω_1, is used to obtain its flexural stiffness, EI, (1a to 2a). The dynamic amplitude of displacement, a, and the damping ratio, ξ, are used to obtain the equivalent static displacement, a_s, (1b to 2b). With the flexural stiffness and the static displacement, and using a static numerical model, the moment load, M, necessary to force such a static displacement is estimated, (2a and 2b to 3). Using the moment load, the flexural stiffness of the cantilever and the equivalent static displacement, a numerical static model is used to estimate the stiffness of the 6 springs, K, evenly distributed along the embedded 3mm height, (3 to 4). Finally, the two verification steps are performed. Using the spring stiffness together with the flexural stiffness of the cantilever, the resonance frequency of the embedded transducer is calculated by a numerical dynamic model, and compared with the monitored value, (4 to 5a). Using the spring stiffness and a static numerical model, a static displacement is calculated and compared with the estimated value, (4 to 5b).

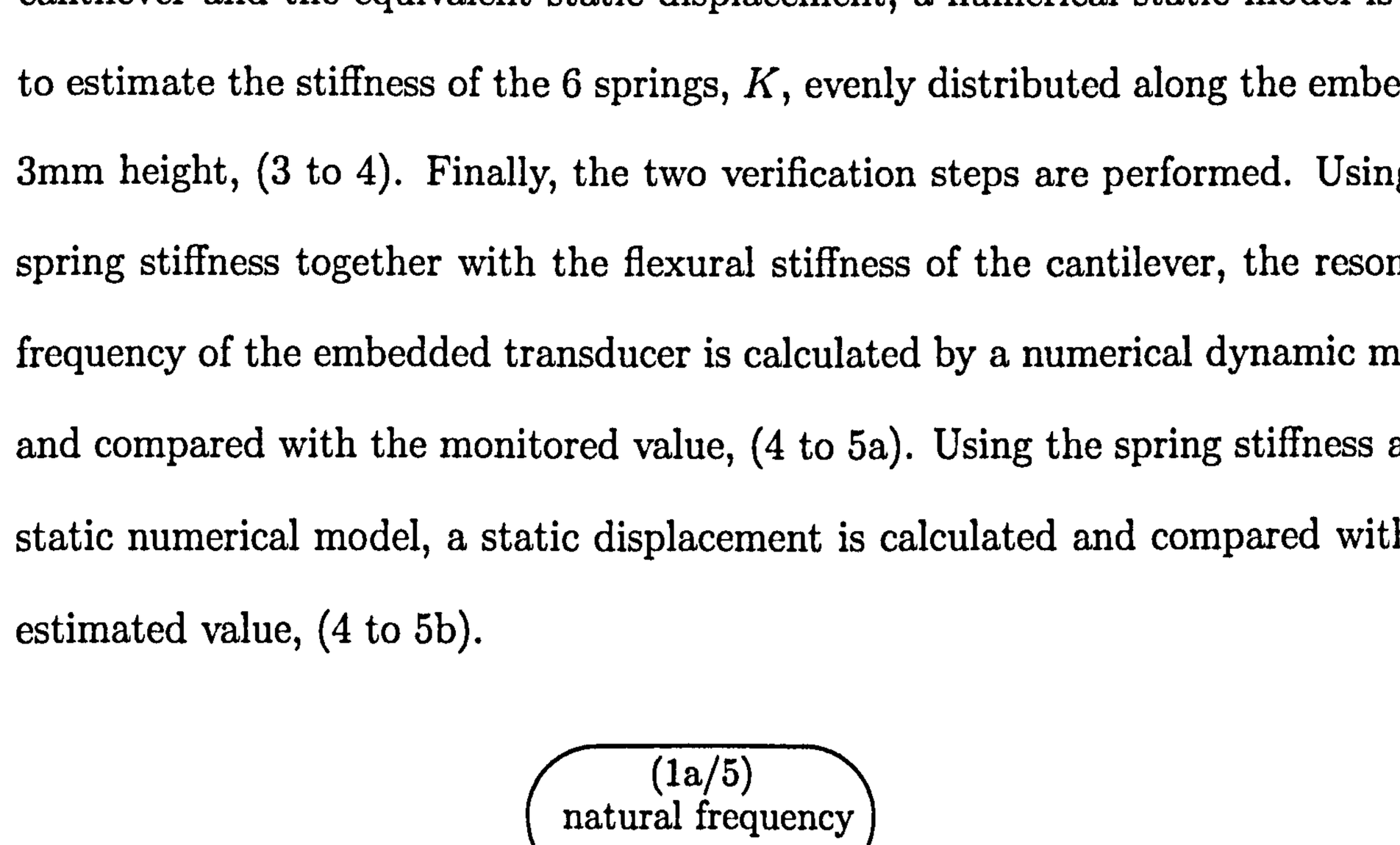

Figure 5.23: Scheme of multi-step bender element transducers modelling using the observed properties from the laser velocimeter monitoring

The mass per unit length is calculated considering the transducer tip to be a composed section. It is composed of piezoelectric ceramic and of epoxy resin. The epoxy resin used as coating in the manufacture of bender element has a density of around 1000kg.m^{-3}, (Vosschemie, 2002). The density of piezoelectric ceramic is around 7800kg.m^{-3}, (Piezo, 2005). Knowing the partial area of each section component, it is then possible to calculate the equivalent density and mass per length unit of the composite section. These calculations are presented in equation 5.11 for the tips of the UCL-BE and CIS-BE transducers.

	epoxy	piezoceramic		bender element
UCL-BE	$\rho = 1000\text{kg.m}^{-3}$ $A = 6.8 \times 10^{-6}\text{m}^2$	$\rho = 7800\text{kg.m}^{-3}$ $A = 3.0 \times 10^{-6}\text{m}^2$	$\Rightarrow$	$\rho = 3100\text{kg.m}^{-3}$ $A = 9.8 \times 10^{-6}\text{m}^2$ $m = 3.02 \times 10^{-2}\text{kg.m}^{-1}$
CIS-BE	$\rho = 1000\text{kg.m}^{-3}$ $A = 13.0 \times 10^{-6}\text{m}^2$	$\rho = 7800\text{kg.m}^{-3}$ $A = 5.0 \times 10^{-6}\text{m}^2$	$\Rightarrow$	$\rho = 2900\text{kg.m}^{-3}$ $A = 18.0 \times 10^{-6}\text{m}^2$ $m = 5.22 \times 10^{-2}\text{kg.m}^{-1}$

(5.11)

The piezoelectric plate ceramic used to manufacture the CIS-BE is from the same maker as the one used to manufacture the UCL-BE and has the same thickness of 0.5mm. The densities of the composed sections of the UCL-BE and CIS-BE are calculated to be 3100kg.m^{-3} and 2900kg.m^{-3} respectively, giving mass per length unit values of 3.02×10^{-2}kg.m^{-1} and 5.22×10^{-2}kg.m^{-1}.

The estimated values of flexural stiffness, equivalent static displacement, equivalent static load and equivalent springs stiffness are presented in table 5.7. Damping causes the system to resonate at frequencies slightly lower than the actual charac-

teristic frequencies, (Clough and Penzien, 1993). The necessary relation between the damped and undamped natural frequencies is given in equation 3.76. The calculation procedure steps defined in figure 5.23 are also presented in table 5.7.

It was not possible to obtain a satisfactory value of equivalent damping coefficient for the embedded CIS-BE, due to complex model behaviour expressed in the respective magnitude response curve, (figure 5.17(a)). Two distinct modes of vibration occur at close frequencies, possibly interfering with each other. The equivalent damping ratio obtained for the UCL-BE is used in the calculations concerning CIS-BE, since the transducers are constituted by similar materials. The value of damping ratio is only used to estimate the equivalent maximum static displacement. The dynamic verification of the natural frequency is made without considering any damping at all.

			UCL-BE		CIS-BE		step
			free	embed.	free	embed.	
damped natural frequency	f_D	Hz	3400	5000	2200	3200	
natural frequency	f_n	Hz	3401	5164	2207	3305	
	ω	rad.s^{-1}	21370	32446	13867	20766	1a
flexural stiffness	EI	N.m^2	4.57×10^{-3}		8.12×10^{-3}		2a
Young modulus	E	Pa	2.50×10^{9}		2.41×10^{9}		
dynamic displacement	a	μm	$\pm$18.00	$\pm$1.12	$\pm$2.95	$\pm$1.41	1b
damping coefficient	ξ	—	2.5%	25.0%	8.0%	25.0%	1b
magnification factor	D_f	—	20.0	2.0	6.3	2.0	
static displacement	a_s	μm	$\pm$0.90	$\pm$0.56	$\pm$0.47	$\pm$0.71	2b
moment load	M	N.m	1.95×10^{-4}		1.60×10^{-4}		3
spring stiffness (×6)	K	N.m^{-1}	—	10500	—	8100	4
verification							
natural frequency	f_n	Hz	—	5164	—	3305	5a
static displacement	a_s	μm	—	$\pm$0.38	—	$\pm$0.31	5b

Table 5.7: Estimated flexural stiffness, static displacements, moment load and equivalent spring stiffness for UCL-BE and CIS-BE, using the observed natural frequency, dynamic displacement and damping ratio.

The estimated flexural stiffness of the free UCL-BE, using the observed natural frequency of 3.4kHz, is of $EI = 4.57\times10^{-3}$N.m^2, which for the respective section produces a Young modulus of $E = 2.50\times10^{9}$Pa. A similar calculation is carried out for the free CIS-BE, now with a natural frequency of 2.2Hz, and considering its different section geometry, $A = 1.5 \times 12.0$mm^2, and cantilever height, $L =$ 10mm, produces a Young modulus of $E = 2.41\times10^{9}$Pa. These two values of Young modulus are relatively similar, confirming the initially assumed similarities between the transducers, namely the CIS-BE mass per unit length. They also demonstrate how well the Bernoulli-Euler flexural model is capable of relating the beam properties with their first flexural mode of vibration.

The observed maximum dynamic displacement of the UCL-BE, at resonance, was of $\pm18.00\mu$m and the equivalent damping ratio was estimated at 2.5%. These values were obtained from a clear resonance peak of the magnitude response curve in figure 5.10. The dynamic magnification factor was estimated at $D_f = 20.0$ using the given damping ratio and knowing the dynamic displacement is the maximum displacement obtained when exciting the transducer at its resonance frequency, giving $\beta = 1$. The equivalent static displacement of $a_s = \pm0.90\mu$m is therefore obtained. Using the static model of a free cantilever, the concentrated moment load at the top end of the transducer's tip which produces such static displacement is $M = 1.95\times10^{-4}$N.m.

Two new numerical models are used, one static and the other dynamic, in which 6 springs of identical stiffness, K, equally distributed at the top 3mm of the bender element tip, are located. These springs model the resistance to displacements offered by the medium in which the transducer is embedded. The obtained static load is used in the static model to obtain the spring stiffness, which, all other things being equal, produces the static displacement of $a_s = \pm0.56\mu$m for the UCL-BE. The dynamic model is used to independently estimate the spring stiffness, which results in an undamped first flexural mode of vibration frequency of 5.2kHz. A spring

stiffness of $(6\times)K = 10500\text{N.m}^{-1}$ was necessary to produce a natural frequency of 5.2kHz. Using this spring stiffness the static spring model gives a static displacement of $\pm 0.38\mu$m. No value for spring stiffness could match both the natural frequency and static displacement of the system. The spring stiffness that matches the natural frequency is valued above the static displacement since there is a greater degree of uncertainty about the viscous damping ratio, about its estimated value but also about its nature, (section 3.9), where for simplicity a viscous damping is assumed when a closer concept is that provided by a more complex linear hysteretic damping.

The natural frequency of the CIS-BE was determined from a more complex magnitude response curve, (figure 5.11); in fact, the continuous and pulse signals produce different natural frequency estimates, $f = 2.2$kHz and $f = 3.4$kHz, (table 5.6). Of the two, the natural frequency at $f = 2.2$kHz is the one that produces a flexural stiffness and static load that best match the values obtained for the UCL-BE. For this reason, they are preferred to characterise the CIS-BE transducer simple two-dimensional flexural behaviour. For a characteristic frequency for the first mode of flexural at 2.2kHz, a mass per unit length of $5.22\times 10^{-2}\text{kg.m}^{-1}$, a flexural stiffness of $EI = 8.12\times 10^{-3}\text{N.m}^2$ is obtained. This value of flexural stiffness, in turn, can be decomposed to obtain the Young modulus, $E = 2.41\times 10^{9}$Pa. To obtain values of Young modulus for the two transducers so similar, using independently monitored resonance frequencies, validates the assumption of similarities between them as well as increases the confidence in the methods used to obtain those values.

The dynamic maximum displacement of the free CIS-BE at resonance is $\pm 2.95\mu$m and the related damping ratio 8.0%. A static displacement is then estimated at $\pm 0.47\mu$m. This value of static displacement can also be obtained in the corresponding static numerical free model by a load of $M = 1.60\times 10^{-4}$N.m. This load is in the same range as the one obtained for the UCL-BE. Even though the transducers have different sections they are excited using similar signals, with the same amplitude

and using the same equipment. It is not clear whether the loads for each different transducer should be similar or proportional to the piezoelectric ceramic plates dimensions and capacities.

The piezoelectric ceramic capacity of the plates, being from the same maker, is equivalent. Therefore, only their dimensions or lifetime could justify a difference in electric capacity. According to the estimated values of moment load, it appears that this load is similar for both transducers, independent of the dimensions of the piezoelectric plate. If the load was proportional to the piezoceramic plate, then the moment load for the CIS-BE would be significantly higher then the one for the UCL-BE. In fact, it is slightly lower. The two transducers have different origins, the piezoelectric ceramic plates have different lifetimes, and both factors can influence the piezoelectric capacity, therefore no conclusive remarks can be made about the actual relation between excitation and response capacity of the piezoelectric ceramic plates.

Leong *et al.* (2005) presented an equation to determine the maximum force generated by a bender element. Equation 5.12 is presented for the acting force of a series polarised and wired bender element,

$$F_{\max} = \frac{3}{8} E d_{31} \left(\frac{T}{l_b}\right) W \left(1 + \frac{t_s}{T}\right) V R \tag{5.12}$$

where E is the Young modulus, d_{31} is the piezoelectric strain constant, T is the thickness, l_b is the embedment length, W is the width of the transducer, t_s is the thickness of the centre metallic shim between piezoelectric plates, V is the applied voltage and R is an empirical weighting factor. In Piezo (2005) a slightly different version of this expression is presented, here given by equation 5.13.

$$F_{\max} = \frac{2}{3} \frac{VWT}{Lg_{31}} \tag{5.13}$$

where L is the length of the piezoceramic plate and g_{31} is a piezoelectric voltage constant.

According to either equation 5.12 and 5.13, and considering that the properties for the two transducers are the same, except for their width and slightly different lengths, then a force proportional to their widths is expected. The force exerted by the CIS-BE would be around twice as high as the force exerted by the UCL-BE. The obtained results do not confirm this prediction. The observed lack of efficiency of the first flexural modes of vibration of the CIS-BE, (section 5.5), could also explain the relatively low value of dynamic displacement from which, after several steps, the moment load was estimated, hence making a comparison in the linear static terms, presented by Leong *et al.* (2005), invalid.

An important point about equations 5.12 and 5.13 is that they refer to a static loading, and in the case of equation 5.12, the length of the piezoceramic plate is not even considered. This renders the comparison with values from a dynamic analysis impractical. Also, it is worth noting that the mentioned equations do not consider the piezoceramic plate coating, generally in epoxy resin, that contribute significantly to the overall mechanical behaviour of the bender element, both static and dynamic.

The estimated spring stiffness for the embedded CIS-BE was of $K = (6\times)\,8100\text{N.m}^{-1}$ obtained from the dynamic model first flexural mode characteristic frequency of 3.3kHz. This estimate of spring stiffness gives, in the static model, a displacement of $a_s = \pm 0.31\mu\text{m}$. The obtained value of static displacement is lower than the estimated value using the observed dynamic displacement and damping ratio, $\pm 0.71\mu\text{m}$. With the UCL-BE, the verification of the static displacement produced a value also in the same range as the initially estimated value at around half that value. This might indicate that a consistent error might be associated either with the initial estimate, with the verification calculations or with both procedures.

The spring stiffness result, as estimated from the natural frequency, is preferred

to that of the damping coefficient, since this second result is more susceptible to error. This has to do with the use of an estimated damping ratio, from the magnitude response curve, which is, among the initial presented values, the one most prone to error, particularly if using a response curve with a resonance response which is not very clear, as was the case of CIS-BE, (figure 5.17). Even though the resonance frequency can be influenced by the damping of the system, this influence is relatively low. The error associated with the damped resonance frequency is the square root of the error associated with the damping ratio, (equation 3.76). Besides, the results concerning the natural frequency of the systems agree quite well with each other, for example, when estimating the Young's modulus of the transducer's tip sections.

5.6.1 Bender Element Displacement

The laser velocimeter monitoring the bender elements was pointed towards the centre of the embedded height, 1.5mm from the transducer's tip end, out of a possible 3mm. The displacement of other points along the transducer tips are estimated using the observed displacement and the static model with springs, (figure 5.22). The displacement distribution of the nodes, obtained from the numerical model, is used to estimate the dynamic maximum displacement of those nodes, proportional to the value obtained by direct observation. The respective displacement results of the UCL-BE and CIS-BE are presented in figure 5.24

The maximum displacements estimated for the top ends of the UCL-BE and CIS-BE tips are in the range of $\pm 2\mu$m for a driving voltage of 20V. It is important to acknowledge that this is the single largest strain forced on the sample caused by bender element testing. As the disturbance created by the transmitting transducer propagates through the sample, the related strains attenuate, and so never equal the magnitude of the initial forced strain. In terms of actual displacement it is not possible to make the same observation because some modes of vibration actually amplify

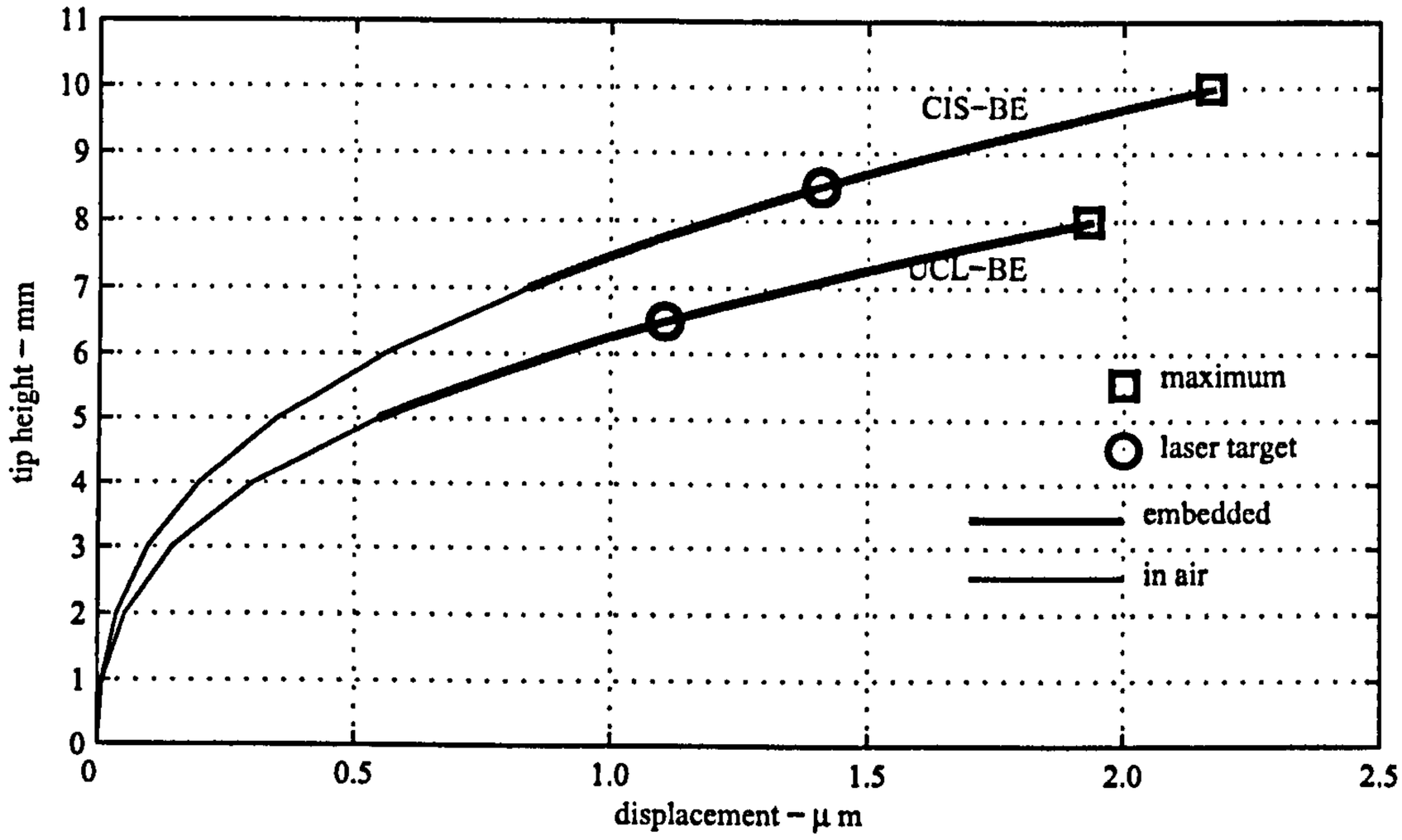

Figure 5.24: Dynamic displacement amplitudes of UCL-BE and CIS-BE tips.

displacements felt at the source. Shirley and Hampton (1978) predicted a maximum displacement of $\pm 0.56\mu$m for the bender elements used in their testing. This displacement was calculated using the piezoelectric constant, $d_{31} = 5.8 \times 10^{-11}\text{m.V}^{-1}$, relating mechanical strain with the applied voltage, 100V. The boundary conditions for the mentioned maximum displacement, free or embedded, were not specified but are assumed to have been for the free case. Then, the obtained displacement is in the same range as the equivalent static displacement for both the UCL-BE and CIS-BE, $\pm 0.90\mu$m and $\pm 0.47\mu$m respectively. Nevertheless, Shirley and Hampton (1978) used a higher voltage, 100V>20V, for a much bulkier transducer with 8.5 times the thickness of UCL-BE and CIS-BE, 12.7mm>1.5mm.

Piezo (2005) presented an equation, also proposed by Leong *et al.* (2005), which enables the calculation of the maximum displacement of the receiving bender element,

$$x_{\max} = \frac{3L^2 V_r d_{31}}{2T^2} \tag{5.14}$$

where L and T are the length and thickness of the piezoceramic plate respectively,

V is the applied maximum voltage and d_{31} is a piezoelectric strain constant.

The obtained equivalent static displacements for the free UCL-BE and CIS-BE, 0.90μm and 0.47μm, do not agree with equation 5.14. In both cases, all the relevant parameters are the same except for the free length, 8mm and 10mm, assuming that the coating for both transducers has an equivalent influence on their mechanical behaviour. Thus equation 5.14 would provide a displacement for UCL-BE around 1.6 times lower than for CIS-BE. Equation 5.14 therefore does not provide a satisfactory explanation for the observed displacements. In this case, the transducers and respective boundary conditions are not formally contemplated by equation 5.14 and therefore no comparison can be performed.

Equation 5.14 was observed to have little applicability at estimating the flexural displacement of an embedded bender element. If this is the case then it can be assumed that, as the pressure under which the medium is confined increases, such as during the consolidation of a soil sample in a oedometer, equation 5.14 looses even more meaning, since the medium will therefore hold the bender element even tighter.

5.6.2 Pressure Distribution

Having calculated the displacement of different nodes along the bender element tip, both for the 3mm embedded length and along the remaining not embedded length, and having estimated the equivalent spring stiffness at the embedded part, the next logical step is to calculate the pressure exerted by the transducer on the embedding medium. The dynamic displacements, obtained as described in section 5.6.1, are used together with the springs stiffness to estimate the maximum dynamic pressure exerted by the bender element tip on the embedding medium. The maximum pressure results for the UCL-BE and CIS-BE are presented in figure 5.25.

The maximum pressure exerted by UCL-BE, as presented in figure 5.25(a), varies

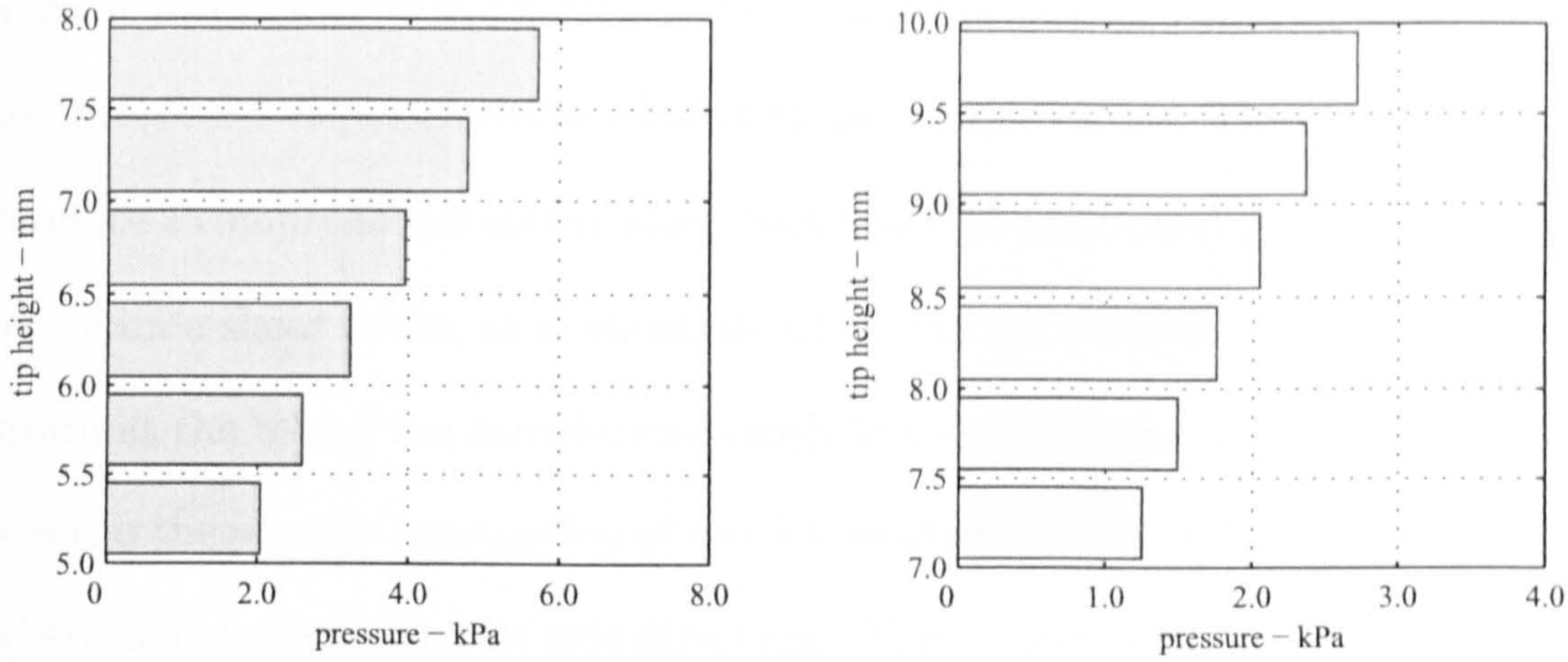

(a) UCL-BE

(b) CIS-BE

Figure 5.25: Pressure exerted by bender element against the embedding medium for a maximum dynamic displacement.

between 2200Pa at the bottom node of the embedded height and 6400Pa at the top of the tip. For the CIS-BE these values are of 1400Pa and 3100Pa, about half of those provided for the UCL-BE. This difference can be explained, since the dynamic displacements are relatively similar, at 1.12μm and 1.41μm, by the different width and consequent areas of contact of each transducer with the medium, one being roughly two-fold the other.

5.6.3 Strain Level

The strain level caused by the displacement of the transmitting bender element tips on the sample can be obtained from the observed and calculated dynamic displacements, being the ratio of deformation over length. Assuming the transducer's tip is well coupled with the sample, as in Shirley and Hampton (1978), the deformation of the sample is equivalent to the displacement of the transducer.

The laser monitoring of the embedded bender elements was performed with the tip embedded on a rubber sample with a diameter of 38mm. The calculation of the shear strain could be made assuming the displacement of the transducer tip to be

a shear displacement in relation to the sample height, or could be assumed to be compressional displacement in relation to the sample radius. The second case would produce a compressional strain which could then be multiplied by the Poisson's ratio to obtain a shear strain, as in equation 5.15. It is not possible to easily estimate the strain at the top of the sample, and much less assume it to be non-existent. There remains the possible assumption of a null lateral surface strain in the radial direction, where it is unrestrained in this direction. The second solution for the calculation of strain level is then preferred. Equation 5.15 presents the simple relation between compressional strain, shear strain and Poisson's ratio,

$$\varepsilon_s = \nu \varepsilon_d \tag{5.15}$$

where ε_s and ε_d are the shear and compression strains respectively and ν is the Poisson's ratio, (Gere, 2001). The Poisson's ratio was assumed to be $\nu = 0.45$, close to the maximum value, for rubber-like materials, (Feldman and Barbalata, 1996). From the maximum dynamic displacement of the UCL-BE, $a_s = 1.9\mu$m, results a compression strain of $\varepsilon_d = 1.9\mu\text{m} \times 19\text{mm} \approx 1 \times 10^{-2}\%$. Then using equation 5.15, one obtains $\varepsilon_s = 0.45 \times 1 \times 10^{-2} \approx 5 \times 10^{-3}\%$.

A number of shear strain level ranges have been proposed by Dyvik and Madshus (1985), Leong *et al.* (2005) and Pennington (1999), (section 1.3). Dyvik and Madshus (1985) and Leong *et al.* (2005) used a force conversion ratio relating the signal voltage with displacement. Leong *et al.* (2005) presented a shear strain estimate method making use of a equation used initially by White (1965),

$$\varepsilon_s = \frac{\dot{u}_s}{V_s} \tag{5.16}$$

where $\dot{u}_s$ is the velocity of the transducer and V_s the estimate of the characteristic

shear wave velocity.

Using equation 5.16, again for the maximum displacement of the UCL-BE, and knowing it occurred at a vibration frequency of 5.0kHz, (table 5.6), then integrating the displacement back into a velocity, $\dot{u_s} = u_s \times f$, one obtains $\dot{u_s} = 5.6 \times 10^{-3}\text{m.s}^{-1}$. Assuming the shear wave velocity of the rubber to be $V_s \approx 50\text{m.s}^{-1}$, (section 6.2), one obtains $\epsilon = 11.2 \times 10^{-3}\%$. For the CIS-BE, a similar process can be achieved, where a maximum dynamic displacement of $u_s = 1.41\mu\text{m}$ produces strain level values of $3.3 \times 10^{-3}\%$ and $9.0 \times 10^{-3}\%$, using equations 5.15 and 5.16 respectively.

The method of strain level evaluation proposed by Leong *et al.* (2005), using the equation provided by White (1965), estimates the shear strain level to be roughly twice as large as the values obtained through the calculation of the compression strain level along the radius. It is reassuring to know the values obtained using the compression strain are in the same range as the values obtained using the shear wave velocity, providing further confidence to the laser velocimeter monitoring method. The difference between the values is nevertheless significant, although being consistent. This would indicate that this difference is not due to an observation error but probably due to an error in the assumptions used to calculate the compression shear rate. It could indicate that this compression strain decreases to zero before the lateral surface, as soon as half that length.

Figure 5.26 contains the initial assumption of linear displacement distribution between the transducer and the lateral surface, reaching a zero displacement only at that surface, pictured on the left. On the right side of the figure is the linear and parabolic displacement distribution, which sees the displacement reduced to, or near to, zero at half the length between the transducer and the lateral surface, as predicted by the use of equation 5.16.

Considering either the first or second case of shear strain estimation, the obtained values are significantly higher than the proposed strain level range for which soft

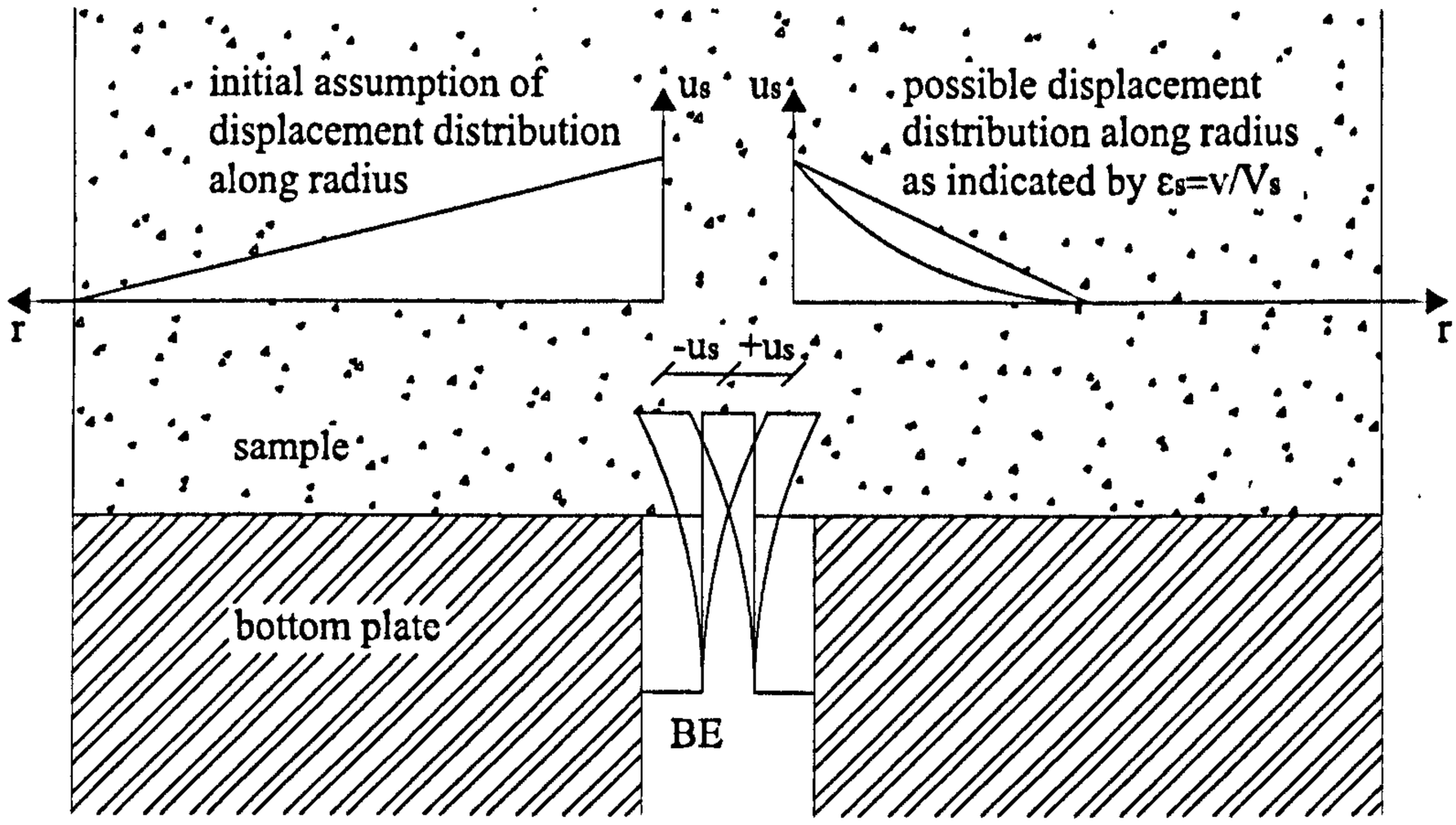

Figure 5.26: Displacement distribution from flexed bender element tip to lateral surface along radius.

soils are considered to have linear elastic behaviour, (figure 1.1) or (Atkinson, 2000). The shear strain level values obtained by Dyvik and Madshus (1985), Pennington (1999) and Leong *et al.* (2005), appear to have been obtained not using a direct observation of the oscillation velocity but through indirect methods, for example by estimating the displacement using equation 5.14 and then differentiating the obtained value to obtain a velocity and finally by using equation 5.16. The problem with using such a method instead of obtaining the velocity directly is that first and foremost, equation 5.16 and other similar equations provided by Piezo (2005) are for static cases, therefore they underestimating the actual dynamic strain. Also, there might be some unverifiable error associated with the use of the piezoelectric constants, the boundary conditions of the base and tip are not considered and the epoxy resin coating is also not considered, and neither is its influence on the overall mechanical behaviour of the transducers.

Having observed shear strain level values which are relatively high, rising above the linear elastic limit for soft soils, there are nevertheless some circumstances which

might explain why such large values were obtained and provide a reasonable justification for still use bender elements and considering a linear elastic behaviour of soils. The rubber used for the synthetic samples is quite soft, even when compared with soft clay soils, so a harder soil might provide more resistance to the transmitting transducer oscillation, which would imply lower strains. Furthermore when testing in a triaxial cell, the sample is contained by hydraulic pressure and a latex membrane.

The mechanical model was based on the observations of the transducer's tip embedded in a rubber sample. To achieve this, a small opening had to be cut from sample so that the laser beam could be successfully reflected from it. This opening, although small, might significantly affect the coupling between the sample and the transducer, and also offer less sample surface to resist the transducer's oscillation. The signal amplitude diminishes significantly from the transmitter to receiver, so its amplitude is expected to fall well inside the accepted linear elastic range not far from the source. Finally, when inserting the bender element tip in a soil sample, disturbances with consequent strains rates higher than 1.0% are caused, which are at 3 orders of magnitude higher than possible disturbances caused by the dynamic oscillation of the transmitting transducer. This means that if the dynamic oscillation of the transmitting bender element does disturb the soil's elastic behaviour, is to a far lesser degree than the actual insertion of the transducer, and only locally since such disturbance is not significantly felt along most of the wave travel path.

5.7 Tip-to Tip Monitoring

A similar set-up as the one used by Lee and Santamarina (2005) and Leong *et al.* (2005) was attempted, with a receiving transducer touching the transmitter. Apart from obtaining the response values from the receiver, the laser velocimeter was also

aimed at a point on its tip, this time outside the embedded height. Both transmitter and receiver transducers have their tips embedded 3mm into a 6mm height rubber sample. The transducers tested with this set-up are characterised as UCL-BE, (table 5.2). An illustration of the basic set-up is presented in figure 5.27.

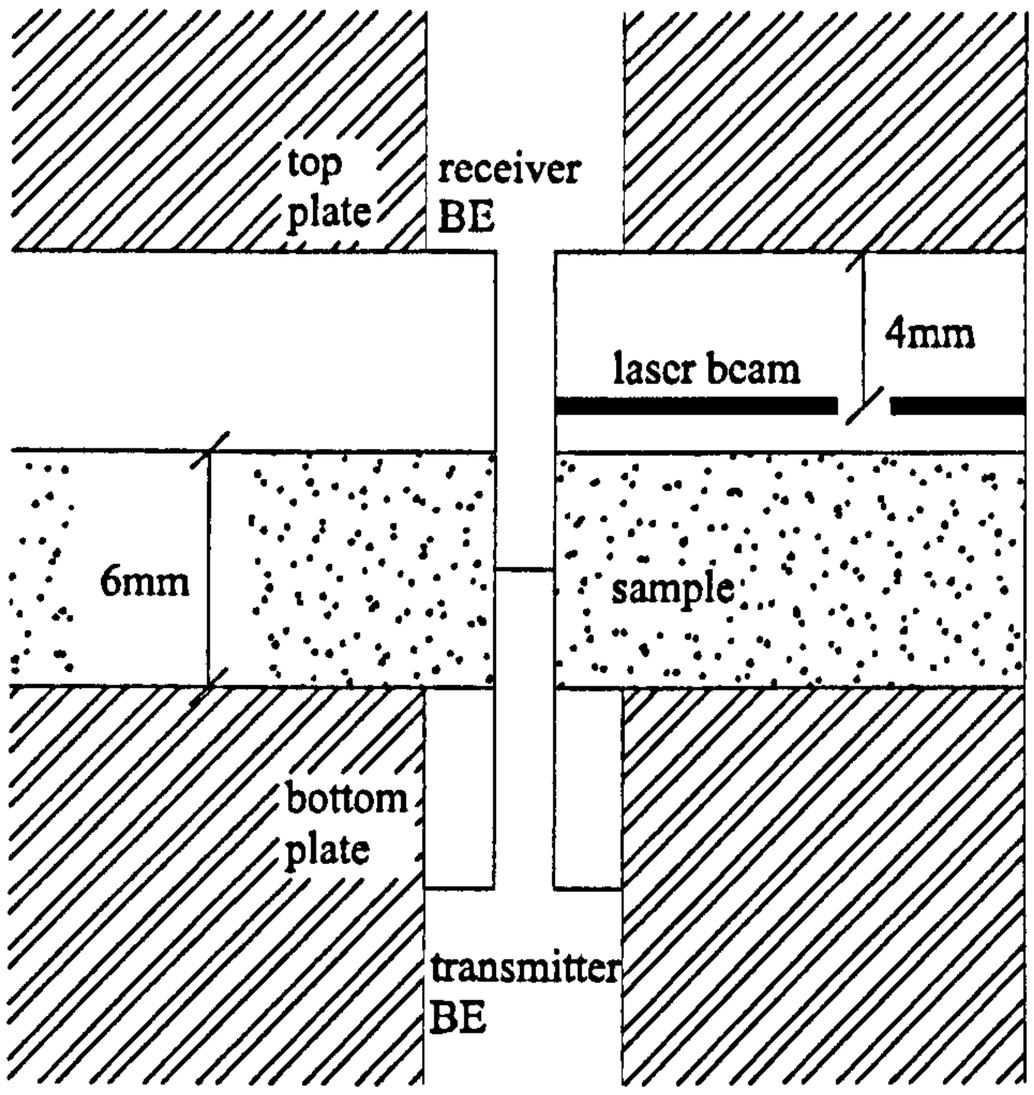

Figure 5.27: Touching bender elements set-up, both tips embedded, with laser beam monitoring the behaviour of the receiving transducer.

A mechanical model of the embedded touching bender elements is proposed in figure 5.28 where a hinge couples the transmitting and receiving transducer cantilevers. The hinge provides a mechanical link between the transducers compatible with the assumption that the receiver transducer tip is capable of perfectly emulating the bending or flexural movement of the transmitter. This assumption was not explicit in the works of Lee and Santamarina (2005) and Leong *et al.* (2005), but without it any analysis would be meaningless. Since the bender elements are embedded in the sample, again a number of equally distributed springs are placed evenly along the respective embedded modelled lengths.

The signals obtained by the laser velocimeter have a very low amplitude and are significantly affected by noise. In figure 5.29, the results of one of the few discernible

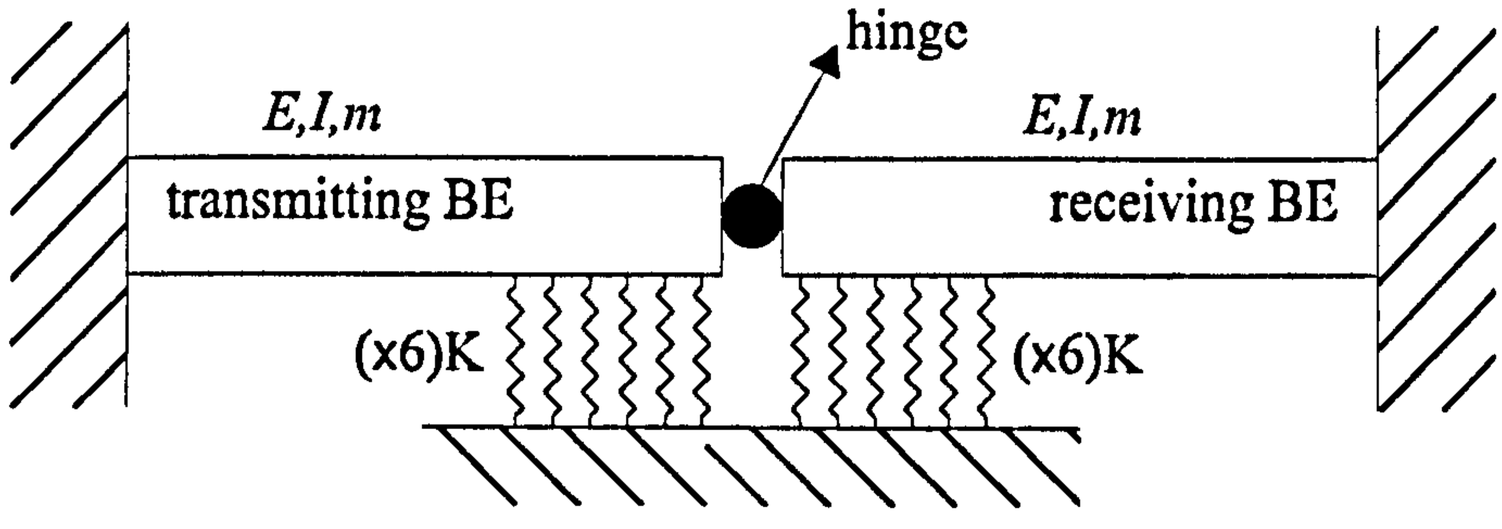

Figure 5.28: Mechanical model of two bender element tips touching, both embedded in an elastic medium.

results, namely its time history and correspondent magnitude response curve, are presented. These results concern a transmitted sweep signal.

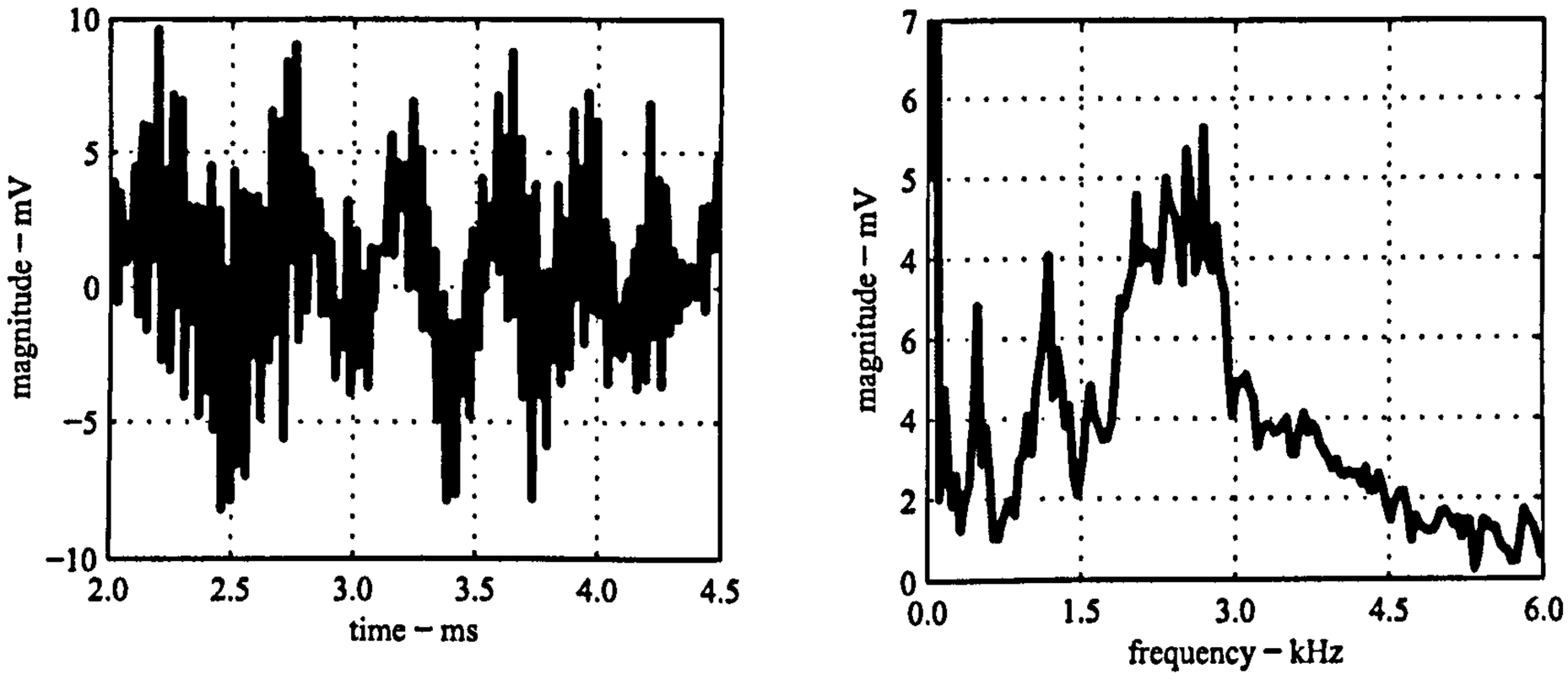

(a) time history

(b) magnitude

Figure 5.29: Time history and magnitude response of receiving UCL-BE, touching the transmitter, both embedded in a short rubber sample.

Even though the interpretation of the results, as presented in figure 5.29, is not straightforward, it is possible to estimate the maximum oscillation of the targeted point to be in the range of $a = \pm 4\text{mV} \equiv \pm 0.15\mu\text{m}$ and the resonance frequency of the system to be around 3.0kHz. The results from the signal produced by the receiver are presented in figure 5.30 in the form of the magnitude and phase delay response curves.

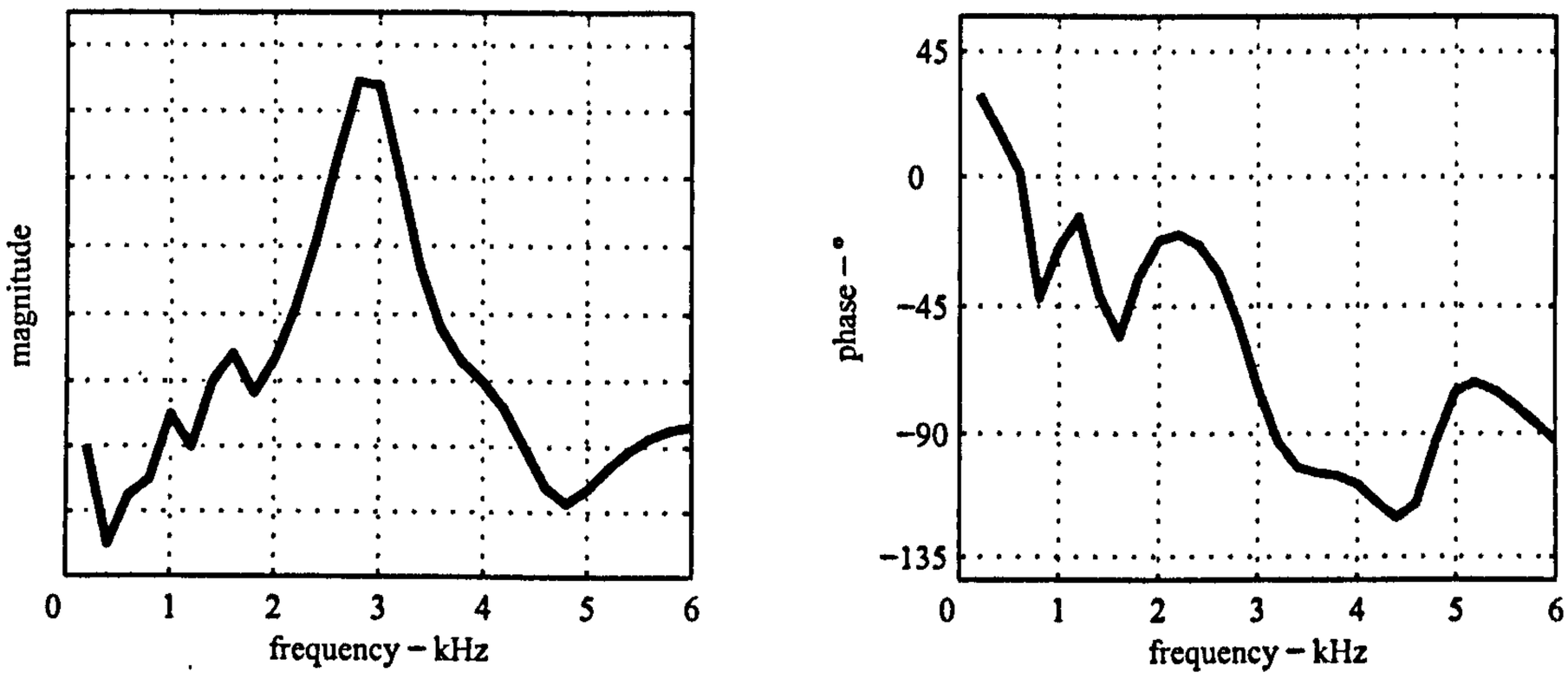

(a) magnitude

(b) phase

Figure 5.30: Response magnitude and phase delay curves of the output signal of the receiving bender element touching the transmitter.

The results from the receiving transducer confirm the observations made using the laser velocimeter, namely the resonance frequency of the system, 3.0kHz, (figures 5.30(a) and 5.30(b)).

The sample used is similar to the samples tested so far in this section. The mechanical model described in table 5.7 of a cantilever beam with springs is again used to determine the displacement at the middle of the receiving transducer's tip and estimate the corresponding displacement of the tip end. In this way the same flexural stiffness of the beam and the spring stiffness are considered for the new double-hinged cantilever model. The estimated maximum dynamic displacement of the receiving transducer is then $a = 0.97\mu$m. This value is around half the value estimated for the tip end of the single transmitting bender element, $a = 1.9\mu$m. Using equation 5.16, a shear strain level of $\varepsilon_s = 5.8 \times 10^{-3}\%$ can be obtained from the dynamic tip end displacement.

The difference in displacement and strain observed between the results for the transmitting transducer and the receiving transducer touching the transmitter can be attributed to loss of energy due to an imperfect mechanical transmission process,

or to different mechanical boundary conditions introduced by making the transducers touch each other, or a combination of these two. For this reason, the strain level obtained from the touching transducers is considered to be less reliable than the one obtained monitoring the transmitting with a laser beam. Not only are the touching transducers less reliable but, it is a clear case where the monitoring process significantly alters the subject being monitored.

It is worth noting the resonance response of the system at around 3.0kHz in figure 5.30. This frequency value is lower than the corresponding resonance frequency of the single transmitting bender element at 5.0kHz. The numerical model of the embedded touching bender elements, as illustrated in figure 5.28, estimated the natural frequency of the complex system at 5.9kHZ, significantly higher than the value observed. A corresponding dynamic amplitude of displacement of $a = \pm 0.37\mu$m was also calculated using the numerical model. This value of displacement amplitude is smaller than the one estimated from the observed response, $a = 0.97\mu$m.

Clearly, as demonstrated by the difference in the natural frequencies and dynamic displacements, the real contact between the elements is not a perfect hinge as modelled in the corresponding numerical model. The proposed numerical model is therefore not suitable to predict the real behaviour of touching embedded transducers. It also means that the touching transducers are not an appropriate method of monitoring the behaviour of bender elements. Not only does the contact between the transmitting and receiving transducers change the actual individual behaviour of each bender element, but the contact between the two is not a perfect hinge, which disproves the assumption that the receiver perfectly emulates the transmitter.

5.8 Discussion

The monitoring of the dynamic behaviour of bender element transducers confirms that they behave, as expected, as Newtonian mechanical systems. The transducers responded with characteristic magnitude and phase delay curves, enabling the identification of the resonance frequencies for different modes of vibration. In light of these observations, any assumptions of a bender elements response which perfectly emulates the electric signals can no longer be pursued.

When used to determine the small-strain shear stiffness of soil or any other medium, the mechanical properties of the bender elements must be taken into account. Several aspects of their mechanical behaviour are worth mentioning, in terms of the influence on the overall performance of the test system, i.e., they have a characteristic mechanical response to an external excitation and they behave as frequency filters.

If bender elements behave as mechanical frequency filters, this means that either left free to vibrate or with their tips embedded in a sample, in either case there is a maximum frequency after which the response is no longer discernible. The value of such maximum frequency is a property of the bender elements themselves, but also of the medium in which they might be embedded, since when embedded in a medium, the overall mechanical response of the bender elements is stiffened proportionately to the stiffness of the medium and to the degree of coupling obtained between the medium and the bender elements. The overall conclusion is that when testing with bender elements, this maximum frequency must be taken into account.

If behaving as a Newtonian mechanical system, with finite mass and stiffness, and therefore with significant inertia, bender elements have different responses to excitations with short and long duration. If pulse signals are used to excite a bender element, then only a transient response can be obtained, which is dominated by

the natural frequency of the transducer rather than the frequency of the signal. Because dispersive phenomena are frequency-dependent, this means that if pulse signals are used to excite the bender elements, such phenomena cannot be effectively controlled. The establishment of a steady-state of vibration, can be achieved when using harmonic continuous signals, and so the use of this type of signal is therefore advisable.

In all four set of tests with the two different bender element transducers, free to vibrate or embedded in a rubber sample, an apparent initial time delay can be observed. In figures 5.12, 5.14, 5.18 and 5.20 0.02ms separate the recorded beginning of the input and received signals, independent of input signal frequency. Therefore, such a time delay can only be attributed to a loss in the group of electric and electronic devices that compose the test circuit, i.e., the bender element cable, the light travel time to and from the target and the processing time of the laser velocimeter. Such a time difference can be quite significant in terms of determining wave travel times, since for shorter samples it represents about 10% of the travel time $\approx$ 0.17ms, section 6.6.1). For higher samples, with longer travel distances and hence longer travel times, the observed time delay is less significant, contributing about 2% of the total travel time.

Considering the mechanical behaviour of bender elements, more specifically the time and phase delays between load and response, the use of bender elements to directly compare the transmitted and received signals in the time domain is not ideal. A actual time delay is added by the necessity of the eletric signals to travel along the circuit as well as frequency dependent phase delay is added at each mechanical interface of the bender element test system. In a normal bender element test, four such interfaces exist, and as a consequence any direct time comparison between the transmitted and received electric signals is inevitably affected. A signal comparison, done in relative terms by comparing different received signals in the frequency do-

main, is capable of overcoming the effect of the mentioned delays at each interface, and its use is therefore advisable.

The mechanical limitations of bender elements as dynamic transducers must be acknowledged if they are to be used effectively.

Chapter 6

Parametric Study of Synthetic Soil

In an unbounded and unloaded elastic solid medium, wave propagation depends only on the intrinsic properties of the medium itself such as its density, stiffness and damping coefficient. When studying a soil sample in the laboratory, using triaxial cells or oedometer, a number of boundary conditions can interfere with its dynamic behaviour including the properties of the wave propagation, which might render the behaviour model of unbounded wave propagation unsuitable.

The testing of a soil sample in a triaxial cell apparatus with bender elements depends on a great number of parameters, medium properties and boundary conditions. Some of these are listed in table 6.1.

One of the listed boundary conditions which is believed to have a significant effect on the dynamic behaviour of the system is the sample's geometry, (Arroyo *et al.*, 2006; Rio *et al.*, 2003; Santamarina, 2001). A parametric study was conducted with the main objective of observing, understanding and quantifying the influence of sample geometry on bender element test systems' behaviour and consequent influence on the results. Other objectives are the study of radiation phenomena such as the near-field effect, the study of the correct wave travel distance and the comparison between results from the time and frequency domains.

Soil Properties
void ratio
current effective stress state (confining pressure and anisotropic stress state)
degree of saturation
sedimentation environment
post sedimentation stress-strain history, including mechanical overconsolidation
anisotropy
cementation
particle size distribution, particle shape, particle crushability, mineralogy, etc.
mechanical properties
stiffness
Poisson's ratio
density
damping
triaxial cell controlled conditions
axial load, confining pressure and pore water pressure
load history and path
drainage of sample
excitation signal and wave properties
signal amplitude (proportional to strain)
signal frequency
signal wave form
wave polarisation and direction
bender element
geometry (length, width, thickness)
stiffness
density
other boundary conditions
sample geometry (shape, height, width, etc.)
latex membrane
fixity of sample to end plates
fixity of bender element to end plates
fixity of end caps
coupling between sample and bender element tip
existence and length of protrusion
other measurement instruments attached to the sample

Table 6.1: List of soil properties and triaxial cell bender element test parameters and boundary conditions.

6.1 Test Description

6.1.1 Sample Properties

Synthetic samples of polyurethane rubber were used to conduct the geometry parametric study. The advantages of using a synthetic material such as polyurethane rubber instead of real soil are discussed in chapter 4. In summary, when testing with bender elements, soft soils are assumed to have a linear-elastic behaviour only at low levels of shear strain, in the order of $10^{-3}\%$ and $10^{-4}\%$, (Burland, 1989). Rubber materials are also considered elastic at such strain ranges and even up to much higher strains, $\varepsilon > 100\%$. There is also the issue of viscosity, with both soft soil and rubber-like materials being recognised for having viscous-like behaviour, (Fodil *et al.*, 1997). When disturbed at high frequencies, being a time-dependent phenomenon, viscosity becomes less relevant in the overall behaviour of the disturbed media. The tested samples are excitated at frequencies in the range of $f \in [0.2\ \ 20.0]$kHz or higher, at which their viscous properties become less relevant, and so can be expected to behave as incompressible non-viscous solids.

The parametric study is conducted using bender elements to test a number of synthetic rubber samples with different geometries, in a similar fashion to soil sample testing. All the samples have a cylindrical shape with different diameters and heights. The cylindrical shape was selected for three main reasons. First because it is a sample shape commonly used in triaxial cells and oedometers apparatus, (Head, 1998). Secondly, because due to the symmetry around the central axis, the dynamic behaviour of cylinders is theoretically well studied and understood, (Achenbach, 1973; Graff, 1975; Redwood, 1960). The third reason has to do with the moulding process of the samples. It was easier to prepare cylindrical moulds with set diameters in which the height of the samples could be varied and from which the samples could be easily demoulded.

The cylindrical samples were of three different diameters, 38mm, 50mm and 75mm. These diameters were chosen because both $D = 38$mm and $D = 75$mm are commonly used for soil samples tested in triaxial cells and oedometer[1] apparatus respectively. The 50mm diameter was chosen so that an intermediate diameter could be studied. The third and larger diameter of 75mm was the maximum achievable diameter for which polyurethane rubber could be easily moulded. It was not possible to manufacture moulds with larger diameters hence the chosen maximum diameter of 75mm. The time it takes for the liquid rubber to vulcanize and set also limits the volume of the samples since once the vulcanization process begins, there are only 10 minutes left to proceed with the mixing and pouring of the liquid mixture into the moulds. The dimensions of all the tested samples are presented in table 6.2. Figure A.1 contains a graphic representation of these samples which can be used as a companion to this chapter.

At the moulding stage, sets of four different samples were prepared simultaneously where the moulds were filled from the same batch of liquid rubber mixture. This group of 4 samples consists of 3 samples with different diameters and the same height and a fourth sample with fixed dimensions of $h76 \times d38$mm. Henceforth each one of these groups is referred to as a 'set'.

Apart from comparing samples from the same set, with the same height and different diameters, the influence of the sample height is also studied. Different sets of samples were therefore moulded with different heights. From each set, the 3 samples with different diameters and constant height were used in the parametric study itself. The fourth sample, with 76×38mm, was used for control purposes in order to normalise the results from each set. This control and normalisations procedure exists because even though synthetic rubber was used to obtain constant

[1]The standard diameter for oedometers is 76mm and not 75mm.
[2]Sample used for repeatability testing.

Height (mm)	Travel Distance (mm)	Diameter (mm)			Control
		38	50	75	$h76 \times d38$
06	00	S01	S02	S03	S04
10	04	S05	S06	S07	S08[2]
20	14	S09	S10	S11	S12
30	24	S13	S14	S15	S16
40	34	S17	S18	S19	S20
50	44	S21	S22	S23	S24
60	54	S25	S26	S27	S28
76	70	S29	S30	S31	S29

Table 6.2: Dimensions and reference of rubber samples. Figure A.1 contains a graphic representation of the samples and can be used as a pull-out to accompany the reading of this chapter.

properties for all samples, some minor variation might exist between sets, due to factors unaccounted in the samples moulding process, and can be henceforward taking into account

Synthetic rubber is a very resilient material, (Feldman and Barbalata, 1996), and hence it is quite difficult to cut the gaps in which to insert the bender element tips. For this reason, a pair of gaps needed to be moulded in each sample. These gaps were designed with dimensions slightly smaller than those of the bender element tips to achieve a closer fit, and the coupling maximised between the transducers and the sample. The moulded gaps allow the bender element tips to protrude the sample 3.0mm each. At the first stage of the parametric study, the wave travel distance was assumed to be measured from tip-to-tip, (Viggiani and Atkinson, 1995). Therefore, for each sample, the travel distance was obtained as the difference between sample height and two times the embedment height, $td = H - 2 \times 3.0$, (table 6.2).

6.1.2 Laboratory Set-Up

The laboratory set-up for the parametric study is illustrated in figure 6.1. A pair of bender elements was used, one at each end of the cylindrical sample, fixed to steel plates. A function generator and a computer sound card were used to generate the transmitted signal. Both the transmitted and received signals were captured by the oscilloscope, which then sent them to the personal computer, to be visualised, stored and processed. The input signals were determined prior to the testing and remained the same for all of the samples, (section 6.1.3).

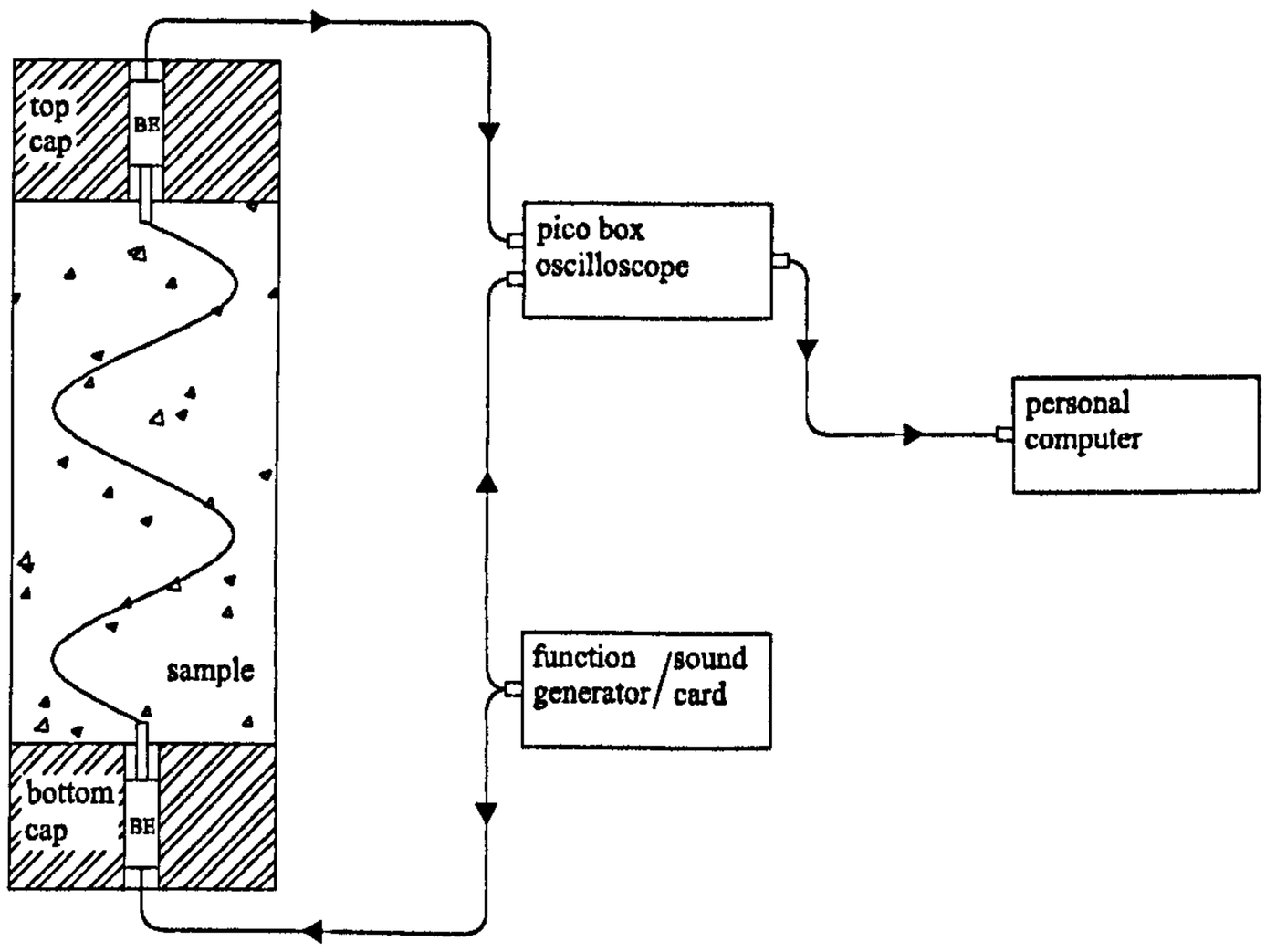

Figure 6.1: Typical bender element test set-up used in the parametric study.

The configuration of the system was kept constant during the test, so as to minimise any possible influence over its behaviour and consequently the results. This translated into using the same pair of bender element transducers for all samples, each consistently performing the function of transmitter or receiver. The transducers were placed always with the same polarisation, i.e., facing the same way relative to each other and to the remaining equipment of the test system such as the top plates. The sample was consistently placed in the vertical position, with the transmitting

bender element placed on the bottom plate and the receiving bender element on the top plate.

The bender elements used during the parametric study have been described in table 5.2, where they were referred to as UCL-BE. These bender elements were designed and manufactured at UCL to take part in this study. Their dynamic behaviour, on their own or in a normal test set-up, is described in chapter 5. These transducers, when fixed, have a resonance frequency of 3.4kHz with their tips free, and of 5.0kHz with their tips embedded in a synthetic rubber sample, (table 5.6).

6.1.3 Signal Properties

In order to understand the influence of sample geometry in bender element testing, the dynamic behaviour of each sample must be consistently determined to enable a thorough comparison of results. A useful representation of each system's dynamic behaviour is given by its response curves. The response of a dynamic system is complex, being usually described by two curves, one containing the magnitude and the other containing the phase delay of the response.

A total of three types of input signals were used. They were the sinusoidal pulse signal, the harmonic sinusoidal continuous signal and the sinusoidal sweep signal. The general use of these signals is described with detail in sections 2.1 to 2.4. The specific characteristics of the signals used during the parametric test, such as their frequency and amplitude, are shown in table 6.3.

The pulse and continuous signals were supplied by the function generator. The sweep signal was supplied by the computer sound card, hence its lower signal amplitude. These pieces of hardware equipment are described in table 5.4.

[3]The signal amplitude is the maximum provided by the respective hardware source.
[4]In the case of pulse signals, the values refer to the central frequency of the pulses.

Signal	Source	Amplitude[3]	Frequency[4]
pulse	function generator	±10V	[0.2 5.0]kHz in steps of 0.2kHz [5.0 10.0]kHz in steps of 0.5kHz [10.0 20.0]kHz in steps of 1.0kHz
continuous	function generator	±10V	[0.2 5.0]kHz in steps of 0.2kHz [5.0 10.0]kHz in steps of 0.5kHz
sweep	sound card	±2V	twice the cycle from 0.0kHz to 20.0kHz and back, with a variation rate of $\dot{\omega} = 2\pi \times 10^6 \text{rad.s}^{-2}$

Table 6.3: Properties of the signals used to excite the transmitting bender element during the parametric study.

6.1.4 Overview

The parametric study consisted of three parts. In the first part, a repeated test of the same sample, S08 - $h76 \times d38$mm, was carried out. This was to verify the repeatability of the testing procedure and the variation of the synthetic rubber sample properties with time and room temperature. During the second part of the parametric study, a control sample from each set was tested and the obtained results compared. The objective of this second procedure was to evaluate the dissimilarities between the synthetic rubber properties from each set. The third and main part of the parametric study dealt with the testing of 24 samples, each with different geometry. This was to evaluate the influence of sample geometry on their dynamic behaviour, namely their body vibration and wave propagation properties.

The repeatability study focused on sample S08. This sample was selected arbitrarily from all the control samples with standard dimensions of $h76 \times d38$mm. It was tested repeatedly and the results compared. There were 6 tests in total over a period of 82 days from the time the samples were first casted. Each test was independent from the others in the sense that both sample and equipment were reset each time. All the tests had the same laboratory configuration and used the

same signal combination, equal to the main parametric study. The parameters, which were known to vary between control tests, were the age of the sample and the room temperature. Besides these two factors, the repeatability control testing also served to evaluate possible human error related with the equipment set-up and the interpretation of results.

At the control sample study, a sample from each set was tested and the results compared. From each set of samples, one was moulded with the aim of taking part in this control study. Each tested sample has the same dimensions of $h76 \times d38$mm. Slightly different material properties might exist between sample sets, due to variations during the moulding stage, (section 4). So, the objective of this study was to analyse the difference in the properties of each set of samples in the form of bender element test results so that the results could later be normalised.

An independent monitoring of the samples' dynamic response was also conducted. With the same laser equipment used in chapter 5, it was possible to monitor without interference the dynamic response of various samples to external excitations. In this was it was possible to estimate the elastic properties of the medium which could later be compared with the estimates obtained from the actual bender element testing.

6.2 Torsional and Flexural Resonance

An independent monitoring of the dynamic behaviour of three of the rubber samples is presented in this section. The tested samples were subjected to an impact torsional load and left to vibrate freely. Their dynamic response in terms of torsional and flexural motion was monitored using a laser velocimeter. While vibrating freely, the samples are expected to oscillate mainly at their torsional natural frequencies. From the value of resonance frequency, it is then possible to evaluate the shear stiffness of

the samples using the respective frequency equations, as in resonant column testing, (ASTM-D-4015, 2000).

The main objective of this test was the excitation of the natural torsional mode of vibration of the samples, since the impact load is primarily torsional. But, since the load is applied manually, it was not possible to avoid some flexural excitation as well. For this reason both the torsional and flexural response of the samples are analysed, as done previously by Cascante *et al.* (1998) and Fratta and Santamarina (1996).

6.2.1 Test Set-Up and Description

A scheme of the torsional resonant column set-up is presented in figure 6.2. The samples were set up in the same way as when tested with bender elements with a few exceptions. These exceptions are the laser beam pointed at the top end of the sample, a small target with 5mm in diameter painted on the sample and a small steel rod attached to the top end plate where the forces were applied. The mentioned differences do not significantly influence the behaviour of the system compared with its set-up for the parametric study since the laser beam has no measurable influence on the behaviour of the sample, and neither does the small painted target. The rod attached to the top plate weights 0.9g, which is less than 0.5% of the weight of any of the used plates, and was therefore also assumed to be insignificant.

The laser velocimeter used to monitor the behaviour of the samples is the same as the one described in section 5.2, also known as LDV. The LDV can only detect movement in a direction collinear with the direction of the laser beam. For it to detect the torsional movement of the sample, it had to be aimed at a point deviated from the main axis of the samples, (figure 6.2). Only points which are not in the plane formed by the sample axis and the laser beam have movement that can be detected when the sample is oscillating in torsion. This set-up of the LDV enables

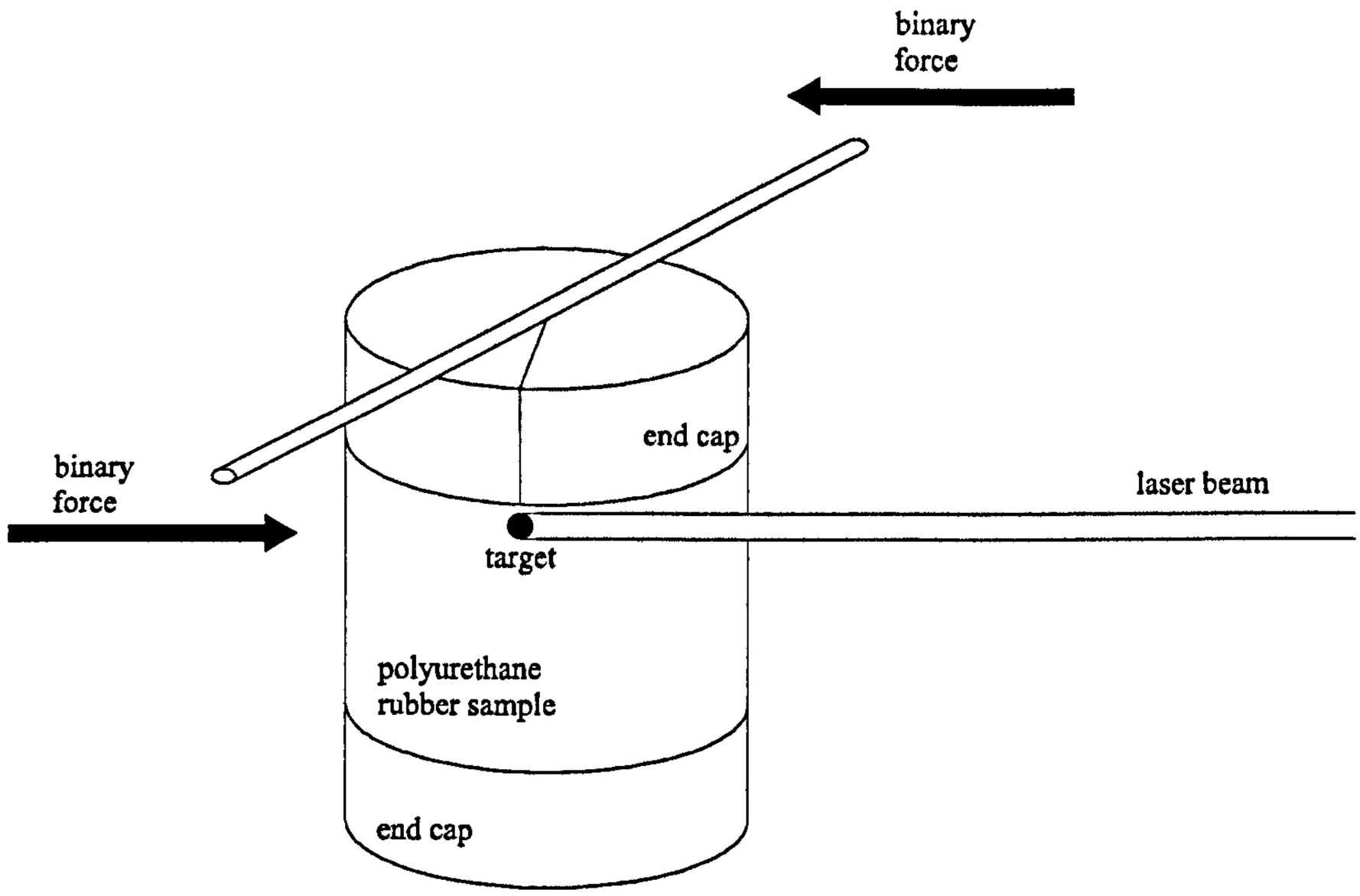

Figure 6.2: Resonance test of rubber samples set-up, monitored with laser velocimeter.

the detection not only of the torsional motion but also of the flexural motion of the sample, since both motions have movement components collinear with the laser beam. The LDV measures the oscillation velocity rather than displacements. Nevertheless, the signal's frequency properties are revealed in the velocity time history of the oscillation, just as they would be at the equivalent displacement time histories, (equation 5.9).

The samples chosen to be tested were S21 - $h50 \times d38$mm, S22 - $h50 \times d50$mm, S23 - $h50 \times d75$mm and S24 - $h76 \times d38$mm, described in table 6.2. These 4 samples are from the same mould set, and therefore assumed to have exactly the same material properties.

The resonant column test system is fixed at one end and free at the other end, behaving as a cantilever with a mass at the free end. A suitable dynamic model of behaviour is the Bernoulli-Euler beam, capable of relating the resonance frequency of the beam with its stiffness, (Karnovsky and Lebed, 2001). The necessary analytical

tools to model the first mode of torsional and flexural vibrations are presented in sections 3.8 and 3.11. The torsional vibration of the system is described by equation 3.107 and the specific boundary conditions expressed in equation 3.110. The flexural vibration behaviour of the system was modelled using equation 3.101 and its boundary conditions expressed by equation 3.103.

The system was characterised by its equivalent shear-wave velocity, V_s rather than by its Young's modulus, E, shear-stiffness, G, or Poisson's ratio, ν. The relations between these values are given in equations 3.12 and 3.2. In these models the Poisson's ratio was assumed to be $\nu = 0.45$, since rubber-like materials are highly elastic and suffers next to no volume variation with strains up to 100%, (section 4.3) or (Doi, 1996).

6.2.2 Results

An example of a typical result obtained by LDV monitoring is presented in figure 6.3, for sample S22 - $h50 \times d50$mm. The actual time history of the observed motion is presented in figure 6.3(a) and the corresponding response magnitude, also known as frequency content, obtained using a fast Fourier transform FFT, is presented in figure 6.3(b).

The response in figure 6.3(a) resembles the undercritically damped free vibration of a simple mechanical system, (section 3.8.4). If that is the case, the natural frequency of the system can be obtained directly by measuring the time difference between some of the observed peak features. The damping coefficient could also be estimated using the free-vibration decay method mentioned in section 3.9.1. The uncharacteristic sharp variations in figure 6.3(a) can be attributed to environment noise such as ground vibration due to people moving near the equipment.

The magnitude response in figure 6.3(b) describes a more complex response case than that of a SDOF system. Two peaks, corresponding to two resonance frequen-

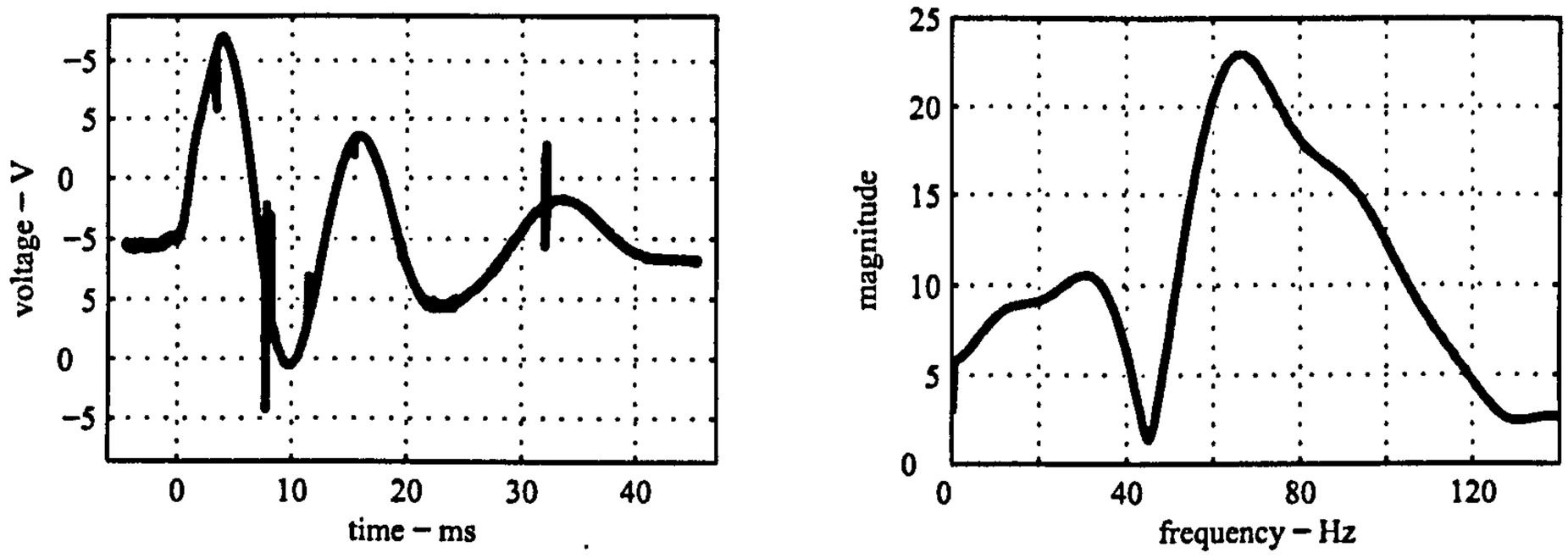

(a) time history (b) FFT

Figure 6.3: Time history and corresponding frequency content of resonant column response of polyurethane rubber sample S22, as monitored by a laser velocimeter.

cies, can be observed, the clearest one occurring at 67Hz and another at 31Hz. Each one of these resonance frequencies is associated to a different mode of vibration. As will be subsequently confirmed, the resonance frequency at 67Hz corresponds to the initially intended first torsional mode of vibration. The other resonance at 31Hz corresponds to the first flexural mode of vibration.

Being characterised by a lower frequency, is seems likely that the sample started out oscillating in a torsional mode as initially intended. Since it was vibrating freely, it then reverted to its 'more natural' flexural mode, a similar process to the one observed by Fratta and Santamarina (1996). The samples was manually disturbed, so it was not possible to guarantee a perfect torsional input; therefore they might be expected to have been excited at other vibration modes. Also, the excitation was impulsive, meaning it had a relatively broad frequency content, making possible the excitation of more than one mode of vibration, (Ewins, 2000).

Using the magnitude components of the response, it is possible to detect the damped resonance frequencies of the system and to estimate their correspondent damping coefficient, using the half-power bandwidth method, (section 3.9.2). The damped resonance frequencies ω_D, are associated with the natural resonance fre-

quencies ω, (equation 3.76), which can be used in the Bernoulli-Euler beam analysis to obtain the elastic stiffness properties of the sample, (Clough and Penzien, 1993).

Figure 6.4 presents the estimated equivalent shear-wave velocities obtained from the torsional and flexural resonance frequencies.

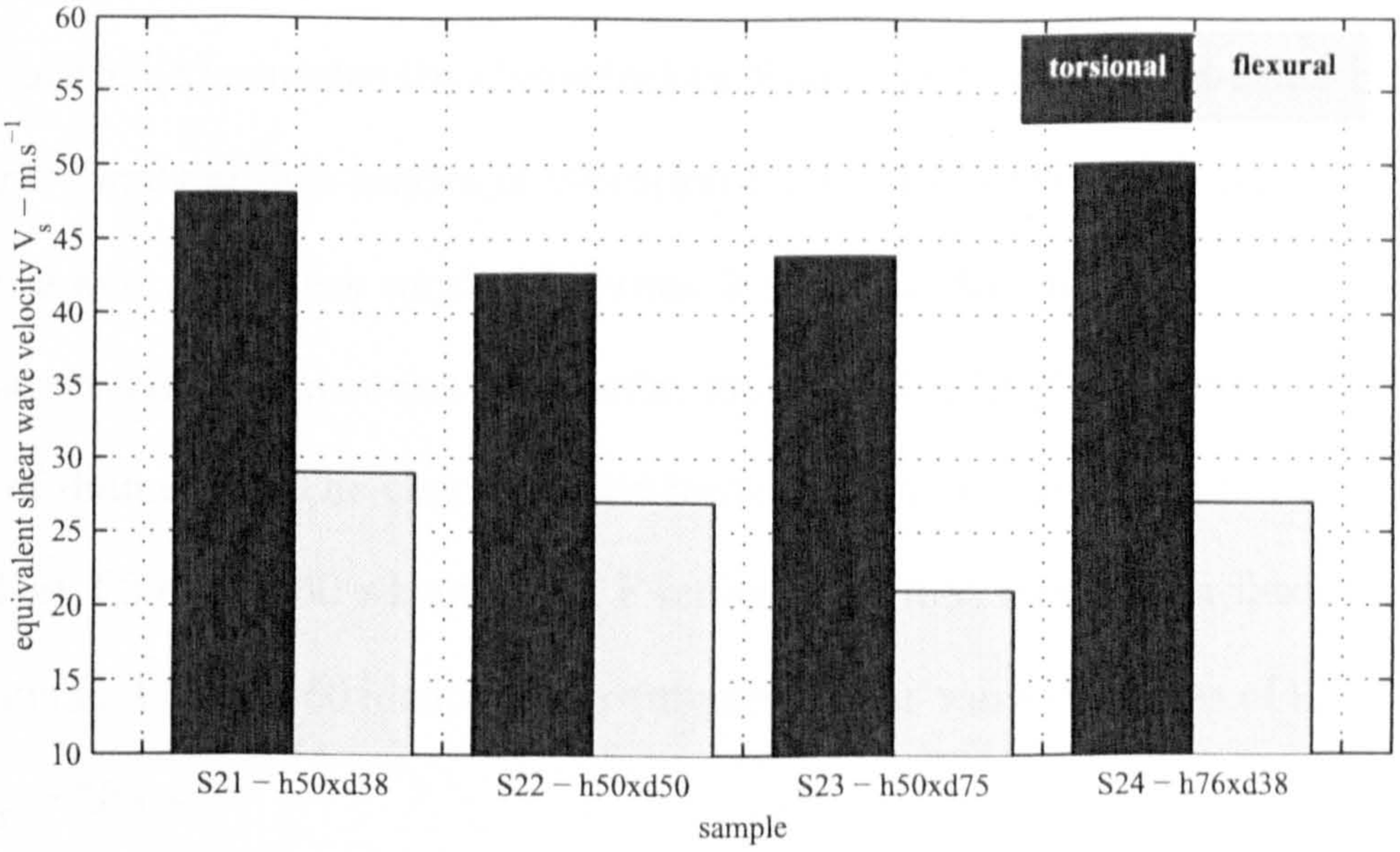

Figure 6.4: Equivalent shear wave velocities obtained from the torsional and flexural resonance frequencies for samples S21, S22, S23 and S24.

The velocities presented in figure 6.4 vary between 42m.s^{-1} and 50m.s^{-1} for the torsional mode, and between 21m.s^{-1} and 29m.s^{-1} for the flexural mode. There is a discrepancy in velocity results of about 8m.s^{-1} between the maximum and minimum torsional results. A similar discrepancy of 8m.s^{-1} between the flexural results is also present. The discrepancy between the torsional and flexural results is much greater, around 20m.s^{-1}. The interference between the torsional and flexural modes might explain the observed discrepancies. If these two distinct modes of vibration occur at similar frequencies, their expression in terms of local peaks in the magnitude response curve might shift due to presence of the other, resulting in a curve that is harder to interpret.

To better understand the possible interference between the first modes of tor-

sional and flexural vibration, their characteristic frequencies for an equivalent cantilever model, with the properties of the rubber samples, are presented in figure 6.5. The characteristic frequencies for each mode are determined for equivalent shear-wave velocities of $V_s = 30\text{m.s}^{-1}$ and $V_s = 50\text{m.s}^{-1}$, so that a significant range of values can be compared.

Figure 6.5(a) contains the characteristic frequencies of Bernoulli-Euler beam flexural and torsional first modes of vibration for a cylindrical cantilever with a height of 50mm and diameters varying between 30mm and 80mm. Figure 6.5(b) contains the characteristic frequencies of a similar model with a height of 76mm and the same range of diameters. The characteristic frequency curves are identified by references T30, T50, F30 and F50 where T and F indicate the first torsional or flexural mode of vibration and 30 and 50 identify the equivalent shear-wave velocities of $V_s = 30\text{m.s}^{-1}$ and $V_s = 50\text{m.s}^{-1}$.

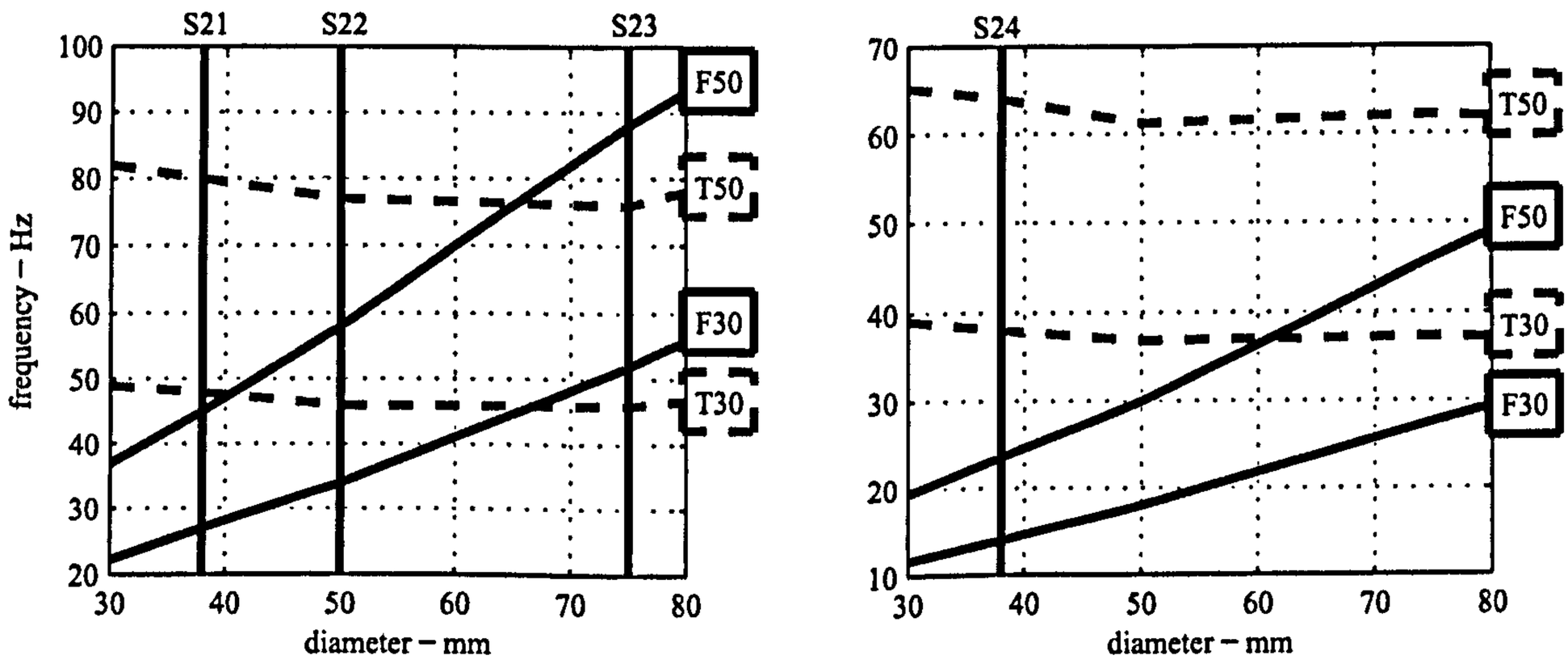

(a) $H = 50\text{mm}$ (b) $H = 76\text{mm}$

Figure 6.5: First flexural and torsional modes of vibration characteristic frequencies for sample heights of $H = 50\text{mm}$ and $H = 76\text{mm}$ and varying diameters.

For samples S22 and S23, the torsional and flexural modes occur at very similar frequencies. For samples S21 and S24, the ones with higher slenderness ratios, the torsional and flexural modes occur at more distinct frequencies. The results of

sample S22 - $h50 \times d50$mm, presented in figure 6.3, can serve as an example of mode interference. In the time history presented in figure 6.3(a) a subtle shift in signal frequency at around 22ms can be observed. The frequency content of the signal was obtained a second time, now separately for two time histories, before and after the 22ms mark. The frequency content of the two separate time histories are presented in figure 6.6, marked as M1 and M2. The original magnitude response of sample S22 is also presented, marked as M0.

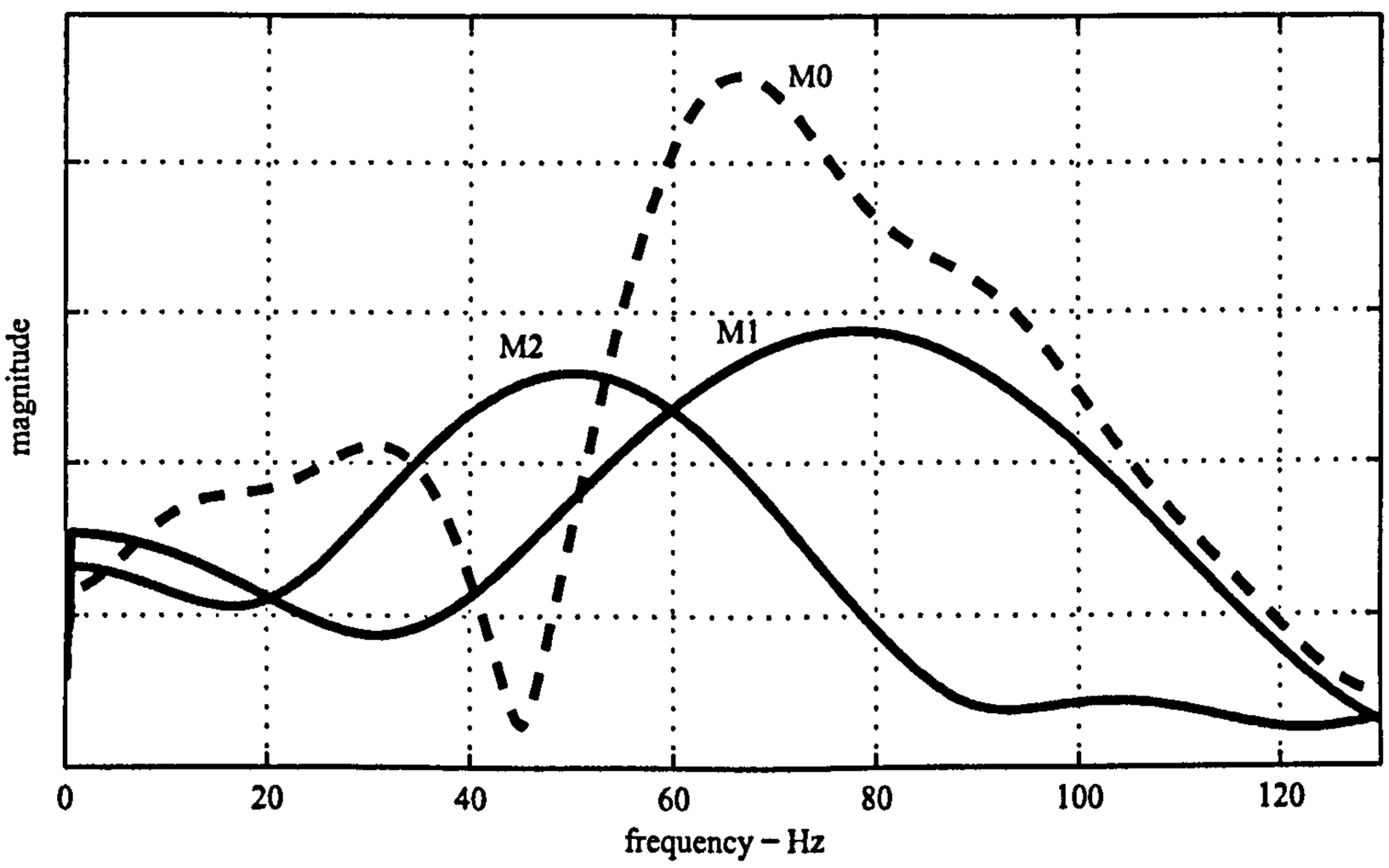

Figure 6.6: Frequency content of sample S22 - $h50 \times d50$mm partial and total time histories.

In figure 6.6, the separate peak features of each time history segment are now much more clear than that of the complete signal. The peak features found in M0 at 67Hz, related with the torsional mode, shifted to 77Hz in M1. The peak feature at 31Hz in M0, related with flexural mode, is now located at 50Hz in M2. These results are a clear indication of mode interference and of how the sample oscillation does shift from one frequency to another. The two corrected characteristic frequencies now estimate the shear wave velocity at $V_s = 50\text{m.s}^{-1}$ and $V_s = 44\text{m.s}^{-1}$ for the torsional and flexural modes respectively. The corrected estimate for the torsional

mode of sample S22 is closer to the value obtained for sample S24, where possible mode interference is less significant, (figure 6.5(b)). The corrected value of the estimated shear wave velocity given by the flexural mode is even more significantly changed, from $V_s = 27\text{m.s}^{-1}$ up to $V_s = 44\text{m.s}^{-1}$. This value is now much closer to the torsional mode estimates.

The local minimum feature in curve M0 at 45Hz roughly corresponds to the peak feature of M1. The peak feature of M2 at 77Hz also roughly corresponds to a local minimum of M0. These local minima of the composed modal curve M0, coinciding with the actual resonance frequencies of each separate mode, are a well known property of mode interference known as anti-resonance, (Ewins, 2000), confirming the proposed hypothesis of mode interference.

The time histories of remaining samples S21, S23 and S24 do not present such a clear breakpoint in their vibration time histories. For this reason, it is not possible to calculate their frequency contents for separate modes of vibration. Nevertheless, a fair estimate of $V_s = 50\text{m.s}^{-1}$ is proposed, considering the results from the torsional modes of samples S21, S24 and the corrected estimate of sample S22. The velocity estimates obtained from the first torsional mode are selected rather than those obtained from the first flexural mode. This is because the torsional mode was the one initially intended to be excited. This is revealed in its dominance over the flexural mode, (figure 6.6). It is also, because the first torsional mode of vibration, according to linear vibration theory, is the only non-dispersive mode of vibration, (section 3.4.1). This is the reason why the first torsional mode is chosen in resonant column geotechnical testing, (section 3.11) or (ASTM, 1978).

6.3 Repeatability and Control Sample Tests

Repeatability test results have already been presented in section 4.6, but are worth revisiting, and compared to the control sample results, providing a benchmark from which to evaluate the variations observed at the control sample tests. During the repeatability tests the parameters known to have varied are the sample age and the room temperature. Other sources of error were associated with the equipment set-up and human factors in result interpretation. During the control sample tests, the most important varying parameter was the use of different samples from different sets. The sample age and the room temperature were again controlled and the possible sources of error acknowledged. The controlled test parameters are listed in tables 6.4 and 6.5.

For each test, a large number of results were collected. From these, various techniques of evaluating the wave travel time were used both in the time and frequency domains. The results presented in this section, for the repeatability and control sample tests, were obtained using estimates from the time and frequency domain techniques, namely the direct travel time measured between pulse signals and the gradient of the phase delay curves. The same signal processing parameters were used for all the estimates.

For a general error estimation, the set of composed results, as presented in figures 6.7 and 6.8, provides a simple and coherent tool. A distinction between results obtained using different signal processing techniques, together with an explanation of the choice of processing parameters, are given with detail in sections 6.4 and 6.5.

---

[5]Sample age is expressed in days.

Repeatability Tests			
Test	Sample	Age[5]	Temperature
1	S08	7	26.0°
2	S08	12	26.0°
3	S08	14	23.5°
4	S08	16	23.5°
5	S08	79	25.5°
6	S08	81	24.5°

Table 6.4: Repeatability study parameters.

Control Sample Tests			
Test	Sample	Age	Temperature
1	S04	<60	24.5°
2	S08	<60	26.0°
3	S12	<60	25.5°
4	S16	<60	24.5°
5	S20	<60	25.0°
6	S24	<60	25.0°
7	S28	<60	25.0°
8	S29	<60	24.0°

Table 6.5: Control sample study parameters.

6.3.1 Repeatability

An estimate of the wave travel velocity for each of the repeatability tests is given in figure 6.7.

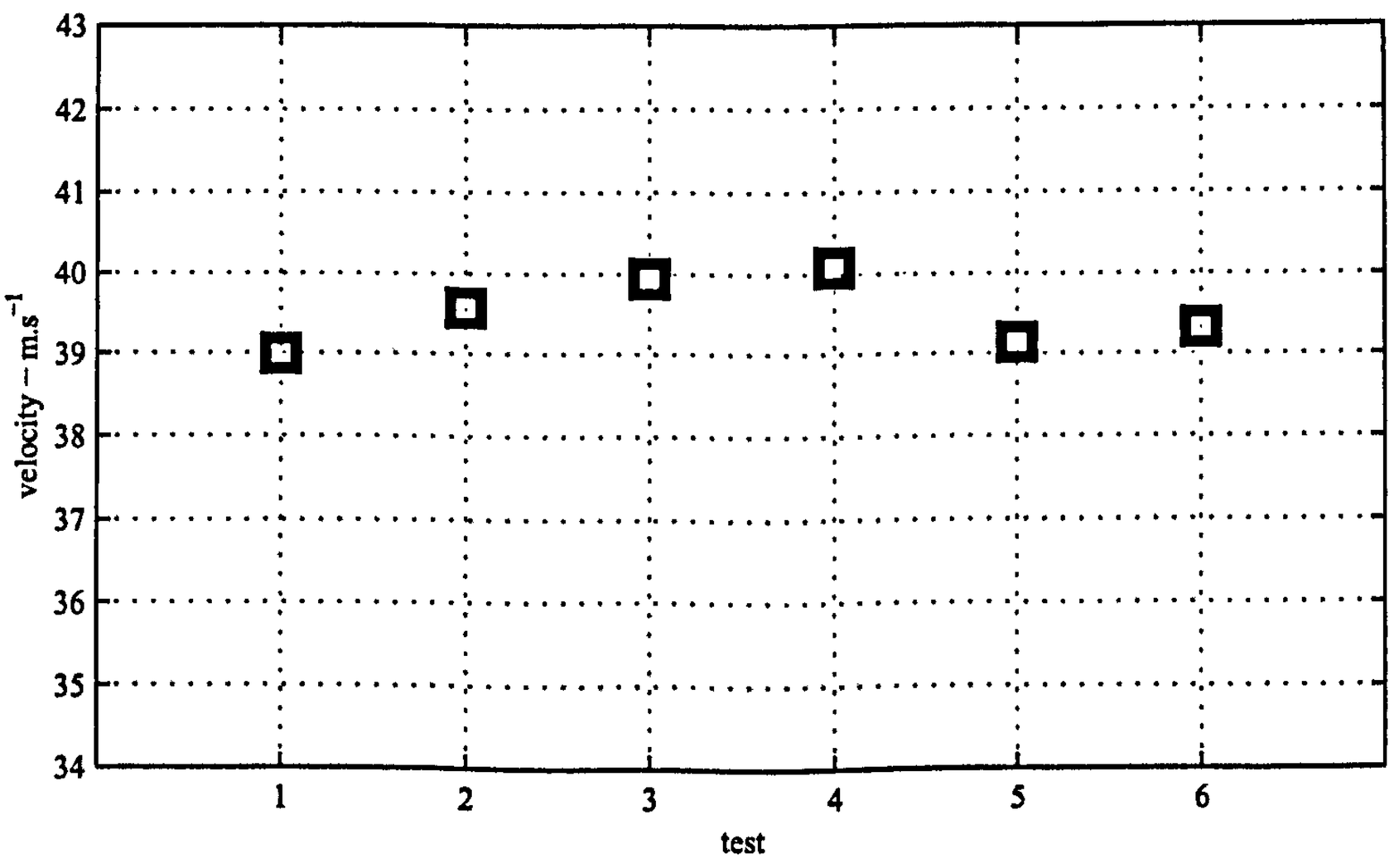

Figure 6.7: Wave travel velocity estimates for the repeatability study.

The velocity estimates for the repeatability tests, in figure 6.7, have a maximum

value of 40m.s^{-1} and a minimum value of 39m-s^{-1}. This means there is a maximum difference of 1m.s^{-1} between any two estimates of wave velocity. The mean deviation from the average wave velocity estimates, considering all the repeatability test results, is of ±1.5%. As discussed in section 4.6, there are no particular relationships between the estimated wave velocities and the sample age or room temperature. The repeatability results therefore indicate a wave velocity estimate somewhat affected by an error attributed, in bulk, to sample age, room temperature and possibly to human error setting up the equipment and processing the results. This estimate of error obtained for the repeatability study will henceforth be referred to as 'baseline error'.

Arroyo *et al.* (2003*b*) obtained surprisingly high uncertainties of around 30% and 50% in the determination of the medium shear stiffness for pulse signal tests. Bodare and Massarsch (1984) obtained similar uncertainty values for cross-hole tests. The estimate of baseline error is not entirely compatible with these uncertainty results since it is concern with the repeatability of the tests and not with the actual determination of the shear stiffness. Nevertheless, since for this study the sample's properties were comparatively maintained constant it was possible to isolate the error or uncertainty due primarily to the test-set up and other aspects such as room temperature and sample age.

6.3.2 Control Sample

The estimated wave velocities for each of the control sample tests are given in figure 6.8.

The wave velocities obtained for the control sample tests, (figure 6.8), vary between 36m.s^{-1} and 41m.s^{-1}. This constitutes a maximum difference in velocity results in the range of 5m.s^{-1}, approximately 13% of the average velocity of 39.2m.s^{-1}.

The density of each of the rubbers constituting the control samples is given in

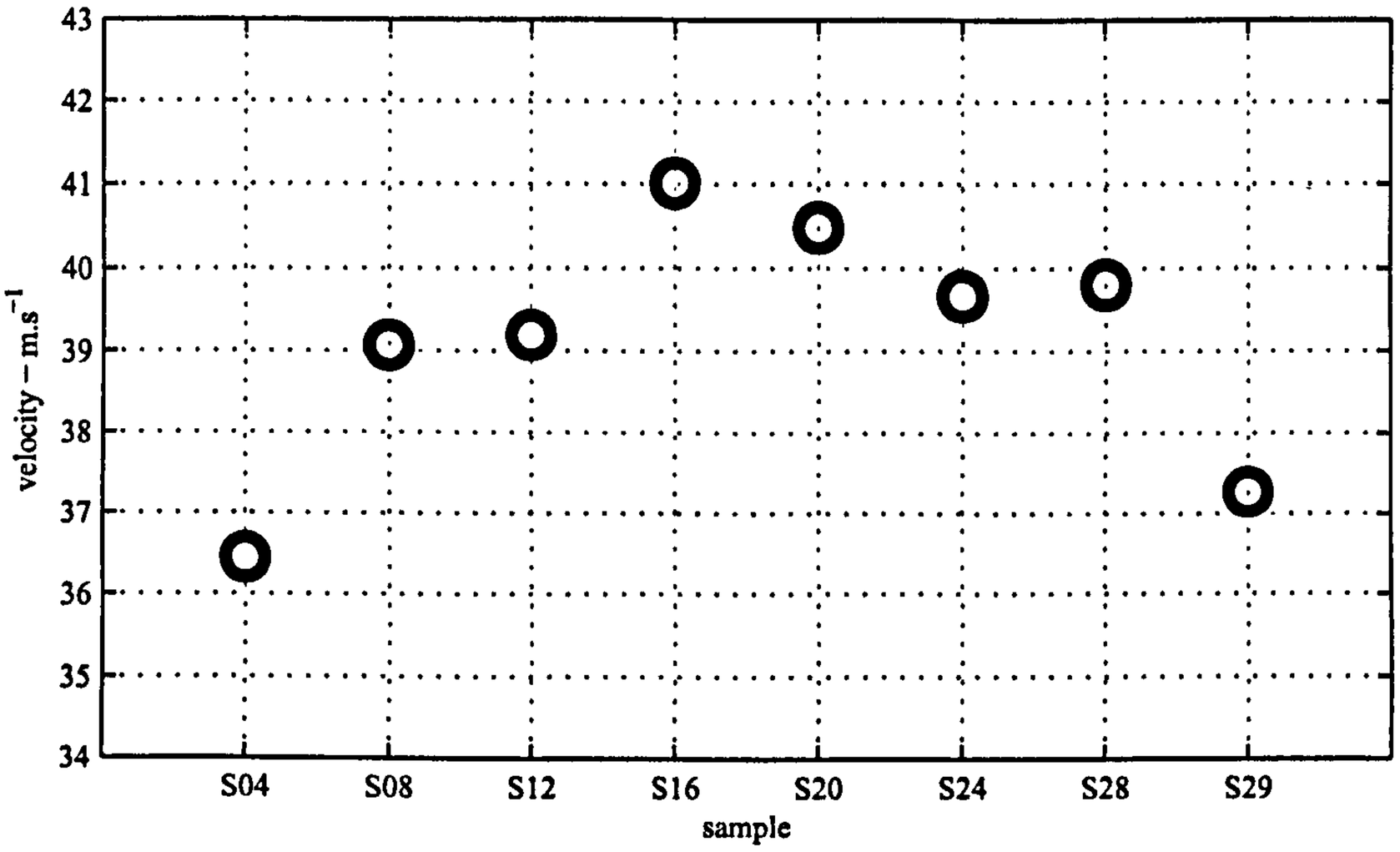

Figure 6.8: Wave travel velocity estimates for the control sample study.

table 6.6 together with the obtained wave velocity. No relation could be established between the two presented characteristics of the tested rubbers meaning the degree of variation in wave velocity results can not be attributed to the rubber density.

Sample	Density (kg.m^{-3})	Velocity (m.s^{-1})
S04	1052	36.5
S08	1076	39.1
S12	1046	39.3
S16	1053	41.0
S20	1046	40.5
S24	1045	39.8
S28	1040	39.9
S29	1037	37.2

Table 6.6: Control Sample Density.

During the repeatability study, the tested samples were all 81 days old or younger, the room temperature varied between 23.5° and 26.0° and the maximum difference obtained between wave velocity estimates was 1m.s^{-1}, with no particular relation

between sample age, room temperature and equipment set-up detected during the study. During the control sample study, the tested samples were all under 60 days old and the room temperature varied between 24.0° and 26.0°. These values of sample age and room temperatures for the control study are within the range of values covered during the repeatability study. Moreover, in both the repeatability and control sample studies, the equipment set-up remained constant, with the same care applied into the handling the equipment and the data. This means that any difference between wave velocity estimates higher than $1 m.s^{-1}$, for the control sample study, must be attributed to the medium properties of the samples.

In summary, when results are compared between samples from the same set, the baseline error must be considered together with the difference in sample geometry. When results are compared between samples of different sets, the variations obtained during the control sample study must also be considered. This consideration can be made in the form of result normalisation, using the differences between estimated wave velocities presented in figure 6.8

6.4 Frequency Domain

A dynamic system can be described by its response to a given excitation. The system's response is complex and can be defined by two curves, that of the phase delay and that of the magnitude. The phase delay curve describes the phase difference between the excitation and the response at each frequency. In the case of bender element testing, the excitation and the response of the system are usually given by the input and output signals. The magnitude curve describes the ratio between the amplitudes of the excitation and the response at each frequency. The response curves describe the system, but also provide a tool to determine the wave travel time. For example, the gradient of a tangent of the phase delay curve is directly related with

the wave's phase velocity at that frequency. The equivalent curve secant is related with the wave's group velocity, (section 2.2). The detection of resonance frequencies in the form of peak features at the magnitude response curves can also be associated with certain modes of vibration and with the respective stiffness properties of the medium, as was done in section 6.2

Different responses from different samples to the same signal excitation are presented in figures 6.9 and 6.10. In this example, the response curves of three polyurethane rubber samples with different heights and diameters were chosen, samples S15 - $h30 \times d75$mm, S22 - $h50 \times d50$mm and S29 - $h76 \times d38$mm, (table 6.2). The response curves for all three samples were obtained by exciting each sample with the same sweep signal, similar to the one described in table 6.3.

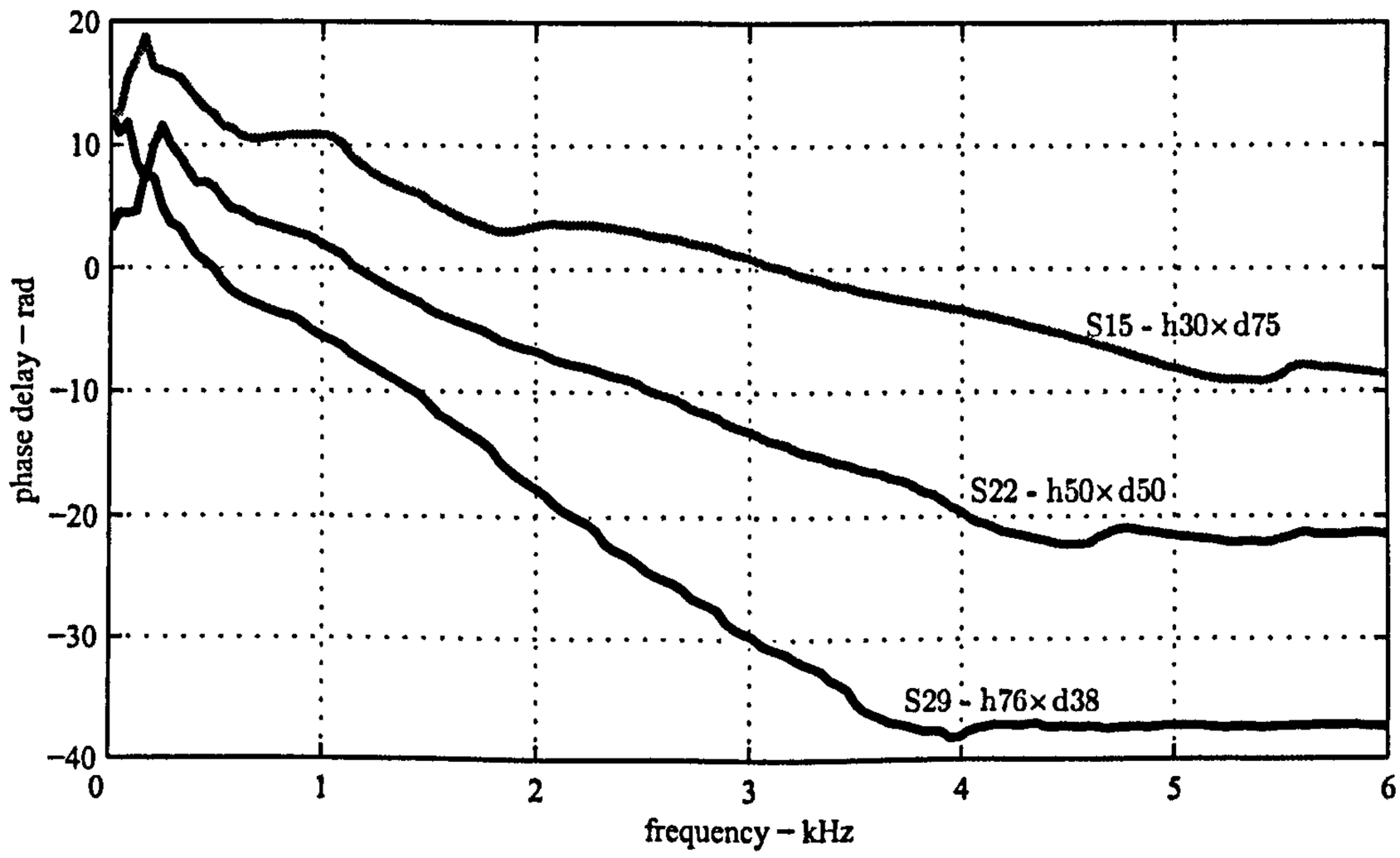

Figure 6.9: Example phase delay curves for samples S15, S22 and S29.

The dynamic behaviour of the three samples have apparent differences. The phase delay curves of the three samples, (figure 6.9), have different gradients. The phase delay gradient of sample S29 is clearly higher than the gradient of S22, which in turn is higher than S15. Knowing that the higher the gradient the higher the travel time, the observed difference is primarily an expression of each sample's height, and

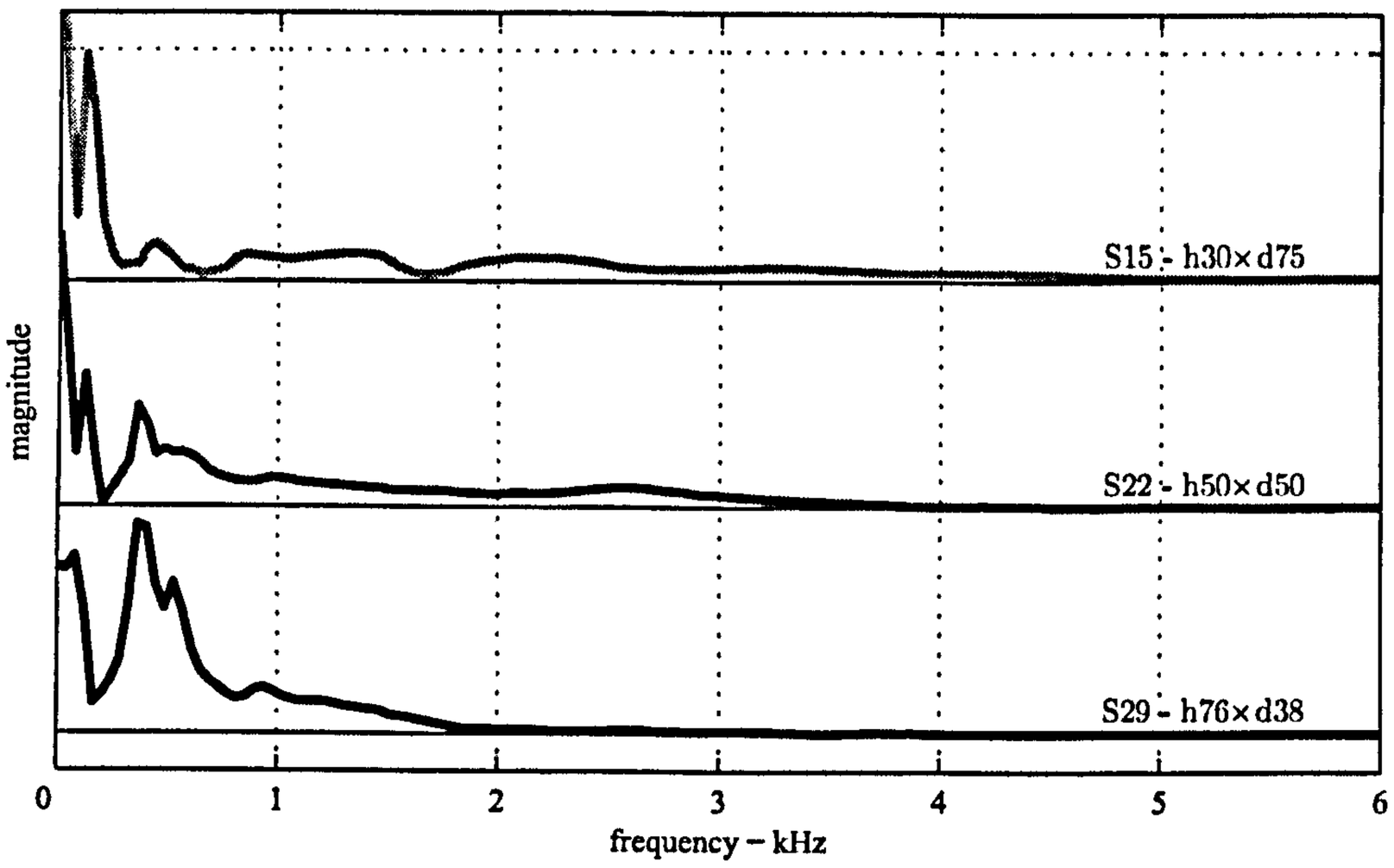

Figure 6.10: Example magnitude curves for samples S15, S22 and S29.

therefore of its different travel path length.

The three phase delay curves flatten from a certain frequency onwards. The frequency at which this occurs coincides with the frequency at which the magnitude curve nears zero. These features of both phase delay and magnitude curves enable the evaluation of the maximum frequency that can be successfully propagated along each sample.

The magnitude response curves, (figure 6.10), are also different for each sample. The magnitude curves are plotted with a vertical offset from each other for clarity purposes. Knowing that a peak in the magnitude curve corresponds to a particular resonance of the system, different resonances at different frequencies can be detected for each of the samples. At frequencies lower than 1.0kHz each magnitude curve has three or four peaks at distinct frequencies. For higher signal frequencies notice the very damped peak for sample S15 is near 3.1kHz, a similar peak at 2.6kHz for sample S22, and no similar noticeable peak for sample S29.

The mentioned features of the response curves are explored with more detail in sections 6.4.1 and 6.4.2. At this stage, it is sufficient to point at the noticeable

differences in behaviours of each sample, expressed in the differences between their responses. This observation raises the possibility of such differences in behaviour being attributed to the sample's different geometries.

6.4.1 Maximum Frequency Content

As seen in figures 6.9 and 6.10, the response curves of each sample show different dynamic behaviours. One such difference is the observed maximum frequency content or cut-off frequency. The notion of maximum frequency is related with the frequency at which the received signal is no longer significant. The maximum frequency or cut-off frequency is an important factor, since it translates the dynamic capacity of each sample in allowing, or impeding, waves with different frequencies to propagate successfully through it.

A number of parameters can be used to determine such maximum frequency. One such parameter is the signal-to-noise ratio, the concept of which is self-explanatory. When this parameter approaches a predetermined minimum value, it is possible to declare that the maximum frequency has been reached, (Bendat and Piersol, 2000). For the present study, another set of combined parameters is going to be used. Thus, in this study, the maximum frequency is said to be attained when both the gradient of the phase delay curve and the value of the magnitude curve approach a value of zero. In order to gain some objectivity, a value lower than 10% of the maximum magnitude, if it coincides with a null gradient of phase delay curve, is proposed. Figure 6.11 illustrates an example of the maximum frequency determination for sample S21 - $h50 \times d38$mm. The frequency at which the phase curve becomes horizontal coincides with the frequency at which the magnitude curve reaches zero.

Using this combined analysis of the response curves, the maximum frequency content was determined for all samples that took part in the parametric study.

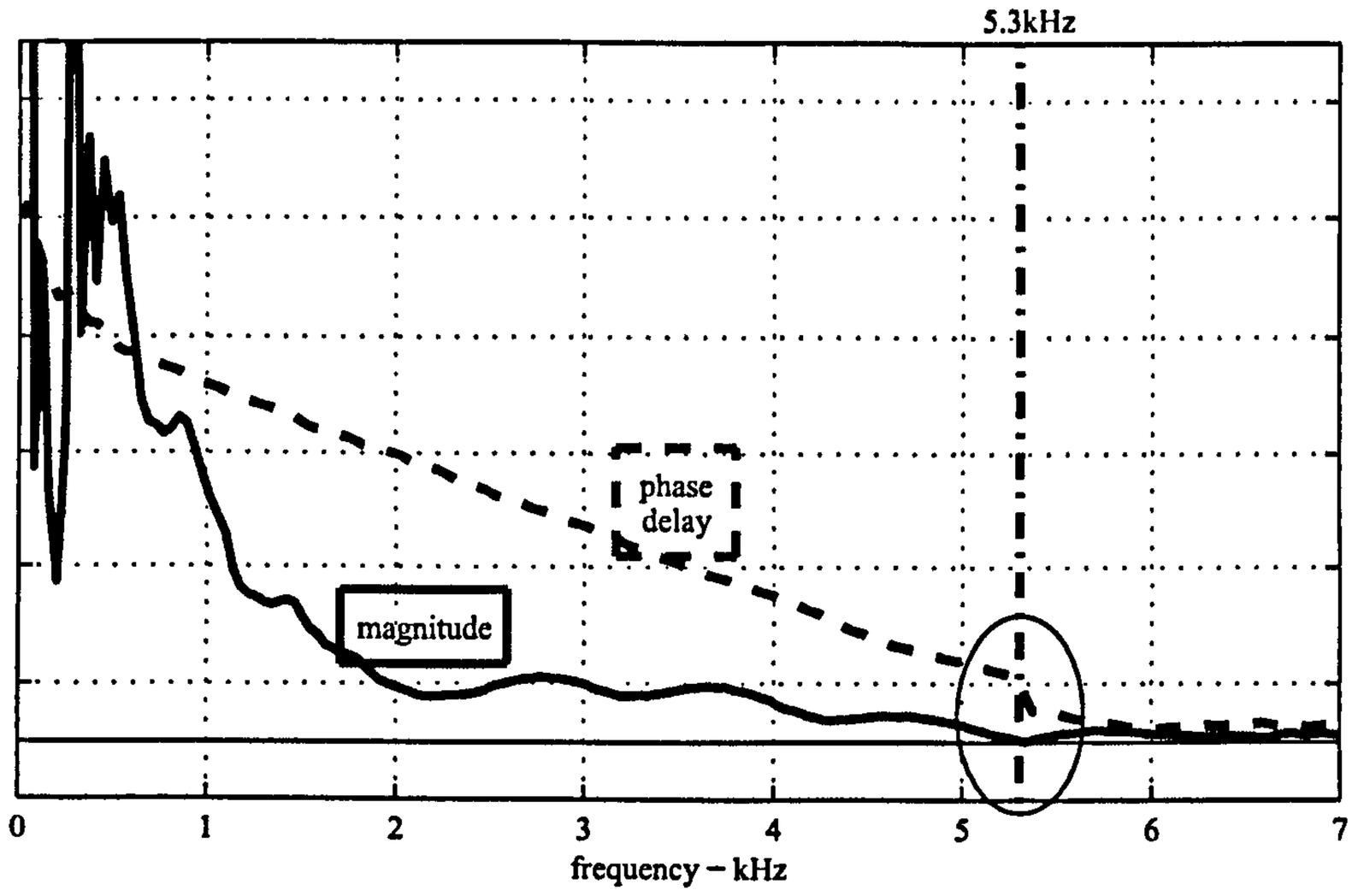

Figure 6.11: Maximum frequency determination for sample S21 - $h50 \times d38$mm using the phase delay and magnitude response curves.

The obtained results are presented in figure 6.12 according with sample height and diameter.

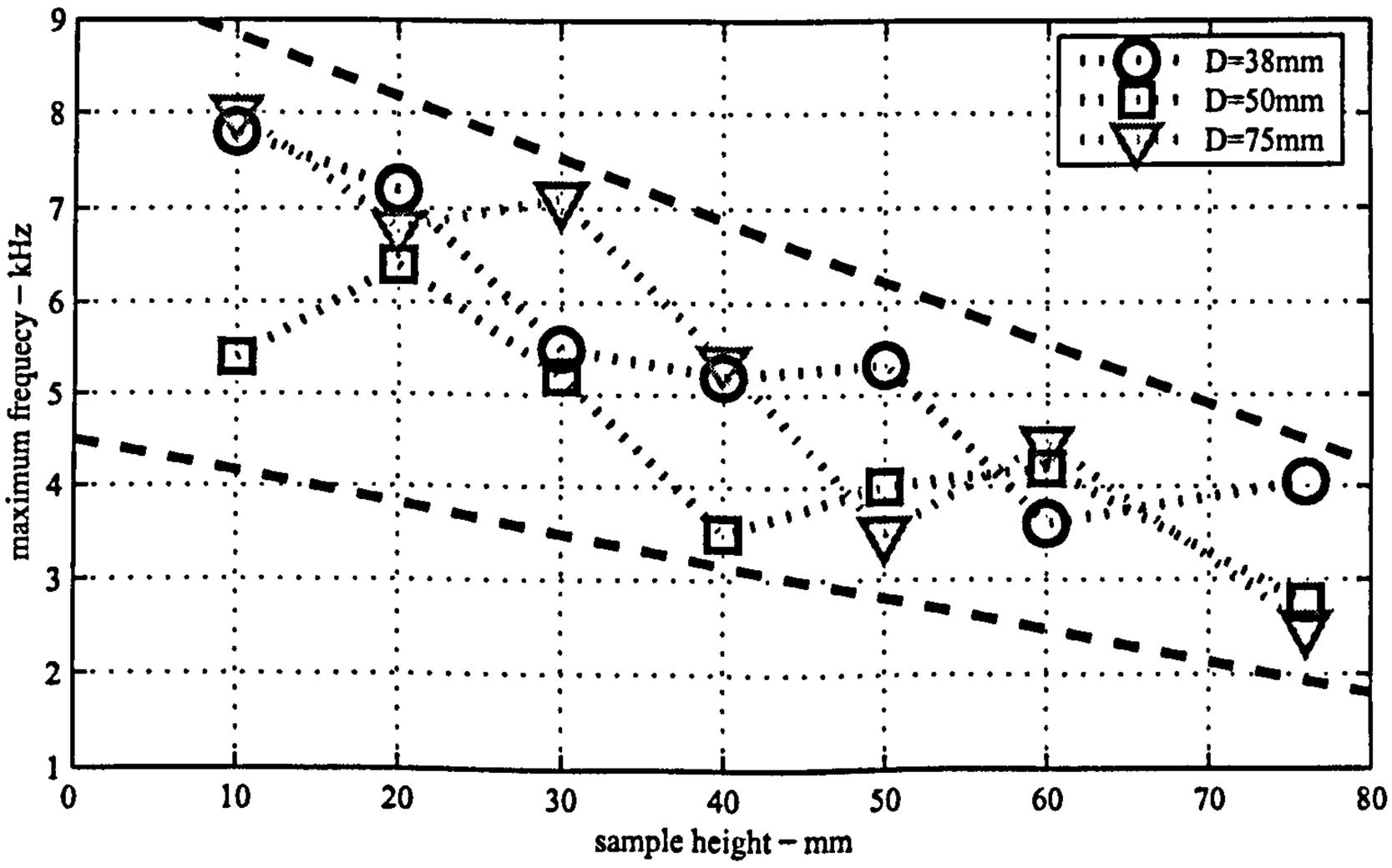

Figure 6.12: Maximum frequency detected at response curves of synthetic rubber samples.

The analysis of the maximum frequency results in figure 6.12 leads to relevant observations. The downward trend with sample height is observed for all three dif-

ferent diameters. The highest maximum frequency contents are detected for the lowest samples, 10mm height, reaching value between 5.5kHz and 8.0kHz. The lowest maximum frequencies are detected for the highest samples, with maximum frequency values between 2.5kHz and 4.0kHz. This translates into a maximum difference of up to 100% between the capacity of maximum frequency wave transmission of two samples. It is worth remembering that the samples are made of the same material, their geometry is the main difference between them. From the presented results, there appears to be no clear relation to sample diameter.

At this point, a clear indication of the influence of sample geometry has been established. The sample height influences the maximum frequency content capable of being transmitted through a given cylindrical sample. The higher the sample the lower the maximum frequency content. This verification confirms that the samples work as mechanical frequency filter, as any solid with mass should, (Doyle, 1977), where the lower the flexural stiffness the lower the maximum frequency able to propagate. It is then justifiable, for anyone wishing to set-up a bender element test, to establish if the tested samples are capable or not of propagating a signal with a desired frequency, or which signal frequencies can be successfully propagated along the studied sample.

6.4.2 Dynamic Response

The peaks observed at the magnitude response curves indicate particular resonances of the system. The tested system, composed by one rubber sample, a pair of bender elements and the end plates is relatively complex. The equipment set-up is maintained constant and only the rubber samples change with their different geometries. Since the geometry of the samples is the main parameter varying during the tests, the possible observed differences in the responses can be attributed to it.

If the bender element test system, pictured in figure 6.13(a), is to be studied

using an analytical model, the boundary conditions which need to be considered are those of a cantilever with a mass at its free end, (figure 6.13(b)). The dynamic behaviour of such a cantilever system can be modelled with some simplicity as a Bernoulli-Euler beam, (Clough and Penzien, 1993). It is even possible to model the system as having a single degree of freedom, SDOF, or a simple multiple degree of freedom, MDOF. This is possible if the beam properties are evenly distributed along its length, (section 3.10).

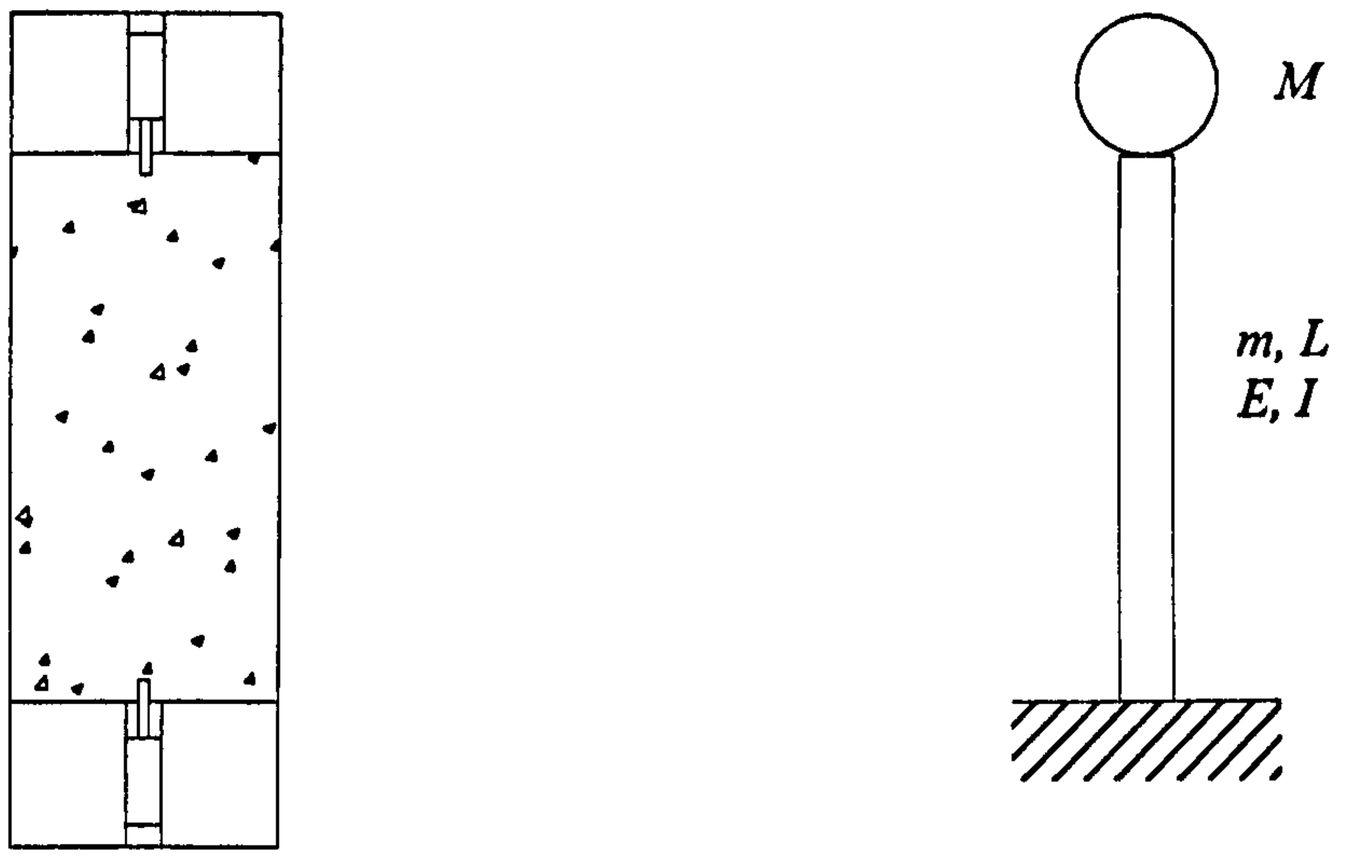

(a) sample, bender element and steel plates (b) MDOF cantilever with mass at free end

Figure 6.13: Bender element test system and equivalent mechanical model.

The flexural motion of the bender element is anti-symmetric in relation to the sample and any possible shear and compressional wave components that reach the lateral boundaries of the samples are assumed to be reflected back into the medium. For these reasons, the bending motion of the transmitting bender element is assumed to excite the system mainly into modes of flexural vibration, (section 3.4.1) or (Redwood, 1960). This means the most influential parameter of the sample, in terms of its vibration behaviour, is its flexural stiffness, given by EI/L. All other things being equal, slender samples, higher H/D, have less flexural stiffness than bulkier samples. Therefore, slender samples might be expected to resonate at lower

frequencies, and bulkier samples to resonate at higher frequencies. An example of how the response magnitudes vary between samples with different heights is given in figures 6.14.

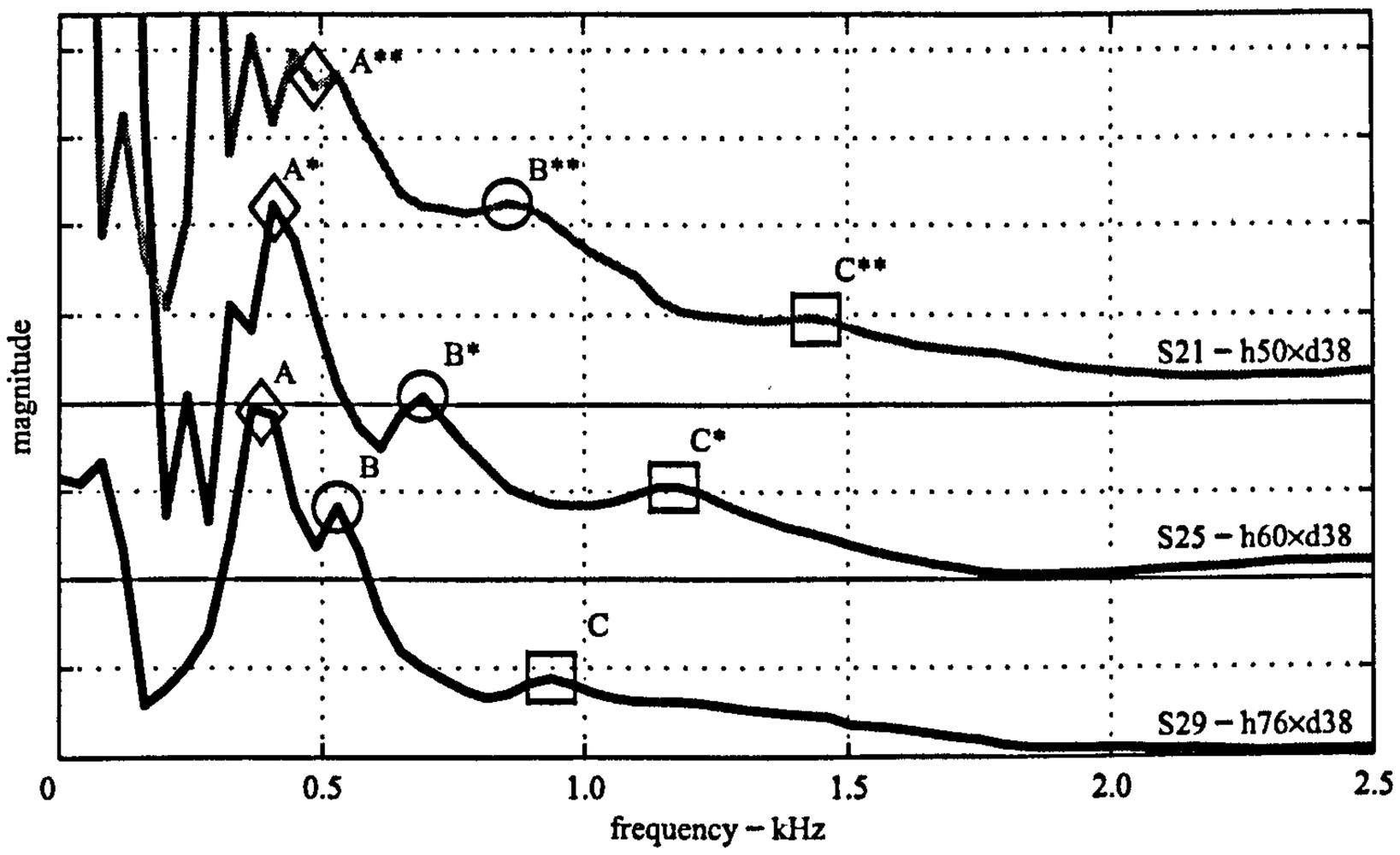

Figure 6.14: Peak features of response magnitude curves of samples S21, S25 and S29.

Figure 6.14 contains the response magnitude curves of samples S21, S25 and S29. These samples all have the same diameter of 38mm and different heights of 50mm, 60mm and 76mm respectively. Three local peaks from each magnitude curve were marked as A, B and C. Considering the marked peaks to indicate curves features related with each other, where A marks the same feature as A* and A**, etc. For each feature, the related frequency decreases with sample height. These tendency is compatible with the expected dynamic behaviour of a MDOF system, where the respective resonance frequency of a particular mode of vibration increases with bar stiffness, which is what happens to the flexural or torsional stiffness of the samples with decreasing height.

A second example is given in figure 6.15 where the sample diameter is the varied geometric parameter. The response magnitude curves of samples S29, S30 and

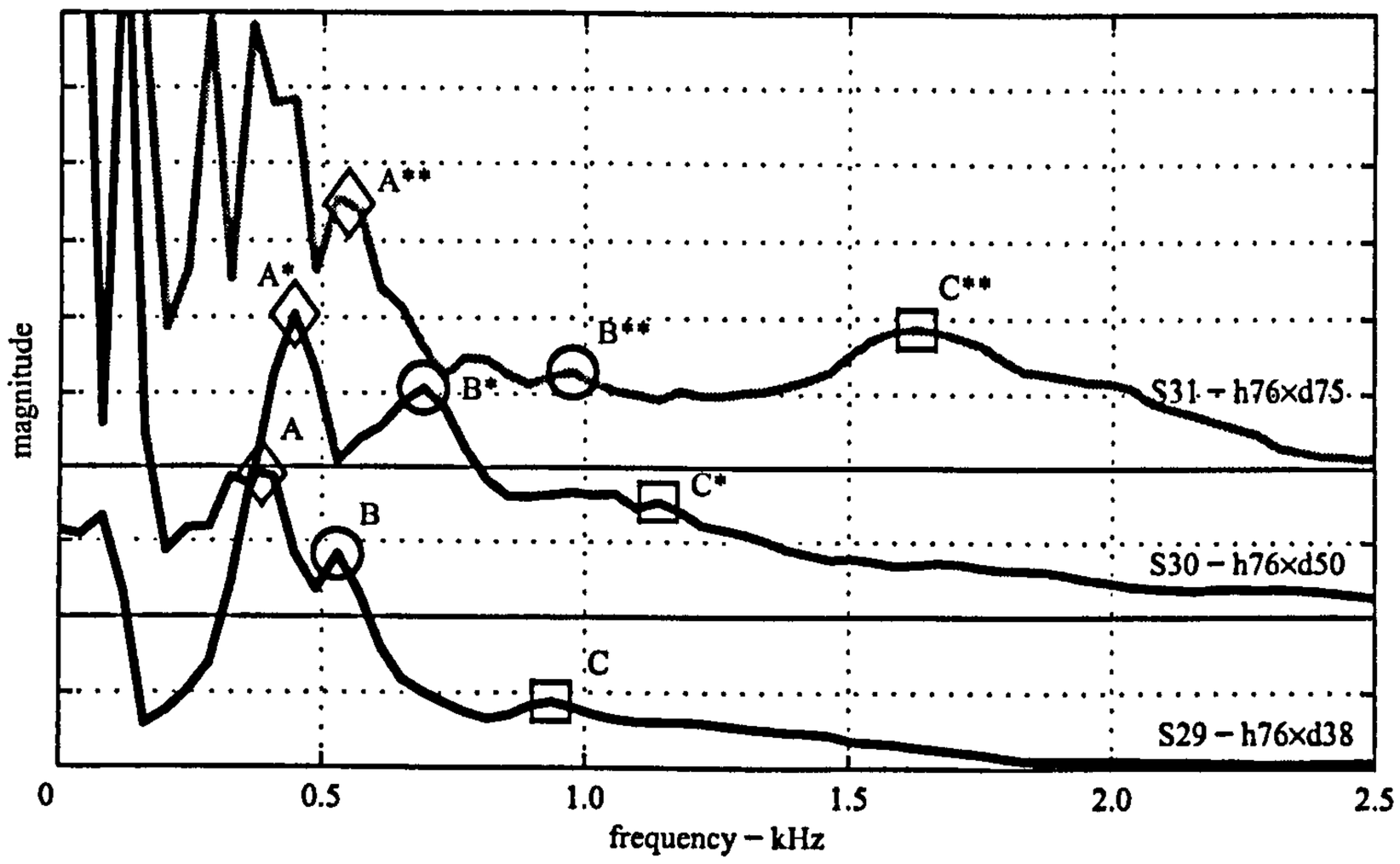

Figure 6.15: Peak features of response magnitude curves of samples S29, S30 and S31.

S31 are presented. These samples all have the same height of 76mm, but different diameters of 38mm, 50mm and 75mm. Once again, three peak features on each magnitude curve were marked. A tendency of increased resonance frequency with increased diameter is noticeable for each of the features. Since for a constant height, the flexural stiffness of a beam increases with its diameter, namely its moment of inertia I, the observation of system stiffening made in figure 6.15 is also compatible with the dynamic behaviour of an MDOF system.

The two examples presented for varying sample height and diameter are another indication that the studied samples have a relatively normal dynamic behaviour. As observed, their behaviours is so far explained by the analytical model predictions, such as the proposed Bernoulli-Euler beam. Since the given examples showed encouraging signs of predictable dynamic behaviour, this subject is explored further for the remaining samples.

Figure 6.16 presents the relationship between the frequency of magnitude curve peak features and sample height for samples with constant diameter, $D = 38$mm.

These samples have varying heights ranging between 20mm and 76mm. The presented peak features are consistent with the ones seen in figure 6.14, and are marked using the same references: A, B and C. By using a logarithmic scale is appears that the results vary exponentially with sample height.

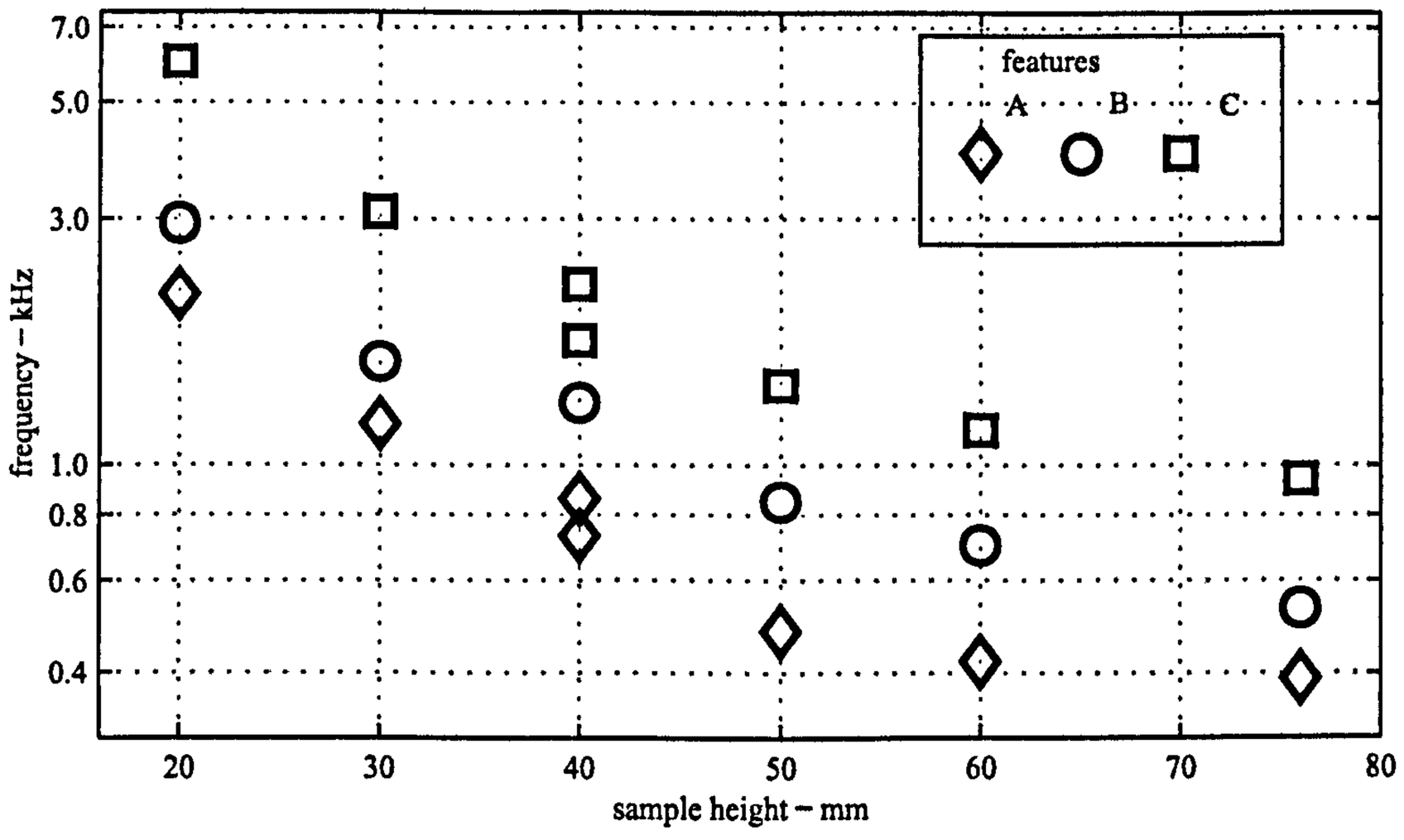

Figure 6.16: Response magnitude peak features from samples with constant diameter, $D = 38$mm, and varying heights.

In figure 6.16 it can be seen that the frequency at which all of the peak features occur decreases with sample height. Feature A decreases from 2.0kHz for a sample height of 20mm down to 0.4kHz for a sample height of 76mm. A similar observation can be made for features B and C, decreasing from 3.0kHz and 6.0kHz down to 0.5kHz and 0.9kHz respectively. The rate at which the frequency of each the peak features occurs is similar for the three presented features cases. This decrease seams to be exponential with sample height, being compatible with the relation between sample height and flexural resonance frequencies given in equation 3.101.

The observed result trends seen in figures 6.14 and 6.15, and again in figure 6.16, appear to be similar to the general behaviour of a Bernoulli-Euler beam. These results are explored further by calculating the equivalent theoretical analytical res-

onance frequency results and comparing them.

Equation 3.101, (section 3.10.2), was used to determine the characteristic frequencies for the first three modes of flexural vibration of the equivalent beam models, with the same density and geometry. Equation 3.107 was used in a similar fashion to determine the characteristic frequencies for the first three modes of torsional vibration. The boundary conditions of the analytical models, namely their fixity, were determined with the use of equation 3.103 and 3.110.

The dynamic behaviour of an analytical model has already been explored in section 6.2 with an estimated equivalent shear-wave velocity of $V_s \cong 50\text{m.s}^{-1}$ obtained from the first torsional mode of vibration. A similar procedure for the first flexural mode of vibration produces an estimate of $V_s = 44\text{m.s}^{-1}$. In the control and repeatability tests, in section 6.3, wave velocity estimates in the range of $V_s \cong 40\text{m.s}^{-1}$ were also obtained. Considering all the shear wave estimates obtained so far, two values of $V_s = 30\text{m.s}^{-1}$ and $= 50\text{m.s}^{-1}$, were chosen to establish a range of possible wave velocities to be used in the comparison of the magnitude response curve and the dynamic analytical models.

The parameters used to define the properties of the cantilever beam and mass on top model are given in table 6.7.

Parameter	Symbol	Units	value		
diameter	D	mm	38	50	75
concentrated mass[6]	M	g	210	384	836
density	ρ	kg.m^{-3}	1000		
Poisson's ratio	ν	no units	0.45		
shear wave velocities	V_s	m.s^{-1}	$= 30$ / $= 50$		
length	L	mm	$\in [\,10 \;\; 110\,]$		

Table 6.7: Properties of the Bernoulli-Euler cantilever beam model.

[6]The weight of the steel plates used in the parametric study.

The theoretical results were calculated for a range of elastic properties, expressed in the equivalent shear wave velocities but also for a range of different beam geometries, corresponding to the actual geometries of the polyurethane samples. The use of different end plates, corresponding to different sample diameters, were also taken into account by considering the actual weight of the different steel plates. The density of the beam's medium is equal to that of the polyurethane rubber. Such rubber-like materials have little elastic volumetric variation and therefore high Poisson's coefficients, thus a value of $\nu = 0.45$ was chosen.

In figure 6.17, the peak feature A and the second mode of flexural vibration results are highlighted. These results are presented for samples with constant diameter, $D = 38$mm and variable heights. The flexural mode characteristic frequencies were calculated for two different equivalent shear-wave velocities of $V_s = 30$ and $V_s = 50\text{m.s}^{-1}$, identified by references F2V30 and F2V50 respectively.

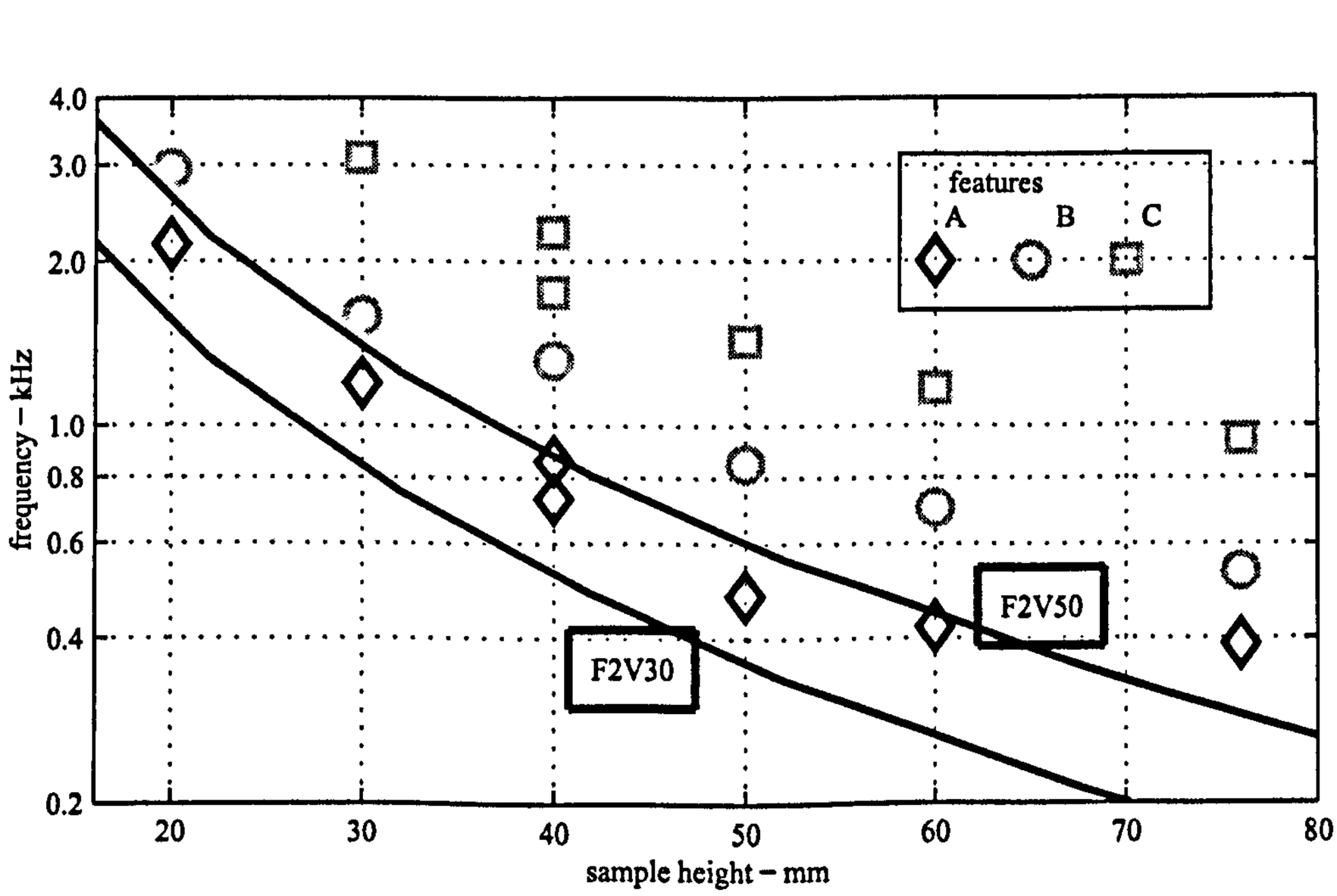

Figure 6.17: Peak features A and characteristic frequency curves of second mode of flexural vibration, for samples with constant diameter, $D = 38$mm.

In figure 6.17, feature A results can be observed to be contained within the range of the second flexural mode of vibration frequencies, except for sample heights

$H > 76$mm. This result indicates that the chosen feature A is related with the second mode of flexural vibration. It also indicates that the equivalent shear wave velocity of the studied rubber is in the proposed range, which agrees with the observation made in section 6.2.2.

Figure 6.18 highlights the peak feature B and the third mode of torsional vibration. This figure is similar to figure 6.17, where now the characteristic frequency curves of the third mode of torsional vibration are identified as T3V30 and T3V50.

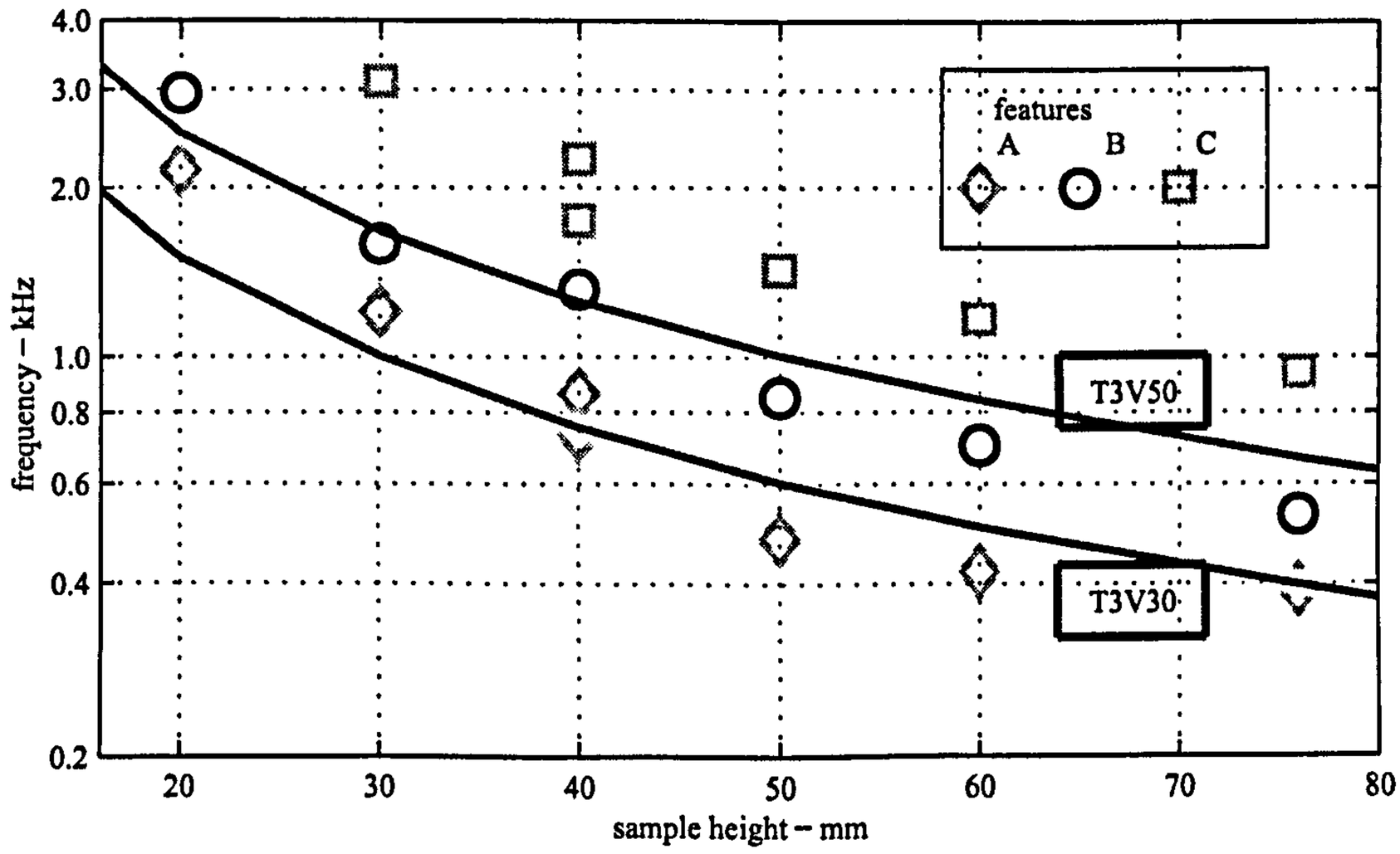

Figure 6.18: Peak features B and characteristic frequency curves of the third mode of torsional vibration, for samples with constant diameter, $D = 38$mm.

The chosen peak features B and frequency curves of the third mode of torsional vibration, in figure 6.18, also appear to be related. This relation is more evident for higher samples, where the proposed range clearly encloses the peak features.

In figure 6.19 are highlighted the third peak features, feature C; and the frequency curves of the third mode of flexural vibration. These theoretical curves are identified as F3V30 and F3V50.

In figure 6.19, the theoretical results of curves F3V30 and F3V50 seem to be

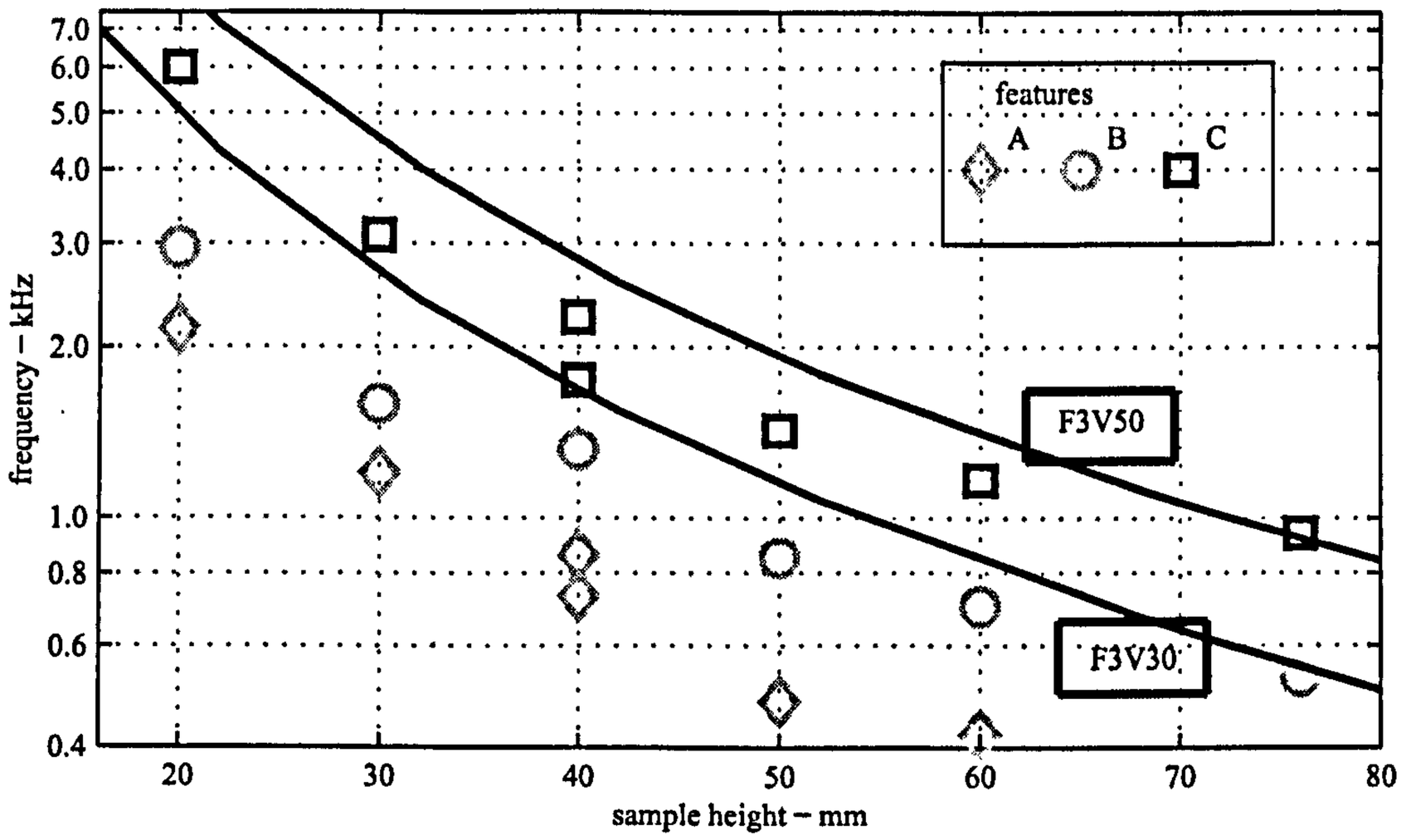

Figure 6.19: Peak features C and characteristic frequency curves of the third mode of flexural vibration, for samples with constant diameter, $D = 38$mm, and variable heights.

related with feature C results. As with feature A and the second mode of flexural vibration in figure 6.17, the frequency curves agree better with feature C for lower sample heights.

Having established the relation between the chosen peak features and the theoretical frequency curves for the second and third modes of flexural vibration as well as for the third mode of torsional vibration, a second type of comparison was attempted. The peak feature results are now compared with theoretical frequency curves in terms of sample diameter variation.

The peak features serving as an example in figure 6.15 correspond to three samples with the same height, $H = 76$mm, and different diameters $D = 38$mm, 50mm and 75mm. These response magnitude curve features are marked as A, B and C, as in figure 6.20, together with the characteristic frequency curves of the second and third modes of flexural vibration. The vertical frequency axis is now linear, since the variation of characteristic frequencies with diameter for flexural vibration also

varies linearly, (equation 3.101).

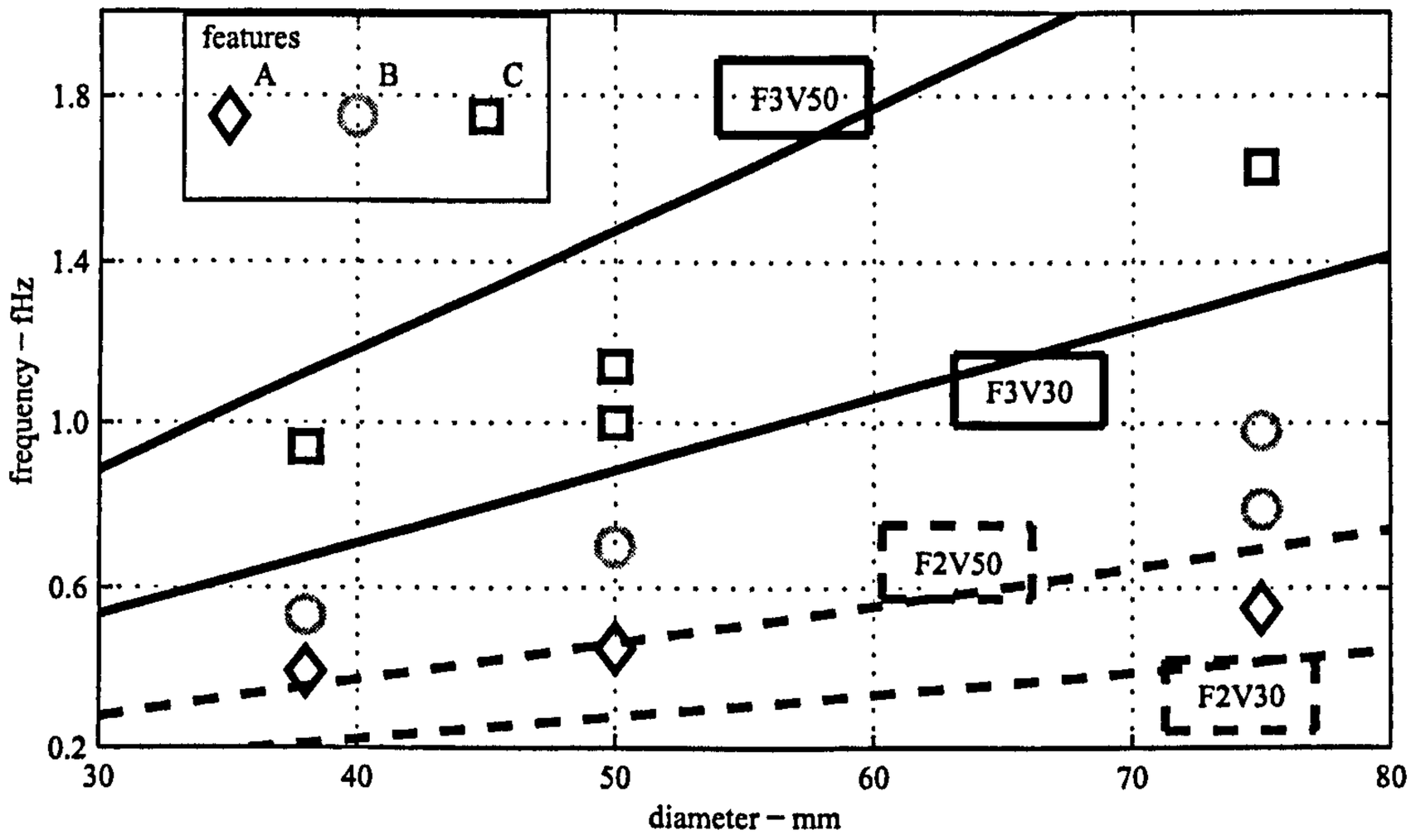

Figure 6.20: Peak features A and C and characteristic frequency curves concerning samples with constant height, $L = 76$mm, and variable diameters.

In figure 6.20 features A and C are generally well within reach of the proposed frequency curve ranges. These results, together with the similar observation made for sample height variations, confirm the relationship between these features and the proposed modes of flexural vibration. At this point, little doubt can remain as for the suitability of the proposed theoretical models of dynamic behaviour of the samples when tested with bender elements.

The comparison between peak feature B and the third torsional mode of vibration's characteristic frequencies for constant sample height of $H = 76$mm and variable diameter is illustrated in figure 6.21.

The results in figure 6.21 show that feature B results are not related to the third torsional mode of vibration, as previously thought and indicated in figure 6.18. Even though, for the diameter $D = 38$mm, feature B is well inside the range of torsional characteristic frequencies, the same is not true for higher diameters. It can be seen that the torsional mode presents near constant values for the range of considered

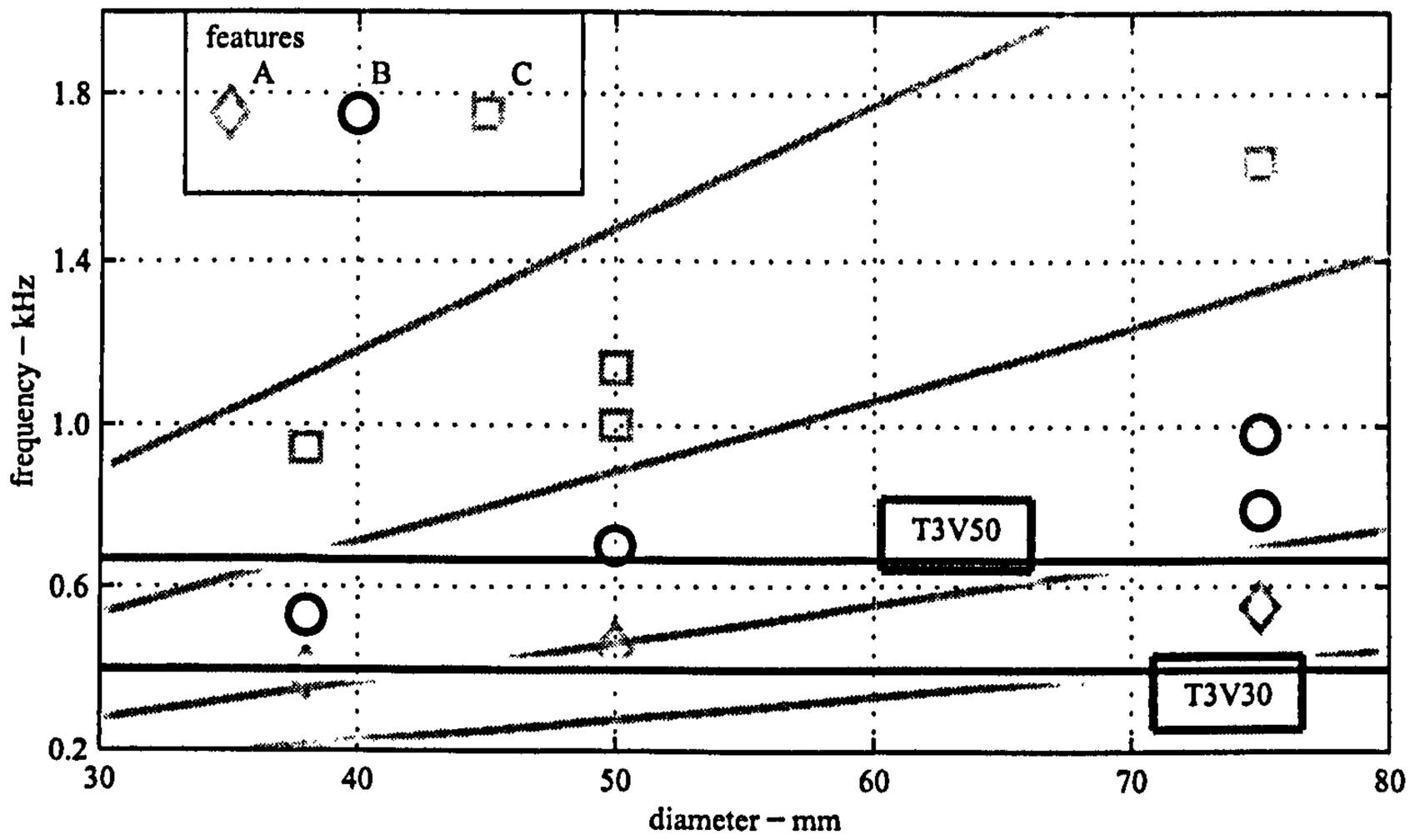

Figure 6.21: Peak features B and characteristic frequency curves concerning samples with constant height, $L = 76$mm, and variable diameters.

diameters, unlike the flexural mode results, which grow linearly with diameter. Even though feature B results are not in the proposed range for the second and third modes of flexural vibration, it follows a similar upwards trend. This might indicate that, even though it is not related with the proposed modes, it is also a feature of flexural behaviour.

A clear unequivocal relation between the cylindrical samples' dynamic behaviour, when excited by a bender element, and the Bernoulli-Euler beam flexural behaviour has been established. It is then important of acknowledging this form of sample behaviour and the consequences it carries in terms of bender element signal interpretation. Early assumptions, explicit or not, of unbounded shear wave propagation regardless of sample geometry, must therefore be corrected, especially since they are misleading in terms of describing the possibility of a simple shear wave propagation, rather than a more complex group of wave components propagating in a flexural mode, (Blewett *et al.*, 1999; Dyvik and Madshus, 1985). It is also important to clarify the possibility that other sources of dispersion are present. When assuming

flexural modes of wave propagation, geometric or waveguide dispersion, as described in section 3.4.1, must also be considered.

6.4.3 Phase Delay Curve

The results for the frequency domain analysis were obtained using sweep signals. These signals provided a complete set of response curves formed by the phase delay and magnitude curves, (section 2.4). Harmonic continuous signals were also used and referred to as continuous signals and pi points, as described in sections 2.2 and 2.3. Since all three types of signal are able to produce phase delay response curves, the resulting curves are compared to confirm the validity of using sweep signals, which have a greater potential in terms of number of data quality but are not so commonly used. In figure 6.22 the obtained phase delay curves for two samples with significantly different geometries are compared. The phase delay curves are identified as 'pip' for pi point results, as 'cs' for continuous signal results and as 'sweep' for sweep signal results.

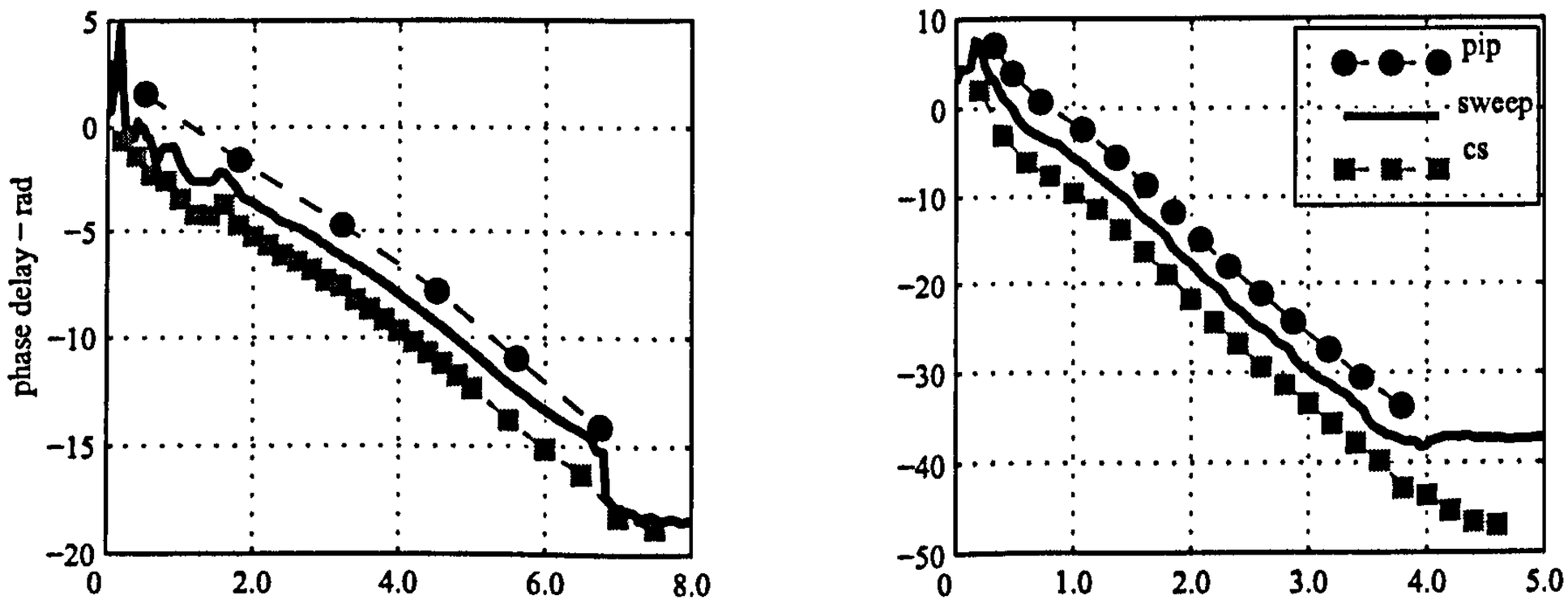

(a) S11 - $h20 \times d75$mm

(b) S29 - $h76 \times d38$mm

Figure 6.22: Comparisons between phase delay curves of sweep signals, pi points and continuous signals for samples S21 and S29.

In both test cases, sample S11 - $h20 \times d75$mm in figure 6.22(a) and sample S29 -

$h76 \times d38$mm in figure 6.22(b), the agreement between the three phase delay curves is very good. Since the three input signals produced similar results, there is no reason to distinguish between them. All three signals are used for all of the samples in the parametric study, but the sweep signals are consistently used to produce most of the presented results due to giving results with better data density, i.e., more data points for each sample.

When obtaining a wave travel time from a phase delay response curve, it is necessary to choose a frequency range from which to calculate the curve's gradient. The selection of such frequency range deserves some attention, since different ranges would produce different travel time estimates. The reason why different results can be obtained is linked to the nature of the phase delay response curve. Three reasons have been identified as being responsible for such difference in gradients: dispersion, phase shifts and noise.

It is worth pointing out that when estimating a wave velocity from a gradient of a range or group of frequencies, from a particular phase delay curve, what is in fact being measured is the group wave velocity. In simple terms, group velocity is the average of the phase velocity of each member of the group. It is important to distinguish between these two concepts, since they produce significantly different results, for instance in terms of dispersion, (Redwood, 1960). For the time domain pulse signal results, only two curve features are used to estimate the wave velocity, one of the input and another of the output signals. What is being measured is therefore the phase velocity of a particular wave component. The differences between phase and group velocity are discussed in section 3.2.

Noise, whenever present, might contaminate the results. It terms of frequency range selection, noise might be a problem if it is felt differently at different frequencies. This means that different frequency ranges might be affected by it in different ways. For the present study, the only source of noise which could not be avoided was

cross-talk, (section 2.6). This form of noise has a relatively low constant magnitude and therefore its interference increases with decreasing magnitude of the received signal. Unfortunately, it was not possible to successfully remove cross-talk noise from the sweep signal responses, as done for harmonic continuous and pulse signals. The reason is that the algorithm prepared for this purpose was not efficient when dealing with sweep signals, (section 2.6.3). Therefore, cross-talk noise must be taken into consideration when determining a frequency range from which to calculate the gradient. For higher frequencies, when the received signal has lower magnitudes, the effect of cross-talk noise is more significant and so these frequency ranges should be avoided.

Figure 6.23 presents an example of the selection of a frequency range. It refers to sample S29 - $h76 \times d38$mm, making use of both its phase delay and magnitude curves. Three frequency ranges are highlighted, the first from 0.3kHz to 0.6kHz, the second from 0.8kHz to 1.7kHz and a third range from 2.0kHz to 3.4kHz. Average wave group velocity estimates of 22.0m.s^{-1}, 37.5m.s^{-1} and 39.5m.s^{-1} correspond respectively to these frequency ranges.

The first range is disregarded because it coincides with a clear response peak of the system, as expressed by the magnitude curve, also plotted in figure 6.23. This resonance is also indicated by the phase delay curve in the form of a phase shift, although quite damped. Such resonances are associated with phase shifts between the input and output signals. The third proposed range is disregarded because it coincided with relatively low values of the magnitude response curve, also because for these frequencies, in the present study, cross-talk noise is expected to have a significant effect on the received signal.

The second frequency range is therefore chosen due to the exclusion of the other two possible frequency ranges. By selecting this frequency range, it is possible to avoid the phase shift that occurs at the resonance peak detected in the first range. It

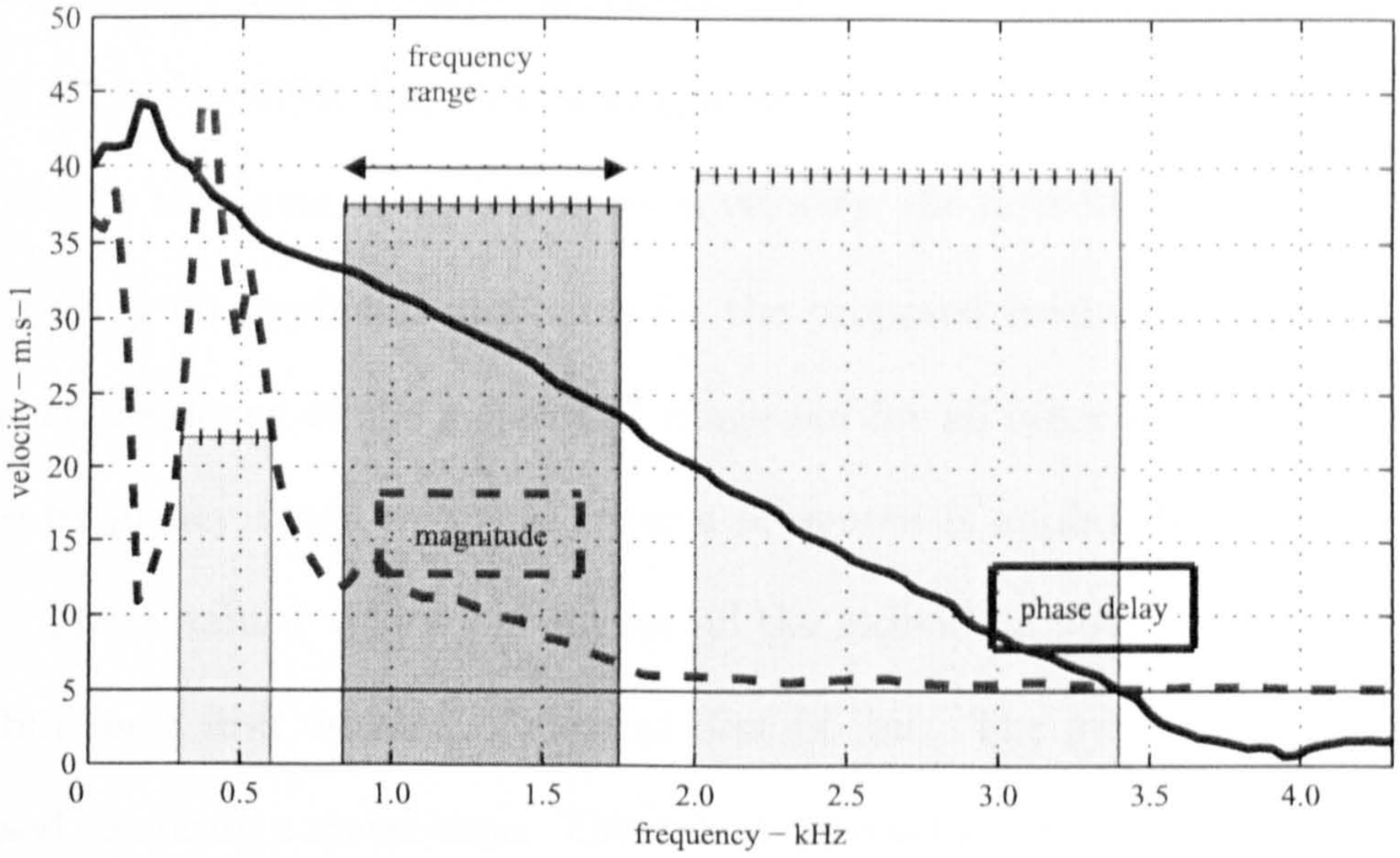

Figure 6.23: Selection of the frequency range used to determine the group wave velocity. Obtained from the phase delay and magnitude response curves, for sample S29 - $h76 \times d38$mm.

is also possible to avoid any significant contribution from the cross-talk noise present in the third frequency range.

While calculating the phase delay and magnitude response curves it is also possible to obtain a coherence curve relative to the input and output signals, as explained in section 2.4. The coherence curve describes the degree of relation of the output signal to the input signal, presented as percentage per frequency. At frequencies where the coherence is near the maximum value of 100% it is possible to admit the output signal to have enough quality, not being too afected by noise of phase-shifts, and should therefore provide trustworthy travel time estimates.

Other potential sources of disturbance related with wave dispersion remain. For the present example the near-field effect is calculated considering the most conservative case of a maximum equivalent shear-wave velocity of $V_s = 50\text{m.s}^{-1}$ and a minimum travel distance from tip-to-tip of $td = 76 - 2 \times 3 = 70$mm, (section 3.6). For the lowest frequency of the proposed range, $f = 0.8$kHz, the near-field shear-

wave component has a relative amplitude of $N_s/F_s = 0.15$ and a phase-velocity ratio of $V_s^n/V_s^f = 0.98$. So, with a weight of around 15% and with a velocity that is practically the same as the shear-wave velocity, the near-field effect can be ruled out as having no significant influence for the proposed frequency range, neither at the lowest frequency of the mentioned range nor for all other higher frequencies.

The frequency range selection criteria presented is applied to all of the sample results. The obtained velocity is not for all the individual points in the phase delay curve but for a first degree polynomial best fit line. The gradient of this curve is then used to obtain a travel time. This travel time is for a group of wave components with slightly different frequencies, and therefore the obtained velocities are the group velocities.

Arroyo *et al.* (2003*a*) proposed a frequency limit concerning the near-field effect. This limit, as given in equation 3.67, can be used with the objective of obtaining the near-field wave components propagation velocity which are less than 5% different than the characteristic compression and shear wave velocities.

6.4.4 Wave Velocity

The wave travel time results obtained for each sample cannot be compared directly between samples with different heights, they need to be normalised into velocities. The velocity results were, at this stage, calculated using a travel distance measured tip-to-tip, (section 1.5).

Some estimates of shear wave velocity have been obtained so far. These values are summarised in table 6.8.

The initial velocity estimates for the parametric study are presented in figure 6.24. The reference wave velocities of 30m.s^{-1} and 50m.s^{-1} are highlighted, defining a range for which the samples' shear stiffness is expected to be at. The proposed

[7]Laser Doppler Velocimeter

Test	Device	V_s
torsional resonance	LDV[7]	$\approx$50m.s^{-1}
flexural resonance	LDV	$\approx$44m.s^{-1}
flexural vibration (2nd and 3rd modes)	bender elements	$\in [30, 50]$m.s^{-1}

Table 6.8: Estimated shear-wave velocity using various dynamic methods.

velocity range is based on the independent sample monitoring presented in section 6.2, and from the analysis of the bender element tested dynamic modal behaviour given in section 6.4.2.

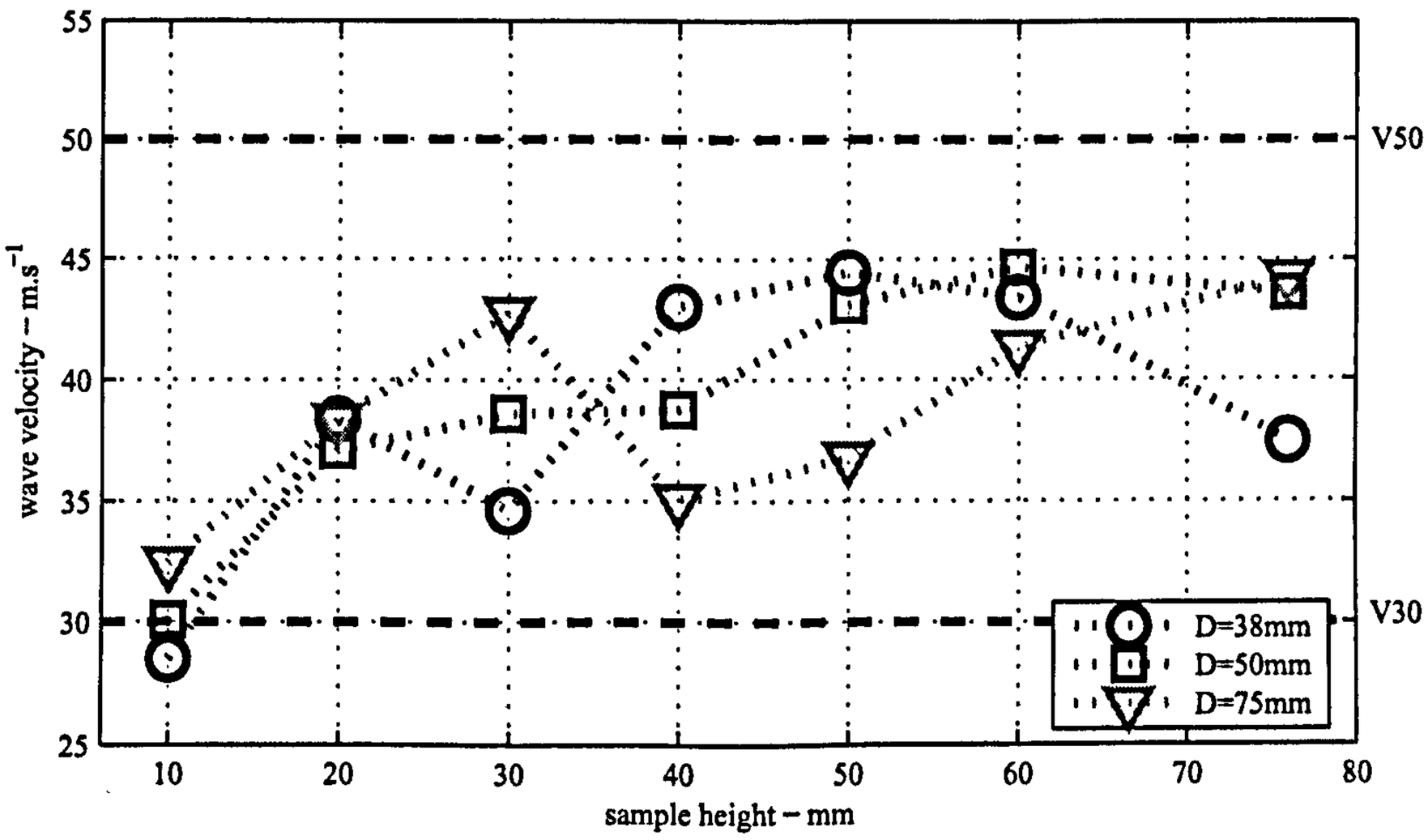

Figure 6.24: Frequency domain wave velocities for parametric study of rubber samples.

Even though the synthetic rubber constituting the samples had similar properties for all sets of samples, some minor differences in stiffness were observed, (section 6.3). These differences, having been quantified, (figure 6.8), are used to normalise the results. Sample S08, the control sample from the sample set with characteristic heights of 10mm, is used as the reference for the normalisation of the remaining sample velocity results. The normalised wave velocities are presented in figure 6.25.

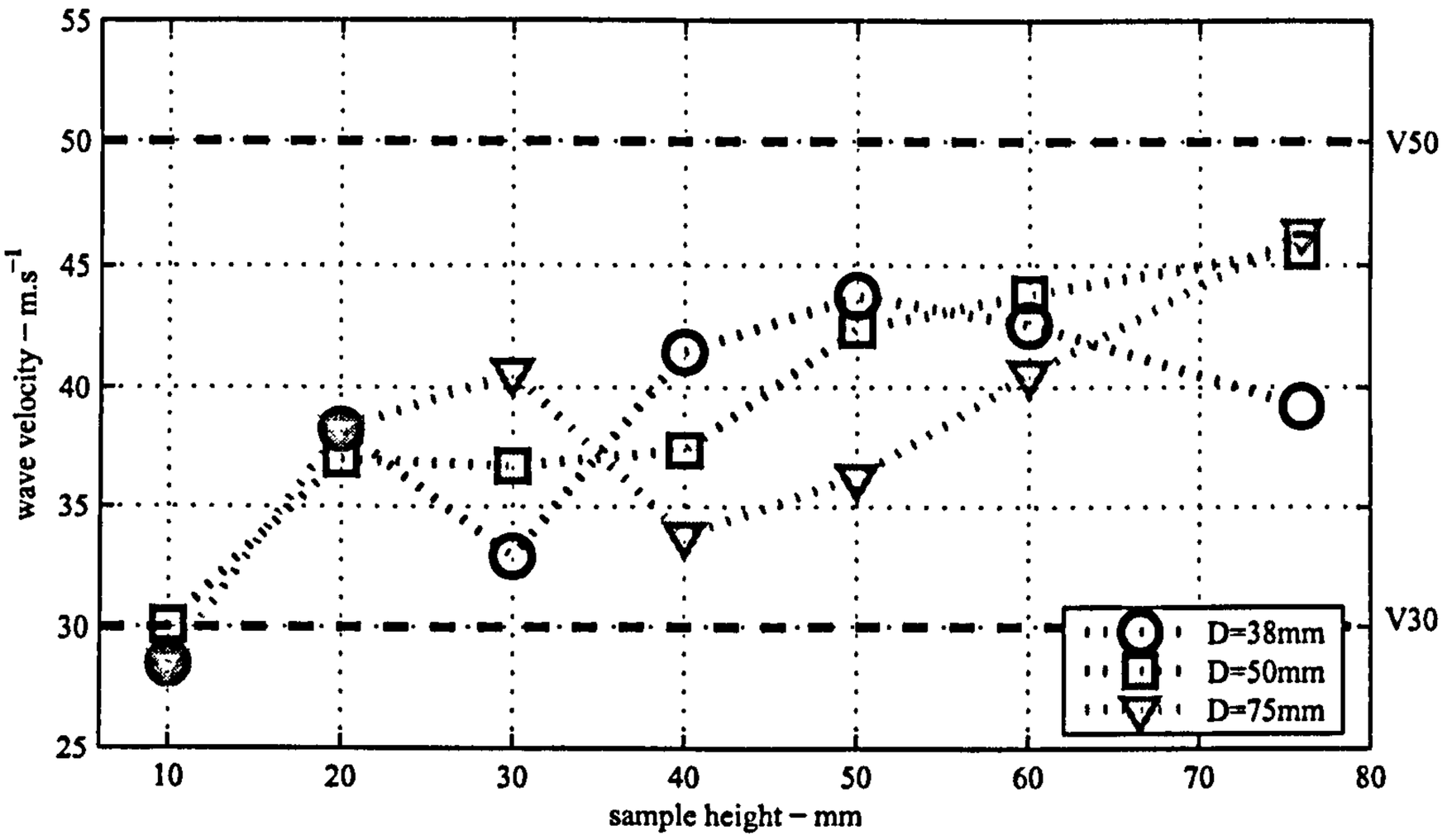

Figure 6.25: Frequency domain normalised wave velocities for parametric study of rubber samples.

The results from figure 6.24 and figure 6.25, one for the non-normalised results and the other for the normalised results, appear to be quite similar. This means that the differences obtained in the control sample tests are not significant which indicates how consistent the properties of the synthetic rubber were.

The analysis of results in either figure 6.24 or 6.25 enables the observation of an overall lower wave velocities for shorter samples. The wave velocity seems to generally increase with sample height. Acknowledging the results for sample of the same diameter, they vary in a similar fashion with sample height; all three curves can be observed to start by increasing, then diminishing and again increasing with increasing sample height. These features of the proposed curves are common for all of them, despite occurring at different heights. The importance of this observation will become apparent in section 6.6.2, where the relation with sample geometry is further explored.

Another characteristic of the results deserves some attention. The fact that for all sample diameters the results from the shortest samples, $H = 10$mm, are

significantly lower than the remaining results, and will also be explored further in section 6.6.1 in relation to wave travel distance.

6.5 Time Domain

In this section the results of the parametric study are studied mainly in the time domain. The wave velocity results are obtained directly from the time histories of the transmitted and received pulse signals. Pulse signals are commonly used when testing soil samples with bender elements. This methodology has its roots in the practice of cross-borehole testing, in which pulse signals are also employed. Moreover, the signal time histories, and especially those of pulse signals, provide a very intuitive reading.

6.5.1 Bender Element Performance

It has already been shown that the transmitted signal and the corresponding transmitting bender element motion are not the same for a short duration input signal such as a sinusoidal pulse, (chapter 5). The actual bender element movement does not stop at the same time as the input signal does, it carries on oscillating in what looks like the vibration of a damped MDOF system. Also, there is a clear phase delay between the input signal and the bender element movement, which varies with the frequency of the input signal. Like in a simple dynamic system, a significant phase shift could be observed at the natural frequency of the bender element. Finally, it is worth mentioning that for pulse signals, the transducers are only capable of achieving a transient response state, which means that its response, namely the frequency of its response is controlled by the dynamic properties of the transducer and not those of the excitation signal.

To summarise, it has been demonstrated in chapter 5 that the input signal does

not correspond to the actual movement of the transmitting bender element. This observation carries a significant consequence in that when using any feature of the transmitted signal as a reference against which to measure the travel time, the chosen feature might not correspond to any feature of the actual transducer vibration. This observation can also be extended to the receiving transducer. Hence, if a feature from each signal is used, then the measured travel time might have no correspondence with the actual wave behaviour.

Dispersion is another factor which must also be considered when dealing with the time histories of the transmitted and received signals. If a propagating wave is formed by components with different frequencies and if each of these components travel at different velocities then the wave signal will not look the same at any two separate points of the sample, including the transmitting and receiving end of the sample, i.e., the propagating signal will become increasingly distorted with travel distance. Two forms of dispersion have been established so far, the near-field effect and the geometric or waveguide dispersion, (section 3.7). Sinusoidal pulse signals, such as those normally used to excite bender elements, have a broad frequency content, (figures 5.15 and 5.21). Besides, the actual transmitted wave might not be equal to the transmitted signal. For these reasons, when using pulse signals, little control over the frequency content of the actual transmitted wave is left for the test operator and therefore little or no control over the frequency dependent dispersion phenomena.

For all these reasons, it does not seem reasonable to use the time histories from pulse signals to determine a medium's equivalent shear wave velocity. Yet, because they are so frequently used and because they provide such intuitive results, their properties are further explored in this section.

6.5.2 Differences and Similarities Between Signals

Figure 6.26 contains the time history responses from samples S09 - $h20 \times d38$mm, S10 - $h20 \times d50$mm and S11 - $h20 \times d75$mm for an input signal of 3.0kHz. These three samples are from the same set, i.e., have the same height but different diameters.

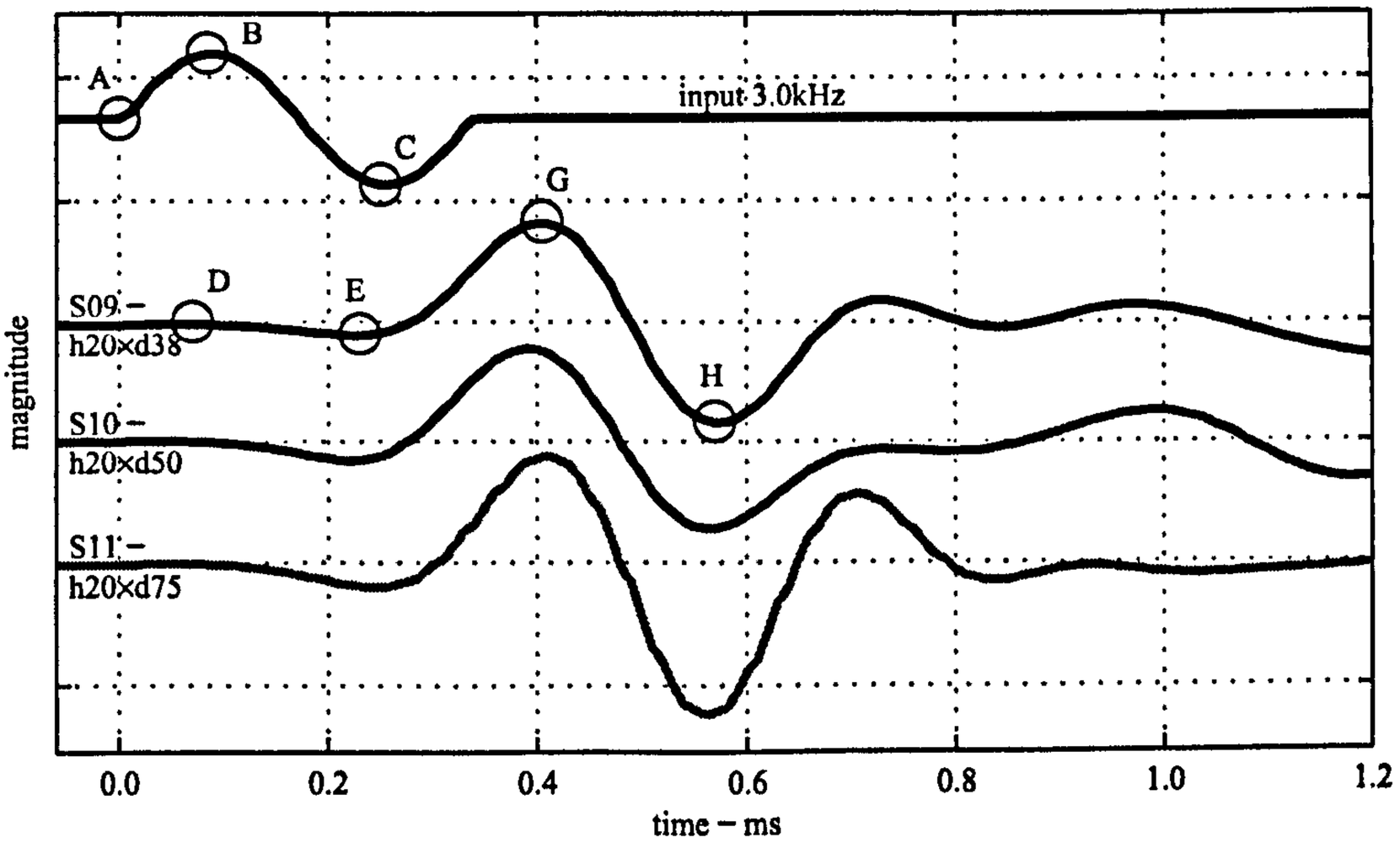

Figure 6.26: Received pulse signals in samples S09, S10 and S11, for an input of 3.0kHz.

The response signals in figure 6.26 are clearly similar to each other. Some signal features occur at around the same time: the first offset at around 0.1ms, the first local minimum at around 0.23ms, the first maximum at around 0.4ms, and the following minimum at around 0.56ms, are present in all the signals. Despite being similar, these features noticeably do not occur at exactly the same time, with the signals becoming even more distinguishable after a time of around 0.56ms.

The mentioned features of the studied responses, first arrival, first local minimum or first inflexion, first maximum and following minimum, are commonly used in pulse signal time history interpretation. They have been identified in figure 2.2 as D, E, G and H respectively and are presented again in figure 6.26.

The magnitude of the first local minimum at around 0.23ms, takes different

values for each signal, both in absolute terms but also in relation to other signal features such as the first maximum at around 0.4ms. This first local minimum is a common feature of pulse signal responses when testing with bender elements, and their origin is subject to discussion. Being usually associated with the near-field effect, (Hardy *et al.*, 2002), the observed magnitude variation with diameter might help to clarify their presence.

The example time histories in figure 6.26 have already been noted by their similarities as well as differences. In fact, they are one of the studied sample set cases where the time domain results most resemble each other. Other comparisons between the responses of samples of the same set proved to be significantly more dissimilar. Figure 6.27 presents a second example for samples S29 - $h76 \times d38$mm, S30 - $h76 \times d50$mm and S31 - $h76 \times d50$mm. Again, the proposed three samples are from the same set and therefore considered to have exactly the same material properties. The signal used is a sinusoidal pulse signal with a central frequency of 3.0kHz.

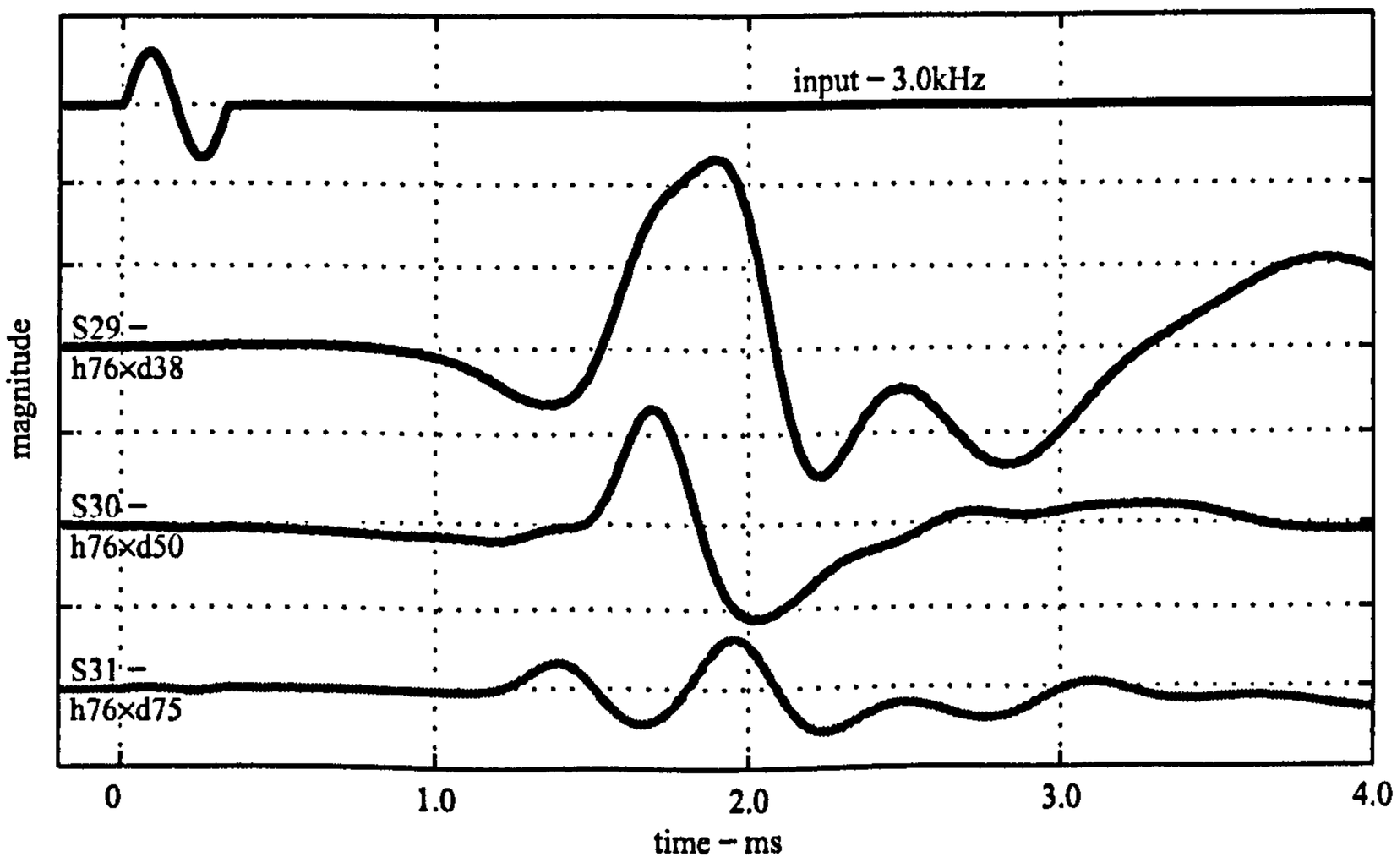

Figure 6.27: Received pulse signals in samples S29, S30 and S31, for an input of 3.0kHz.

Figure 6.27 presents the response time histories of samples S29, S30 and S31. The received signals are quite different from each other, despite having used the same excitation signal and having traveled the same distance on the same medium. The first offset can be detected at around 0.75ms for sample S29, at either 0.4ms or 1.2ms for S30 and at around 1.1ms for S31. The first local minimum feature is located at 1.36ms for S29, at either 1.2ms or 1.4ms for S30 and at around 1.1ms for S31. The following peak features, i.e., the first maximum and the following minimum, also do not coincide in terms of time or magnitude.

If any of the curve features were to be used to estimate the wave travel time, than three different results would be obtained for three samples made of the same material and with the same height. These results would also be different depending on the chosen signal feature. For example, the first local minimum provides an estimated wave velocity of $52m.s^{-1}$, $50m.s^{-1}$ and $64m.s^{-1}$ for samples S29, S30 and S31 respectively. These values are manifestly different from each other, with a variation in the range of 16%. This for a test where the samples are made from exactly the same material and a great deal of effort was placed in the test set-up. Such a variation in results is remarkable, especially when compared with the obtained repeatability baseline error of 1%, (section 6.3). And, for sample S31, the obtained result is significantly outside the range of estimated shear wave results obtained so far, check table 6.8.

Table 6.9 contains the different wave velocity estimates for the three samples, for each of the curve features. The corresponding pulse signal features notation is illustrated in figure 2.2 or 6.26.

The difference between travel times obtained using the same signal features can vary by as much as 30%. The variation between travel times obtained using different features is even greater. For sample S29, the results obtained using A-D is 160% greater than the result from C-H. Knowing the samples are made from exactly

Feature	S29 - $h76 \times d38$	S30 - $h76 \times d50$	S31 - $h76 \times d75$	Variation
A-D	93m.s^{-1}	58m.s^{-1}	64m.s^{-1}	30%
A-E	52m.s^{-1}	50m.s^{-1}	64m.s^{-1}	16%
B-G	39m.s^{-1}	44m.s^{-1}	54m.s^{-1}	18%
C-H	35m.s^{-1}	40m.s^{-1}	50m.s^{-1}	20%

Table 6.9: Wave velocity estimates from figure 6.27.

the same medium, and that the travel distance is the same for all cases, than the differences between signals can only be explained by geometry dependent dispersion, also refered to as waveguide dispersion. Remembering how the frequency of the response can not be controled using pulse signals, then there is no feasable way of obtaining conclusive results for the present example using pulse signals.

6.5.3 Pulse Signal Features

In order to observe the evolution with input signal frequency of the identified features of the response time histories, the corresponding travel times were recorded for various frequencies. The travel times were measured directly between the transmitted and received signal features. Figure 6.28 presents the travel time results from sample S11 - $h20 \times d75$mm, chosen for being a good example of a bulk sample and having been used in the example of figure 6.26. The equivalent travel times for the shear wave velocity estimates of $V_s = 30\text{m.s}^{-1}$ and $V_s = 50\text{m.s}^{-1}$ are also presented and are identified by references V30 and V50, located at 0.47ms and 0.28ms respectively.

The travel time results obtained for different signal features, (figure 6.28), indicate a distortion between the transmitted and received signals, that varies with input signal frequency. An undistorted signal would produce similar travel time estimates for all of the chosen features. What can be observed is that at most frequencies, the features produce different travel times estimates. In summary, the distortion of

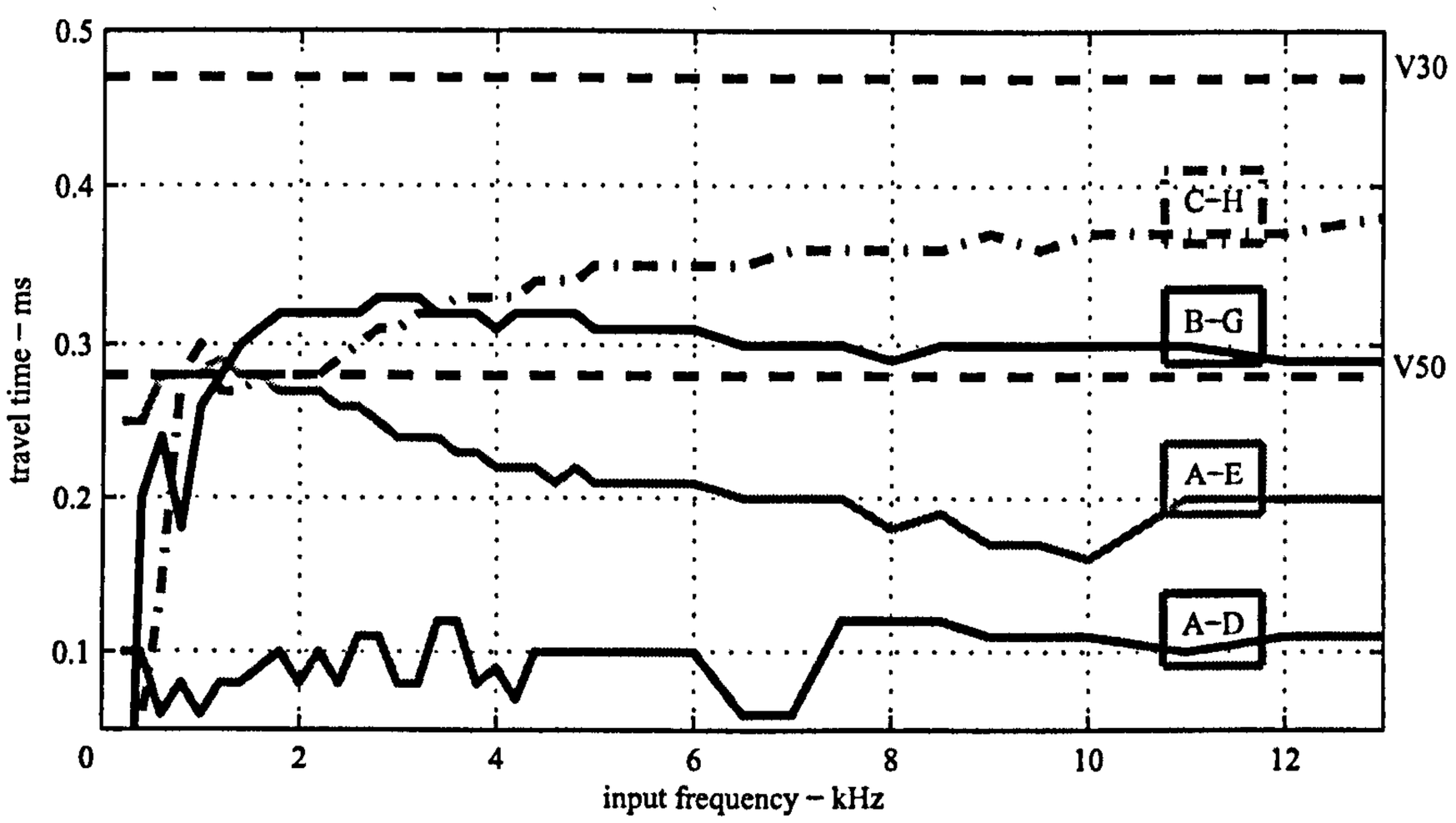

Figure 6.28: Different travel times estimates for sample S11, for varying input frequencies.

the propagated wave can be introduced by a number of factors, such as the actual mechanical response of the benders to the existing signals, (section 5.5), and the mechanical response of the sample itself, (section 6.4.2). It can also be caused by dispersion phenomena.

In figure 6.28, the travel time measured between the first offset of the transmitted and received signals, A-D, gives travel times in the range $tt_{\text{A-D}} = 0.1\text{ms}$, falling substantially below the range of V50. This travel time value corresponds to a wave velocity of around $V = 140\text{m.s}^{-1}$, meaning it is clearly a consequence of dispersion. The travel time measured between the transmitted signal first offset and the received signal first local minimum, A-E, varies between 0.30ms at lower frequencies of around 2kHz and decreases almost linearly reaching travel times of 0.16ms at signal frequencies of 10kHz. This minimum travel time is equivalent to a wave velocity of $V = 88\text{m.s}^{-1}$, again well outside the proposed range of wave velocities, indicating it might consistently overestimate the wave velocity.

The travel times measured between transmitted and received signals first max-

ima, B-G, and the travel time measured between the second minimum of the transmitted and received signals, C-H, both reach stable results of around $tt_{\text{B-G}} = 0.30\text{ms}$ and $tt_{\text{C-H}} = 0.38\text{ms}$ that correspond to wave velocities of $V = 47\text{m.s}^{-1}$ $V = 37\text{m.s}^{-1}$, well within the proposed range.

In figure 6.29 similar results to the ones in figure 6.28 are presented, now for sample S29 - $h76 \times d75\text{mm}$, the most slender geometry in contrast to sample S11. The objective of using two samples with such different geometries is to maximise the range of possible results that can be obtained from samples made of from the same material, when using the time domain pulse signal technique.

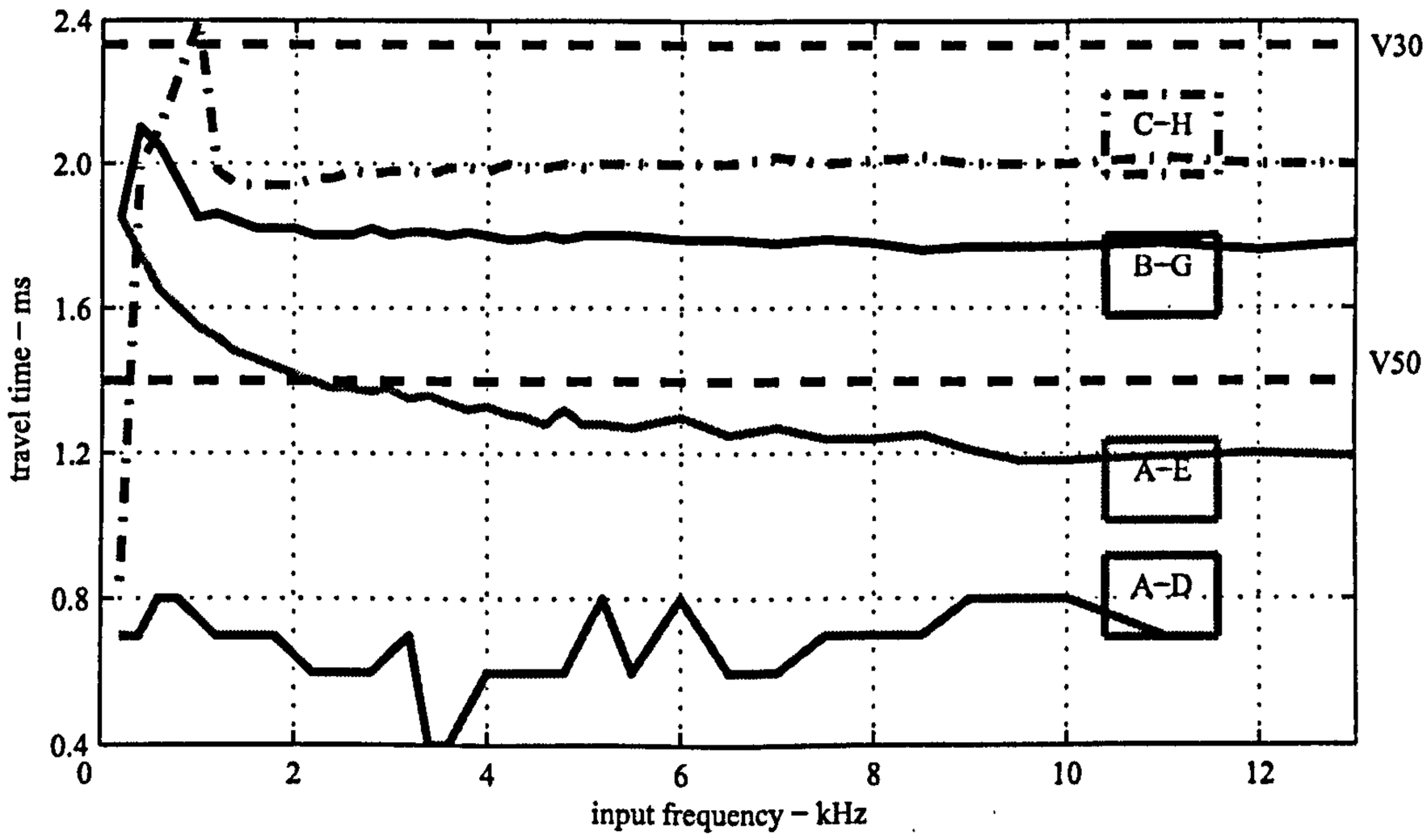

Figure 6.29: Different travel times estimates for sample S29, for varying input frequencies.

Again the received signal is distorted in relation to the transmitted signal. Comparing with the results of sample S11, it can be seen that both cases present similar travel time curves with input signal frequency, with greater variations at lower frequencies, gradually growing more stable for higher frequencies. One observable difference is that for the case of sample S29, this stabilisation occurs at lower frequencies and appears to be more regular.

The travel time results for features B-G and C-H are again within the proposed range defined by V30 and V50. The results for features A-E go out of the mentioned range. They do so for higher frequencies, reaching more reasonable travel time values. A travel time of 1.4ms is equivalent to a wave velocity of 58m.s^{-1} for sample S29. Nevertheless, the estimates from features A-D are, as for S11, very low, producing wave velocities in the range of 100m.s^{-1}.

Having analysed the results from two samples with remarkably distinct geometries, the fact that the results in figures 6.28 and 6.29 are apparently similar is considered relevant. Both cases present a clear distortion between transmitted and received signals, except for a few input frequencies. Both give features B-G and C-H results within the expected range of shear wave velocities and are the ones that indicate the most suitable travel times estimation. Features A-E in both examples give results which estimate relatively high wave velocities of $\geq$ 55m.s^{-1}. Both examples produce features A-D results, which produce very high wave velocities of $\geq$ 140m.s^{-1} and $\geq$ 100m.s^{-1}, for S11 and S29 respectively. Keeping in mind that for a shear wave velocity of $V_s = 50$m.s^{-1} and a Poisson's coefficient of $\nu = 0.45$, the compression wave velocity would be $V_p = 170$m.s^{-1}, the first arrival is neither due to pure compression wave components or to a shear wave component. It must therefore be attributed to dispersion phenomena. For example, travel velocities faster than the characteristic shear wave velocity can be obtained for wave phase velocity dispersion, (figure 3.16).

6.5.4 Frequency Content of Received Pulse Signals

The frequency content of the received pulse signals in samples S11 - $h20 \times d75$mm and S29 - $h76 \times d38$mm are studied in this section, with the objective of studying the transformation the signals suffer after being propagated though the samples.

The frequency content was determined for response signals corresponding to in-

put signals with different central frequencies. The frequency content of each signal was obtained using the fast Fourier transform, FFT. Figure 6.30 presents the frequency content of 6 received pulse signals in sample S11, with input frequencies between 1kHz and 11kHz. Figure 6.31 presents the frequency contents of 6 received pulse signals in sample S29, with input frequencies between 0.4kHz and 2.4kHz. Different frequencies are used for each sample, since each sample is limited in terms of the range of frequencies they can successfully propagate, (section 6.4.1).

In figure 6.30, the frequency content for an input signal of 1kHz in sample S11 has two peaks, one at 0.6kHz and another at 1.0kHz. These peaks occur at frequencies within the range at which the theoretical characteristic frequencies of the first mode of flexural vibration and second mode of torsional vibration of a similar bar would occur. These characteristic frequencies were obtained using a Bernoulli-Euler beam model of the sample, i.e., a cantilever with a mass on the free top end, (section 6.4.2).

The following responses for higher input frequencies can be observed to present a broad peak, ranging from 3kHz to 4kHz. These responses seem to be independent from the frequency of the input signals. The bender elements, when embedded in a similar rubber sample, have been observed to have a flexural resonance frequency around this same range of frequencies, 5.0kHz, (figure 5.16). It is then possible that, for the shorter sample S11, the observed responses for higher input frequencies are dominated by the response of the bender elements.

The test system formed by sample S11 and bender element transducers respond distinctly to different pulse input frequencies. For lower frequencies, the sample's dynamic properties dominate the response of the system. For higher frequencies, the transducers' dynamic properties appear to dominate the response of the system. This distinction highlights the importance of considering the dynamic properties of both the sample and the transducers.

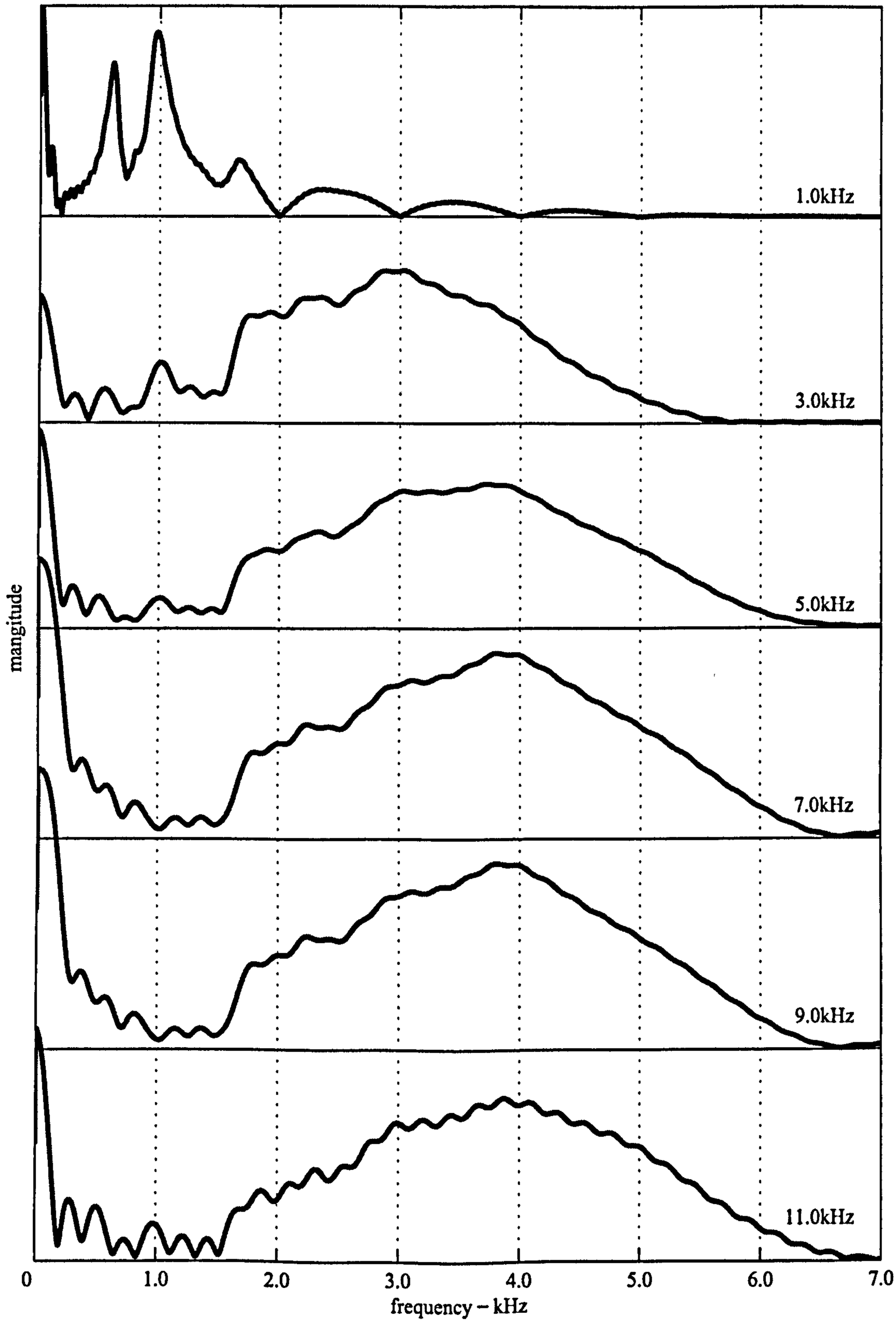

Figure 6.30: Frequency content of received pulse signals in sample S11 - $h20 \times d75$mm, for different frequency inputs.

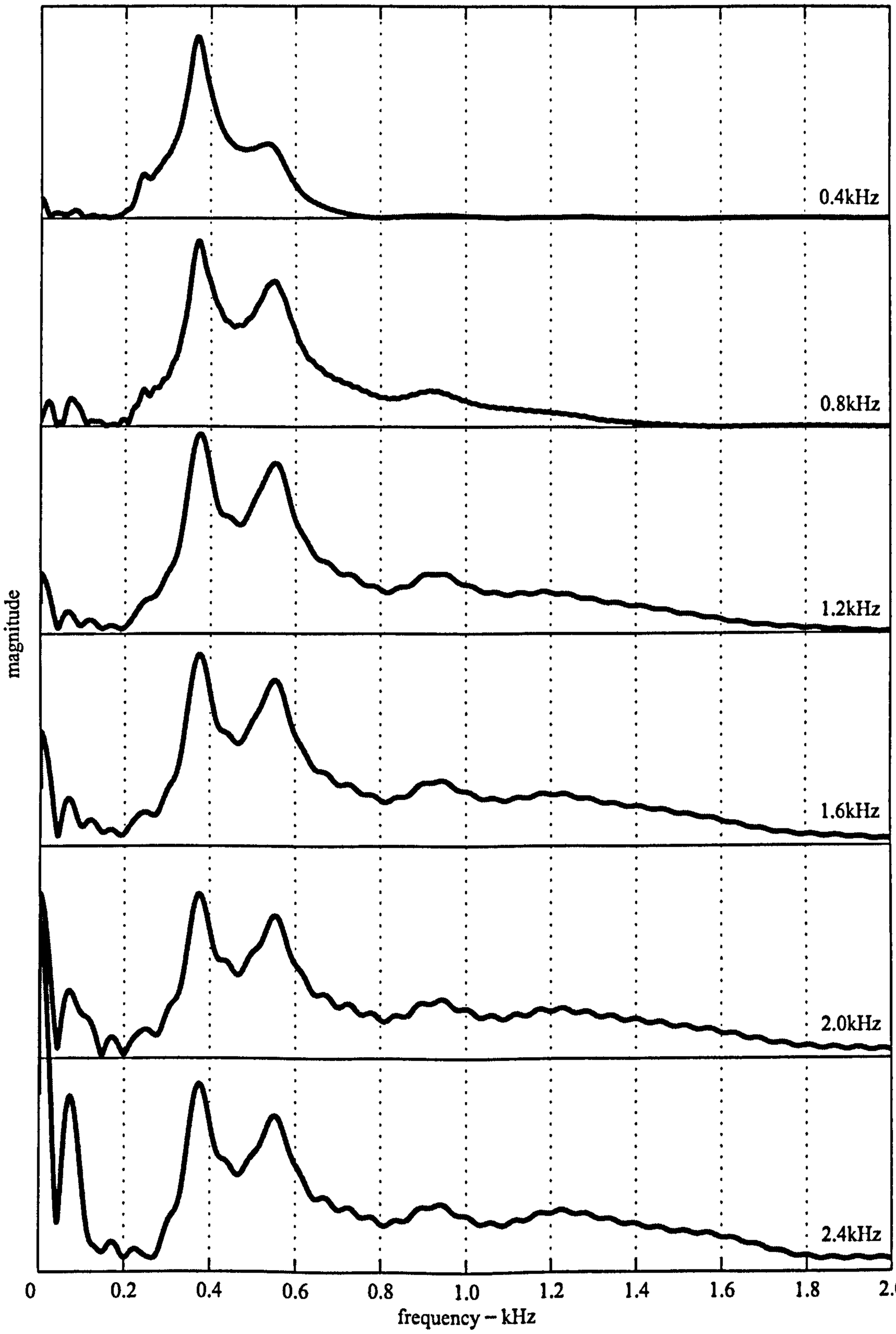

Figure 6.31: Frequency content of received pulse signals in sample S29 - $h76 \times d38$mm, for different frequency inputs.

The frequency contents of the pulse responses obtained for sample S29 are given in figure 6.31. The presented results are for input signals with frequencies up to 2.4kHz after which no significant changes occur to the shape of the received signal. Signals with higher frequencies gave similar results, where only the magnitude of the response attenuates.

Independently from the frequency of the input signal, all of the presented responses can be observed to have two clear peak features, one at 0.38kHz and another at 0.55kHz. These features have already been identified in section 6.4.3, especially the feature at 0.38kHz, which was associated with the second flexural modes of vibration of this sample. The feature at 0.55kHz was thought to be related with the second mode of torsional vibration, although this result has not been confirmed, (figure 6.21).

Comparing the behaviour of the dynamic systems comprising samples S11 and S29, a number of observations can be made. In sample S11, for most of the input signals, the dynamic properties of the transducers dominated the response. For sample S29, the dynamic properties of the sample itself dominated the response. As observed in section 6.4.1, taller samples limit the maximum frequencies which can successfully propagate through them. This means that the wave that reaches the receiving bender element does not have enough frequency content to excite it at its own natural frequency, and so its contribution to the overall response of the system is not as significant. Another empiric way of explaining this behaviour is that for the system where 'less sample separates' the transducers, the overall behaviour is dominated by the dynamic properties of the transducers. For a test system where 'more sample' separates the transducers, the overall behaviour is dominated by the dynamic properties of the sample.

It is worth relating the frequency content presented in figures 6.30 and 6.31 with the peak features results given in figures 6.28 and 6.29. In the case of sample S11,

the frequency at which the response indicates some form of resonance, at frequencies around 3kHz and 4kHz, coincides with the frequency range at which less distortion can be observed from the feature results. Around these frequencies, for the two most significant pair of signal features, B-G and C-H, the correspondent travel time estimated values are most similar. For sample S29, the travel time estimates for signal features B-G and C-H are most similar for lower input frequencies, but it is not possible to make a direct comparison, since for input frequencies lower than 1kHz, the peak feature results are most unstable.

Having observed the relation between two aspects of the dynamic response of the tested systems, i.e, the minimum received signal distortion for input pulse signals' central frequencies near their resonance frequencies, such input frequencies were henceforward chosen to provide the responses used for the time domain parametric study. So, for each sample, multiple input pulse signals with different frequencies were used and the result for the one producing the least distorted response was chosen.

The pair of features B-G and C-H, measuring the travel time between the main maximum and minimum features of the transmitted and received signals, were chosen to estimate the travel time value used in the parametric study. This travel time was calculated as the average of the two B-G and C-H estimates. This way, a consistent collection of results based on a set of concepts which can be replicated in other test systems, obtaining travel time estimates for signals with minimum distortion between input and output, and at which a significant frequency content is observable in the response. Moreover, as seen in figures 6.28 and 6.29, among the possibly signal features, these were the ones leading to the most credible estimates in terms of previously observed wave velocity of the samples, (table 6.8).

6.5.5 Dispersion in Results

The received pulse signals were analysed again, now with the objective of better understanding the two distinct dispersion phenomena associated with bender element testing, geometry dispersion and near-field effect. The received signal feature E, as illustrated in figure 2.2, is usually associated with the near-field effect, (Brignoli *et al.*, 1996). The travel time results presented so far, (figures 6.28 and 6.29), include the travel times obtained using the received signal first inflexion marked as feature E. These seem to correspond to travel times faster that the proposed range of possible shear-wave travel times. Thus, for the results obtained so far, the received signals have a clear presence of dispersion that can be associated with received signal feature E.

In section 3.6, the results concerning the near-field effect are presented as a ratio between the near-field and the far-field wave component magnitudes and velocities. In order to determine the relation of feature E with the near-field effect, feature G was chosen as being associated with the far-field wave components, since it provides travel time results well within the proposed range. The ratio between the magnitude of the signal associated with these two features, E and G, is calculated for a number of pulse signals and for all the samples used in the present parametric study. The signal feature notations E and G must not be mistaken with the Young's modulus, E, or shear stiffness, G.

Figure 6.32 presents the ratio between the magnitudes of features E and G, as identified in figure 2.2, for samples S11 and S29. These results were obtained for a range of the input signal frequencies. The consequences of dispersion due to wave reflection and near-field effect are expected to be different for these two samples. For sample S11 - $h20 \times d75$mm, which is low and broad, the lateral boundaries are distant from the direct wave travel path and the receiver is near the source. So

dispersion due to wave reflection is expected not to be relevant and dispersion due to near-field effect is expected to be quite significant. Sample S29 - $h76 \times d38$mm, on the other hand, has lateral boundaries nearer the direct travel path, in absolute and in relative terms, and has a much longer absolute travel path. Sample S29 can therefore be expected to have dispersion dominated by different causes, i.e., to have a relevant dispersion due to wave reflection and less due to near-field effect.

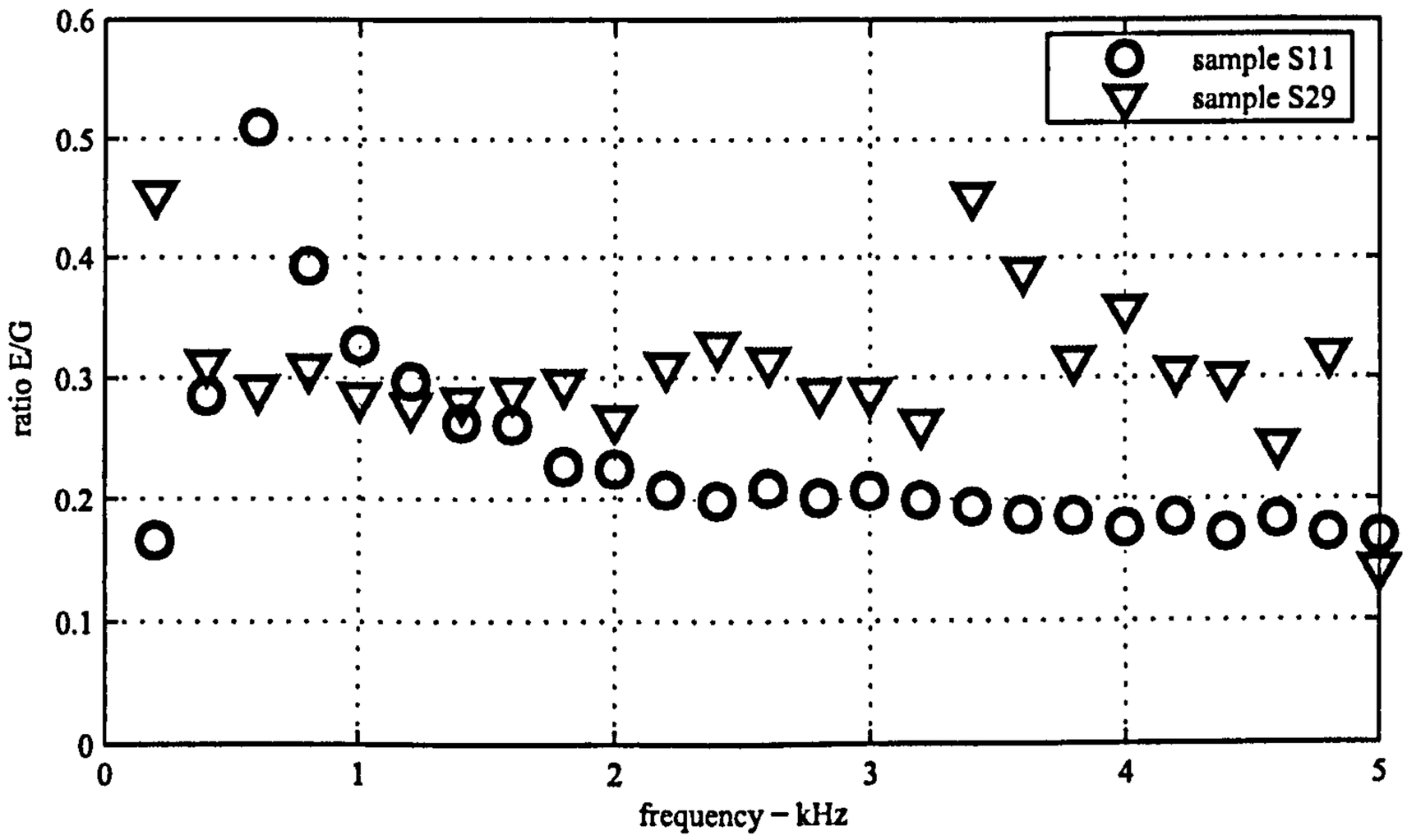

Figure 6.32: Ratio between signal features E/G for samples S11 and S29 collected for a range of input signal frequencies.

In figure 6.32, in the case of sample S11, the ratio can be observed to decrease sharply from its initial maximum value, stabilises at around 0.2. For sample S29, the ratio also has an initial maximum and stabilises at around 0.3. The ratio values, for sample S29, becomes more scatared for input frequencies higher than 3kHz. Theoretical calculations for the near-field effect only place a similar magnitude ratio at 0.15 and 0.20 for samples S11 and S29, using their respective travel distances and dominating received signal frequencies. Hence, the theoretical values of near-field ratio do not match the values obtained with features E and G, but predict a higher near-field effect for sample S29. The fact that the predictions do not match

the observed ratios, being in fact lower than them, might be another indicator that wave reflection must also be a contributor to the observed dispersion.

The same E/G ratio was also calculated for all the samples taking part in the parametric study. The corresponding results are presented in figure 6.33, according to sample diameter and height. The theoretical near-field effect was also calculated for equivalent travel distances and input signal frequencies used. It is presented in the form of the ratio given by the shear wave near-field component over the shear wave far-field component, N_S/F_S. These theoretical results were calculated according to the method presented in section 3.6 and illustrated in figure 3.19(b). Assuming that feature E is related to dispersion, the objective of comparing the E/G ratio with the equivalent near-field ratio is to distinguish which dispersion is due to near-field and which is due to the presence of the geometric boundaries and wave reflection.

In figure 6.33(a), the results concerning the samples with diameters $D = 38$mm are presented. The near-field theoretical results are quite similar to the E/G ratio from the received pulse signals, for lower sample heights $H \leq 30$mm. For taller samples, the E/G ratio produces values considerably higher than the near-field results. For lower samples, the direct wave travel distance is much smaller than any possible reflected wave path. For this reason the lateral boundaries, believed to contribute to the geometric wave dispersion, have less influence on the overall wave propagation. As the sample height increases, the reflected travel paths become more similar to the direct ones, hence increasing the influence of sample geometry as the origin of dispersion.

In figure 6.33(b), the results for samples with intermediate diameters, $D = 50$mm, are presented. The near-field estimates are now similar to the E/G ratio for samples up to 40mm height. The same principles explained for the 38mm diameter samples would also explain this observation and why the similarity in results is

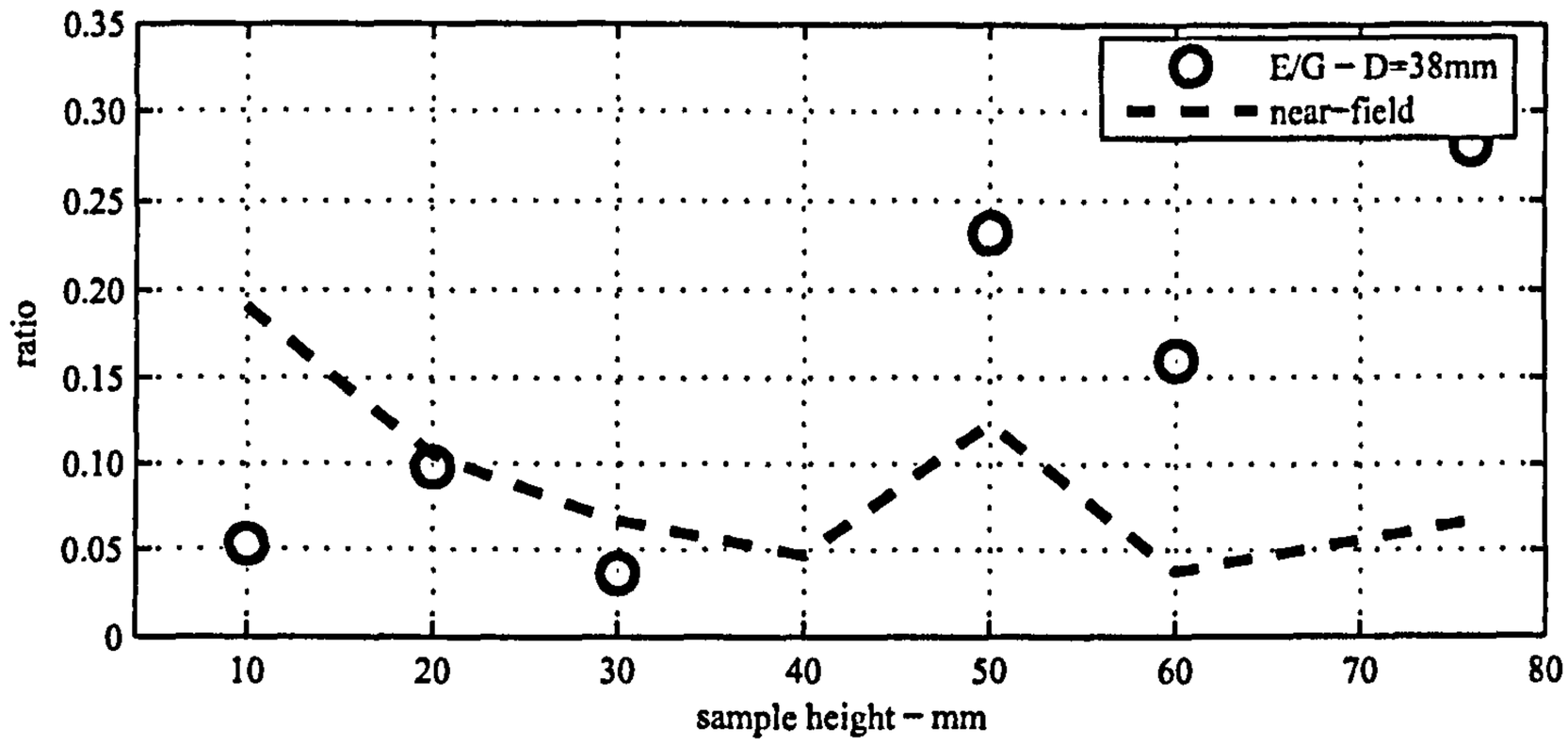

(a) $D = 38\text{mm}$

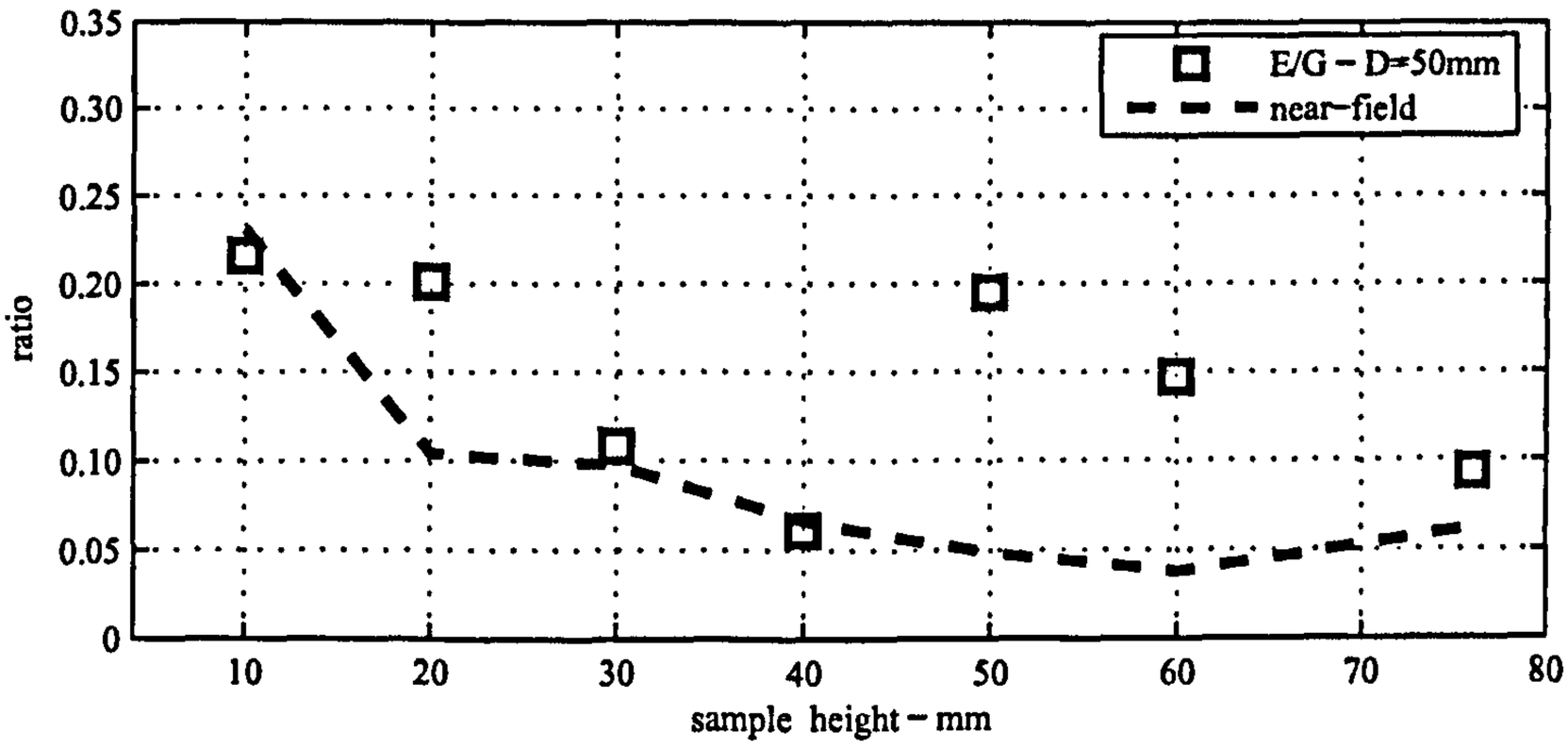

(b) $D = 50\text{mm}$

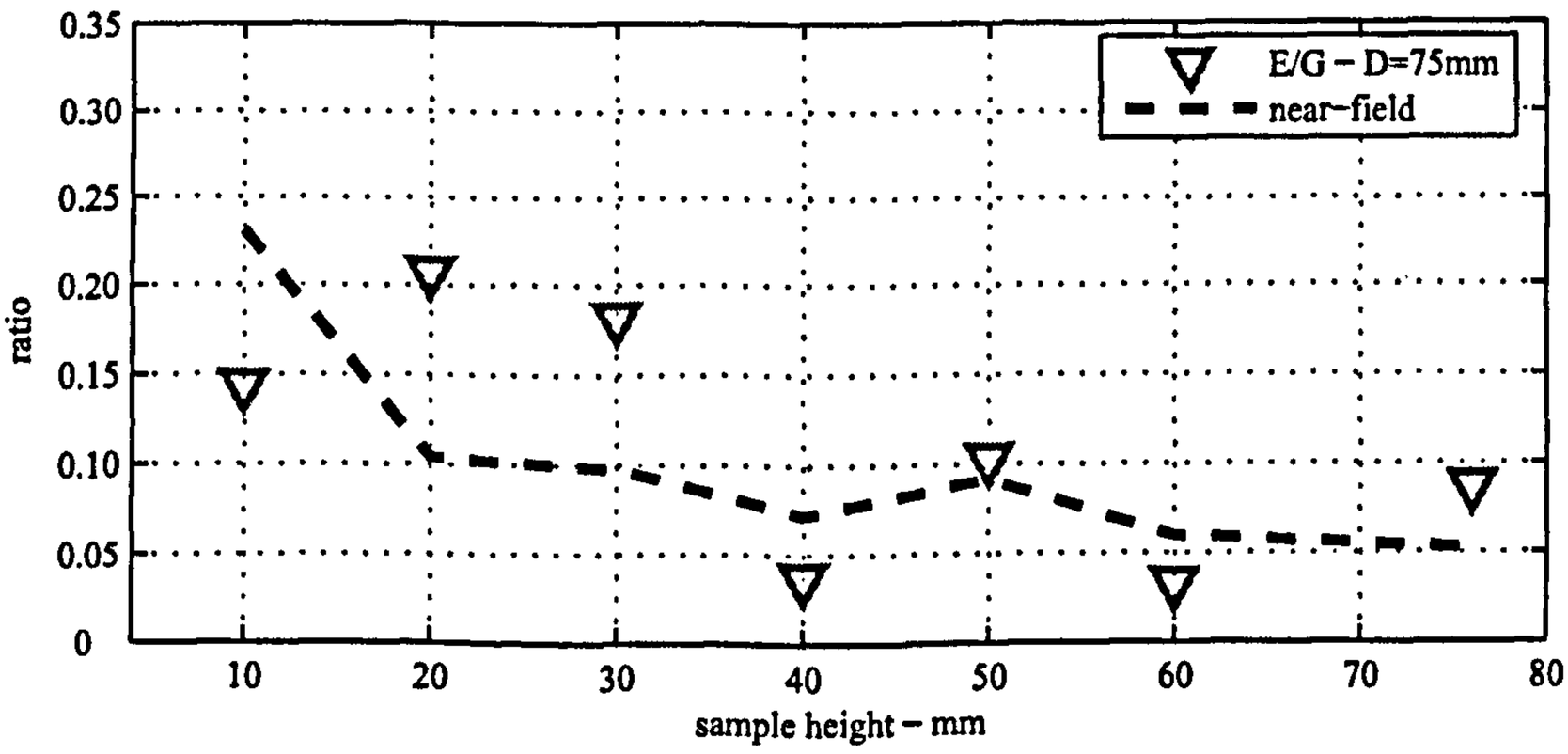

(c) $D = 75\text{mm}$

Figure 6.33: Features E/G ratio in received pulse signal and theoretical near-field effect.

present up to taller samples. Since their diameters are larger, only for taller samples does the reflected wave travel paths become more similar to the direct travel path.

In figure 6.33(c), the results for samples with the largest diameter, $D = 75$mm, are presented. This is the case where for all of the sample heights the E/G ratio seems to be more closely related with the near-field estimates. The same principle of direct and reflected travel paths presented for the previous two cases is not only again valid but further reinforced.

The irregular variation with sample height of the theoretical near-field results occurs because the frequency used to determine each N_S/F_S ratio is the same as that of the input signal chosen to test each sample. Since different frequencies were chosen for the input pulse signals, according to the actual response of each sample, then different values of near-field effect were also obtained.

Together, the analysis of all the E/G ratio allows a number of observations. All samples have some form of dispersion present. In lower and broader samples, dispersion is mainly caused by the near-field effect. In taller and narrower samples, dispersion is caused by both the presence of wave reflection and the near-field effect. So, it is important to consider not only near-field, but also the significant dispersion caused by presence of geometric boundaries.

The objective of eliminating dispersion from the received pulse signal might not be possible to achieve. It has been shown that the dynamic behaviour of the bender element transducer and of the samples, (section 5.8, 6.2 and 6.4.2), cannot be controlled by the frequency of the input pulse signal. Neither the transmitting bender element nor the sample can be made to vibrate at frequencies higher than their own natural frequencies when excited by a short duration signal, such as a pulse signal. In terms of near-field effect. the remaining option would be to increase the travel distance, but by itself this is not an effective solution, since the waveguide dispersion increases for slender samples. Another possibility is to increase the height

and the diameter of the sample, so as to minimise the near-field and the waveguide dispersions. This last option is also not practical, especially if the bender element tests need to be conducted in a standard-size sample as for example the $h76 \times d38$mm of the triaxial cell. For such standard geometry samples the effects of dispersion might be an unavoidable side effect of testing with pulse signals.

6.5.6 Pulse Signal Velocity

Up to 45 pulse signals with different central frequencies were used to test each of the 24 samples included in the parametric study, (table 6.2). The determination of the wave travel time, as explained generally in section 2.1, was made using the transmitted and received signals maxima and minima features, identified as B-G and C-H, and illustrated in figure 2.2. The reasons for choosing these two features, rather than the first arrival, have already been presented in section 6.5.4. The wave velocity estimates were obtained by averaging the travel time recorded for each of the two mentioned signal features for a transmitted pulse signal with a frequency chosen so as to have minimum signal distortion, as well as a significant received signal frequency content. This frequency coincides with the input signal frequency at which the two travel time estimates are most similar.

Figure 6.34 presents the wave velocity estimates obtained from the measured travel times using pulse signals in the indicated manner and for a wave travel distance measured tip-to-tip. These velocity estimates are presented according to sample diameter and height. The presented values for each sample set are corrected according to the observed differences between sets of samples as measured in the control samples, (section 6.3).

From figure 6.34 it can be observed that the wave velocities significantly increase with sample height up to 40mm, down from around 25m.s^{-1} up to around 50m.s^{-1}, which is a very significant increase. Up to sample heights of 40mm, the velocity

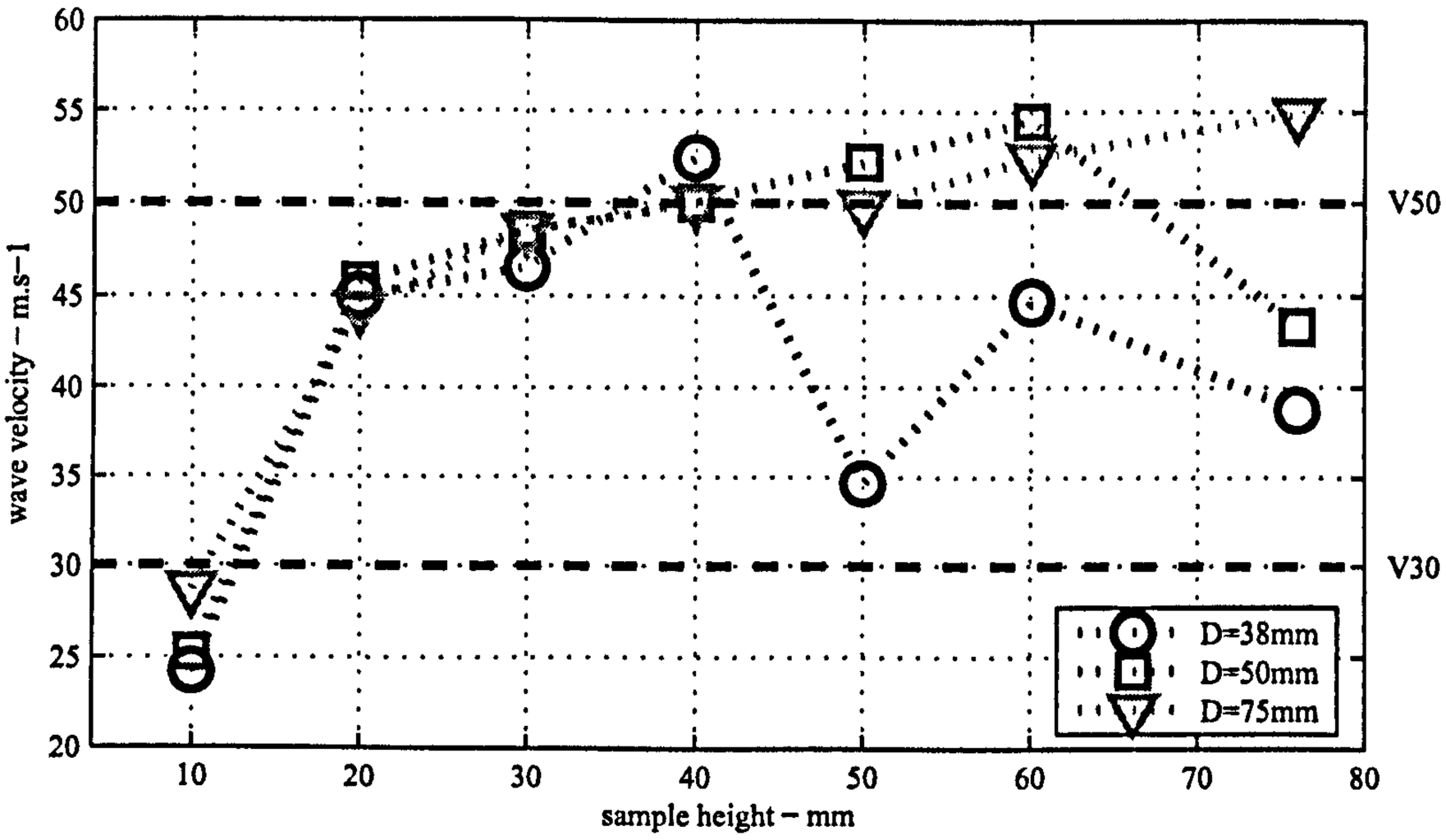

Figure 6.34: Corrected wave velocity estimates from pulse signals, according to sample height and diameter.

estimates for different sample diameters agree well with each other. Referring back to equivalent results from the frequency domain tests presented in figure 6.25, such a good agreement between samples with the same diameter could not be observed.

The velocity estimates for samples with $H > 40$mm are more scattered than for shorter samples where, independent from sample diameter, the results are consistent with each other. Eventually there is 'step down' to values of around 35m.s^{-1} and 45m.s^{-1} as the sample height increases.

Considering the velocity range, given by V30 and V50, to evaluate the reliability of the obtained wave velocity estimates, it is worth noting how the obtained results can vary between significantly low and high values of velocity. In both instances beyond the proposed range. Comparing the presented results with the equivalent frequency domain results, (figure 6.25), the frequency domain results are more scattered but are also more coherent in terms of being within the proposed velocity range.

6.6 Discussion

6.6.1 Travel Distance

So far, all of the presented velocity results have considered the travel distance to be measured tip-to-tip. The background on travel distance estimation in bender element testing is presented in section 1.5. In summary, the work developed by Dyvik and Madshus (1985), Viggiani and Atkinson (1995) and Brignoli *et al.* (1996) has, in all cases, pointed at the travel distance as being that measured on transducers tip-to-tip.

The travel distance contribution to the uncertainty associated with determination of wave velocity is usually considered to be less significant than the travel time, (Arroyo *et al.*, 2003*a*). As there is uncertainty about wave travel time, and since these travel time results are needed to verify the correct travel distance in the bender element problem, then surely the estimation of travel distance is also affected by uncertainty.

For this reason, the estimation of travel distance is now readdressed using the results from the time and frequency domains. When dealing with a first arrival scenario, it is intuitive to imagine the transmitter tip end to be the source of the propagating wave front. It is also intuitive to imagine the receiver's tip end to be the first to pick it up. But, even though many authors directly using the time histories of the signals still use the first offset of the transmitted signal, often they do not use the very first arrival of the received signal. There are many examples where other features of the received signal are used, such as its first local minimum or inflexion, (Brignoli *et al.*, 1996). If the first arrival of the received signal is not used, than any other feature of this signal is obtained at a time when the receiving transducer is already fully engaged, and not only its end extremity.

An estimate of the pressure exerted by the transmitting bender element on the

surrounding medium is presented in section 5.6 in figure 5.25. Considering the results of the UCL-BE, which are the transducers used in the present geometry parametric study, their pressure distribution diagram is parabolic, varying with embedment height. The centre of pressure, for the proposed model, is localised at 1.78mm from the sample base, i.e., 60% of the transducer's embedded tip height, 3mm.

It was not possible to monitor the behaviour of the receiving transducer with the same detail used for the transmitting transducer. This is because the amplitude of its movement fell below the precision limit of the laser equipment. Nevertheless, the receiver bender element is similar to the transmitter bender element, i.e., same materials, geometry, wiring, etc. Therefore, its mechanical behaviour can be expected to be the same and so, when coupled with the medium and engaged and forced by it to oscillate, it can be assumed that the applied pressure has a similar distribution. If that is the case, than the centre of exerted pressure is also at 60% of the embedded height.

The test results presented by Viggiani and Atkinson (1995) are for three samples with heights varying between 35mm and 85mm and constant embedment of 3mm per transducer. The results presented by Brignoli *et al.* (1996) concern embedment relative heights of 3% and 14% for samples with 100mm height. The samples used in the present parametric study permit the study of a broader range of travel distances. The parametric tests concern 7 different sample heights, varying between 10mm and 76mm, with a constant transducer embedment height of 3mm. This produces relative embedment heights between 8% and 60%. Thus the study of lower samples with large relative embedment heights becomes possible. This is important because travel distance assumptions are more relevant for lower travel distance tests. On the other hand, is was not possible to compare results from different stress states. The studied ranges of travel distance for the present study as well as those covered by the mentioned authors are presented in figure 6.35. This figure indicates the suitability

of the range of sample geometries used in the parametric study, to determine the correct travel distance compared to the other mentioned studies.

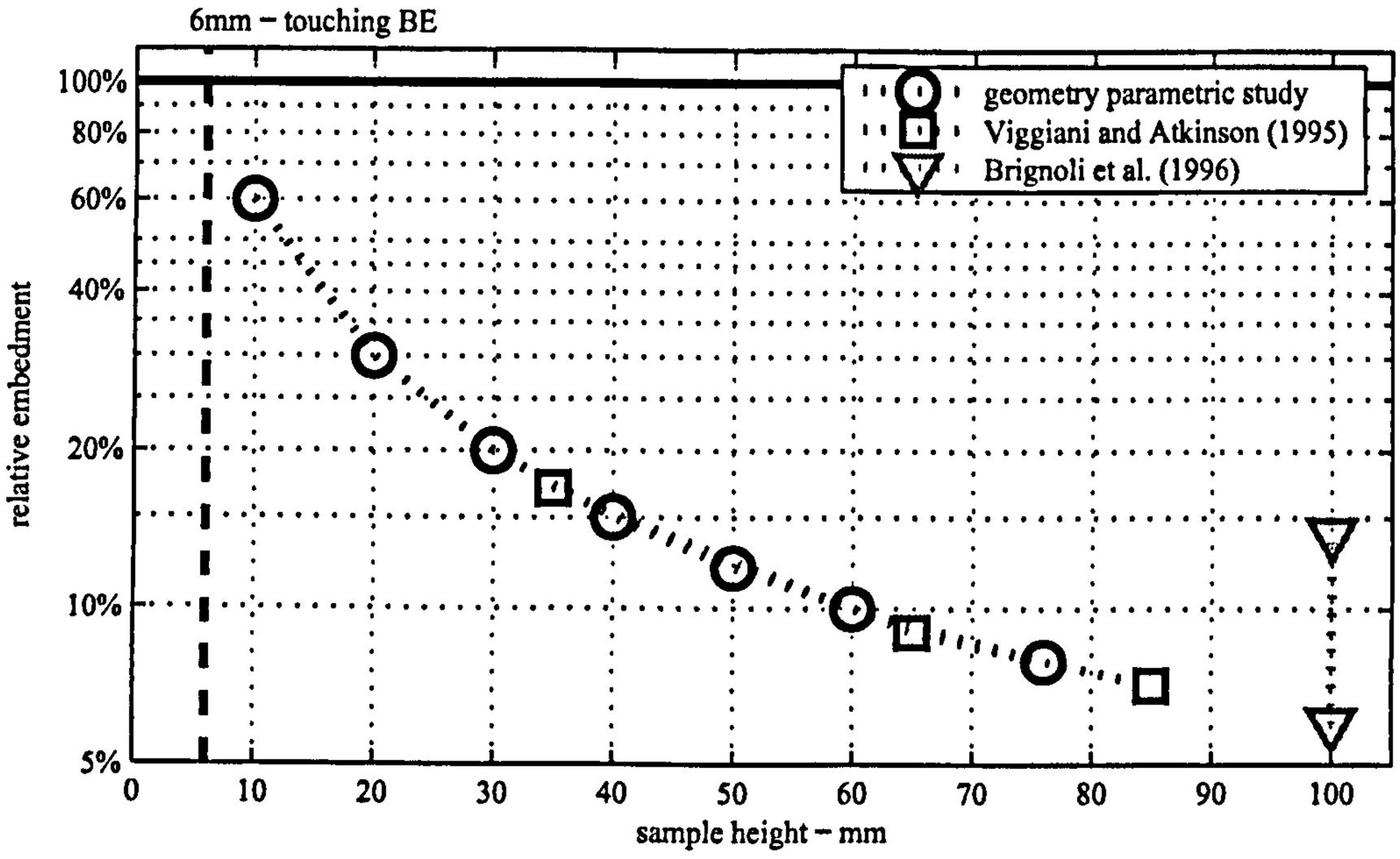

Figure 6.35: Range of studied sample heights and relative embedment in the determination of travel distance for the present parametric study and those covered by Viggiani and Atkinson (1995) and Brignoli *et al.* (1996).

The influence of the travel distance is directly related with the sample height. For a sample of 10mm height and with a bender element embedment of 3mm, the potential maximum error associated with considering the wrong travel distance is $10/(10 - 2 \times 3) = 2.5 \equiv 150\%$. For the tallest sample considered, $H = 76$mm, the equivalent maximum error associated with travel distance would be of $76/(76 - 2 \times 3) = 1.09 \equiv 9\%$. This analysis is quite important, because it implies that considering the wrong travel distance might have different consequences for different sample heights and also highlights how big the potential error associated with considering the wrong travel distance can be for shorter samples. A test in a triaxial cell has a potential of error due to considering the wrong travel distance much lower than if a sample is tested in an oedometer, where the sample is shorter and the relative error can be much higher.

Referring to the velocity results obtained from the frequency domain, namely the wave velocities presented in figure 6.25, the most remarkable result is that for the samples with 10mm height, the velocity results are apparently much lower than those for other sample heights. A similar observation can be made from the time domain results presented in figure 6.34. In both cases there is an upward tendency in wave velocity with sample height, starting with uncharacteristically low velocity values.

Dispersion is usually associated to faster wave velocities in the context of bender element testing. Therefore, it would not be expected to be able to justify the observed lower wave velocities. It is worth mentioning that dispersion, both due to the presence of geometry boundaries and to the near-field effect, in terms of wave group velocities, can produce lower values than the characteristic wave velocities, (figures 3.13, 3.15 and 3.17). Nevertheless, the results from the time domain are associated with the wave phase velocity, since single points are considered when estimating the travel time. Since the frequency domain results agree with the time domain results, dispersion is disregarded as a cause for the observed low wave velocities.

An incorrect travel distance consideration is left as the remaining possible cause for the observed low wave velocities. In order to verify this possibility, the travel time results from the parametric study, both for the frequency and time domains, were re-evaluated with the travel distance in mind.

Figure 6.36 presents travel time results for the same rubber samples used in the parametric study. These results were obtained using the gradient of the phase delay curve in the frequency domain. A best-fit line was plotted to indicate the travel distance which best agrees with the time results. For reference purpose, the total bender element penetration of 6mm was also marked. Figure 6.37 presents equivalent results to those seen in figure 6.36 obtained in the time domain.

The best-fit line for the frequency domain travel time results, in figure 6.36,

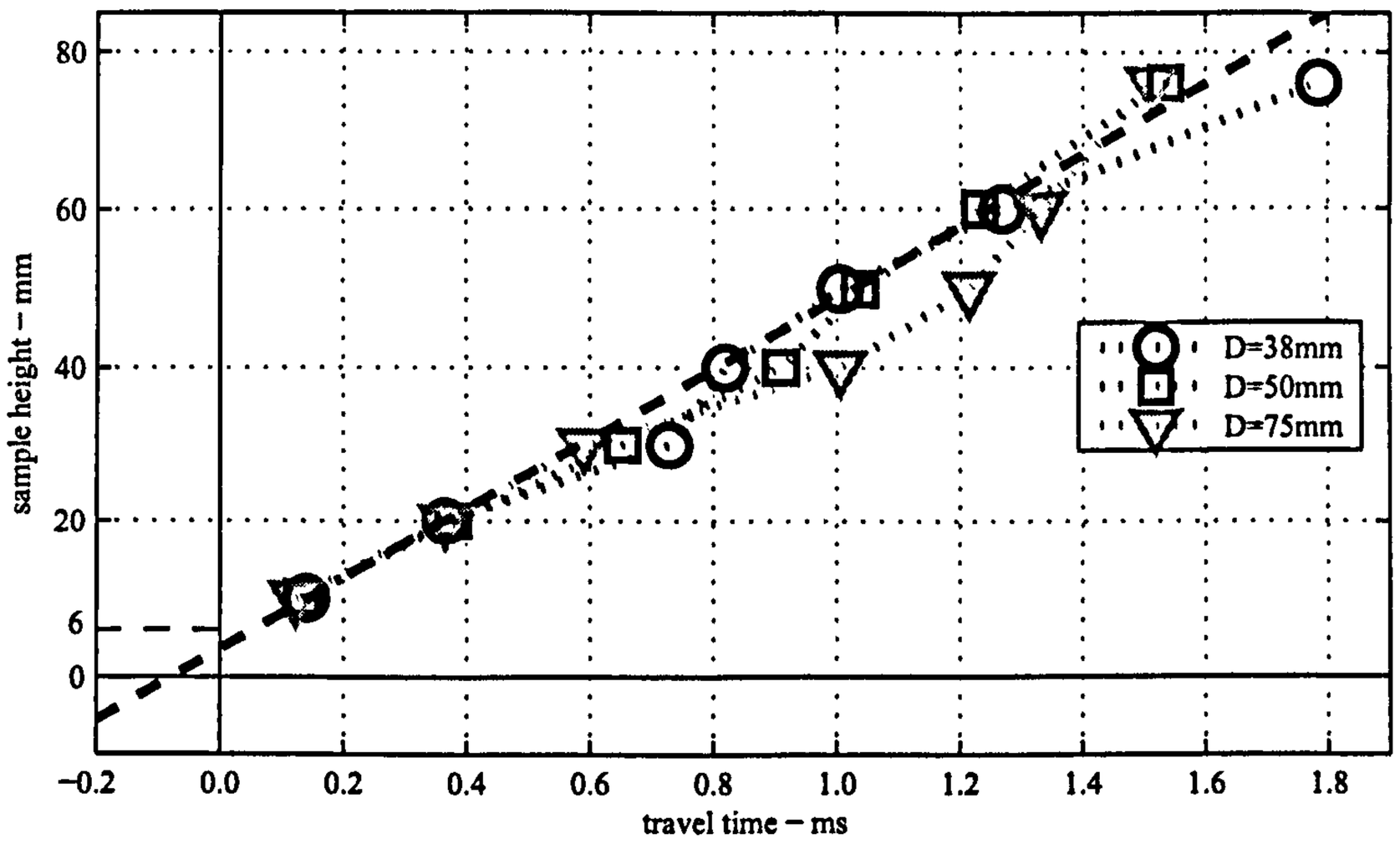

Figure 6.36: Travel time results using a frequency domain method for the parametric study samples.

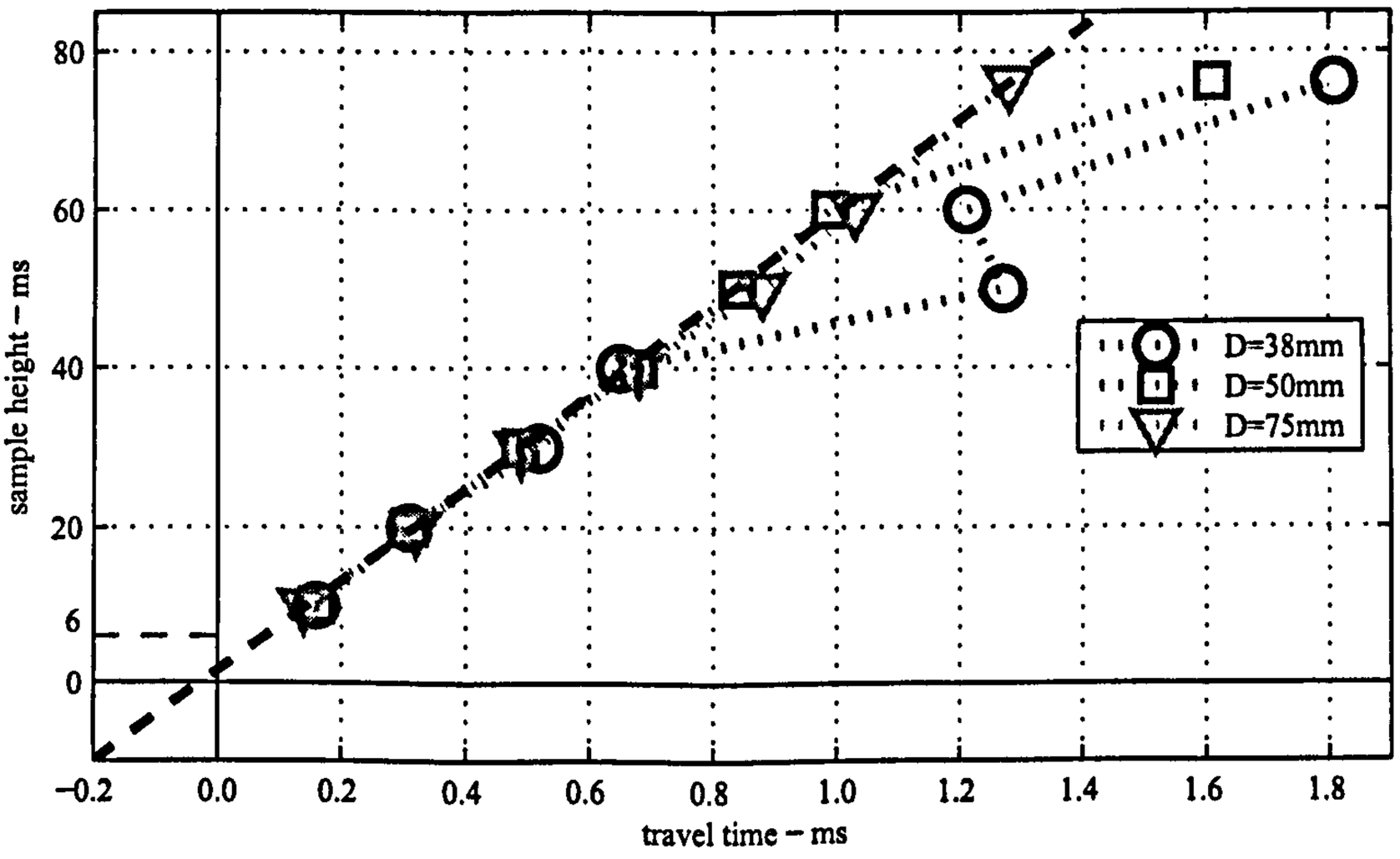

Figure 6.37: Travel time results using time domain method for the parametric study samples.

crosses the vertical sample height axis at 3.56mm. This value indicates that the travel distance should be measured from a point in the embedded bender element tip 1.86mm from the base of the sample, or 62% of the embedded height. Such a travel distance is quite similar to the one obtained using the static pressure distribution

model, which pointed to a value of 1.78mm from the sample base.

The time domain travel time results in figure 6.37 are best fitted by a line that crosses the vertical height axis at 1.64mm. This value indicates a travel distance measured 0.82mm from the sample base, 27% of the embedded height. In spite of indicating a travel distance relatively different from the frequency domain and pressure distribution, the time domain results also indicate a longer distance than the tip-to-tip travel distance.

A proposed explanation for such a high travel distance obtained for the time domain results might be the observed phase delay between the transmitted and the received signals and the actual bender element movement. In figure 5.18 a time delay of around 2×10^{-2}ms could be observed, for a wave velocity of around 50m.s^{-1}. This time delay would decrease the ideal travel distance by 1mm at the transmitting transducer. If the receiving transducer is assumed to have a similar time delay, a total of 2mm need to be added to the corrected travel distance. This would bring the best fit line to cross the vertical axis at $1.64+2\times1.00 = 3.64$mm. This corrected travel distance is very similar to the values obtained for the frequency domain travel time results, which are unaffected by the mentioned phase and time delay. They are also very similar to the travel distance obtained using the centre of pressure from the dynamic pressure distribution model. A total of three separate indicators, one of which is independent from the other two, point to a correct travel distance measured between bender element pressure centres. Table 6.10 presents the various proposed travel distances.

The velocities presented in figures 6.25 and 6.34 were recalculated using the travel times obtained from the frequency and time domain results and using the respective corrected travel distances. These reviewed velocity results are presented in figures 6.38 and 6.39 for the frequency and time domain results respectively.

In figure 6.38, the frequency domain results are still rather scattered. Yet, the

Description	height from base	relative height	travel distance
tip-to-tip	3.00mm	100%	height−6.00mm
pressure distribution	1.78mm	59%	height−3.56mm
frequency domain	1.83mm	61%	height−3.66mm
time domain	0.82mm	27%	height−1.64mm
corrected time domain	0.82+1.00=1.82mm	61%	height−3.64mm

Table 6.10: Travel distances according to different estimates and methods.

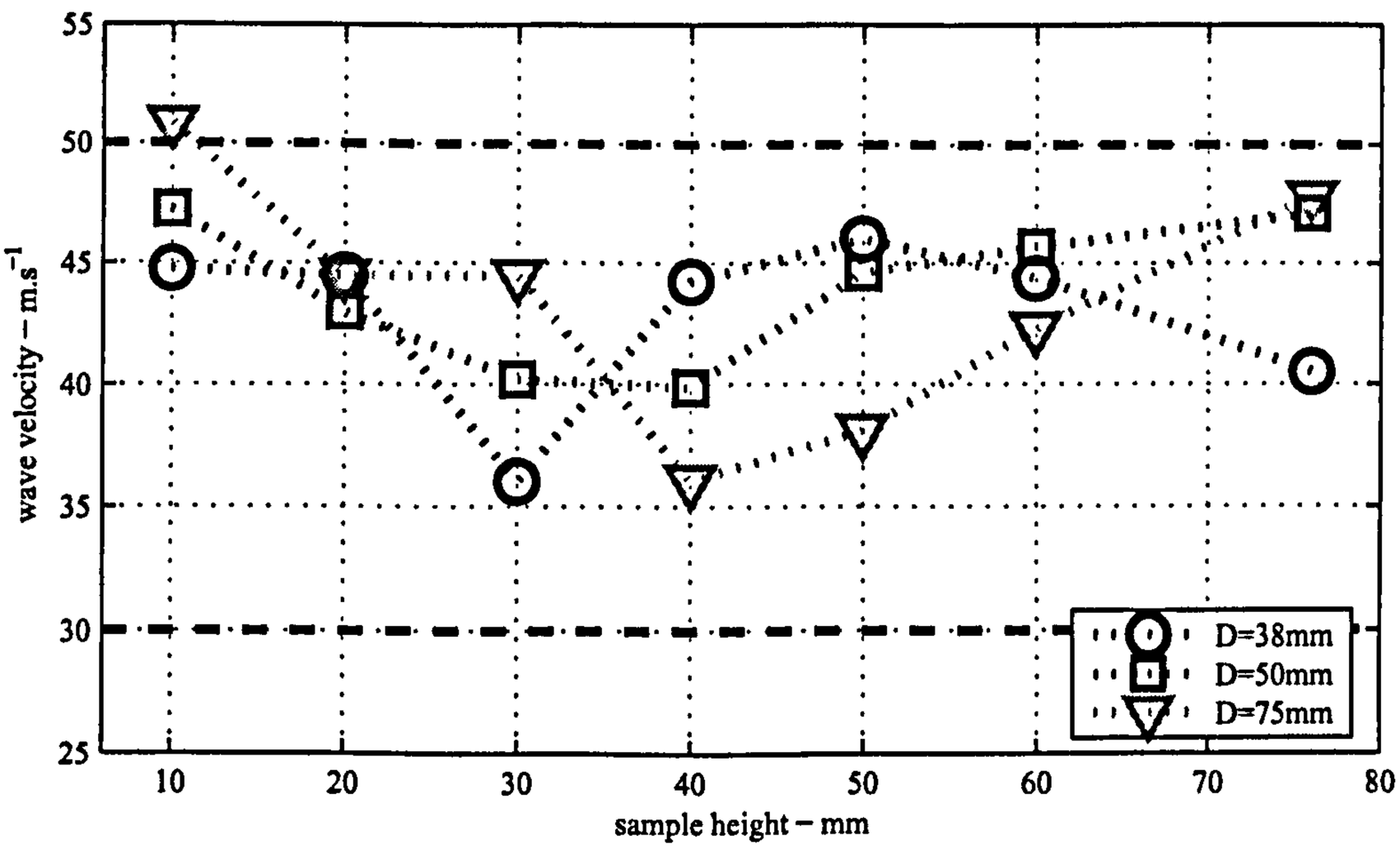

Figure 6.38: Corrected frequency domain wave velocities. Travel distance measured between 1.83mm of transducers' embedded heights.

trend of increasing wave velocity with sample height is no longer present. For the time domain results, in figure 6.39, the increasing trend, also noticeable in the original results seen in figure 6.34, is also no longer present. The corrected time domain results give wave velocity estimates which are quite high, being most of them out of the proposed velocity range. Nevertheless, the coherence between the corrected time domain wave velocity is worth noting.

In general, the travel distance measured between transducers tip-to-tip appeared to be unsuitable for a typical bender element analysis. The obtained results for a

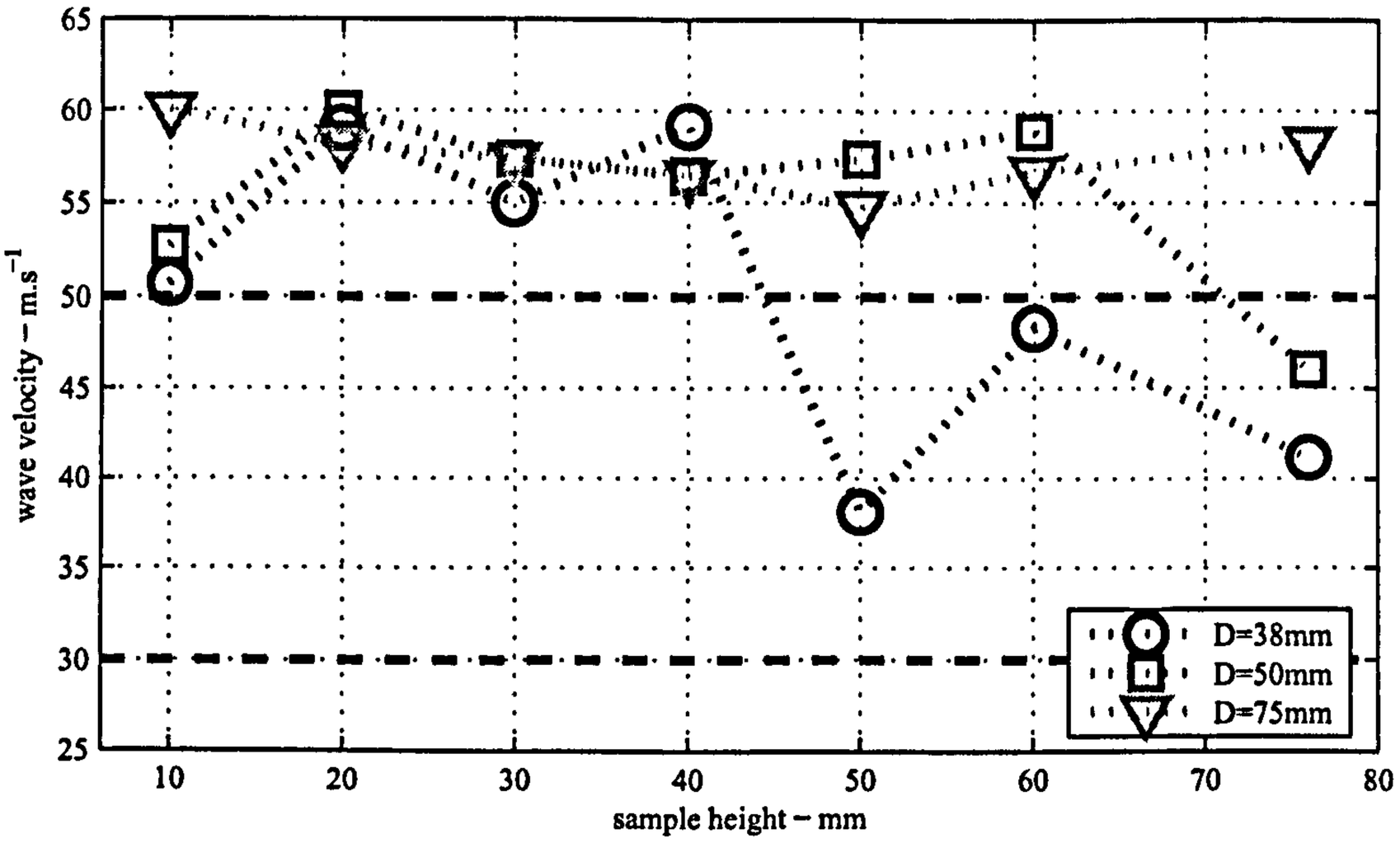

Figure 6.39: Corrected time domain wave velocities. Travel distance measured between 0.82mm of transducers' embedded heights.

large range of sample geometries and confirmed by the estimated pressure distribution along the transducer's embedded length indicate that the travel distance should be measured between the centre of dynamic pressure of those transducers, roughly at 60% of the embedded height.

6.6.2 Geometry Influence in the Frequency Domain

The subject of sample geometry and wave propagation has been addressed generally in section 3.2. Geometric boundaries have been shown to cause incoming wave components to be reflected back into the medium as one or more different wave components, including surface waves, (Redwood, 1960). As all outgoing wave components are reflected back into the medium, they contribute to the overall propagating wave, possibly interfering with the wave front. A bounded medium, by forcing outgoing waves to reflect back into it and guide them, is also known as a waveguide. Cylindrical bars are well-known cases of waveguides, they are often studied and serve as example due to the simplifications introduced in the analysis due

to their cross-section axial symmetry, (Achenbach, 1973). For example, Fratta and Santamarina (1996) have devised a specific test where a cylindrical soil samples was considered to behave as waveguides.

Waves propagating in cylindrical bars are characterised by three distinct fundamental modes of propagation: longitudinal, torsional and flexural, (section 3.4.1). These modes of wave propagation are generally dispersive. There is one exception, the first mode of torsional wave propagation is non-dispersive. This non-dispersive torsional mode is at the base of torsional resonant column testing, (section 3.11).

Soil samples tested with bender elements in triaxial cells and oedometers are usually cylindrical in shape, and thus the principles of wave propagation in cylindrical bars must apply. Nevertheless, since the tested samples do not have an infinite length, there might be cases where for bulkier sample, they can behave more as an unbounded medium than as a waveguide. There are other limitations related to the elastic and linear characteristics of the medium. For the range of applied stresses and strains, the tested samples are assumed to be linear elastic. Even though none of the cylindrical samples have infinite lengths, a distinction can be made between slender samples which are expected to behave as theoretically predicted cylindrical bars, and bulkier samples which are expected to behave more like laterally unbounded media. Slender samples have a higher possibility of having propagating wave fronts influenced by reflected wave components, since the lateral boundaries are relatively nearer the main propagating path, between transducers. Bulkier samples can be expected to propagate wave fronts undisturbed by reflected wave components.

The near-field effect, discussed in section 3.6, is also related to the sample geometry, namely its height. Near-field wave components dissipate much faster than the far-field wave components and so quickly lose their influence with increasing travel path lengths.

Some aspects of sample geometry influence have already been observed. In sec-

tion 6.4.1, the frequency content of the received signals was analysed. It was possible to establish a relation between sample heights and frequency content as taller samples allowed narrower frequency contents through. In section 6.4.2 and 6.2, a relation between the dynamic behaviour of the samples and their geometries has been established.

There was also the question of wave travel distance addressed in section 6.6.1. If the wave travel distance is not correctly selected, a potentially significant error can result in the estimation of wave velocities. Such error would also be different for each sample height, creating a signal distortion which is increasingly significant for lower sample heights.

The last stage of the geometry influence analysis is to look at the wave velocity results and verify the presence of any significant sample geometry influence. The wave velocities obtained from the frequency domain results were presented in figure 6.25. It was possible to observe that the results for the three different diameters have some similarities, namely a local minimum at an intermediate sample height. The relation between this and other features and the sample geometry are further studied by looking at different horizontal axes, revealing different geometric relations of the samples. In figure 6.40, the velocity results, using the tip-to-tip travel distance, are plotted using a horizontal slenderness ratio axis of height over diameter, H/D.

The relation between the three curves, for different sample diameters, presented in figure 6.40, is now more obvious. For the three different diameters, each curve can be seen to follow a similar pattern of initial increase, followed by a local minimum and ending with a local maximum. The fact that the behaviour of so many different samples can be seen to follow a similar pattern related with their geometry indicates that the results, and the mentioned curve features, are not arbitrary, some relation does exist between the results and the sample geometry.

Another geometric parameter is attempted as the horizontal axis in figure 6.41,

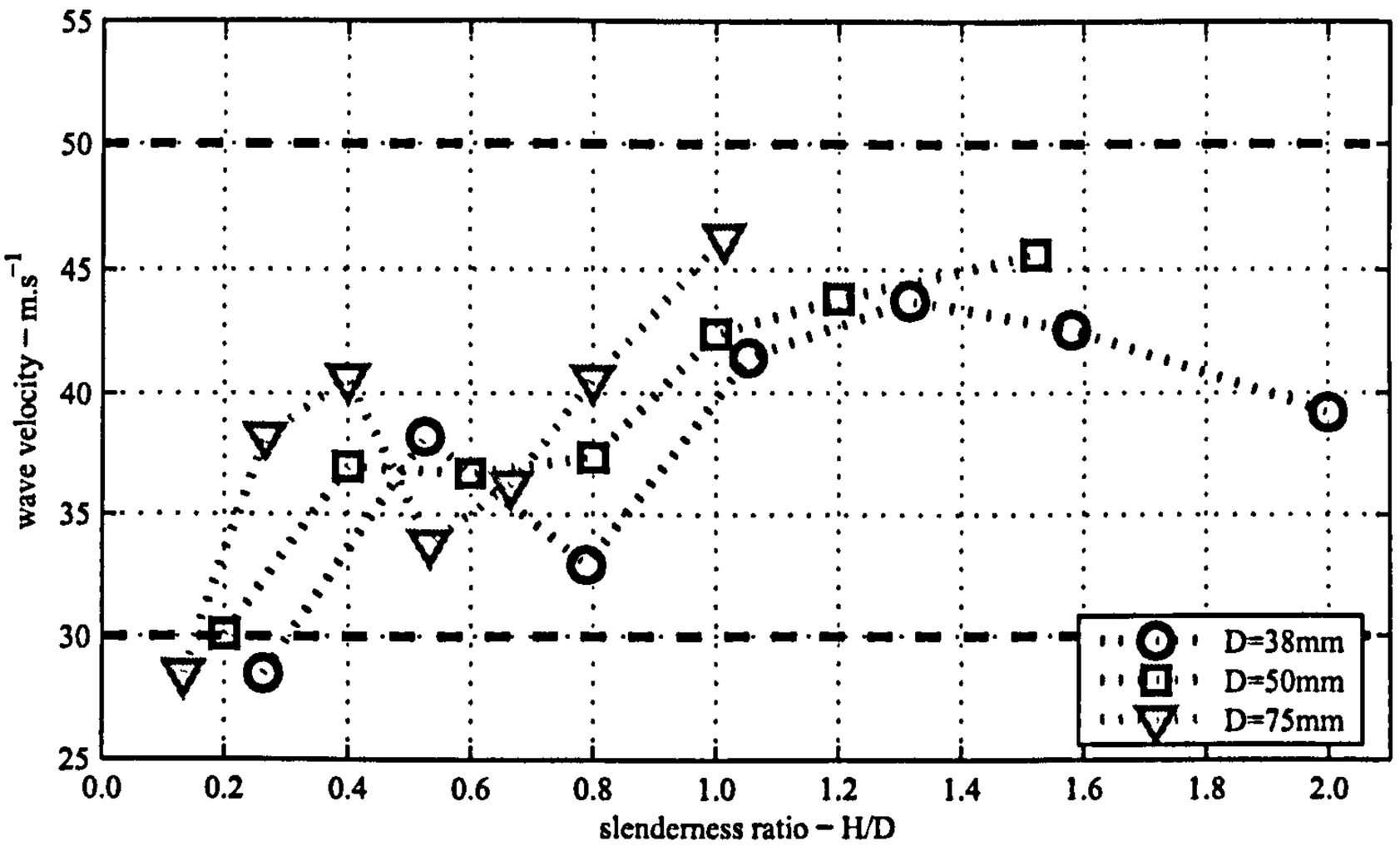

Figure 6.40: Wave velocity comparison with slenderness ratio, H/D,for frequency domain results.

where the square of the sample height over the diameter, H^2/D, is used.

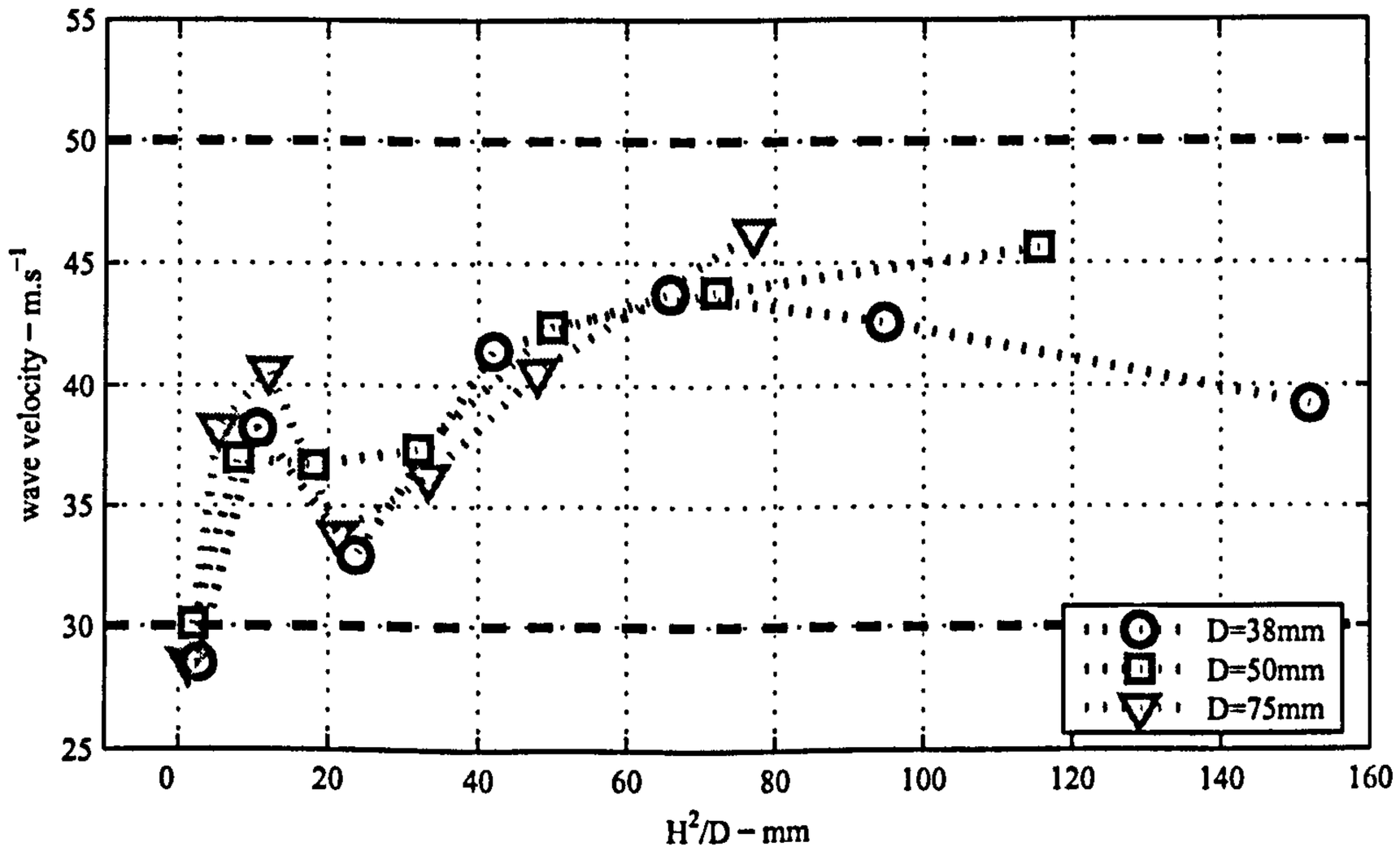

Figure 6.41: Comparison between wave velocity and geometric parameter, H^2/D, for frequency domain results.

When plotted versus the geometric parameter H^2/D, the velocity results from the frequency domain of all of the tested samples now seem to be even more closely related. The three velocity-diameters curves are now very similar to each other.

The curve features now occur at the same values of H^2/D. The parameter H^2/D is not as 'elegant' or universal as the slenderness ratio, but the obtained results show the clearest relation between the frequency domain velocity result and a geometry parameter. Initially the obtained results seemed very scattered and the fact that for the proposed geometry parameter they became so coherent is a clear indication of this parameter relevance. Furthermore, the fact that results from samples with significantly different heights and diameters consistently produce similar wave velocity results in accordance with H^2/D also serves as a clear indicator of the geometry's influence. What might have been considered erratic results now have to be considered in terms of their relevance to explain the influence of sample geometry in terms of wave propagation.

The results presented so far were normalised using the travel distance measured from tip-to-tip. In figure 6.42 are presented the frequency domain velocities now obtained using a corrected travel distance measured between the transducers' centre of dynamic pressure, (section 6.6.1). Once again, the geometry parameter given by the ratio H^2/D is used at the horizontal axis.

The velocity-diameter curves in figure 6.42 are similar to the ones shown in figure 6.41, except for the lowest values of H^2/D. These now produce higher wave velocity estimates.

When the transmitting bender element disturbs the medium, the resulting mechanical waves propagate in all directions. For a bulkier sample, a direct wave propagation is expected to reach the receiver with little or no interference from reflected wave components. Reflected wave components have a travel path which can be much longer, hence becoming significantly more damped and also taking longer to reach the receiver. This means that the wave components which travel directly between transducers in a bulk sample can be assumed to travel in an unbounded medium. As the samples become slender, the reflected wave components, namely

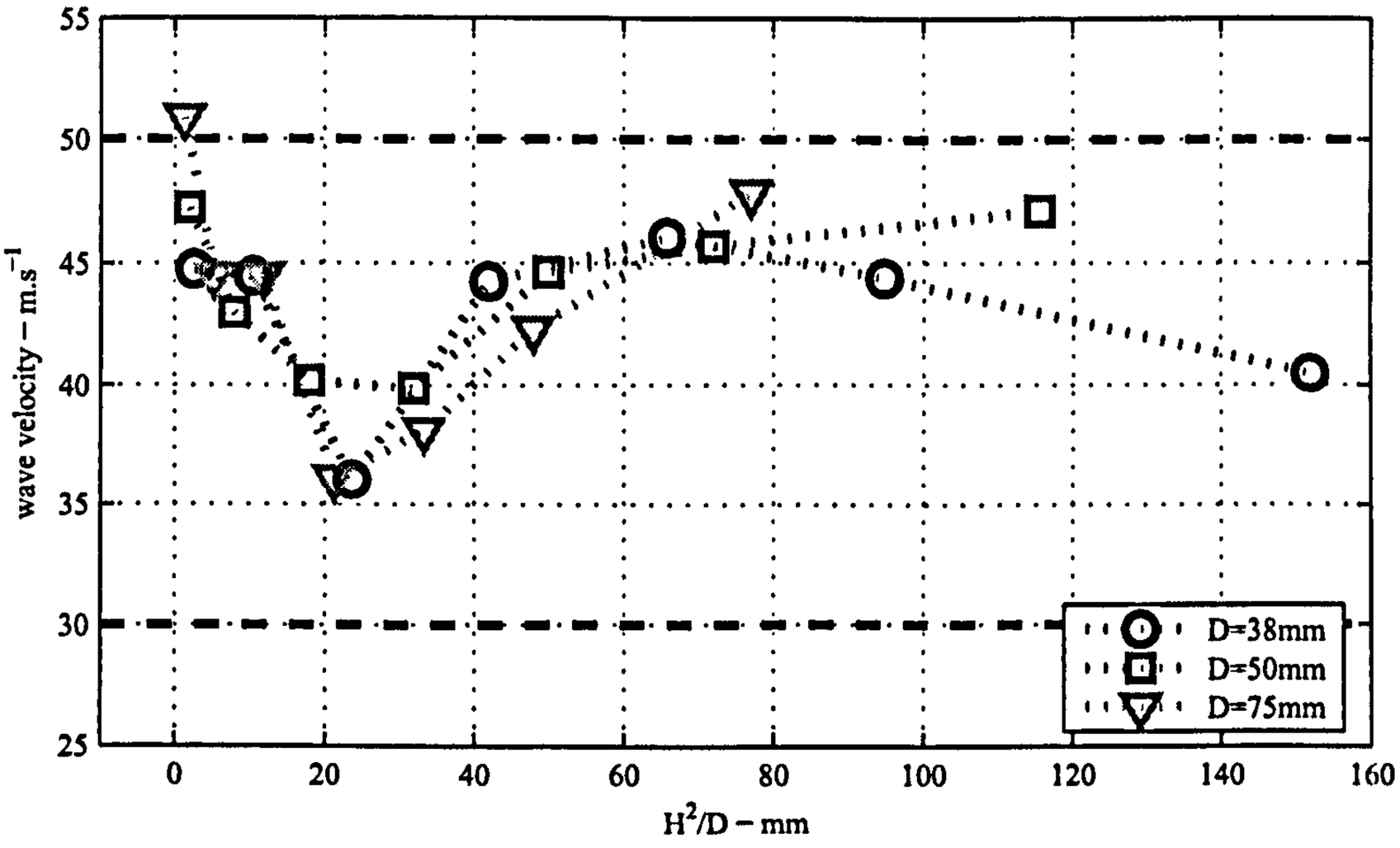

Figure 6.42: Wave velocity for frequency domain results, with a travel distance measured between 60% of the transducer's embedded height, as calculated in section 6.6.1.

those that reach the receiver, have travel paths with similar lengths to the direct travel path, meaning that they start to interfere significantly with the received wave front.

The far-field shear wave components propagate, in an unbounded medium, at the characteristic shear wave velocity, V_s, (Claxton, 1958). In a cylindrical waveguide, an anti-symmetric shear disturbance is expected to produce waves which propagate in a combination of flexural modes. These modes of wave propagation are dispersive. The determination of the relative amplitude of each flexural mode is quite complex and difficult to obtain, (Redwood, 1960). Nevertheless, it is generally assumed that, at higher frequencies, the overall group velocity for each mode tends to be less dispersive, pointing at the characteristic shear wave velocity. At lower wave velocities, the first mode of wave propagation is dominant with an overall significant dispersive behaviour. The estimation of group wave velocity at these lower frequencies is therefore rendered more difficult. The dispersion curves for a rubber cylinder with

similar properties as the ones used in the parametric study can be found in figures 3.16 and 3.17.

Before proceeding to the analysis of the wave velocities for the parametric study in figure 6.42, it is worth remembering that the range of frequencies for which the phase delay gradient was calculated is different for each sample. Taller samples had their wave velocity calculated for lower frequency ranges, due to their lower maximum frequency, as presented in section 6.4.1. This means that with an increasing sample height, one might expect less dispersion due to near-field effect and more dispersion due to wave reflection, both because of the increasing slenderness of the samples and because of their lower maximum frequency ranges.

It is worth trying to fit the proposed wave propagation models to the frequency domain wave velocity results. So, for bulkier samples, say $(H^2/D) < 15$mm, a direct wave propagation undisturbed by reflected wave components is assumed. For this model, dispersion is caused by near-field effect only. For slender samples, say $(H^2/D) > 50$mm, the waves propagate as in a waveguide, and for high enough frequencies the group velocity is the same as the characteristic shear wave velocity.

Two more groups of results can be observed. The velocity results for geometry parameters $15 < (H^2/D) < 45$mm and $(H^2/D) > 85$mm. The first range can be assumed to correspond to a group of transition sample geometries. For this first range of geometry parameters the samples behave neither predominantly as an unbounded medium, nor as a waveguide. Some form of transitional, more complex behaviour takes place. The second range, $(H^2/D) > 85$mm, is characterised by the scattering of the velocities results. This could be explained by the fact that the corresponding results were obtained using frequency ranges at lower frequencies at which the flexural modes of wave propagation are more dispersive. These behaviour models are presented in figure 6.43.

From figure 6.43, the shear wave velocity is estimated to be around $V_s = 45\text{m.s}^{-1}$.

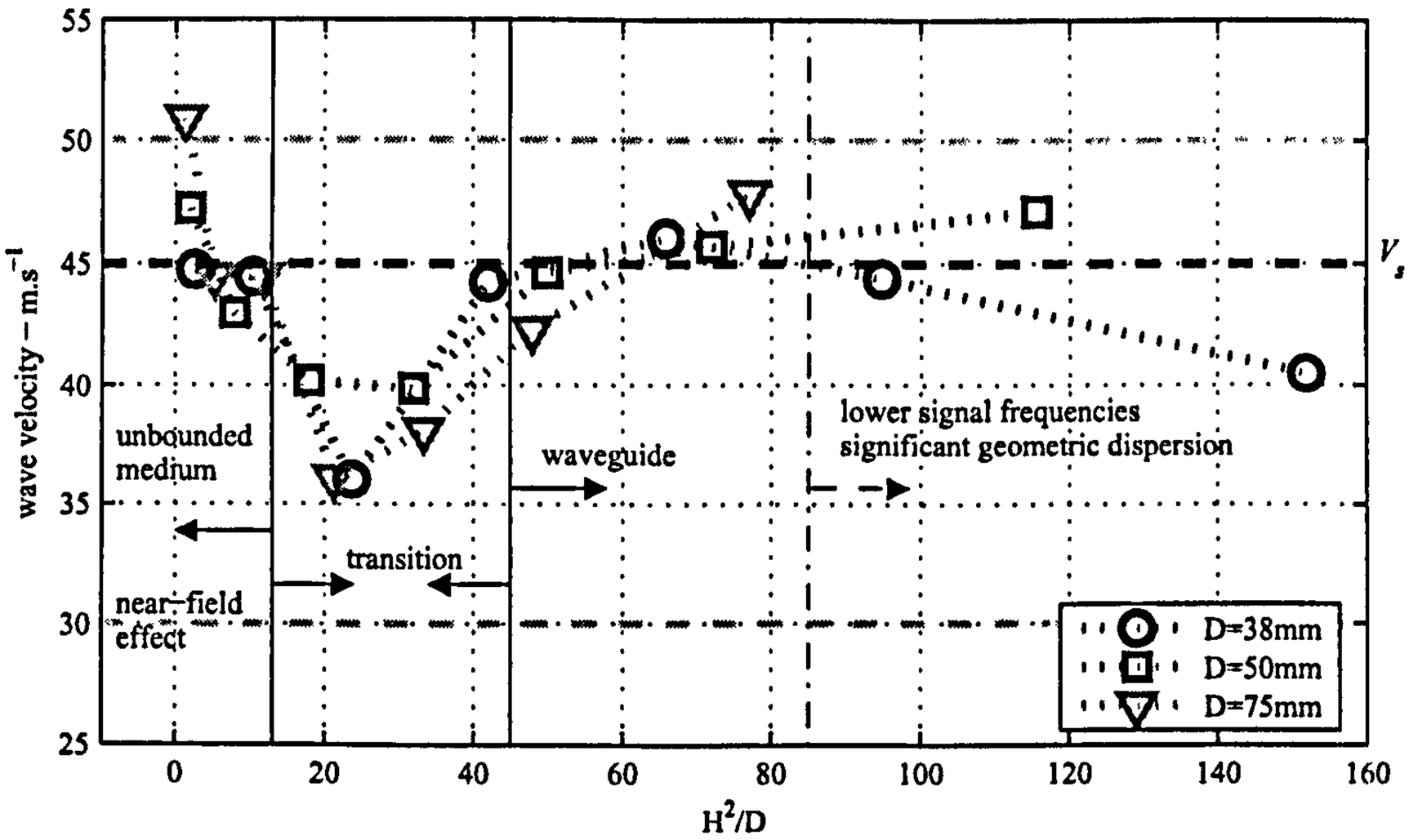

Figure 6.43: Sample behaviour model according to geometry parameter H^2/D for frequency domain velocity results.

This value is obtained considering the wave velocity values obtained for a waveguided behaviour of the sample for which high enough frequencies are able to propagate through.

The proposed models of sample behaviour were related with sample geometry, namely with the geometric factor H^2/D.

$$\begin{aligned} \text{unbounded medium} &\rightarrow H^2/D < 15\text{mm} \\ \text{waveguide} &\rightarrow H^2/D > 45\text{mm} \end{aligned}$$

This relationship has been established for the tested rubber samples. Actual soil samples would still be expected to behave as linear-elastic media, but their different elastic properties mean that the proposed geometric limits of sample behaviours might be found at other values of geometric parameters. Testing with different boundary conditions such as confining pressure or with a protecting latex membrane might also alter the limits distinguishing the models of behaviour. Nevertheless, the

mechanical response appears to present a clear distinction as a function of sample geometry.

Without making a parametric study for each new set of bender element tests, the available option is to use a significantly bulkier or slender sample to guarantee its behaviour is either clearly that of an unbounded medium or that of a waveguide, and not something in between. The standard sample dimensions for an oedometer or triaxial cell places them well within these categories. The same cannot be said of other test set-ups such as anisotropy studies, where the transducers can sometimes be placed at the sides of the samples.

Having established the behaviour models of the studied samples, it becomes necessary to guarantee a minimum of dispersion by controlling the frequency of the continuous signal. For this purpose, the near-field effect for unbounded models and the near-field effect and dispersion curves for the waveguide must be estimated. The near-field effect has been well studied so far and the limit proposed by Arroyo *et al.* (2003*a*) given in equation 3.67 is both practical and simple to use.

In order to evaluate the waveguide dispersion, one option is to calculate the specific dispersion curves of each studied sample. This is a complex numerical task that requires considerable effort. For this reason a simple limit is proposed based on the generic dispersion curves of the flexural modes of propagation presented by Redwood (1960). According to his work, the first mode of flexural wave propagation becomes quite less dispersive after $D/2\Lambda > 0.35$ for a Poisson's ratio of $\nu = 0.29$. This result can be presented as:

$$f_{\text{wd}} > \frac{1.4V_s}{D} \tag{6.1}$$

where f_{wd} is the limit frequency in Hertz for which minimum waveguide dispersion can be expected, V_s is the estimated shear wave velocity and D is the sample diam-

H (mm)	D (mm)	H^2/D (mm)	limit[8] (kHz)	Frequency Range (kHz)	Velocity ($m.s^{-1}$)	Variation (%)
76	38	152	$f_{wd} > 1.7$	[1.0 1.8] - **KO**	**40.5**	**10%**
60	38	95	$f_{wd} > 1.7$	[2.5 3.7] - OK	44.4	1%
50	38	66	$f_{wd} > 1.7$	[2.5 3.1] - OK	46.0	2%
76	50	116	$f_{wd} > 1.3$	[0.8 2.0] - **KO**	**47.1**	**5%**
60	50	72	$f_{wd} > 1.3$	[1.6 3.7] - OK	44.7	1%
50	50	50	$f_{wd} > 1.3$	[2.5 3.1] - OK	44.6	1%
76	75	77	$f_{wd} > 1.0$	[1.1 1.9] - OK	47.7	5%
60	75	47	$f_{wd} > 1.0$	[2.5 3.7] - OK	42.3	6%

Table 6.11: Velocity variation according to waveguide dispersion frequency limit.

eter. This result was obtained using a safety coefficient of 2.0 to further maximise the limit frequency. Equation 6.1 must not be considered as an absolute limit but only as a preliminary reference proposed by the author.

The suitability of the proposed frequency limit presented in equation 6.1 is measured using the velocity results given in figure 6.43.

The application of the waveguide dispersion frequency limit to the frequency domain results appears to suit the results. Since it has a theoretical justification, its confirmation for the available parametric study is quite encouraging. For samples assumed to behave as waveguides, a maximum error of 6% is present for results obtained using a frequency range within the proposed limit. If the results for the bulkier samples, with diameters of 75mm are disregarded, then the maximum error obtained is around 2%. These are favourable results which, nevertheless, do not fully confirm the validity of the proposed limit. A number of other parametric tests on materials with different elasticity properties would be necessary in order to corroborate the results obtained so far.

Noting that the results in figure 6.43 were obtained using a travel distance mea-

[8]Obtained using an estimated shear wave velocity of $V_s = 45 m.s^{-1}$

sured using the transducer's centre of dynamic pressure and not the most usual tip-to-tip distance. Nevertheless, for the considered samples, i.e, those with waveguide behaviour, their relatively large heights makes their results less susceptible to either choice of travel distance. For this reason, the proposed limit is, if valid, applicable to either case.

6.6.3 Geometry Influence in the Time Domain

The time domain wave velocity results for a corrected travel distance, as presented in figure 6.34, are now analysed in terms of their variation with the two geometric parameters explored so far, H/D and H^2/D. The corresponding curves are presented in figures 6.44 and 6.45.

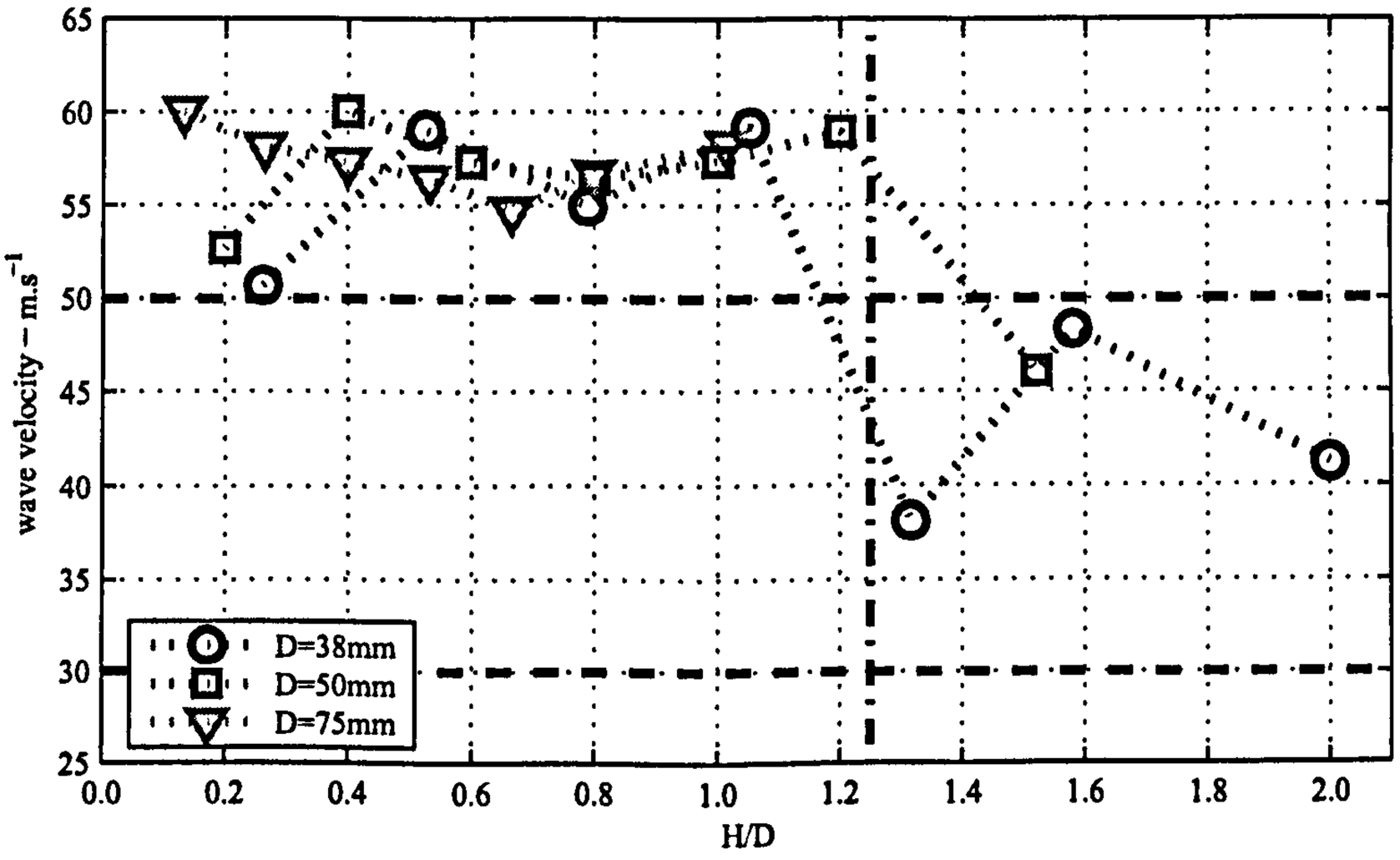

Figure 6.44: Time domain wave velocities variation with slenderness ratio H/D.

From the two proposed geometric parameters, the slenderness ratio, H/D, seems to be the one for which a clear relationship can be established between the velocity results and the sample geometry. In figure 6.45 a clear step in wave velocity can be observed for $H/D > 1.25$. At this slenderness ratio the wave velocity estimates present a shift from values in the range of $V \approx 58\text{m.s}^{-1}$ down to $V \approx 45\text{m.s}^{-1}$.

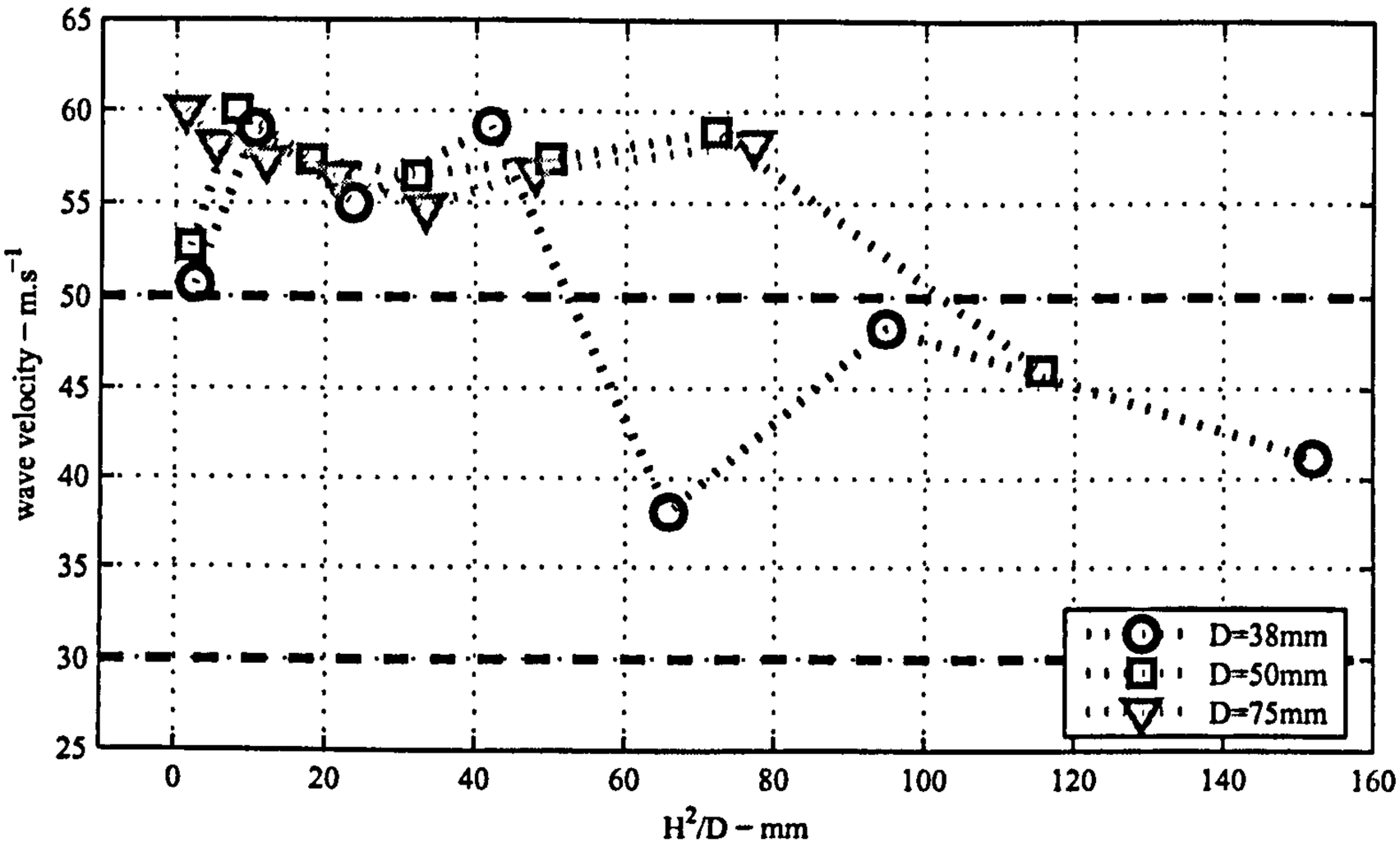

Figure 6.45: Time domain wave velocity variation with geometric parameter H^2/D.

There is a phase shift between excitation and response at each mechanical interface: between transmitted electric signal and transmitting bender element vibration, between transmitting bender element vibration and soil vibration, between soil vibration and receiving bender element vibration and between receiver bender element vibration and received electric signal. This behaviour is characteristic for any simple mechanical system. It was also verified in the monitoring study conducted in section 5. For these reasons, the direct measurement of travel time between transmitted and received electric signals becomes insignificant, since it is only remotely related to the propagating wave in the soil. However, it is noticeable that for low slenderness ratios, $H/D < 1.25$, the measured wave velocities are quite high and well outside the proposed range. This range has been established with results from the independent laser monitoring, the vibration analysis of the response curves and the frequency domain results. For higher slenderness ratios, the velocities 'step down' and fall within the proposed velocity range. They also agree well with the velocities obtained in the frequency domain, at around $v \approx 45\text{m.s}^{-1}$.

It is still quite worrying that most of the obtained results for $H/D < 1.25$ appear to over-estimate the wave velocity, being also quite coherent with each other. Some form of dispersion could explain the wave velocities which are significantly higher than the estimated shear wave velocity, and the proposed range of velocities. The near-field effect is worth considering since, when testing with pulse signals, the transmitted wave frequency content is quite broad, (figures 6.30 and 6.31). This means that even if the signal's reference central frequency would indicate no significant near-field effect, the lower frequency content of such a broadbanded signal could still excite significant near-field wave components. In section 6.5.5 the expected theoretical near-field was compared with the proposed values of measured total dispersion. This total dispersion was evaluated in the form of an amplitude ratio between the first signal minimum, feature E, and the first signal maximum, feature G. These pulse signal notations are identified in figure 2.2.

Samples with diameters of $D = 38$mm were observed to have no significant near-field effect above heights 40mm. Similar observations were made for samples with diameters of $D = 50$mm and $D = 75$mm for sample heights of $H = 50$mm and $H > 76$mm respectively. It is worth presenting the relation between dispersion and sample geometry. Figure 6.46 contains the ratio between estimated near-field and total measured dispersion, varying with sample slenderness ratio. For dispersion ratios lower than 0.5, the near-field effect is assumed to be non-dominant in terms of the overall observed dispersion. Since the other known source of dispersion is the waveguide dispersion, one must assume that for dispersion ratios lower than 0.5, the waveguide dispersion is the dominant form of dispersion.

Again, a relationship between sample geometry and signal properties is quite clear. Figure 6.46 shows how the near-field effect becomes less significant with increasing slenderness ratio. The presented results are quite crude and must be treated with some caution. For example, results where the dispersion ratio is higher

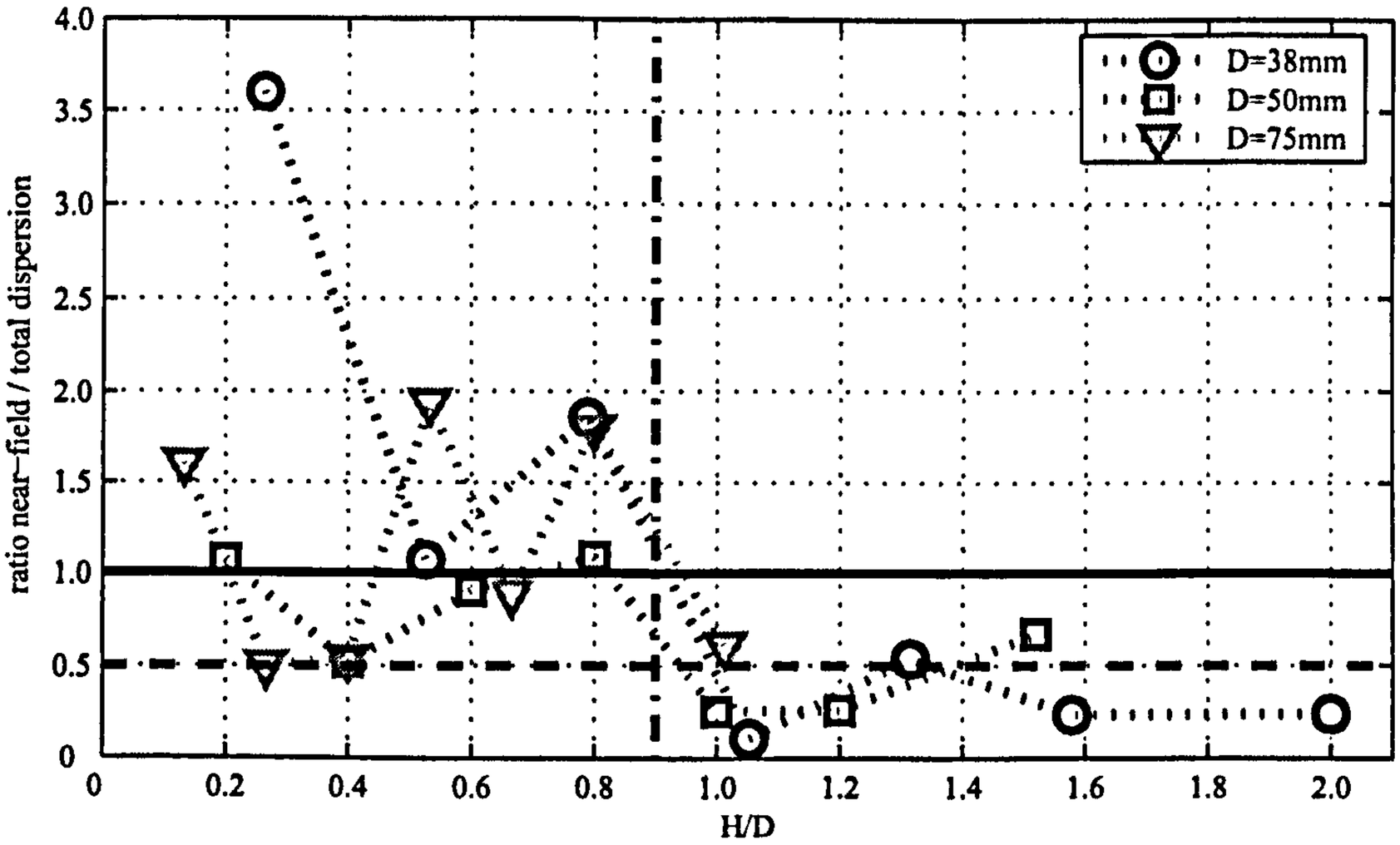

Figure 6.46: Ratio between the theoretical unbounded near-field effect and total measured dispersion.

than 1 indicate that the observed total dispersion is lower than the theoretical near-field effect. This can only mean that the method of measuring dispersion is flawed. Yet, it is remarkable to observe the clear trend which for $H/D \geq 1.0$ indicated little near-field effect. This result produces a limit slenderness ratio quite similar to the one observed in figure 6.44, $H/D = 1.25$mm. Some relationship can therefore be established with the decreased impact of near-field effect with the observed step decrease in (measured) wave velocity, in terms of sample slenderness ratio.

A significant range of slenderness ratios was covered during the parametric study. The calculation of the direct and reflected wave paths allows an interesting observation, if the direct travel distance is the length of the straight line between the transducers, and the reflected travel distance is the sum of the lengths of two sides which close the isosceles triangle which has the direct travel distance as its hypotenuse.

In figure 6.47 assume TD_d as the length of the direct travel path and TD_r as the length of the reflected travel path. The ratio between the direct and reflected travel path lengths is presented in figure 6.48 for the geometric parameters H/D

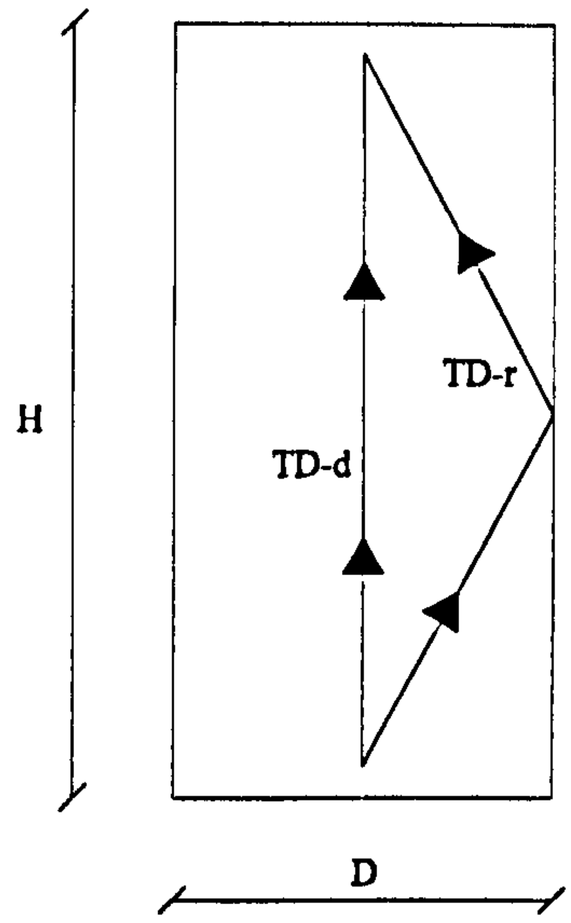

Figure 6.47: Direct and reflected travel distances.

and H^2/D.

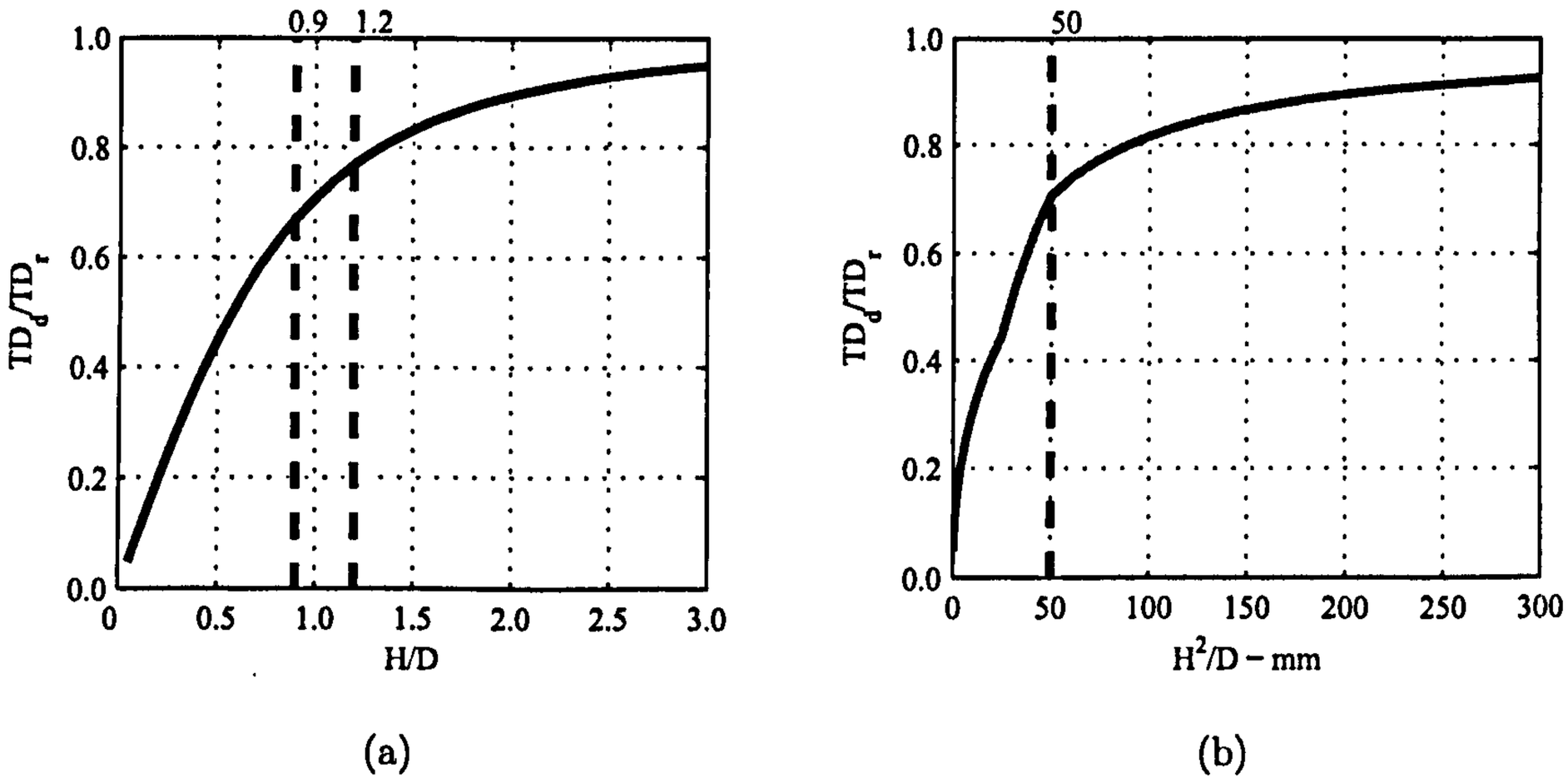

Figure 6.48: Study of direct and reflected travel distances ratio variation with geometry parameters.

The relationships between direct and reflected travel paths provide interesting reading. In figure 6.48(b), a distinction in the travel path ratio curve can be observed at a $H^2/D \approx 50$mm. This value limits a range for which the reflected travel path length could be assumed to be similar to the length of the direct travel path. Such travel path length distinction at $H^2/D \approx 50$mm coincides with the establishment

of a waveguide behaviour for the samples when tested in the frequency domain, as proposed in figure 6.43. The occurrence of this feature feature strengthens the argument in favour of the proposed distinction between models of sample behaviour and its relation with sample geometry, namely the geometric parameter H^2/D.

Returning to the time domain results, in terms of travel time, a distinction was established for sample slenderness ratio of around $H/D = 1.2$. A similar analysis in terms of near-field effect and total dispersion provided a distinction in behaviour at slenderness ratio of $H/D = 0.9$. These two values were highlighted in the relation between reflected and direct travel path lengths given in figure 6.48(a). At the proposed values of slenderness ratios, such a clear break feature is not noticeable as in the case of the frequency domain results observed in figure 6.48(b). However, some distinction can be made between the travel path lengths before and after the range given by $H/D \in [0.9\ 1.2]$.

6.6.4 Frequency Domain Vs Time Domain

Signal processing and interpretation methods using results in the time and frequency domains both aimed at obtaining the correct wave travel time. In the time domain the travel time results are measured directly between chosen features of the transmitted and received electric signals. In the frequency domain, namely through the use of the phase delay response curve gradient, the travel time results are obtained in relative terms, i.e., the correlation between the phase difference of two or more results at different frequencies are used to provide a travel time.

Apart from the waveguidance effect of model conversion at a reflecting boundary, two well-known phenomena in wave propagation and body vibration theory are also believed to be relevant; the phase shift and mode conversion that occurs at the transmission of energy between two media interface, (Doyle, 1977). So at each interface, the response might be different to the excitation in terms of their

relative phases, and wave mode since a modal conversion can occur, where a longitudinal wave components might be transmitted as a flexural wave component for example. When testing with bender elements, a minimum of four interfaces exists, those between transmitted electric signal and transmitting bender element, between transmitting bender element and sample, between sample and receiving bender element, and finally between receiving bender element and received electric signal. At each of these four interfaces the mentioned phenomena could be expect.

The monitoring of a transmitting bender element using a laser velocimeter, (chapter 5), permitted the observation of a minimum time delay between transmitted signal and actual bender element vibration of around 0.01ms, (figures 5.12 and 5.18). This time delay was attributed to actual travel time of the signal in the electric circuit. It also permitted the observation of a phase shift which in practise translates into an apparent second time delay of around 0.03ms. The relative importance of such direct and indirect time delays on the overall travel time determination depends on the flexural stiffness of the medium, as well as on the total travel distance. One important characteristic of each possible time delay at each interface is that they are cumulative.

For the example of the tested synthetic rubber with $V_s \approx 45\text{m.s}^{-1}$, and for a sample height of 20mm, with the transducers embedded 3mm each in the sample and a travel distance measured between their centres of dynamic pressure, the expected shear wave travel time would be $tt = (0.02 - 2 * 0.00182)/45 = 0.36\text{ms}$. The mentioned apparent and real time delays of 0.01ms and 0.03ms at the transducer interface can have an importance of 2.8% and 8.3% each, bringing the total time delay up to 11%, just for one of the possible time delays present in a simple bender element testing system. Assuming a similar value was measured at the receiving transducer, the total time delays would be of 22%.

The contribution of the mentioned apparent delays between each interface can be

significant and cannot be avoided when dealing with the results in the time domain. The frequency domain results are obtained using relative readings. Possible time delays at different signal frequencies are therefore not considered. Even if such time delays exist and vary with signal frequency, when measuring the phase delay between two similar frequencies, they cannot be expected to have much impact. When measuring the phase delay between two responses with similar frequency, both results are influenced by approximately the same time delay and so the relative results should be, all other things being equal, independent from it.

The cumulative delays possible in each interface of the test system, and the difficulty in quantifying them, justifies the use of frequency domain techniques to measure the wave travel times.

6.6.5 Continuous Signal Vs Pulse Signal

Both continuous and pulse signals can be used to excite the transmitting bender element. Pulse signals, either square or sinusoidal, have been used since the start of bender element testing, inherited from another dynamic soil tests such as the cross-borehole test, (Bodare and Massarsch, 1984; Shirley and Hampton, 1978).

Pulse signals are, by definition, short in duration. This carries two important consequences. One, is that they are quite broadbanded, i.e, they have a large frequency content, as can be confirmed in figure 5.13. It entails that the frequency with which the signal is referred to is only partially related to it. It also means that there might be some confusion between the frequency content one might wish to transmit and the frequency content actually being transmitted. The second consequence has to do with the mechanical response of Newtonian systems to short duration excitations, considering their mass and therefore their inertia. This response is referred to as a transient response, (Clough and Penzien, 1993). A transient response of a system is dominated by the properties of the system itself where, for example, the

frequency at which it vibrates is its own natural frequency rather than the excitation frequency (figures 5.12 and 5.18). This is true for short signals such as pulse signals with frequency content that is higher than the natural frequency of the mechanical system excited. Thus, even if the reference frequency of a pulse signal is lower than the natural frequency of a transducer, part of its broad frequency content can still be capable of exciting it in a transient manner.

Bender elements are no exception, and respond in a transient manner, as other simple mechanical systems, to short duration excitations. In fact, the problem is not limited to the response of the transducers as the response of the sample to short duration excitation is also a transient response and again, its own natural frequencies dominate its behaviour, (section 6.5). When testing with pulse signals there is in fact little or no control over the frequency of the response. The operator of a bender element test might therefore be misguided into the actual degree of control he has over the system's response. Even though he controls the central frequency of the transmitted pulse signals, he does not control the frequency of the response of the transmitting transducer and that of the sample, their own mechanical properties do.

When testing with pulse signals, there is little control over the actual frequency of the system's response or its components. This means that there is also no control over dispersion phenomena which are frequency-dependent. These dispersion phenomena have already been discussed and were referred to as the near-field effect and the waveguide dispersion. In cross-borehole testing, even when using square pulse signals, which have even broader ranges of frequency content than sinusoidal pulse signals, frequency dependent dispersion phenomena are most often not relevant. In cross-borehole tests the receivers are placed at a considerable distance from each other and also apart from the wave source. This means that the near-field effect can be disregarded since the near-field wave components decay much faster with distance from the wave source than the far-field wave components do. Furthermore,

they also become less dispersive with distance from source. In terms of waveguide dispersion, again the geometric nature of cross-borehole testing explains why it is not significant. The geometric boundaries from which wave components could be reflected from are quite distant from the direct wave travel path. Hence, possible reflected wave components do not influence the received waves. This means that the transmitted pulses can be considered to propagate as in an unbounded medium, and consequently, with no waveguide dispersion.

Continuous signals such as harmonic continuous signals have relatively much narrower banded frequency contents when compared with pulse signals. For example, the frequency content of a sinusoidal pulse signal and a sinusoidal continuous signal, both with a central frequency of 3.0kHz, are presented in figures 2.4 and 2.6 respectively.

Harmonic continuous signals, with a relatively long duration, are able to excite a simple mechanical system into a steady state of vibration. In terms of wave propagation, this steady state is known as a standing wave, (Achenbach, 1973). The response, namely its amplitude and phase delay, varies with the amplitude and the frequency of the excitation. Nevertheless, the frequency of the excitation and of the response are the same. When using a harmonic continuous signal, it is possible to control the frequency of the system's response. This way it is possible to steer this response clear of significant near-field effect and of the highly dispersive nature of the flexural modes of wave propagation at low frequencies.

Continuous signals are not a panacea for testing with bender elements with minimum dispersion. A system's response can be driven to vibrate at a chosen frequency, but the magnitude of such response might be too low to enable a successful bender element analysis. Every mechanical system with mass is a frequency filter, for which there is a maximum frequency after which no significant vibration can be transmitted. Bender elements and soil samples are such systems. An analysis of the

maximum frequency transmitted through a bender element / rubber sample system was presented in section 6.4.1. It was possible to establish a maximum frequency for each tested sample. It was also possible to observe how this maximum frequency decreases with sample height.

An example of an unsuccessful test, using harmonic continuous signals, is presented in figure 6.42. The velocity result for sample S29 - $h76 \times d38$mm, obtained at a low frequency range, is lower than the estimated equivalent shear wave velocity. Precisely because signals with relatively low frequencies could be received, a highly geometric dispersive behaviour could not be avoided resulting in the obtention of an uncharacteristic velocity result. The observation of the impact of low frequency results leads to the proposition of a frequency limit based in the flexural modal behaviour of the sample and a function of the sample's properties. This frequency limit is expressed in equation 6.1.

6.6.6 Overview

The study of the parametric results permitted the conclusion that a universal formula for testing with bender element is not possible. It has been demonstrated that different types of signal, signal frequency, and sample geometry, all influence the dynamic behaviour of the samples and consequently the obtained estimate wave velocities.

In terms of sample geometry, it was possible to distinguish between three different models of behaviour. Bulk samples, propagating waves as if in an unbounded medium, slender samples behaving as waveguides, and samples with intermediate geometries, behaving in a transient, more erratic, way.

For any given sample, dispersion can only be controlled with signal frequency, both due to near-field effect and wave reflection. When using pulse signals, only a transient response can be obtained from the tested system. This means that little

control over the frequency of the response is available. For this reason, continuous signals should be used, enabling a steady state response from the system.

Even when using continuous signals, there is no complete control over the dynamic response of the system. Since each component of system behaves as a frequency filter, the geometry of the sample or of the transducers, as well as their elastic properties, limit the range of frequencies at which an optimum response can be obtained. It is therefore possible that a particular sample can only be tested with minimum dispersion at a frequency for which its response is negligible. In other words, there might be sample and transducer set-ups which cannot be successfully tested.

The observations made so far concern samples made of a particular soft rubber material, with a Young's modulus in the range of $E \approx 10\text{MPa}$, a density of $\rho = 1000\text{m.s}^{-3}$ and a Poisson's ratio of $\nu \approx 0.45$. Soft soils are generally stiffer $E \approx 100\text{MPa}$, denser $\rho \approx= 1700\text{m.s}^{-3}$ and have various Poisson's coefficients, (Atkinson, 2000). Nevertheless, the generic mechanic response, considering linear-elastic behaviour, must be similar and only the observed values of geometry parameters and signal frequency might vary. For example, a medium which is stiffer than the used rubber will have, all other things being equal, resonances at higher frequencies and also faster wave velocities, leading to the possibility of it being capable of propagating signals with higher frequencies. The main goal of the parametric study was to present a set of theoretical principles which can be considered to guide the behaviour of a bender element test system. Other goals were also the demonstration of the importance of moving past the initial behaviour model of unbounded wave propagation into a more realistic, and not necessarily more complicated models, with solid theoretical background that enable the interpretation of results taking into consideration a number of factors such as the sample geometry. This goal is believed to have been accomplished in a satisfactorily manner.

Chapter 7

Numerical Analysis

This chapter is concerned with the numerical analysis of a finite difference dynamic model of a soil sample and bender element transducers system. Laboratory testing results have confirmed the complex modal dynamic behaviour of soil samples and bender element transducers alike. Some indications have already been obtained that such behaviours can be explained by well-known dynamic theories of wave propagation, body vibration, and corresponding analytical models. Nevertheless, there are no closed-form solutions for this specific dynamic problem, (Hardy, 2003). Therefore, a numerical analysis becomes a suitable tool to pursue a better understanding of general and specific phenomena related with the use of bender elements.

7.1 Literature Review

Numerical analysis related to bender element testing has been performed for different aspects of this particular mechanical process by a number of authors. In table 7.1, a summary of some of these authors and respective computer programs used in their studies is presented.

Author	Type	Model	Program
Jovičić *et al.* (1996)	finite elements	plane shear - 2D	SOLVIA 90[1]
Arulnathan *et al.* (1998)	finite elements	plane shear - 2D	GeoFEAP[2]
Hardy (2003)	finite elements	plane shear - 2D	ICFEP[3]
Hardy (2003)	finite elements	Fourier series - 3D[4]	ICFEP
Arroyo *et al.* (2002)	finite differences	plane shear- 3D	FLAC3D[5]

Table 7.1: Summary of numerical computer programs used in the analysis of bender element problems.

Jovičić *et al.* (1996) used a finite element program to model a two-dimensional, plane strain, normally consolidated Speswhite kaolin soil sample as an isotropic, elastic and drained medium. The medium's properties were a Young's modulus of $E = 118\text{MPa}$ and a density of $\rho = 2000\text{kg.m}^{-3}$. A confining stress of 200kPa was also applied. This study focused on the wave propagation caused by forcing a soil node to oscillate transversely in a single cycle sinusoidal pulse. The time histories of the displacements of the source point and of a second point, representing the receiving bender element, were then compared to obtain a wave travel time. Two pulse signals with different central frequencies were used. These frequencies were chosen so that a particular dimensionless relation between shear wave velocity and wave length of $R_d = 1.1$ and $R_d = 8.1$ could be obtained, where R_d is given as:

$$R_d = \frac{td \times f}{V_s} \tag{7.1}$$

and where td is the travel distance, f is the frequency and V_s is the shear wave velocity.

The obtained results were compared with actual test results of a Speswhite kaolin

[1]As seen in AB (2005).
[2]Geotechnical Finite Element Analysis Program, (Bray *et al.*, 1995).
[3]Imperial College Finite Element Program, (Potts, 2005).
[4]Not a full 3D analysis but an alternative for fewer memory storage and processing time needs.
[5]Fast Lagrangian Analysis of Continua in Three-Dimensions, (Itasca, 2002).

soil sample. The numerical results appear to agree well with the pre-determined shear wave velocity. However, some complex response components attributed to the near-field effect were identified. It was also possible to observe from the numerical results that the frequency of the received signals might not have the same frequency as the transmitted signal. Similar frequency disagreements have been also observed for practical tests, as presented in section 6.5.4 for example.

Arulnathan *et al.* (1998) prepared a finite element model with the objective of evaluating the sources of travel time determination errors, namely the interference of the end plates, the transfer function between electric signal and the actual mechanical oscillations and near-field effect. The error associated with the assumption of one-dimensional wave propagation is also mentioned. A two-dimensional finite element model of a soil sample with plane strain and with linear elasticity was used. The transmitting and receiving bender element pair were modelled together with the soil sample. The transmitted signals were sinusoidal pulses. A parametric study was conducted varying the input pulse signal central frequency, sample size, mesh scale, bender element length, soil stiffness and Poisson's ratio.

The results presented by Arulnathan *et al.* (1998) agree with some observations already made in chapters 5 and 6. For example, a phase lag between the excitation load and the actual tip displacement was observed, as was also seen in section 5.5. Different methods of evaluating the wave travel time were used, cross-correlation and direct time reading using different peak features of the transmitted and received signals. The numerical results from these different methods do not match and neither do they precisely match the actual predetermined equivalent shear wave velocity. It is also interesting to note how, using direct time readings, different travel times were estimated using different curve features. The disparity between these results increases for lower input signal frequencies. Similar results, for practical tests, were obtained in section 6.5.3.

Hardy (2003) presented a thorough numerical analysis of the bender element test, also presented in Hardy *et al.* (2002) where three different types of models were used. The first two models were two-dimensional and considered a plane strain wave propagation. The first model only considered the soil medium, which was in fact forced to behave as if though it were one-dimensional. This was achieved by forcing the lateral surfaces to have no longitudinal movement hence stopping any wave reflected components from reaching the receiver. If no wave reflection exists, then in principle no waveguide dispersion can occur. The second model considered both the soil sample and a pair of bender elements. The third model, also considering the soil and bender elements, was calculated using a Fourier series, which together with some considerations of symmetry, enabled it to emulate a three-dimensional behaviour. The time step, as well as the mesh scale, were tested for various values in order to optimise the quality of the results.

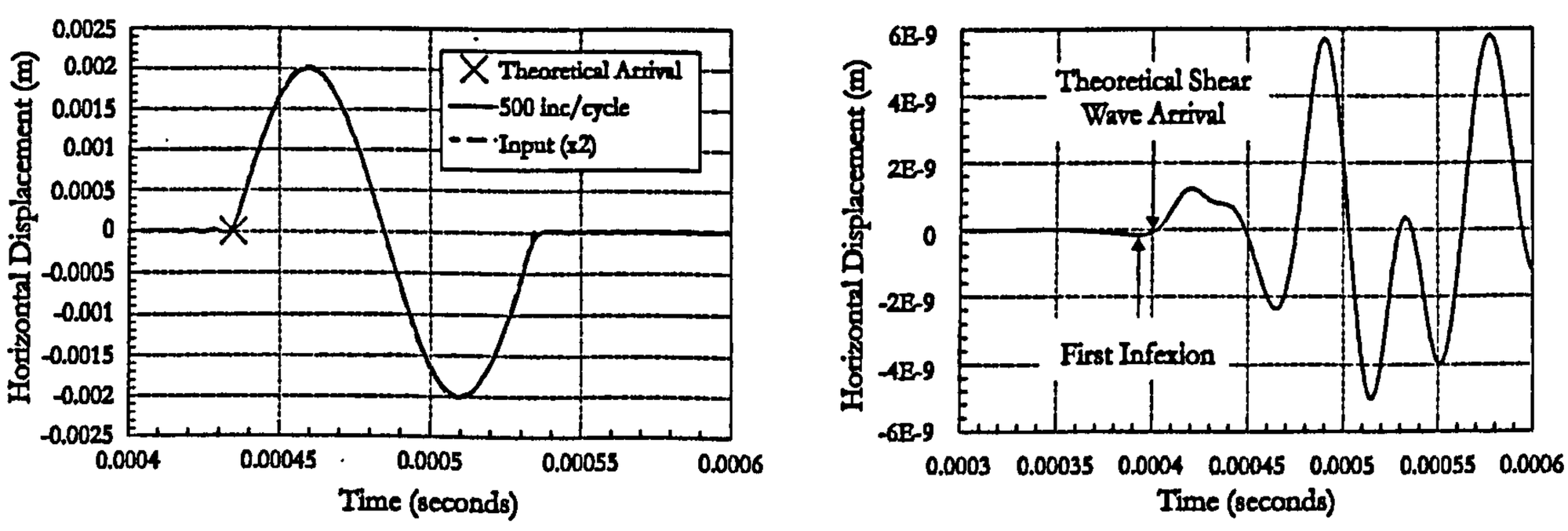

(a) 1st model - 1D unbounded

(b) 2st model - 2D bounded

Figure 7.1: time history of the received signals for the 1D unbounded and the 2D bounded numerical modes, extracted from Hardy (2003).

The first model, with an example result seen in figure 7.1(a), behaving as a one-dimensional model, is capable of propagating a shear wave with little or no distortion, depending on the time step used. For time steps small enough, the received signal is an exact scaled copy of the transmitted signal. This test is useful, since it provides a benchmark to determine the necessary boundary conditions that

need to exist so that an undistorted wave propagation can occur, and consequently for which unbounded wave propagation assumptions can be supported.

The second model, with an example result seen in figure 7.1(b), appears to produce more realistic results. The time history of the received signals, obtained using different input signal frequencies, indicates no specific feature, which can be reliably and consistently associated with the actual shear wave velocity. Nevertheless, the first inflexion, for the particular sample elastic properties and geometry used, does seem to be the feature from the received curve which provided the most approximate results in terms of expected wave velocity. It was also observed that signs of dispersion affecting the reading of the first arrival diminish with increasing input signal frequency. Issues of dispersion were only associated with near-field effects and no mention to waveguide dispersion, or to sample modal behaviour was made. This significantly limits the mentioned analysis. Hardy (2003) does not mention the apparent constant frequency of the received signals for higher frequency input signals. If, as observed, the received signals have a constant independent frequency, then any possible relation between input signal frequency and observed dispersion is limited, since the actual received signal frequency is where the dispersion should be analysed.

The second numerical model used by Hardy (2003) was also excited using a continuous signal in order to perform a phase-sensitive detection method. It was thus possible to avoid transient states of vibration. However, the results from this model were not so satisfactory. A number of frequencies were determined for which the transmitted and received signals should have been in-phase, but that was not the case. This could be explained, for example, by an incorrect assumption of travel distance. Hardy (2003) assumed the travel distance to be that between transducers tip-to-tip. A challenge to this assumption can be found in section 6.6.1.

The third model, approximating a three-dimensional analysis, leads to results

similar than the results from the plain two-dimensional second model. This model produces a more complex received signal, for which the determination of first arrival is less objective. It is also interesting to notice that, in this case, the increasing of input signal frequency does not eliminate the signs of dispersion. On the contrary, it increases them. Again, this might indicate that more than near-field effect dispersion might be present.

The comparison between the results of the first and second models, as given by Hardy (2003), and partially represented in figure 7.1, provides a useful observation. The first model, for which no wave components can be reflected at the lateral boundaries, shows received signal with very little signs of distortion and very little signs of dispersion, for small enough time steps. An analytical calculation following the steps given in section 3.6 and the material properties given in Hardy (2003), estimated the near-field wave components to have a magnitude of around 4% of the far-field wave components. This estimate agrees with the results presented by Hardy (2003). For the second model, the same material properties were used, with no restrictions applied to the lateral boundaries of the sample. In this case, the received signal appears to be more realistic, showing clear signs of distortion and of dispersion. Considering the travel distance to be measured between bender element tips, the theoretical near-field effect for the second model would still have around 4% of the far-field wave magnitude.

The main differences between the two models are the boundary conditions at the lateral surface and the inclusion of bender elements on the second model. If the inclusion of the bender elements, modelled as perfectly coupled to the soil sample, is considered not to have a significant effect in the way waves propagate along the sample, then the great increase in distortion, observed in the second model, can surely only be attributed to the changes in the lateral surface boundary conditions. Since the near-field effect is theoretically predicted to be similar in both models,

the observed increase in dispersion cannot be attributed exclusively to the near-field effect. This leaves the wave reflection phenomena, also referred in the present study as waveguide dispersion, as another significant source of dispersion.

Arroyo *et al.* (2002) created a true three-dimensional numerical model using a less conventional finite difference model. According to the authors, finite difference models are numerically less expensive for small wavelengths and might introduce less numerical dispersion, due to the employed discretization algorithms, (Zienkiewicz *et al.*, 2000). A parametric study was performed where the sample diameter and height were varied in order to understand their influence on the overall behaviour. Arroyo *et al.* (2002) have only modelled the transmitting bender element having used the oscillation of a node at the other end of the sample to evaluate the received signal. The influence of the lateral boundaries was also studied by making them absorbing or non-absorbing, affecting their capacity for wave reflection.

Arroyo *et al.* (2002) obtained a received signal with no clear first arrival, and no feature that could be associated with a theoretical first arrival, as Jovičić *et al.* (1996), Arulnathan *et al.* (1998) and Hardy (2003) had. In the case of Arroyo *et al.* (2002), the first inflexion and the theoretical first arrival are the least related of the presented cases.

For all the results produced by the mentioned authors, the time history of the received signals are significantly different from the input signals. The fact that four different authors using different software packages and different modelling techniques produced received signals which were distorted in relation to the input signals is a sign that the used numerical models are capable of simulating at least some of the mechanical phenomena which leads to such distortion. The observed distortions are common in laboratory practical results and make a strong case against the possibility of undistorted wave propagation. It means that boundary condition assumptions related with undistorted wave propagation are not reliable, such as the assumption

of unbounded wave propagation. The fact that, in general, these authors were also not able to match the theoretical first arrival of a propagating shear wave with any particular feature of the received signal time history is also a strong case for the inherent difficulties of avoiding wave dispersion, casting more doubts about the reliability of travel time determination using the time history of the transmitted and received signals. Arulnathan *et al.* (1998) goes further in demonstrating the phase lag between the excitation load and oscillation movement of the transmitting bender element, further strengthening the case of unreliability of direct time readings.

7.2 Introduction to FLAC3D

The software package used for the present work was FLAC3D[6]. This programme was used because it offered the possibility of true three-dimensions modelling, with only reasonable processing costs. Two-dimensional modelling is believed to be insufficient to study the influence of the sample geometry over its dynamic behaviour when excited by a bender element. Even though the tested samples were often cylindrical, the transversal motion caused by the transmitting bender element was anti-symmetric, causing equivalent positive and negative strains on each side of the transducer. Moreover, different wave components propagate in different directions and are reflected differently once they reach the cylindrical or other shape of the sample lateral surface. Such a complex wave propagation can only be modelled if all aspects of the sample geometry are considered.

FLAC3D uses an explicit finite difference method of modelling the behaviour of geomechanical structures. It is capable of modelling linear and non-linear, elastic and plastic behaviour. In three-dimensional models, the constitutive elements forming the grid assume various semi-regular polyhedron shapes, such as bricks and

[6]Thanks to the much appreciated collaboration of Prof. Luis Medina at Universidade Da Coruña.

wedges. Besides static analysis, FLAC is capable of linear and non-liner dynamic analysis, creep analysis, thermal analysis and fluid flow analysis. Only linear elastic dynamic analysis is used for the present study.

By using a finite difference method of modelling, FLAC does not need to build and store stiffness matrices. For this reason it is able of using a lower processing capacity than standard finite element programs to run similar models or more complex models using the same processing capacity. The processing capacity limitations mentioned by Hardy (2003) and the cause for not running full three-dimensional models are therefore possible to overcome.

7.2.1 Damping

While using analytical models to study the dynamic behaviour of bender element transducers and soil-like samples, a simple form of viscous damping was used. This form of damping, presented in section 3.9, is ideal for use in analytical models, due to its simplicity compared to more realistic hysteretic forms of damping. Viscous damping is a simpler concept but has its limitations, it is frequency-dependent, which is not a trait of real mechanical damping.

FLAC permits the use of two types of hysteretic damping. One such form of damping is the Rayleigh damping, often used in time-domain programs. Rayleigh damping is frequency-independent only within a particular range of frequencies, being frequency-dependent outside that range, (Bathe and Wilson, 1976). It is independently proportional to the mass and to the stiffness of the system, and it is therefore necessary to define it by determining two respective damping constants.

The other form of damping offered by FLAC is called local damping. This form of damping is, for simple cases, frequency independent. It is modelled by adding and removing mass to oscillating elements, proportional to the mass and acceleration of that element. The addition and subtraction of mass is made so that there is an

overall conservation of mass in the system. This model of damping is not fully tested and must be used with some care for complex systems with multi-modal behaviour, (Itasca, 2002).

As in Arroyo *et al.* (2002), local damping is used. This way, since the model is relatively simple, non-frequency dependence can be assumed for the range of excited frequencies used. Local damping only needs one dimensionless parameter, unlike Rayleigh damping, which needs two. This makes its estimation more intuitive. Also, local damping is less expensive in terms of computational processing capacity.

7.2.2 Grid Size and Time Step

The wave frequencies that can be correctly propagated along the model are dependent of the grid dimensions, namely its maximum dimensions. In Itasca (2002), the following limit is proposed,

$$\Delta l \leq \frac{\lambda}{10} \tag{7.2}$$

where Δl is the maximum grid element dimension and λ is the wavelength.

The time step used in the calculations does not need to be determined by the user, it is automatically calculated by FLAC. Depending on the use of local or Rayleigh damping, the dynamic time step takes different values, for numerical stability reasons. The time step expression when using local damping is given as:

$$\Delta t = \min \left\{ \frac{V}{c_p A_{max}} \right\} \frac{1}{2} \tag{7.3}$$

where V is the model sub-zone volume, A_{max} is the maximum face area associated with the respective model sub-zone and c_p is the longitudinal wave velocity. The minimum function includes all of the model's sub-zones.

7.3 Simple Parametric Study

Two separate numerical studies were conducted using FLAC3D. In this section is presented the study of a simple parametric study based in the work presented by Arroyo *et al.* (2002) and further developed in Arroyo *et al.* (2006). The numerical model described as model A was used to prepare a second model with the same properties but with a larger diameter. The main objective is to be able to compare the results from the two models and to evaluate the influence of the sample's diameter on the wave propagation phenomenon.

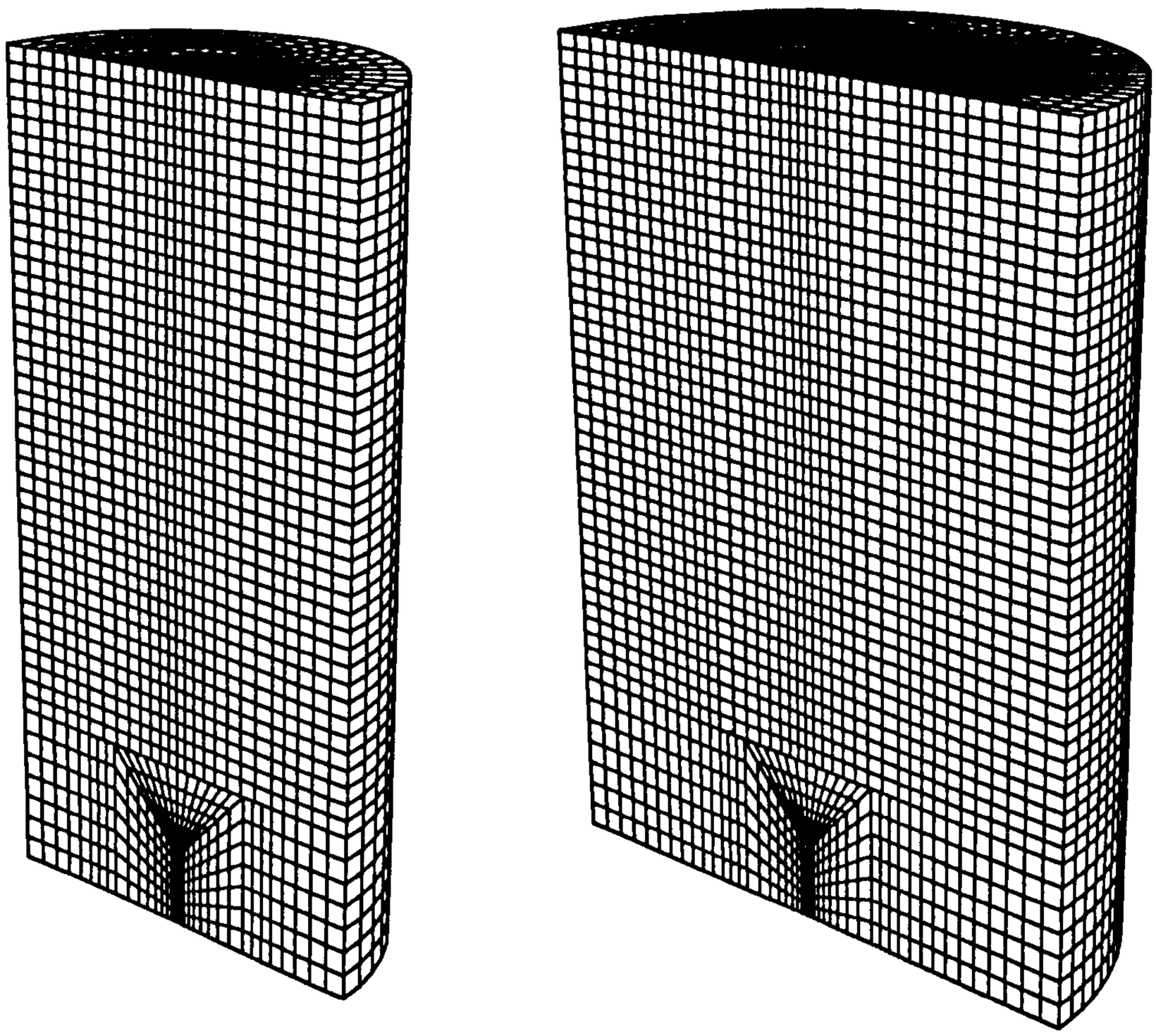

(a) Model A - $D50 \times H100$ (b) Model B - $D75 \times H100$

Figure 7.2: representation of finite difference grids of models A and B.

7.3.1 Model Description

Two models of a cylindrical soil sample with diameters of 50mm and 75mm were used with a height of 100mm. These models include a transmitting bender element

at the bottom end which is 2mm thick, 10mm high and 10mm wide and is completely embedded in the sample. Figure 7.2 shows the graphical representation of grids of the two distinct models.

The soil sample and bender element were modelled as two different media. The properties of the soil medium are given in table 7.2. The elastic properties of the bender element were modelled as being ten times higher than those of the soil. This was to ensure that the transducer is significantly stiffer than the soil. In this way, the bender element transducers have a Young's modulus of around $E = 630$MPa. This value is nearly four times smaller than the stiffness value estimated in section 5.6. The reason for this discrepancy is that the numerical study was performed before the monitoring study. The remaining properties of the bender element are the same as those of the soil, i.e., the same Poisson's ratio and density.

Model A - $D50 \times H100$mm / Model B - $D75 \times H100$mm

Property	Symbol	Units	Value
Bulk Modulus	k	Pa	26.4×10^6
Shear Modulus	G	Pa	28.6×10^6
Poisson's ratio	ν	—	0.10
Density	ρ	$kg.m^{-3}$	2000
Compression Wave Velocity	V_p	$m.s^{-1}$	180
Shear Wave Velocity	V_s	$m.s^{-1}$	120

Table 7.2: Properties of the soil medium for numerical models A and B, in FLAC3D.

The cylindrical models are in fact modelled as half cylinders. The vertical plane that crosses the vertical axis of the sample and the bender element width is capable of providing a symmetry plane, in terms of geometry and motion. A horizontal restraint is applied to the displacement of the nodes along this symmetry plane.

This way only half the processing capacity is needed. The necessity of full three-dimensional models to correctly simulate the complex behaviour of wave propagation generated by bender element has been stated. Precisely due to the non-symmetric wave components radiation from the transducer, as well as non-symmetric wave reflection from the cylindrical lateral surface of the sample, it might now seem incoherent to use symmetry to simplify the model. Take the pressure distribution of a circular section presented in figure 7.3, obtained for the displacement of a node in its centre, estimated from a similar pressure distribution presented by McSkimin (1956). It can be observed that there is a plane of symmetry along the vertical axis that crosses the circle centre. This observation provides the premisses which allow the modelling of just half a cylinder and still assume the results to be similar to those of a full cylinder.

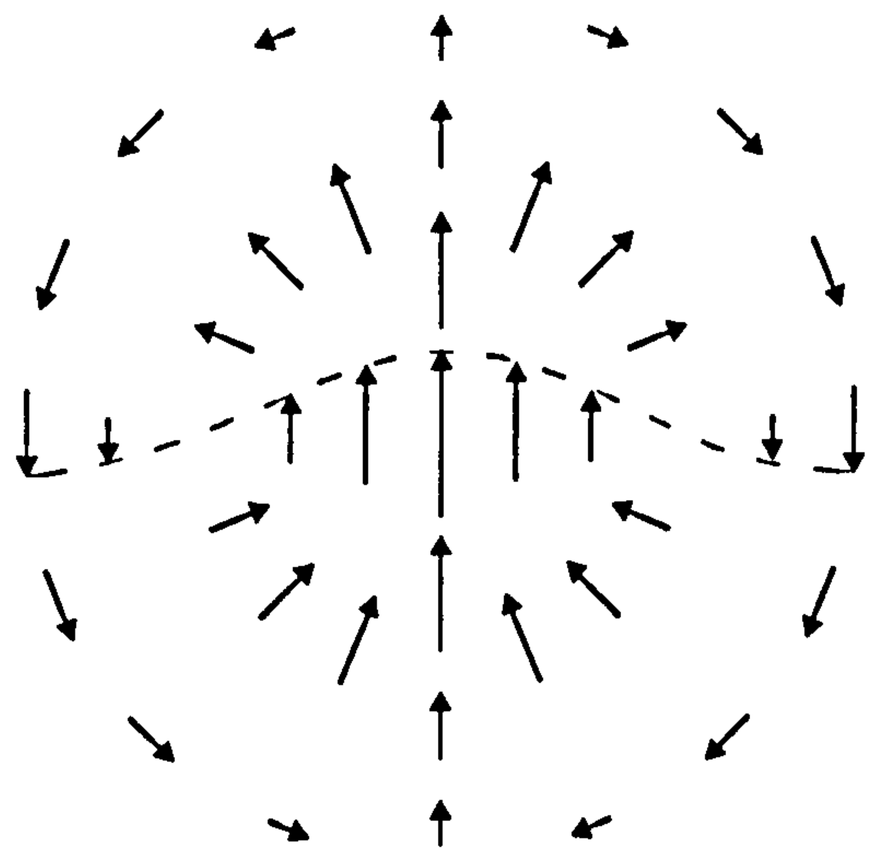

Figure 7.3: pressure distribution on a circular section, subjected to the displacement of a node in its centre.

The boundary conditions of both models are similar. They are horizontally fixed along the vertical face of symmetry. Their bottom end face is vertically fixed but left with free horizontal movement. Their top end surface is absorbent, so as not to introduce any reflected wave components back into the system and hence avoiding

further complexity of behaviour. The models are also confined by an isotropic pressure of 100kPa.

The excitation is applied in the form of a forced motion. The bender element is forced to move by application of a displacement history, parabolically distributed along the transducer's height, so as to simulate it deformation when bending as if excited by an electric signal with its based fixed. The displacement history consists of a single cycle of a sinusoidal function with a frequency of 4.0kHz, null phase delay and an amplitude reached by the top nodes of 0.1mm, represented by:

$$u(t) = \begin{cases} 0.1\,\sin(2\pi 4000t + 0) & \text{(mm)} \quad \text{for} \quad 0 \leq t \leq 1/4000 \\ 0 & \quad \text{for} \quad t > 1/4000 \end{cases} \text{(s)}$$

where time, t, is in seconds and the displacement, $u(t)$, is in millimetres.

Besides modelling the two described samples with similar properties and different diameters, another study case was also tested where the samples have absorbing lateral surface. These tests enable the simulation of almost no wave components being reflected from these boundaries back into the sample. In this way it is possible to estimate the behaviour of the model as if the sample was unbounded in terms of wave propagation, such as Blewett *et al.* (2000) attempted in actual laboratory testing. The absorbing boundary condition is a particular feature of FLAC, it does not provide an 100% effective absorbance, losing eficiency for wave components reflecting at lower angles from the surface.

7.3.2 Results

Figure 7.4 displays the time histories of the horizontal displacements of the node at the top of the sample symmetry axis for models A and B with reflecting boundaries. The equivalent time response for model B with absorbing lateral surface is also

presented. For reference purposes, the input signal as well as the equivalent travel time correspond to a shear wave velocity of $V_s = 120\text{m.s}^{-1}$.

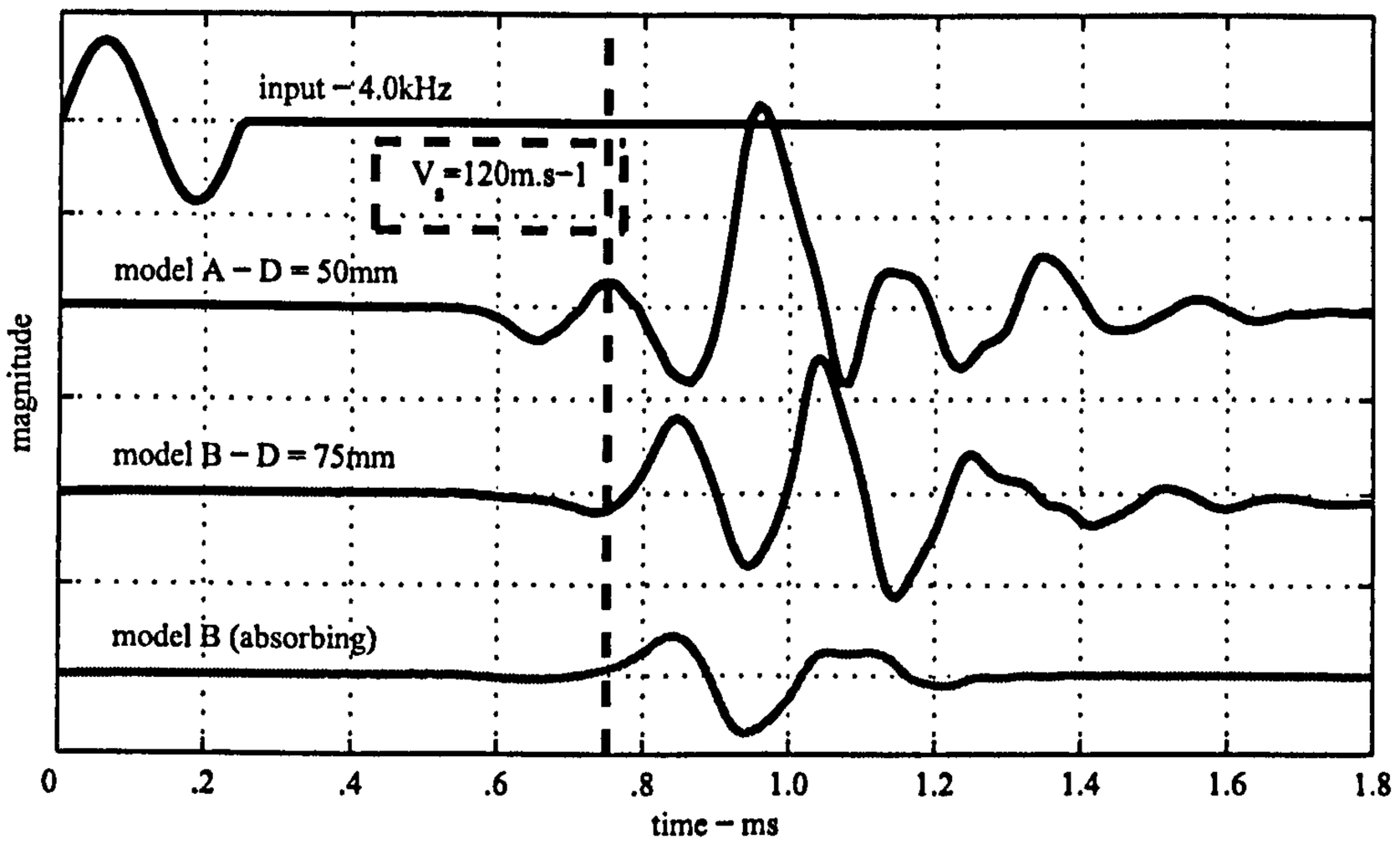

Figure 7.4: time history of received pulse signals at top of the sample, for model A and model B.

The response of model A appears to be realistic, similar to a characteristic response of a bender element test. This result is encouraging in terms of validity of the numerical analysis carried out. It can be observed that the first arrival occurs sooner than the shear wave velocity would indicate, which is also a not very uncommon result. The response in model B is apparently similar to that of model A except for having a slightly lower magnitude and of having its main peak feature arriving at a later time. The very first arrival in model B also does not occur at the expected time of 0.75ms. The response of model B with absorbing lateral surfaces is the one with apparent less distortion. It lasts only one and a half cycles and has a first arrival nearest to the expected arrival time. The response for the absorbing model B is the most similar to the response obtained by Hardy (2003) for his unbounded model. This partially confirms the capacity of using absorbing surfaces to model unbounded conditions. It also strengthens the perception of which boundary conditions need to

be present for unbounded wave propagation to occur.

The comparison of the time response results for models A, B and absorbing model B, (figure 7.4), provides an analysis of the responses for samples with decreasing influence from laterally reflected wave components and consequent lower waveguide dispersion. The other studied cause of dispersion, the near-field effect, does not vary for these three cases since the signal frequency and the travel distance is the same for all. For these reasons, any changes in the received signal, namely changes which indicate dispersion, can be attributed exclusively to waveguide dispersion, (section 3.2).

A clear indication of the influence of the reflected wave components in the received signal can be seen to develop with sample geometry. For a supposedly unbounded sample, found in the absorbing model B, the received signal is the least distorted, with the latest first arrival occurring nearer to the expected shear wave arrival. As the possibility of wave reflection increases, i.e., with decreasing sample diameter, the received signal indicates larger distortion. The number of oscillation cycles can be seen to increase, the first arrival occurs earlier, and the difference between first arrival and expected shear wave first arrival increases. These observations confirm the observation already made about the significant influence the sample geometry has on the propagation of bender element generated waves, (chapter 6).

Figure 7.5 presents an attempt of wave decomposition. Assuming that a simple decomposition case of the received signal between direct and reflected wave components is possible. The response of the reflecting model A is the total response, including direct and reflected wave components. The response of absorbing model A is produced exclusively by the direct wave components, since no reflection could occur at the lateral surfaces. The difference between the reflecting and absorbing responses should produce the response caused exclusively by the reflected wave

components.

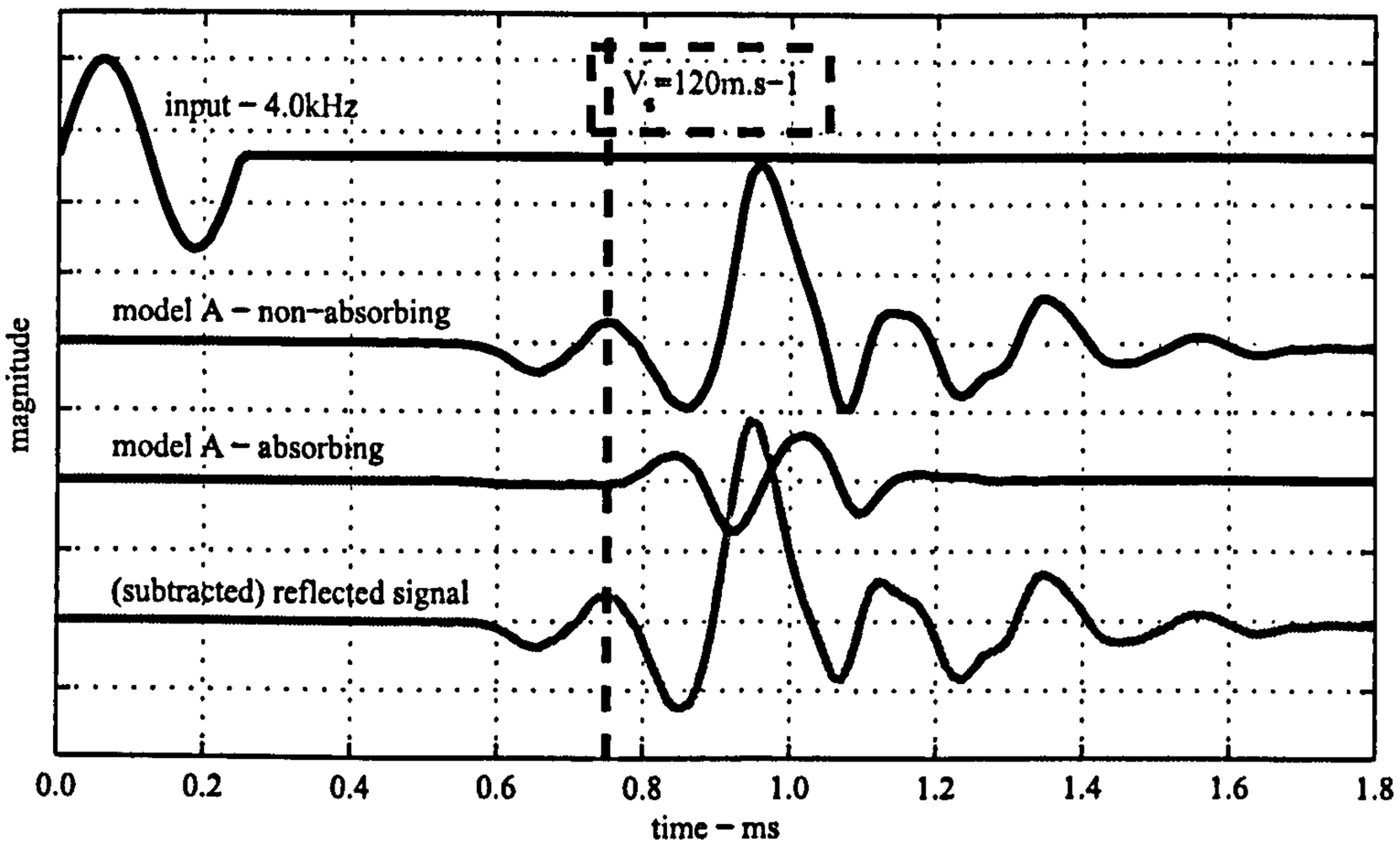

Figure 7.5: reflected wave signal obtained as the difference between the non-absorbing signal and the absorbing signal, for model A.

The comparison between the responses of the reflecting or non-absorbing model A and the absorbing modal A- $h100 \times d50$ indicates a larger complexity of the non-absorbing response. The non-absorbing model A also produces a response with an earlier first arrival. The exclusively reflected wave response is very similar to the non-absorbent response, (figure 7.5). This indicates that the non-absorbent received signal is dominated by the reflected wave components. The importance of the reflected wave components, which are not considered when assuming unbounded wave propagation, is therefore further acknowledged by these numerical results.

A similar analysis is made for model B- $h100 \times d75$ and presented in figure 7.6. This time, by comparing a model with a larger diameter, slightly smaller reflected wave components influence might be expected, since the travel path for these is now slightly longer.

Comparing the results of figure 7.6 for model B - $h100 \times d75$ with the results in figure 7.5 for model A - $h100 \times d38$, it is possible to observe discrepencies between

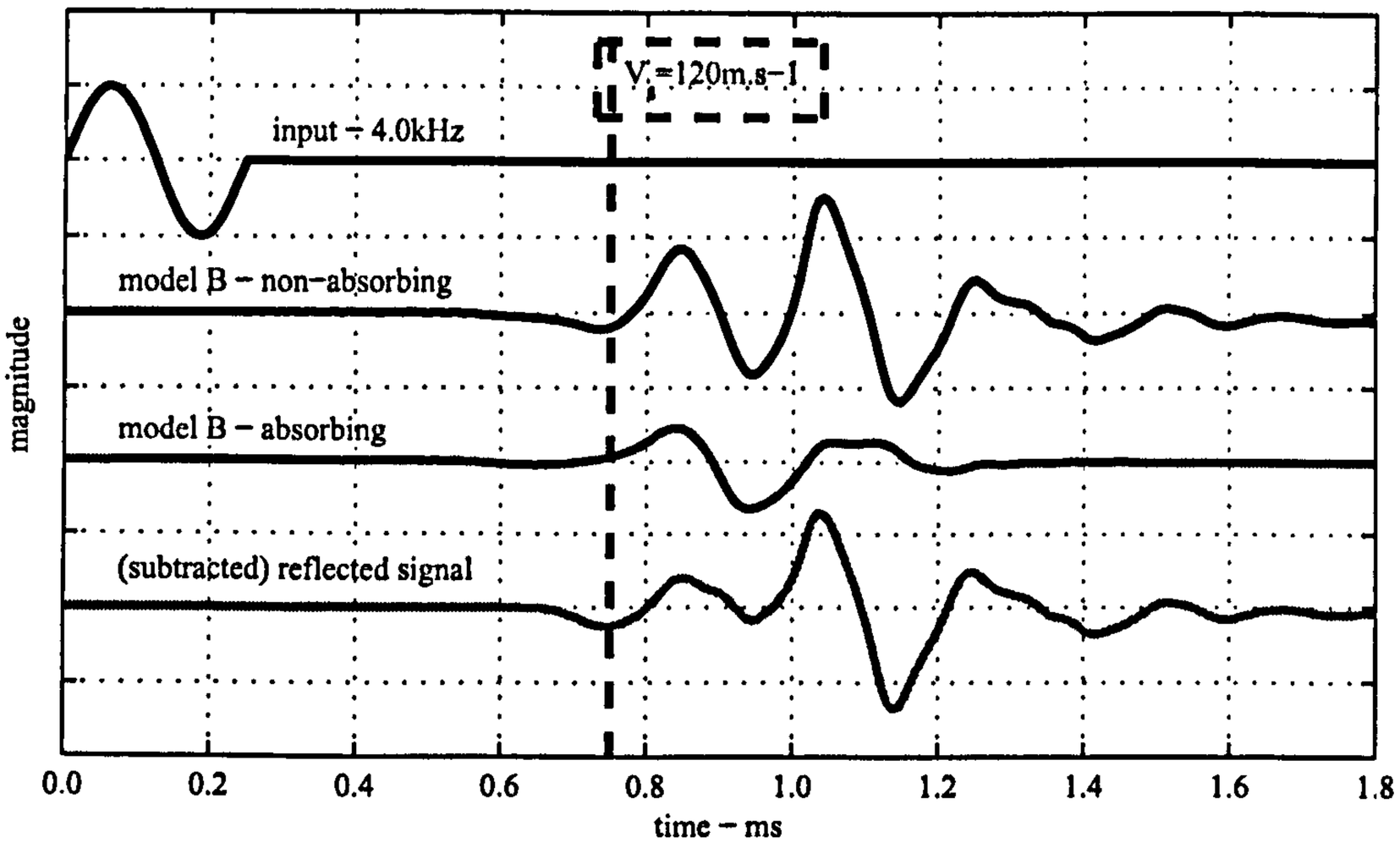

Figure 7.6: reflected wave signal obtained as the difference between the non-absorbing signal and the absorbing signal, for model B.

the subtracted results. In the case of model B, the subtraction produces a reflected wave signal less similar to the original non-absorbing signal. This indicates that the reflected wave components are now less significant than the direct wave components given by the absorbing model. It is also interesting to note how influential the dispersion caused by waves reflection is, and in the present case, how significant it is when compared with other sources of dispersion such as the near-field effect.

Both in the case of model A and model B, the received signal is mainly composed of reflected wave components, more so for model A with a slenderness ratio of $H/D = 1.0$. This observation indicates that, for the present simulations, with the present material properties, any wave velocity estimation using unbounded wave propagation assumptions is erroneous, leading to more or less significant underestimations of shear wave travel time and consequent overestimations of shear wave velocity and small-strain shear stiffness. Take for example the use of the first bump as the first arrival, given by feature E in figure 2.2, the concerning results are presented in table 7.3.

Model	Travel Time	V_s	G_0	Error
A&B	0.75ms	120.0m.s^{-1}	28.8MPa	0.0%
A	0.66ms	136.4m.s^{-1}	37.2MPa	29.2%
B	0.73ms	123.3m.s^{-1}	30.4MPa	5.6%

Table 7.3: Small-strain shear stiffness G_0 estimation error using first arrival for numerical models A and B.

In model A, the estimate of the material's small-strain shear stiffness using the wave's first arrival in the time domain produces an error of 29%, which is quite significant. For model B, the reflected wave compoenents are less significant and consequently the error in stiffness estimation, 6%, is lower.

When using a pair of bender elements to study the dynamic behaviour of a sample of any medium, an important limitation is present. Such a test set-up can only be used to monitor the behaviour of a single point of the studied sample, which in turn has to be at or near the surface. There are rare exceptions of using more than one receiver, (Belloti *et al.*, 1996; Lee and Santamarina, 2005). The use of numerical models permits to vanquish this limitation of bender element use. Using numerical models, it is possible to monitor the behaviour of any node of the sample. The models A and B were calculated registering the motion history of around 40 nodes along the samples main axis. The presentation of results for all these nodes in a combined fashion allows not only the study of each node, but also the study of the way in which the transmitted wave propagates.

Figure 7.7 shows a surface formed by the motion time history of 40 nodes along the sample's main central axis. These nodes are equidistantly separated 2mm from each other between the sample heights of 20mm and 100mm. The motion of the transmitting bender element tip at a height of $H = 10$mm, and of the nodes at $H = 20$mm, $H = 50$mm and $H = 100$mm are highlighted to assist the interpretation of the surface. The theoretical first arrival for a shear wave velocity of

$V_s = 120\text{m.s}^{-1}$ is marked in the corresponding highlighted response time history. The travel time is obtained considering a travel distance measured from the tip of the transducer. Figures 7.8 and 7.9 show similar surfaces for model B with non-absorbent and absorbing lateral surface respectively. The motion time histories are not presented with their actual relative magnitude. Since they decrease exponentially with travel distance, any direct comparison is difficult. Their magnitudes were therefore presented as normalised to each other.

A first comparison between the surfaces in figures 7.7, 7.8 and 7.9 shows a decreasing complexity in terms of wave propagation. As the lateral surfaces are moved further away from the studied wave travel path, the less interference can be observed, and consequently the simpler the wave propagation appears to become. This observation serves to reinforce the relation between the presence of lateral boundaries and the complexity of wave propagation.

Take the case of model A - $h100 \times d50$ with non-absorbing lateral surfaces, presented in figure 7.7. Of the three presented cases this is the one with the most complex surface. Notice how at $H = 10\text{mm}$, $H = 20\text{mm}$ and $H = 50\text{mm}$ the theoretical first arrival coincides with the same feature of node motion, i.e., assumed to coincide with the apparent wave front. For the case of $H = 100\text{mm}$ this is no longer the case, the first arrival occurs significantly later than the arrival of the wave front. Notice also how the mentioned wave front appears to propagate in a linear fashion up to a height of approximately $H \approx 60\text{mm}$, after which it is deviated. The apparent wave front carries on propagating up to the sample maximum height also in a linear fashion but with a different inclination in the horizontal plane. This different inclination translates into a different propagating velocity.

The assumption that up to $H \approx 60\text{mm}$ the wave-front was formed by undisturbed wave components, travelling directly from the source, was confirmed by the good correlation between this wave-front travel time and the theoretical wave equivalent first

arrivals. Is is also possible to assume that at the mentioned height of $H \approx 60$mm reflected wave components, faster but with a longer travel path, reach the wave-front. From then on, the wave-front is defined by the reflected wave components, which introduce faster than expected first arrivals. The propagating wave-fronts inclinations or velocities, in figure 7.7, for direct and reflected wave components, are not parallel. This implies that it is not possible to assume any particular feature on the received pulse signal, $H = 100$mm, to be related with the direct wave propagation. Similar results for direct and reflected wave propagation and consequent sample behaviour have already been clearly observed and explored in sections 6.4 and 6.5.

For example in section 6.4, the parametric study in the frequency domain of sample geometry provided a clear distinction in behaviour for samples with different geometries, (figure 6.43). Results for pulse signals and time domain velocity estimates also presented differentiated behaviours for different sample geometries. In figure 6.44, a clear phenomenon could be observed, where distinct wave velocities were obtained for samples with slenderness ratios lower and higher than $H/D = 1.25$.

The results for model B with absorbing boundaries, (figure 7.9), shows a very stable wave propagation. Of the three presented cases, it is the one where the original transmitted pulse signal appears to be less distorted as it propagates along the sample. Since for this case little or no wave reflected components are expected to interfere with the transmitted wave propagation, it is also an ideal case to observe any possible near-field effect, which should be the only source of dispersion. The near-field wave components would be expected to travel at higher, non-constant, decreasing velocities than the far-field components. They would also be expected to attenuate significantly faster than the far-field components, (figures 3.19 and 3.20). No such feature is apparent in figure 7.9. This raises the possibility of FLAC3D dynamic model not being capable of modelling near-field phenomena.

Assume, as for the results in figure 7.6, that only non-reflected wave components

propagate along the sample's main axis for the absorbing model A and model B. Then by subtracting their motion time histories to those of the non-absorbing models, the motion time histories of the reflected wave components, exclusively, can be obtained. The surfaces constructed by plotting these results for the nodes along the main sample axis are presented in figures 7.10 and 7.11 for model A and model B respectively.

When comparing the reflected wave results of model A, in figure 7.10, with the equivalent non-absorbent results, in figure 7.7, it is possible to observe how, at lower sample height, the reflected wave components are detected much later. For a sample height of 20mm, the normal non-absorbent wave is first detected at around 0.1ms. The reflected wave is only detected at around 0.25ms. This means the reflected wave components arrive later than the direct wave components, at the sample height of h= 20mm, by a factor of three. Having already speculated from the results in figure 7.7, it can now be confirmed that the wave front of the reflected wave components intersects the theoretical first arrival at a sample height of around 60mm. The theoretical first arrival coincides with different features from the reflected wave at different sample heights, with no apparent relation with any of them.

Comparing the results from model A and model B, in figures 7.10 and 7.11 respectively, the reflected wave components are detected significantly later in the case of model B. At a sample height of 20mm, the first arrival for model A occurs at around 0.25ms and for model B it occurs at around 0.40ms. This strengthens the assumptions that the presented surfaces actually correspond to reflected wave components. Since model B has a larger diameter than model A, 75 > 50mm, the reflected travel path is longer, explaining the difference in reflected wave first detection.

For model A the reflected wave-front intersects the theoretical first arrival at a sample height of around $H = 60$mm, and at around $H = 87$mm for sample B, (fig-

ures 7.10 and 7.11). These sample heights, when divided by the respective sample diameters, produce slenderness ratios of 1.20 and 1.16 respectively. Referring back to the parametric study in chapter 6, more specifically to the estimated wave velocity results for pulse signals presented in figure 6.44 and the near-field relative dispersion in figure 6.46, these results also presented significantly different behaviour for samples with slenderness ratios lower and higher than 1.25 and 0.9 approximately. Distinguishable behaviours with clear break points at not very different slenderness ratios have been established for non-related laboratory and numerical tests. This is an extra confirmation of the importance of sample geometry in wave propagation. Namely, how distinct behaviours for lower or higher slenderness ratios can be obtained, in terms of determining the first arrival of the received signal.

The inclination of the two distinct wave components, direct and reflected, as they propagate along the sample, indicates different propagation velocities, for the direct wave propagation, a wave velocity of around $V = 120\text{m.s}^{-1}$ was obtained, compatible with the theoretical shear wave velocity. The reflected wave components propagate at a wave velocity of around $V = 230\text{m.s}^{-1}$. This value is in fact higher than compression wave velocity of $V_p = 180\text{m.s}^{-1}$. This indicated that these reflected wave components are clear signs of waveguidance dispersion, which explains such high velocities, (figure 3.16). Actual wave velocities with relative high velocities were also observed in section 6.5.

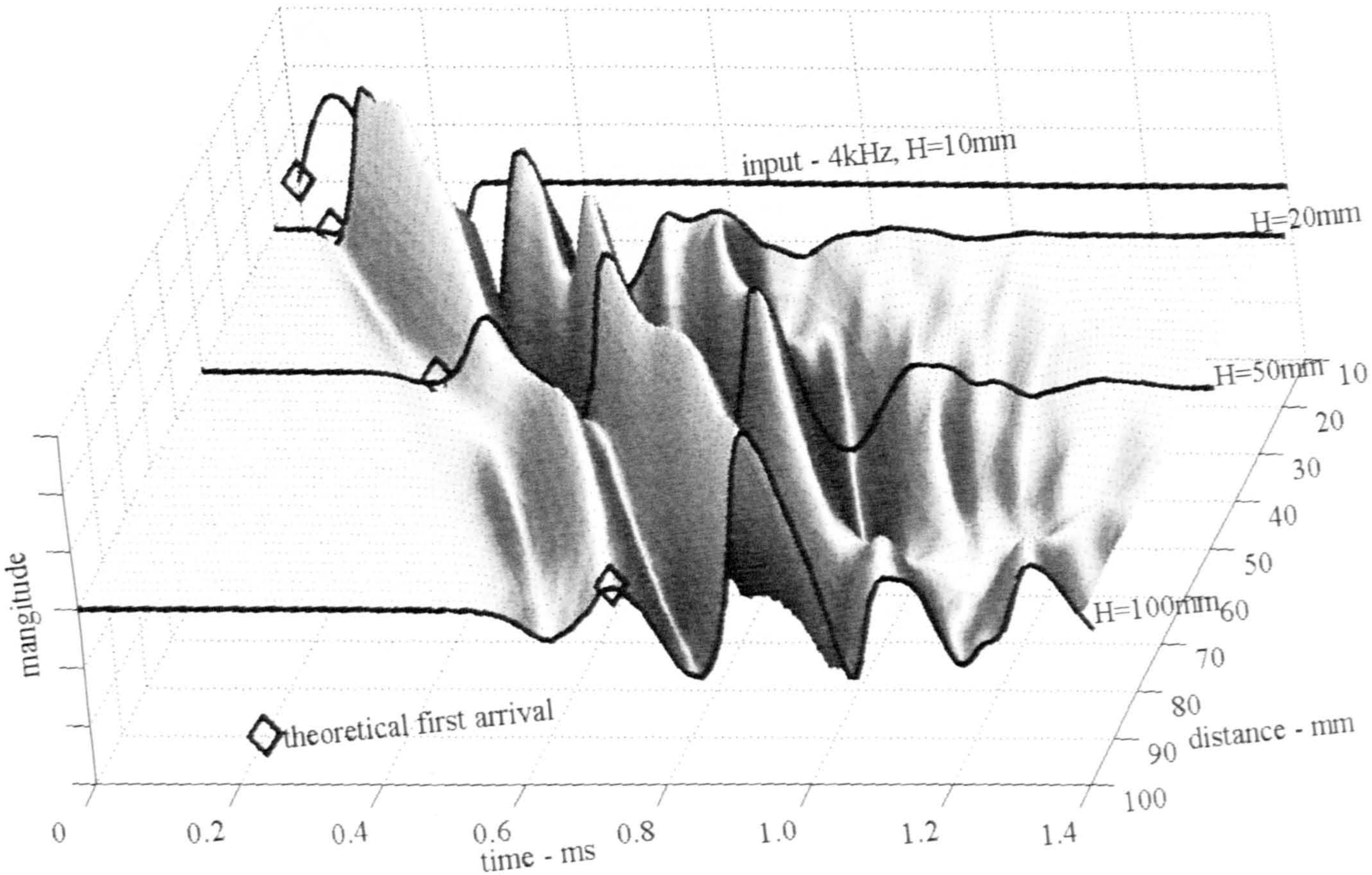

Figure 7.7: Wave propagation along the sample's main axis for model A - $h100 \times d50$mm, with non-absorbing lateral surface.

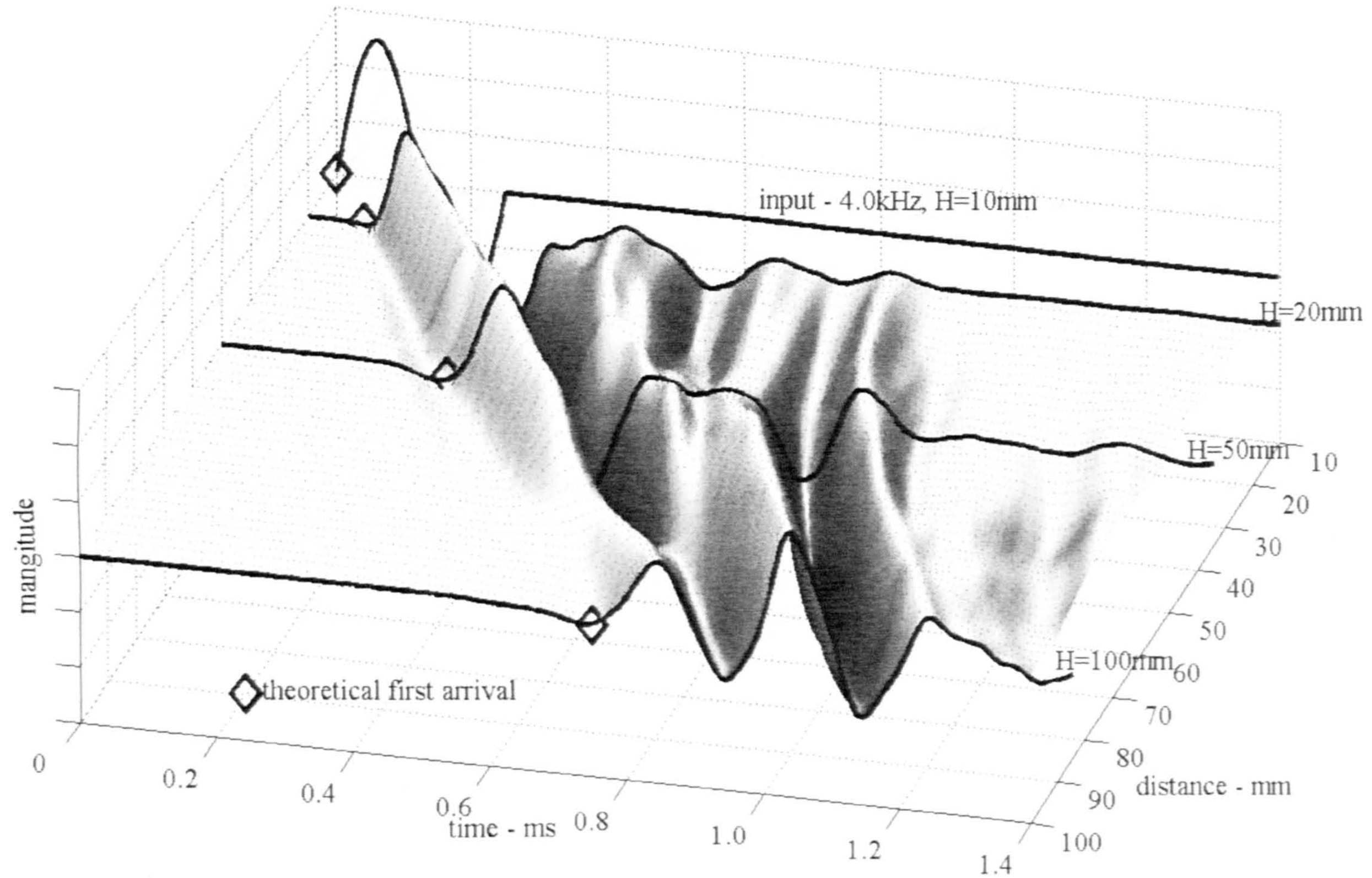

Figure 7.8: Wave propagation along the sample's main axis for model B - $h100 \times d75$mm, with non-absorbent lateral surface.

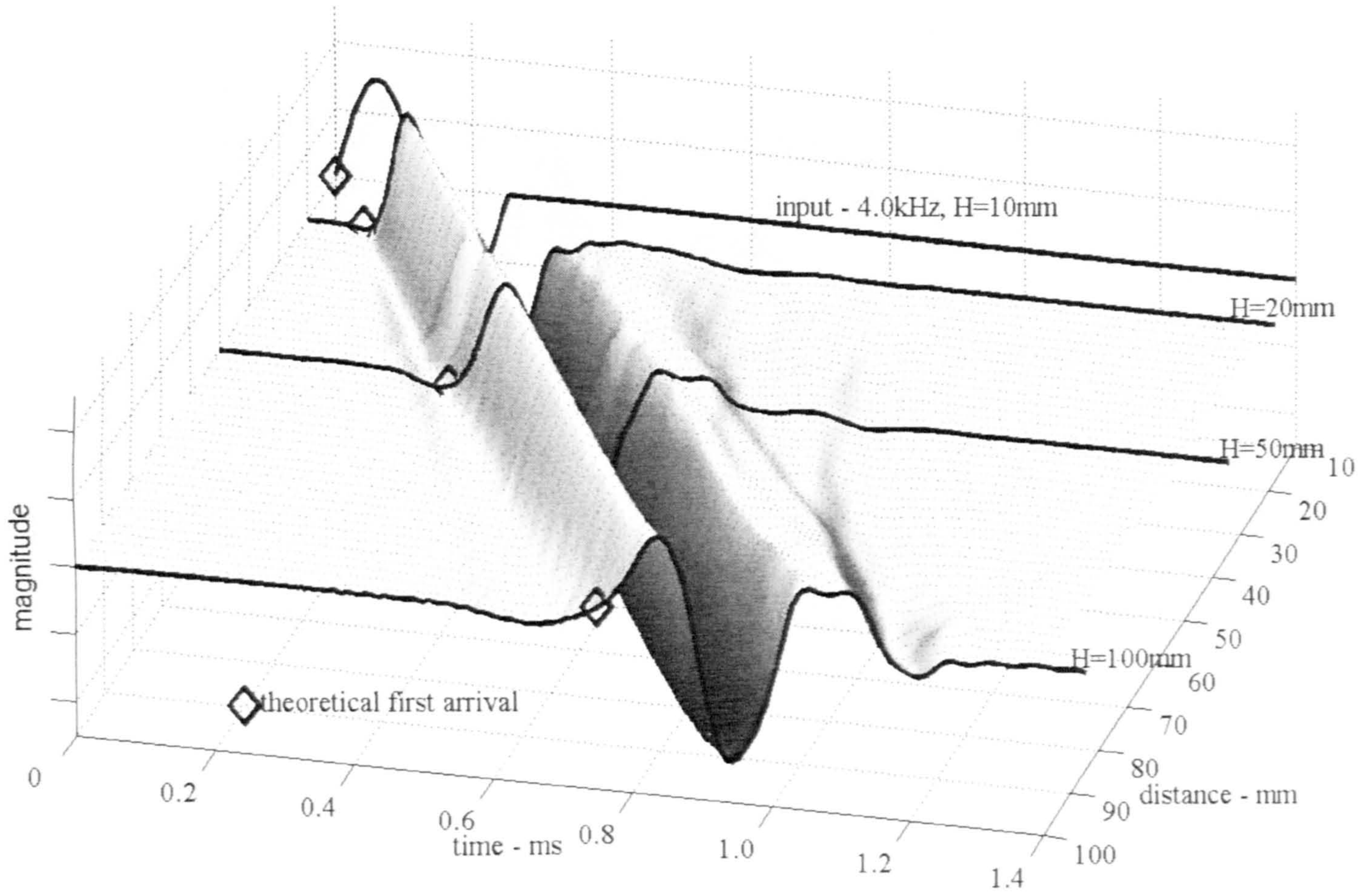

Figure 7.9: Wave propagation along the sample's main axis for model B - $h100 \times d75$mm, with absorbing lateral surface.

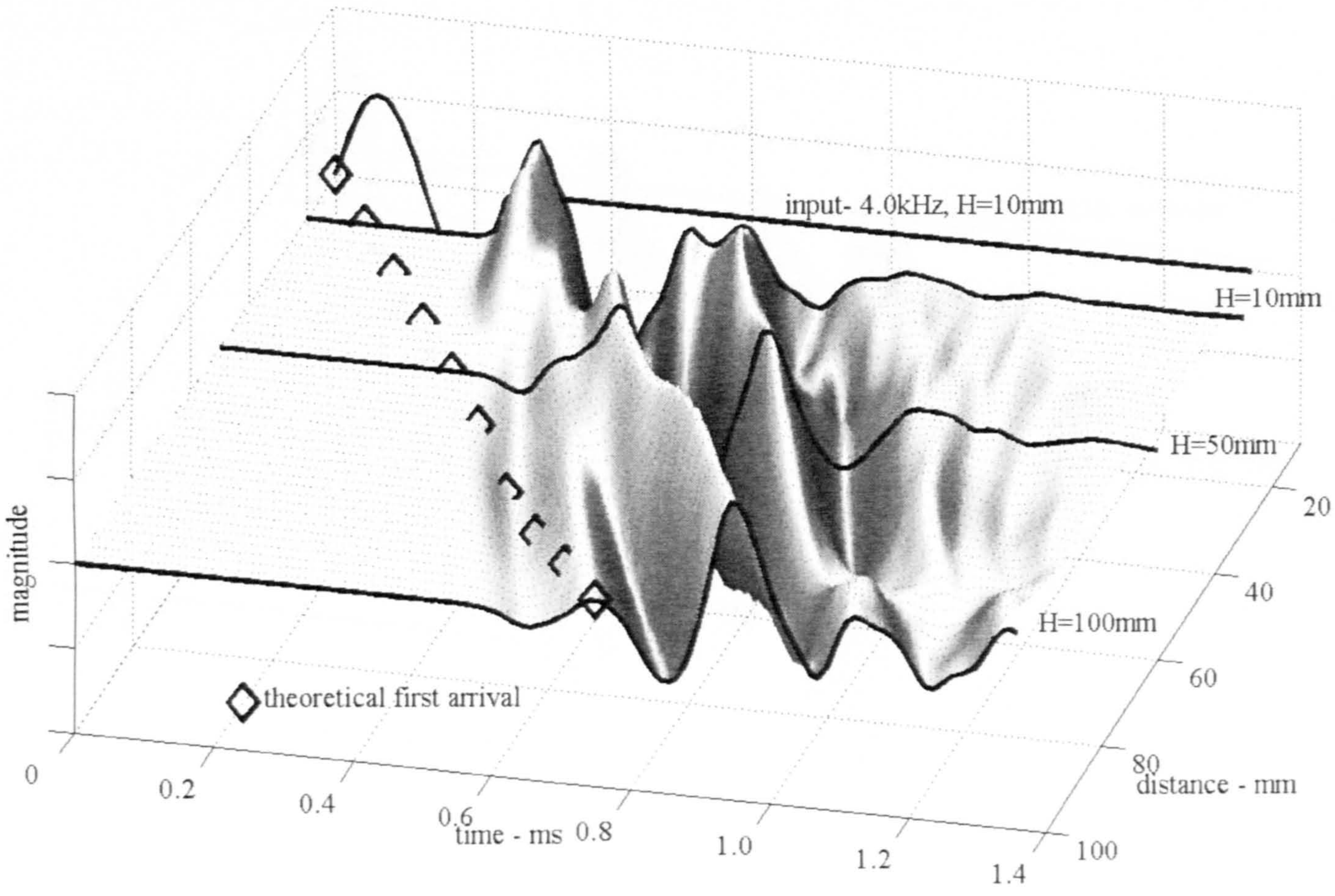

Figure 7.10: Reflected wave components propagating along the sample's main axis for model A - $h100 \times d50$mm.

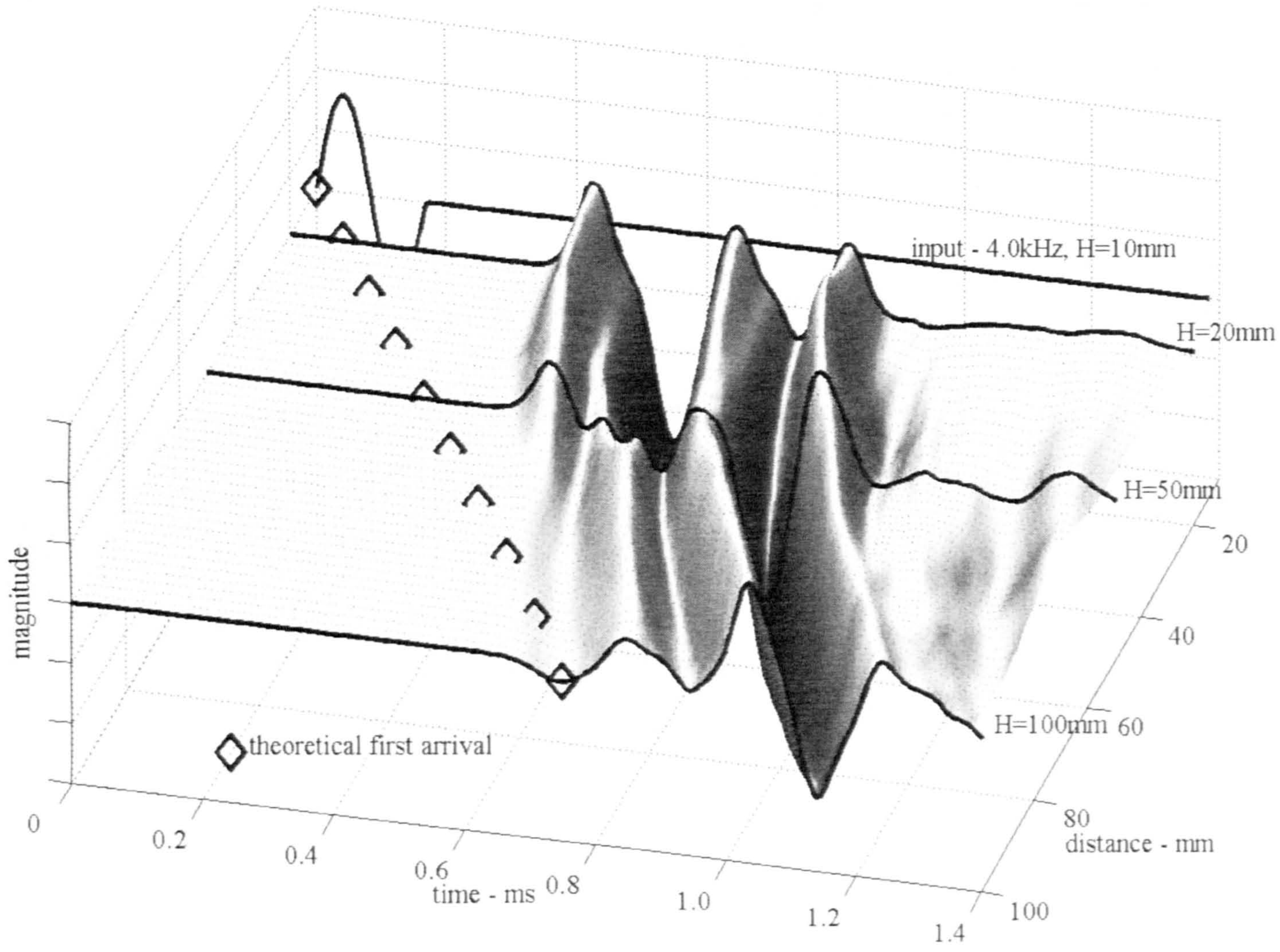

Figure 7.11: Reflected wave components propagating along the sample's main axis for model B - $h100 \times d75$mm.

7.4 Second Parametric Study

A second parametric study was conducted using a new set of FLAC3D models. These were prepared from scratch with the objective of refining some aspects of the previous models, such as the inclusion of a receiving transducer and the use of a load, instead of a forced displacement, to excite the transmitting bender element. Finally, the model properties were calibrated with the results of an actual tri-axial bender element soil test.

Time constraints to the use of the software license meant that the models could not be perfected in order to obtain the same standards of results quality obtained in the previous numerical study. The results were affected by some numerical errors which, although not disabling a comparative analysis, do remove some degree of confidence.

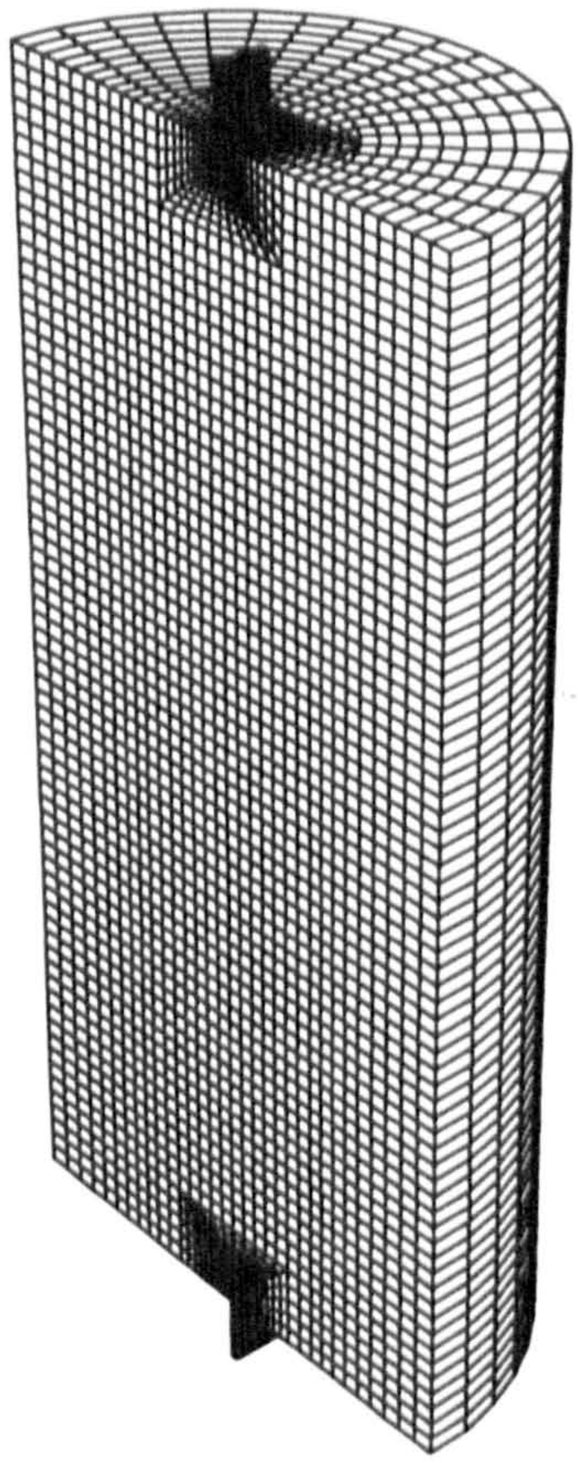

Figure 7.12: representation of generic finite difference model, including transmitting and receiving bender elements.

7.4.1 Model Description

A new set of 8 FLAC3D models was prepared to further study the influence of sample geometry in wave propagation. These models include the transmitting and receiving bender element transducers and the soil sample. The bender element transducers still have 10mm width and 10mm length but only have 1mm thickness. The bender element pair is embedded in the soil by 2mm, and the opposed end is fixed, making them behave as cantilevers.

The soil properties were modelled so as to emulate a residual granite soil, similar to the one described in Ferreira *et al.* (2004) and Greening *et al.* (2003). The main objective was to obtain a shear wave velocity estimated at $V_s = 190\text{m.s}^{-1}$, for a soil with a density of $\rho = 1900\text{kg.m}^{-3}$ and a characteristic Poisson's coefficient of $\nu = 0.35$. These and other properties of the soil are summarised in table 7.4.

Property	Symbol	Units	Value
Bulk Modulus	K	Pa	205.8×10^6
Shear Modulus	G	Pa	68.6×10^6
Poisson's ratio	ν	—	0.35
Density	ρ	kg.m^{-3}	1900
Compression Wave Velocity	V_p	m.s^{-1}	396
Shear Wave Velocity	V_s	m.s^{-1}	190

Table 7.4: Properties of the soil medium for second parametric study numerical models.

The sample's height and diameter were varied, much in the same way as was done in chapter 6, and tested separately. Again, the understanding of their influence over the perceived dynamic behaviour of the sample is the main objective. The values for the different heights and diameters, as well as for the resulting slenderness ratios, are presented in table 7.5.

Model	Height H(mm)	Diameter D(mm)	Slenderness H/D(mm)
M81	140	70	2.00
M82	140	60	2.33
M83	140	50	2.80
M84	140	40	3.50
M85	110	70	1.57
M86	90	70	1.29
M87	70	70	1.00
M88	50	70	0.71

Table 7.5: Geometry of FLAC3D models used in second parametric study.

The properties of the bender element transducer, namely its elastic parameters, are again modelled as being ten times higher than those of the soil. At the time these numerical simulations were performed, the monitoring of actual transducer properties, as presented in section 5.6, had not been performed, and this is why more approximated values were not used. The same procedure of multiplying the soil's stiffness parameters by ten, as done by Arroyo *et al.* (2002), and in the previous section, was again chosen to simulate transducers significantly stiffer than the soil they are testing.

The transmitting bender element is excited by applying a binary force at the top and bottom end of the transducer. This binary force follows a sinusoidal function during a single cycle, much like in section 7.3.1, with a central frequency of 2.0kHz and with a maximum amplitude of 2.5×10^{-4}N. The force binary amplitude was chosen in order to obtain a maximum displacement of the bender element tip of around 1.0μm, which is a relatively small value. The maximum displacement observed for an embedded transducer of similar dimensions was of 10.0μm, see results

in section 5.6.3.

7.4.2 Results

The travel time estimates in the time domain were made using the first maximum and minimum values of the transmitted and received signals, as done in section 6.5, and described in figure 2.2 as curve features B to E and C to G. The obtained travel times, one for each pair of features, were averaged to produce a single travel time.

In the frequency domain, a transfer function was obtained relating the transmitted and received signals. From its phase delay component, the gradient for a range of frequencies near the input signal central frequency of 2.0kHz was used to estimate the wave travel time. The time and frequency domain results are presented next in figure 7.13.

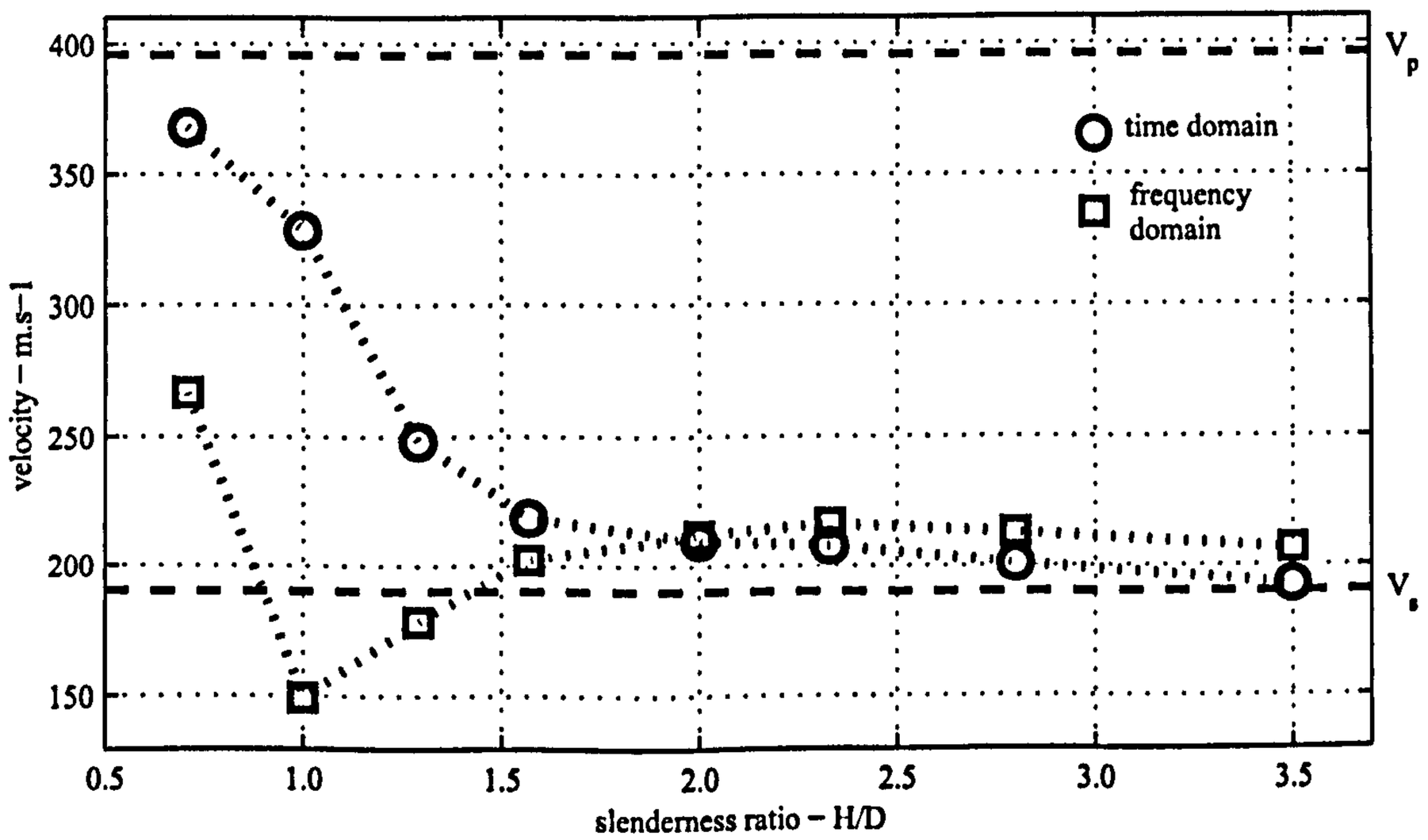

Figure 7.13: wave velocity for numerical parametric simulation, obtained through results in the time and frequency domains.

The results in figure 7.13 appear to present some relevant trends. It can be observed that the time domain velocities decrease with the sample slenderness ratio, approaching the theoretical value of V_s for larger ratios. The frequency domain

velocities, except for the value corresponding to the lowest slenderness ratio, increase significantly, from lower than theoretical velocity values up to the theoretical shear wave velocity. It is also relevant to point how the different results appear to agree with each other and with the theoretical velocity value, for slenderness ratios higher than 2.0.

7.5 Discussion

In laboratory tests, innumerable factors cannot be precisely repeated from test to test. When dealing with numerical simulations, there is complete control over chosen properties of the system. Besides, in laboratory, some of the differences between tests might occur without the knowledge of the operator and therefore go unaccounted for. On the other hand, numerical modelling cannot simulate all the properties and boundary conditions of a real system. Also, they involve complex numerical calculations which are not easily understood by most users and which can produce significant numerical errors. These are in turn often dealt using a trial and error approach. Still, for simple simulations where only a single geometry parameter is varied, differences in the results can most certainly be attributed to such parameter.

The numerical results from the two separate numerical studies in section 7.3 clearly show the influence of the sample geometry in the results obtained from bender element generated wave propagation. It was possible to distinguish between exclusively directly propagated waves and exclusively reflected propagated waves. From these two type of waves, which constitute the normal propagated wave, the impact of the reflected wave components could be observed, dominating the response at the receiving end, more so for the sample with the smallest diameter.

Another observation made from the first simulation series was the actual propagation of the transmitted wave along the main axis of the sample. In this analysis,

it was possible to observe how the direct and reflected wave components travel at different velocities. The reflected wave components were detected with an initial delay but, by travelling faster than the direct wave components, intersect them, eventually distorting the observed first arrival.

The second series of numerical simulations also provided indications of a sample geometry influence. Moreover, it was possible to obtain and compare results from the time and frequency domains. These matched for samples with higher slenderness ratios, but are quite different for lower slenderness ratios.

Only sinusoidal pulse signals were used in the presented numerical simulations. This leaves an important gap since the response of cylindrical samples, as already discussed in chapters 5 and 6, is more stable when a steady state of oscillation is reached. This is not the case when using pulse signals, where only a transient state of vibration can be obtained. Further testing needs to be done in order to clarify the understanding of wave propagation in cylindrical samples as well as their dynamic responses. Specifically the use of continuous signals, which have already been used in Hardy (2003).

The elastic properties assumed for the bender elements were not their actual properties but very rough estimates with the single objective of ensuring that their stiffness was significantly higher than that of the soil. Since the properties of the bender elements are now better known, there is no reason not to use their actual values in future simulations.

In the second group of simulations the properties of an actual soil, as well as those of its corresponding bender element test, were used. The simulation and the soil tests were not performed simultaneously neither were they coordinated with each other. It would then be interesting to, in future simulations, have a better prepared calibration between actual and numerical studies, so that each of them can support and justify the other's results and conclusions.

Chapter 8

Conclusions and Recommendations

8.1 Conclusions

The experimental, numerical and analytical results obtained and presented in this dissertation confirm the general applicability of well known theoretical concepts of body vibration and wave propagation to bender element testing. These provides a concrete background to the phenomena involved, and a robust platform over which further discussion, developments and improvements can be built upon. Debatable issues such as the ideal signal type, signal processing method and dispersion minimisation approach, are made more clear and the process of decision-making more straightforward, when contextualised under a mechanical point of view.

The choice of the best type of input signal to use in bender element testing is a clear example of where the understanding of the mechanical properties of the test system provides a clear answer. Given the choice between pulse signals and harmonic continuous signals, the monitoring of the bender elements behaviour confirms the theoretical prediction of a transient response for pulse signals and of a steady-state

response for harmonic continuous signals. During a transient response, the behaviour of a mechanical system is dominated by its own properties, namely its frequency of vibration. Therefore, if control over the frequency of vibration of the system is required, for example to try and avoid the near-field effect, than the pulse signal is not a suitable excitation signal. This argument needs to keep being reinforced due to the more traditional and persistent practise of using pulse signals.

Harmonic continuous signals, unlike pulse signals, are able to establish a steady-state response from the transmitting bender element, and of the tested sample as as well. Consequently, this type of signal permits the control of the frequency of vibration of the transducer as well as of the tested sample. For this reason, harmonic continuous signals are a better choice than pulse signal when control over the frequency of the response is required, such as when minimising frequency dependent dispersive phenomena.

A clear distinction between signal processing methods can be made regarding the domain in which the data is handled, the time domain or the frequency domain. One of the main differences between analysis in these domains is that in the time domain the results are usually compared in absolute terms, and in the frequency domain the results are compared in relative terms. The transmission of vibration energy between two different mediums, such as between a bender element and a sample, has an inherent phase delay between the excitation and the response, which has also been confirmed in the results of the bender element monitoring. Therefore, if comparing features from the transmitted and received signals directly in the time domain, the phase delays that occur at each of the interfaces of the test system render the obtained travel time almost meaningless.

Even when comparing the very first arrival of the transmitted and received signals, which marks the discontinuity between stationary and moving particles of the medium, the introduction of phase delays at each interface can also induce the per-

ception of time delays. These time delays can have a significant impact on relatively short travel distances, such as the ones present in laboratory geotechnical testing of soil. In the studied case of a synthetic rubber with a height of $H = 76$mm and a small-strain shear stiffness of approximately $G_0 = 2.0$GPa, the introduced time delay was estimated at 20% of the total wave travel time. For shorter samples with shorter travel paths and for stiffer mediums the importance of the introducing such a time delay increases.

When comparing signals in relative terms, for example by comparing two received signals rather than a transmitted and received signal, as done in the frequency domain, then any phase or time delays cumulatively introduced at each interface will have approximately the same impact on any two signals with similar frequency. For this reason, when comparing two such signals the influence of the phase delay at each mechanical interface can be avoided. The travel time results obtained in the frequency domain, such as by using the gradient of the phase delay curve to estimate wave travel time, are consequently more suitable than the results obtained using direct time domain readings.

When calculating the wave velocity, the travel distance is as relevant as the travel time, since the velocity varies linearly with either factor. The travel distance has, for some time, been taken as the tip-to-tip distance between bender elements, subject which has been left mostly unchallenged. The results presented in this dissertation, covering a large range of sample heights, travel distances and relative embedment heights indicate that the wave travel distance should be measured not between transducers tip-to-tip but between about 60% of the transducer's embedment height, coinciding with the estimated centres of dynamic pressure exerted by the transmitter bender element on the sample. Since the initial assumption of travel distance measured tip-to-tip was based in tests covering a smaller and less relevant ranges of sample heights, the present study must therefore at least lead to further

discussion concerning this subject.

On the issue of dispersion; when considering the test sample to behave as a linear-elastic mechanical continuum, dispersion can be caused by the near-field effect and by wave reflection or wave-guidance. Both these phenomena are influenced by the geometry of the sample, where bulkier samples are mostly affected by the near-field effect and slender samples can be affected by the near-field effect and by waveguidance, and both these dispersion phenomena are frequency dependent. A limit for the signal frequency after which the near-field effect can be avoided has previously been proposed based on wave radiation theory, and is presented in equation 3.67. Following a similar theoretical approach, a limit for signal frequency concerning waveguide dispersion is proposed for the first time in the context of bender element testing, and presented in equation 6.1.

The classification of sample geometry permits an objective choice of which theoretical model of behaviour is most suitable to describe the relevant dynamic phenomena of body vibration and wave propagation. A concrete distinction of what constitutes a bulkier or slender sample was attempted based on the results of the geometry parametric study. In general terms, bulkier models were observed to behave similarly to an unbounded medium and the slender samples were observed to behave more similarly to waveguides. In terms of bender element testing, the distinction between sample geometries influences the necessity of considering the waveguide dispersion or not. A geometry parameter was obtained, based in the parametric study results, to distinguish between the two mentioned models of behaviour, as well as to indicate where the samples might have a transient, more unpredictable dynamic response. These geometry limits are presented in equation 6.1.

Finally, the studied numerical models confirmed the objective influence of sample geometry in terms of wave propagation. They provided a clear picture of unbounded

wave propagation, of waveguided wave propagation and of wave reflection, along the main axis of the sample. And of the meaningful contribution of such reflected waves, in the overall received signal.

8.2 Recommendations

The study of the influence of the sample geometry in bender element testing was the primary subject of this dissertation. Nevertheless, other relevant issues concerning bender element testing where also analysed, sometimes with surprising observations.

The wave travel distance, according to the results obtained in the parametric study, was observed to be measured not between the transducers tip-to-tip, as commonly assumed in bender element testing, but measured between about 60% of the transducers embedded heights. Further testing, concerning specifically the subject of wave travel distance, might help to clarify this subject.

The independent monitoring of the transmitting bender element permitted the observation of shear strains in excess of $\varepsilon > 10^{-3}\%$, which might imply the induction of local non-linear behaviour of the soil near the transmitting transducer. Therefore, it is necessary to veryfing these results and also to quantify its influence on the overall behaviour of the system, and consequent validity of the linear-elastic behaviour assumptions.

The numerical modelling of dynamic bender element test systems has shown so far, a good agreement with laboratory results. They provide a powerful tool where the properties of the medium are defined prior to testing, and with the added advantage of considering the vibration of as many nodes as desired, in more than one direction, unlike real bender element testing where a not much more than one pair of transducers are commonly used.

The presented analytical study of the relevant dynamic phenomena was made

using the Bernoulli-Euler beam model of behaviour, with considerable success. This model is quite simple providing easy to use frequency equations, yet it does not consider the effect of shear deflection and rotary inertia. Other, more complete models, such as the Timoshenko beam model, which considers the mentioned effects, have the potential of predicting the dynamic response of relatively bulk samples even better. For this reason, its use might further increase the quality of analytical results, despite being its added complexity.

When interpreting test results, besides the sample geometry other factors that might affect the dynamic behaviour of the system, must be considered. For example, the wave propagation analysis presented in this dissertation only considered wave reflection at the lateral boundaries of the sample. The consideration of wave reflection at the top and bottom boundaries is a relevant subject which merits further study. Other elements of the test system, described in table 6.1, could also be responsible for significant alterations to the dynamic behaviour of the test system. These other factors, such as the latex membrane protecting the sample, or the application of other test equipment such as local LVDT's, must be quantified in future work related with bender element testing, in order to obtain a more realistic picture of how a bender element test system really behaves.

Appendix A

Sample Geometry

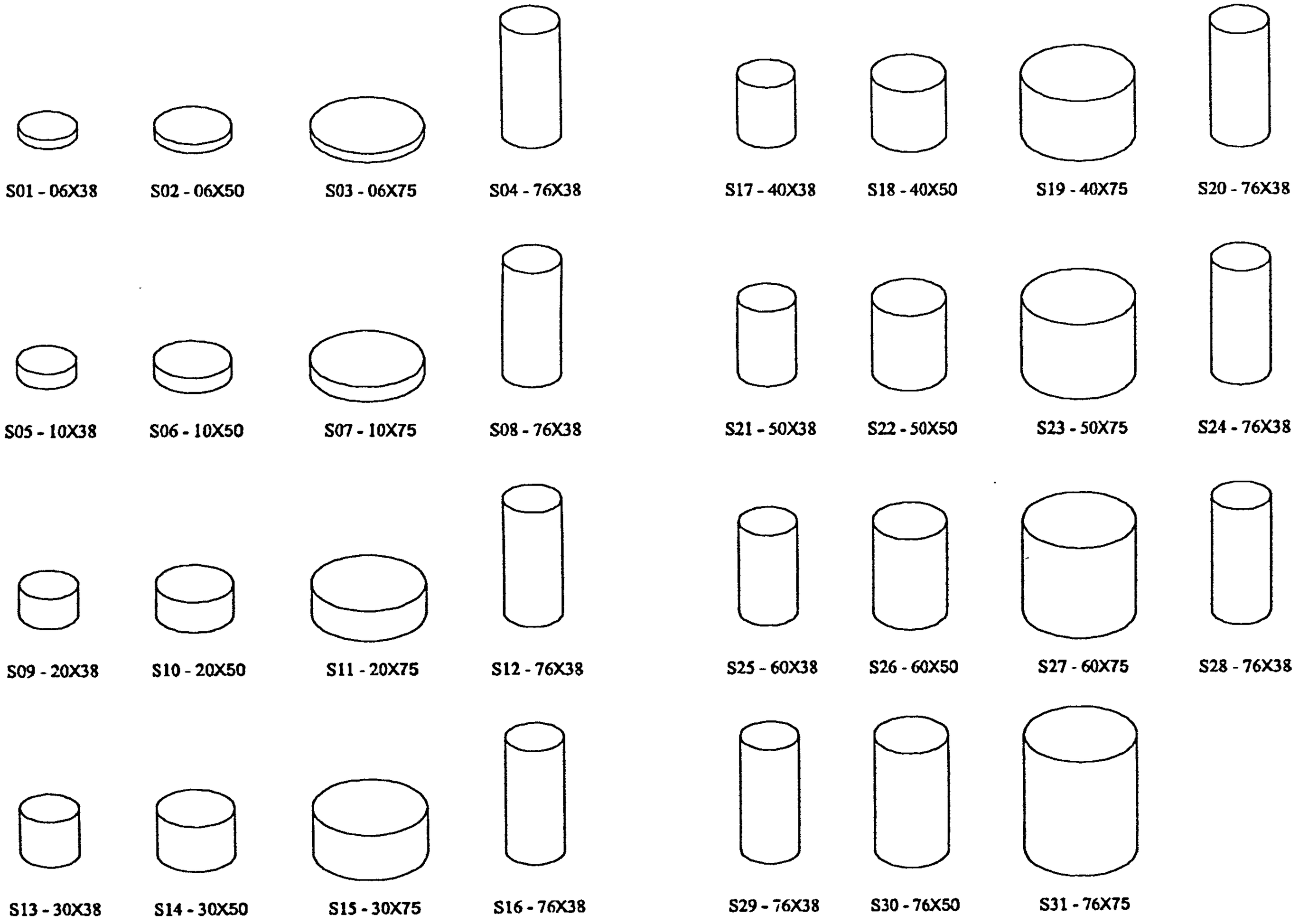

Figure A.1: Rubber sample geometries used in parametric study. This page may be used as a pull-out companion to chapter 6.

Appendix B

Conclusions Summary (or Bender Elements Use Guide)

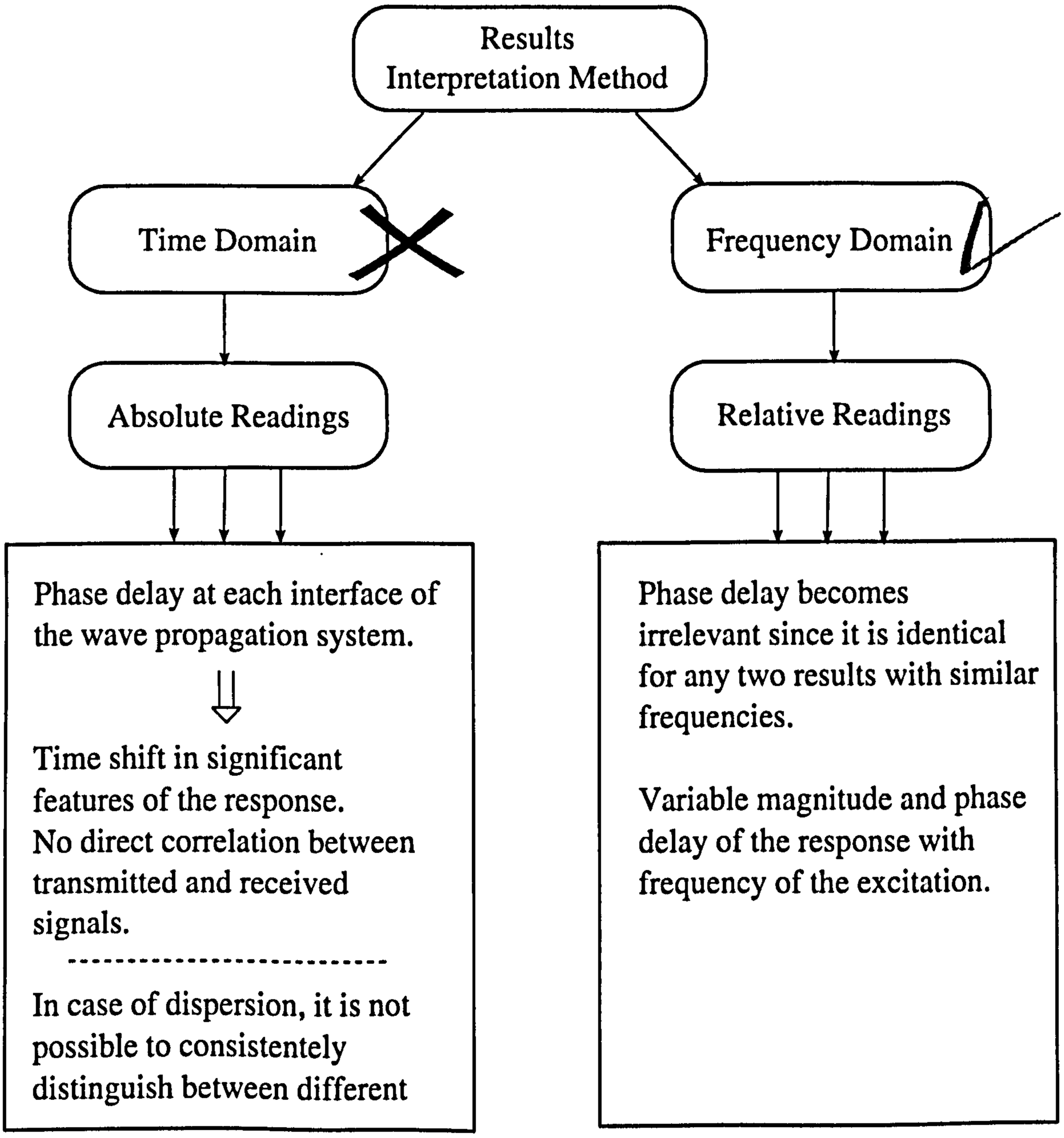

Figure B.1: Interpretation Method

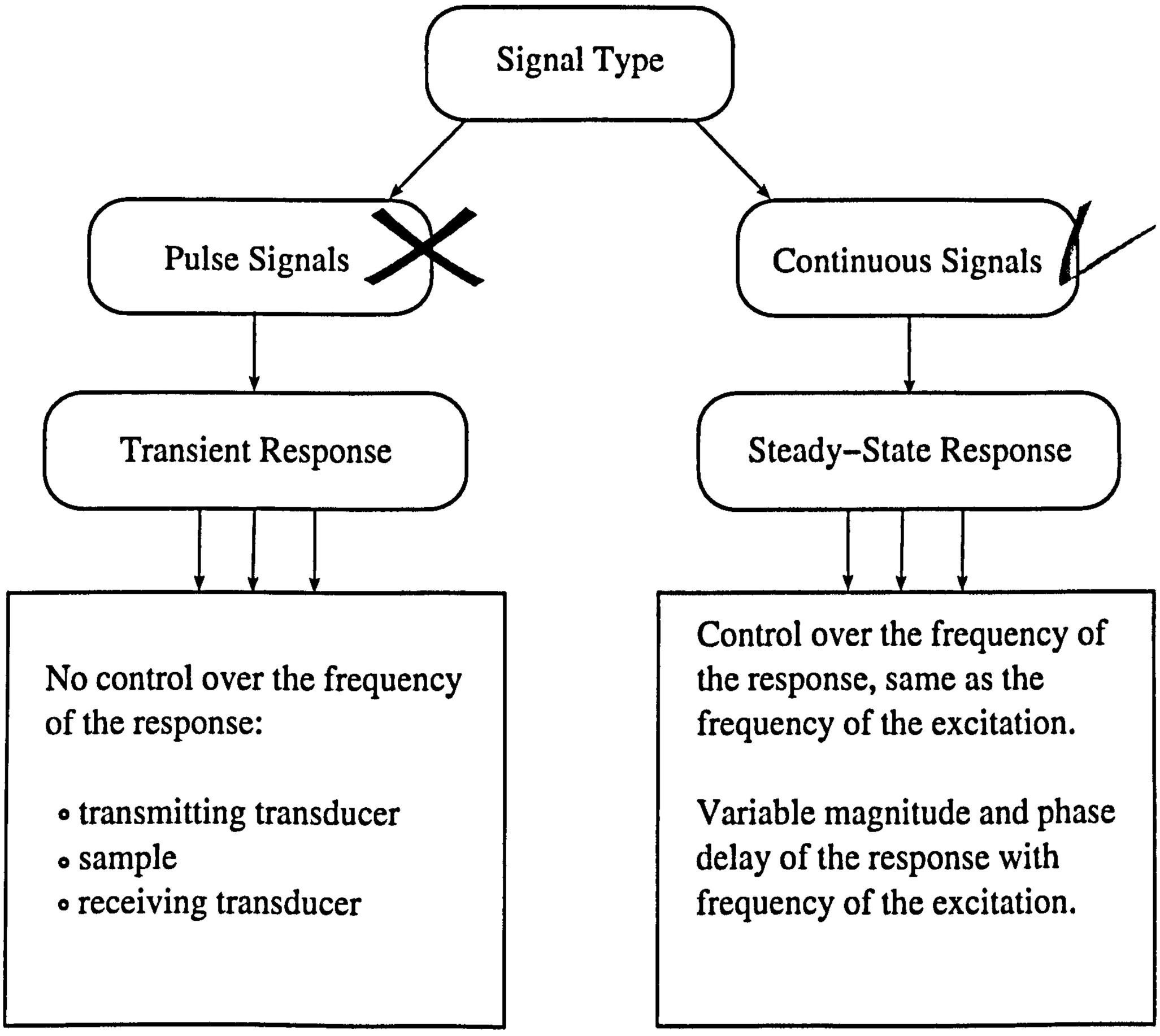

Figure B.2: Signal Type

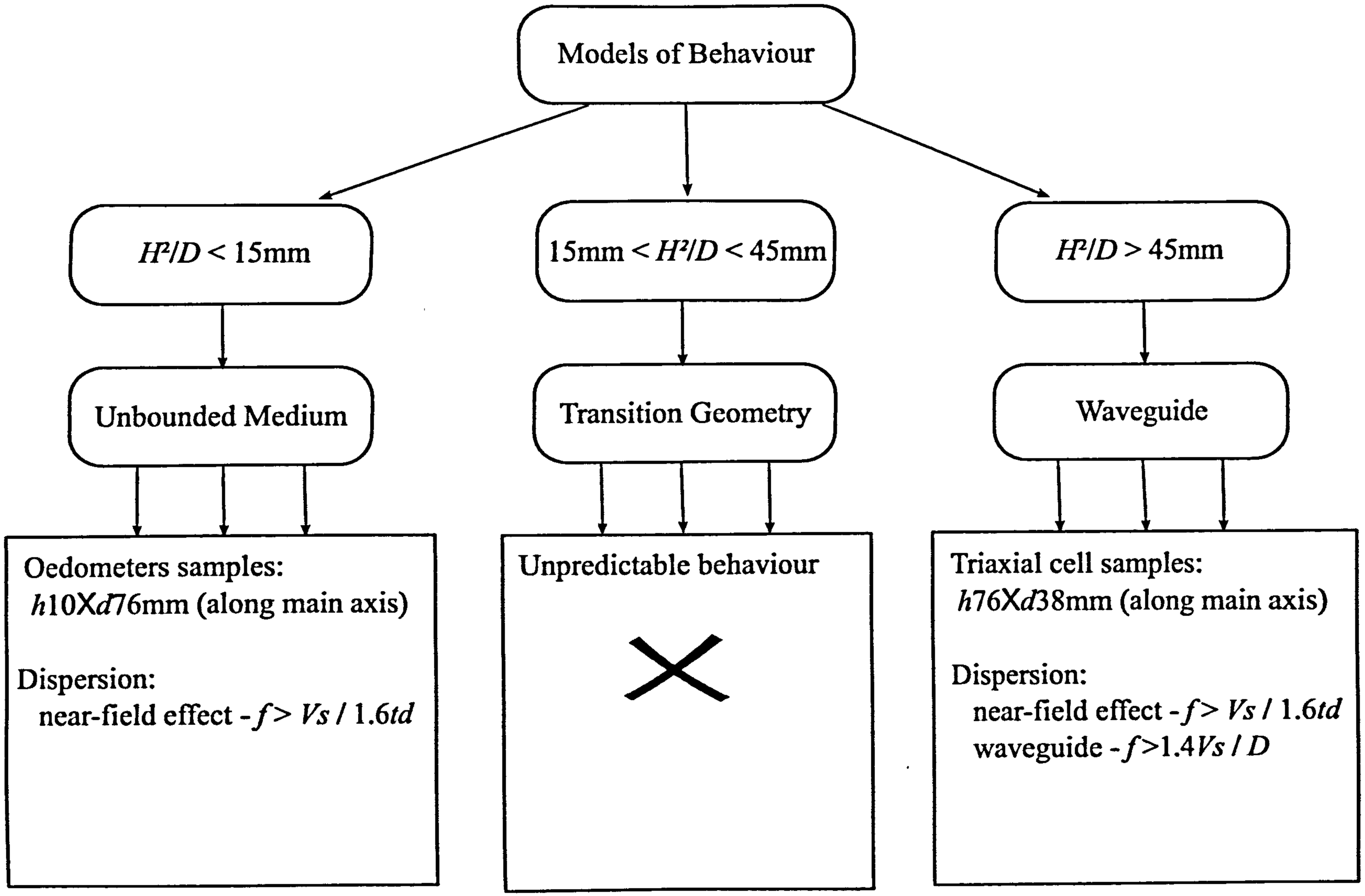

Figure B.3: Models of Behaviour

References

AB, SOLVIA Engineering (2005). Solvia, finite element system. Computer Program.

Achenbach, J. D. (1973). *Wave propagation in elastic solids.* Vol. 16 of *Applied mathematics and mechanics.* North-Holland publishing company. Amsterdam.

Ahn, J., S. J. and D. Kim (2001). Fabrication of piezoelectrically driven micro-cantilever using pb (zrti) o3 films. *Proceedings of the 12th IEEE International Symposium* pp. 721–724.

Aki, K. and P. G. Richard (2002). *Quantitative seismology.* 2nd ed.. University Science Books. California.

AnhDan, L., J. Koseki and T. Sato (2002). Comparison of youn's moduli of dense sand and gravel measured by dynamic and static methods. *Geotechnical Testing Journal.*

Arroyo, M. (2001). Pulse Tests in Soil Samples. Thesis/dissertation. University of Bristol.

Arroyo, M. and D. Muir-Wood (2003). Simplifications related to dynamic measurements of anisotropic g0. *Proc. Int. Symp. Deformation Characteristics of Geomaterials, ISLyon03.*

Arroyo, M., D. Muir-Wood and P. D. Greening (2003*a*). Source near-field effects and pulse tests in soil samples. *Géotechnique* **53**(3), 337–345.

Arroyo, M., D. Muir-Wood, P. D. Greening, L. Medina and J. F. Rio (2006). Effects of sample size on bender-based axial g_0 measurements. *Géotechnique* **56**(1), 39–52.

Arroyo, M., L. Medina and D. Muir-Wood (2002). Numerical modelling of scale effects in bender-based pulse tests. In: *NUMOG VIII*. Pande G. N. and Pietruszczak, S. (eds). pp. 589–594.

Arroyo, M., P. D. Greening and D. Muir-Wood (2003*b*). An estimate of uncertainty in current laboratory pulse test practice. *Rivista Italiana di Geotecnica* **37**(1), 17–35.

Arulnathan, R., R. W. Boulanger, B. L. Kutter and W. K. Sluis (2000). New tool for shear wave velocity measurements in model tests. *Geotechnical Testing Journal* **23**(4), 444–453.

Arulnathan, R., Ross W. Boulanger and M. F. Riemer (1998). Analysis of bender element tests. *Geotechnical Testing Journal* **21**(2), 120–131.

Ashmawy, A. K. and V. P. Drnevich (1994). A general dynamic model for the resonant column/quasi-static torsional shear apparatus. *Geotechnical Testing Journal* **17**(3), 337–348.

ASTM (1978). *STP 654, Dynamic Geotechnical Testing*. ASTM international.

ASTM-D-4015 (2000). *D 4015-92, Standard Test Methods for Modulus and Damping of Soils by the Resonant-Column Method*. Vol. 4.08 of *Book of ASTM Standards*. ASTM international.

Atkinson, J. H. (2000). Non-linear soil stiffness in routine design. *Géotechnique* **50**(5), 487–508.

Audisio, A., S. Bonani and S Foti (1999). Advances in spectral analysis for sasw test. In: *Pre-failure Deformation of Geomaterials*. Jamiolkowski, Lancellotta & Lo Presti (eds). pp. 395–402.

Bardet, J. P. (1992). A viscoelastic model for the dynamic bahaviour of saturated poroelastic soils. *Journal of applied mechanics* **59**, 128–135.

Bates, C. R. (1989). Dynamic soil property measurements during triaxial testing. *Géotechnique* **39**(4), 721–726.

Bathe, K. J. and E. L. Wilson (1976). *Numerical methods in finite element analysis.* Prentice-Hall. Englewood Cliffs, New Jersey.

Belloti, R., M. Jamiolkowski, D. C. F. Lo Presti and D. A. O'Neill (1996). Anisotropy of small stiffness in ticino sand. *Géotechnique* **46**(1), 115–131.

Bendat, J. S. and A. G. Piersol (2000). *Random Data Analysis and Measurement Procedures.* 3 ed.. John Wiley and Sons. New York.

Biot, M. A. (1956). Theory of propagation of elastic waves in a fluid-saturated porous solid. *Journal of Acoustical Society of America.*

Blewett, J., I. J. Blewett and P. K. Woodward (1999). Measurement of shear-wave velocity using phase-sensitive detection techniques. *Canadian Geotechnical Journal* **36**(5), 934–939.

Blewett, J., I. J. Blewett and P. K. Woodward (2000). Phase and amplitude responses associated with the measurement of shear wave velocity in sand by bender elements. *Canadian Geotechnical Journal* **37**, 1348–1357.

Bodare, A and K. R. Massarsch (1984). Determination of shear-wave velocity by different cross-hole methods. Generic.

Bray, J. D., R. D. Espinoza, K. Soga and R. L. Taylor (1995). Geofeap - geotechnical finite element analysis program. Report.

Brignoli, E. G. M., M. Gotti and K. H. Stokoe (1996). Measurement of shear waves in laboratory specimens by means of piezoelectric transducers. *Geotechnical Testing Journal* **19**(4), 384–397.

Brocanelli, D. and V. Rinaldi (1998). Measurement of low-strain material damping and wave velocity with bender elements in the frequency domain. *Canadian Geotechnical Journal* **6**(35), 1032–1040.

Burland, J. B. (1989). Ninth laurits bjerrum memorial lecture: 'small is beautiful´- the stiffness of soils at small strains. *Canadian Geotechnical Journal* **26**, 499–516.

CALFEM (1999). Calfem, a finite element toolbox to matlab.. Electronic Citation.

Campanella, R. G. and J. K. Mitchell (1968). Influence of temperature and variations on soil behaviour.. *Journal of the Soil Mechanics and Foundations Division, ASCE* **94**(3), 709–734.

Cascante, G. and J. C. Santamarina (1997). Low strain measurments using ramdom noise excitation. *Geotechnical Testing Journal* **20**(1), 29–39.

Cascante, G., J. C. Santamarina and Najwa Yassir (1998). Flexural exitation in a standard torsional-resonant column device. *Canadian Geotechnical Journal* **35**, 478–490.

Cascante, G., John Vanderkooy and Wilson Chung (2005). A new mathmatical model for the resonant-column measurements including eddy-current effects. *Canadian Geotechnical Journal* **42**, 121–135.

Chopra, Anil K. (1995). *Dynamic of structures, Theory and Applications to Earthquake Engineering*. 1st ed.. Prentice Hall. New Jersey.

Claxton, W. E. (1958). Stress-strain equation for rubber in tension. *Journal of Applied Physics* **29**(10), 1398–1406.

Clayton, C. R. I., M Theron and A. I. Best (2004). The measurement of vertical shear-wave velocity using side-mounted bender elements in the triaxial apparatus. *Géotechnique* **54**(7), 495–498.

Clough, R. W. and Joseph Penzien (1993). *Dynamic of structures*. 2nd ed.. McGraw-Hill. Singapore.

Connolly, T. M. and R. Kuwano (1999). The measurement of gmax in a resonant column, bender element, torsional shear apparatus. Generic.

Cooley, J. W. and J. W. Tukey (1965). An algorithm for the mechane calculation of complex fourier series. *Mathmatics of Computation* **19**, 297–301.

Craig, R. F. (1997). *Soil Mechanics*. 6th ed.. E and FN SPON. London.

Cuccovillo, T. and M. R. Coop (1997). The measurement of local axial strains in triaxial tests using lvdts. *Géotechnique* **47**(1), 167–171.

Da-Re, G., Maria C. Santagata and John T. Germaine (2001). Lvdt based system for the measurement of the prefailure bahaviour of geomaterials. *Geotechnical Testing Journal* **24**(3), 288–298.

Dano, C. and Pierre-Yves Hicher (2002). Evolution of elsatic shear modulus in granular materials along isotropic and deviatoric stress paths. *15th ASCE Engineering Mechanics Conference.*

Dano, C., Hocine Hareb and Pierre Y. Hicher (2003). Characterization of loire river sand in the small strain domain using new bender-extender elements. *16th ASCE Engineering Mechanics Conference.*

Dano, C., P.-Y. Hicher and S. Tailiez (2004). Engineering properties of grouted sands. *Journal of Geotechnical and Geoenvironmental Engineering* **130**(3), 328–338.

Doi, M. (1996). *Introduction to Polymer Physics.* Clarendon Press. Oxford.

Doyle, J. F. (1977). *Wave propagation in structures.* 2nd ed.. Springer.

Drnevich, V. P., B. O. Hardin and D. J. Shippy (1978). Modulus and damping of soils by the resonant column method. In: *STP 654, Dynamic Geotechnical Testing.* pp. 91–125. ASTM international.

Durst, F., A. Melling and J. H. Whitelaw (1981). *Principles and practice of Laser-Doppler anemometry.* 2nd ed.. Academic Pres. London.

Dyvik, R. and C. Madshus (1985). Laboratory measurements of gmax using bender elements. *Advances in the engineering* (161), 117–137.

Ewins, D. J. (2000). *Modal Testing.* 2nd ed.. Research Studies Press. Baldock.

Fam, M. and J. C. Santamarina (1995). Study of geoprocesses with complementary mechanical and electromagnetic wave measurements in an oedometer. *Geotechnical Testing Journal* **18**(3), 307–314.

Fan, Y., Farhang Honarvar, Anthony N. Sinclair and Mohammad-Reza Jafari (2003). Circumferential resonance modes of solid elastic cylinders excited by obliquely acoustic waves. *Journal of the Acoustical Society of America* **113**(1), 102–113.

Feldman, D. and Alla Barbalata (1996). *Synthetic Polymers.* Chapman and Hall. London.

Ferreira, C., A. A. Mendonça and A. Viana da Fonseca (2004). Avaliação da qualidade de amostragem em campos experimentais de solos residuais de granito do porto. In: *9º Congresso Nacional de Geotecnia - 2º Congresso Luso-Brasileiro de Geotecnia, Aveiro, Portugal.* SPG. pp. 27–38.

Fioravante, V. (2000). Anisotropy of small strain stiffness of ticino and kenya sands from seismic wave propagation measured in triaxial testing. Generic.

Fioravante, V. and Roberto Capoferri (2001). On the use of multi-directional piezoelectric transducers in triaxial testing. *Geotechnical Testing Journal* **24**(3), 243–255.

Fodil, A., W. Aloulou and P. Y. Hicher (1997). Viscoplastic behaviour of soft clay. *Géotechnique* **47**(3), 581–591.

Fratta, D. and J. C. Santamarina (1996). Wave propagation in soils: Multi-mode, wide-band testing in a waveguide device. *Geotechnical Testing Journal* **19**(2), 130–140.

Gemant, A. and W. Jackson (1937). The measurement of internal friction in some solid materials. *Philosophical Magazine.*

Gere, J. M. (2001). *Mechanical of Materials.* 5 ed.. Nelson THornes Ltd. Cheltteham.

Graff, K. F. (1975). *Wave motion in elastic solids.* Clarendon Press. Oxford.

Greening, P. D. and D. F. T. Nash (2004). Frequency domain determination of g0 using bender elements. *Geotechnical Testing Journal* **27**(3), 288–294.

Greening, P. D., D. F. T. Nash, N. Benahmed, C. Ferreira and A. Viana da Fonseca (2003). Comparison of shear wave velocity measurements in different materials using time and frequency domain techniques. *Procedings Deformation Characteristics of Geomaterials, IS-Lyon.*

Hardy, S. (2003). The implementation and application of dynamic finite element analysis to geotechnical problems. Thesis/dissertation.

Hardy, S., L. Zdravkovic and D. M. Potts (2002). Numerical interpretation of continuously cycled bender element tests. NUMOG. Sweets and Zeitlinger. pp. 595–600.

Head, K. H. (1998). *Manual of soil laboratory testing.* Vol. 3. second ed.. John Wiley and Sons. Chichester.

Heymann, G., C. R. I. Clayton and G. T. Reed (1997). Laser interferometry to evaluate the performance of local displacement transducers. *Géotechnique* **47**(3), 399–405.

Hoar, R. J. and K. H. Stokoe (1979). Field and laboratory measurements of material damping of soil in shear. Generic.

Hope, V. S., C. R. I. Clayton and A. P. Butcher (1999). In situ determination of g(hh) at bothkennar using a novel seismic method. *Quarterly Journal of Engineering Geology* **32**, 97–105.

Image, Automation (2000). *Ometron VH300+ user manual.* Image Automation.

Intel (2004). Intel® 82801ba i/o controller hub 2 (ich2). Electronic Citation.

Itasca, HC (2002). Flac3d, fast lagrangian analysis of continua in 3 dimentions. Computer Program.

Jovičić, V. and M. R. Coop (1997). Stiffness of coarse-grained soils at small strains. *Géotechnique* **47**(3), 545–561.

Jovičić, V. and M. R. Coop (1998). The measurement of stiffness anisotropy in clays with bender elements in the triaxial apparatus. *Geotechnical Testing Journal* **21**(1), 3–10.

Jovičić, V., M. R. Coop and M. Simić (1996). Objective criteria for determining g(max) from bender element tests. *Geotechnique* **2**(46), 357–362.

Kalinski, M. E. and M. S. R. Thummaluru (2005). A new free-free resonant column device for measurement of gmax and dmin at higher confining stresses.. *Geotechnical Testing Journal.*

Karnovsky, I. A. and O. I. Lebed (2001). *Formulas for Structural Dynamics.* McGraw-Hill. New York.

Kawaguchi, T., T. Mitachi and S. Shibuya (2001). Evaluation of shear wave travel time in laboratory bender element test. *15th international conference on soil mechanics and geotechnical engineering* **1**, 155–158.

Kelvin, Lord W. T. (1887). Stability of fluid motion: rectilinear motion of viscous fluid between two parallel planes. *Philosofical magazine* **24**(5), 188–196.

Kim, D. S. and G. C. Kweon (2000). Calibration of testing equipment for reliable small-strain deformation measurments using synthetic speciments. *Geotechnical Testing Journal* **23**(4), 454–463.

Kim, D. S. and K. H. Stokoe (1994). Torsional motion monitoring system for small strain (10-5 to 10-3) soil testing. *Geotechnical Testing Journal* **17**(1), 17–26.

Kumar, P. and E. Foufoula-Georgiou (1997). Wavelet analysis for geophysical applications. *Reviews of geophysics* **35**(4), 385–412.

Kuwano, R, T. M. Connolly and R. J. Jardine (2000). Anisotropic stiffness measurements in a stress-path triaxial cell. *Geotechnical Testing Journal* **23**(2), 141–157.

Kuwano, R., T. M. Connolly and R. Kuwano (1999). Shear stiffness anisotropy measured by multi-directional bender element transducers. *Pre-failure Deformation Characteristics of Geomaterials* pp. 205–212.

Lawrence, F. V. (1963). Propagation of ultrasonic waves through sand. Report.

Lee, J. S. and J. C. Santamarina (2005). Bender elements: Performance and signal interpretation. *Journal of Geotechnical and Geoenvironmental Engineering* **131**(9), 1063–1070.

Leong, E. C., S. H. Yeo and H. Rahardjo (2005). Measuring shear wave velocity using bender elements. *Geotechnical Testing Journal* **28**(5), 488–498.

Lings, M. L. and P. D. Greening (2001). A novel bender/extender element for soil testing. *Géotechnique* **51**(8), 713–717.

Lo Presti, D. C. F., O. Pallara, M. Jamiolkowski and A. Cavallaro (1999). Anisotropy of small strain stiffness of undisterbed and reconstituted clays. *Pre-failure Deformation Characteristics of Geomaterials* pp. 3–9.

Love, A. E. H. (1944). *A treatise on the mathematical theory of elasticity.* 4th ed.. Dover Publications. New York.

M., E. and H. Yi. Ko (1994). A study of an anisotropically overconsolidated silt by the resonant column method. *Geotechnical Testing Journal* **17**(3), 315–324.

Mah, M and D. R. Schmitt (2001). Experimental determination of the elastic coefficients of an orthorhombic material. *Geophysics* **66**(4), 1217–1225.

Mancuso, C, A. L. Simonelli and F Vinale (1989). Numerical analysis of in situ s-wave measurements. *Ist. Geotecnica* pp. 277–280.

Marques, M. E. S., S. Leroueil and M. S. S. Almeida (2004). Viscous behaviour of st-roch-de-l'achigan clay, quebec. *Canadian Geotechnical Journal* **41**, 25–38.

Maxwell, J. C. and W. D. Niven (1890). *The scientific papers of James Clerk Maxwell.* Vol. 2.

McSkimin, H. J. (1956). The propagation of longitudinal waves and shear waves incylindrical rods at high frequencies. *Journal of the Acoustical Society of America* **28**, 484–494.

Meng, J. and G. J. Rix (2003). Reduction of equipment-generated damping in resonant column measurements. *Géotechnique* **53**(5), 503–512.

Mitchell, J. K. (1964). Shearing resistance of soils as a rate process. *Journal of the Soil Mechanics and Foundations Division, ASCE* **95**(5), 1219–1246.

Muscolino, G., A. Palmari and F. Ricciardelli (2005). Time-domain response of linear hysteretic systems to deterministic and random excitations. *Earthquake engineering and structural dynamics* **34**(9), 1129–1147.

Nagaraj, T. S. and M. Norihiko (2001). *Soft Clay Behaviour, Analysis and Asscss-ment.* 1 ed.. A.A.Balkema. Rotterdam.

Nash, D. F. T., M. L. Lings and D. S. Pennington (1999). The dependence of anisotropic go shear moduli on void ratio ans stress state for reconstituted gault clay. Generic.

Nazarian, S. and K. H. Stokoe (1984). In situ shear wave velocities from spectral analysis of surface waves. *8th World Conference on Earthquake Engineering* pp. 31–38.

Pennington, D. S. (1999). The Anisotropic Small Strain Stiffness of Cambridge Gault Clay. Thesis/dissertation.

Pennington, D. S., D. F. T. Nash and M. L. Lings (2001). Horizontally mounted bender elements for measuring anisotropic shear moduli in triaxial clay specimens. *Geotechnical Testing Journal* 24(2), 133–144.

Pico, Technology L. (2005). Pico adc-216 oscilloscope specifications. Electronic Citation.

Piezo, Systems I. (2005). Piezoceramic materials and properties. Catalog.

Podesta, M. D. (2002). *Understanding the properties of matter.* 2nd ed.. Taylor and Francis. London.

Potts, D. M. (2005). Icfep, imperial college finite element program. Computer Program.

Rayleigh, J. W. S. and Robert B. Lindsay (1945). *The theory of sound.* Vol. 1 of *Dover Classics of Science and Mathematics.* Dover Publications. New York.

Redwood, M. (1960). *Mechanical waveguides.* Pergamon Press.

Richart, F. E., J. R. Hall and R. D. Woods (1970). *Vibration of soils and foundations.* Prentice Hall. Englewood Cliff, New Jersey.

Rio, J. F., P. D. Greening and L. Medina (2003). Influence of sample geometry on shear wave propagation using bender elements. *Procedings of the Third International SYmposium on Deformation Characteristics of Geomaterials, IS Lyon 2003* pp. 963–967.

Rix, G. J. and J. Meng (2005). A non-resonance method for measuring dynamic soil properties. *Geotechnical Testing Journal.*

Sanchez-Salinero, I. (1987). Analytical investigation of seismic methods used for engineering applications. Thesis/dissertation. University of Texas. Austin.

Santamarina, J. C. (2001). *Soisl and waves.* John Wiley and Sons. Chichester.

Saunders, J. H. and K. C. Frisch (1962). *Polyurethanes, Chemistry and Technology.* Vol. 1. 1st ed.. John Wiley and Sons. New York.

Schultheiss, P. J. (1981). Simultaneous measurement of p and s wave velocities during conventional laboratory soil testing procedures. *Marine Geotechnology* 4(4), 343–367.

Schultheiss, P. J. (1982). The influence of packing structures on seismic wave velocity in sediments. *Marine Geological Report.*

Seco, F., J. M. Martín, A. Jiménez, J. L. Pons, L. Calderón and R. Ceres (2002). Pcdisp, a tool for the simulation of wave propagation in cylindrical waveguides. 9th international congress of sound and vibration.

Shibuya, S., S. C. Hwang and T. Mitachi (1997). Elastic shear modulus of soft clays from ashear wave velocity measurement. *Géotechnique* 47(3), 593–601.

Shirley, D. J. (1978). An improved shear wave transducer. Generic.

Shirley, D. J. and L. D. Hampton (1978). Shear-wave measurements in laboratory sediments. Generic.

Smith, G. N. (1990). *Elements of Soil Mechanics.* Vol. 9. 6 ed.. Blackwell Science.

Sørensen, K. K., B.e A. Baudet and F. Tatsuoka (2006). Coupling of ageing and viscous effects in artificially structured clays. *Geotechnical Symposium in Roma, 2006.*

Stokes, G. G. (1845). on the theories of the internal friction of fluids in motion, and of the equilibrium and motion of elastic solids. *Cambrige Philosophical Society Transcripts.*

Stokoe, K. H., D.-S. Kim and R. Andrus (1990). Development of synthetic specimens for calibration and evaluation of mr equipments. *Transportation Research Record* (1278), 63–71.

Stokoe, K. H., S. K. Hwang, J. M. Roesset and C. W. Sun (1994). Laboratory measurement of small-strain material damping of soil using free-free resonant column. In: *Earthquake Resistant Construction and Design: Proceedings of the Second International Conference on Earthquake Resistant Construction and Design.* pp. 195–202.

Tabor, D. (1991). *Gases, liquids and solids and other states of matter.* third ed.. Cambridge University Press. Cambridge.

Terzaghi, K. and R. B. Peck (1967). *Soil Mechanics in Engineering Practice.* 2 ed.. John Wiley and Sons. New York.

The British Association of Synthetic Rubber Manufacturers (1970). *Not From Trees Alone, The Story of Synthetic Rubber.* The British Association of Synthetic Rubber Manufacturers. London.

Thomann, T. G. and R. D. Hryciw (1990). Laboratory measurement of small strain shear modulus under ko conditions. *Geotechnical Testing Journal* **13**(2), 97–105.

Thurlby, T. I. L. (1994). *TTi TG1010 User Manual.* Thurlby Thandar Instruments Ltd. Huntingdon.

Treloar, L. R. G. (1958). *The physics of rubber elasticity.* 2 ed.. Oxford University Press. Oxford.

Viggiani, G. and J. H. Atkinson (1995). Interpretation of bender element tests. *Géotechnique* **45**(1), 149–154.

Viggiani, G. and J. H. Atkinson (1997). Interpretation of bender element tests, discussion. *Géotechnique* **47**(4), 873–877.

Voigt, W. (1887). Theoretische studien über die elasticitätsverhältnisse der krystalle. *Göttingen Abhandlungen.*

Vosschemie (2002). Epoxy glosscoat. Catalog.

Wang, Y. H., G. Cascante and J. C. Santamarina (2003). Resonant column testing: The inherent counter emf effect. *Geotechnical Testing Journal.*

Warner, M. and E. M. Terentjev (2003). *Liquid Crystal Elastomers.* 1st ed.. Clarendon Press. Oxford.

Wegel, R. L. and H. Walther (1935). Internal dissipation in solids for small cyclic strains. *Physics* **6**(4), 141–157.

White, J. E. (1965). *Seismic Waves.* McGraw-Hill. New York.

Zeng, X. W. and B. X. Ni (1998). Application of bender elements in measuring g(max) of sand under k-0 condition. *Geotechnical Testing Journal* **21**(3), 251–263.

Zienkiewicz, O. C., R. L. Taylor and J. Z. Zhu (2000). *The finite element method, ITS Basis and Fundamentals.* Butterworth-Heinemann. Oxford.